

nature

HIGH AND RISING

Satellite images reveal an increasing number of people and places exposed to floods

Species swaps

How rapidly changing ecosystems could spell trouble for biodiversity

Making waves

Probe quantum mechanics with experiments in space

Early animals

Potential sponge fossil could rewrite timeline for life on Earth

Nature.2021.08.07

[Sat, 07 Aug 2021]

- [This Week](#)
- [News in Focus](#)
- [Books & Arts](#)
- [Opinion](#)
- [Work](#)
- [Research](#)

| [Next section](#) | [Main menu](#) |

Donation

| [Next section](#) | [Main menu](#) |

This Week

- **[It's time to expand the definition of 'women's health'](#)** [04 August 2021]
Editorial • Research in this area deserves more attention — and not only for conditions related to reproduction.
- **[Cash payments in Africa could boost vaccine uptake](#)** [03 August 2021]
World View • When doses finally arrive, use cash incentives to overcome hesitancy.
- **[Your blood teems with a unique set of stealthy 'anelloviruses'](#)** [29 July 2021]
Research Highlight • A single individual harbours tens to hundreds of variants of this DNA-based virus, which can move from one person to another in donated blood.
- **[A grim future awaits many children with type 2 diabetes](#)** [28 July 2021]
Research Highlight • Long-term follow up finds that more than half of children and adolescents with the disease develop complications within 15 years of diagnosis.
- **[A caffeine buzz gives bees flower power](#)** [28 July 2021]
Research Highlight • Bumblebees dosed with caffeine can more easily remember the scent of sugar-heavy blossoms.
- **[The unnoticed eye motions that help us see the world](#)** [27 July 2021]
Research Highlight • Eye movements lasting only a few hundredths of a second create an information-laden 'smear' on the retina.
- **[Toxic mercury rides rivers into the sea](#)** [23 July 2021]
Research Highlight • Research suggests that rivers are a bigger source of mercury in coastal waters than is the atmosphere — a finding that contradicts some global models.
- **[Mini 'metavehicles' zip and swerve on light power](#)** [28 July 2021]
Research Highlight • Light can be used to both propel and steer tiny vehicles made with materials that have distinctive optical properties.
- **[Far-off planet has a nursery for baby moons](#)** [27 July 2021]
Research Highlight • Researchers spy a dusty, moon-forming disk surrounding a planet beyond the Solar System.

| [Next section](#) | [Main menu](#) | [Previous section](#) |

- EDITORIAL
- 04 August 2021

It's time to expand the definition of 'women's health'

Research in this area deserves more attention — and not only for conditions related to reproduction.





•

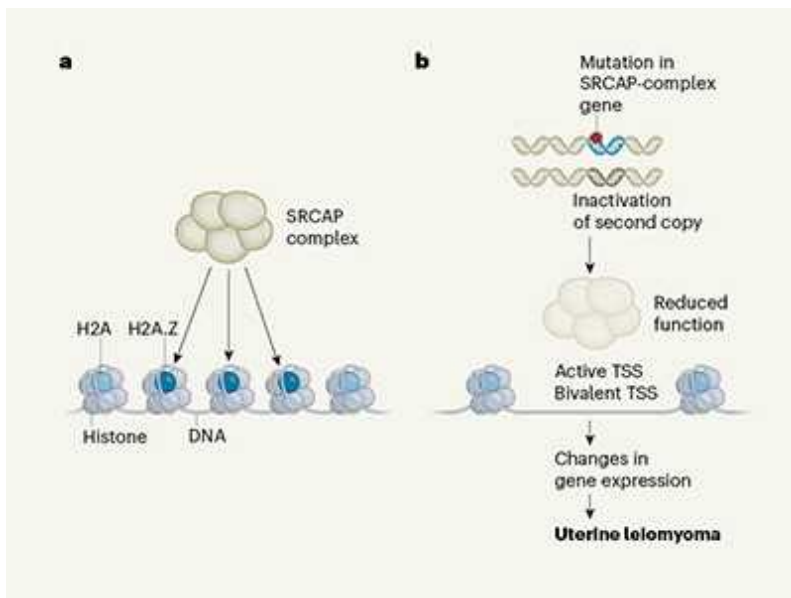
[Download PDF](#)



Common conditions such as cardiovascular diseases are understudied in women, making diagnosis, prognosis and treatment in women less straightforward.Credit: BSIP/UIG/Getty

More than one-eighth of the world's population has a condition that can cause pain, heavy bleeding and reduced fertility, all potential consequences of benign tumours called uterine leiomyomas, or fibroids. Fibroids can be debilitating, and are a common reason for surgical removal of the uterus.

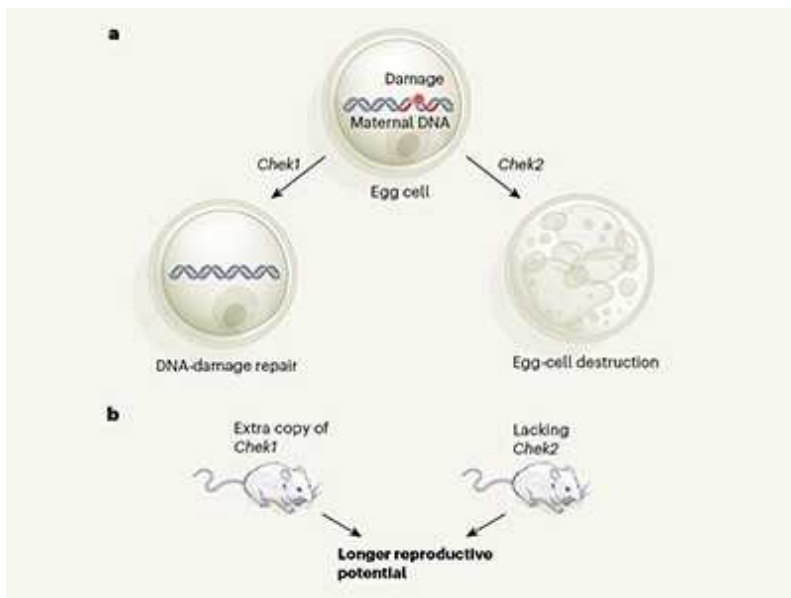
Yet fibroids have received relatively little attention from scientists, either in academia or at pharmaceutical companies. The root cause of the condition — and how to reduce its impact on fertility — has been a matter of debate for decades, leaving physicians unsure how best to treat people.



Deranged chromatin drives uterine fibroid tumours

Unfortunately, fibroids are just one of many understudied aspects of health in people assigned female at birth. (This includes cisgender women, transgender men and some non-binary and intersex people; the term ‘women’ in the rest of this editorial refers to cis women.) Clinical and pre-clinical studies alike tend to focus on men: only one-third of people participating in clinical trials relating to cardiovascular disease are women, and an analysis of neuroscience studies published in six journals in 2014 found that 40% of them used only male animals. Two studies and a feature published in *Nature* on 5 August spotlight the achievements of research into women’s health — and the need for much more.

One study looks at the [molecular origins of fibroids](#) and uncovers a potential mechanism of tumour formation. Drugs that target key molecular players in this process could, with further study, provide new treatment options.



Genomic analysis identifies variants that can predict the timing of menopause

The other study takes a multidisciplinary approach in looking at both the [genetic mechanisms and epidemiological factors involved in ovarian ageing](#), which leads to menopause and loss of fertility. The age at which women experience menopause varies widely — with a range in healthy women of about 20 years — and fertility can decline drastically as much as a decade before its onset.

This work has expanded the list of genes that contribute to early ovarian ageing, and pinpoints the importance of DNA-repair mechanisms in establishing the age at which women experience menopause.

Both studies illustrate the progress that can be made when women's health challenges are brought to the fore. But women's health advocates caution that the field is often still viewed too narrowly. The study of health and disease in women should not be limited to conditions that affect only women. Conditions such as type 2 diabetes, Alzheimer's disease and heart disease affect men and women differently. Such diseases must be studied in both men and women, with the recognition that diagnosis, prognosis and treatment might need to be different between the sexes.

Heart attacks, for example, are a leading killer of both women and men, but women don't always experience the 'typical' symptoms usually seen in men. Women are also more prone to blood clots after a heart attack, yet less likely to be prescribed anti-clotting medication by their doctors. Women are 50% more likely than men to receive an initial misdiagnosis after a heart attack, and are less likely to be prescribed medicines to reduce the risk of a second attack, according to the British Heart Foundation.



Why sports concussions are worse for women

When it comes to sport, women face a risk of serious long-term injury if we continue to model training and head-injury management on data from men. As our News Feature reports, it's becoming increasingly clear that [women experience and recover from head injuries very differently from men](#).

Research from across many disciplines will be needed if we are to understand why women are almost twice as likely as men to suffer a concussion in sports such as soccer and rugby — and to understand why women take longer to recover from such injuries.

So far, the evidence is sparse, but preliminary data point to structural differences in the brain. Axons in women's brains are wired up with thinner microtubules, which rupture more easily; hormonal fluctuations are also thought to contribute. Biomechanics, too, could be playing a part — in rugby, for instance, it seems that women fall differently when tackled, which

could raise the risk of concussion. Training regimes designed specifically for women might help to mitigate these injuries.

But the clear message from those researching the sport is that it is no longer acceptable to use data solely from men in these studies. And when women are included, the data need to be disaggregated by sex and involve a sufficient number of women. A recent study looking at MRI images from elite rugby players did include women ([K. A. Zimmerman *Brain Commun.* 3, fcab133; 2021](#)), but of the 44 elite players only 3 were women.

But the relative dearth of women on grant review panels and scientific advisory boards has meant that few of these decision makers have direct personal experience of women's health needs or research gaps. This makes it all the more important that funding bodies consult the public when they come to set research priorities.

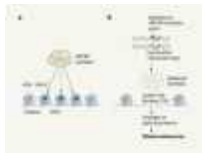
Since 2016, the US National Institutes of Health has required researchers to carry out pre-clinical studies in both male and female animals, tissues and cells, or to provide an explanation for why it is not appropriate to study both sexes. Now it is up to other funders, researchers and journals to amplify the impact of this change by taking care to report sex-specific data in publications. Funders should also bolster the resources given to support studies of health and disease in women, and track how much money goes to supporting such research across all domains, not merely gynaecological conditions. That which gets measured gets done.

Nature **596**, 7 (2021)

doi: <https://doi.org/10.1038/d41586-021-02085-6>

Related Articles

-  [Why sports concussions are worse for women](#)



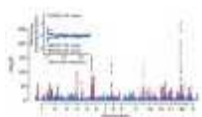
- Deranged chromatin drives uterine fibroid tumours



- Genomic analysis identifies variants that can predict the timing of menopause



- Read the paper: Deficient H2A.Z deposition is associated with genesis of uterine leiomyoma



- Read the paper: Genetic insights into biological mechanisms governing human ovarian ageing



- Why autoimmunity is most common in women



- Why the sexes don't feel pain the same way



- Inequality in medicine



- [A heartfelt plea](#)
- [Medical research often ignores differing health outcomes for men and women](#)

Subjects

- [Medical research](#)
- [Health care](#)
- [Diseases](#)
- [Genetics](#)

nature careers

[Jobs](#) >

- [Translational Biologist, Oncology](#)

Astex Pharmaceuticals Limited

Cambridge, United Kingdom

- [Postdoctoral Researcher – studying the histopathology of acute ischaemic stroke blood clots and the correlation of composition with impedance measurements\(CÚRAM\), NUIG RES 158-21](#)

National University of Ireland Galway (NUI Galway)

Galway, Ireland

- [Summer Laboratory Technician](#)

Oklahoma Medical Research Foundation (OMRF)

Oklahoma City, United States

- [PhD student \(m/f/d\) Hormonal programming of hepatic chromatin landscapes](#)

Technical University of Munich (TUM)

Munich, Germany

Nature Briefing

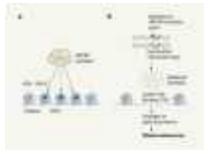
An essential round-up of science news, opinion and analysis, delivered to your inbox every weekday.

[Download PDF](#)

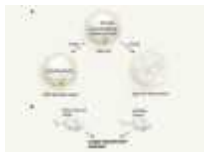
Related Articles



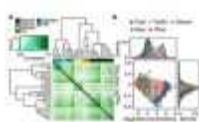
- [Why sports concussions are worse for women](#)



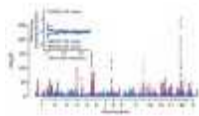
- [Deranged chromatin drives uterine fibroid tumours](#)



- [Genomic analysis identifies variants that can predict the timing of menopause](#)



- [Read the paper: Deficient H2A.Z deposition is associated with genesis of uterine leiomyoma](#)



- [Read the paper: Genetic insights into biological mechanisms governing human ovarian ageing](#)



- [Why autoimmunity is most common in women](#)



- [Why the sexes don't feel pain the same way](#)



- [Inequality in medicine](#)



- [A heartfelt plea](#)

- [Medical research often ignores differing health outcomes for men and women](#)

Subjects

- [Medical research](#)

- [Health care](#)
 - [Diseases](#)
 - [Genetics](#)
-

This article was downloaded by **calibre** from <https://www.nature.com/articles/d41586-021-02085-6>

| [Section menu](#) | [Main menu](#) |

- WORLD VIEW
- 03 August 2021

Cash payments in Africa could boost vaccine uptake



When doses finally arrive, use cash incentives to overcome hesitancy.

- [Rabah Arezki](#) 0

1. [Rabah Arezki](#)

1. Rabah Arezki is the chief economist of the African Development Bank and a senior fellow at Harvard's Kennedy School of Government. Twitter: [@rabah_arezki](#)

[View author publications](#)

You can also search for this author in [PubMed](#) [Google Scholar](#)





•

[Download PDF](#)

Any global-health researcher can tell you that solving one problem at a time is not enough. As the COVID-19 pandemic surges in Africa, securing access to vaccines is the dominant focus. But more must be done to ensure citizens will get them. The best option, in my view, is cash incentives.

There is a debate across the globe on how best to incentivize immunization. Regions of the United States have offered entry into prize lotteries, and even US\$100 savings bonds. Uptake is particularly important in Africa.

Only about 1.4% of Africa's 1.3 billion people have been fully vaccinated. Since the start of the year, cases have more than doubled, with Botswana, Namibia, South Africa and Tunisia reporting their highest jumps in cases since the pandemic began. Right now, the problem is vaccine availability. Rich countries have more vaccine than they need, and African countries have been left with only 2% of the total supply.

Outrage at this disparity (plus the potential for more-dangerous viral variants to evolve where infection rates are high) has prompted promises of one billion doses to poorer countries alongside other initiatives and the ramping up of vaccine production.



[World Bank grants for global vaccination — why so slow?](#)

Attention must now be paid to getting shots into arms. Already, vaccine hesitancy has cost Africa. Several African countries, including the Democratic Republic of the Congo, Malawi and South Sudan, have had to destroy or return vaccines because doses could not be used before their expiry date.

As chief economist at the African Development Bank in Abidjan, Côte d'Ivoire, and, before that, for the World Bank's Middle East and North Africa Region, I have evaluated many programmes and studies on cash transfers. I know the idea is controversial. Some critics argue that all efforts

should be focused on securing vaccines. Others counter that the capacity to implement a cash-transfer programme on this scale does not exist. Still others say that offering cash incentives to people for behaviours that benefit them is ethically problematic, coercive or erosive of trust.

When I first heard of cash transfers, in a 2008 employment programme in Liberia, I was sceptical. But I have seen them used carefully and effectively. For instance, a programme targeting women of childbearing age in Nigeria significantly increased tetanus immunization. These programmes encourage vaccine uptake even as logistical challenges such as maintaining the vaccines in cold storage and distributing them are managed.

That means that a cash-transfer programme would complement other ‘supply side’ efforts, including logistics, communication and community engagement. (Of course, cash transfers must be combined with other mechanisms, such as mobile clinics, to ensure that people who want vaccines can get them.)

In another example of their effectiveness, cash transfers to families in Indonesia for bringing children in for routine health care and enrolling them in school showed significant results, reducing stunted growth in children by up to 23%.

These programmes are so well established that they are being used to benchmark other interventions. Both development banks and non-governmental organizations (NGOs) have developed best practices for designing and implementing these programmes at scale, including targeting them to vulnerable communities.



COVID-19 vaccines: how to ensure Africa has access

I envisage a programme that would offer each individual eligible for vaccination in West African countries a payment for receiving the shot, say, 6,000 West African CFA francs (US\$11). That amount is 10% of the monthly guaranteed minimum wage in Côte d'Ivoire.

In 2019, Africa received about \$58 billion in foreign aid. I estimate that an effective cash payment would add some \$9 billion to an estimated \$15 billion for providing and administering COVID-19 vaccines across Africa. The bulk of the money would come after the second dose — or full payment be made at once in the case of one-shot vaccines. Funding would come from the world's richest countries, foundations and corporations, particularly those with business interests in the continent. This programme would reduce vaccine inequity, save lives and bolster hard-hit economies where the pandemic has plunged many into poverty.

The infrastructure to carry out such a payment programme is already in place: about half of Africans have mobile phones, and programmes designed around these have improved childhood vaccination rates in Bangladesh. By transferring money directly through mobile phones, authorities can better ensure that funds go to the intended recipient. For those without a phone, beneficiaries would receive a voucher with a unique identifier that could be redeemed for cash. Again, there is precedent. During

the Ebola crisis, a vast cash-transfer programme used many delivery methods, including direct payments to people in the most remote areas without mobile phones.

The vaccine-incentive fund could be administered by development banks working with public-health bodies, NGOs and telecom operators.

Blockchain technology could record doses and payments, to ensure traceability and limit corruption. The technology to record doses has been put in place by airline corporations and British hospitals.

This would be a huge benefit for Africa, and would be in donors' self-interest. Arresting the virus's spread in Africa would both revive a major global market and reduce the chances of the virus mutating into more-dangerous forms.

Nature **596**, 9 (2021)

doi: <https://doi.org/10.1038/d41586-021-02086-5>

Competing Interests

The author declares no competing interests.

Related Articles

-  [COVID-19 vaccines: how to ensure Africa has access](#)
-  [World Bank grants for global vaccination — why so slow?](#)

Subjects

- [SARS-CoV-2](#)
- [Vaccines](#)
- [Developing world](#)
- [Health care](#)
- [Economics](#)

nature careers

[Jobs](#) >

- [Translational Biologist, Oncology](#)

Astex Pharmaceuticals Limited

Cambridge, United Kingdom

- [Postdoctoral Researcher – studying the histopathology of acute ischaemic stroke blood clots and the correlation of composition with impedance measurements\(CÚRAM\), NUIG RES 158-21](#)

National University of Ireland Galway (NUI Galway)

Galway, Ireland

- [Summer Laboratory Technician](#)

Oklahoma Medical Research Foundation (OMRF)

Oklahoma City, United States

- [PhD student \(m/f/d\) Hormonal programming of hepatic chromatin landscapes](#)

Technical University of Munich (TUM)

Munich, Germany

Nature Briefing

An essential round-up of science news, opinion and analysis, delivered to your inbox every weekday.

[Download PDF](#)

Related Articles



- [**COVID-19 vaccines: how to ensure Africa has access**](#)



- [**World Bank grants for global vaccination — why so slow?**](#)

Subjects

- [SARS-CoV-2](#)
- [Vaccines](#)
- [Developing world](#)
- [Health care](#)
- [Economics](#)

This article was downloaded by **calibre** from <https://www.nature.com/articles/d41586-021-02086-5>



Blood transfusions can spread the infectious agents called anelloviruses, which are thought to be harmless, from blood donor to recipient. Credit: Mauro Fermariello/Science Photo Library

Virology

29 July 2021

Your blood teems with a unique set of stealthy ‘anelloviruses’

A single individual harbours tens to hundreds of variants of this DNA-based virus, which can move from one person to another in donated blood.





•

A deep analysis of a family of viruses found in human blood has revealed the vast variety of these typically harmless ‘anelloviruses’, and shows that every person hosts their own unique community of resident viruses.

Nathan Yozwiak at Ring Therapeutics, a biotechnology company in Cambridge, Massachusetts, and his colleagues sequenced anelloviruses obtained from blood donors and from people who received transfusions of the donated blood.

The authors analysed viral DNA and showed that anelloviruses have diversified into many more lineages than have eight other viruses and virus families that infect people. The analysis suggests that a person’s resident

anelloviruses frequently swap DNA, leading to a diverse and individual ‘anellome’.

The team also compared the genetic signatures of anelloviruses in people who received a blood transfusion with those in the blood donors. This showed that some lineages from a donor persisted in the recipient.

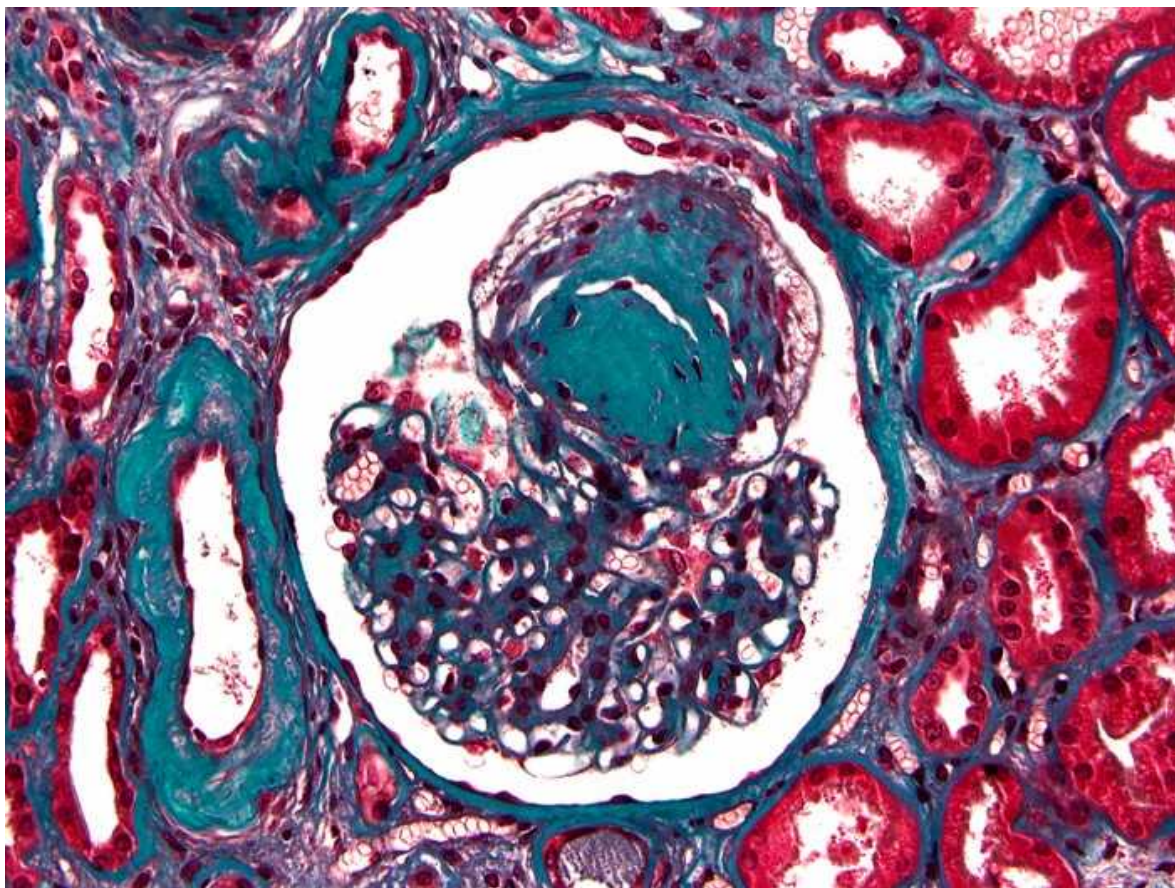
The authors suggest that anelloviruses could be useful as biomarkers of immune health after organ transplants, or as viral vectors to deliver treatments.

[Cell Host Microbe \(2021\)](#)

- [Virology](#)

This article was downloaded by **calibre** from <https://www.nature.com/articles/d41586-021-02075-8>

| [Section menu](#) | [Main menu](#) |



A damage-related nodule (turquoise) in the kidney of a person with diabetes. People with childhood type 2 diabetes are at risk of kidney problems in their twenties. Credit: PR J. L. Kemeny — ISM/Science Photo Library

Medical research

28 July 2021

A grim future awaits many children with type 2 diabetes

Long-term follow up finds that more than half of children and adolescents with the disease develop complications within 15 years of diagnosis.





•

Children with type 2 diabetes are at high risk of developing grave complications — ranging from hypertension to heart failure — by the time they are in their twenties or early thirties, according to a 15-year study of hundreds of young people with the condition.

Type 2 diabetes is characterized by an inability to regulate blood sugar levels. In the United States, the number of children with type 2 diabetes rose by almost 5% per year from 2002 to 2012.

To examine this trend's long-term effects, Kimberly Drews at the George Washington University in Rockville, Maryland, and her colleagues began

monitoring 500 children aged 11 to 17 who had been diagnosed with type 2 diabetes an average of eight months earlier.

The researchers found that by the end of the 15-year study period, 60% of participants — who were an average of 26 years old by that time — had developed at least one diabetes-related complication, such as kidney disease. Almost one-third had nerve disease, four had had a stroke and six had died.

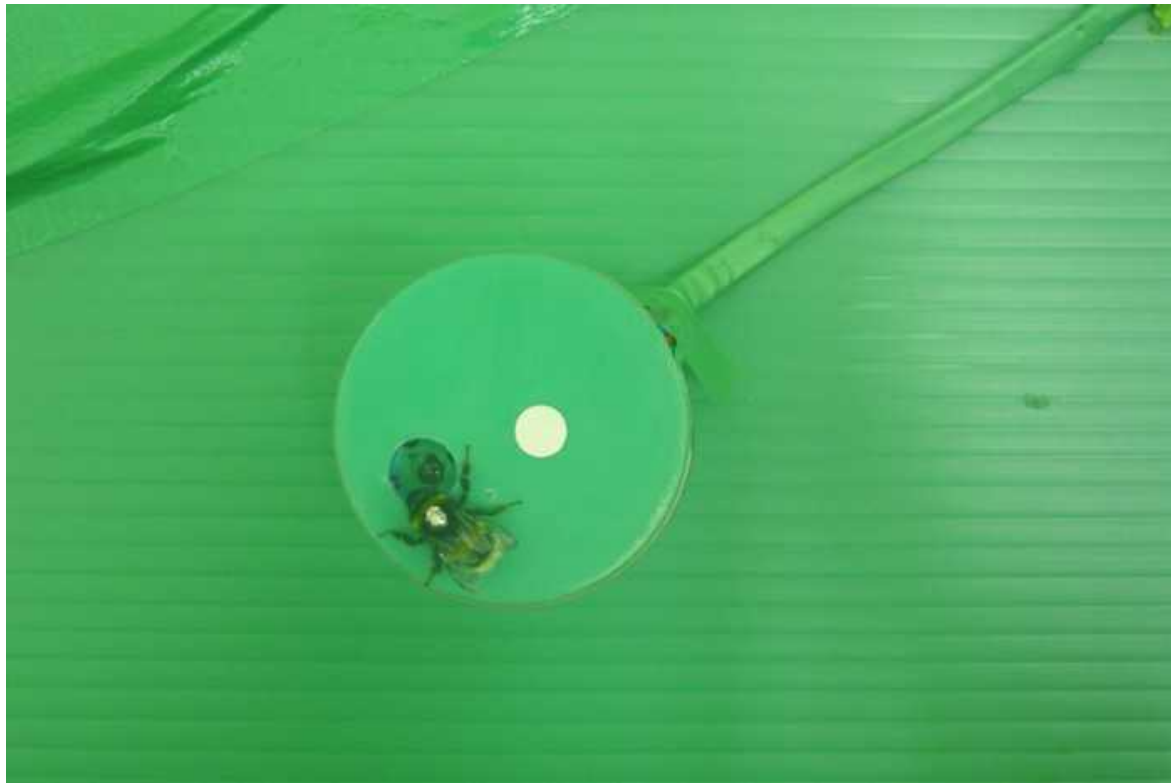
The authors say their findings have major implications for public health.

N. Engl. J. Med. (2021)

- [Medical research](#)

This article was downloaded by **calibre** from <https://www.nature.com/articles/d41586-021-02074-9>

| [Section menu](#) | [Main menu](#) |



A bumblebee visiting a robotic flower receives a drop of sugar water as a reward. Credit: Jan-Hendrik Dudenhöffer

Animal behaviour

28 July 2021

A caffeine buzz gives bees flower power

Bumblebees dosed with caffeine can more easily remember the scent of sugar-heavy blossoms.





•

A jolt of caffeine can help bumblebees to learn to find flowers with a specific scent.

Previous research suggests that bees tend to make repeated visits to a source of caffeine-laden nectar. But is that because the caffeine boosted the insects' ability to remember a food-rich site? Or were the bees simply craving a buzz?

To find out, Sarah Arnold at the University of Greenwich, UK, and her colleagues taught bumblebees (*Bombus terrestris*) to associate the smell of strawberry flowers with the taste of nectar. The researchers also slipped caffeine to the bees during this training. The team released the trained,

caffeinated bees into an arena dotted with robotic flowers containing nectar without caffeine. Half of those flowers emitted the strawberry floral smell; the rest wafted a standard floral scent.

The bees were more likely to make their first visit to the strawberry-scented flowers than to the other flowers — despite the lack of a caffeine reward. This suggests that the slug of caffeine had boosted the bees' ability to remember the 'right' scent and to find flowers with that fragrance.

[Curr. Biol. \(2021\)](#)

- [Animal behaviour](#)

This article was downloaded by **calibre** from <https://www.nature.com/articles/d41586-021-02072-x>

| [Section menu](#) | [Main menu](#) |



As we look at a scene, high-speed eye motions create ‘streaks’ (right) on the retina that we do not perceive but that the eye uses to maintain a coherent view. Credit: Martin Rolfs

Neuroscience

27 July 2021

The unnoticed eye motions that help us see the world

Eye movements lasting only a few hundredths of a second create an information-laden ‘smear’ on the retina.





•

When we look at a scene, our eyes dart from one point to another an estimated three times per second. Although we don't perceive this rapid-fire jitter, experiments reveal that it produces visual information that helps us to make sense of the world around us.

To see in sharp detail, a person's eyes frequently shift to focus on objects in their peripheral vision. These extremely rapid eye movements create 'motion streaks', visual smears on the back of the eye. A motion streak stretches from an object's starting position on the retina to its position after eye movement.

Richard Schweitzer and Martin Rolfs at the Humboldt University of Berlin showed six differently patterned objects to volunteers and asked them to focus on one object. While the volunteers' eyes were moving towards that target, the objects' positions changed. The researchers then overlaid all of the objects with the same pattern to make them indistinguishable.

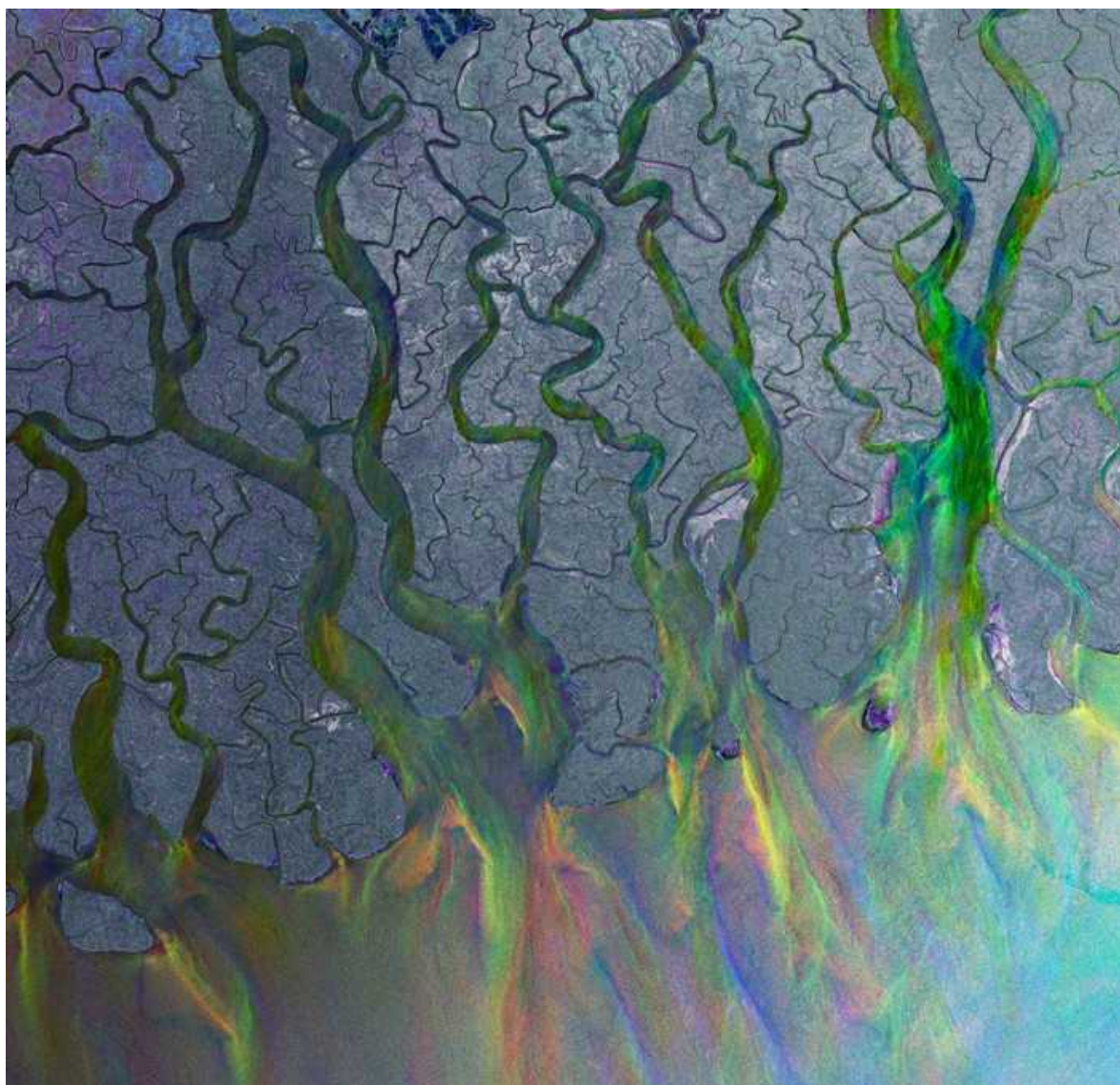
Participants successfully found the target in most cases, but were more likely to do so if its movement had generated a motion streak. This suggests that information gleaned from the streaks helps our jittering eyes to keep track of where objects are.

[Sci. Adv. \(2021\)](#)

- [Neuroscience](#)

This article was downloaded by **calibre** from <https://www.nature.com/articles/d41586-021-02058-9>

| [Section menu](#) | [Main menu](#) |



The Ganges River is one of the biggest contributors of mercury into coastal oceans. Credit: ESA/Shutterstock

Geochemistry

23 July 2021

Toxic mercury rides rivers into the sea

Research suggests that rivers are a bigger source of mercury in coastal waters than is the atmosphere — a finding that contradicts some global models.





•

Rivers pour one million kilograms of the toxic element mercury each year into the oceans, where it can poison fishes and the people who eat them.

Mercury comes from both natural sources, such as volcanoes, and non-natural sources, such as power plants. Once in the atmosphere, it can travel long distances before settling onto land and sea. Some global models assume that all mercury entering the oceans arrives from the atmosphere.

Xuejun Wang at Peking University in Beijing, Peter Raymond at Yale University in New Haven, Connecticut, and their colleagues combined data on mercury in rivers with models of how much water and sediment are carried by rivers to the sea. The scientists estimate that rivers add three times

as much mercury to coastal oceans as atmospheric deposition does. Large rivers, such as the Amazon and the Ganges, are the biggest contributors.

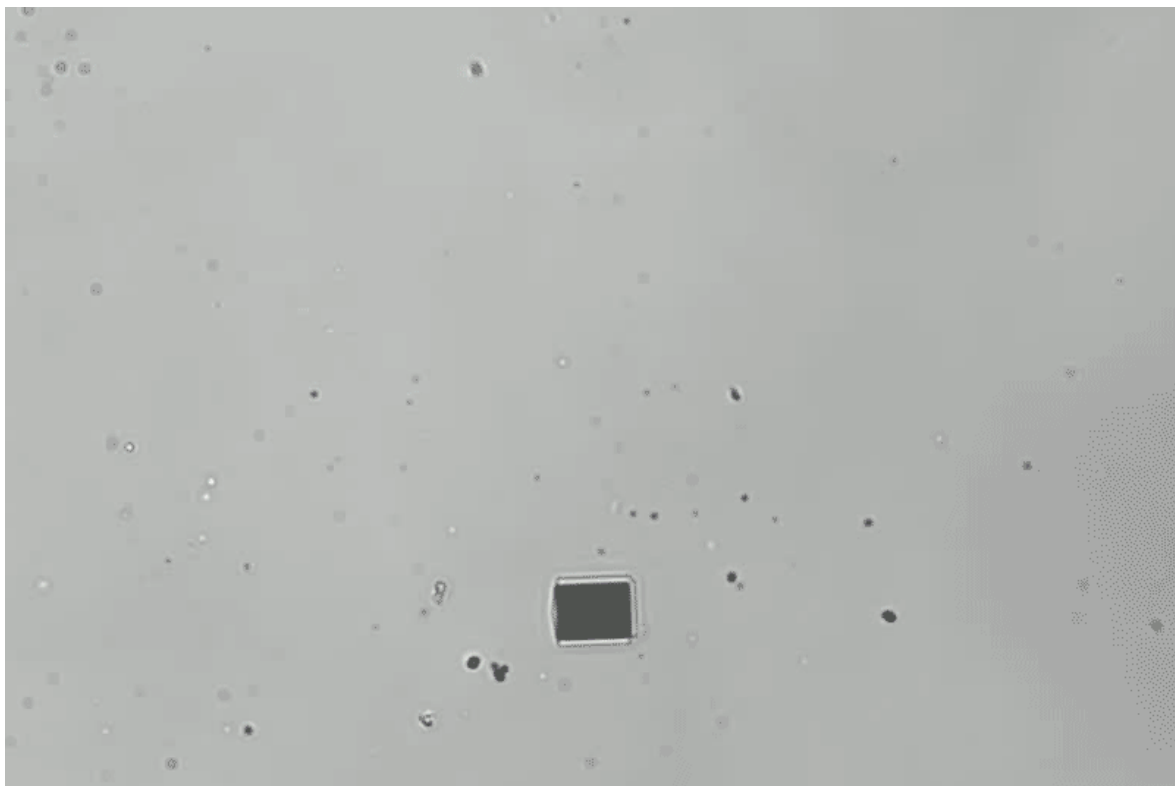
Although the new estimate is lower than one previous estimate, it is higher than others, underscoring that rivers are an important and often underestimated contributor to the planet's mercury budget.

[Nature Geosci. \(2021\)](#)

- [Geochemistry](#)
-

This article was downloaded by **calibre** from <https://www.nature.com/articles/d41586-021-02026-3>

| [Section menu](#) | [Main menu](#) |



A vehicle roughly 10 micrometres long can trace a circular path under the command of polarized light. Credit: D. Andrén *et al.*/Nature Nanotechnol.

Materials science

28 July 2021

Mini ‘metavehicles’ zip and swerve on light power

Light can be used to both propel and steer tiny vehicles made with materials that have distinctive optical properties.





•

Microscopic vehicles can be powered and steered by light, and even used to transport tiny cargoes, such as single-celled organisms.

Optical metasurfaces are ultrathin materials that can change incoming light's direction and polarization — that is, the orientation of the light's electromagnetic waves. Typically, these materials are viewed as being unaffected by the light that they alter. But Daniel Andrén at Chalmers University of Technology in Sweden and his colleagues have shown that this perspective is not always correct.

The authors made minute vehicles consisting of optical metasurfaces embedded in microscopic particles. Laser light propels these ‘metavehicles’

across a surface, and they can be steered by changing the light's polarization.

To maximize this effect, the team used simulations and experiments to refine the metasurfaces' structure. They discovered that vehicles incorporating the optimized materials could move in complex patterns, self-correct their orientation and transport tiny objects, including polystyrene beads and yeast cells.

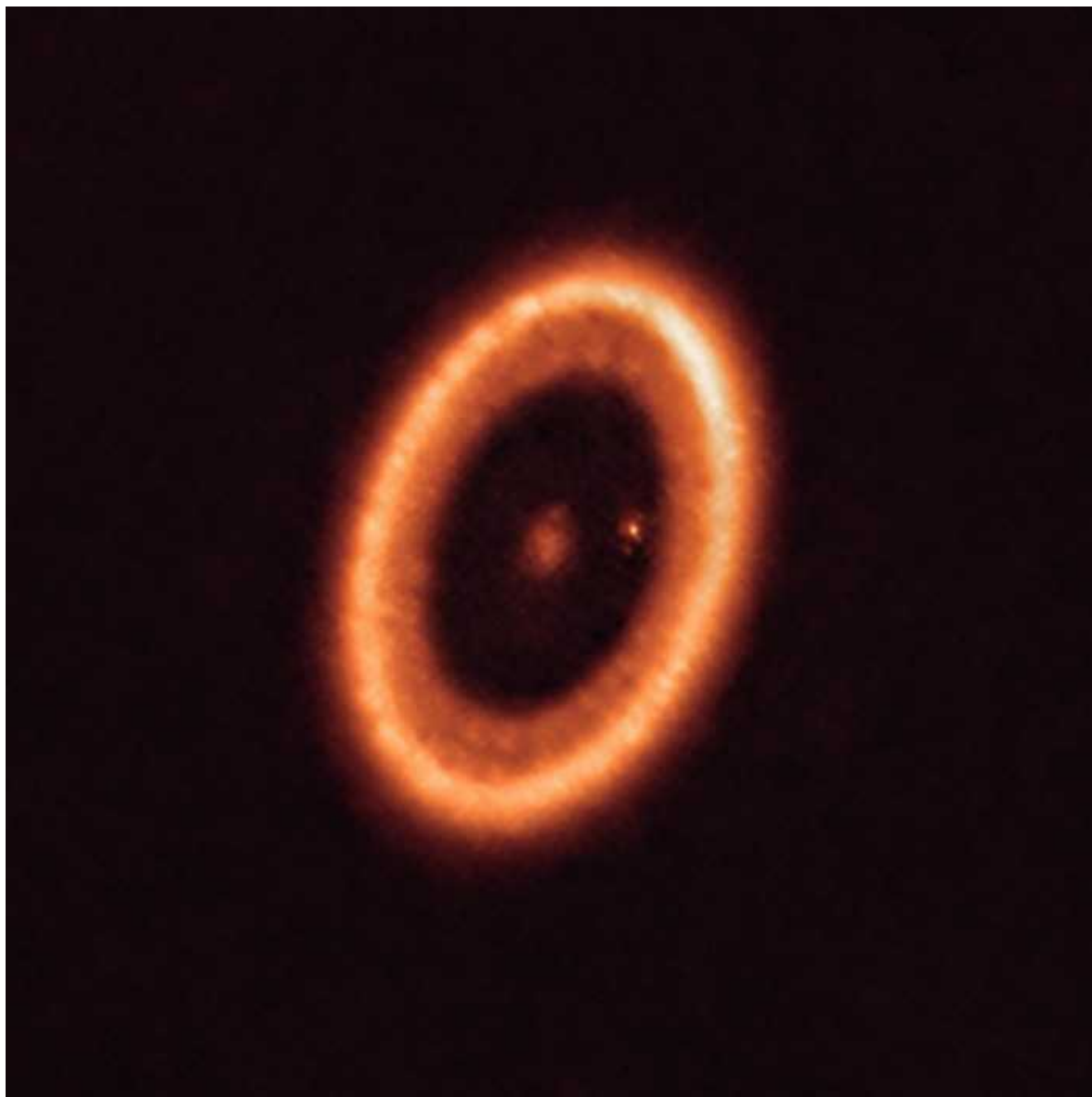
The team says that given the wide range of optical metasurfaces that could be used in these vehicles, they have many potential applications, including in molecular sensing.

[Nature Nanotechnol. \(2021\)](#)

- [Materials science](#)
-

This article was downloaded by **calibre** from <https://www.nature.com/articles/d41586-021-02057-w>

| [Section menu](#) | [Main menu](#) |



The star PDS 70 is orbited by a ring of material and by a planet (bright dot) that is itself encircled by a disk of moon-forming material. Credit: ALMA (ESO/NAOJ/NRAO)/Benisty *et al.*

Planetary science

27 July 2021

Far-off planet has a nursery for baby moons

Researchers spy a dusty, moon-forming disk surrounding a planet beyond the Solar System.





•

Astronomers gazing at a distant planet have noticed that it is surrounded by a ring of gas and dust, where newborn moons might be coalescing.

Myriam Benisty at Grenoble Alps University in France and her colleagues used the Atacama Large Millimeter/submillimeter Array in Chile to peer at a star called PDS 70, which lies 112 parsecs from Earth. Scientists had previously detected two ‘gas giant’ planets — gas-rich worlds as big as Jupiter or larger — orbiting the star.

New images reveal that one of the planets is surrounded by a dusty disk, which extends to a distance roughly the same as that between Earth and the Sun. Moons might be forming in this disk as its gas and dust clumps

together, just as planets form from similar disks around stars. There is enough material in the disk to create up to three moons the size of Earth's Moon.

The images offer the clearest glimpse yet of one of these moon-forming disks, providing clues to how planetary systems form.

[*Astrophys. J. Lett. \(2021\)*](#)

- [Planetary science](#)
-

This article was downloaded by **calibre** from <https://www.nature.com/articles/d41586-021-02052-1>

| [Section menu](#) | [Main menu](#) |

News in Focus

- **[COVID vaccine enthusiasm, astronomy bullies and an enzyme chip](#)** [04 August 2021]
News Round-Up • The latest science news, in brief.
- **[NASA investigates renaming James Webb telescope after anti-LGBT+ claims](#)** [23 July 2021]
News • Some astronomers argue the flagship observatory — successor to the Hubble Space Telescope — will memorialize discrimination. Others are waiting for more evidence.
- **[COVID vaccines slash viral spread – but Delta is an unknown](#)** [27 July 2021]
News • Studies show that vaccines reduce the spread of SARS-CoV-2 by more than 80%, but the Delta variant is creating fresh uncertainty.
- **[Water transformed into shiny, golden metal](#)** [28 July 2021]
News • Electrons from a droplet of sodium and potassium turn water into a metallic material that conducts electricity.
- **[Sponge-like fossil could be Earth's earliest known animal](#)** [28 July 2021]
News • Fossil discovered in northwestern Canada could rewrite the early history of animal life — but some palaeontologists are not convinced it's real.
- **[China's space station is preparing to host 1,000 scientific experiments](#)** [23 July 2021]
News • Researchers around the world are eagerly awaiting the completion of Tiangong, to study topics from dark matter and gravitational waves to the growth of cancer and pathogenic bacteria.
- **[The world's species are playing musical chairs: how will it end?](#)** [04 August 2021]
News Feature • Many communities aren't losing biodiversity, but ecosystems are changing rapidly and the future is far from rosy.
- **[Why sports concussions are worse for women](#)** [03 August 2021]
News Feature • As women's soccer, rugby and other sports gain popularity, scientists are racing to understand how the female brain responds to head injury.

| [Next section](#) | [Main menu](#) | [Previous section](#) |

- NEWS ROUND-UP
- 04 August 2021

COVID vaccine enthusiasm, astronomy bullies and an enzyme chip

The latest science news, in brief.





•

[Download PDF](#)



Vaccines for COVID-19 are administered in Rwanda, where survey results show high acceptance of the jab. Credit: Habimana Thierry/Anadolu Agency/Getty

Less-affluent countries more eager for COVID jab

People in low- and middle-income countries tend to be [much more willing to receive a COVID-19 vaccine](#) than are those in the United States, according to an analysis that included poll results from a dozen countries.

Researchers surveyed people between June 2020 and January 2021, asking whether they would be vaccinated once COVID-19 jabs became available in their countries, and the reasons for their decisions.

The analysis found that 80% of individuals in ten low- and middle-income countries in Asia, Africa and South America were willing to receive a COVID-19 vaccine, compared with 65% in the United States ([J. S. Solís](#)

[Arce et al. *Nature Med.* <https://doi.org/gqh7>; 2021](https://doi.org/gqh7)). Worries about side effects and efficacy were the top reasons people would refuse a COVID-19 vaccine.

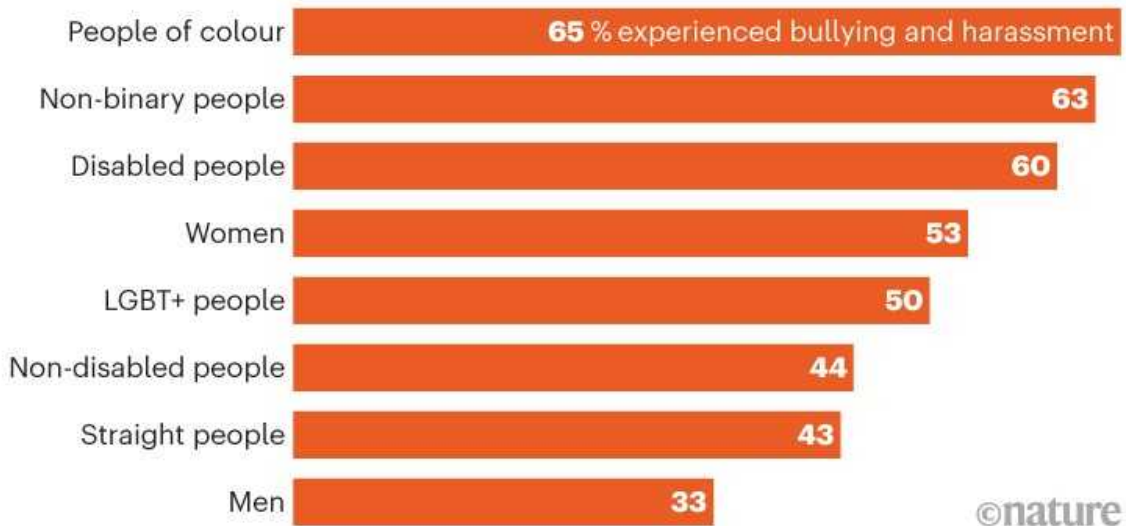
The study authors say the results suggest that ensuring equitable access to COVID-19 vaccines worldwide is not only a moral imperative, but also a powerful way to stem the spread of the virus: lower levels of hesitancy make widespread vaccination easier.

Bullying and harassment widespread in astronomy

Astronomy and geophysics have [high rates of bullying and harassment](#) in Britain and perhaps other regions, according to the results of a survey conducted last year by the Royal Astronomical Society (RAS) in London. Among 661 researchers polled, more than half of whom were in the United Kingdom, 44% said they had experienced issues in the previous two years.

BULLYING AND HARASSMENT IN ASTRONOMY

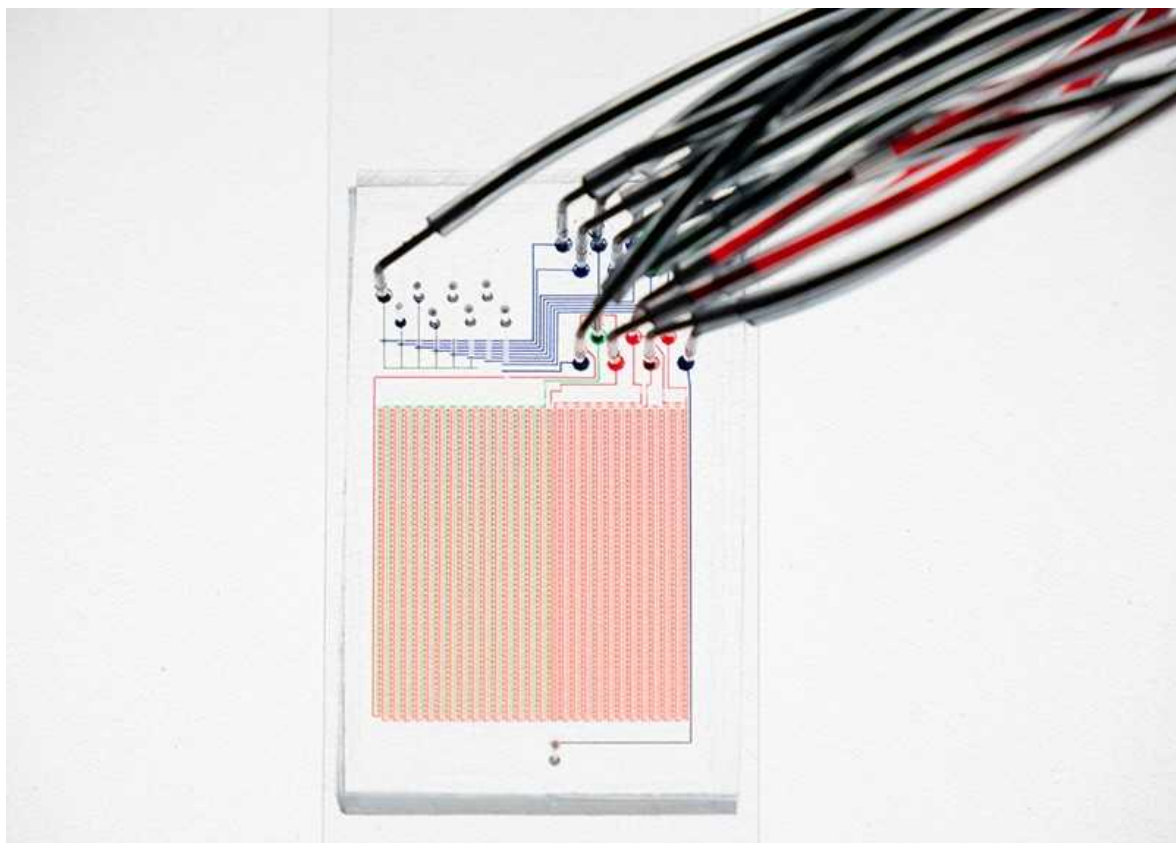
A survey of 661 astronomers and geophysicists found that 44% of respondents had experienced bullying and harassment in the past two years — but people from certain demographics and marginalized groups reported more negative experiences than others.



Source: Royal Astronomical Society

RAS diversity officer Aine O'Brien, who co-conducted the survey, says: “We knew from anecdotal data and other evidence that there was likely to be a sector-wide problem, and I wasn’t super shocked by the trends of the findings — but I was certainly shocked by the extent.”

The survey finds that the problems are worse for women, for people with marginalized sexual orientations or gender identities (LGBT+ people), for disabled people and for Black people and those from other minority ethnic groups. Half of the LGBT+ astronomers and geophysicists polled said they had been bullied in the previous year, and disabled, Black and minority-ethnic astronomers and geophysicists were 40% more likely to be bullied than were non-disabled and white researchers.



The silicone microfluidic chip has an array of 1,568 reaction chambers. Channels etched in the chip connect the chambers to control pipes attached to the top. Credit: Daniel Mokhtari

Chip does massively parallel enzyme tests

Finding out how a protein or enzyme works requires altering hundreds of the molecule's amino acid building blocks one by one. Researchers then produce each mutated enzyme in the lab and test how it affects the enzyme's ability to carry out its job.

Now, a polymer chip etched with tiny channels could greatly reduce the time this takes by [allowing researchers to test more than 1,000 mutations at a time](#). A 22 July paper in *Science* describes how the new system, called High-Throughput Microfluidic Enzyme Kinetics (HT-MEK), could provide a faster way for scientists to study disease-causing proteins, develop enzymes that break down toxins and understand the evolutionary relationships between species ([C. J. Markin *et al. Science* 373, eabf8761; 2021](#)).

Because it can screen so many mutants at a time, the system could allow researchers to look beyond mutations in the active site — the part of an enzyme that actually carries out its main function and usually attracts the most research attention. Mutations in other regions might still affect an enzyme's function by changing how it folds or binds to other proteins, for instance.

Nature **596**, 13 (2021)

doi: <https://doi.org/10.1038/d41586-021-02087-4>

Subjects

- [SARS-CoV-2](#)
- [Drug discovery](#)
- [Vaccines](#)
- [Astronomy and astrophysics](#)

nature careers

[Jobs](#) >

- [Translational Biologist, Oncology](#)

Astex Pharmaceuticals Limited

Cambridge, United Kingdom

- [Postdoctoral Researcher – studying the histopathology of acute ischaemic stroke blood clots and the correlation of composition with impedance measurements\(CÚRAM\), NUIG RES 158-21](#)

National University of Ireland Galway (NUI Galway)

Galway, Ireland

- [Summer Laboratory Technician](#)

Oklahoma Medical Research Foundation (OMRF)

Oklahoma City, United States

- [PhD student \(m/f/d\) Hormonal programming of hepatic chromatin landscapes](#)

Technical University of Munich (TUM)

Munich, Germany

Nature Briefing

An essential round-up of science news, opinion and analysis, delivered to your inbox every weekday.

[Download PDF](#)

Subjects

- [SARS-CoV-2](#)
- [Drug discovery](#)

- [Vaccines](#)
 - [Astronomy and astrophysics](#)
-

This article was downloaded by **calibre** from <https://www.nature.com/articles/d41586-021-02087-4>

| [Section menu](#) | [Main menu](#) |

- NEWS
- 23 July 2021

NASA investigates renaming James Webb telescope after anti-LGBT+ claims

Some astronomers argue the flagship observatory — successor to the Hubble Space Telescope — will memorialize discrimination. Others are waiting for more evidence.

- [Alexandra Witze](#)
 1. Alexandra Witze
[View author publications](#)

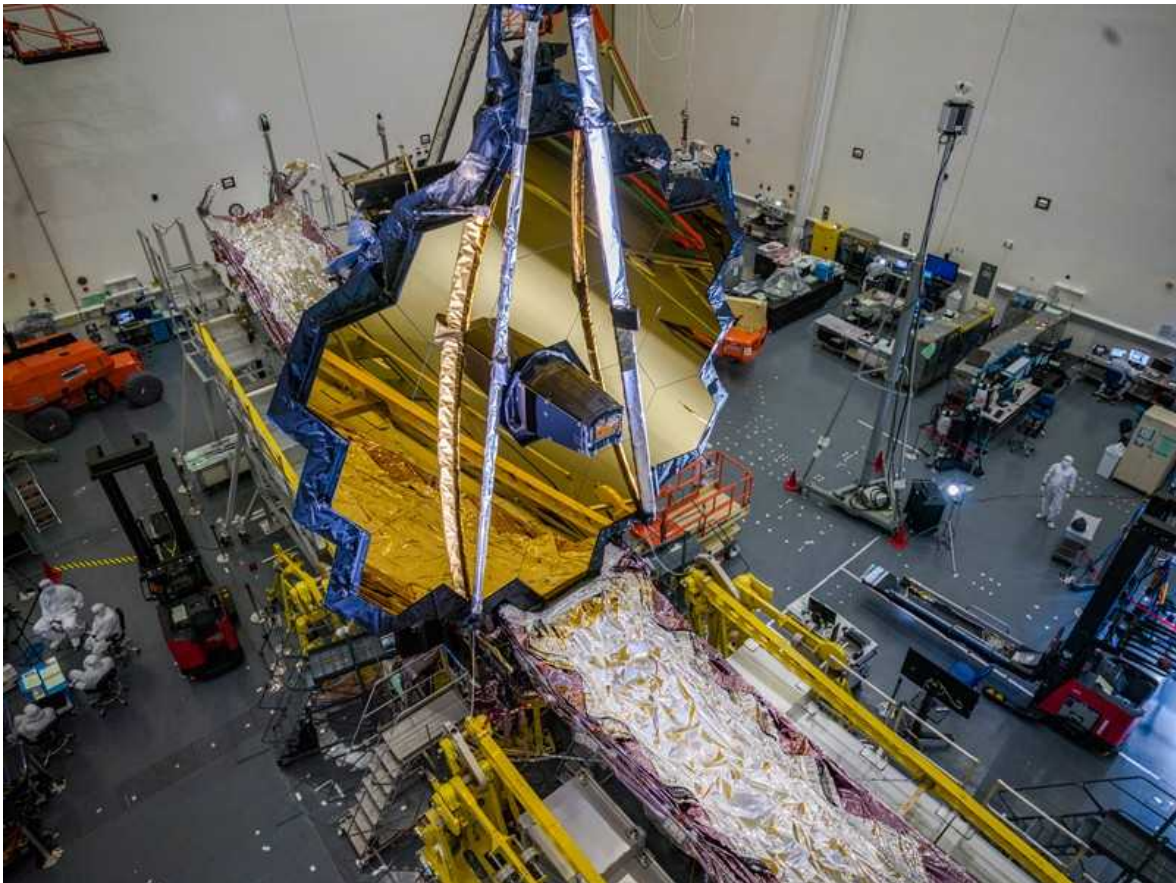
You can also search for this author in [PubMed](#) [Google Scholar](#)





•

[Download PDF](#)



The James Webb Space Telescope, which is scheduled to launch this year.Credit: NASA/Chris Gunn

NASA is considering whether to rename its flagship astronomical observatory, given reports alleging that James Webb, after whom it is named, was involved in persecuting gay and lesbian people during his career in government. Keeping his name on the US\$8.8-billion James Webb Space Telescope (JWST) — set to launch later this year — would glorify bigotry and anti-LGBT+ sentiment, say some astronomers. But others say there is not yet enough evidence against Webb, who was head of NASA from 1961 to 1968, and they are withholding judgement until the agency has finished an internal investigation.

The JWST, which will peer into the distant reaches of the cosmos, is NASA's biggest astronomical project in decades, so the stakes are high. In May, citing Webb's purported involvement in discrimination, four prominent astronomers launched a petition to change the telescope's name. It has

amassed 1,250 signatories, including scientists who have been awarded observing time on the telescope.



[Coronavirus pandemic threatens launch of world's most-expensive telescope](#)

NASA's acting chief historian, Brian Odom, is working with a non-agency historian to review archival documents about Webb's policies and actions, according to agency officials. Only after the investigation concludes will NASA decide what to do.

“We must make a conscious decision,” Paul Hertz, head of NASA’s astrophysics division, told an agency advisory committee on 29 June. “We must be transparent with the community and with the public for the rationale for whichever decision we make.”

Searching the archives

Former NASA administrator Sean O’Keefe named the JWST after Webb in 2002, when the telescope was in the early stages of development. It was a unilateral decision that took many by surprise, because NASA’s telescopes are typically named after scientists. Webb, who died in 1992, was a bureaucrat who held several administrative roles in the US government.



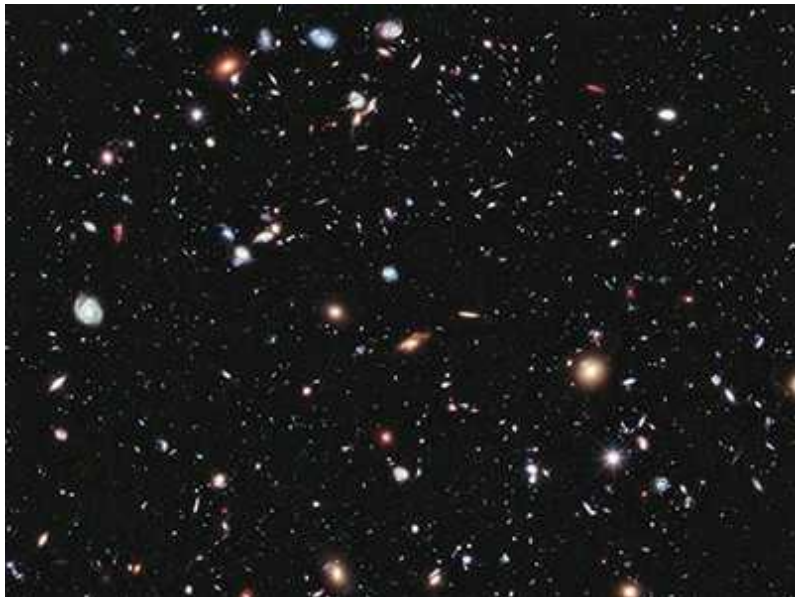
James Webb was NASA's second-ever administrator, running the agency from 1961 to 1968. Credit: NASA

O'Keefe chose the name because Webb had advocated that NASA keep science as a key part of its portfolio in the 1960s, even as the Apollo programme of human space exploration soaked up most of the agency's attention and budget. O'Keefe tells *Nature* he was not aware of the accusations when he picked the name, and he supports keeping it unless more information surfaces. "Without James Webb's leadership, there may have been no telescope or much of anything else at NASA noteworthy of a naming controversy," he says.

As Webb was beginning his career with the US government in the late 1940s, gay and lesbian employees were being systematically rooted out and fired because of their sexual orientation — a campaign encouraged by several prominent members of Congress. The period is known as the lavender scare, echoing the anti-Communist 'red scare' with which it was often intertwined. During the lavender scare, gay people were cast, untruthfully, as perverts who might be desperate to keep their sexual orientation secret and thus be susceptible to revealing government secrets

under blackmail. Its epicentre was the Department of State, which handles foreign policy.

The four astronomers leading the renaming petition say that when Webb worked for the state department in the high-ranking position of undersecretary from 1949 to 1952, he passed a set of memos discussing what was described as “the problem of homosexuals and sex perverts” to a senator who was leading the persecution. They point to records found in the US National Archives by astronomer Adrian Lucy at Columbia University in New York City. “The records clearly show that Webb planned and participated in meetings during which he handed over homophobic material,” [the petition leaders wrote earlier this year](#) in an opinion piece in *Scientific American*.



[US astronomers plot wish list for the next decade](#)

The four astronomers are Lucianne Walkowicz at the Adler Planetarium in Chicago, Illinois; Chanda Prescod-Weinstein at the University of New Hampshire in Durham; Brian Nord at the Fermi National Accelerator Laboratory in Batavia, Illinois; and Sarah Tuttle at the University of Washington in Seattle. “We felt that we should take a public stand on naming such an important facility after someone whose values were so questionable,” they write in an e-mail to *Nature*. “It’s time for NASA to stand up and be on the right side of history.”

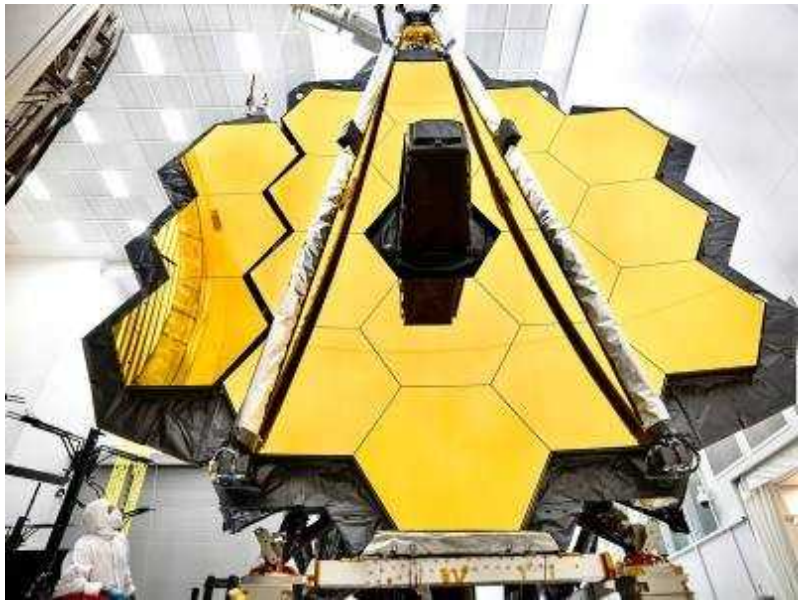
David Johnson, a historian at the University of South Florida in Tampa who wrote the 2004 book *The Lavender Scare*, says he knows of no evidence that Webb led or instigated persecution. Webb did attend a White House meeting on the threat allegedly posed by gay people, but the context of the meeting was to contain the hysteria that members of Congress were stirring up. “I don’t see him as having any sort of leadership role in the lavender scare,” says Johnson.

Walkowicz and their colleagues note that as a leader, Webb bore responsibility for discriminatory policies enacted at his agency. They also note the case of Clifford Norton, who was fired from his job at NASA because he was suspected to be gay in 1963, when Webb was NASA administrator. “We believe the known historical record speaks clearly in favour of renaming the telescope,” they say.

NASA has given no estimate of when its investigation might be complete. Odom says that the COVID-19 pandemic has limited historians’ access to archival records.

A reflection of values

The push to rename the telescope falls into [the broader reckoning](#) over naming buildings, facilities and other objects after questionable historical figures. Last year, an aerospace executive began an as-yet unsuccessful effort to rename a NASA centre in Mississippi that is named after John Stennis, a senator who voted repeatedly in favour of racial segregation in the 1960s. In the past year or so, NASA has tried to address past discrimination against Black scientists and against women by naming its Washington DC headquarters after Mary Jackson, the first Black female engineer at the agency, and announcing that the flagship space telescope after the JWST will be named after Nancy Grace Roman, NASA’s first chief astronomer.



Delays mount for NASA's \$8-billion Hubble successor

The JWST debate comes near the end of a long and exhausting push to launch the observatory into space. Originally conceived in 1989 as the successor to the iconic Hubble Space Telescope, the craft is many years and billions of dollars over budget.

To some, the telescope's potential to transform astronomy makes it even more important that the JWST carry a name that reflects modern values. "For me, it really comes down to what kind of message we want to send to the more junior folks and students in our field," says Peter Gao, a planetary scientist at the University of California, Santa Cruz. "The people we choose to celebrate by naming our telescopes after them is a reflection of our values."

The final decision lies with NASA administrator Bill Nelson, who has not said anything publicly on the matter. There is no clear list of alternative names, although many people have made unofficial suggestions. Walkowicz and the other astronomers who are leading the petition suggest Harriet Tubman, after the formerly enslaved woman who fought to end slavery in the United States in the nineteenth century and used the stars to guide Black people to freedom. Saurabh Jha, an astronomer at Rutgers University in New Brunswick, New Jersey, suggests Cecilia Payne-Gaposchkin, whose work

revolutionized astronomers' understanding of the composition of the Universe in the early twentieth century.



Hubble telescope spies water raining on distant world

Some astronomers who plan to use the JWST are already thinking about what they will do if the telescope is not renamed. One idea is to acknowledge LGBT+ rights in the acknowledgements sections of papers published using JWST data, says Johanna Teske, an astronomer at the Carnegie Institution for Science in Washington DC.

Many are keen to see what the NASA investigation might unearth. “It’s important to look at what happened and what the facts are,” says Rolf Danner, an astronomer at NASA’s Jet Propulsion Laboratory in Pasadena, California, who is chair of the American Astronomical Society’s committee on sexual orientation and gender minorities in astronomy. “And then really ask ourselves — would we make that choice again?”

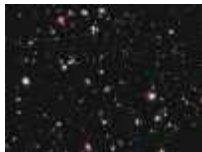
Nature **596**, 15-16 (2021)

doi: <https://doi.org/10.1038/d41586-021-02010-x>

Related Articles



- [Coronavirus pandemic threatens launch of world's most-expensive telescope](#)



- [US astronomers plot wish list for the next decade](#)



- [Delays mount for NASA's \\$8-billion Hubble successor](#)
- [Exoplanet hunters rethink search for alien life](#)



- [Hubble telescope spies water raining on distant world](#)

Subjects

- [Scientific community](#)
- [History](#)
- [Astronomical instrumentation](#)
- [Astronomy and astrophysics](#)

nature careers

[Jobs](#) >

- [Translational Biologist, Oncology](#)

Astex Pharmaceuticals Limited

Cambridge, United Kingdom

- [Postdoctoral Researcher – studying the histopathology of acute ischaemic stroke blood clots and the correlation of composition with impedance measurements\(CÚRAM\), NUIG RES 158-21](#)

National University of Ireland Galway (NUI Galway)

Galway, Ireland

- [Summer Laboratory Technician](#)

Oklahoma Medical Research Foundation (OMRF)

Oklahoma City, United States

- [PhD student \(m/f/d\) Hormonal programming of hepatic chromatin landscapes](#)

Technical University of Munich (TUM)

Munich, Germany

Nature Briefing

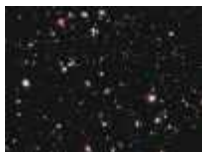
An essential round-up of science news, opinion and analysis, delivered to your inbox every weekday.

[Download PDF](#)

Related Articles



- [Coronavirus pandemic threatens launch of world's most-expensive telescope](#)



- [US astronomers plot wish list for the next decade](#)



- [Delays mount for NASA's \\$8-billion Hubble successor](#)
- [Exoplanet hunters rethink search for alien life](#)



- [Hubble telescope spies water raining on distant world](#)

Subjects

- [Scientific community](#)
- [History](#)
- [Astronomical instrumentation](#)
- [Astronomy and astrophysics](#)

This article was downloaded by **calibre** from <https://www.nature.com/articles/d41586-021-02010-x>

- NEWS
- 27 July 2021

COVID vaccines slash viral spread – but Delta is an unknown

Studies show that vaccines reduce the spread of SARS-CoV-2 by more than 80%, but the Delta variant is creating fresh uncertainty.

- [Smriti Mallapaty](#)
 1. Smriti Mallapaty
[View author publications](#)

You can also search for this author in [PubMed](#) [Google Scholar](#)





•

[Download PDF](#)



A dose of the Pfizer–BioNTech COVID-19 vaccine is administered at the Sheba Medical Center near Tel Aviv, Israel. Credit: Jack Guez/AFP/Getty

Many vaccines have been shown to provide strong protection against COVID-19. Now, growing evidence finds that they also substantially reduce the risk of passing on the virus SARS-CoV-2 — crucial information for governments making decisions about how best to control the pandemic.

However, the studies were done before the highly transmissible Delta variant became prevalent — and scientists say it might be more easily spread by vaccinated people than are earlier variants.

Two studies^{1,2} from Israel, posted as preprints on 16 July, find that two doses of the vaccine made by pharmaceutical company Pfizer, based in New York City, and biotechnology company BioNTech, based in Mainz, Germany, are 81% effective at preventing SARS-CoV-2 infections. And vaccinated people who do get infected are up to 78% less likely to spread the virus to household members than are unvaccinated people. Overall, this adds up to very high protection against transmission, say researchers.

The studies reflect population-level trends, say researchers. “It’s good news,” says Natalie Dean, a biostatistician at Emory University in Atlanta, Georgia. “But it’s not quite good enough,” she notes, because it means that vaccinated people can still occasionally spread the infection.

And the highly transmissible [Delta variant](#) is a major source of uncertainty. The Israeli studies and others are based on the circulation of earlier variants, in particular Alpha, but research suggests that vaccines offer slightly reduced protection against Delta.

Robust estimates

The studies “help us understand why cases were falling in most highly vaccinated populations before the emergence of the Delta variant”, says Marm Kilpatrick, an infectious-disease researcher at the University of California, Santa Cruz. “If that variant hadn’t arisen and spread, it’s likely that case burdens would be very, very low in many countries” with high rates of vaccination, he says.

The studies provide robust estimates for various aspects of transmission that had previously been inferred through multiple studies, says Kilpatrick.



[Six months of COVID vaccines: what 1.7 billion doses have taught scientists](#)

The first study¹, co-authored by researchers in Israel and France, looked at transmission in 210 households of infected people who worked at the Sheba Medical Center near Tel Aviv, which is Israel's largest hospital. The data come from between December 2020 and April 2021 — a time when a massive vaccination drive in Israel was competing with a surge in cases driven by Alpha.

The second study², co-authored by researchers in Israel and the United States, was based on a retrospective analysis of data from about 66,000 multiperson households with at least one infected member, collected by Maccabi Healthcare Services, a large health-care provider based in Tel Aviv, Israel, between June 2020 and March 2021.

Both studies found that two doses of the Pfizer–BioNTech vaccine were 81% effective at preventing infections. Those who did get infected were also less likely to pass the infection to household members than were unvaccinated individuals.

The first study saw a drop of 78%, and the second 41%, in reduction of infectiousness — with the large difference in numbers perhaps explained by the fact that the estimates are based on a very small number of vaccinated people who were infected and then infected others.

Reduce infectiousness

Nevertheless, “both papers provide good evidence of a substantial reduction in infectiousness”, says Elizabeth Halloran, a biostatistician at the Fred Hutchinson Cancer Research Center in Seattle, Washington.

And whereas the studies provide an insight into transmission within households, the protection could be even higher outside the home, where people might be exposed to smaller doses of virus, notes Kilpatrick.

Although most of the benefit is because vaccines prevent infection in the first place, “the fact that they also reduce the infectiousness of breakthrough cases is important and reassuring”, says Virginia Pitzer, an infectious-

diseases modeller at Yale School of Public Health in New Haven, Connecticut, and co-author of one of the Israel studies².

The results correspond well with [studies conducted elsewhere](#). One analysis³ of some 365,000 households in the United Kingdom, published on 23 June, estimated that individuals infected with SARS-CoV-2 were 40–50% less likely to spread the infection if they had received at least one dose of the Pfizer–BioNTech vaccine or that developed by the University of Oxford, UK, and pharmaceutical company AstraZeneca, based in Cambridge, UK, at least three weeks previously

A study⁴ from Finland, posted as a preprint on 10 July, found that spouses of infected health-care workers who had received a single dose of the Pfizer–BioNTech vaccine or that produced by Moderna in Cambridge, Massachusetts, were 43% less likely to get infected than were spouses of unvaccinated health workers.

Confounding factor of Delta

But studies on Alpha and other variants cannot be easily generalized to Delta, says Steven Riley, an infectious-diseases researcher at Imperial College London.

So far, there are no published data on how vaccines affect infections and infectiousness with Delta, but a UK study⁵ published on 21 July shows that the Pfizer–BioNTech and Oxford–AstraZeneca vaccines both protect slightly less well against symptomatic disease caused by Delta than against that caused by Alpha. This could also mean a drop in how well they protect against transmission of Delta, but there is still a lot of uncertainty, says Dean.



[COVID vaccines to reach poorest countries in 2023 — despite recent pledges](#)

Unpublished [preliminary data](#) from Israel's Ministry of Health show that Delta could chip away at some of the reduction in transmission provided by the Pfizer–BioNTech vaccine. And case numbers have risen sharply in Israel following Delta's arrival, despite more than 60% of the population being fully vaccinated. This hints at what might happen elsewhere, say researchers.

Even if vaccines are just as effective at preventing infections with Delta as with earlier variants, if Delta is more infectious, transmission in households could still increase, says Dean.

A study⁶ from China, posted as a preprint on 12 July, found that the concentration of viral particles — a proxy for infectiousness — in people infected with Delta was roughly [1,000 times](#) that in people infected with the original strain of SARS-CoV-2.

Delta's increased infectiousness could mean that the proportion of people in a population who need to be vaccinated to bring the pandemic under control will be larger than would have been required with earlier variants.

Nature **596**, 17–18 (2021)

doi: <https://doi.org/10.1038/d41586-021-02054-z>

References

1. 1.

Layan, M. *et al.* Preprint at
<https://doi.org/10.1101/2021.07.12.21260377> (2021).

2. 2.

Prunas, O. *et al.* Preprint at
<https://doi.org/10.1101/2021.07.13.21260393> (2021).

3. 3.

Harris, R. J. *et al.* *N. Engl. J. Med.*
<https://doi.org/10.1056/NEJMc2107717> (2021).

[Article](#) [Google Scholar](#)

4. 4.

Salo, J. *et al.* Preprint at <https://doi.org/10.1101/2021.05.27.21257896> (2021).

5. 5.

Lopez Bernal, J. *et al.* *N. Engl. J. Med.*
<https://doi.org/10.1056/NEJMoa2108891> (2021).

[PubMed](#) [Article](#) [Google Scholar](#)

6. 6.

Li, B. *et al.* Preprint at <https://doi.org/10.1101/2021.07.07.21260122> (2021).

[Download references](#)

Related Articles

-  [Can COVID vaccines stop transmission? Scientists race to find answers](#)
-  [Six months of COVID vaccines: what 1.7 billion doses have taught scientists](#)
-  [Scientists zero in on long-sought marker of COVID-vaccine efficacy](#)

Subjects

- [Infection](#)
- [Public health](#)
- [Vaccines](#)
- [SARS-CoV-2](#)

nature careers

[Jobs >](#)

- [Translational Biologist, Oncology](#)

Astex Pharmaceuticals Limited

Cambridge, United Kingdom

- [Postdoctoral Researcher – studying the histopathology of acute ischaemic stroke blood clots and the correlation of composition with impedance measurements\(CÚRAM\), NUIG RES 158-21](#)

National University of Ireland Galway (NUIG Galway)

Galway, Ireland

- [Summer Laboratory Technician](#)

Oklahoma Medical Research Foundation (OMRF)

Oklahoma City, United States

- [PhD student \(m/f/d\) Hormonal programming of hepatic chromatin landscapes](#)

Technical University of Munich (TUM)

Munich, Germany

Nature Briefing

An essential round-up of science news, opinion and analysis, delivered to your inbox every weekday.

[Download PDF](#)

Related Articles

-  [Can COVID vaccines stop transmission? Scientists race to find answers](#)



- **Six months of COVID vaccines: what 1.7 billion doses have taught scientists**



- **Scientists zero in on long-sought marker of COVID-vaccine efficacy**

Subjects

- Infection
- Public health
- Vaccines
- SARS-CoV-2

This article was downloaded by **calibre** from <https://www.nature.com/articles/d41586-021-02054-z>

- NEWS
- 28 July 2021

Water transformed into shiny, golden metal

Electrons from a droplet of sodium and potassium turn water into a metallic material that conducts electricity.

- [Davide Castelvecchi](#)
 1. Davide Castelvecchi
[View author publications](#)

You can also search for this author in [PubMed](#) [Google Scholar](#)





•

[Download PDF](#)



Electrons from a droplet of sodium and potassium diffuse onto a thin layer of water, turning it golden and giving it metallic properties. Credit: Philip E. Mason

If you can't turn water into gold like a good alchemist would, the next best thing might be to transform water itself into a shiny, metallic material. Researchers have achieved that feat by forming a thin layer of water around electron-sharing alkali metals.

The water stayed in a metallic state for only a few seconds, but the experiment did not require the high pressures that are normally needed to turn non-metallic materials into electrically conductive metals.

Co-author Pavel Jungwirth, a physical chemist at the Czech Academy of Sciences in Prague, says that seeing the water take on a golden shine was a

highlight of his career. The team published its findings on 28 July in *Nature*¹.

“This is a most important advance,” says Peter Edwards, a chemist at the University of Oxford, UK. “Who would have thought it … bronze, metallic water?”

Metallic non-metals

In theory, most materials are capable of becoming metallic if put under enough pressure. Atoms or molecules can be squeezed together so tightly that they begin to share their outer electrons, which can then travel and conduct electricity as they do in a chunk of copper or iron. Geophysicists think that the centres of massive planets such as Neptune or Uranus host water in such a metallic state, and that high-pressure metallic hydrogen can even become a superconductor, able to conduct electricity without any resistance.

Turning water into a metal in this way would require an expected 15 million atmospheres of pressure, which is out of reach for current lab techniques, says Jungwirth. But he suspected that water could become conductive in an alternative way: by borrowing electrons from alkali metals. These reactive elements in group 1 of the periodic table, which includes sodium and potassium, tend to donate their outermost electron. Last year, Jungwirth and his colleague Phil Mason — a chemist who is also known for making science videos on YouTube — led a team that demonstrated a similar effect in ammonia². The fact that ammonia can turn shiny in such conditions was known to the British chemist Humphry Davy in the early nineteenth century, Edwards points out.



A video of the experiment shows how water on the surface of the droplet turns shiny and metallic for a few seconds.Credit: Philip E. Mason

The team wanted to try the same approach with water instead of ammonia, but faced a challenge: alkali metals tend to react explosively when mixed

with water. The solution was to design an experimental set-up that would dramatically slow the reaction so that it would not be explosive. The researchers filled a syringe with sodium and potassium, a mixture that is liquid at room temperature, and placed it in a vacuum chamber. They then used the syringe to form droplets of the metal mixture and exposed them to small amounts of water vapour. The water condensed onto each droplet and formed a layer one-tenth of a micrometre thick. Electrons from the droplet then quickly diffused into the water — together with positive metallic ions — and, within a few seconds, the water layer turned golden.

Timing is crucial

Experiments at a synchrotron in Berlin confirmed that the gold reflections produced the signatures expected of metallic water. The key to avoiding an explosion, Jungwirth says, was to find a window of time in which the diffusion of electrons was faster than the reaction between the water and the metals. “They have managed to get to a quasi-steady state such that the physics of metallization wins over chemical decomposition,” Edwards says.

“We were not sure at all that we would find it,” Jungwirth says. “It was amazing, like [when] you discover a new element.”

Jungwirth says the experiment was a refreshing break from his day job, which is to run computer simulations in organic chemistry, and a reminder that science can be fun. “It’s not something you can get grant money for, but something you can do on your weekends,” he says. It’s not the first time he has collaborated with Mason on a practical experiment: in 2015, the two researchers and their colleagues revealed the mechanism that makes sodium explode when it touches water³ — an experiment they set up on a balcony at their institute, because they didn’t have access to a lab. “That pissed everybody off, because that was where people went smoking,” he recalls. “We said: could we have the balcony for explosions?”

Nature **596**, 18 (2021)

doi: <https://doi.org/10.1038/d41586-021-02065-w>

References

1. 1.

Mason, P. E. *et al.* *Nature* <https://doi.org/10.1038/s41586-021-03646-5> (2021).

[Article](#) [Google Scholar](#)

2. 2.

Buttersack, T. *et al.* *Science* **368**, 1086–1091 (2020).

[PubMed](#) [Article](#) [Google Scholar](#)

3. 3.

Mason, P. E. *et al.* *Nature Chem.* **7**, 250–254 (2015).

[PubMed](#) [Article](#) [Google Scholar](#)

[Download references](#)

Related Articles

- [Sodium explosion caught on camera](#)
- [Physicists doubt bold report of metallic hydrogen](#)
- [First room-temperature superconductor excites — and baffles — scientists](#)

Subjects

- [Chemistry](#)
- [Physics](#)
- [Geophysics](#)

nature careers

Jobs >

- [Translational Biologist, Oncology](#)

Astex Pharmaceuticals Limited

Cambridge, United Kingdom

- [Postdoctoral Researcher – studying the histopathology of acute ischaemic stroke blood clots and the correlation of composition with impedance measurements\(CÚRAM\), NUIG RES 158-21](#)

National University of Ireland Galway (NUI Galway)

Galway, Ireland

- [Summer Laboratory Technician](#)

Oklahoma Medical Research Foundation (OMRF)

Oklahoma City, United States

- [PhD student \(m/f/d\) Hormonal programming of hepatic chromatin landscapes](#)

Technical University of Munich (TUM)

Munich, Germany

Nature Briefing

An essential round-up of science news, opinion and analysis, delivered to your inbox every weekday.

[Download PDF](#)

Related Articles

- [Sodium explosion caught on camera](#)
- [Physicists doubt bold report of metallic hydrogen](#)
- [First room-temperature superconductor excites — and baffles — scientists](#)

Subjects

- [Chemistry](#)
- [Physics](#)
- [Geophysics](#)

This article was downloaded by **calibre** from <https://www.nature.com/articles/d41586-021-02065-w>

| [Section menu](#) | [Main menu](#) |

- NEWS
- 28 July 2021

Sponge-like fossil could be Earth's earliest known animal

Fossil discovered in northwestern Canada could rewrite the early history of animal life — but some palaeontologists are not convinced it's real.

- [Max Kozlov](#)
 1. Max Kozlov
[View author publications](#)

You can also search for this author in [PubMed](#) [Google Scholar](#)





•

[Download PDF](#)



A black horny sponge (*Scalarspongia scalaris*) growing off the coast of France. Some types of horny sponge are today harvested for bath sponges. Credit: Biosphoto/Alamy

Most major groups of animals — including arthropods, molluscs and worms — first appear in the fossil record during the Cambrian explosion, 541 million years ago. But according to a paper published today in *Nature*¹, sponge fossils from northwestern Canada could be 350 million years older, significantly pushing back the date of Earth's earliest-known animals.

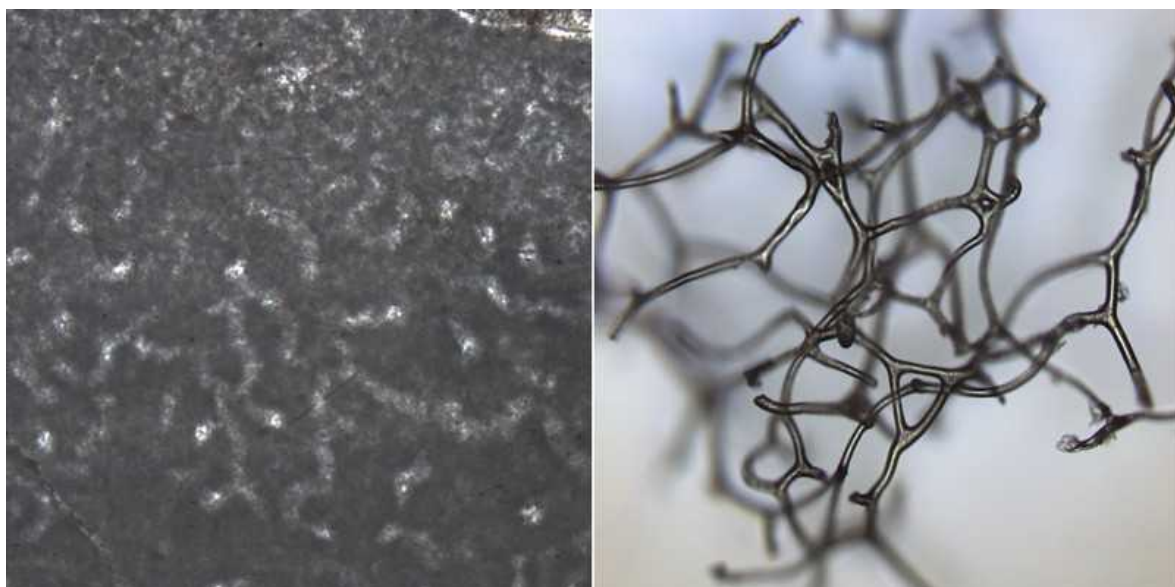
The ancient discovery is igniting debate among palaeontologists, who have long contested when complex animal life first evolved.

“If I’m right, animals emerged long, long before the first appearance of traditional animal fossils,” says study author Elizabeth Turner, a sedimentary geologist at Laurentian University in Sudbury, Canada. “That would mean there’s a deep back history of animals that just didn’t get preserved very well.”

Weird and wonderful shapes

Some scientists, however, are not convinced that the microscopic patterns in Turner's 890-million-year-old fossils indicate an ancient sponge, given the evidence provided in the study.

"It's such a big claim that you really have to eliminate all the other possibilities," says Rachel Wood, a geoscientist at the University of Edinburgh, UK, who researches fossil reefs. "Microbes, for example, produce weird and wonderful shapes and forms." Sometimes crystals also grow in a way that looks like patterns formed by living organisms, she says, meaning that the rock samples Turner found might not be fossils at all.



Crystalline tubes seen in rocks (left) might have been formed when the collagen-like skeleton of an 890-million-year-old sponge decayed and fossilized. Some modern sponges have internal scaffolding (right) that resembles the shapes in the rocks. Credit: Elizabeth C. Turner

Turner counters that none of the known reef-building organisms that existed 890 million years ago, such as cyanobacteria or algae, can explain the complex structures in her samples.

She collected the purported fossils from ancient microbial reefs preserved in the rocks of Canada's remote Northwest Territories, starting during her

graduate studies in the 1990s.

When Turner examined slices of the rock under a microscope, she saw branching networks of crystalline tubes. She later realized that these structures resemble the internal scaffolding of modern horny sponges, and line up with the expected decay and fossilization patterns of spongin, a collagen protein that forms their scaffolding.

“These rocks are beautiful, but you don’t expect to find something that complicated or weird in them,” she says.

Early history of animal life

It wasn’t until the past few years, when she saw studies that described similar structures in much younger rocks — from a time when sponges were known to exist — that Turner felt confident in publishing her results. But those studies, too, are disputed on the grounds that they might not be actual sponge fossils.

The authors of one of these papers² took photographs of many thin slices of their rock sample and used them to generate a 3D model of the purported sponge. Wood says that a similar piece of evidence would have strengthened Turner’s claim.

If Turner’s structures do prove to be sponge fossils, says David Gold, a geobiologist at the University of California, Davis, “it would be very exciting, and help us nail down the early story of animal evolution”, a subject that has been hotly debated for decades.

But although “it’s easy to find things that look like sponges in the fossil record”, he says, it’s more difficult to back them up with other evidence. He and other researchers, for instance, have supported³ fossil claims by pointing to rock samples containing traces of biological molecules that are linked to sponges. Unfortunately, given the sheer age and type of Turner’s rock samples, this type of preservation isn’t really possible, he adds.

It’s not inconceivable that sponges could have pre-dated the Cambrian explosion, says Phoebe Cohen, a geobiologist at Williams College in

Williamstown, Massachusetts. Scientists estimate how long ago the ancestors of groups of living animals diverged using ‘molecular clocks’, which measure the rate of mutation in DNA and proteins over time.

The majority of these estimates suggest that the last common ancestor of all animals alive today evolved before the Cambrian explosion, but not by as much as 350 million years, says Cohen. Nevertheless, she says she could be convinced that Turner’s samples are sponge fossils if she saw more evidence, including studies on how horny sponges fossilize.

Molecular-clock estimates

The palaeontological community is split on whether the dearth of animal fossils from before the Cambrian period is because the creatures that lived then rarely survived as fossils to the present day, or because molecular-clock estimates of animal origins are wrong. Gold is convinced there were sponges before the Cambrian, but says that exactly how far back is a big, unresolved question.



Ancient worm fossil rolls back origins of animal life

If the ancestors of modern sponges really were alive 890 million years ago, then it means early animals survived through very trying conditions for life,

such as extremely low levels of oxygen and ‘snowball Earth’ periods during which the surface of the planet almost entirely froze over, says Gold.

Turner argues that sponges could have survived the low-oxygen environment by eking out a living in cavities and crevices in the microbial reef next to photosynthetic cyanobacteria, which release oxygen. The sponges might also have been nourished by organic ooze that the bacteria produced. “There was probably a delicious and very copious supply of ‘snot’ for these filter-feeding organisms to have eaten,” she says.

Scientists are passionate about their views of when animal life started on Earth. The paper could reinvigorate the debate that has been quietly simmering for decades, says Gold. “But I suspect it’s not going to change a lot of minds for those who have made a decision about how old animals are.”

Nature **596**, 19 (2021)

doi: <https://doi.org/10.1038/d41586-021-02066-9>

References

1. 1.

Turner, E. C. *Nature* <https://doi.org/10.1038/s41586-021-03773-z> (2021).

[Article](#) [Google Scholar](#)

2. 2.

Luo, C. & Reitner, J. *Naturwissenschaften* **101**, 467–477 (2014).

[PubMed](#) [Article](#) [Google Scholar](#)

3. 3.

Gold, D. A. *et al.* *Proc. Natl Acad. Sci. USA* **113**, 2684–2689 (2016).

[PubMed](#) [Article](#) [Google Scholar](#)

[Download references](#)

Related Articles



- [These bizarre ancient species are rewriting animal evolution](#)



- [What sparked the Cambrian explosion?](#)



- [Ancient worm fossil rolls back origins of animal life](#)



- [Earliest skeletal animals were reef builders](#)

Subjects

- [Evolution](#)
- [Palaeontology](#)
- [Geology](#)

nature careers

[Jobs](#) >

- **Translational Biologist, Oncology**

Astex Pharmaceuticals Limited

Cambridge, United Kingdom

- **Postdoctoral Researcher – studying the histopathology of acute ischaemic stroke blood clots and the correlation of composition with impedance measurements(CÚRAM), NUIG RES 158-21**

National University of Ireland Galway (NUIG Galway)

Galway, Ireland

- **Summer Laboratory Technician**

Oklahoma Medical Research Foundation (OMRF)

Oklahoma City, United States

- **PhD student (m/f/d) Hormonal programming of hepatic chromatin landscapes**

Technical University of Munich (TUM)

Munich, Germany

Nature Briefing

An essential round-up of science news, opinion and analysis, delivered to your inbox every weekday.

[Download PDF](#)

Related Articles



- These bizarre ancient species are rewriting animal evolution



- What sparked the Cambrian explosion?



- Ancient worm fossil rolls back origins of animal life



- Earliest skeletal animals were reef builders

Subjects

- Evolution
- Palaeontology
- Geology

This article was downloaded by **calibre** from <https://www.nature.com/articles/d41586-021-02066-9>

- NEWS
- 23 July 2021

China's space station is preparing to host 1,000 scientific experiments

Researchers around the world are eagerly awaiting the completion of Tiangong, to study topics from dark matter and gravitational waves to the growth of cancer and pathogenic bacteria.

- [Smriti Mallapaty](#)
 1. Smriti Mallapaty
[View author publications](#)

You can also search for this author in [PubMed](#) [Google Scholar](#)





•

[Download PDF](#)



Chinese astronaut Nie Haisheng works inside the Tianhe module.Credit: Jin Liwang/Xinhua/eyevine

China launched the core of its space station in April, and sent three astronauts up in June. But although the space station probably won't be complete until late 2022, there is already a long queue of experiments from across the world waiting to go up. Scientists in China told *Nature* that the China Manned Space Agency (CMSA) has tentatively approved more than 1,000 experiments, several of which have already been launched.

Before April, the International Space Station (ISS) was the only space laboratory in orbit, and many researchers say Tiangong (or ‘heavenly palace’) is a welcome addition for astronomical and Earth observation, and for studying how microgravity and cosmic radiation affect phenomena such as bacterial growth and fluid mixing.



[China has landed its first rover on Mars — here's what happens next](#)

However, others argue that crewed space stations are costly, and serve more of a political than a scientific purpose.

“Increased scientific access to space is of scientific benefit globally, no matter who builds and operates platforms,” says Julie Robinson, chief scientist for human exploration and operations at NASA Headquarters in Washington DC.

“We need more space stations, because one space station is definitely not enough,” adds Agnieszka Pollo, an astrophysicist at the National Centre for Nuclear Research in Warsaw who is part of a team sending an experiment to study γ -ray bursts.

Open to the world

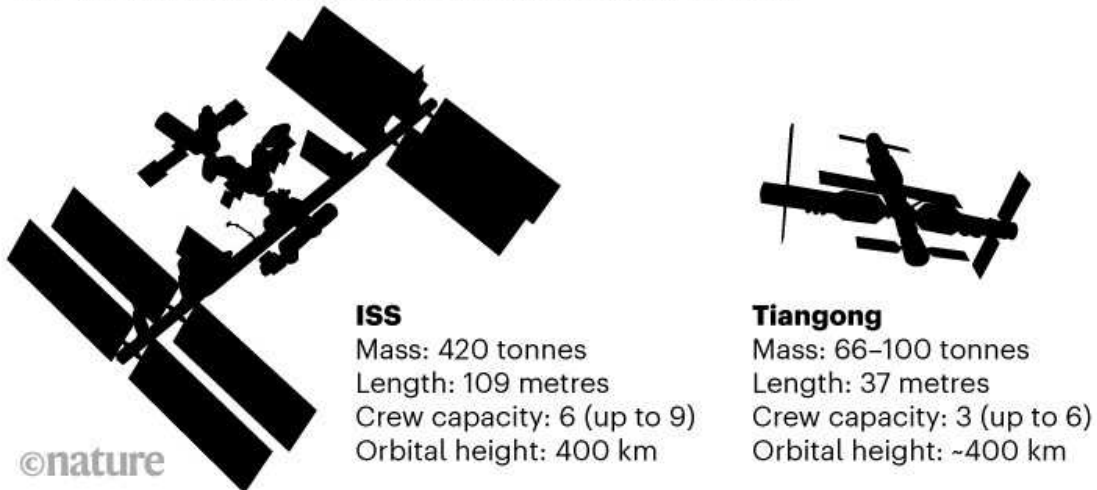
The ISS was launched in 1998, as a partnership between space agencies from the United States, Russia, Europe, Japan and Canada (see ‘Variations on a theme’). It has housed [more than 3,000 experiments](#) since then, but China is barred from it because of US rules that prohibit NASA from using funds for collaboration with China.

Although most experiments slated for Tiangong will involve Chinese researchers, China says that its space station will be open to collaboration from all countries, including the United States.

In June 2019, the CMSA and the United Nations Office for Outer Space Affairs (UNOOSA), which promotes collaboration in space, [selected nine experiments](#) — in addition to the 1,000 that China has tentatively approved — to go up once the space station is complete. Simonetta Di Pippo, director of UNOOSA in Vienna, says these involve 23 institutions in 17 nations.

VARIATIONS ON A THEME

Tiangong will be much smaller than the International Space Station (ISS), but will still have space for plenty of scientific experiments.



China previously launched two small [space labs](#) — Tiangong-1 and Tiangong-2. These hosted more than 100 experiments, circling Earth for a number of years, but are [no longer in orbit](#).

The space station offers brand new facilities, and China is encouraging experiments not attempted in space before, says Tricia Larose, a medical researcher at the University of Oslo, who is leading a project planned for 2026. “They’re saying, yes, build your hardware, make it brand new, do something that has never been done before, and send it up to us.”

Even though most projects approved so far are led by Chinese researchers, many have international collaborators, says Zhang Shuang-Nan, an

astrophysicist at the Chinese Academy of Sciences (CAS) Institute of High Energy Physics in Beijing, who advises the CMSA.

‘The playrooms of scientists’

The first section of Tiangong to arrive was a core module known as Tianhe ('harmony of the heavens'). In late May, a cargo ship named Tianzhou-2 ('heavenly ship') was sent up and docked, delivering fuel, space suits and experimental equipment. In June, three Chinese astronauts — or 'taikonauts' — aboard Shenzhou-12 ('divine vessel') also docked, entering the 17-metre-long chamber that will be their home for the next three months.

Over the next year or more, the CMSA will send another eight missions to Tiangong. Two will deliver the Wentian ('quest for heavens') and Mengtian ('dreaming of heavens') modules, which will mainly house scientific experiments (see 'China's first space station').

CHINA'S FIRST SPACE STATION

China aims to finish construction of Tiangong in late 2022. The station will be used to test technologies for human space exploration and as a laboratory for scientific experiments.

□ Set to launch in 2022

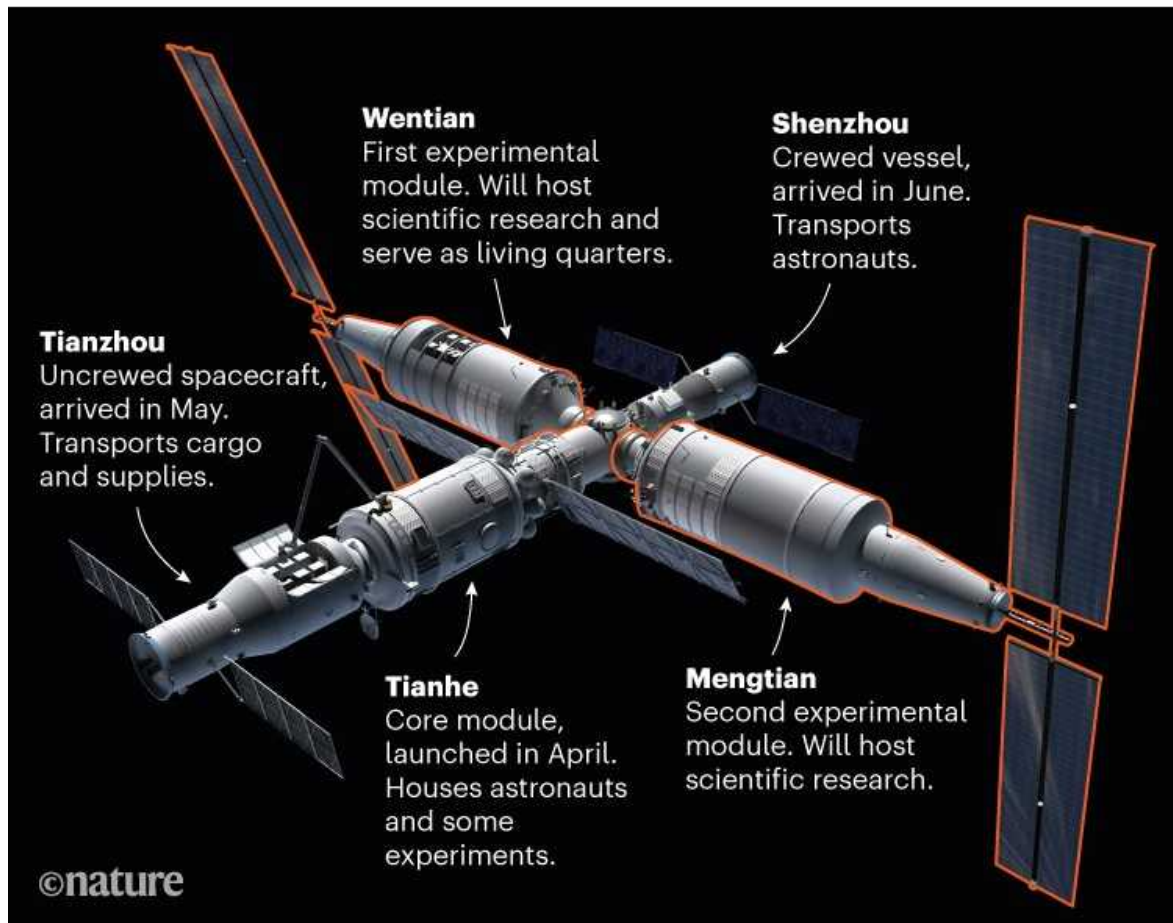


Image credit: Adrian Mann/Stocktrek Images/Alamy

These will be “the playrooms of scientists”, says Paulo de Souza, a physicist at Griffith University in Brisbane, Australia, who develops sensors used in space.

The space station will have more than 20 experimental racks, which are mini-labs with closed, pressurized environments, says Yang Yang, director of international cooperation at the CAS Technology and Engineering Center for Space Utilization in Beijing. Outside, there will be 67 connection points for research hardware facing Earth or the sky, says Yang. A powerful central

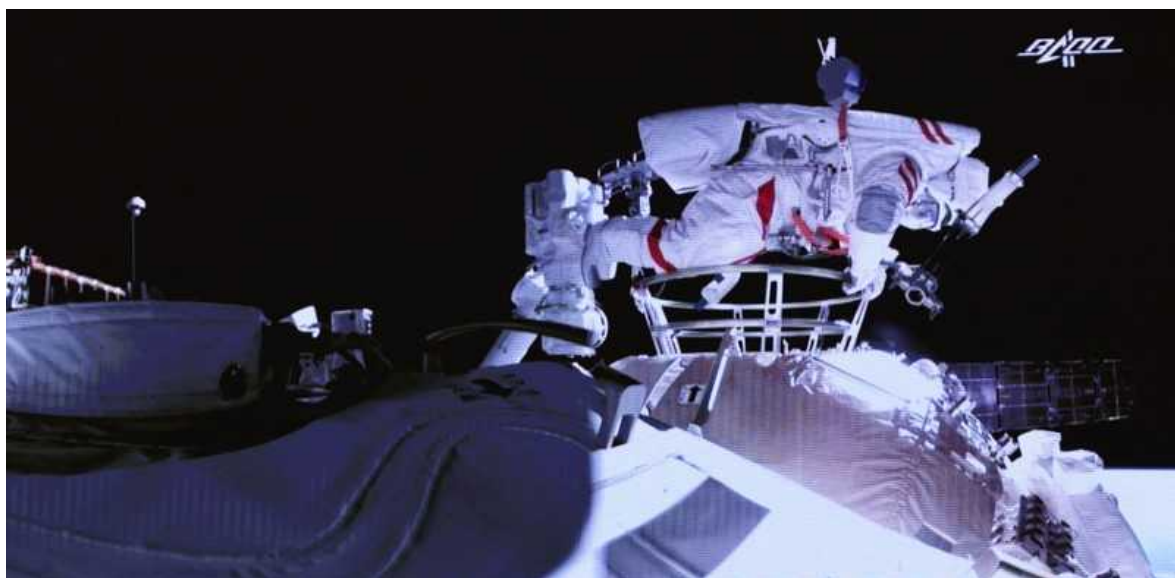
computer will process data from experiments before beaming them back to Earth.

Organoids and dark matter

The experiments being sent up to the new space station encompass numerous fields. Zhang is the principal investigator for HERD (High Energy Cosmic-Radiation Detection facility), which is a partnership involving Italy, Switzerland, Spain and Germany, slated for 2027. This particle detector will study dark matter and cosmic rays, and will cost some 1 billion to 2 billion yuan (US\$155 million to \$310 million), says Zhang.

Zhang and Pollo are also involved in POLAR-2, which will study the polarization of γ -rays emitted from large and distant explosions, with the goal of clarifying the properties of γ -ray bursts, and possibly even gravitational waves.

Larose plans to send up 3D blobs of healthy and cancerous intestinal tissue, known as organoids. She wants to find out whether the very-low-gravity environment will slow or stop the growth of the cancerous cells, which might lead to new therapies.



‘Taikonaut’ Liu Boming performs China’s second ever spacewalk after arriving at Tiangong in June.Credit: Jin Liwang/Xinhua/eyevine

Other projects from scientists in India and Mexico will study ultraviolet emissions from nebulae and infrared data from Earth, to study meteorological conditions and what drives intense storms.

Despite many of the projects being partnerships between Chinese and Western scientists, geopolitical tensions have made collaborations more difficult, notes Larose. She says Norway has yet to sign a bilateral agreement with China that would give her project the green light. Merlin Kole, an astrophysicist at the University of Geneva in Switzerland, who is also working on POLAR-2, adds that stricter adherence to export regulations means there is added bureaucracy around sending electronic hardware to China.

But Di Pippo says that tensions have so far had no impact on the progress of projects selected by UNOOSA, adding that the agency is discussing plans with the CMSA to send more experiments to Tiangong by the end of next year.

Scientific bang for buck

Some scientists have argued that crewed space stations are a waste of money — the cost of Tiangong has not been made public, but the ISS cost some €100 billion (US\$118 billion) to build and maintain for its first decade.

“You’d get a much bigger scientific bang for the buck with robotic missions,” says Gregory Kulacki, an analyst on China security issues for the Union of Concerned Scientists, an advocacy group headquartered in Cambridge, Massachusetts. “Within China, as within the United States, there has been a tension between scientists who want to do the best science they possibly can and who prefer robotic missions, and governments who want to use human space-flight programmes largely for political purposes.”



China's daring mission to grab Moon rocks is under way

But other researchers point out that although satellites offer an alternative for some observations, for many experiments, particularly those requiring microgravity, crewed space stations are essential. They provide a home for long-term observations, data-processing capacity and access for astronauts who can perform maintenance tasks and run the experiments.

Furthermore, as well as housing experiments from researchers, Tiangong is intended to test human space-travel technologies to support China's space-exploration goals, says Zhang.

With current ISS funding running only until sometime between 2024 and 2028, it's also possible that Tiangong will eventually become Earth's only space station in operation.

Tiangong is projected to operate for at least a decade, and China already has plans to launch other spacecraft to work in tandem with it. The China Survey Space Telescope, or Xuntian ('survey the heavens'), is a two-metre optical telescope that will rival NASA's Hubble Space Telescope and will periodically dock with Tiangong for refuelling and maintenance. Set to launch in 2023, it will have a larger field of view for peering into the deep Universe than does Hubble.

Nature **596**, 20-21 (2021)

doi: <https://doi.org/10.1038/d41586-021-02018-3>

Related Articles



- [China reveals scientific experiments for its next space station](#)



- [China has landed its first rover on Mars — here's what happens next](#)

Subjects

- [Space physics](#)
- [Astronomy and astrophysics](#)
- [Geophysics](#)

nature careers

[Jobs](#) >

- [Translational Biologist, Oncology](#)

Astex Pharmaceuticals Limited

Cambridge, United Kingdom

- [Summer Laboratory Technician](#)

Oklahoma Medical Research Foundation (OMRF)

Oklahoma City, United States

- [PhD student \(m/f/d\) Hormonal programming of hepatic chromatin landscapes](#)

Technical University of Munich (TUM)

Munich, Germany

- [Postdoctoral Researcher – studying the histopathology of acute ischaemic stroke blood clots and the correlation of composition with impedance measurements\(CÚRAM\), NUIG RES 158-21](#)

National University of Ireland Galway (NUI Galway)

Galway, Ireland

Nature Briefing

An essential round-up of science news, opinion and analysis, delivered to your inbox every weekday.

[Download PDF](#)

Related Articles



- [China reveals scientific experiments for its next space station](#)
- [China's quest to become a space science superpower](#)



- [China has landed its first rover on Mars — here's what happens next](#)

Subjects

- [Space physics](#)
- [Astronomy and astrophysics](#)
- [Geophysics](#)

This article was downloaded by **calibre** from <https://www.nature.com/articles/d41586-021-02018-3>

| [Section menu](#) | [Main menu](#) |

- NEWS FEATURE
- 04 August 2021

The world's species are playing musical chairs: how will it end?

Many communities aren't losing biodiversity, but ecosystems are changing rapidly and the future is far from rosy.

- [Gayathri Vaidyanathan](#) ⁰

1. Gayathri Vaidyanathan

1. Gayathri Vaidyanathan is a freelance reporter in Bangalore, India.

[View author publications](#)

You can also search for this author in [PubMed](#) [Google Scholar](#)





•



The number of plant species in New Zealand has doubled since humans settled there about 800 years ago. Credit: Matthew Lovette/Education Images/UIG/Getty

[Download PDF](#)

In June 2018, 180 cars fanned out across Denmark and parts of Germany on a grand insect hunt. Armed with white, funnel-shaped nets mounted on their car roofs, enthusiastic citizen naturalists roamed through cities, farmlands, grasslands, wetlands and forests. The drivers sent the haul from their

‘InsectMobiles’ to scientists at the National History Museum of Denmark in Copenhagen and the German Centre for Integrative Biodiversity Research in Leipzig.

The researchers dried and weighed the collections to determine the total mass of flying insects in each landscape. They expected some bad news. The previous year, scientists in Germany had found that the flying-insect biomass in their nature reserves had plunged by 76% over 27 years¹. Similar studies had led to news headlines that screamed of an ongoing “insectageddon” and “insect apocalypse”. British columnist George Monbiot wrote in *The Guardian*: “Insectageddon: farming is more catastrophic than climate breakdown”.

But when the researchers tallied the InsectMobile results², they didn’t see evidence of declines everywhere. Insect biomass totals were higher than expected in agricultural fields, and indeed in all places except cities in their study, which is yet to be peer reviewed². Aletta Bonn, an entomologist at the Leipzig centre and a co-author of the study, says this could be because the fertilizers that farmers use are leading to lush plant life, which is reverberating through the ecosystem. That said, she cautions, not every insect species in the study area might be doing well; some could be thriving, others not so much.

“We do need to understand better what kind of insects are affected and to which degree,” Bonn says. “I think the generalization that all agriculture is bad — I wouldn’t say so.”

The findings resonate with what biologist Mark Vellend and his colleagues have seen in their studies of trees at the edge of boreal forests in eastern Canada. They’ve found that spruce, eastern white cedar, eastern hemlock and American beech have been struggling to maintain their roothold since European and American settlers began clearing land more than a century ago. But poplar, paper birch, maple and balsam fir are thriving³. Vellend, who teaches at the University of Sherbrooke in Quebec, Canada, poses a question to his students every year: if they were to count the plant species in the province, would the number have gone up or down since Europeans arrived?

Most students so far have got it wrong. “Many of them are surprised to learn that there’s 25% more [species] than there were 500 years ago, before people of European origin laid a foot here,” Vellend says.



Humans are driving one million species to extinction

Something odd is going on in biodiversity studies. Scientists have long warned that animal and plant species are disappearing at an alarming rate. In 2019, an international group of hundreds of researchers produced the most comprehensive report on biodiversity ever assembled, and they concluded that some [one million animals and plant species are facing extinction](#). On top of that, humans have cleared landscapes and chopped down nearly one-third of the world’s forests since the Industrial Revolution — all of which bodes poorly for protecting species.

So, scientists naturally assumed that they would find precipitous declines in biodiversity nearly everywhere they looked. But they haven’t. And a consensus is emerging that, even though species are disappearing globally at alarming rates, scientists cannot always detect the declines at the local level. Some species, populations and ecosystems are indeed crashing, but others are ebbing more slowly, holding steady or even thriving. This is not necessarily good news. In most places, new species are moving in when older ones leave or blink out, changing the character of the communities. And that has important implications, because biodiversity at the small scale

has outsize importance; it provides food, fresh water, fuel, pollination and many ecosystem services that humans and other organisms depend on.

“Ecosystems don’t work at the global scale,” says Maria Dornelas, an ecologist at the University of St Andrews, UK. “I’m interested in what is happening to biodiversity at the local scale, because that’s the scale that we experience.”

Scientists say it’s clear that there’s a biodiversity crisis, but there are many questions about the details. Which species will lose? Will new communities be healthy and desirable? Will the rapidly changing ecosystems be able to deal with climate change? And where should conservation actions be targeted?

To find answers, scientists need better data from field sites around the world, collected at regular intervals over long periods of time. Such data don’t exist for much of the world, but scientists are trying to fill the gaps in Europe. They are planning a comprehensive network, called EuropaBON, that will combine research plots, citizen scientists, satellite sensors, models and other methods to generate a continuous stream of biodiversity data for the continent. The effort will inform European policymakers, who are pushing for a strong and verifiable global biodiversity agreement when nations next meet to renew the United Nations’ Convention on Biological Diversity (CBD) — an international pact to halt and reverse biodiversity loss.

How to measure biodiversity

Biological diversity is a shape-shifting term that has been used in many ways. The CBD takes a broad approach, defining it as “the variability among living organisms from all sources”. This includes, it says, “diversity within species, between species and of ecosystems”.

“Everybody could sign up to such a definition,” says Chris Thomas, an ecologist at the University of York, UK. “It means that different people can pick on different aspects that are all included within that all-encompassing definition, and find almost whatever trend they want.”

Scientists measure biodiversity through many metrics, but the most common is species richness: a simple count of the number of species in the area. They also check the relative abundance of different organisms — a metric called species evenness — and track the identity of species to learn the ‘community composition’. Further complicating matters, scientists sometimes tally biomass instead of species richness, especially when it comes to insects.

Using such measures, the clearest signal that the world is losing biodiversity comes from the bookkeeper of species, the International Union for Conservation of Nature. It has found that 26% of all mammals, 14% of birds and 41% of amphibians are currently threatened globally. Insufficient data are available for other groups, such as most plants and fungi. Extinction rates in the past few centuries are much higher than they had been before humans started to transform the planet; some estimates suggest current rates are 1,000 times the background level. One calculation estimates that, if high rates continue, then within 14,000 years, we could enter the sixth mass extinction — an event similar to the one that wiped out about three-quarters of the planet’s species, including dinosaurs, 65 million years ago⁴. For the most critically endangered species, the death knell could come within decades.



Lionfish have invaded the Red Sea, one example of species changes seen in many places. Credit: Alexis Rosenfeld/Getty

More bad news comes from the United Nations-backed Intergovernmental Science-Policy Platform on Biodiversity and Ecosystem Services (IPBES) — the organization behind the 2019 report warning that about one million species were threatened by extinction. The report also found that the abundance of native species in local terrestrial ecosystems has dropped by an average of around 20% as a result of human activities.

Another biodiversity report that draws considerable attention comes from the conservation organization WWF and the Zoological Society of London, among other groups. Every year, they produce the Living Planet Index, which has amassed data for 27,695 populations of 4,806 vertebrate species. Last year, the report stated that population sizes of birds, mammals, fish, amphibians and reptiles declined, on average, by 68% between 1970 and 2016.

Some researchers worry that such averaged figures can hide a lot of nuance, because many people might assume incorrectly that the average applies to

most species. Dornelas likes to illustrate the danger by pointing out that the ‘average human’ has one breast and one testicle, and doesn’t exist.



Why deforestation and extinctions make pandemics more likely

Last year, Brian Leung, a biologist at McGill University in Montreal, and his colleagues re-analysed the Living Planet Index data from 2018 and found that a handful of populations are declining catastrophically, strongly pulling down the average. If these outliers are dropped from the computation, 98.6% of the populations on the index are holding steady or increasing or declining more slowly⁵. “We’re not saying there are not problems,” says Leung, who stresses that declines are still bad. “But there should be some caution about using these really broad-based global metrics, even though they are pretty powerful statements. But they can mask a whole lot of variation and be driven by extreme outliers.”

When scientists talk about the world entering a sixth mass extinction, what sometimes gets lost is the timescale. Extinction rates for past periods of Earth’s history are calculated per one million years, and at present, researchers are seeing vertebrate species disappear at a rate of about 1% every century, and most of that has happened on islands.

It’s clear there is a biodiversity crisis right now, although the pace is uncertain, says Henrique Pereira, a conservation biologist at the German Centre for Integrative Biodiversity Research , and a co-chair of an IPBES

expert group. “It doesn’t mean that there is no decline. It means that if there is a decline, it’s much smaller than what maybe we thought.”

So is the sixth mass extinction happening? “Well, not yet, if you want my scientific assessment of it. But is it going to be starting? Yes, maybe starting,” says Pereira.

Difficult message

In 2012, Vellend and his colleagues decided to see what’s happening with plant biodiversity by looking at a collection of individual field sites around the world. They compiled more than 16,000 studies in which scientists had monitored plants for at least 5 years, and found that only 8% of the studies noted a strong decline in the total number of species. Most plots showed either no change, smaller declines or even an increase in biodiversity⁶.

The study was rejected by *Nature*, and one reviewer worried that journalists would garble the results and give the false impression that there were no problems with biodiversity. A *Nature* spokesperson says the peer-review process is confidential and that editorial decisions are not driven by considerations of potential media coverage. (*Nature*’s news team is editorially independent of its journal team.)



An experiment to trap and identify moth species in the Netherlands.Credit: Edwin Giesbers/Nature Picture Library

Vellend eventually published the study in the *Proceedings of the National Academy of Sciences* in 2013⁶.

His conclusions were soon backed up by Dornelas and her colleague Anne Magurran, an ecologist at the University of St Andrews, who have been compiling a database of biodiversity field studies, called BioTIME, since 2010. The database now has more than 12 million records for about 50,000 species from 600,000 locations around the world.

In a study of 100 field sites worldwide, Dornelas and her colleagues had expected to find declines in species richness and abundance, but the data showed otherwise. Many sites were declining in biodiversity, but an equal proportion were improving. And about 20% showed no change over time. Overall, there wasn't a clear trend⁷.

At first, the researchers didn't believe the results, so they reanalysed the data several ways and finally published the findings in 2014.

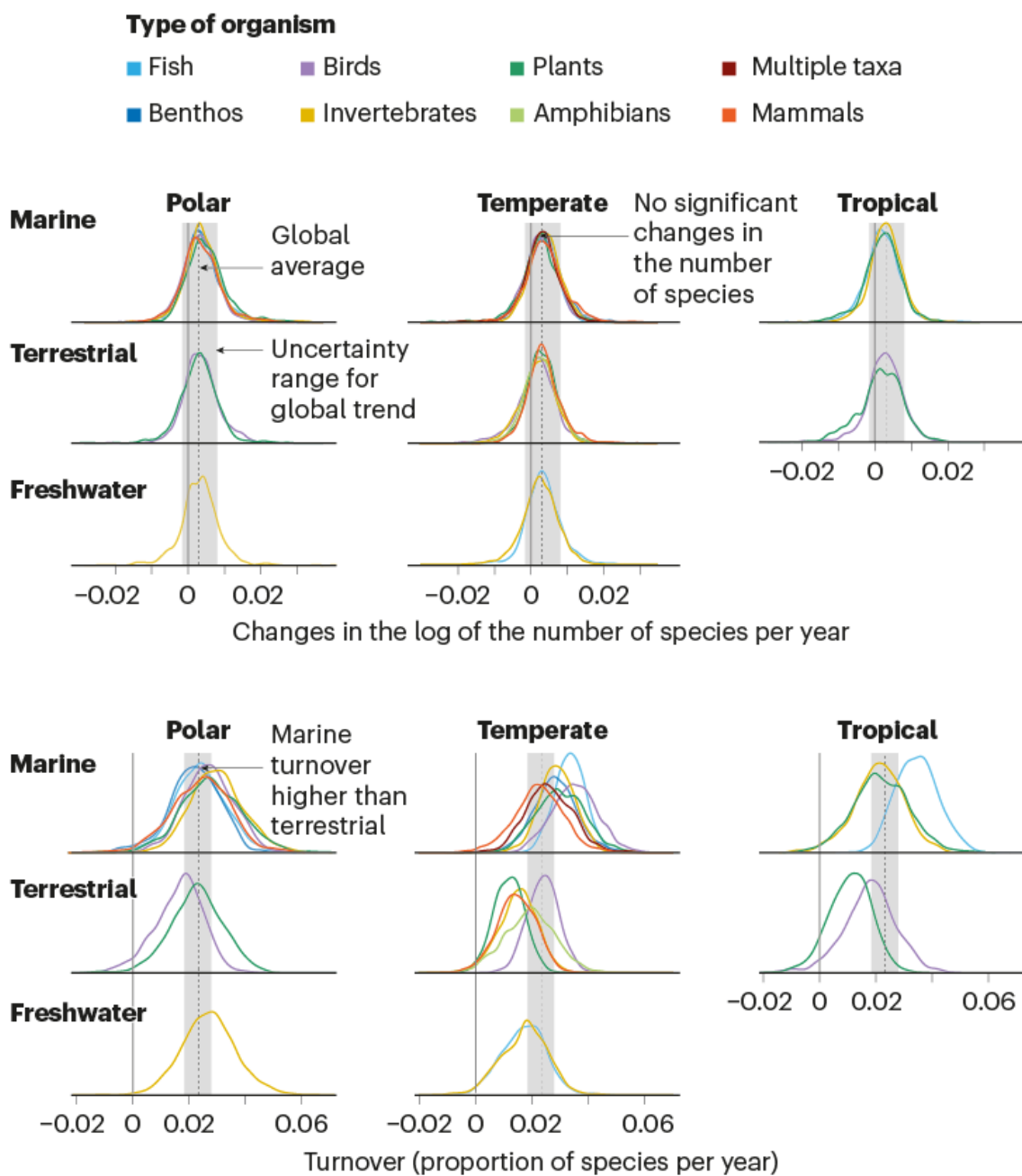
“It was this tremendous shock. What’s going on?” says Pereira, who wasn’t involved in the study.

Dornelas says reactions were mixed. Some people worried that the results could be misconstrued to suggest that everything’s fine with biodiversity. Others went even further. “Some people questioned our integrity, which is something that I take offence at, because being an ethical scientist is at the core of what I do,” she says. “But other people reached out to us and said, ‘Oh, interesting, that sort of matches my experience.’”

Since then, many studies looking at biodiversity in the oceans, rivers, among insects — almost any grouping or biome one can think of — have found that there is no clear trend of decline. But that doesn’t mean the ecosystems are remaining static. Dornelas and her colleagues have continued to mine the BioTime database and have found that the mix of species in local communities is changing rapidly almost everywhere on Earth⁸ (see ‘Life on the go’). As some inhabitants disappear, colonizers move in and add to species richness, so the ‘average ecosystem’ shows no change or even an increase in the number of species, she says, with her usual cautions about averages⁹.

LIFE ON THE GO

A meta-analysis of 239 biodiversity studies found that, at the local level, there was not much change in species richness — the number of organisms in a community — over the span of each study. But there was considerable turnover in most groups and locations, as some species left and others moved in.



©nature

Source: Ref. 8

“Species are at the moment playing musical chairs,” says Dornelas.

This can be seen most clearly on isolated islands, where 95% of the world’s extinctions have happened. Take New Zealand, where there were no mammalian predators before humans first settled there, less than 800 years ago. Since then, nearly half of New Zealand’s endemic birds have gone extinct.

But despite the extinctions, biodiversity, measured by species richness, has improved over time in New Zealand, Vellend says. Continental birds have replaced the lost endemics. Plant biodiversity is doing well; fewer than 10 native species have gone extinct, and there are now 4,000 plant species on the islands, up from 2,000 before human settlers. And there are more than two dozen new land mammals.

The lesson is that species richness or abundance figures might not tell the whole story, says Dornelas. Rather, scientists need to know the identity of all the species in a community, and track their relative abundances. This will allow them to learn which species are declining and which could be targeted for conservation.

The story is similar on the continents, except with fewer complete extinctions. In Denmark over the past 140 years, 50 plant species have declined in abundance and range, but 236 have expanded their habitats. The large majority are holding steady¹⁰. Scientists looking at Europe’s birds since 1980 have found that 175 species are declining while 203 are increasing¹¹. Rare birds are doing better than more common species, such as the house sparrow (*Passer domesticus*). A study of vertebrates in North America and Europe by Leung and his colleagues found that, whereas amphibians are declining across the board, other taxa have winners and losers in roughly equal measure¹².

Even corals seem to show the same pattern: between 1981 and 2013, 26 genera in the Caribbean and Indo-Pacific became more abundant, while 31 declined¹³.

With studies piling up, it’s become increasingly acceptable for scientists to say that biodiversity isn’t declining everywhere and for all taxa, says Dan

Greenberg, an ecologist at University of California, San Diego. “The tide is turning,” he says, “but the field is grappling with how to translate that to a public audience, or what does that mean in terms of social consequences.”

That doesn’t mean there’s no biodiversity crisis, stresses Helmut Hillebrand, an ecologist at the University of Oldenburg in Germany. Some scientists worry that unusually high turnover, together with signals of instability in some populations, could itself portend ecological collapse. Humans are carrying species into new environs, leading to colonization. Whereas climate change is spurring warm-loving species to expand into new zones, cold-adapted species are losing out. Plus, generalist species that are fast-growing and less particular about where they live are thriving in human-modified landscapes.

Specialists that need highly specific environments or that disperse poorly get easily isolated, which increases their extinction risk, says Greenberg. Case in point: amphibians. “If something changes in that environment, you can’t really hop over to another site very easily,” he says.



The battle for the soul of biodiversity

Turnover could lead to distant communities that increasingly resemble each other — a process called homogenization that has been documented in particular regions and taxa. In 2015, César Capinha, a biogeographer at the

University of Lisbon, and his colleagues found that snail populations in temperate regions as far flung as Virginia, New Zealand and South Africa had species in common, thanks to human travel and trade¹⁴. Similarly, in the plant study in Denmark, scientists found that plant communities are increasingly looking like each other and are dominated by generalists. Scientists worry that such landscapes might not be resilient to environmental change.

Dornelas urges caution in interpreting the changes seen so far. There hasn't yet been a robust global study of homogenization to know the extent to which this is happening. And there is also increased habitat fragmentation, which can counter this process. "We don't often talk about both of those at the same time," Dornelas says. "I've now learned not to assume I know what's going on until I've seen what the data show."

Scientists have also observed cases in which a colonizer mixes with a resident to rapidly form a new hybrid species, especially in plants, says Thomas. But it's unclear how long these hybrids will persist, and most other groups usually take one million years or so to form new species. Many of the beasts of today could go extinct before that process can catch up, says Dolph Schlüter, an evolutionary biologist at the University of British Columbia in Vancouver, Canada. "We are going to lose a lot of the ancients. And no amount of evolution in the short term is going to replace those," Schlüter says.

Keeping tabs on life

Global studies of biodiversity have important biases owing to data gaps. Most of the records of species come from Europe and North America; there are very few data from the tropics, where rainforests house half of all species in just 7% of the Earth's surface. And even in the most richly monitored places on Earth, such as Europe, the data are patchy. "We are trying to read the book, but we have only a few letters," says Pereira.

Pereira and his colleagues are designing a top-down monitoring network in Europe called EuropaBON that can add in more letters, and maybe even sentences. The project has received 3 million (US\$3.5 million) from the

European Commission, and was launched last December. Pereira and Jessica Junker, the scientific coordinator of EuropaBON and a conservationist at Martin Luther University Halle-Wittenberg in Germany, have assembled a 350-strong community of national conservation authorities, non-governmental organizations, scientists and government officials. Among the first goals is to create a map that identifies data gaps as well as a list of metrics to be tracked, Pereira says. At the end of the initial three-year stage, EuropaBON aims to set up a coordinating centre for the monitoring network.

It'd have to be affordable to be replicable and maintained over time. Lack of funds has hampered a global version of this project, called GEO BON, on which EuropaBON is based, says Dornelas. To contain costs, EuropaBON intends to use existing long-term monitoring sites. Where there are data gaps, the scientists would launch new tracking efforts using technology such as sensors, weather radar and drones, or citizen volunteers, who already do 80% of the biodiversity monitoring in Europe.

EuropaBON would also use satellite data of land cover, vegetation growth and other indicators of local biodiversity. The data streams would be combined with modelling to generate seamless biodiversity data over time and across Europe. The plan is that data from the project will help the European Commission to decide what research to fund on the continent's biodiversity, says Pereira. In a stakeholder meeting in May for EuropaBON, Humberto Delgado Rosa, the director for natural capital at the European Commission, said that the European Union wants to make "huge leaps internationally in biodiversity, as it has done with climate in Paris". EuropaBON should help Europe to meet its international commitments to report on its biodiversity, Rosa said.

"This new global biodiversity framework needs quantification, measurability," he said. "In a nutshell, we need knowledge."

Dornelas, who is also part of EuropaBON, says she would like to expand this initiative across the world. Canada is exploring a national version, called CanBON. But for now, monitoring remains sparse in the poorer parts of the world, where most of the planet's biodiversity remains.

“Europe is one of the best monitored parts of the planet, and where we’re really, really missing data is from other parts of the world,” she says. “But I guess we got to start somewhere.”

Nature **596**, 22–25 (2021)

doi: <https://doi.org/10.1038/d41586-021-02088-3>

References

1. 1.

Hallmann, C. A. *et al.* *PLoS ONE* **12**, e0185809 (2017).

[PubMed](#) [Article](#) [Google Scholar](#)

2. 2.

Svenningsen, C. S. *et al.* Preprint at bioRxiv
<https://doi.org/10.1101/2020.09.16.299404> (2020).

3. 3.

Danneyrolles, V. *et al.* *J. Ecol.* **109**, 273–283 (2021).

[Article](#) [Google Scholar](#)

4. 4.

McGill, B. J., Dornelas, M., Gotelli, N. J. & Magurran, A. E. *Trends Ecol. Evol.* **30**, 104–113 (2015).

[PubMed](#) [Article](#) [Google Scholar](#)

5. 5.

Leung, B. *et al.* *Nature* **588**, 267–271 (2020).

[PubMed](#) [Article](#) [Google Scholar](#)

6. 6.

Vellend, M. *et al.* *Proc. Natl Acad. Sci. USA* **110**, 19456–19459 (2013).

[PubMed](#) [Article](#) [Google Scholar](#)

7. 7.

Dornelas, M. *et al.* *Science* **344**, 296–299 (2014).

[PubMed](#) [Article](#) [Google Scholar](#)

8. 8.

Blowes, S. A. *et al.* *Science* **366**, 339–345 (2019).

[PubMed](#) [Article](#) [Google Scholar](#)

9. 9.

Dornelas, M. *et al.* *Ecol. Lett.* **22**, 847–854 (2019).

[PubMed](#) [Article](#) [Google Scholar](#)

10. 10.

Nielsen, T. F., Sand-Jensen, K., Dornelas, M. & Bruun, H. H. *Ecol. Lett.* **22**, 1650–1657 (2019).

[PubMed](#) [Article](#) [Google Scholar](#)

11. 11.

Burns, F. *et al.* Preprint at Authorea

<https://doi.org/10.22541/au.162557488.83915072> (2021).

12. 12.

Leung, B., Greenberg, D. A. & Green, D. M. *Divers. Distrib.* **23**, 1372–1380 (2017).

[Article](#) [Google Scholar](#)

13. 13.

Edmunds, P. J. *et al.* *PLoS ONE* **9**, e107525 (2014).

[PubMed](#) [Article](#) [Google Scholar](#)

14. 14.

Capinha, C., Essl, F., Seebens, H., Moser, D. & Pereira, H. M. *Science* **348**, 1248–1251 (2015).

[PubMed](#) [Article](#) [Google Scholar](#)

[Download references](#)

Related Articles



- [**The battle for the soul of biodiversity**](#)



- [**Humans are driving one million species to extinction**](#)



- [**Why deforestation and extinctions make pandemics more likely**](#)



- [Fewer than 20 extinctions a year: does the world need a single target for biodiversity?](#)

Subjects

- [Biodiversity](#)
- [Ecology](#)
- [Environmental sciences](#)

nature careers

[Jobs](#) >

- [Translational Biologist, Oncology](#)

Astex Pharmaceuticals Limited

Cambridge, United Kingdom

- [Postdoctoral Researcher – studying the histopathology of acute ischaemic stroke blood clots and the correlation of composition with impedance measurements\(CÚRAM\), NUIG RES 158-21](#)

National University of Ireland Galway (NUI Galway)

Galway, Ireland

- [Summer Laboratory Technician](#)

Oklahoma Medical Research Foundation (OMRF)

Oklahoma City, United States

- [PhD student \(m/f/d\) Hormonal programming of hepatic chromatin landscapes](#)

Technical University of Munich (TUM)

Munich, Germany

Nature Briefing

An essential round-up of science news, opinion and analysis, delivered to your inbox every weekday.

[Download PDF](#)

Related Articles



- [The battle for the soul of biodiversity](#)



- [Humans are driving one million species to extinction](#)



- [Why deforestation and extinctions make pandemics more likely](#)



- [Fewer than 20 extinctions a year: does the world need a single target for biodiversity?](#)

Subjects

- [Biodiversity](#)
 - [Ecology](#)
 - [Environmental sciences](#)
-

This article was downloaded by **calibre** from <https://www.nature.com/articles/d41586-021-02088-3>

| [Section menu](#) | [Main menu](#) |

- NEWS FEATURE
- 03 August 2021

Why sports concussions are worse for women

As women's soccer, rugby and other sports gain popularity, scientists are racing to understand how the female brain responds to head injury.

- [Katharine Sanderson](#) ⁰
 1. Katharine Sanderson is a freelance journalist based in Cornwall, UK.

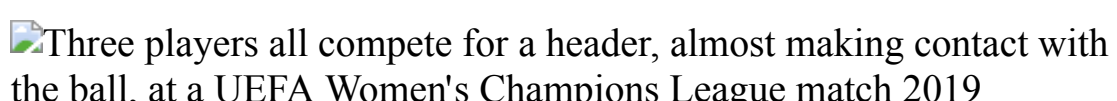
[View author publications](#)

You can also search for this author in [PubMed](#) [Google Scholar](#)





•



Football players jump for a header at a UEFA women's Champions League match in Décines-Charpieu, France, in March 2019. Credit: Jeff Pachoud/AFP/Getty

[Download PDF](#)

Liz Williams was standing pitchside at a women's rugby match, and she did not like what she was seeing. Williams, who researches forensic biomechanics at Swansea University, UK, had equipped some of the players

with a mouthguard that contained a sensor to measure the speed of head movement. She wanted to understand more about head injuries in the brutal sport. “There were a few instances when my blood went cold,” Williams said.

When the women fell in a tackle, their heads would often whiplash into the ground. The sensors showed that the skull was accelerating — indicating an increased risk of brain injury. But medical staff at the match, not trained to look out for this type of head movement as a cause of injury, deemed the women fine to play on. Such whiplash injuries are much rarer when males play.

Williams’ observations highlight an increasingly apparent problem. A growing body of data suggests that female athletes are at significantly greater risk of a traumatic brain injury event than male athletes. They also fare worse after a concussion and take longer to recover. As researchers gather more data, the picture becomes steadily more alarming.

Female athletes are speaking out about their own experiences, including Sue Lopez, the United Kingdom’s first semi-professional female football player in the 1970s, who now has dementia — a diagnosis she has linked to concussions from heading the ball.



[Head-injury risk higher for female soccer players, massive survey finds](#)

Researchers have offered some explanations for the greater risk to women, although the science is at an early stage. Their ideas range from differences in the microstructure of the brain to the influence of hormones, coaching regimes, players' level of experience and the management of injuries.

Given that most, if not all, sports-concussion protocols are based on data from men, female athletes ranging from schoolgirls to this year's Olympic football squads are being put at risk of serious injury. "We take all of these data, primarily from studies on men; we apply them to women. That's just got to change," says Michael Grey, who researches rehabilitation neuroscience at the University of East Anglia in Norwich, UK.

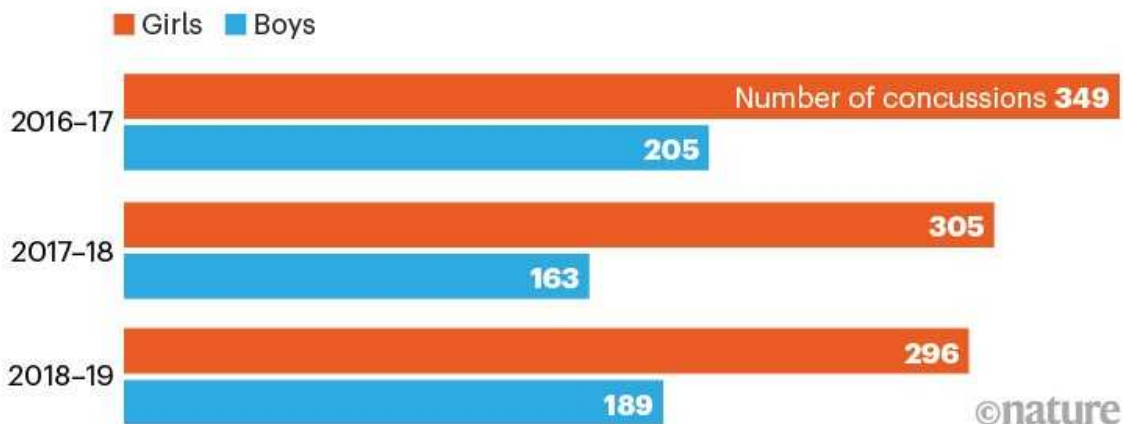
Head injuries in sport have had a high profile for many years, with hundreds, if not thousands, of participants in American football, rugby, football, boxing and other sports experiencing dementia or memory loss thought to be linked to recurrent blows to the head decades earlier. Coaching protocols at all levels are changing to try to prevent injury, but these have generally neglected to include a huge cohort: women.

Bigger risk

Studies from US collegiate sports have shown that female athletes are 1.9 times more likely to develop a sports-related concussion than are their male contemporaries in comparable sports¹. Those female students also missed many more study days as they recovered. Neuropathologist Willie Stewart at the University of Glasgow, UK, co-authored a study published earlier this year² of [more than 80,000 secondary-school soccer players in the United States](#), with similar results (see 'Concussion risk').

CONCUSSION RISK

A survey of more than 80,000 secondary-school soccer players in Michigan found that girls are nearly twice as likely as boys to experience concussions.



Source: Ref. 2

It's not just the number of head injuries that differs between women and men, but also their nature. A review of 25 studies of sport-related concussion suggests that female athletes are not only more susceptible to concussion than are males, but also sustain more-severe concussions³.

Athletics trainer and sports scientist Tracey Covassin at Michigan State University in East Lansing was one of the first to look at the differences between the sexes, starting in the early 2000s. She was interested in concussion, but noticed that all the data were coming from male-dominated sports in the United States: ice hockey, boxing and American football. In more than 20 papers over almost two decades, Covassin has shown that there are sex differences in concussion rates and recovery times. In 2013, for instance, she published work on concussed soccer players in the United States⁴, and showed that the female players scored lower in memory tests and experienced more symptoms than did their male contemporaries.

As-yet-unpublished research by Williams on female rugby players — among the first studies to analyse sex-specific mechanisms of head injury in the sport — showed that more than 50% of the 25 female participants experienced injuries caused by their head whiplashing into the ground,

whereas only one male player did. “I didn’t expect that. That’s an important discovery,” says Grey, who has seen Williams’s results.

The actions leading to head injuries in female players might also be different. In Stewart’s soccer study², the girls were most likely to injure themselves when they made contact with an object (such as the ball, when heading it for example), whereas the boys were more likely to make contact with another player. Whether this is a matter of coaching, an individual’s level of playing experience or something else isn’t yet known.

Why women fare worse

The damage that causes concussion can be quite subtle. The brain can’t move that much in the skull, explains Stewart. “The brain virtually fills the intracranial cavity, and there’s a little thin film of fluid that fills up what space is left.” But, in the split second after an impact, the head rapidly decelerates, and the resulting forces transmit deep inside the brain. The gelatinous grey matter undergoes significant shear forces when the head stops suddenly, pushing and pulling the brain tissue in a way that can cause structural damage.



A player is treated for a head injury during this year's Women's Six Nations rugby tournament.Credit: Andrew Milligan/PA Images/Alamy

And those forces can affect the brains of men and women in profoundly different ways. Doug Smith at the University of Pennsylvania's Penn Center for Brain Injury and Repair in Philadelphia uncovered evidence that could be crucial for explaining some of the different outcomes seen in women versus men: their brain cells are structurally different.

Every neuron has a major fibre called the axon, which is responsible for transmitting electrical signals from cell to cell. Damage to axons, through strong shear forces, is thought to be the main reason that concussions occur. "Your brain literally can break," says Smith, holding up some silly putty during a video call to demonstrate. When stretched gently, the silly putty deforms and then relaxes back into shape. When yanked violently, it snaps.

Inside each axon, tiny protein tunnels, called microtubules, that give cells their structure behave similarly, Smith says. These microtubules, only 25 nanometres wide, carry proteins in the axons and help them to function. If a microtubule is damaged, its protein cargo builds up, causing inflammation and ultimately a breakage, explains Smith. "And if you disconnect an axon, it's gone forever."

Smith's team knew from imaging and brain-tissue studies that axon fibres from the brains of female rats and humans are slimmer than those from males. They wanted to know more about the differences and what effect they might have on brain injury, so they cultured rat neurons and then damaged them by exposing them to a rapid air blast. In the neurons from female rats, the axons were smaller and the microtubules narrower and more susceptible to damage than in the cells from males. The same was true for cultured human neurons⁵.

Knowing the extent of axonal damage could be an indicator of how well someone could recover from a concussion. In a sports setting, this could be used to determine when an athlete is safe to return to the field, perhaps in the form of a blood test. Smith is now trying to find biomarkers of axonal damage in the blood — for instance, proteins that leak from axons when they are harmed. He's doing studies on professional ice-hockey players and

measuring axonal protein levels in blood before and after injury. “We did find out that some of these proteins and protein fragments, at a certain level, will actually predict who’s going to have a poor outcome,” says Smith.



A rugby player is fitted with a sensor-equipped mouthguard during a study in New Zealand. Credit: Joe Allison/World Rugby/Getty

Grey urges caution in extrapolating too much from Smith’s work on neurons in culture, which is mainly in rats. “Now that’s not to say that I disagree,” he adds. “It’s just that we need to be cautious. This is one study. I personally think there are other issues that are more important.”

One of those might be differences in neck strength, which some researchers think could have a considerable role in mitigating the damage wrought by concussion. Williams’ mouthguard study also measured neck strength to see what sex differences there are. She found that female players’ necks were 47% weaker than men’s. Williams is working on improving neck strength in female rugby players to understand whether specific training could lessen the likelihood of concussion.

Not everyone agrees, however, that neck strength is the problem, or the answer. Stewart isn't convinced by any of the studies showing that neck strength is a factor in increasing the risk of a concussion, or a factor in improving the outcome of concussions.



Researchers seek definition of head-trauma

Some researchers, including Grey, favour the idea that concussion is aggravated by the hormones that govern the menstrual cycle.

In 2014, Jeff Bazarian, a physician specializing in brain injury at the University of Rochester Medical Center in New York, published a paper⁶ that showed a clear correlation between the menstrual cycle and how women recover from a traumatic brain injury. His team found that women who arrived at the emergency department with a head injury sustained while they were in the luteal phase of the menstrual cycle, which begins after ovulation and is when progesterone levels are highest, fared worse a month later than did women who hit their heads during the follicular stage, which marks the start of a new cycle and ends at ovulation. Women who were taking oral contraceptives, which balance out hormone levels, also fared better.

Initially, this seems counter-intuitive, because progesterone has been shown to have a neuroprotective effect⁷, and the luteal phase is when that hormone peaks. But other studies have reported an association between progesterone

and concussion⁸. Martina Anto-Ocrah, a reproductive epidemiologist at the University of Rochester who has continued Bazarian's work, says this is because the brain injury causes progesterone levels to abruptly plummet⁹.

Anto-Ocrah became interested in concussion and female sexual health after seeing evidence from the US National Football League that some 30 years after sustaining concussions, male athletes were experiencing low testosterone levels and erectile dysfunction. "But there was nothing in the literature for women. I started thinking, why are we not looking at how concussion affects female reproduction, female menstruation, female sexual health?" she says.



A doctor examines an athlete for injuries during a boxing match at the Tokyo Olympics in July 2021.Credit: Ueslei Marcelino/Getty

Anto-Ocrah is discovering signs that not only does the menstrual cycle have an impact on concussion but, conversely, head injuries can affect the menstrual cycle and other aspects of reproductive function by interfering with the brain regions that, in tandem with other glands in the body, help to control levels of oestrogen and progesterone.

Treating women differently

One thing scientists agree on is the need for more research about women who sustain head injuries. In sports, this could transform the concussion treatment protocols, recovery experiences and the return to play. In July, World Rugby, rugby union's global governing body, made a [statement committing to conduct research into injury-prevention programmes specific to women](#), and stressing the need for such initiatives. Grey says he knows of no sports bodies that have actually implemented woman-specific concussion measures or protocols.

Research funders are beginning to recognize the need to study sports concussions separately in men and women. The US National Institute of Neurological Disorders and Stroke (NINDS) has allotted a total of US\$6.8 million over five years to two large projects studying sex differences in concussion and its assessment.

As part of this push for more data, in 2019, Stewart and his collaborator Katherine Snedaker, who runs PINK Concussions, an advocacy group for women's head injury, put out a call for more female athletes to pledge their brains to the Glasgow traumatic brain-injury archive he curates. Stewart's team plans to use the archive to investigate further how traumatic brain injury harms brain tissue and alters gene expression, and how it might go on to cause degenerative brain disease. Of the 1,800 or so donated brains in the archive, 75% are from men; fewer than 200 are from athletes and none of those is from a woman, although a number of high-profile UK-based female athletes have pledged their brains, including Scottish footballer Rose Reilly, judo international Connie Ramsay and Scottish rugby star Lee Cockburn.

Prompted by what she saw on the pitch, and facing some enforced downtime during the COVID-19 pandemic, Williams put together a survey of almost 2,000 female rugby players from 56 countries, who answered questions about their experiences of concussion. Early results suggest that players vary hugely in their knowledge of how to recognize and deal with brain injuries.

Williams says that her work, and that of others, is slowly gaining traction. In April, the University of Otago in Dunedin, New Zealand, [announced the](#)

[start of a study](#) in collaboration with World Rugby that will use a mouthguard to quantify aspects of head injuries in both male and female rugby players.

There are bright spots, but at the moment, Grey says, sports bodies mostly ignore the steadily building knowledge about sex differences in concussion. The male game is still the priority, says Stewart. “There’s this general focus on male sport, male injury and male outcomes, and less on female. It’s terrible neglect.”

Nature **596**, 26-28 (2021)

doi: <https://doi.org/10.1038/d41586-021-02089-2>

References

1. 1.

Bretzin, A. C. *et al. Am. J. Sports Med.* **46**, 2263–2269 (2018).

[PubMed](#) [Article](#) [Google Scholar](#)

2. 2.

Bretzin, A. C., Covassin, T., Wiebe, D. J. & Stewart, W. *JAMA Netw. Open* **4**, e218191 (2021).

[PubMed](#) [Article](#) [Google Scholar](#)

3. 3.

McGroarty, N. K., Brown, S. M. & Mulcahey, M. K. *Orthop. J. Sports Med.* **8**, 2325967120932306 (2020).

[PubMed](#) [Article](#) [Google Scholar](#)

4. 4.

Covassin, T., Elbin, R. J., Bleeker, A., Lipchik, A. & Kontos, A. P. *Am. J. Sports Med.* **41**, 2890–2895 (2013).

[PubMed](#) [Article](#) [Google Scholar](#)

5. 5.

Dollé, J.-P. *et al. Exp. Neurol.* **300**, 121–134 (2018).

[PubMed](#) [Article](#) [Google Scholar](#)

6. 6.

Wunderle, K., Hoeger, K. M., Wasserman, E. & Bazarian, J. J. *J. Head Trauma Rehabil.* **29**, E1–E8 (2014).

[PubMed](#) [Article](#) [Google Scholar](#)

7. 7.

Wei, J. & Xiao, G.-M. *Acta Pharmacol. Sin.* **34**, 1485–1490 (2013).

[PubMed](#) [Article](#) [Google Scholar](#)

8. 8.

di Battista, A. P. *et al. Sci. Rep.* **9**, 18605 (2019).

[PubMed](#) [Article](#) [Google Scholar](#)

9. 9.

Snook, M. L., Henry, L. C., Sanfilippo, J. S., Zeleznik, A. J. & Kontos, A. P. *JAMA Pediatr.* **171**, 879–886 (2017).

[PubMed](#) [Article](#) [Google Scholar](#)

[Download references](#)

Related Articles

-  [Head-injury risk higher for female soccer players, massive survey finds](#)
-  [Researchers seek definition of head-trauma](#)
-  [Head injuries in sport must be taken more seriously](#)

Subjects

- [Biomechanics](#)
- [Brain](#)
- [Medical research](#)

nature careers

[Jobs](#) >

- [Translational Biologist, Oncology](#)

Astex Pharmaceuticals Limited

Cambridge, United Kingdom

- [Summer Laboratory Technician](#)

Oklahoma Medical Research Foundation (OMRF)

Oklahoma City, United States

- [PhD student \(m/f/d\) Hormonal programming of hepatic chromatin landscapes](#)

Technical University of Munich (TUM)

Munich, Germany

- [Postdoctoral Researcher – studying the histopathology of acute ischaemic stroke blood clots and the correlation of composition with impedance measurements\(CÚRAM\), NUIG RES 158-21](#)

National University of Ireland Galway (NUI Galway)

Galway, Ireland

Nature Briefing

An essential round-up of science news, opinion and analysis, delivered to your inbox every weekday.

[Download PDF](#)

Related Articles



- [Head-injury risk higher for female soccer players, massive survey finds](#)



- **Researchers seek definition of head-trauma**



- **Head injuries in sport must be taken more seriously**

Subjects

- Biomechanics
- Brain
- Medical research

This article was downloaded by **calibre** from <https://www.nature.com/articles/d41586-021-02089-2>

Books & Arts

- **[The COVID vaccine makers tell all](#)** [02 August 2021]

Book Review • A book from the Oxford–AstraZeneca team, and a documentary, go behind the scenes in the race to vaccinate the world.

- **[Cooperation's pros and cons, construction decarbonized, and into the wild: Books in brief](#)** [16 July 2021]

Book Review • Andrew Robinson reviews five of the week's best science picks.

- BOOK REVIEW
- 02 August 2021

The COVID vaccine makers tell all

A book from the Oxford–AstraZeneca team, and a documentary, go behind the scenes in the race to vaccinate the world.

- [Heidi Ledford](#)
 1. Heidi Ledford
[View author publications](#)

You can also search for this author in [PubMed](#) [Google Scholar](#)





•

[Download PDF](#)



Catherine Green (left) and Sarah Gilbert developed a COVID-19 vaccine. Credit: Lewis Khan

Vaxxers: The Inside Story of the Oxford AstraZeneca Vaccine and the Race Against the Virus *Sarah Gilbert & Catherine Green* Hodder & Stoughton (2021)

The Vaccine Directors: *Catherine Gale & Caleb Hellerman* Wingspan (2021)

Last August, biologist Catherine Green was camping with her daughter in Wales when a chance conversation at the pizza van turned to a familiar topic: COVID-19. “We don’t know what they put in these vaccines,” a fellow camper told her. “I don’t trust them. They don’t tell us the truth.”

Green was uniquely placed to know. She runs a clinical biomanufacturing facility at the University of Oxford, UK, and is part of a team that had developed a COVID-19 vaccine that was in clinical trials at the time. Pharmaceutical company AstraZeneca of Cambridge, UK, aims to produce three billion doses of this vaccine for distribution around the world by the

end of 2021, significantly protecting people from severe disease and death. Yet, nearly a year after Green's encounter, conspiracy theories continue to stymie take-up of COVID-19 vaccines, risking lives both in regions where doses are abundant, and in those where there are precious few. In April, the non-profit Kaiser Family Foundation, based in San Francisco, California, found that 54% of US adults either believe common misinformation about COVID-19 vaccines or think that it might be true (see go.nature.com/3fyfaoi).

It was with the epidemic of misinformation in mind, Green says, that she and Oxford vaccinologist Sarah Gilbert decided to write *Vaxxers*, a behind-the-scenes story that attempts to humanize vaccine-making in the hope of boosting trust. The book, along with *The Vaccine* — a documentary commissioned by the BBC and CNN Films — offers a welcome glimpse inside the race to develop COVID-19 vaccines in the middle of a raging pandemic.



[Vaccines stop diseases safely — why all the suspicion?](#)

The book and documentary are a useful pairing. The film follows five research groups as they forgo sleep and family time to develop vaccines using approaches ranging from tried-and-true inactivated viruses to cutting-edge messenger RNA techniques. The book is a deep dive with one team as it juggles funding stress, press interviews and domestic responsibilities. All

the groups painstakingly balance the need to be careful and methodical with the pressure to create and test a vaccine faster than ever before. They carry the hopes of the world — and they know it.

The film's images reveal the toll of relentless stress. At the University of Queensland in Brisbane, Australia, virologist Keith Chappell's eyes grow progressively redder and his clothing more dishevelled. The slump in his shoulders after he learns in December that his protein vaccine must be abandoned is heartbreakingly clear. Wu Guizhen, a biosafety specialist at the Chinese Center for Disease Control and Prevention in Beijing, describes her coping mechanisms: "When it feels like you're too tired to go forward," she says, "my solution is to sleep for a bit while standing."

The documentary occasionally slips into a prominent narrative of the time: the idea of a race between the groups to build a vaccine first. Media stories sometimes framed this as a quest for profit, but the real race, Green and Gilbert repeatedly emphasize, was always against the virus and its mounting death toll, not the other groups.

Leap into action

The Oxford–AstraZeneca story begins around 2014, as Gilbert hops between grants and contracts at Oxford, scraping together laboratory funds. They look for ways first to develop an Ebola vaccine and then to prepare for a future epidemic "Disease X". The identity of this illness was uncertain, but its eventual arrival was never in doubt.

Soon after news of SARS-CoV-2 arrives in early January 2020, Gilbert and Green decide that COVID-19 could be Disease X. They risk their reputations and a substantial amount of Oxford's money to prepare a vaccine, even before the need becomes clear. Although I have reported on many aspects of COVID-19 vaccine development over the past year, I was surprised to learn the extent to which they had to gamble in those early days, without knowing if funding would come through — and that the vials of vaccine used in the first clinical trials were filled by hand at Oxford's facility.



COVID vaccines: time to confront anti-vax aggression

From April, a collaboration with AstraZeneca boosts their manufacturing capabilities. But it comes with a dash of culture clash between the small, nimble academic lab and the corporate behemoth. This collaboration, as well as one with the Serum Institute of India in Pune, and an early insistence on minimizing the price and making the vaccine available to the world, have helped to ensure that Gilbert and Green's early gambles have global impact.

There are details about some of the more frustrating moments in the Oxford–AstraZeneca vaccine's development. This includes an explanation of why some clinical-trial participants received different amounts of vaccine, and waited for different lengths of time between doses. Both of these incidents complicated interpretation of study results.

Other key moments get less attention. There is no reference to South Africa's February decision not to use its doses of the Oxford–AstraZeneca vaccine, because the jab failed to prevent infections with the Beta variant of SARS-CoV-2 sweeping the region. And safety concerns over an extremely rare but potentially deadly blood-clotting disorder that might be associated with the vaccine are mentioned only briefly. Yet the resulting fears and roll-out pauses threw a huge spanner in the works.

Hidden heroes

Still, the book highlights the under-sung research behind vaccines, and the need to promote it. The authors repeatedly emphasize how development was accelerated not by skipping safety steps, but by taking financial risks, such as running various testing stages concurrently. Developers must usually ensure that one step is successful before moving to the next.

Throughout, food metaphors make the people and science relatable. The first viral cultures are like a sourdough starter; the conventional process of getting a lab result, then applying for funding for the next step, is like having to make a separate run to the shops for each ingredient in a roast dinner. The biggest mystery, ultimately, is how the authors found time to write the book in the middle of it all.

Although the chronology of events and science sometimes get jumbled — readers are given a detailed explanation of the chewy “replication-deficient recombinant simian adenoviral-vectored vaccine” well before they are introduced to the basics of how vaccines work — Green and Gilbert lay everything out clearly, from molecular biology to clinical-trial design. There is even a handy appendix listing the ingredients of the vaccine and what each does.

It would be wonderful if that were enough to quell the sort of concerns Green heard at the campsite. Sadly, it is hard to imagine that even her down-to-earth charm can compete with the flood of anti-vaccine propaganda that fills social-media feeds. Even so, it is worth a try.

Nature **596**, 29-30 (2021)

doi: <https://doi.org/10.1038/d41586-021-02090-9>

Competing Interests

The author declares no competing interests.

Related Articles



- [Six months of COVID vaccines: what 1.7 billion doses have taught scientists](#)



- [Vaccines stop diseases safely — why all the suspicion?](#)



- [COVID vaccines: time to confront anti-vax aggression](#)



- [Vaccines — lessons from three centuries of protest](#)



- [COVID-19 vaccines: how to ensure Africa has access](#)

Subjects

- [SARS-CoV-2](#)
- [Drug discovery](#)
- [Medical research](#)
- [Public health](#)

Jobs >

- [Translational Biologist, Oncology](#)

Astex Pharmaceuticals Limited

Cambridge, United Kingdom

- [Postdoctoral Researcher – studying the histopathology of acute ischaemic stroke blood clots and the correlation of composition with impedance measurements\(CÚRAM\), NUIG RES 158-21](#)

National University of Ireland Galway (NUI Galway)

Galway, Ireland

- [Summer Laboratory Technician](#)

Oklahoma Medical Research Foundation (OMRF)

Oklahoma City, United States

- [PhD student \(m/f/d\) Hormonal programming of hepatic chromatin landscapes](#)

Technical University of Munich (TUM)

Munich, Germany

Nature Briefing

An essential round-up of science news, opinion and analysis, delivered to your inbox every weekday.

[Download PDF](#)

Related Articles

-  [Six months of COVID vaccines: what 1.7 billion doses have taught scientists](#)
-  [Vaccines stop diseases safely — why all the suspicion?](#)
-  [COVID vaccines: time to confront anti-vax aggression](#)
-  [Vaccines — lessons from three centuries of protest](#)
-  [COVID-19 vaccines: how to ensure Africa has access](#)

Subjects

- [SARS-CoV-2](#)
- [Drug discovery](#)
- [Medical research](#)
- [Public health](#)

This article was downloaded by **calibre** from <https://www.nature.com/articles/d41586-021-02090-9>

| [Section menu](#) | [Main menu](#) |

- BOOK REVIEW
- 16 July 2021

Cooperation's pros and cons, construction decarbonized, and into the wild: Books in brief

Andrew Robinson reviews five of the week's best science picks.

- [Andrew Robinson](#) 0
 - 1. [Andrew Robinson](#)
 - 1. Andrew Robinson's many books include *Lost Languages: The Enigma of the World's Undeciphered Scripts* and *Einstein on the Run: How Britain Saved the World's Greatest Scientist*. He is based in London.

[View author publications](#)

You can also search for this author in [PubMed](#) [Google Scholar](#)





•

[Download PDF](#)

The Social Instinct

How Cooperation Shaped the World



Nichola Raihani

The Social Instinct

Nichola Raihani *Jonathan Cape* (2021)

Cooperation is a double-edged sword. Within totalitarian nations and between democratic ones, it dominated the Second World War. But working together also created a post-war consensus that paved the way for the UK National Health Service and gender equality. If used well, cooperation delivers riches, but “in the wrong hands or used in the wrong ways”, it brings ruin, observes psychologist Nichola Raihani. Her rewarding analysis ranges from genetics to politics, and from the individual to the international, including the COVID-19 pandemic.



ROOTS TO SEEDS

400 YEARS OF OXFORD BOTANY

Stephen A. Harris

Roots to Seeds

Stephen A. Harris *Bodleian Library Publishing* (2021)

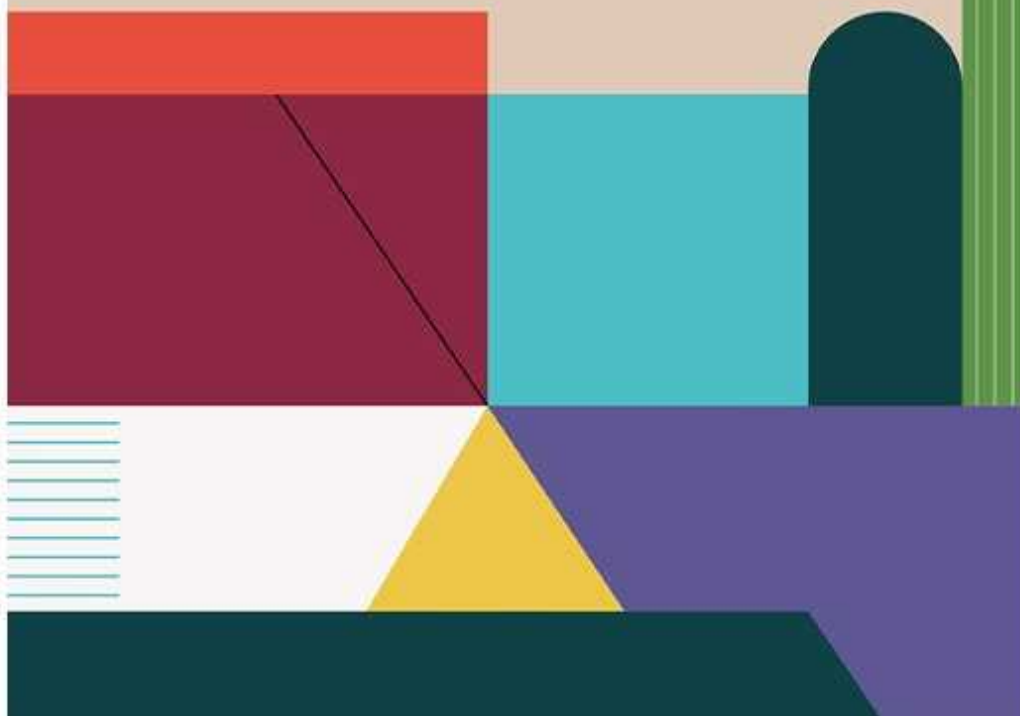
The University of Oxford's botanical garden was founded in 1621 as the Physic Garden, to support medical training. Early plants included the mandrake, with a homunculus-like root thought to emit a lethal shriek if pulled up, notes plant scientist Stephen Harris. His history of the garden, accompanying a Bodleian Library exhibition, displays diverse illustrations and portraits. Authoritative and gorgeous, it is also honest: "Oxford's success at both the generation of botanical knowledge and its dispersal over four centuries has been very patchy."

A PELICAN BOOK

Architecture

From Prehistory to Climate Emergency

Barnabas Calder



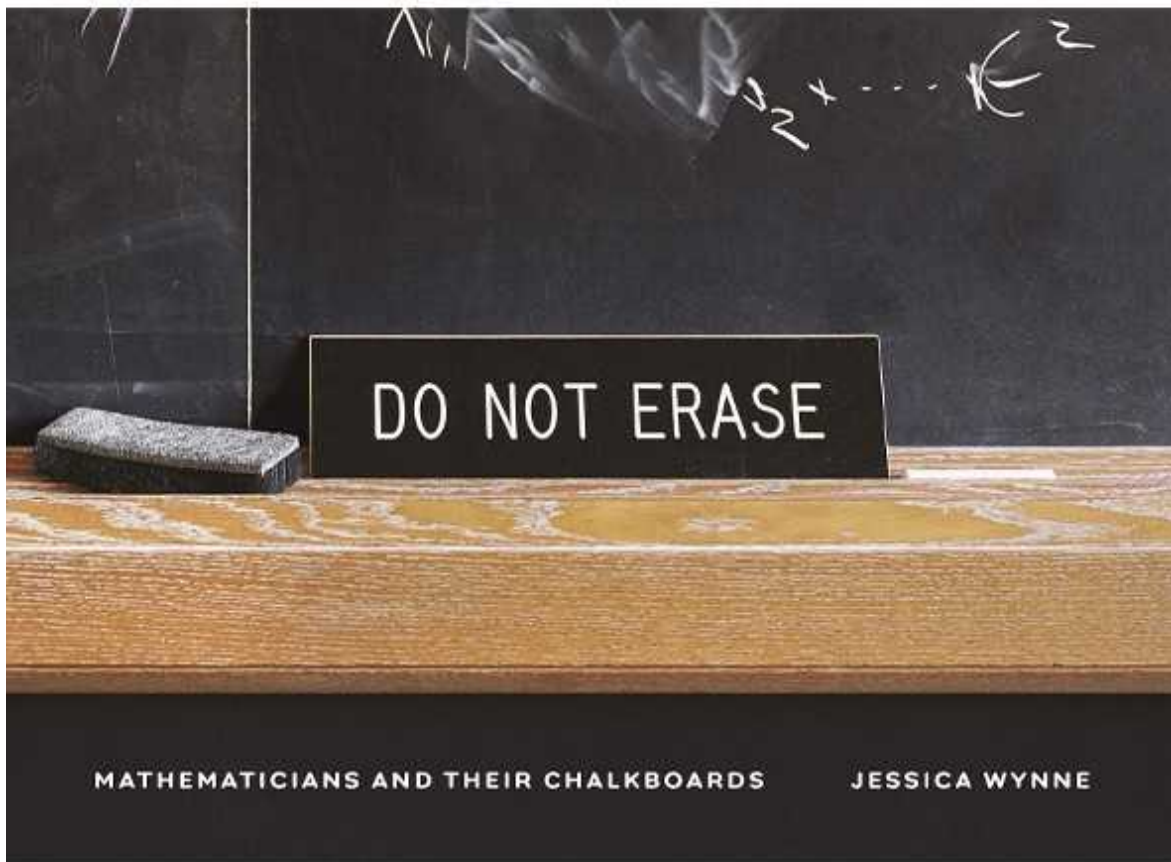
Architecture

Barnabas Calder *Pelican* (2021)

Constructing and running buildings produces 39% of global human greenhouse-gas emissions, notes historian Barnabas Calder in his powerful, disturbing account of architecture and energy since ancient times.

Construction of Egypt's Great Pyramid of Giza used less energy than is consumed over the lifetimes of seven average modern US residents; stone has a strength-to-carbon-footprint ratio 25 times better than concrete's.

Calder argues that architecture must end its reliance on fossil fuels by learning from the past, including ancient Rome.



Do Not Erase

Jessica Wynne *Princeton Univ. Press* (2021)

A blackboard filled with mathematics by Albert Einstein takes pride of place in a museum in Oxford, UK. Ironically, Einstein opposed its preservation — unlike 111 mathematicians whose hugely varying chalkboards feature in photographs by Jessica Wynne. The simplest, by Tadashi Tokieda, shows a white circle outlined against black, labelled ‘WHITE’; a second circle, filled with white, is labelled ‘BLACK’. Tokieda compares watching a board being chalked with listening to music “note by note”. This is an original, elegant, if baffling book.

WILD SOULS

FREEDOM
AND
FLOURISHING

IN THE
NON-HUMAN
WORLD

"Everybody who
cares about animals
should read this
fascinating book."

-TEMPLE GRANDIN

AUTHOR OF RAMBUNCTIOUS GARDEN

EMMA MARRIS

BLOOMSBURY

Wild Souls Emma Marris Bloomsbury (2021)

Environment writer Emma Marris begins her colourful study of wild animal–human interactions with a helicopter ride to a sanctuary in Hawaii. There, conservationists are trying to save eight bird species threatened by human influences, including mosquito-borne viruses brought in by ship in 1826. She also considers Australian bilbies, Peruvian monkeys and wolves reintroduced to Oregon. “Ecosystems are built on death”, she muses, so which ‘wild’ animals should be preserved, and which allowed to die?

Nature **596**, 30 (2021)

doi: <https://doi.org/10.1038/d41586-021-01973-1>

Competing Interests

The author declares no competing interests.

Subjects

- [Arts](#)
- [Culture](#)

nature careers

[Jobs](#) >

- [Translational Biologist, Oncology](#)

Astex Pharmaceuticals Limited

Cambridge, United Kingdom

- [Postdoctoral Researcher – studying the histopathology of acute ischaemic stroke blood clots and the correlation of composition with impedance measurements\(CÚRAM\), NUIG RES 158-21](#)

National University of Ireland Galway (NUI Galway)

Galway, Ireland

- [Summer Laboratory Technician](#)

Oklahoma Medical Research Foundation (OMRF)

Oklahoma City, United States

- [PhD student \(m/f/d\) Hormonal programming of hepatic chromatin landscapes](#)

Technical University of Munich (TUM)

Munich, Germany

Nature Briefing

An essential round-up of science news, opinion and analysis, delivered to your inbox every weekday.

[Download PDF](#)

Subjects

- [Arts](#)
- [Culture](#)

This article was downloaded by **calibre** from <https://www.nature.com/articles/d41586-021-01973-1>

Opinion

- **Test quantum mechanics in space — invest US\$1 billion** [02 August 2021]
Comment • Shooting glass beads across the inside of a satellite could probe the limits of quantum wave behaviour. Here's how.
- **Genomics of African American remains — limits must not compound inequity** [03 August 2021]
Correspondence •
- **Declare how you are limiting your environmental impact** [03 August 2021]
Correspondence •
- **India's cyclones: hasten mitigation measures** [03 August 2021]
Correspondence •

- COMMENT
- 02 August 2021

Test quantum mechanics in space — invest US\$1 billion

Shooting glass beads across the inside of a satellite could probe the limits of quantum wave behaviour. Here's how.

- [Alessio Belenchia](#)⁰,
- [Matteo Carlesso](#)¹,
- [Sandro Donadi](#)²,
- [Giulio Gasbarri](#)³,
- [Hendrik Ulbricht](#)⁴,
- [Angelo Bassi](#)⁵ &
- [Mauro Paternostro](#)⁶

1. Alessio Belenchia

1. Alessio Belenchia is a postdoctoral researcher at the Institute for Theoretical Physics, Eberhard Karls University Tübingen, Germany, and a visiting scholar at the Centre for Theoretical Atomic, Molecular and Optical Physics, Queen's University, Belfast, UK.

[View author publications](#)

You can also search for this author in [PubMed](#) [Google Scholar](#)

2. Matteo Carlesso

1. Matteo Carlesso is a postdoctoral researcher at the Centre for Theoretical Atomic, Molecular and Optical Physics, Queen's

University, Belfast, UK.

[View author publications](#)

You can also search for this author in [PubMed](#) [Google Scholar](#)

3. Sandro Donadi

1. Sandro Donadi is a postdoctoral researcher at the National Institute for Nuclear Physics (INFN), Trieste, Italy.

[View author publications](#)

You can also search for this author in [PubMed](#) [Google Scholar](#)

4. Giulio Gasbarri

1. Giulio Gasbarri is a postdoctoral researcher in the Department of Physics, Autonomous University of Barcelona, Spain.

[View author publications](#)

You can also search for this author in [PubMed](#) [Google Scholar](#)

5. Hendrik Ulbricht

1. Hendrik Ulbricht is a professor of physics in the School of Physics and Astronomy, University of Southampton, UK.

[View author publications](#)

You can also search for this author in [PubMed](#) [Google Scholar](#)

6. Angelo Bassi

1. Angelo Bassi is professor of physics in the Department of Physics, University of Trieste, Italy, and member of the National Institute for Nuclear Physics (INFN), Trieste, Italy.

[View author publications](#)

You can also search for this author in [PubMed](#) [Google Scholar](#)

7. [Mauro Paternostro](#)

1. Mauro Paternostro is a professor of quantum optics and quantum information science and head of the School of Mathematics and Physics, Queen's University, Belfast, UK.

[View author publications](#)

You can also search for this author in [PubMed](#) [Google Scholar](#)

•



•

[Download PDF](#)



Christina Koch on the International Space Station, with hardware used to probe the quantum effects of gases chilled to almost absolute zero. Credit: NASA

Where does the shift from quantum to classical reality take place? To find out, physicists are testing whether molecules of ever-larger size behave like waves. When these particles are shot through narrow slits, they produce a striped interference pattern, just like light or water waves would.

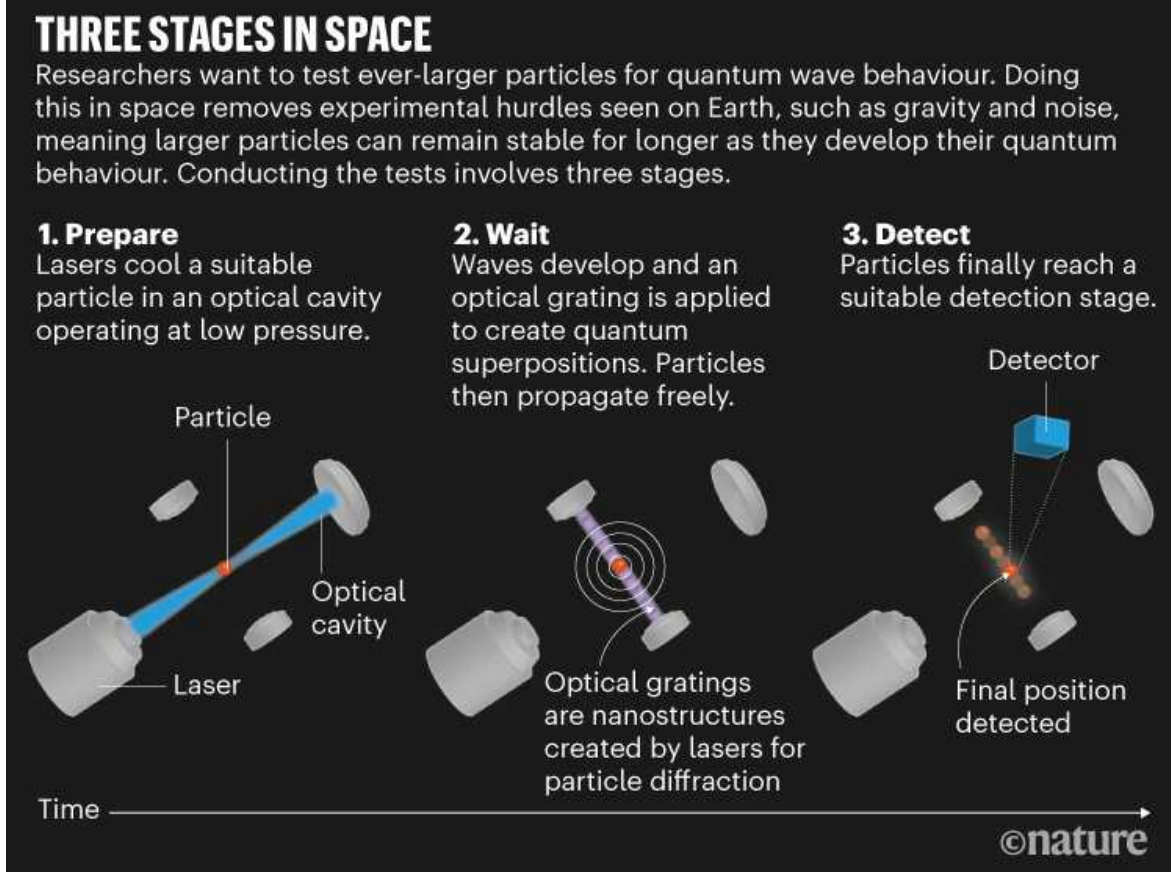
The holder of the current size record for this wave behaviour is a molecule thousands of times smaller than a speck of dust or a bacterium (these span tens to hundreds of nanometres or more). Called oligoporphyrin, it is made of 2,000 atoms, measures 5–6 nanometres across and weighs around 25,000 atomic mass units^{1,2} (amu; 1 amu is one-twelfth the mass of an atom of carbon-12). The technological implications of finding even larger objects displaying quantum behaviour are tantalizing.

But there are limits to what can be done in the laboratory³. Quantum-matter interferometers are complex, bulky and difficult to calibrate. The apparatus must be shielded from outside gases, light and vibrations. The larger a

particle gets, the more likely it is to interact with its surroundings, washing out its quantum behaviour. It takes longer to produce interference, because the quantum waves spread more slowly. That means keeping the particle stable for longer.

Gravity is a limitation. Tabletop experiments can run for only a few seconds before the particles fall onto the bench. Particles larger than a few tens of nanometres would require tens of seconds to generate an interference pattern (for example, it would take 100 seconds for particles with a mass of 10^{11} amu to reveal fringes). Introducing lasers or magnetic fields to buoy up the particles adds noise and complications.

The answer is to work in space (see ‘Three stages in space’).



Source: Source: Belenchia *et al.*

Orbital offers

In microgravity, test particles would float freely for minutes. They would fall towards Earth at the same rate as the satellite they were in. An equivalent experiment on Earth lasting 100 seconds would be like controlling a particle while it drops from a height of 50 kilometres.

Major challenges must be overcome. The whole set-up should be designed for the specific particles being deployed — taking into account their sizes and electric charges, for example. And it must be able to operate in the harsh environment of space, showered with cosmic rays, solar wind and ionizing radiation. The experiment's size and weight must be constrained. The satellite's motion needs to be considered, and noise (such as vibrations from engines) will have to be minimized.

Interest in taking quantum technology into space is growing. Yet, so far, most nations have focused on devices that have commercial or security applications. For example, in 2016, the Chinese satellite Micius demonstrated quantum-encrypted communication between Beijing and Vienna⁴. A [German team in 2017](#) and a [NASA collaboration in 2020](#) produced a Bose–Einstein condensate in space — a quantum system with potential for sensing and metrology.

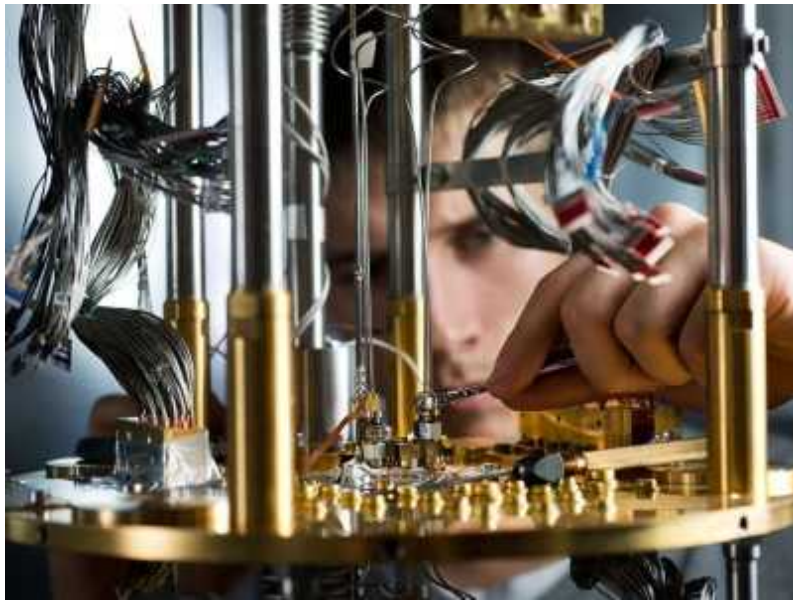
A quantum interferometer for large particles would be much more complicated. Putting one in orbit would require great technical, technological and scientific leaps. Here we set out the main research challenges and make the case for establishing a billion-dollar international collaboration to achieve this breakthrough.

Quantum physicists and space engineers need to do the following.

Select particles

Physicists need to assess the mass, size and shape of the test particles that would be used, as well as their chemical, electrical and optical properties. All of these will dictate the experiment's design. The payload must be able to handle particles with a range of masses and sizes, to track how quantum behaviour scales. Charges will need to be controlled down to the level of individual electrons, to minimize noise. The nanoparticles should be able to

interact with the lasers used to control and detect them, yet not absorb stray light.



Keep quantum computing global and open

Glass nano-beads are good test candidates. These nanometre-sized spheres made of silica or hafnium dioxide are already widely used in ground-based experiments. Other materials, such as gold or diamond, might also be suitable.

A large number of experimental runs will be needed to assure the particles' quality and to prove that the experiment works. Techniques will need to be developed for repeating experiments reliably and efficiently, under stable conditions and with minimal interventions. Physicists will need to design automated methods for loading, capturing and reusing the nano-particles. Promising approaches being explored include using piezoelectric transducers to catapult particles to the spot where they will be used, or nebulizers that spray particles stored in solution.

Choose gratings and detectors

A grating — a series of slits — must be placed along the path of the particles to reveal their quantum behaviour (see ‘Quantum test’). This is typically a

solid mask. However, such masks can trap large particles, reducing the grating's effectiveness. Optical gratings are an alternative widely used on the ground, in which laser light acts as a grid. Precise modelling will be required to understand how the particles interact with the light. Industry will need to develop lasers that remain stable for lengthy experiments, as well as modulators that can change light intensity in milliseconds.

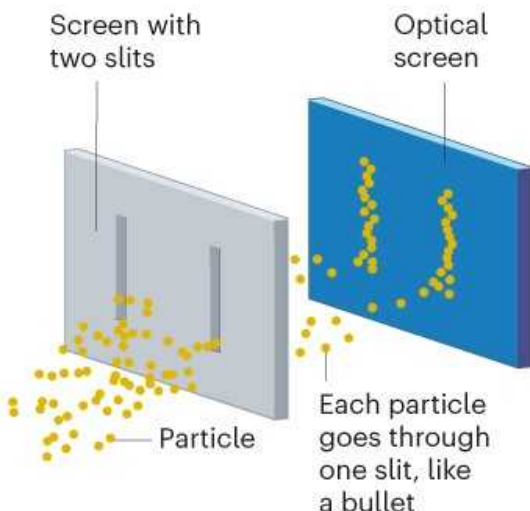
Finally, the particles' positions must be detected after they have passed through the grating. At a minimum, devices should be able to measure the locations to within one-tenth of the distance between interference fringes. Capturing light scattered by the particle is an established technique that can be translated into space.

QUANTUM TEST

Physicists fire particles through slits or gratings to test whether they behave like quantum waves.

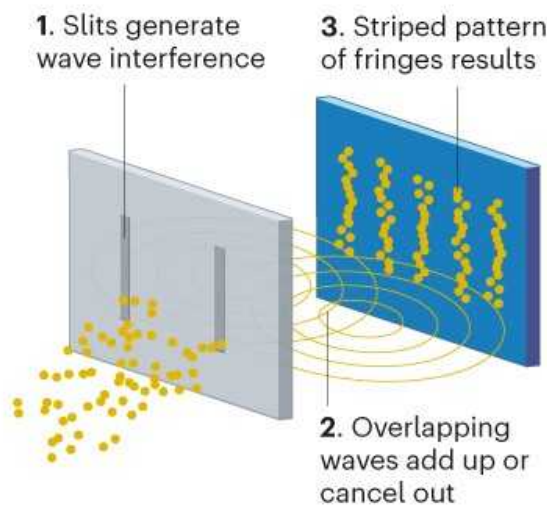
Classical

Particles pile up behind slits.



Quantum

Particles act as waves.



©nature

Source: Belenchia *et al.*

Address cooling, vacuum and noise

Before test particles enter the interferometer, they must be cooled to states that have minimal energy and motion (around 10^{-6} kelvin). This can be done

using lasers, with methods used on the ground. The whole experimental apparatus would also need to be cooled down. Temperatures of 0.1 K have been achieved in space using cryostat devices based on mixtures of helium isotopes. However, the amount of helium required limits the mission's lifetime. Researchers need to weigh up such trade-offs.

Ultra-high vacuum conditions are also essential. Collisions with gas molecules or dust motes, brought from Earth, would disrupt the nanoparticles' quantum behaviour. A vacuum pressure of around 10^{-11} pascals or less would be needed to hold nanospheres with masses larger than 10^{11} amu stable for the 100 seconds it takes to measure fringes, for example. Although this is possible on the ground, it is much harder in an enclosed chamber in space, because vacuum pumps generate vibrations. One solution is to coat the inside of the chamber with films that catch stray gas particles, such as an alloy based on titanium, zirconium and vanadium, which is being developed at CERN, Europe's particle-physics lab near Geneva, Switzerland.



[Quantum computing's reproducibility crisis: Majorana fermions](#)

All sources of noise must be minimized. These include mechanical vibration, interactions with gases, and showers of solar radiation, micro-meteoroids and ions. Quantum physicists working with engineers at the European Space Agency (ESA) have drawn up technical plans for dealing

with each of these, for future missions⁵. However, the techniques have yet to be demonstrated together in a single experiment.

Techniques for isolating vibrations have been developed, for example, by the LISA Pathfinder mission. This spacecraft, launched in 2015, tested technologies for the Laser Interferometer Space Antenna (LISA), an ESA-led gravitational-wave observatory planned for launch in 2034. LISA Pathfinder controlled noise well enough to measure relative accelerations between two masses (each weighing 2 kg) of up to $10^{-14} g$, where g is the acceleration caused by the gravitational pull of Earth (see go.nature.com/3zkawmp). So far, this is one of the best performances reported. By comparison, that's like tracking a mass as it takes one day to travel one-tenth of a millimetre. Interferometric quantum experiments will need to reach similar levels with much smaller masses.

Find stable orbits

Space engineers must establish which orbits to put the satellite in to avoid jostling the particles. The main aim is to minimize acceleration and other changes in gravitational forces.

Suitable paths have been suggested. For example, the spacecraft effectively ‘hovers’ at points where the gravitational pulls and centrifugal forces of its orbital motion balance each other. ESA supports the idea of a satellite orbiting around such a point 1.5 million kilometres directly ‘behind’ Earth as viewed from the Sun — known as L2. Earth is always visible at this position, making communication easier. (The Planck satellite currently sits here, as will the James Webb Space Telescope.)

Alternatives include the L1 point, where the gravitational forces of the Sun and Earth on the satellite are opposed. At L1, also about 1.5 million kilometres from Earth, the satellite orbits the Sun at the same angular speed as Earth does. (This spot is currently home to the Solar and Heliospheric Observatory satellite.)

Invest and collaborate

When implemented in space, the costs of testing the limits of quantum superposition — being in two or more different physical states at the same time, which is the fundamental property of quantum systems — will exceed current national research budgets. LISA Pathfinder cost more than €430 million (US\$508 million), the Chinese Micius was more than \$100 million and the NASA-led experiment taking a Bose–Einstein condensate on the (already very costly) International Space Station was about \$70 million. By comparison, UK support for its Quantum Technologies for Fundamental Physics programme is only £31 million (\$43 million). Tabletop interferometry experiments cost just a few million euros.

Instead, a supranational collaboration needs to be established with an overall budget of at least €1 billion, including Earth-based activities. By comparison, this is the entire budget of the [EU Quantum Flagship programme](#). Skills need building and collaborations strengthening: between public and private sectors, academics, agencies and companies that have track records at the interface of quantum and space technology (such as Airbus Defense and Space in Portsmouth, UK, OHB System in Bremen, Germany and Thales Alenia Space in Cannes, France)⁶.



[Four steps to global management of space traffic](#)

Europe has taken the lead. Large-particle interferometry is one of three priority areas (together with cold atoms and entangled photon experiments)

in the most recent ESA Intermediate Strategic Report, issued in 2017. A dedicated mission might be launched by the late 2030s⁵. Large-mass quantum tests are slated for later medium-class missions, as highlighted in ESA's longer-term road map, Voyage 2050, announced in June.

Since 2017, the European Union has invested €500,000 in QTSpace, a project aimed at building a quantum space community involving researchers and companies from 46 countries (www.qtospace.eu). The Quantum Space Network initiative — a parallel body to the Quantum Community Network established within the EU Quantum Flagship programme — is liaising with policymakers, funding bodies and ESA. Other nations, scientists, agencies and companies now need to get on board. Fragmenting efforts will only delay progress. European researchers have already seen how pooling effort through the EU has sped up the pace of advances.

Critics will say that it's unnecessary to set up yet another billion-dollar programme in fundamental physics, especially in a world grappling with COVID-19 and climate change. We contend that the payback could be vast in terms of new knowledge and technologies, even within a decade. Investments in the space sector will contribute to the recovery of the global economy.

Such a dialogue should begin at the next European Quantum Technology Virtual Conference, being held online at the end of November. Membership of the Quantum Space Network and Quantum Community Network should be extended to representatives of NASA and the Micius team at the Chinese Academy of Sciences, as well as to other major players in the quantum space race, from Canada to Singapore and Japan.

Protection of intellectual property and sharing of technologies and data security should be high on the agenda. These issues have hindered the establishment of a transcontinental framework in quantum tech before. In this respect, the recent EU decision to allow non-EU countries such as the United Kingdom and Israel to bid for Horizon Europe funding in quantum and space programmes is a positive signal.

doi: <https://doi.org/10.1038/d41586-021-02091-8>

References

1. 1.

Fein, Y. Y. *et al.* *Nature Phys.* **15**, 1242–1245 (2019).

[Article](#) [Google Scholar](#)

2. 2.

Gerlich, S. *et al.* *Nature Phys.* **3**, 711–715 (2007).

[Article](#) [Google Scholar](#)

3. 3.

Gasbarri, G., Belenchia, A., Paternostro, M. & Ulbricht, H. *Phys. Rev. A* **103**, 022214 (2021).

[Article](#) [Google Scholar](#)

4. 4.

Liao, S.-K. *et al.* *Nature* **549**, 43–47 (2017).

[PubMed](#) [Article](#) [Google Scholar](#)

5. 5.

European Space Agency. *CDF Study Report. QPPF: Assessment of Quantum Physics Payload Platform* (ESA, 2018).

[Google Scholar](#)

6. 6.

Jones, K. L. *Public–Private Partnerships: Stimulating Innovation in the Space Sector* (Center for Space Policy and Strategy, 2018).

[Google Scholar](#)

[Download references](#)

Competing Interests

The authors declare no competing interests.

Related Articles



- [Quantum computing's reproducibility crisis: Majorana fermions](#)



- [Universe's coolest lab creates bizarre quantum matter in space](#)



- [Minuscule drums push the limits of quantum weirdness](#)



- [Keep quantum computing global and open](#)

-  [Explore space using swarms of tiny satellites](#)
-  [Four steps to global management of space traffic](#)

Subjects

- [Quantum physics](#)
- [Space physics](#)

nature careers

[Jobs](#) >

- [Translational Biologist, Oncology](#)

Astex Pharmaceuticals Limited

Cambridge, United Kingdom

- [Postdoctoral Researcher – studying the histopathology of acute ischaemic stroke blood clots and the correlation of composition with impedance measurements\(CÚRAM\), NUIG RES 158-21](#)

National University of Ireland Galway (NUI Galway)

Galway, Ireland

- [Summer Laboratory Technician](#)

Oklahoma Medical Research Foundation (OMRF)

Oklahoma City, United States

- [PhD student \(m/f/d\) Hormonal programming of hepatic chromatin landscapes](#)

Technical University of Munich (TUM)

Munich, Germany

Nature Briefing

An essential round-up of science news, opinion and analysis, delivered to your inbox every weekday.

[Download PDF](#)

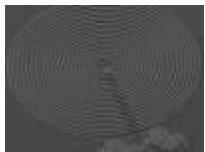
Related Articles



- [Quantum computing's reproducibility crisis: Majorana fermions](#)



- [Universe's coolest lab creates bizarre quantum matter in space](#)



- [Minuscule drums push the limits of quantum weirdness](#)

-  [Keep quantum computing global and open](#)
-  [Explore space using swarms of tiny satellites](#)
-  [Four steps to global management of space traffic](#)

Subjects

- [Quantum physics](#)
- [Space physics](#)

This article was downloaded by **calibre** from <https://www.nature.com/articles/d41586-021-02091-8>

| [Section menu](#) | [Main menu](#) |

- CORRESPONDENCE
- 03 August 2021

Genomics of African American remains — limits must not compound inequity

- [Fatimah Jackson](#)⁰,
- [Carter Clinton](#)¹ &
- [Joseph Graves](#)²

1. [Fatimah Jackson](#)

1. Howard University, Washington DC, USA.

[View author publications](#)

You can also search for this author in [PubMed](#) [Google Scholar](#)

2. Carter Clinton

1. Pennsylvania State University, University Park, USA.

[View author publications](#)

You can also search for this author in [PubMed](#) [Google Scholar](#)

3. Joseph Graves

1. North Carolina Agricultural and Technical State University, Greensboro, USA.

[View author publications](#)

You can also search for this author in [PubMed](#) [Google Scholar](#)

-



•

[Download PDF](#)



Students at Howard University in Washington DC survey a former African American cemetery. Credit: Robert A. Reeder/The Washington Post via Getty

We agree that African American skeletal remains must be treated with dignity and diligence (see [J. Dunnivant et al. Nature 593, 337–340; 2021](#)). But we caution against any stifling of high-quality, ethical, quantitative genomic inquiry that might be imposed by an African American Graves Protection and Repatriation Act (AAGPRA). Restrictions must not compound existing disadvantages in health and education. DNA studies can support oral histories; they can provide the strongest objective case for reparations for past offences of enslavement and institutionalized racism; and they can increase opportunities for precision medicine.

Rather than being constrained, researchers working with the consent of and on behalf of African American communities should feel empowered to use DNA analysis to take charge of hypothesis testing and define the resulting interpretative narrative. Such analyses do not always require the destruction of skeletal remains. In an unpublished investigation of the seventeenth- and eighteenth-century New York African Burial Ground, we detected human-

associated bacteria in 69 soil samples; we generated human microbiome profiles for each individual and identified pathogenic bacteria in some cases. This information creates a form of identity for the buried person and helps us to learn more about their living conditions and possible cause of death.

Furthermore, such ethical genomic enquiry helps to close the representation gap for people of African descent in genomic databases. This gap denies access to gene therapy and precision medicine ([G. Sirugo et al. Cell 177, 26–31; 2019](#)).

Therefore, we propose that the AAGPRA be explicitly crafted to do several things in addition to those Dunnivant *et al.* propose. It should: require the recruitment and training of Black and brown forensic scientists in each of the facilities currently curating remains (see [go.nature.com/36qcks7](#)); increase genetic ancestry studies among African Americans and continental Africans (see [go.nature.com/3f10izf](#)); develop publicly available databases on African-American biological histories to increase interdisciplinary research on this population; and drive the identification of disease biomarkers in African American skeletal remains that inform medicine relevant to the descendant population.

Crucially, the AAGPRA should also mandate the development of standard operating protocols for future discoveries of remains, delineating the appropriate curation and research applications of data. These protocols must be guided by the priorities of both the descendant community and the engaged scientific community. Nothing must magnify the dearth of knowledge that limits African Americans' opportunities now and in the future.

Nature **596**, 35 (2021)

doi: <https://doi.org/10.1038/d41586-021-02129-x>

Competing Interests

The authors declare no competing interests.

Related Articles

- [See more letters to the editor](#)

Subjects

- [Genetics](#)
- [History](#)
- [Society](#)

nature careers

[Jobs](#) >

- [Translational Biologist, Oncology](#)

Astex Pharmaceuticals Limited

Cambridge, United Kingdom

- [Postdoctoral Researcher – studying the histopathology of acute ischaemic stroke blood clots and the correlation of composition with impedance measurements\(CÚRAM\), NUIG RES 158-21](#)

National University of Ireland Galway (NUI Galway)

Galway, Ireland

- [Summer Laboratory Technician](#)

Oklahoma Medical Research Foundation (OMRF)

Oklahoma City, United States

- [PhD student \(m/f/d\) Hormonal programming of hepatic chromatin landscapes](#)

Technical University of Munich (TUM)

Munich, Germany

Nature Briefing

An essential round-up of science news, opinion and analysis, delivered to your inbox every weekday.

[Download PDF](#)

Related Articles

- [See more letters to the editor](#)

Subjects

- [Genetics](#)
- [History](#)
- [Society](#)

This article was downloaded by **calibre** from <https://www.nature.com/articles/d41586-021-02129-x>

| [Section menu](#) | [Main menu](#) |

- CORRESPONDENCE
- 03 August 2021

Declare how you are limiting your environmental impact

- [Paul Grogan](#)⁰,
- [Kate M. Buckeridge](#)¹ &
- [Anders Priemé](#)²

1. [Paul Grogan](#)

1. Queen's University, Kingston, Ontario, Canada.

[View author publications](#)

You can also search for this author in [PubMed](#) [Google Scholar](#)

2. Kate M. Buckeridge

1. Luxembourg Institute of Science and Technology, Belvaux, Luxembourg.

[View author publications](#)

You can also search for this author in [PubMed](#) [Google Scholar](#)

3. Anders Priemé

1. University of Copenhagen, Denmark.

[View author publications](#)

You can also search for this author in [PubMed](#) [Google Scholar](#)





•

[Download PDF](#)

Every research activity — from data collection and computational analysis to laboratory experiments and fieldwork — has an environmental impact. Many scientists recognize this, but most overlook it because they are overwhelmed by other priorities. We therefore urge funding agencies, academic institutions and publishers to ask scientists to declare what steps they will take, or have taken, to minimize the environmental impact of their work.

Scientists have a responsibility to assess each proposed research activity as a trade-off between knowledge gains and negative impacts. Consequently, some minimize the use of electricity and plastics, reuse materials where possible, share equipment and reduce air travel for conferences and fieldwork (see [J. Rosen *Nature* 546, 565–567 \(2017\)](#) and [J. Madhusoodanan *Nature* 581, 228–229; 2020](#)).

Asking scientists to declare their efforts to safeguard the environment in their grant proposals and in appendices of research papers and theses (see examples in [P. Grogan *Front. Ecol. Environ.* 19, 143; 2021](#)) will raise awareness and inspire others to change their behaviour.

Nature 596, 35 (2021)

doi: <https://doi.org/10.1038/d41586-021-02130-4>

Competing Interests

The authors declare no competing interests.

Related Articles

- [See more letters to the editor](#)

Subjects

- [Authorship](#)
- [Funding](#)
- [Publishing](#)
- [Sustainability](#)

nature careers

[Jobs](#) >

- [Translational Biologist, Oncology](#)

Astex Pharmaceuticals Limited

Cambridge, United Kingdom

- [Postdoctoral Researcher – studying the histopathology of acute ischaemic stroke blood clots and the correlation of composition with impedance measurements\(CÚRAM\), NUIG RES 158-21](#)

National University of Ireland Galway (NUIG Galway)

Galway, Ireland

- [Summer Laboratory Technician](#)

Oklahoma Medical Research Foundation (OMRF)

Oklahoma City, United States

- [PhD student \(m/f/d\) Hormonal programming of hepatic chromatin landscapes](#)

Technical University of Munich (TUM)

Munich, Germany

Nature Briefing

An essential round-up of science news, opinion and analysis, delivered to your inbox every weekday.

[Download PDF](#)

Related Articles

- [See more letters to the editor](#)

Subjects

- [Authorship](#)
 - [Funding](#)
 - [Publishing](#)
 - [Sustainability](#)
-

This article was downloaded by **calibre** from <https://www.nature.com/articles/d41586-021-02130-4>

| [Section menu](#) | [Main menu](#) |

- CORRESPONDENCE
- 03 August 2021

India's cyclones: hasten mitigation measures

- [Joyita Roy Chowdhury](#)⁰,
- [Yashobanta Parida](#)¹ &
- [Prakash Kumar Sahoo](#)²

1. [Joyita Roy Chowdhury](#)

1. FLAME University, Pune, Maharashtra, India.

[View author publications](#)

You can also search for this author in [PubMed](#) [Google Scholar](#)

2. Yashobanta Parida

1. FLAME University, Pune, Maharashtra, India.

[View author publications](#)

You can also search for this author in [PubMed](#) [Google Scholar](#)

3. Prakash Kumar Sahoo

1. Vikram Deb (Autonomous) College, Jeypore, India.

[View author publications](#)

You can also search for this author in [PubMed](#) [Google Scholar](#)





•

[Download PDF](#)

Two severe cyclones, Tauktae and Yaas, made landfall in India in May. They killed 199 people and affected 37 million more, damaging houses, infrastructure and agriculture at an estimated cost of 320 billion rupees (US\$4.3 billion). As cyclones become more frequent, putting further measures in place to mitigate the effects of such disasters is increasingly urgent.

Cyclones regularly hit India's 7,500-kilometre coastline, and about 7% of the world's tropical cyclones originate in the North Indian Ocean. Since

1999, such events have killed more than 12,000 people and caused damage worth \$32.6 billion. Improvements in early-warning systems and disaster management have helped to reduce the death toll but not the economic hit.

Embankments that are resilient to storm surges are needed urgently, along with improved prevention of flooding from swollen rivers. Shelter-belt plantations should be widened and coastal mangrove habitats regenerated. Such measures could markedly reduce the impact of India's cyclones.

Nature **596**, 35 (2021)

doi: <https://doi.org/10.1038/d41586-021-02131-3>

Competing Interests

The authors declare no competing interests.

Related Articles

- [See more letters to the editor](#)

Subjects

- [Climate sciences](#)
- [Environmental sciences](#)

nature careers

[Jobs](#) >

- [Translational Biologist, Oncology](#)

Astex Pharmaceuticals Limited

Cambridge, United Kingdom

- **Postdoctoral Researcher – studying the histopathology of acute ischaemic stroke blood clots and the correlation of composition with impedance measurements(CÚRAM), NUIG RES 158-21**

National University of Ireland Galway (NUIG Galway)

Galway, Ireland

- **Summer Laboratory Technician**

Oklahoma Medical Research Foundation (OMRF)

Oklahoma City, United States

- **PhD student (m/f/d) Hormonal programming of hepatic chromatin landscapes**

Technical University of Munich (TUM)

Munich, Germany

Nature Briefing

An essential round-up of science news, opinion and analysis, delivered to your inbox every weekday.

[Download PDF](#)

Related Articles

- **See more letters to the editor**

Subjects

- **Climate sciences**

- [Environmental sciences](#)

This article was downloaded by **calibre** from <https://www.nature.com/articles/d41586-021-02131-3>

| [Section menu](#) | [Main menu](#) |

Work

- **[Pandemic upheaval offers a huge natural experiment](#)** [02 August 2021]
Career Feature • The disruption that the coronavirus has caused to daily life has created unique research opportunities for scientists.
- **[The hunt for red fluorescent proteins](#)** [03 August 2021]
Technology Feature • By pushing fluorescent proteins further into the red, bioengineers are expanding the palette and penetration depth of biological imaging.
- **[A race against time to feed the world](#)** [02 August 2021]
Where I Work • Agrochemical scientist Sarah Iveson is excited about digital agriculture's potential to make crops more resilient to climate change as the global population grows.

- CAREER FEATURE
- 02 August 2021

Pandemic upheaval offers a huge natural experiment

The disruption that the coronavirus has caused to daily life has created unique research opportunities for scientists.

- [Julia Rosen](#) ⁰
1. Julia Rosen
 1. Julia Rosen is a freelance journalist in Portland, Oregon.

[View author publications](#)

You can also search for this author in [PubMed](#) [Google Scholar](#)





•

[Find a new job](#)

[Download PDF](#)



The project Our Ocean in COVID-19 launched in 2020 to track human–ocean interactions during the coronavirus pandemic. Credit: Andrea Marshall

Soon after COVID-19 lockdowns began in March 2020, physicians in certain nations noticed something unexpected: the number of premature births seemed to plummet. Preliminary research in one region of Ireland documented a 73% decrease in very-low-birth-weight babies¹. And scientists in Denmark measured a roughly 90% country-wide drop in extremely premature births compared with the previous five years². In Nepal, however, researchers reported³ that the risk of preterm birth — before 37 weeks of gestation — jumped by 30% during lockdown, a pandemic trend that scientists expect to find in other economically disadvantaged nations. In some countries, reports of increased numbers of stillbirths further complicated the picture⁴.

Amid this confusion, scientists saw an opportunity. “If it is real and we’re seeing differences, can we use that as a natural experiment?” says Sarah Stock, who studies maternal and fetal medicine at the University of Edinburgh, UK. Researchers still don’t understand exactly what triggers preterm birth — the leading cause of infant mortality globally — or how to prevent it. But by upending daily life in disparate ways around the world, the pandemic is offering scientists a chance to try to tease apart the role of

suspected factors such as air pollution, hygiene, access to maternity care and stress.

In wealthier nations, for instance, pregnant people might have enjoyed cleaner air and developed fewer infections while sequestered at home than they would while commuting, for example. In parts of Africa, however, stay-at-home orders might have increased exposure to smoke from cooking fires and amplified economic anxieties, says Kofi Amegah, an epidemiologist at the University of Cape Coast in Ghana. “Basically, we are locked down, we are home, we don’t have money to feed the family, and it equals to add up to stress,” he says.

Amegah, Stock and more than 150 other researchers from around the world are now analysing these differences as part of the International Perinatal Outcomes in the Pandemic (iPOP) study. The goal is to “leverage the most disruptive and widespread ‘natural experiment’ of our lifetime to make rapid discoveries about preterm birth”, the team wrote in a paper describing the study’s protocol⁵.

The effort is one of many aimed at finding a small but significant silver lining to the pandemic by using it to further scientific understanding and improve human life. By assembling and mining large data sets, asking creative questions and using careful statistical approaches to assess cause and effect, researchers can use the havoc wrought by the coronavirus to tackle a wide range of scientific questions (see ‘Seize the moment’). “We can’t underplay the horror of the pandemic,” Stock says. “But I think we’ve got to learn as much as we can from this.”

Seize the moment

The pandemic has created a natural experiment of unprecedented proportions. Here is advice for gleaning lessons from the tragic events of the past year.

Start with the obvious. See whether you find what you expect. If so, the pandemic can help to test existing hypotheses. The pandemic also provides opportunities to generate new hypotheses by revealing previously hidden mechanisms.

Leverage big data. Think creatively about how to use existing data sources. Take advantage of mobility tracking, social-media trends, satellite observations and other data sources. Make use of existing scientific databases and environmental monitoring programmes.

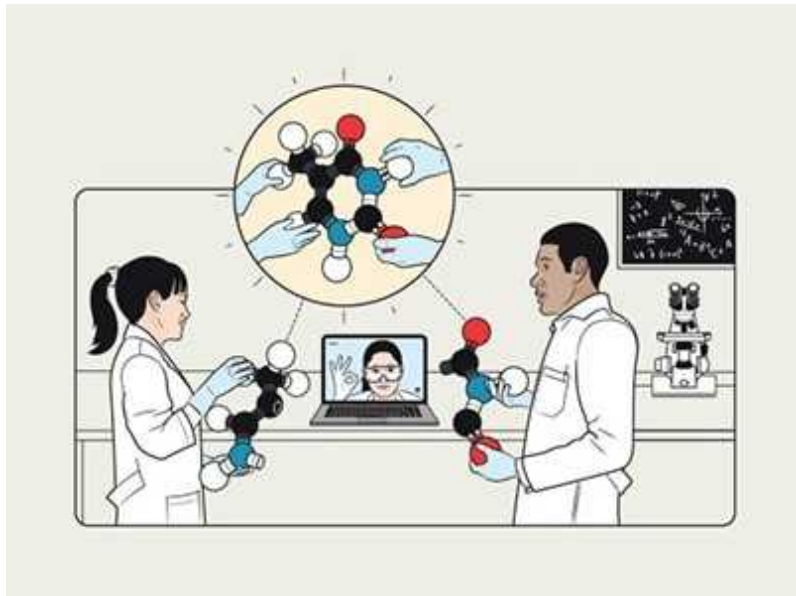
Be careful with causality. Think of all the possible factors that could influence the outcome of interest, then try to account for them. Team up with other researchers studying similar questions in other places. Remember that you cannot generate and confirm hypotheses with the same data.

Don't stop now. The pandemic is still raging, and recovery could be just as disruptive. Continue collecting data, even if there's no time to analyse them. The information could prove crucial for future studies.

The sky is the limit

Researchers have long relied on natural experiments to probe subjects that would be difficult — or unethical — to investigate through conventional methods such as randomized controlled trials. For example, they have studied the lifelong effects of stress in early life by tracking the progress of young children who experienced weather disasters⁶.

Scientists have also learnt from political upheavals, such as the collapse of the Soviet Union in 1991. Researchers found⁷ that in Russia, increased alcohol consumption probably contributed to a significant drop in life expectancy between 1984 and 1994. In Cuba, which had close ties to the Soviet Union, the fall triggered a period of food and fuel shortages that led to nationwide weight loss — and to reduced rates of diabetes and diabetes-related deaths⁸.



Nature special: How to collaborate in science

Now, COVID-19 has created a similar opportunity, says Blake Thomson, a principal scientist for cancer-disparity research at the American Cancer Society in Atlanta, Georgia, who wrote a 2020 article in the cardiovascular disease journal *Circulation* about learning from the pandemic⁹. Many people skipped cancer screenings during the pandemic out of fear of catching the virus, which has deeply concerned physicians. But it also presents an opportunity “to look for areas in which, actually, we are over-diagnosing or over-treating certain people or certain conditions”, Thomson says. (Doctors cannot ask some patients to forgo routine screening to serve as a control group in clinical trials.)

Industrial shutdowns also provided a rare real-world chemistry experiment for atmospheric scientists such as Guy Brasseur at the Max Planck Institute for Meteorology in Hamburg, Germany. “We’re always saying, to clean up the air, we need to shut down the emission sources,” he says. “Well, we’re doing that.” So Brasseur and his colleagues tracked changes in air pollutants around the world and compared them with a widely used computer model. The results agreed “reasonably well”, the team wrote in a study this year, validating their current understanding of atmospheric chemistry and highlighting areas for further research¹⁰.



Guy Brasseur used the pandemic as an opportunity to track air pollutants worldwide. Credit: Rebecca Hornbrook/NCAR

Other researchers are using the pandemic to study the effects of increased screen time on physical activity in children¹¹, of decreased tourism on beach ecosystems¹² and of reduced exposure to colds and allergens on children with asthma^{13,14}. And that's just the tip of the iceberg, Thomson says. "The sky is really the limit — it's a matter of creativity."

Go big on data

Some studies, such as Brasseur's, extract knowledge by focusing on the peak of disruption. Others will unfold slowly as scientists track the long-term effects of the pandemic on people with cancer, for instance, or on children who experienced remote learning. "There's clearly research to be done right now and in the coming months and years," Thomson says. "For decades, we'll be wanting to revisit this."

Either way, scientists need to find or collect data that capture the perturbations caused by the virus and related lockdown measures. Already,

researchers have capitalized on mobility reports from Apple and Google to study changes in human activity during lockdowns. Scientists can also dig through data from such sources as social media, satellite observations, wearable sensors and sales trends, Thomson says. He encourages researchers to collect as many extra data as possible while the pandemic continues to enable more future research.



What polar researchers have learnt from the pandemic

For health studies, Thomson recommends databases such as the UK-based Biobank, which contains genetic and health information for half a million people, and the All of Us research programme, run by the US National Institutes of Health, which launched in 2018 and includes a wide diversity of participants. The iPOP study has partnered with the International COVID-19 Data Alliance (ICODA), a new initiative funded by groups such as the Bill and Melinda Gates Foundation and the biomedical research funder Wellcome, and operated by Health Data Research UK. ICODA compiles health data from around the world to support research on COVID-19 and other public-health issues.

Amegah and his colleagues are currently digitizing birth records from hospitals around Ghana to contribute to the database. He says that the project is an example of how researchers in low- and middle-income countries, who often face funding constraints, can turn the natural

experiment of the pandemic to good use, because it is relatively inexpensive to round up and analyse existing data. “That is a golden opportunity that we cannot miss,” he says.

In addition to participating in iPOP, Amegah plans to track the effects of increased hand washing on childhood mortality in Ghana. In a September 2020 comment article in the medical journal *The Lancet Global Health*, he hypothesized that better hygiene during the pandemic is likely to have reduced cases of common diarrhoeal diseases, which can be fatal if untreated¹⁵. He says he will look for clues in the next round of data from the Demographic and Health Surveys Program, which focuses on low- and middle-income countries and is funded by the US Agency for International Development.

Not all researchers have had success finding the data they need, so some have launched projects to fill the gaps. When Chile entered partial lockdown in March 2020, Eduardo Silva-Rodríguez scrambled to set up wildlife cameras in several major cities to investigate reports of urban carnivore sightings. He is a conservation biologist at the Austral University of Chile in Valdivia and, like many researchers, was curious about how wildlife would respond to the unprecedented lull in human activity that some have dubbed the Anthropause.



Unused boats in Cameroon. Researchers are studying the effects of reduced fishing on sharks. Credit: Lionel Yamb

Silva-Rodríguez and his colleagues managed to get camera traps installed in Valdivia and Concepción. They documented several animals rarely seen in urban areas, including a small wildcat called a güiña (*Leopardus guigna*) and the endangered southern river otter (*Lontra provocax*)¹⁶. But because the researchers weren't studying cities before the pandemic, they don't know whether the animals' behaviour changed. So they will continue the study as lockdowns ease to see what happens. "It's not optimal," Silva-Rodríguez admits. "We had two options: doing nothing or doing what we could."

Silva-Rodríguez has contributed his team's results to the COVID Cameratrap Comparison Collaboration, which was first announced in a September 2020 tweet from Roland Kays, a zoologist at North Carolina State University in Raleigh. Many researchers are joining these kinds of international partnerships in the hope that similar studies conducted in different locations can offer a form of replication. But they caution that scientists must always consider the circumstances surrounding each individual project. "People have to know that the pandemic has not affected places in the world in the same way," says Lionel Yamb, a marine ecologist

at Cameroon's Institute of Agricultural Research for Development in Yaoundé.

Yamb is one of dozens of scientists participating in Our Ocean in COVID-19, an effort to understand human–ocean interactions during the pandemic using eOceans, a new platform and app that allows researchers and citizen scientists to collect, share and analyse ocean data. Christine Ward-Paige, a marine scientist based in Dartmouth, Canada, was already building the app when the pandemic hit and decided to release it early. “Maybe it could be used to study the impacts of COVID,” she thought.

Yamb isn't sure yet how the pandemic has affected the sharks he studies in Cameroon. When the crisis struck last year, the government closed many fish markets, effectively grounding fishing boats. Fishers sometimes catch sharks by accident, so Yamb thinks that shark populations might have benefited from the break. If true, such an observation would support proposals to establish seasonal no-catch zones at times when sharks reproduce. Either way, he says, researchers seeking to learn from the pandemic will need to consider how these dynamics vary in every location. “We have to think about a specific protocol that will be carried out in each country,” Yamb says.

Pitfalls and perseverance

Natural experiments require clever approaches to analysing data, such as comparing what happened before and after lockdowns using methods that could include interrupted time series, or between a population that was subject to lockdown and another that was not, which can serve as a control. But determining causality can be tricky, warns Paul Ferraro, an economist at Johns Hopkins University in Baltimore, Maryland, who studies causal relationships in complex systems. “When nature disturbs our human or environmental system, it does it in ways that often have multiple paths to the same outcome,” he says.

Ferraro advises researchers who are attempting to exploit natural experiments to develop a comprehensive model, based on mechanisms, that links not only the variables of interest, but also everything else that could

affect a given outcome. For instance, if researchers want to study the link between telecommuting and worker satisfaction, they have to account for many other factors that could influence employees' well-being, such as pandemic-related anxiety and whether other family members are at home, too.

If comparing locked-down versus open locations, researchers must consider why certain countries or regions shut down at different times, which might depend on political leadership, the presence or absence of trades unions campaigning for workers' jobs or safety, and myriad other factors that could bias the result in question, he says. And every study must somehow account for the effects of COVID-19 itself. Then, Ferraro says, researchers must try to rule out other explanations that could confound their hypothesis. In that sense, the pandemic poses a challenge because it has affected so many aspects of life.

Amanda Bates, a marine ecologist at the University of Victoria in Canada, grappled with this reality last spring. She was sitting at the dinner table when she grabbed one of her daughter's crayons and a piece of cardboard and started sketching out all the ways that the pandemic might affect biodiversity — and what lessons it might contain for conservation. That spontaneous exercise became the basis for a central figure in an August 2020 paper in which Bates and her co-authors exhorted their colleagues to take advantage of the “unprecedented concurrent confinement of nearly two-thirds of the global population” caused by the coronavirus^{[17](#)}.

A follow-up study published in May synthesizes hundreds of reports of pandemic impacts on wildlife and the environment collected over the past year^{[18](#)}. The results paint a complex picture: in some cases, species seem to have benefited from human absence, but in others, they suffered as conservation work ground to a halt. For example, an estimated two million seabird chicks perished in 2020 because people could not reach breeding colonies to remove invasive rodents.

Bates and her co-authors wrote that the pandemic has highlighted the dual role of humans as threats to and custodians of nature, and revealed ways to “favourably tilt this delicate balance” to protect biodiversity. And the experiment isn’t over yet.

Many countries are still in the grip of the coronavirus, and others are racing to revive their economies, creating new risks for species and habitats, Bates says. “What I’m hoping is that people will keep jumping aboard,” she says. There’s still plenty of pandemic disruption to document — and even more to learn.

Nature **596**, 149–151 (2021)

doi: <https://doi.org/10.1038/d41586-021-02092-7>

References

1. 1.

Philip, R. K. *et al.* *BMJ Glob. Health* **5**, e003075 (2020).

[PubMed](#) [Article](#) [Google Scholar](#)

2. 2.

Hedermann, G. Preprint at medRxiv
<https://doi.org/10.1101/2020.05.22.20109793> (2020).

3. 3.

Ashish, K. C. *et al.* *Lancet Glob. Health* **8**, e1273–e1281 (2020).

[PubMed](#) [Article](#) [Google Scholar](#)

4. 4.

Chmielewska, B. *et al.* *Lancet Glob. Health* **9**, e759–e772 (2021).

[PubMed](#) [Article](#) [Google Scholar](#)

5. 5.

Stock, S. J. *et al.* *Wellcome Open Res.* **6**, 21 (2021).

[Article](#) [Google Scholar](#)

6. 6.

Rosales-Rueda, M. J. *Health Econ.* **62**, 13–44 (2018).

[Article](#) [Google Scholar](#)

7. 7.

Leon, D. A. *et al.* *Lancet* **350**, 383–388 (1997).

[PubMed](#) [Article](#) [Google Scholar](#)

8. 8.

Franco, M. *et al.* *BMJ* **346**, f1515 (2013).

[PubMed](#) [Article](#) [Google Scholar](#)

9. 9.

Thomson, B. *Circulation* **142**, 14–16 (2020).

[PubMed](#) [Article](#) [Google Scholar](#)

10. 10.

Gaubert, B. *et al.* *J. Geophys. Res. Atmos.* **126**, e2020JD034213 (2021).

[PubMed](#) [Article](#) [Google Scholar](#)

11. 11.

Schmidt, S. C. E. *et al.* *Sci. Rep.* **10**, 21780 (2020).

[PubMed](#) [Article](#) [Google Scholar](#)

12. 12.

Soto, E. H. *et al.* *Biol. Conserv.* **255**, 108972 (2021).

[Article](#) [Google Scholar](#)

13. 13.

Abe, K., Miyawaki, A., Nakamura, M., Ninomiya, H. & Kobayashi, Y. *J. Allergy Clin. Immunol. Pract.* **9**, 494–496 (2021).

[PubMed](#) [Article](#) [Google Scholar](#)

14. 14.

Kenyon, C. C., Hill, D. A., Henrickson, S. E., Bryant-Stephens, T. C. & Zorc, J. J. *J. Allergy Clin. Immunol. Pract.* **8**, 2774–2776 (2021).

[Article](#) [Google Scholar](#)

15. 15.

Amegah, A. K. *Lancet Glob. Health* **8**, e1110–e1111 (2020).

[PubMed](#) [Article](#) [Google Scholar](#)

16. 16.

Silva-Rodríguez, E. A., Gálvez, N., Swan, G. J. F., Cusack, J. J. & Moreira-Arce, D. *Sci. Total Environ.* **765**, 142713 (2021).

[PubMed](#) [Article](#) [Google Scholar](#)

17. 17.

Bates, A. E., Primack, R. B., Moraga, P. & Duarte, C. M. *Biol. Conserv.* **248**, 108665 (2020).

[PubMed](#) [Article](#) [Google Scholar](#)

18. 18.

Bates, A. E., Primack, R. B., PAN-Environment Working Group & Duarte, C. M. *Biol. Conserv.*
<https://doi.org/10.1016/j.biocon.2021.109175> (2021).

[Article](#) [Google Scholar](#)

[Download references](#)

Related Articles



- [How COVID-19 has stomped on scientists' travel plans](#)



- [What polar researchers have learnt from the pandemic](#)



- [2020: the year of hard-won lessons](#)



- [Nature special: How to collaborate in science](#)

Subjects

- [Careers](#)
- [SARS-CoV-2](#)
- [Scientific community](#)
- [Research data](#)

nature careers

Jobs >

- [Translational Biologist, Oncology](#)

Astex Pharmaceuticals Limited

Cambridge, United Kingdom

- [Postdoctoral Researcher – studying the histopathology of acute ischaemic stroke blood clots and the correlation of composition with impedance measurements\(CÚRAM\), NUIG RES 158-21](#)

National University of Ireland Galway (NUI Galway)

Galway, Ireland

- [Summer Laboratory Technician](#)

Oklahoma Medical Research Foundation (OMRF)

Oklahoma City, United States

- [PhD student \(m/f/d\) Hormonal programming of hepatic chromatin landscapes](#)

Technical University of Munich (TUM)

Munich, Germany

Nature Briefing

An essential round-up of science news, opinion and analysis, delivered to your inbox every weekday.

[Download PDF](#)

Related Articles



- [How COVID-19 has stomped on scientists' travel plans](#)



- [What polar researchers have learnt from the pandemic](#)



- [2020: the year of hard-won lessons](#)



- [Nature special: How to collaborate in science](#)

Subjects

- [Careers](#)
- [SARS-CoV-2](#)
- [Scientific community](#)
- [Research data](#)

This article was downloaded by **calibre** from <https://www.nature.com/articles/d41586-021-02092-7>

- TECHNOLOGY FEATURE
- 03 August 2021
- Correction [05 August 2021](#)

The hunt for red fluorescent proteins

By pushing fluorescent proteins further into the red, bioengineers are expanding the palette and penetration depth of biological imaging.

- [Amber Dance](#) ⁰

1. Amber Dance

1. Amber Dance is a freelance writer in Los Angeles, California.

[View author publications](#)

You can also search for this author in [PubMed](#) [Google Scholar](#)





•

[Download PDF](#)

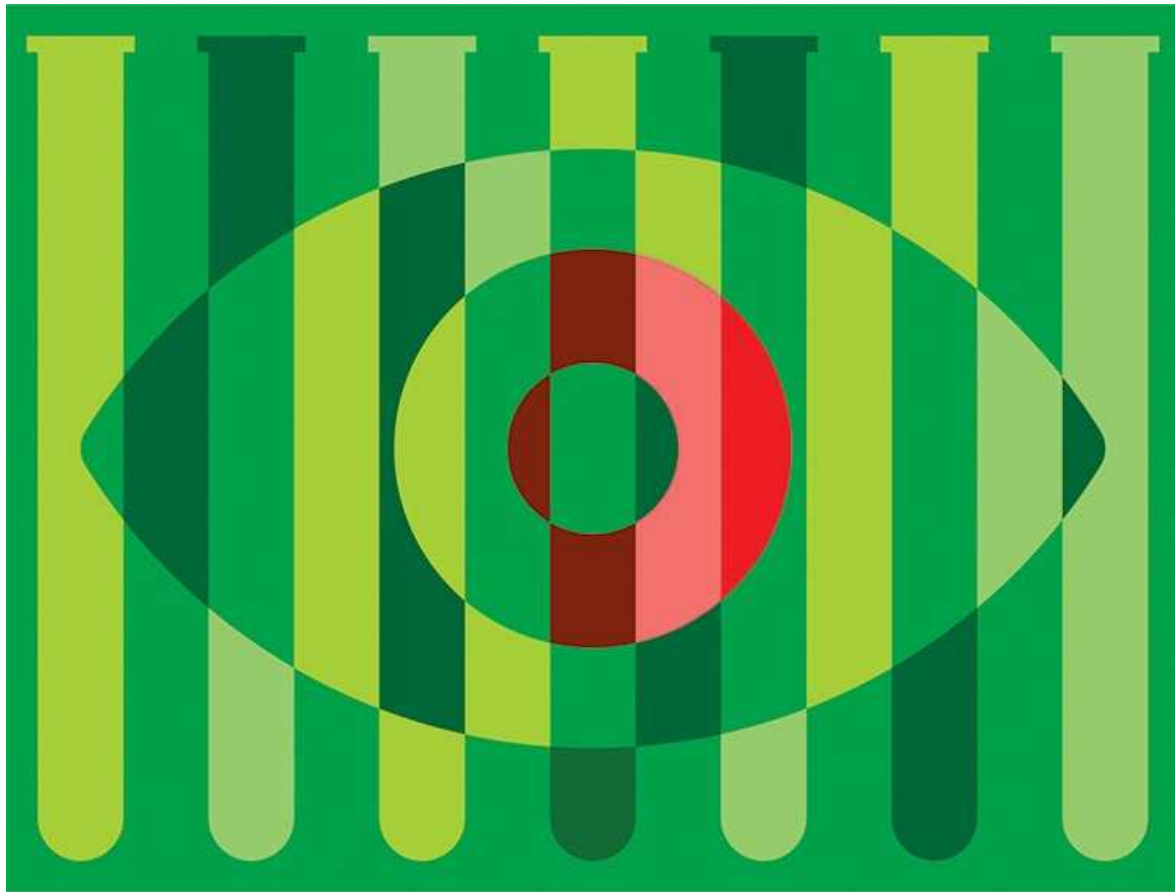


Illustration by The Project Twins

Green fluorescent protein is one of the most popular items in the microscopist's toolbox. It is a Nobel-prizewinning innovation that brilliantly lights up molecules of interest across a diverse range of biological fields, laboratories and techniques. But it does not work for physical chemist Julie Biteen.

Biteen studies gut bacterial communities at the University of Michigan in Ann Arbor, and was eager to use fluorescent proteins to identify individual species in complex mixtures. But gut bacteria don't like oxygen — something green fluorescent protein (GFP) absolutely requires. No oxygen, no fluorescence.

So, she turned to a label that can do without oxygen. A relatively new addition to the fluorescent-protein palette, [IFP2.0](#) fluoresces mainly in the near-infrared — a portion of the electromagnetic spectrum that is barely

visible to the human eye but readily apparent to microscope cameras¹. “We’re really excited,” Biteen says. “We could see single cells and identify them.”

Imaging at the red end of the spectrum offers other advantages, too: lower background fluorescence, reduced toxicity and deeper tissue penetration. “All other factors being the same, redder is better,” says Robert Campbell, a protein engineer who spends half his time at the University of Tokyo and the other half at the University of Alberta in Edmonton, Canada. It also provides a way to add another hue, or two, to experiments. “The more channels we can pack into an experiment, without significant bleed-through, the more interactions we can study,” says Talley Lambert, a microscopist at Harvard Medical School in Boston, Massachusetts.

Reddish fluorescent proteins have existed for decades, but they are still generally no match for GFP in terms of both brightness and hue. Even the ‘red’ fluorescent protein RFP is closer to orange. Scientists are making headway in developing fluorescent proteins that are truly red — often called ‘far red’ to distinguish them from earlier attempts. Infrared offers similar advantages. Development is still in its infancy, but advances in bioprospecting, protein engineering and synthetic chemistry are helping to improve the labels. Most are available, in gene form, on the plasmid repository [Addgene](#).

There’s clearly a need. Scientists are desperate for tags and sensors that they can use alongside standard tools, such as GFP, blue DNA stains and channelrhodopsins, which are activated by green and blue light. Brian Almond, senior manager for product management at Thermo Fisher Scientific in Carlsbad, California, says an alternative hue is often customers’ first request for new fluorescent tools. “Everything is green,” they tell him. “Please, don’t make it green.”

Scarlet solution

A typical fluorescence-microscopy experiment can use around three colours without overlap. But picking labels that will work together is not as simple as yellow-green-blue. There are hundreds of fluorescent proteins to choose

from, and they vary in factors such as hue, brightness and fluorescence longevity. Some are single-unit proteins, but others have the potential to stick to each other and perhaps even glue the protein of interest to others like it, interfering with the results. No one protein will be the best for every application.



Near-Infrared: A fact sheet

When choosing a tag, it's best not to rely too closely on published data, warns Roberto Chica, a protein engineer at the University of Ottawa. Proteins that work well in a test tube might not shine in a model organism, and data tables are often incomplete. It's best to test a few fluorescent proteins and pick the best for your experiments.

Several free online resources can help scientists to choose candidate fluorescent proteins, including Lambert's FPbase; Thermo Fisher's [Fluorescence SpectraViewer](#); and the [Fluorescence Spectra Analyzer](#) developed by BioLegend in San Diego, California. Users can view the excitation and emission curves for hundreds of fluorescent proteins and dyes, and by inputting their light sources, filters and detectors, they can choose accordingly.

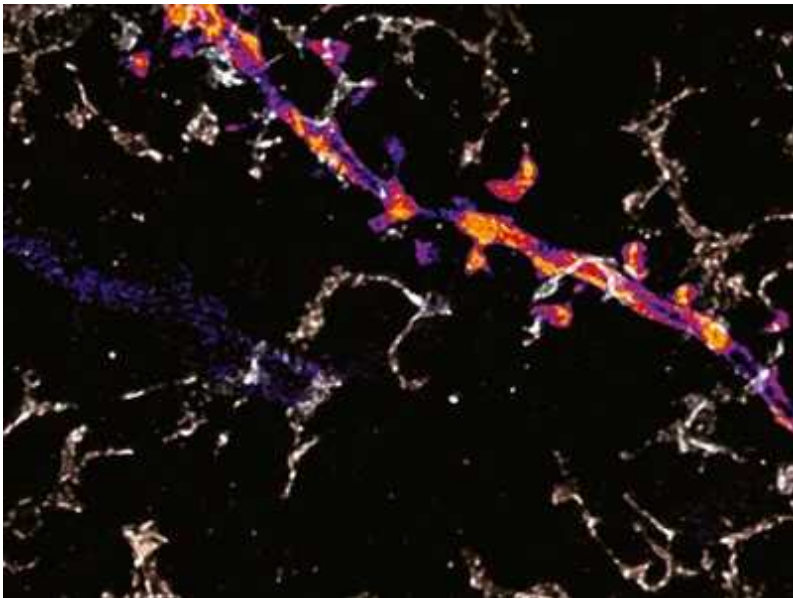
One strategy for using multiple colours is to let computers sort out any overlapping emission spectra after the data are collected. With this

technique, called ‘spectral imaging and linear unmixing’ or ‘fluorescent unmixing’, researchers can probe many more colours — up to 40 tags in the same flow-cytometry experiment, says BioLegend product manager Kenta Yamamoto. But such rainbow panels require careful planning, he warns: for example, rarer proteins might need to be paired with brighter tags if they are to stand out from the crowd.

A simpler approach is to use a colour that doesn’t overlap with any of the others. That’s where far-red and near-infrared labels are handy; they make it easy to get at least four non-overlapping signals from the same cells. In his lab at Westlake University in Hangzhou, China, tool developer Kiryl Piatkevich routinely records five signals from the same microscope slide by using three visible colours and two in the near-infrared range. Such experiments can often be performed without major equipment upgrades.

Where the fluorophore grows

Whereas many fluorescent proteins are found in sea creatures, far-red and near-infrared molecules tend to come from bacteria. But unlike GFP and similar proteins, bacterial light receptors lack a component to absorb light (called a chromophore) of their own; they require the addition of a pigment known as biliverdin. The good news is that biliverdin is a natural intermediate in the breakdown of haem, which binds to oxygen to transport it through the blood, so it’s naturally present in mammals. The bad news is that biliverdin is also quickly degraded, so it’s far from abundant.



Fluorescent protein biosensors

One solution to that problem is to add more biliverdin, either from standard chemical suppliers, or by altering organisms to make more of it. Another is to engineer natural far-red and near-infrared proteins so that they work better outside their usual host, for example by boosting the efficiency of the binding between the protein and the pigment, says Vladislav Verkhusha, a molecular bioengineer at Albert Einstein College of Medicine in New York City. His group induces random mutations in the relevant genes *in vitro*, then expresses those genes in the bacterium *Escherichia coli* and selects for the reddest or brightest products. In one example², the team used 17 rounds of this molecular-evolution approach to obtain a near-infrared protein tag called [miRFP670nano](#). The tag is about 60% of the size of GFP, binds to biliverdin efficiently and fluoresces brightly in mammalian cells.

Piatkevich uses molecular evolution, too, but in mammalian cells, which fold up the proteins such that they match those of the target cells more closely than those evolved in bacteria. His team has used this approach to brighten a near-infrared fluorescent voltage reporter (useful for tracking nerve-cell firing), creating a sensor called [Archon1](#)³.

It's also possible to engineer proteins directly. Timothy Wannier, a synthetic biologist at Harvard Medical School, used both molecular evolution and computer-based protein analysis and design on GFP relatives during his PhD

studies at the California Institute of Technology in Pasadena. His goal was to turn dimeric far-red fluorescent proteins into monomers, which would help to prevent undesirable interactions. But he also had to engineer mutations to stabilize the lone monomers⁴.

One of the resulting tags, [mKelly1](#), caught the eye of Yi Shen, a protein engineer at the University of Alberta, who used it to build far-red calcium sensors named [FR-GECOs⁵](#).

Redder all the time

Despite these advances, far-red and near-infrared fluorescent proteins remain dim bulbs. Whereas some green proteins push the limits of brightness, the best near-infrared tags hover at around 10–20% of the maximum.



[NatureTech hub](#)

One solution is a workaround based on far-red and near-infrared chemical dyes, which are also becoming available more widely. Organic chemist Luke Lavis at the Howard Hughes Medical Institute Janelia Research Campus in Ashburn, Virginia, developed bright, non-toxic dyes that can switch between colourless and fluorescent forms according to their surroundings⁶. Lavis has since teamed up with protein-engineer colleague Eric Schreiter to turn these

dyes into ‘chemigenetic’ cellular sensors that couple a chemical dye with a protein partner.

The pair use the genetically encoded ‘[HaloTag](#)’ as a dock for the synthetic dyes, and hook it up to sensor proteins that change shape in the presence of calcium or electrical voltage⁷. The shape change alters the local environment of the dye such that it fluoresces — and is about ten times brighter than previous red sensors, says Schreiter. Lavis gives the dyes to other scientists free of charge. He is now testing next-generation dyes that he expects will penetrate deeper into tissue for *in vivo* applications.

“The future is bright for this class of sensors,” says Schreiter. He adds that it should be possible to replace GFP in any pre-existing sensor with the HaloTag to create a new, red, chemigenetic sensor. But for the rest of the rainbow, Lavis says, standard fluorescent proteins should suffice “because they’re awesome”.

Nature **596**, 152-153 (2021)

doi: <https://doi.org/10.1038/d41586-021-02093-6>

Updates & Corrections

- **Correction 05 August 2021:** An earlier version of this feature misnamed the protein miRFP670nano as miR670nano.

References

1. 1.

Yu, D. *et al.* *Nature Commun.* **5**, 3626 (2014).

[PubMed](#) [Article](#) [Google Scholar](#)

2. 2.

Oliinyk, O. S., Shemetov, A. A., Pletnev, S., Shcherbakova, D. M. & Verkhusha, V. V. *Nature Commun.* **10**, 279 (2019).

[PubMed](#) [Article](#) [Google Scholar](#)

3. 3.

Piatkevich, K. D. *et al.* *Nature Chem. Biol.* **14**, 352–360 (2018).

[PubMed](#) [Article](#) [Google Scholar](#)

4. 4.

Wannier, T. M. *et al.* *Proc. Natl Acad. Sci. USA* **115**, E11294–E11301 (2018).

[PubMed](#) [Article](#) [Google Scholar](#)

5. 5.

Dalangin, R. *et al.* Preprint at bioRxiv
<https://doi.org/10.1101/2020.11.12.380089> (2020).

6. 6.

Grimm, J. B. *et al.* *Nature Meth.* **17**, 815–821 (2020).

[Article](#) [Google Scholar](#)

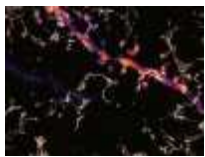
7. 7.

Deo, C. *et al.* *Nature Chem. Biol.* **17**, 718–723 (2021).

[PubMed](#) [Article](#) [Google Scholar](#)

[Download references](#)

Related Articles

-  [Fluorescent protein biosensors](#)
-  [Near-Infrared: A fact sheet](#)
-  [NatureTech hub](#)

Subjects

- [Microscopy](#)
- [Molecular biology](#)
- [Biotechnology](#)
- [Imaging](#)

nature careers

[Jobs](#) >

- [Translational Biologist, Oncology](#)

Astex Pharmaceuticals Limited

Cambridge, United Kingdom

- [Summer Laboratory Technician](#)

Oklahoma Medical Research Foundation (OMRF)

Oklahoma City, United States

- [PhD student \(m/f/d\) Hormonal programming of hepatic chromatin landscapes](#)

Technical University of Munich (TUM)

Munich, Germany

- [Postdoctoral Researcher – studying the histopathology of acute ischaemic stroke blood clots and the correlation of composition with impedance measurements\(CÚRAM\), NUIG RES 158-21](#)

National University of Ireland Galway (NUI Galway)

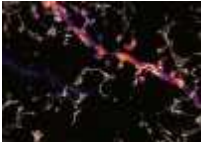
Galway, Ireland

Nature Briefing

An essential round-up of science news, opinion and analysis, delivered to your inbox every weekday.

[Download PDF](#)

Related Articles

-  [Fluorescent protein biosensors](#)
-  [Near-Infrared: A fact sheet](#)
-  [NatureTech hub](#)

Subjects

- [Microscopy](#)
 - [Molecular biology](#)
 - [Biotechnology](#)
 - [Imaging](#)
-

This article was downloaded by **calibre** from <https://www.nature.com/articles/d41586-021-02093-6>

| [Section menu](#) | [Main menu](#) |

- WHERE I WORK
- 02 August 2021

A race against time to feed the world

Agrochemical scientist Sarah Iveson is excited about digital agriculture's potential to make crops more resilient to climate change as the global population grows.

- [Linda Nordling](#) 0

1. Linda Nordling

1. Linda Nordling is a freelance writer in Cape Town, South Africa.

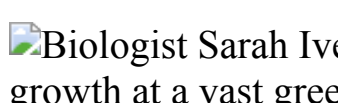
[View author publications](#)

You can also search for this author in [PubMed](#) [Google Scholar](#)





•



Biologist Sarah Iveson inspects sunflower plants in various stages of growth at a vast greenhouse in Toulouse, France.

Sarah Iveson is head of seed development for Europe, Africa and the Middle East for Switzerland-based agrochemical company Syngenta.
Credit: Grégoire Bernardi for *Nature*

[Download PDF](#)

In this picture, I'm in one of our greenhouses at Syngenta's Toulouse Innovation Centre in France. I'm checking the quality of sunflowers grown from our experimental seeds. As Syngenta's head of seed development for

commercial growers in Europe, Africa and the Middle East, I oversee work to improve the performance and stress tolerance of crops such as corn, oilseed rape and sunflowers, used to make sunflower oil.

The sunflower greenhouse is especially lovely in the cold, dark winter (the picture was taken in March). Our greenhouses are climate- and light-controlled, so we can grow crops in ideal conditions year-round. We can speed up the life cycle of the plant and quickly introduce and check new plant traits. Irrigation and nutrient supply lines feed into the soil beds, and sensors tell us what the crops need.

Syngenta is a global company that supplies large- and small-scale commercial growers. I've worked here for 15 years, since I got my undergraduate degree at Lancaster University, UK. These sunflowers have been naturally modified to tolerate pests, including broomrape (*Orobanche*), a parasitic weed. The tallest sunflowers are mature, and we encase them in mesh to stop pollen from contaminating the samples in which we look for genes relevant to specific traits.

Every year, we try to get products into the hands of farmers more quickly. We use light-emitting diodes and different wavelengths of light to create optimum growing conditions.

I'm excited about using digital agriculture to maximize yields. Farmers can put sensors in their fields to detect and predict plant diseases, and can examine satellite data to pick the best seeds for their soil types and local environment. In Europe, especially, farmers are shifting to practices that are kinder to the soil and are more sustainable long-term. With climate change and a growing global population, we need more output from every single field. It's a race against time to meet growers' needs.

Nature **596**, 156 (2021)

doi: <https://doi.org/10.1038/d41586-021-02094-5>

Related Articles



- [Fighting food insecurity with CRISPR at Zimbabwe's first private research institute](#)



- [A deep-rooted appreciation for the health benefits of plants](#)



- [Why industry internships can be your 'golden ticket' to a prosperous career](#)

Subjects

- [Careers](#)
- [Agriculture](#)
- [Plant sciences](#)

nature careers

[Jobs](#) >

- [Translational Biologist, Oncology](#)

Astex Pharmaceuticals Limited

Cambridge, United Kingdom

- [Summer Laboratory Technician](#)

Oklahoma Medical Research Foundation (OMRF)

Oklahoma City, United States

- [PhD student \(m/f/d\) Hormonal programming of hepatic chromatin landscapes](#)

Technical University of Munich (TUM)

Munich, Germany

- [Postdoctoral Researcher – studying the histopathology of acute ischaemic stroke blood clots and the correlation of composition with impedance measurements\(CÚRAM\), NUIG RES 158-21](#)

National University of Ireland Galway (NUI Galway)

Galway, Ireland

Nature Briefing

An essential round-up of science news, opinion and analysis, delivered to your inbox every weekday.

[Download PDF](#)

Related Articles



- [Fighting food insecurity with CRISPR at Zimbabwe's first private research institute](#)



- [A deep-rooted appreciation for the health benefits of plants](#)



- [Why industry internships can be your ‘golden ticket’ to a prosperous career](#)

Subjects

- [Careers](#)
- [Agriculture](#)
- [Plant sciences](#)

This article was downloaded by **calibre** from <https://www.nature.com/articles/d41586-021-02094-5>

| [Section menu](#) | [Main menu](#) |

Research

- **[The fraction of the global population at risk of floods is growing](#)** [04 August 2021]

News & Views • Satellite imaging combined with population data shows that, globally, the number of people living in flood-prone areas is growing faster than is the number living on higher ground — greatly increasing the potential impact of floods.

- **[Private immune protection at the border of the central nervous system](#)** [20 July 2021]

News & Views • At the outer border of the brain and spinal cord, immune cells have been observed that originate from the bone marrow of the adjacent skull and vertebrae. They reach this site through special bone channels, without passing through the blood.

- **[Bouncing droplets mimic spin systems](#)** [04 August 2021]

News & Views • Experiments show that a collection of bouncing fluid droplets can behave like a microscopic system of spins — the intrinsic angular momenta of particles. This discovery could lead to a better understanding of the physics of spin systems.

- **[From the archive](#)** [03 August 2021]

News & Views • Nature's pages feature an account of the unveiling of the theory of natural selection, and a reported sighting of an unusual type of lightning.

- **[Two giants of cell division in an oppressive embrace](#)** [21 July 2021]

News & Views • The enzymes separase and cyclin-dependent kinase are key orchestrators of cell division. Structural data reveal the surprisingly intricate mechanism that renders them both inactive when bound to each other.

- **[The role of retrotransposable elements in ageing and age-associated diseases](#)** [04 August 2021]

Review Article • This Review discusses how the activity of retrotransposons influences ageing and the role of these mobile genetic elements in age-related diseases and their treatment.

- **[Global upper-atmospheric heating on Jupiter by the polar aurorae](#)** [04 August 2021]

Article • High-resolution observations confirm that Jupiter's global upper atmosphere is heated by transport of energy from the polar aurora.

- **[Emergent order in hydrodynamic spin lattices](#)** [04 August 2021]

Article • A macroscopic analogue of a spin system is shown to emerge in an ensemble of droplets bouncing on the surface of a vibrating bath, revealing symmetry-breaking phenomena such as ‘magnetic’ ordering.

- **Quantized nonlinear Thouless pumping** [04 August 2021]
Article • Nonlinearity is shown to induce quantized topological transport via soliton motion; specifically, we demonstrate nonlinear Thouless pumping of photons in waveguide arrays with a non-uniformly occupied energy band.
- **Pseudogap in a crystalline insulator doped by disordered metals** [04 August 2021]
Article • A back-bending band structure and an emerging pseudogap are observed at the interface between a crystalline solid (black phosphorus) and disordered alkali-metal dopants.
- **Aziridine synthesis by coupling amines and alkenes via an electrogenerated dication** [22 June 2021]
Article • The synthesis of aziridines—three-membered nitrogen-containing heterocycles—is achieved by a new method involving the electrochemical coupling of alkenes and amines, via a dicationic intermediate.
- **Satellite imaging reveals increased proportion of population exposed to floods** [04 August 2021]
Article • Satellite imagery for the period 2000–2018 reveals that population growth was greater in flood-prone regions than elsewhere, thus exposing a greater proportion of the population to floods.
- **Possible poriferan body fossils in early Neoproterozoic microbial reefs** [28 July 2021]
Article • Vermiform microstructure in microbial reefs dating to approximately 890 million years ago resembles the body fossils of Phanerozoic demosponges, and may represent the earliest known physical evidence of animals.
- **Molecular architecture of the developing mouse brain** [28 July 2021]
Article • A comprehensive single-cell transcriptomic atlas of the mouse brain between gastrulation and birth identifies hundreds of cellular states and reveals the spatiotemporal organization of brain development.
- **Gut cytokines modulate olfaction through metabolic reprogramming of glia** [21 July 2021]
Article • Glial metabolic reprogramming by gut-derived cytokines in Drosophila results in lasting changes in the sensory system of an ageing organism
- **In vivo monoclonal antibody efficacy against SARS-CoV-2 variant strains** [21 June 2021]

Article • Experiments in mouse and hamster models show that monoclonal antibody combinations, using antibodies that correspond to products in clinical development, largely retain their efficacy in protecting against currently prevailing variant strains of SARS-CoV-2.

- **SARS-CoV-2 mRNA vaccines induce persistent human germinal centre responses** [28 June 2021]
Article • Analysis of antigen-specific B cells in lymph nodes of individuals vaccinated with BNT162b2 reveals lasting germinal centre responses, explaining the robust humoral immunity induced by SARS-CoV-2 mRNA-based vaccines.
- **Adaptive immunity induces mutualism between commensal eukaryotes** [14 July 2021]
Article • Studies of mouse and human IgA responses against Candida albicans and other common fungal species show that host adaptive immunity selects for fungal effectors that promote commensalism and prevent intestinal disease.
- **Phenotype, specificity and avidity of antitumour CD8+ T cells in melanoma** [21 July 2021]
Article • The authors use single-cell profiling and T cell receptor specificity screening to show how tumour antigen recognition shapes the phenotypes of CD8+ T cells and antitumour immune responses.
- **Transcriptional programs of neoantigen-specific TIL in anti-PD-1-treated lung cancers** [21 July 2021]
Article • Single-cell RNA sequencing and T cell receptor sequencing are combined to identify transcriptional programs specific to mutation-associated neoantigen-specific T cells in non-small cell lung cancers treated with anti-PD-1, providing insights into resistance to PD-1 blockade.
- **BANP opens chromatin and activates CpG-island-regulated genes** [07 July 2021]
Article • BANP is identified as the transcription factor that binds the CGCG element in a DNA-methylation-dependent manner, opens chromatin and activates a class of essential CpG-island-regulated genes.
- **Structural basis of human separase regulation by securin and CDK1–cyclin B1** [21 July 2021]
Article • Structures of separase in complex with either securin or cyclin B–CDK1 shed light on the regulation of chromosome separation during the cell cycle.
- **Structure of human Cav2.2 channel blocked by the painkiller ziconotide** [07 July 2021]
Article • Cryo-electron microscopy structures of human Cav2.2 in the presence or absence of ziconotide reveal the molecular basis of the specificity of this painkiller for Cav2.2, and provide insights into electromechanical coupling in Cav channels.

| [Main menu](#) | [Previous section](#) |

- NEWS AND VIEWS
- 04 August 2021

The fraction of the global population at risk of floods is growing

Satellite imaging combined with population data shows that, globally, the number of people living in flood-prone areas is growing faster than is the number living on higher ground — greatly increasing the potential impact of floods.

- [Brenden Jongman](#) 0

1. [Brenden Jongman](#)

1. Brenden Jongman is at the Global Facility for Disaster Reduction and Recovery, World Bank, Washington DC 20433, USA.

[View author publications](#)

You can also search for this author in [PubMed](#) [Google Scholar](#)





•

[Download PDF](#)

Flooding of river and coastal systems is the most frequent and damaging climate-related hazard, affecting thousands of people and causing billions of dollars in losses each year¹. The impacts often fall disproportionately on poor and vulnerable people, who have limited capacity to respond and recover from the shocks caused by floods. Over the past few decades, flood risk has increased globally because of a combination of climate-change-induced increases in the frequency and severity of floods, and because populations and economic activity have increased rapidly in hazard-prone areas (Fig. 1). [Writing in Nature](#), Tellman *et al.*² report a comprehensive assessment of

nearly 1,000 large flood events that occurred between 2000 and 2018, and estimate the magnitude of the impacts. The findings aid our understanding of the underlying drivers of flood risk.



Figure 1 | Flooding in Dhaka, Bangladesh. Tellman *et al.*² report that the proportion of the world's population that lives in flood-prone areas is increasing. Some of the biggest of these population increases have been in Dhaka. Credit: Mamanur Rashid/NurPhoto/Getty

The authors combined a record of flood events with daily satellite observations to develop the Global Flood Database — a resource that stores the footprint of 913 large floods that occurred between 2000 and 2018, across all continents (except Antarctica). For each event, the authors then estimated the area inundated and the number of people living in that area, using geospatial data sets of population density for different years. This analysis improves our understanding of the spatial extent of major floods and, most importantly, allowed the authors to look at changes in population and socio-economic activities in areas prone to inundation.



[Read the paper: Satellite imaging reveals increased proportion of population exposed to floods](#)

Tellman and colleagues show that the population in flood-prone areas rose by an estimated 34.1% during the study period — an increase of between 58 million and 86 million people. By contrast, the global population grew by just 18.6% over the same period. The authors went on to calculate trends in expected flood exposure up to 2030 within the flood footprints identified in the study, using previously developed projections of flood extents and population exposure^{3,4}. They found that the number of people exposed to floods is likely to continue to increase more quickly than the overall population in 59 countries, mostly in Asia and Africa.

Previous studies in this area relied on global flood models that use rainfall statistics and elevation models to map potential riverine and coastal flood zones⁵. Tellman *et al.* instead mapped an unprecedented number of validated events, including various flood types — such as those caused by dam breaks, local rainfall events and snowmelt — that had not been considered in the earlier analyses. As a result, the authors' estimate of the increase in the percentage of people exposed to floods globally is ten times higher than previous estimates.

As with all global assessments, the new work has its limitations. The flood events considered are still just a subset of all the floods that occurred during

the study period. This is because the satellite observations capture only floods above a certain spatial extent and that were followed by a period of cloud-free weather, thereby allowing reliable optical detection. Furthermore, the spatial resolution of the satellite data and the use of global population models do not allow a detailed analysis of flood impact in urban areas. Given that the world is rapidly urbanizing and that urban disaster risk is an increasing concern, future studies should develop improved approaches for estimating global flood risk in cities.



[Five centuries of human observation reveal Europe's flood history](#)

The trends revealed in Tellman and colleagues' study might seem daunting, but there is also good news to be drawn from the statistics: the capacity of communities to manage and respond to floods has increased over time.

Investments in flood protection, drainage infrastructure and early-warning systems, together with improved building standards, schemes for supporting flood-affected people and strengthened government policies enforcing risk-informed land planning, can both prevent floods and buffer the impacts when they occur⁶. The number of fatalities and extent of flood damage, relative to the number of people and economic assets exposed to floods, has declined globally over the past few decades⁷.

As the global population grows and cities expand, natural ecosystems that once provided flood protection will also be under threat. Mangroves, coral

reefs, dune systems and urban parks can damp flood waves, reduce peak flows and significantly reduce flooding and other climate-related hazards⁸. Investments in solutions that restore or construct ecosystems often provide a cost-effective way of reducing flood damage while improving biodiversity and providing other benefits⁹. Satellite technology can track changes in protective ecosystems¹⁰, similarly to its use in monitoring flooding and population changes. However, even the best combination of infrastructure and nature-based approaches might be insufficient to deal with rising sea levels — the only option for some communities will be to manage their retreat out of flood-prone areas¹¹.

Understanding the links between climate change, socio-economic development and flooding is a big scientific challenge, but is essential for developing robust decision-support models that will enable policymakers to calculate and communicate the best mix of measures for future challenges. Tellman and colleagues' improved global estimates of risk are a crucial step in that direction.

Nature **596**, 37–38 (2021)

doi: <https://doi.org/10.1038/d41586-021-01974-0>

References

1. 1.

van Loenhout, J. *et al.* *Human Cost of Disasters 2000–2019* (CRED/UNDRR, 2020).

[Google Scholar](#)

2. 2.

Tellman, B. *et al.* *Nature* **596**, 80–86 (2021).

[Article](#) [Google Scholar](#)

3. 3.

World Resources Institute. *Aqueduct Global Flood Risk Maps* (2015).

[Google Scholar](#)

4. 4.

Winsemius, H. C. *et al. Nature Clim. Change* **6**, 381–385 (2015).

[Article](#) [Google Scholar](#)

5. 5.

Ward, P. J. *et al. Nature Clim. Change* **5**, 712–715 (2015).

[Article](#) [Google Scholar](#)

6. 6.

Browder, G. *et al. An EPIC Response: Innovative Governance for Flood and Drought Risk Management* (World Bank, 2021).

[Google Scholar](#)

7. 7.

Jongman, B. *et al. Proc. Natl Acad. Sci. USA* **112**, E2271–E2280 (2015).

[PubMed](#) [Article](#) [Google Scholar](#)

8. 8.

Girardin, C. A. J. *et al. Nature* **593**, 191–194 (2021).

[PubMed](#) [Article](#) [Google Scholar](#)

9. 9.

Sudmeier-Rieux, K. *et al. Nature Sustain.*
<https://doi.org/10.1038/s41893-021-00732-4> (2021).

[Article](#) [Google Scholar](#)

10. 10.

Crowther, T. W. *et al.* *Nature* **525**, 201–205 (2015).

[PubMed](#) [Article](#) [Google Scholar](#)

11. 11.

Haasnoot, M., Lawrence, J. & Magnan, A. K. *Science* **372**, 1287–1290 (2021).

[PubMed](#) [Article](#) [Google Scholar](#)

[Download references](#)

Competing Interests

The author declares no competing interests.

Related Articles



- [Read the paper: Satellite imaging reveals increased proportion of population exposed to floods](#)



- [Five centuries of human observation reveal Europe's flood history](#)



- [Future of tidal wetlands depends on coastal management](#)
- [See all News & Views](#)

Subjects

- [Climate sciences](#)
- [Environmental sciences](#)
- [Hydrology](#)
- [Geography](#)

nature careers

[Jobs](#) >

- [Translational Biologist, Oncology](#)

Astex Pharmaceuticals Limited

Cambridge, United Kingdom

- [Postdoctoral Researcher – studying the histopathology of acute ischaemic stroke blood clots and the correlation of composition with impedance measurements\(CÚRAM\), NUIG RES 158-21](#)

National University of Ireland Galway (NUI Galway)

Galway, Ireland

- [Summer Laboratory Technician](#)

Oklahoma Medical Research Foundation (OMRF)

Oklahoma City, United States

- [PhD student \(m/f/d\) Hormonal programming of hepatic chromatin landscapes](#)

Technical University of Munich (TUM)

Munich, Germany

Nature Briefing

An essential round-up of science news, opinion and analysis, delivered to your inbox every weekday.

[Download PDF](#)

Related Articles



- [Read the paper: Satellite imaging reveals increased proportion of population exposed to floods](#)



- [Five centuries of human observation reveal Europe's flood history](#)



- [Future of tidal wetlands depends on coastal management](#)

- [See all News & Views](#)

Subjects

- [Climate sciences](#)
 - [Environmental sciences](#)
 - [Hydrology](#)
 - [Geography](#)
-

This article was downloaded by **calibre** from <https://www.nature.com/articles/d41586-021-01974-0>

| [Section menu](#) | [Main menu](#) |

- NEWS AND VIEWS
- 20 July 2021

Private immune protection at the border of the central nervous system

At the outer border of the brain and spinal cord, immune cells have been observed that originate from the bone marrow of the adjacent skull and vertebrae. They reach this site through special bone channels, without passing through the blood.

- [Britta Engelhardt](#) ORCID: <http://orcid.org/0000-0003-3059-9846> 0
 1. [Britta Engelhardt](#)
1. Britta Engelhardt is at the Theodor Kocher Institute, University of Bern, CH-3012 Bern, Switzerland.

[View author publications](#)

You can also search for this author in [PubMed](#) [Google Scholar](#)





•

[Download PDF](#)

Barriers around the brain and spinal cord of the central nervous system (CNS) protect neuronal cells from the changeable milieu of the bloodstream by controlling movement of molecules and cells between the blood and the CNS. These barriers also ensure that the CNS can be kept under surveillance by certain immune cells, but restrict the access of blood-derived immune cells and molecules to specific compartments at the border of the CNS¹. Writing in *Science*, [Cugurra et al.](#)² and [Brioschi et al.](#)³ report that the dura mater, a tissue layer around the outermost barrier of the CNS, sources a private immune protection from nearby bone marrow.

Encasing the brain and the spinal cord are three meningeal membranes^{1,4} (Fig. 1). The outermost membrane, the dura mater, lacks a blood–brain barrier, and so the entry of blood-derived components, including immune cells, into this layer is unrestricted^{1,4}. The arachnoid mater is attached to the inner surface of the dura mater. Between the arachnoid mater and the innermost meningeal layer, the pia mater, is the subarachnoid space, which contains cerebrospinal fluid (CSF) and resident immune cells that enter during embryonic development⁵. The arachnoid mater acts as a blood–CSF barrier between the dura mater and the subarachnoid space. The pia mater lies directly on top of the glia limitans, a thin layer of extracellular-matrix material and cell-protrusion endings at the surface of the CNS tissue⁴. The anatomy of the meningeal layers has been likened to the defences around a medieval castle, with two walls (the arachnoid barrier and the glia limitans) bordering a guard-patrolled moat (the subarachnoid space and its immune cells)⁶.

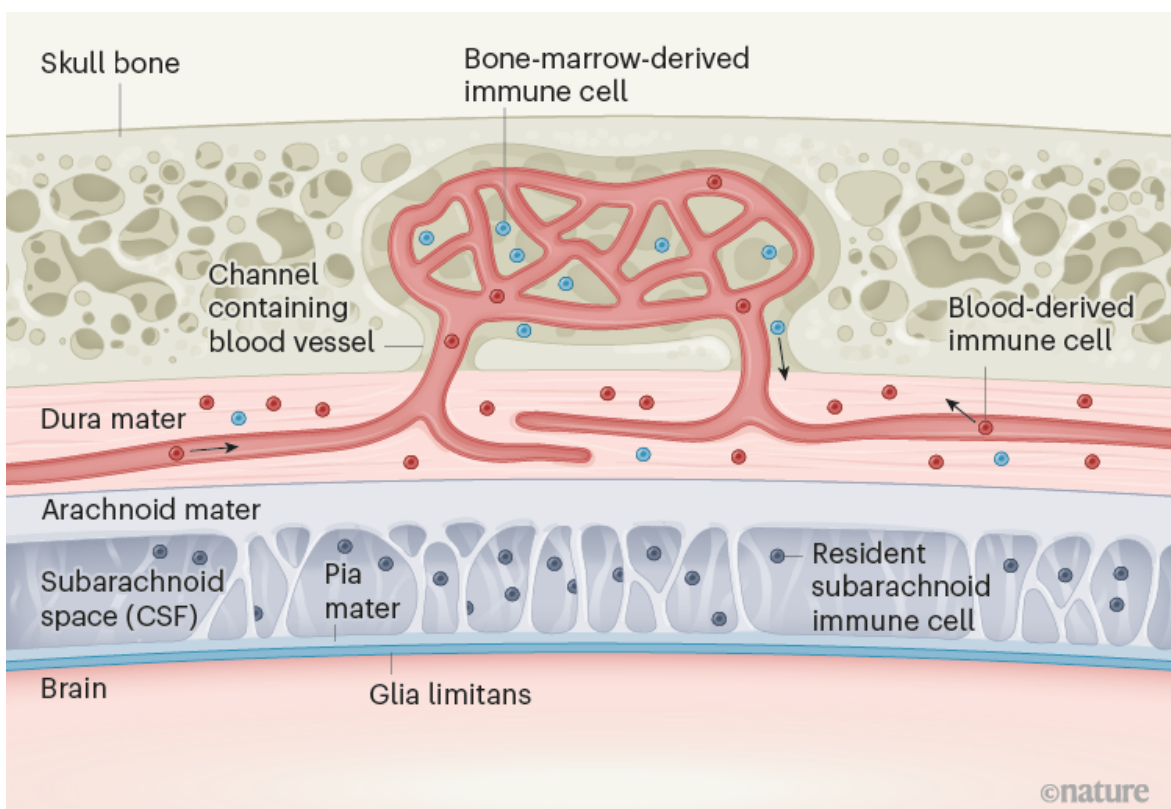
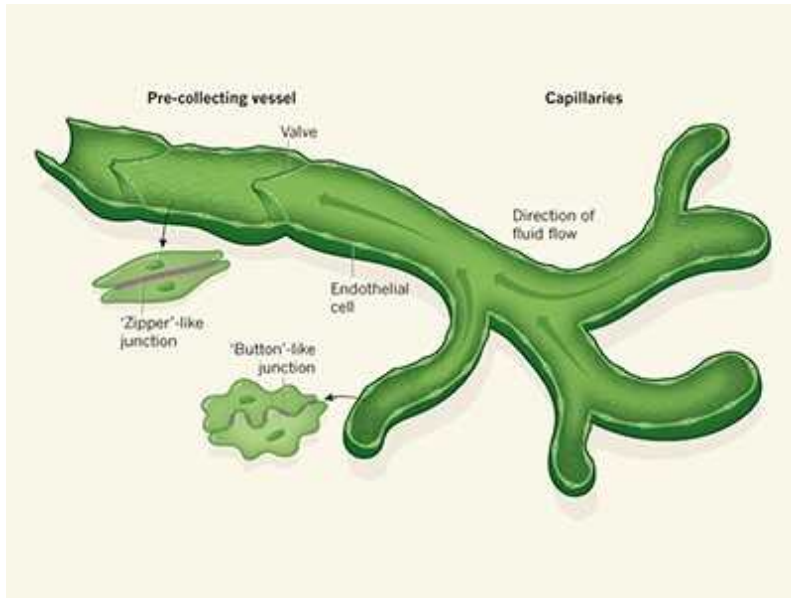


Figure 1 | Immune cells from the bone marrow outside the border of the central nervous system (CNS). Cugurra *et al.*² and Brioschi *et al.*³ studied immune cells in the dura mater, the outermost of three meningeal

membranes that surround the brain and spinal cord. In addition to immune cells derived from the bloodstream, they observed immune cells in the dura mater that originated directly from the neighbouring bone marrow in the skull or vertebrae. Immune cells from the bone marrow enter the dura mater by moving along the outside of blood vessels in channels in the bone. The other two meningeal membranes — the arachnoid mater and pia mater — surround the subarachnoid space, which contains cerebrospinal fluid (CSF) and its own immune cells that enter during embryonic development. The arachnoid mater establishes a cellular barrier between the dura mater and the CNS. Under the pia mater, the glia limitans layer, which is made of extracellular matrix material and cellular processes, establishes a further barrier.

The two new studies focused on different subsets of immune cells, namely, myeloid cells of the innate branch of the immune system (which recognizes stereotypical changes characteristic of infection)² and B cells of the adaptive immune system (which responds to and remembers specific foreign invaders)³. The authors attached the circulatory system of one mouse, in which these subsets of immune cells were fluorescently tagged, to that of a second, untreated, mouse, and made the surprising finding that fewer tagged cells than untagged cells were observed in the dura mater of the second mouse. This finding suggests that a considerable proportion of immune cells in the dura mater do not arrive from the bloodstream, but instead originate from the bone marrow in the skull and the vertebrae of the spine. This shortcut is made possible by the cells crawling along the outside of blood vessels inside small, bony channels, identified previously⁷, between the bone marrow and the dura mater (Fig. 1). Thus, the dura mater sources a private immune protection right outside the outer CNS barrier (the arachnoid mater) from adjacent bone marrow through a previously unrecognized route.



Lymphatic vessels at the base of the mouse brain provide direct drainage to the periphery

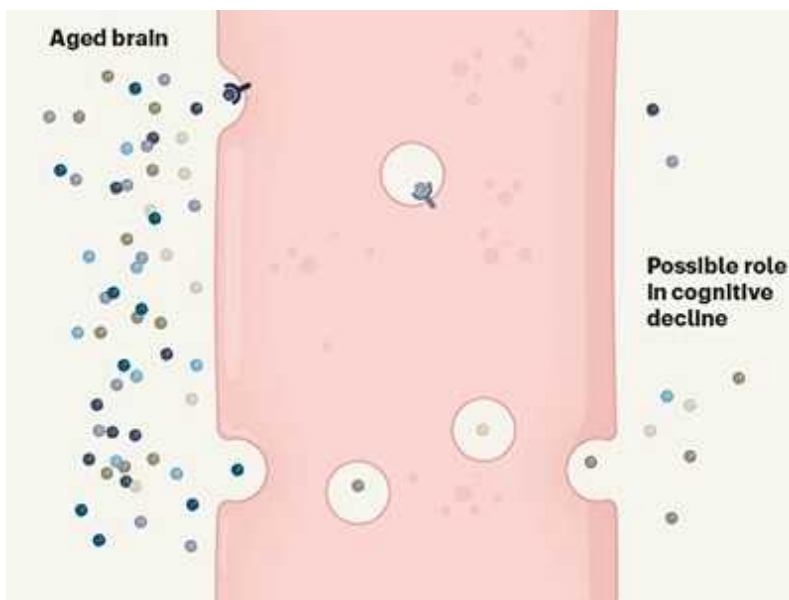
Analysis of gene expression and other characteristics of the individual dura mater immune cells supported the idea that these bone-marrow-derived immune cells are programmed to ensure CNS health, whereas those arriving from the blood tend to be pro-inflammatory and thus more ready to fight potential infections. Moreover, with ageing, increasing numbers of blood-derived immune cells were observed in the dura mater, suggesting a shift in CNS-border immune protection.

Unexpectedly, Cugurra *et al.*² found a large number of a type of bone-marrow-derived immune cell called granulocytes in the dura mater. Granulocytes are not typically resident in tissue: they are short-lived, circulate in the blood and usually infiltrate tissue only during acute inflammation. However, the authors found these cells in the apparently uninflamed dura mater, and, indeed, granulocytes have been observed in healthy meninges previously⁶.

Therefore, the bone-marrow-derived granulocytes might be a special subset of granulocytes with functions different from those of the cells from the blood. This finding is highly relevant to stroke caused by insufficient oxygen reaching the brain, because the presence of granulocytes in the meninges is a major hallmark of such an event^{8,9}, and yet blocking granulocyte infiltration

from the blood had no effect on the outcome of stroke in clinical trials¹⁰. Previous work⁷ showed that the oxygen-deprived brain can recruit granulocytes directly from the skull bone marrow to the brain tissue by way of the same bony channels described in the present studies.

The signals that recruit cells from the bone marrow to the dura mater remain to be identified. Cugurra *et al.* and Brioschi *et al.* propose a role for the chemokine molecule CXCL12 and its cell-surface receptor CXCR4. However, CXCL12 usually promotes immune-cell retention in the bone marrow¹¹, and blocking CXCR4 would release these bone-marrow cells into the blood¹¹. Thus, these roles of CXCL12 and CXCR4 are difficult to reconcile with a role in direct immune-cell recruitment to the dura mater. One possibility is that blocking CXCR4 on bone-marrow granulocytes might enable these cells to sense gradients of the inflammatory chemokines CCL2 and CCL8, which Cugurra and colleagues found to be highly expressed in the dura mater.



Unexpected amount of blood-borne protein enters the young brain

Another indication that the dura mater might provide the CNS with a special form of immune surveillance was that it contains a substantial number of immature B cells³ expressing CXCR4, similar to those in the bone marrow. This suggests that the bone marrow outsources part of its role in B-cell

maturity to the dura mater. Indeed, cells of the dura mater were found to produce CXCL12, thus providing a bone-marrow-like environment for these immature B cells.

The signals that drive movement of premature B cells from the bone marrow to the dura mater remain to be identified. The authors speculate that the brain and spinal cord might program immune cells coming from adjacent bone-marrow niches to provide CNS-tailored immune protection. A key remaining question is how the CNS communicates with the immune cells in the dura mater or the bone marrow in the skull and vertebrae, because they are on different sides of the arachnoid barrier, which establishes a barrier between the CNS and the changing blood milieu.

Notably, in this context, the dura mater sends many blood vessels into the skull bone⁹. And, intriguingly, both studies found high levels of myeloid cells and B cells in the dura mater that encases the dural sinus (the large central vein that drains blood, and probably CSF, from the brain), particularly at sites where blood vessels from the CNS, and the subarachnoid space, join the dural sinus. Previous work from some of the authors of the current studies suggested that the dura mater along the dural sinus constitutes a special neuroimmune interface¹². It is thus tempting to speculate that the signals driving the recruitment of immune cells from the bone marrow to the dura mater, and potentially into the CNS itself, do not cross the arachnoid barrier, but instead move along the walls of blood vessels that form a bridge between brain barriers such as the arachnoid barrier and the glia limitans.

Future research should determine whether skull and vertebra bone marrow are different from bone marrow elsewhere. Furthermore, how do the functions of bone-marrow-sourced immune cells in the dura mater compare with those of the immune cells that keep the subarachnoid space under surveillance? The signals attracting immune cells to the dura mater from the bone marrow, as opposed to from the blood, must also be explored. And how do the bone-marrow-sourced immune cells in the dura mater interact with those from the blood?

The channels connecting the skull and vertebra bone marrow with the dura mater also exist in humans⁷, suggesting that observations of immune-cell

migration and function in mice might translate to humans. Moreover, because the dura mater lacks a blood–brain barrier, immune cells there could be more easily therapeutically targeted than immune cells in the subarachnoid space or in CNS tissue itself. Understanding the precise role of these dura mater immune cells, the signals that control them and how they contribute to CNS immunity could therefore open up entirely new avenues for the design of treatments for disorders involving CNS inflammation.

Nature **596**, 38-40 (2021)

doi: <https://doi.org/10.1038/d41586-021-01962-4>

References

1. 1.

Engelhardt, B., Vajkoczy, P. & Weller, R. O. *Nature Immunol.* **18**, 123–131 (2017).

[PubMed](#) [Article](#) [Google Scholar](#)

2. 2.

Cugurra, A. *et al.* *Science* <https://doi.org/10.1126/science.abf7844> (2021).

[Article](#) [Google Scholar](#)

3. 3.

Brioschi, S. *et al.* *Science* <https://doi.org/10.1126/science.abf9277> (2021).

[Article](#) [Google Scholar](#)

4. 4.

Rua, R. & McGavern, D. B. *Trends Mol. Med.* **24**, 542–559 (2018).

[PubMed](#) [Article](#) [Google Scholar](#)

5. 5.

Mrdjen, D. *et al.* *Immunity* **48**, 599 (2018).

[PubMed](#) [Article](#) [Google Scholar](#)

6. 6.

Engelhardt, B. & Coisne, C. *Fluids Barriers CNS* **8**, 4 (2011).

[PubMed](#) [Article](#) [Google Scholar](#)

7. 7.

Herisson, F. *et al.* *Nature Neurosci.* **21**, 1209–1217 (2018).

[PubMed](#) [Article](#) [Google Scholar](#)

8. 8.

Enzmann, G. *et al.* *Acta Neuropathol.* **125**, 395–412 (2013).

[PubMed](#) [Article](#) [Google Scholar](#)

9. 9.

Zenker, W. & Kubik, S. *Anat. Embryol.* **193**, 1–13 (1996).

[Article](#) [Google Scholar](#)

10. 10.

Enzmann, G., Kargaran, S. & Engelhardt, B. *Ther. Adv. Neurol. Disord.* **11**, 1756286418794184 (2018).

[PubMed](#) [Article](#) [Google Scholar](#)

11. 11.

Lapidot, T. & Kollet, O. *Leukemia* **16**, 1992–2003 (2002).

[PubMed](#) [Article](#) [Google Scholar](#)

12. 12.

Rustenhoven, J. *et al.* *Cell* **184**, 1000–1016 (2021).

[PubMed](#) [Article](#) [Google Scholar](#)

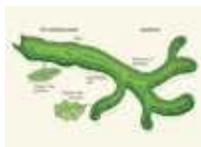
[Download references](#)

Competing Interests

The author declares no competing interests.

Related Articles

- [Read the paper: Skull and vertebral bone marrow are myeloid cell reservoirs for the meninges and CNS parenchyma](#)
- [Read the paper: Heterogeneity of meningeal B cells reveals a lymphopoietic niche at the CNS borders](#)



- [Lymphatic vessels at the base of the mouse brain provide direct drainage to the periphery](#)



- [Unexpected amount of blood-borne protein enters the young brain](#)

- [See all News & Views](#)

Subjects

- [Immunology](#)
- [Brain](#)

nature careers

Jobs >

- [Translational Biologist, Oncology](#)

Astex Pharmaceuticals Limited

Cambridge, United Kingdom

- [Postdoctoral Researcher – studying the histopathology of acute ischaemic stroke blood clots and the correlation of composition with impedance measurements\(CÚRAM\), NUIG RES 158-21](#)

National University of Ireland Galway (NUI Galway)

Galway, Ireland

- [Summer Laboratory Technician](#)

Oklahoma Medical Research Foundation (OMRF)

Oklahoma City, United States

- [PhD student \(m/f/d\) Hormonal programming of hepatic chromatin landscapes](#)

Technical University of Munich (TUM)

Munich, Germany

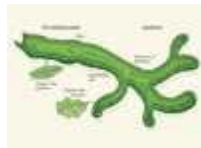
Nature Briefing

An essential round-up of science news, opinion and analysis, delivered to your inbox every weekday.

[Download PDF](#)

Related Articles

- [Read the paper: Skull and vertebral bone marrow are myeloid cell reservoirs for the meninges and CNS parenchyma](#)
- [Read the paper: Heterogeneity of meningeal B cells reveals a lymphopoietic niche at the CNS borders](#)



- [Lymphatic vessels at the base of the mouse brain provide direct drainage to the periphery](#)



- [Unexpected amount of blood-borne protein enters the young brain](#)
- [See all News & Views](#)

Subjects

- [Immunology](#)
- [Brain](#)

This article was downloaded by **calibre** from <https://www.nature.com/articles/d41586-021-01962-4>

| [Section menu](#) | [Main menu](#) |

- NEWS AND VIEWS
- 04 August 2021

Bouncing droplets mimic spin systems

Experiments show that a collection of bouncing fluid droplets can behave like a microscopic system of spins — the intrinsic angular momenta of particles. This discovery could lead to a better understanding of the physics of spin systems.

- [Nicolas Vandewalle](#) ⁰

1. [Nicolas Vandewalle](#)

1. Nicolas Vandewalle is at the GRASP Laboratory, Department of Physics, University of Liège, 4000 Liège, Belgium.

[View author publications](#)

You can also search for this author in [PubMed](#) [Google Scholar](#)

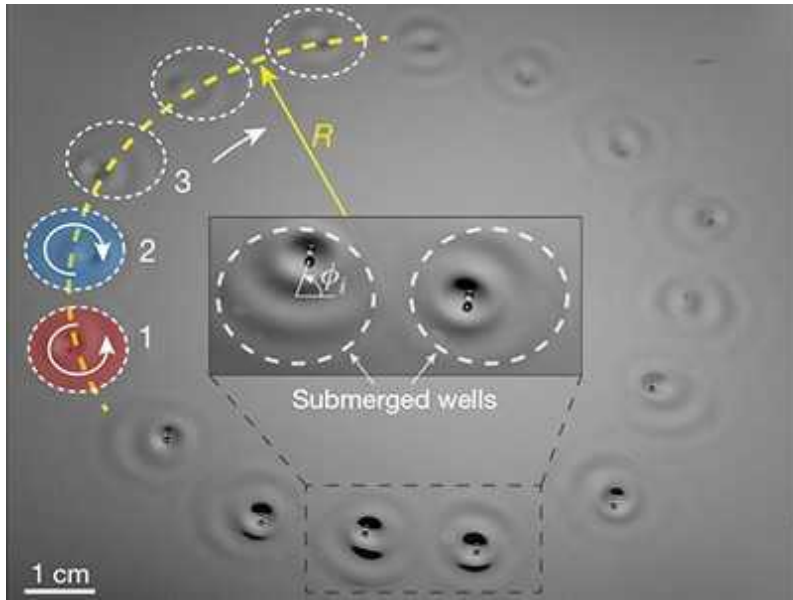




•

[Download PDF](#)

In 2005, researchers found that bouncing fluid droplets on the surface of a vibrating liquid bath can self-propel¹. Remarkably, the dynamical and statistical features of this macroscopic system resemble those of microscopic quantum systems. Building on this work, Sáenz *et al.*² [report in *Nature*](#) that arrays of bouncing droplets can mimic systems of spins (the intrinsic angular momenta of particles). The authors' discovery could increase knowledge of these spin systems, which have uses in spin-based electronics and computing.



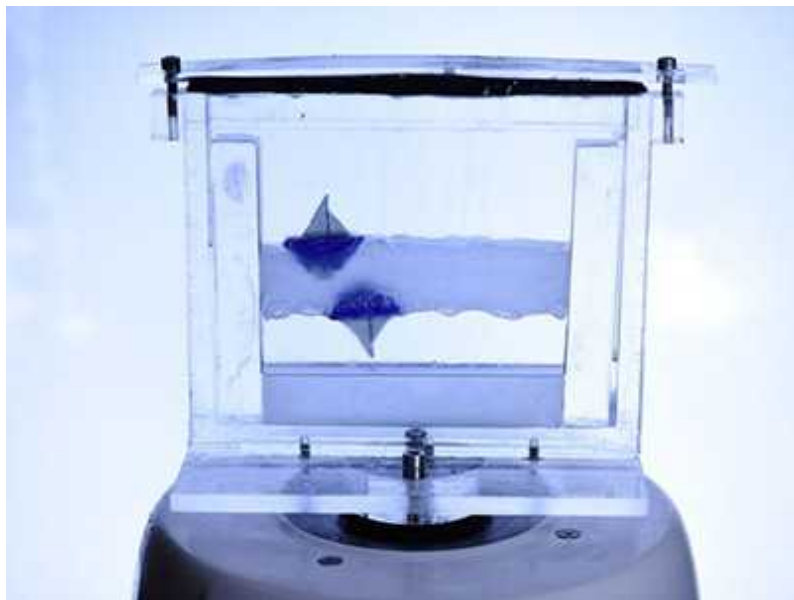
[Read the paper: Emergent order in hydrodynamic spin lattices](#)

In their quest for a better understanding of the emergence of order in typically disordered systems, physicists have developed many models in fields ranging from animal behaviour to materials science. A few of these models have become archetypes that are taught today in advanced physics courses. Let us consider two of them.

The first model concerns the dynamical synchronization of oscillators, which is described in every textbook on nonlinear physics³ — the study of systems in which cause and effect are not directly proportional to each other. Such synchronization is often illustrated by considering the flashing of fireflies. In the model, when one firefly sees others flashing nearby, it speeds up or slows down its own flashing to be in sync with its neighbours. This behaviour explains why, in some areas of south Asia, the synchronicity of fireflies that land on trees at dusk builds up during the night, as shown in an acclaimed 1990 BBC nature documentary series, *The Trials of Life*. In the model, the collective flashing of fireflies results from their subtle interactions mediated by light.

The second model, from statistical physics, is known as the spin model⁴. It was introduced to study ferromagnetism — the familiar type of magnetism found in iron magnets. In the model, spins are arranged on a lattice that is in thermal equilibrium with a reservoir of heat called a thermal bath. A spin

can point either up or down. As with the fireflies, complex physical behaviour emerges when each spin is influenced by its neighbours.



Vibration overcomes gravity on a levitating fluid

The competition between thermal agitation and spin alignment leads to a transition between ordered phases (for strong spin–spin interactions at low temperature) and disordered phases (for weak spin–spin interactions at high temperature). In the ordered phases, the overall symmetry of the spin lattice is broken because the pattern of spins would look different if flipped upside down, whereas in the disordered phases, such symmetry is retained. The properties of this system are therefore governed by the interactions between spins. The ordered phases can correspond to ferromagnetism, in which spins point in the same direction, or antiferromagnetism, in which neighbouring spins point in opposite directions.

Following on from pioneering work^{1,5}, Sáenz and colleagues studied fluid droplets bouncing on the surface of a vertically vibrating liquid bath (Fig. 1a). For particular values of the vibration amplitude and frequency, close to those associated with a surface instability called the Faraday instability, each bounce of the droplets generates a surface wave that causes the droplets to self-propel. Furthermore, these surface waves eventually reach other bouncing droplets, inducing non-trivial droplet–droplet interactions and triggering complex droplet trajectories. Collections of such droplets form

aggregates of interacting bouncing entities. Two droplets can bounce in sync or out of sync with each other⁵. And in some cases, more than two bouncing droplets can share a single surface wave that exhibits a phenomenon known as coherence⁶.

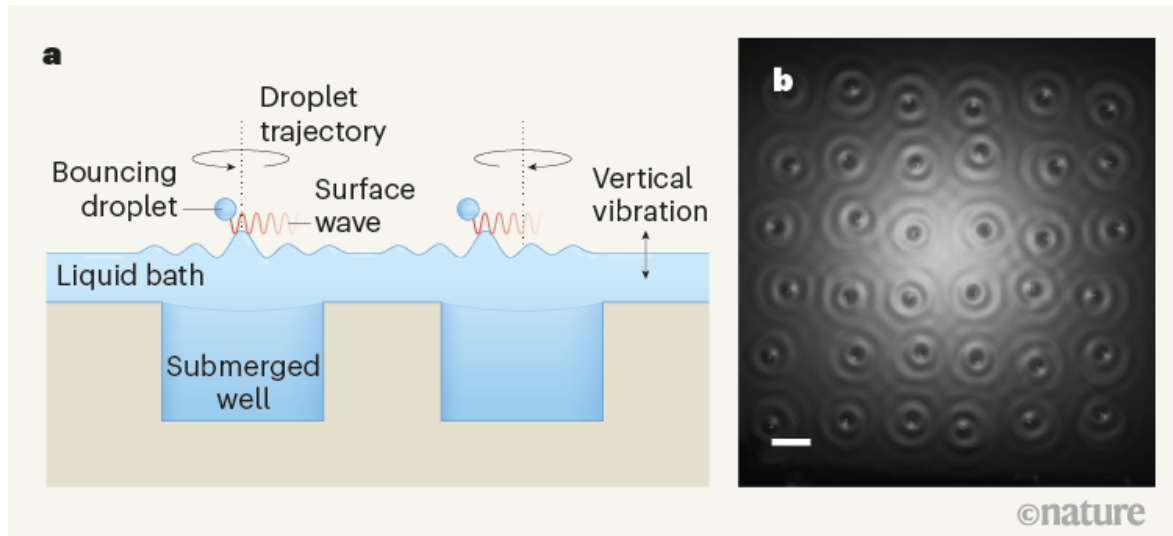
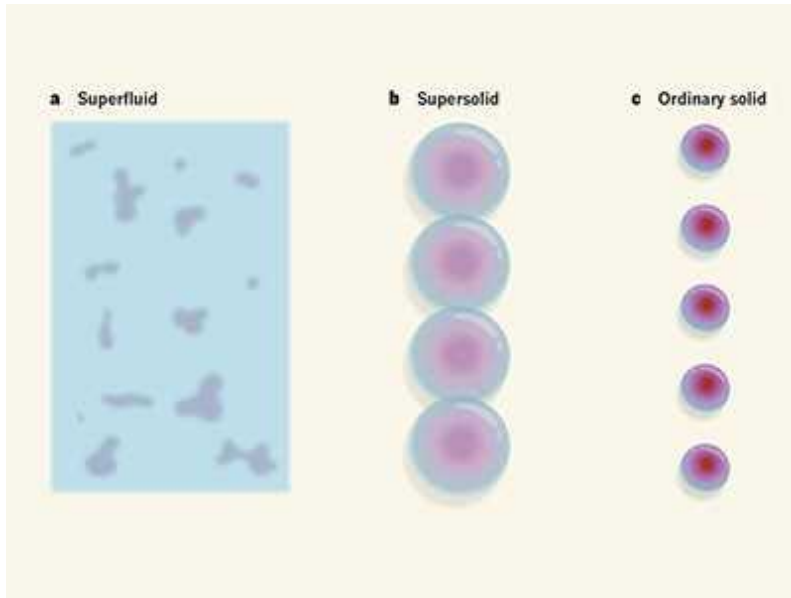


Figure 1 | A system of bouncing droplets. **a**, Sáenz *et al.*² studied the behaviour of fluid droplets bouncing on the surface of a vertically vibrating liquid bath. The depth of the bath varied owing to the presence of submerged wells. Under certain conditions, the droplets generated gradually decaying surface waves that caused the droplets to follow clockwise or anticlockwise circular trajectories and interact with each other in complex ways. **b**, The authors found that arrays of these bouncing droplets (pictured) share many features with systems of spins — the intrinsic angular momenta of particles. Scale bar, 1 centimetre. (Adapted from Fig. 1b and Fig. 4a of ref. 2.)

Sáenz and co-workers considered submerged wells that locally change the depth of the liquid bath. Because these depth variations influence the propagation of the surface waves, the bouncing droplets are piloted along specific paths. In particular, circular submerged wells cause the droplets to follow clockwise or anticlockwise circular trajectories. By analogy with magnetic spin, the spin of such a droplet can be defined as the angular momentum of the droplet's horizontal motion: down for clockwise motion and up for anticlockwise motion.



Quantum gases show flashes of a supersolid

The authors found that when these circular wells are arranged on a one- or two-dimensional lattice with a small (millimetre-scale) lattice spacing, the droplets can be affected by the surface waves emitted by neighbouring droplets (Fig. 1b). Depending on the lattice shape and dimensions, and the experimental conditions, the pattern of droplet spins can resemble the arrangement of magnetic spins in ferromagnetism or antiferromagnetism, meaning that symmetry is broken spontaneously. This ordering of droplet spins emphasizes the complex wave-interaction mechanism that is mediated across the lattice. In spectacular experiments, Sáenz *et al.* discovered that a global angular momentum can be imposed on the system, similar to the way in which an external magnetic field aligns spins and thereby magnetizes materials.

Sáenz and colleagues' work demonstrates that arrays of these droplets can synchronize their bouncing vertical motion just as fireflies synchronize their light flashes. Moreover, it shows that the droplet spins can exhibit pattern formation and symmetry breaking, similar to those seen in magnetic-spin lattices, through subtle hydrodynamic interactions. The system therefore seems to combine the two archetypal models mentioned previously.

Although the hydrodynamic spin lattices presented share many features with magnetic-spin systems, the former are out of equilibrium whereas the latter

are in equilibrium, suggesting that the observed synchronized behaviour might be universal. Sáenz and colleagues' experiments used a limited number of bouncing droplets (fewer than 50), but the authors model larger systems that could be explored in future numerical studies. There is little doubt that these hydrodynamic spin lattices will inspire research at the intersection of statistical physics, nonlinear physics and fluid mechanics.

Nature **596**, 40-41 (2021)

doi: <https://doi.org/10.1038/d41586-021-02077-6>

References

1. 1.

Couder, Y., Protière, S., Fort, E. & Boudaoud, A. *Nature* **437**, 208 (2005).

[PubMed](#) [Article](#) [Google Scholar](#)

2. 2.

Sáenz, P. J. *et al.* *Nature* **596**, 58–62 (2021).

[Article](#) [Google Scholar](#)

3. 3.

Strogatz, S. H. *Nonlinear Dynamics and Chaos* (CRC Press, 2018).

[Google Scholar](#)

4. 4.

Stanley, H. E. *Introduction to Phase Transitions and Critical Phenomena* (Oxford Univ. Press, 1971).

[Google Scholar](#)

5. 5.

Eddi, A., Decelle, A., Fort, E. & Couder, Y. *Europhys. Lett.* **87**, 56002 (2009).

[Article](#) [Google Scholar](#)

6. 6.

Filoux, B., Hubert, M. & Vandewalle, N. *Phys. Rev. E* **92**, 041004 (2015).

[Article](#) [Google Scholar](#)

[Download references](#)

Competing Interests

The author declares no competing interests.

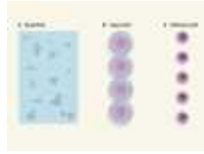
Related Articles



- [Read the paper: Emergent order in hydrodynamic spin lattices](#)



- [Vibration overcomes gravity on a levitating fluid](#)



- [Quantum gases show flashes of a supersolid](#)

- [See all News & Views](#)

Subjects

- [Fluid dynamics](#)
- [Quantum physics](#)
- [Condensed-matter physics](#)

nature careers

[Jobs](#) >

- [Translational Biologist, Oncology](#)

Astex Pharmaceuticals Limited

Cambridge, United Kingdom

- [Postdoctoral Researcher – studying the histopathology of acute ischaemic stroke blood clots and the correlation of composition with impedance measurements\(CÚRAM\), NUIG RES 158-21](#)

National University of Ireland Galway (NUI Galway)

Galway, Ireland

- [Summer Laboratory Technician](#)

Oklahoma Medical Research Foundation (OMRF)

Oklahoma City, United States

- [PhD student \(m/f/d\) Hormonal programming of hepatic chromatin landscapes](#)

Technical University of Munich (TUM)

Munich, Germany

Nature Briefing

An essential round-up of science news, opinion and analysis, delivered to your inbox every weekday.

[Download PDF](#)

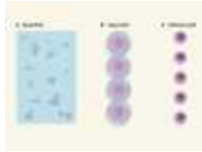
Related Articles



- [Read the paper: Emergent order in hydrodynamic spin lattices](#)



- [Vibration overcomes gravity on a levitating fluid](#)



- [Quantum gases show flashes of a supersolid](#)
- [See all News & Views](#)

Subjects

- [Fluid dynamics](#)
- [Quantum physics](#)
- [Condensed-matter physics](#)

This article was downloaded by **calibre** from <https://www.nature.com/articles/d41586-021-02077-6>

| [Section menu](#) | [Main menu](#) |

- NEWS AND VIEWS
- 03 August 2021

From the archive

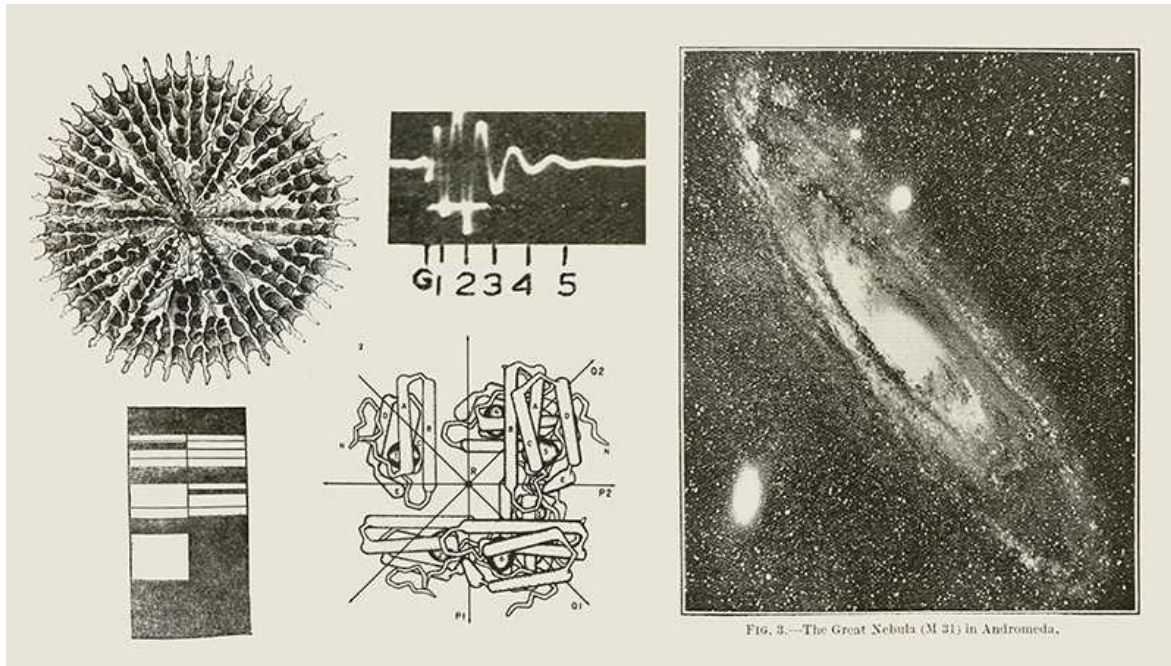
Nature's pages feature an account of the unveiling of the theory of natural selection, and a reported sighting of an unusual type of lightning.





•

[Download PDF](#)



50 years ago

It is a truth of history and an aspect of human behaviour that momentous occasions recalled in later life ... often gain in grandeur and importance with the passing of time. A study of contemporary documents by J. W. T. Moody (*J. Soc. Bibliog. Nat Hist.*, 5, 474; 1971) shows that the presentation of the Darwin–Wallace papers on natural selection to the scientific world on July 1, 1858, was no exception ... [T]he occasion has been said to represent the beginning of a new era in scientific thinking ... but at the time of its presentation it was something of a non-event. [T]he meeting at the Linnean Society ... had been specially called by the president for the election of a new council member ... [T]he secretary read the text of the Darwin and Wallace papers ... Darwin for domestic reasons did not attend the meeting ... [A]t that date agenda were not sent to members, so the fewer than thirty members who attended ... can hardly have expected a momentous meeting ... Moody ... suggests that the audience were not so much stunned by new ideas as they were overwhelmed by the sheer volume of information loaded upon them. No formal discussion took place at the meeting, the audience was expected to switch its attention instantly from the Darwin–Wallace papers to “Notes on the organization of *Phoronis hippocrepis*”.

From *Nature* 6 August 1971

100 years ago

A description of ball lightning seen in the sky at St. John's Wood during a thunderstorm in the early morning of June 26 has recently been received at the Meteorological Office. The phenomenon, a large incandescent mass floating in the air below the clouds and apparently stationary for some minutes, is of great rarity, and the Director of the Meteorological Office, London, S.W.7, would be greatly obliged if persons who observed it on this occasion would communicate with him.

From *Nature* 4 August 1921

Nature **596**, 41 (2021)

doi: <https://doi.org/10.1038/d41586-021-02080-x>

Subjects

- [History](#)
- [Evolution](#)
- [Atmospheric science](#)

nature careers

Jobs >

- [Translational Biologist, Oncology](#)

Astex Pharmaceuticals Limited

Cambridge, United Kingdom

- [Postdoctoral Researcher – studying the histopathology of acute ischaemic stroke blood clots and the correlation of composition with](#)

impedance measurements(CÚRAM), NUIG RES 158-21

National University of Ireland Galway (NUI Galway)
Galway, Ireland

- Summer Laboratory Technician

Oklahoma Medical Research Foundation (OMRF)
Oklahoma City, United States

- PhD student (m/f/d) Hormonal programming of hepatic chromatin landscapes

Technical University of Munich (TUM)
Munich, Germany

Nature Briefing

An essential round-up of science news, opinion and analysis, delivered to your inbox every weekday.

[Download PDF](#)

Subjects

- History
- Evolution
- Atmospheric science

This article was downloaded by **calibre** from <https://www.nature.com/articles/d41586-021-02080-x>

- NEWS AND VIEWS
- 21 July 2021

Two giants of cell division in an oppressive embrace

The enzymes separase and cyclin-dependent kinase are key orchestrators of cell division. Structural data reveal the surprisingly intricate mechanism that renders them both inactive when bound to each other.

- [Silke Hauf](#) 

1. [Silke Hauf](#)

1. Silke Hauf is in the Department of Biological Sciences, Fralin Life Sciences Institute, Virginia Tech, Blacksburg, Virginia 24061, USA.

[View author publications](#)

You can also search for this author in [PubMed](#) [Google Scholar](#)



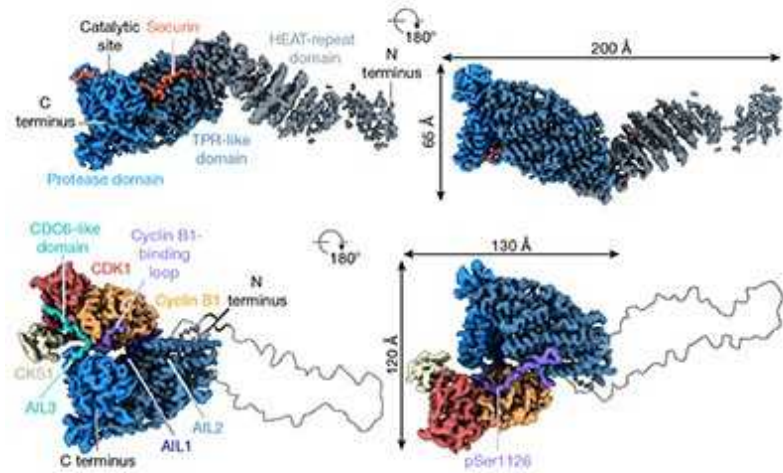


•

[Download PDF](#)

In every dividing cell, a time comes when the two copies of the genome need to be separated. The aptly named enzyme separase springs into action and gets the job done. Unleashing separase at any other time in the life of a cell would be dangerous, so the enzyme is kept well guarded. Human separase is held in check by not one but three mutually exclusive inhibitors. [Writing in Nature](#), Yu *et al.*¹ report structures of human separase in complex with two of these inhibitors. The structures show commonalities but also striking differences. One of the inhibitors snakes along separase to embed itself in the enzyme's active site. The other forces separase to inhibit itself;

at the same time, this inhibitor is itself inhibited by separase in an entangled embrace.



[Read the paper: Structural basis of human separase regulation by securin and CDK1–cyclin B1](#)

Cell division is studied both for its beauty and for the danger that it represents. When all goes well, new healthy cells are born. But when things go awry, newborn cells inherit faulty copies of the genome and might die or become the seed for cancerous growth. Movies of cell division showing this dramatic process never fail to intrigue, and such films have provided an inspiration that has launched renowned scientific careers (see, for example, ref. 2). In the key scene of cell-division movies, chromosomes split abruptly along their length, separating the two copies of the genome destined for the daughter cells. The major force behind the split is separase, which at this crucial moment cleaves a protein complex called cohesin that serves as ‘glue’ between the genome copies³.

Until this pivotal moment, separase activity is blocked by inhibitors. The best-characterized inhibitor is the protein securin, which begins to bind to separase while that enzyme is still being made⁴; it even supports separase synthesis⁵. Genetic and biochemical experiments were the first to hint at the possibility that securin mimics the cohesin substrate and binds to the active site of separase⁶. Structures of budding yeast and nematode separase in

complex with securin confirmed this^{7,8}. One of the structures solved by Yu *et al.* using cryogenic electron microscopy now shows that the same is true for human separase (Fig. 1).

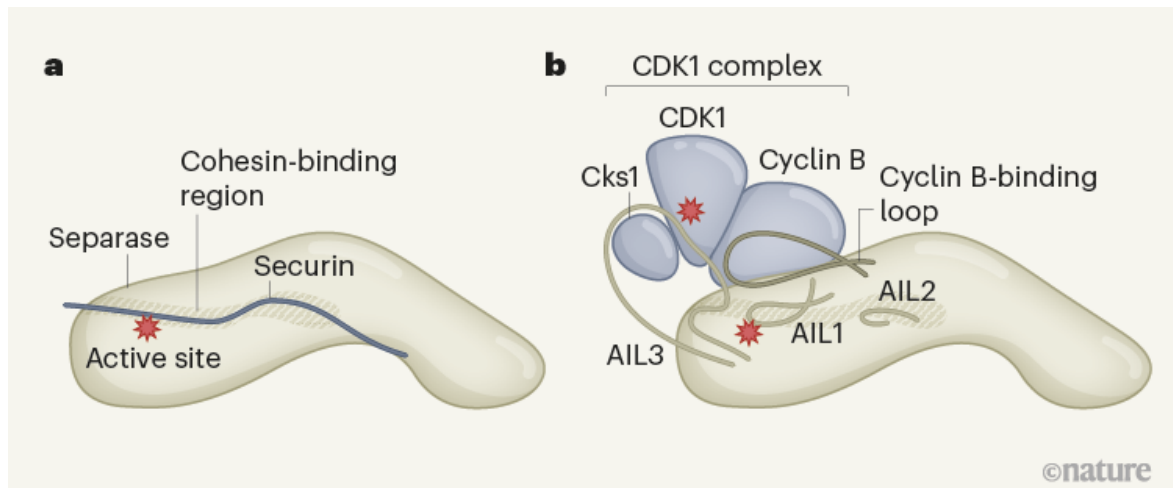


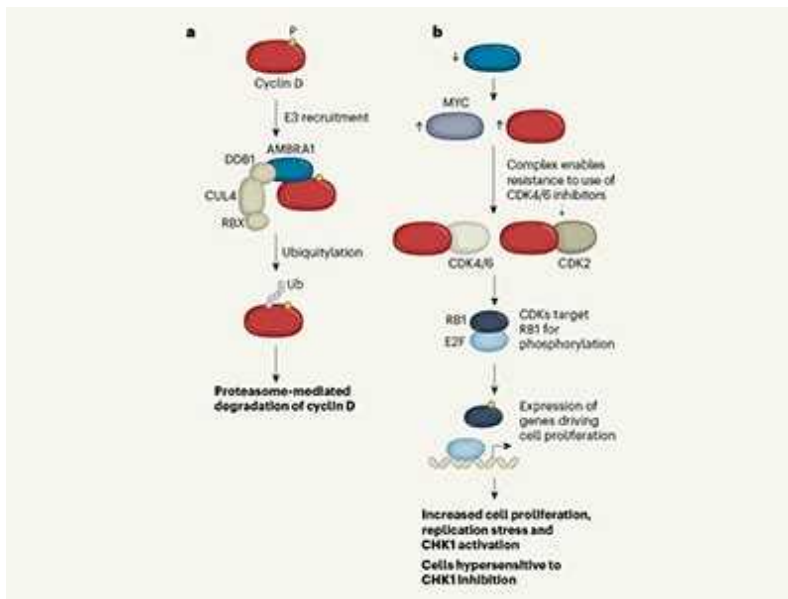
Figure 1 | Structural insights into inhibition of the separase enzyme.

When separase cleaves its target substrate, a protein complex called cohesin, this enables chromosome separation to occur. **a**, The protein securin inhibits separase by binding to a region of the enzyme (shaded area) that normally binds to components of cohesin¹⁴. Securin binding blocks substrate access to the enzyme's active site^{7,8}. Consistent with this earlier work in other species, Yu *et al.*¹ present structural data, obtained using cryogenic electron microscopy, indicating that securin inhibits human separase through this same mechanism. **b**, The authors also obtained structural data revealing how the CDK1 complex (which contains the proteins Cks1, CDK1 and cyclin B) inhibits separase. This occurs through a different mechanism, which relies on separase inhibiting itself. Binding of the CDK1 complex triggers three autoinhibitory loops (AIL1, AIL2 and AIL3) in separase to block parts of the substrate-binding site. In addition, CDK1 is inhibited by AIL3, in agreement with previous biochemical analysis⁹, and cyclin B is inhibited by a fourth separase loop.

The big surprise comes with the second structure that Yu *et al.* solved. This shows separase bound to another of its inhibitors, the cyclin-dependent kinase 1 (CDK1) complex, which consists of the proteins Cks1, CDK1 and cyclin B. This complex is itself a major player in cell division, and it functions by phosphorylating (adding phosphate groups to) hundreds, if not

thousands, of different proteins to bring about the cellular changes required for division. To solve this structure, the authors used a neat trick⁵: they fused separase to a short piece of securin that was long enough to promote separase synthesis but not so long that it impaired binding of the CDK1 complex.

Despite much previous biochemical insight into the interaction between separase and the CDK1 complex⁹, anyone would have been hard-pressed to imagine the structure that Yu *et al.* have solved. The same sites in separase that are used to bind securin are occupied, but now by separase itself, which has become autoinhibitory (Fig. 1). However, unlike securin (and probably cohesin), which binds to separase in a linear fashion (as a continuous stretch of protein), the autoinhibitory elements of separase found in this key binding region are non-contiguous and come from three loops, which the authors call autoinhibitory loops (AIL1, AIL2 and AIL3). AIL3 not only autoinhibits separase; it also inhibits CDK1 by binding to its active site. This loop probably binds to every protein in the complex.

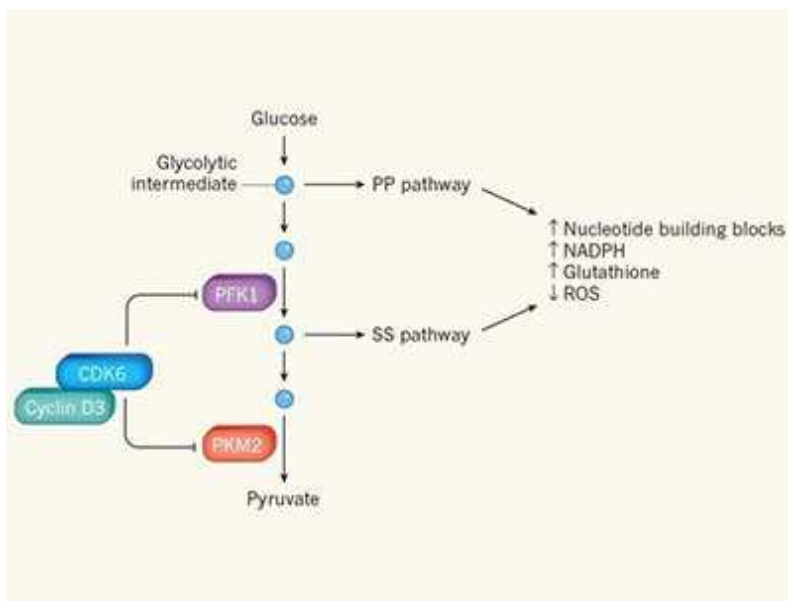


The path to destruction for D-type cyclin proteins

A fourth separase loop wraps around cyclin B and contributes to inhibition of the CDK1 complex. At the centre of this separase loop is a well-characterized phosphorylation site that is required for the formation of this complex⁹. Visualization of this phosphorylation site in the structure revealed

a previously unrecognized phosphate-binding pocket in cyclin B. Seeing the strikingly different types of inhibition achieved by securin and the CDK1 complex makes one wonder what sort of inhibition mechanism the third and most recently discovered¹⁰ separase inhibitor, SGO2/MAD2, might have up its sleeve.

Separase inhibition by securin is probably universal across eukaryotes (organisms with a nucleus), but inhibition by the CDK1 complex seems to be vertebrate specific. Why different inhibition modes evolved, and how labour is distributed between these inhibition options, remain mysterious. Some mammalian cell types crucially rely on separase inhibition by the CDK1 complex¹¹, highlighting the importance of the new structural data that Yu and colleagues report. All three types of separase complex coexist in human cell lines¹⁰. What determines which inhibitor binds to a given separase molecule, and whether separase molecules bound to the various inhibitors execute different functions in the cell once released from inhibition, is unclear. Separase has other roles in cell division beyond that of cohesin cleavage, and perhaps different inhibitors enable spatial or temporal control of separase activity.



Division enzyme regulates metabolism

Interestingly, although separase needs to be released from its inhibitors to trigger chromosome separation, the CDK1 complex also binds to separase

late during cell division, at a time after separase has become active and cohesin has been cleaved. Inhibition of CDK1 in this complex supports the movement of chromosomes into the daughter cells¹².

The formation of this late complex requires the enzyme PIN1¹³, which acts on a site in the separase loop that binds to cyclin B. Curiously, assembly of the CDK1 complex bound to separase in the structure that Yu *et al.* solved did not require PIN1. Human separase not only cleaves cohesin, but also cleaves itself when it becomes active. To solve the structure, the authors made separase catalytically inactive to prevent its auto-cleavage. Did this modification alleviate the requirement for PIN1? And is the reported structure of the CDK1 complex bound to separase representative of a complex found early during cell division, but possibly different from that assembled later on?

Clearly, more remains to be uncovered about the regulation of separase. Further behind-the-scenes footage will be needed before we can not only admire, but also fully understand, cell-division movies.

Nature **596**, 41-42 (2021)

doi: <https://doi.org/10.1038/d41586-021-01944-6>

References

1. 1.

Yu, J. *et al.* *Nature* **596**, 138–142 (2021).

[Article](#) [Google Scholar](#)

2. 2.

Lehmann, R. & Peters, J.-M. *Cell* **184**, 10–14 (2021).

[PubMed](#) [Article](#) [Google Scholar](#)

3. 3.

Uhlmann, F., Wernic, D., Poupart, M.-A., Koonin, E. V. & Nasmyth, K. *Cell* **103**, 375–386 (2000).

[PubMed](#) [Article](#) [Google Scholar](#)

4. 4.

Hellmuth, S. *et al.* *J. Biol. Chem.* **290**, 8002–8010 (2015).

[PubMed](#) [Article](#) [Google Scholar](#)

5. 5.

Rosen, L. E. *et al.* *Nature Commun.* **10**, 5189 (2019).

[PubMed](#) [Article](#) [Google Scholar](#)

6. 6.

Nagao, K. & Yanagida, M. *Genes Cells* **11**, 247–260 (2006).

[PubMed](#) [Article](#) [Google Scholar](#)

7. 7.

Luo, S. & Tong, L. *Nature* **542**, 255–259 (2017).

[PubMed](#) [Article](#) [Google Scholar](#)

8. 8.

Boland, A. *et al.* *Nature Struct. Mol. Biol.* **24**, 414–418 (2017).

[PubMed](#) [Article](#) [Google Scholar](#)

9. 9.

Gorr, I. H., Boos, D. & Stemmann, O. *Mol. Cell* **19**, 135–141 (2005).

[PubMed](#) [Article](#) [Google Scholar](#)

10. 10.

Hellmuth, S., Gómez-H, L., Pendás, A. M. & Stemmann, O. *Nature* **580**, 536–541 (2020).

[PubMed](#) [Article](#) [Google Scholar](#)

11. 11.

Huang, X. *et al.* *Mol. Cell Biol.* **29**, 1498–1505 (2009).

[PubMed](#) [Article](#) [Google Scholar](#)

12. 12.

Shindo, N., Kumada, K. & Hirota, T. *Dev. Cell* **23**, 112–123 (2012).

[PubMed](#) [Article](#) [Google Scholar](#)

13. 13.

Hellmuth, S. *et al.* *Mol. Cell* **58**, 495–506 (2015).

[PubMed](#) [Article](#) [Google Scholar](#)

14. 14.

Lin, Z., Luo, X. & Yu, H. *Nature* **532**, 131–134 (2016).

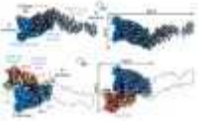
[PubMed](#) [Article](#) [Google Scholar](#)

[Download references](#)

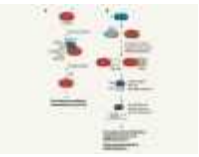
Competing Interests

The author declares no competing interests.

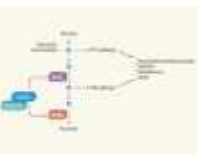
Related Articles



- [Read the paper: Structural basis of human separase regulation by securin and CDK1–cyclin B1](#)



- [The path to destruction for D-type cyclin proteins](#)



- [Division enzyme regulates metabolism](#)
- [See all News & Views](#)

Subjects

- [Cell biology](#)
- [Structural biology](#)

nature careers

[Jobs](#) >

- [Translational Biologist, Oncology](#)

Astex Pharmaceuticals Limited

Cambridge, United Kingdom

- [Postdoctoral Researcher – studying the histopathology of acute ischaemic stroke blood clots and the correlation of composition with impedance measurements\(CÚRAM\), NUIG RES 158-21](#)

National University of Ireland Galway (NUI Galway)

Galway, Ireland

- [**Summer Laboratory Technician**](#)

Oklahoma Medical Research Foundation (OMRF)

Oklahoma City, United States

- [**PhD student \(m/f/d\) Hormonal programming of hepatic chromatin landscapes**](#)

Technical University of Munich (TUM)

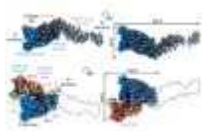
Munich, Germany

Nature Briefing

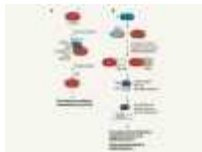
An essential round-up of science news, opinion and analysis, delivered to your inbox every weekday.

[Download PDF](#)

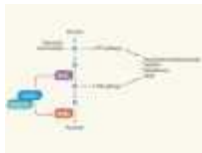
Related Articles



- [**Read the paper: Structural basis of human separase regulation by securin and CDK1–cyclin B1**](#)



- [**The path to destruction for D-type cyclin proteins**](#)



- **Division enzyme regulates metabolism**
- **See all News & Views**

Subjects

- Cell biology
- Structural biology

This article was downloaded by **calibre** from <https://www.nature.com/articles/d41586-021-01944-6>

| [Section menu](#) | [Main menu](#) |

- Review Article
- [Published: 04 August 2021](#)

The role of retrotransposable elements in ageing and age-associated diseases

- [Vera Gorbunova](#) [ORCID: orcid.org/0000-0001-8979-0333](#)^{1,2},
- [Andrei Seluanov](#) [ORCID: orcid.org/0000-0003-3400-538X](#)^{1,2},
- [Paolo Mita](#) [ORCID: orcid.org/0000-0002-2093-4906](#)^{3,4 nAf9},
- [Wilson McKerrow](#)^{3,4},
- [David Fenyö](#) [ORCID: orcid.org/0000-0001-5049-3825](#)^{3,4},
- [Jef D. Boeke](#) [ORCID: orcid.org/0000-0001-5322-4946](#)^{3,4,5},
- [Sara B. Linker](#) [ORCID: orcid.org/0000-0002-6653-1715](#)⁶,
- [Fred H. Gage](#) [ORCID: orcid.org/0000-0002-0938-4106](#)⁶,
- [Jill A. Kreiling](#)^{7,8},
- [Anna P. Petraschen](#)^{7,8},
- [Trenton A. Woodham](#)^{7,8},
- [Jackson R. Taylor](#)^{7,8},
- [Stephen L. Helfand](#)^{7,8} &
- [John M. Sedivy](#) [ORCID: orcid.org/0000-0001-9363-4253](#)^{7,8}

[Nature](#) volume **596**, pages 43–53 (2021) [Cite this article](#)

- 2409 Accesses
- 43 Altmetric
- [Metrics details](#)

Subjects

- [Ageing](#)
- [Senescence](#)
- [Transposition](#)

Abstract

The genomes of virtually all organisms contain repetitive sequences that are generated by the activity of transposable elements (transposons).

Transposons are mobile genetic elements that can move from one genomic location to another; in this process, they amplify and increase their presence in genomes, sometimes to very high copy numbers. In this Review we discuss new evidence and ideas that the activity of retrotransposons, a major subgroup of transposons overall, influences and even promotes the process of ageing and age-related diseases in complex metazoan organisms, including humans. Retrotransposons have been coevolving with their host genomes since the dawn of life. This relationship has been largely competitive, and transposons have earned epithets such as ‘junk DNA’ and ‘molecular parasites’. Much of our knowledge of the evolution of retrotransposons reflects their activity in the germline and is evident from genome sequence data. Recent research has provided a wealth of information on the activity of retrotransposons in somatic tissues during an individual lifespan, the molecular mechanisms that underlie this activity, and the manner in which these processes intersect with our own physiology, health and well-being.

Access options

Subscribe to Journal

Get full journal access for 1 year

\$199.00

only \$3.90 per issue

[Subscribe](#)

All prices are NET prices.
VAT will be added later in the checkout.
Tax calculation will be finalised during checkout.

Rent or Buy article

Get time limited or full article access on ReadCube.

from \$8.99

[Rent or Buy](#)

All prices are NET prices.

Additional access options:

- [Log in](#)
- [Access through your institution](#)
- [Learn about institutional subscriptions](#)

Fig. 1: L1 life cycle.

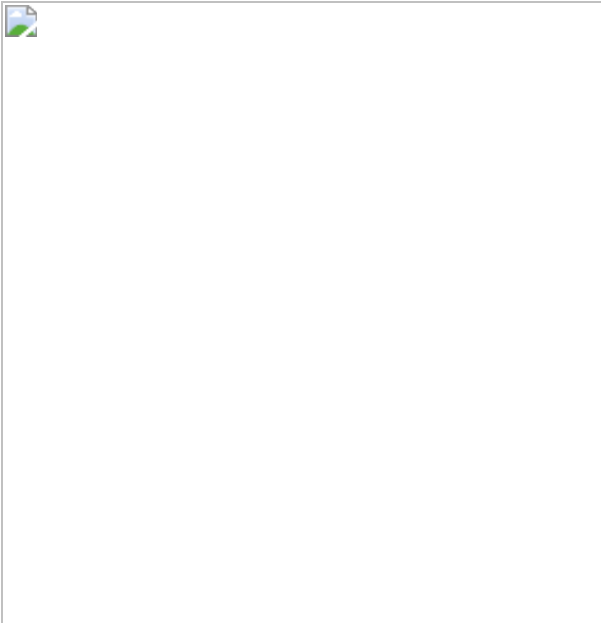


Fig. 2: Retrotransposition mechanisms.

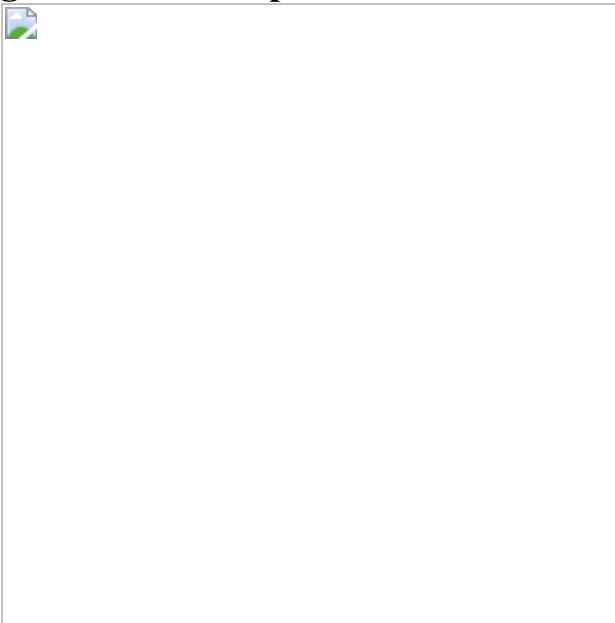


Fig. 3: Surveillance of retrotransposons.

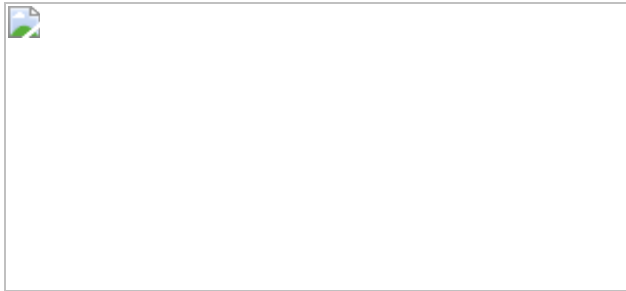
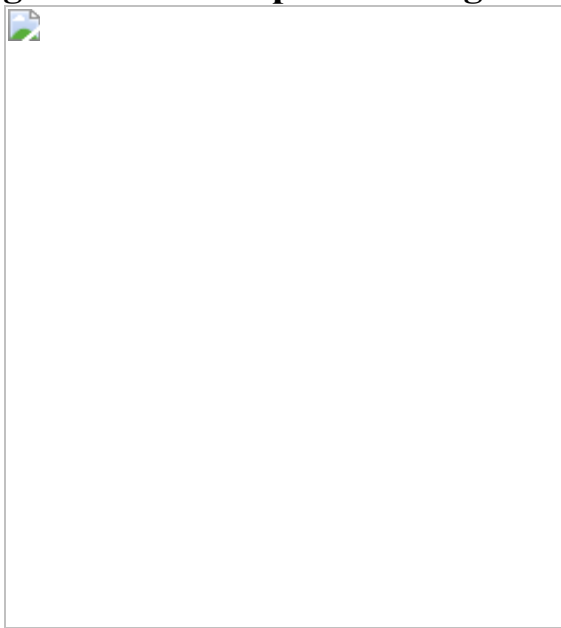


Fig. 4: Retrotransposons as agents of ageing and disease.



References

1. 1.

Huang, C. R., Burns, K. H. & Boeke, J. D. Active transposition in genomes. *Annu. Rev. Genet.* **46**, 651–675 (2012).

[CAS](#) [PubMed](#) [PubMed Central](#) [Article](#) [Google Scholar](#)

2. 2.

Bourque, G. et al. Ten things you should know about transposable elements. *Genome Biol.* **19**, 199 (2018).

[CAS](#) [PubMed](#) [PubMed Central](#) [Article](#) [Google Scholar](#)

3. 3.

Molaro, A. & Malik, H. S. Hide and seek: how chromatin-based pathways silence retroelements in the mammalian germline. *Curr. Opin. Genet. Dev.* **37**, 51–58 (2016).

[CAS](#) [PubMed](#) [PubMed Central](#) [Article](#) [Google Scholar](#)

4. 4.

Cosby, R. L., Chang, N. C. & Feschotte, C. Host-transposon interactions: conflict, cooperation, and cooption. *Genes Dev.* **33**, 1098–1116 (2019).

[CAS](#) [PubMed](#) [PubMed Central](#) [Article](#) [Google Scholar](#)

5. 5.

Pardue, M. L. & DeBaryshe, P. G. Retrotransposons that maintain chromosome ends. *Proc. Natl Acad. Sci. USA* **108**, 20317–20324 (2011).

[ADS](#) [CAS](#) [PubMed](#) [PubMed Central](#) [Article](#) [Google Scholar](#)

6. 6.

Chuong, E. B., Elde, N. C. & Feschotte, C. Regulatory evolution of innate immunity through co-option of endogenous retroviruses. *Science* **351**, 1083–1087 (2016).

[ADS](#) [CAS](#) [PubMed](#) [PubMed Central](#) [Article](#) [Google Scholar](#)

7. 7.

Burns, K. H. Our conflict with transposable elements and its implications for human disease. *Annu. Rev. Pathol.* **15**, 51–70 (2020).

[CAS](#) [PubMed](#) [Article](#) [PubMed Central](#) [Google Scholar](#)

8. 8.

Jacques, P. E., Jeyakani, J. & Bourque, G. The majority of primate-specific regulatory sequences are derived from transposable elements. *PLoS Genet.* **9**, e1003504 (2013).

[CAS](#) [PubMed](#) [PubMed Central](#) [Article](#) [Google Scholar](#)

9. 9.

Mita, P. & Boeke, J. D. How retrotransposons shape genome regulation. *Curr. Opin. Genet. Dev.* **37**, 90–100 (2016).

[CAS](#) [PubMed](#) [PubMed Central](#) [Article](#) [Google Scholar](#)

10. 10.

Brouha, B. et al. Hot L1s account for the bulk of retrotransposition in the human population. *Proc. Natl Acad. Sci. USA* **100**, 5280–5285 (2003).

[ADS](#) [CAS](#) [PubMed](#) [PubMed Central](#) [Article](#) [Google Scholar](#)

11. 11.

Flasch, D. A. et al. Genome-wide de novo L1 retrotransposition connects endonuclease activity with replication. *Cell* **177**, 837–851 (2019).

[CAS](#) [PubMed](#) [PubMed Central](#) [Article](#) [Google Scholar](#)

12. 12.

Sultana, T. et al. The landscape of L1 retrotransposons in the human genome is shaped by pre-insertion sequence biases and post-insertion selection. *Mol. Cell* **74**, 555–570 (2019).

[CAS](#) [PubMed](#) [Article](#) [Google Scholar](#)

13. 13.

Denli, A. M. et al. Primate-specific ORF0 contributes to retrotransposon-mediated diversity. *Cell* **163**, 583–593 (2015).

[CAS](#) [PubMed](#) [Article](#) [Google Scholar](#)

14. 14.

Kulpa, D. A. & Moran, J. V. Cis-preferential LINE-1 reverse transcriptase activity in ribonucleoprotein particles. *Nat. Struct. Mol. Biol.* **13**, 655–660 (2006).

[CAS](#) [PubMed](#) [Article](#) [Google Scholar](#)

15. 15.

Khazina, E. et al. Trimeric structure and flexibility of the L1ORF1 protein in human L1 retrotransposition. *Nat. Struct. Mol. Biol.* **18**, 1006–1014 (2011).

[CAS](#) [PubMed](#) [Article](#) [Google Scholar](#)

16. 16.

Doucet, A. J., Wilusz, J. E., Miyoshi, T., Liu, Y. & Moran, J. V. A 3' poly(A) tract is required for LINE-1 retrotransposition. *Mol. Cell* **60**, 728–741 (2015).

[CAS](#) [PubMed](#) [PubMed Central](#) [Article](#) [Google Scholar](#)

17. 17.

Mita, P. et al. LINE-1 protein localization and functional dynamics during the cell cycle. *eLife* **7**, e30058 (2018).

[PubMed](#) [PubMed Central](#) [Article](#) [Google Scholar](#)

18. 18.

Cost, G. J., Feng, Q., Jacquier, A. & Boeke, J. D. Human L1 element target-primed reverse transcription in vitro. *EMBO J.* **21**, 5899–5910 (2002). **Using biochemical studies, this paper developed the TPRT model of L1 retrotransposition.**

[CAS](#) [PubMed](#) [PubMed Central](#) [Article](#) [Google Scholar](#)

19. 19.

Ardeljan, D. et al. Cell fitness screens reveal a conflict between LINE-1 retrotransposition and DNA replication. *Nat. Struct. Mol. Biol.* **27**, 168–178 (2020).

[CAS](#) [PubMed](#) [PubMed Central](#) [Article](#) [Google Scholar](#)

20. 20.

Mita, P. et al. BRCA1 and S phase DNA repair pathways restrict LINE-1 retrotransposition in human cells. *Nat. Struct. Mol. Biol.* **27**, 179–191 (2020).

[CAS](#) [PubMed](#) [PubMed Central](#) [Article](#) [Google Scholar](#)

21. 21.

Holloway, J. R., Williams, Z. H., Freeman, M. M., Bulow, U. & Coffin, J. M. Gorillas have been infected with the HERV-K (HML-2) endogenous retrovirus much more recently than humans and chimpanzees. *Proc. Natl Acad. Sci. USA* **116**, 1337–1346 (2019).

[CAS](#) [PubMed](#) [PubMed Central](#) [Article](#) [Google Scholar](#)

22. 22.

Küry, P. et al. Human endogenous retroviruses in neurological diseases. *Trends Mol. Med.* **24**, 379–394 (2018).

[PubMed](#) [PubMed Central](#) [Article](#) [CAS](#) [Google Scholar](#)

23. 23.

Wolf, D. & Goff, S. P. Embryonic stem cells use ZFP809 to silence retroviral DNAs. *Nature* **458**, 1201–1204 (2009).

[ADS](#) [CAS](#) [PubMed](#) [PubMed Central](#) [Article](#) [Google Scholar](#)

24. 24.

Castro-Diaz, N. et al. Evolutionally dynamic L1 regulation in embryonic stem cells. *Genes Dev.* **28**, 1397–1409 (2014).

[CAS](#) [PubMed](#) [PubMed Central](#) [Article](#) [Google Scholar](#)

25. 25.

Jacobs, F. M. et al. An evolutionary arms race between KRAB zinc-finger genes *ZNF91/93* and SVA/L1 retrotransposons. *Nature* **516**, 242–245 (2014). **The above three papers show that KZFPs provide DNA sequence specificity to target retrotransposon silencing in mammalian genomes, and uncover the role of KZFPs in the co-evolutionary ‘arms race’ of primate L1s with their hosts.**

[ADS](#) [CAS](#) [PubMed](#) [PubMed Central](#) [Article](#) [Google Scholar](#)

26. 26.

Bulut-Karslioglu, A. et al. Suv39h-dependent H3K9me3 marks intact retrotransposons and silences LINE elements in mouse embryonic stem cells. *Mol. Cell* **55**, 277–290 (2014).

[CAS](#) [PubMed](#) [Article](#) [Google Scholar](#)

27. 27.

Kato, M., Takemoto, K. & Shinkai, Y. A somatic role for the histone methyltransferase Setdb1 in endogenous retrovirus silencing. *Nat. Commun.* **9**, 1683 (2018).

[ADS](#) [PubMed](#) [PubMed Central](#) [Article](#) [CAS](#) [Google Scholar](#)

28. 28.

de Wit, E., Greil, F. & van Steensel, B. Genome-wide HP1 binding in *Drosophila*: developmental plasticity and genomic targeting signals. *Genome Res.* **15**, 1265–1273 (2005).

[PubMed](#) [PubMed Central](#) [Article](#) [CAS](#) [Google Scholar](#)

29. 29.

Ishak, C. A. et al. An RB–EZH2 complex mediates silencing of repetitive DNA sequences. *Mol. Cell* **64**, 1074–1087 (2016).

[CAS](#) [PubMed](#) [PubMed Central](#) [Article](#) [Google Scholar](#)

30. 30.

Liu, N. et al. Selective silencing of euchromatic L1s revealed by genome-wide screens for L1 regulators. *Nature* **553**, 228–232 (2018).

[ADS](#) [CAS](#) [PubMed](#) [Article](#) [PubMed Central](#) [Google Scholar](#)

31. 31.

Van Meter, M. et al. SIRT6 represses LINE1 retrotransposons by ribosylating KAP1 but this repression fails with stress and age. *Nat. Commun.* **5**, 5011 (2014).

[ADS](#) [PubMed](#) [Article](#) [CAS](#) [PubMed Central](#) [Google Scholar](#)

32. 32.

Helleboid, P. Y. et al. The interactome of KRAB zinc finger proteins reveals the evolutionary history of their functional diversification. *EMBO J.* **38**, e101220 (2019).

[PubMed](#) [PubMed Central](#) [Article](#) [CAS](#) [Google Scholar](#)

33. 33.

De Cecco, M. et al. L1 drives IFN in senescent cells and promotes age-associated inflammation. *Nature* **566**, 73–78 (2019). **This study shows that upregulation of L1 triggers an IFN-I response in senescent cells and aged mice that can be therapeutically ameliorated with NRTIs.**

[ADS](#) [PubMed](#) [PubMed Central](#) [Article](#) [CAS](#) [Google Scholar](#)

34. 34.

Simon, M. et al. LINE1 derepression in aged wild-type and SIRT6-deficient mice drives inflammation. *Cell Metab.* **29**, 871–885 (2019). **This study shows that upregulation of L1 triggers an IFN-I response in *Sirt6*-knockout and normal aged mice, and that pathologies and lifespan of *Sirt6* progeroid mice can be improved with NRTIs.**

[CAS](#) [PubMed](#) [PubMed Central](#) [Article](#) [Google Scholar](#)

35. 35.

Wood, J. G. et al. Chromatin-modifying genetic interventions suppress age-associated transposable element activation and extend life span in *Drosophila*. *Proc. Natl Acad. Sci. USA* **113**, 11277–11282 (2016).

Using chromatin-modifying genetic interventions and NRTI treatments in *Drosophila*, this study causally links retrotransposon activation with aging.

[CAS](#) [PubMed](#) [PubMed Central](#) [Article](#) [Google Scholar](#)

36. 36.

Deniz, Ö., Frost, J. M. & Branco, M. R. Regulation of transposable elements by DNA modifications. *Nat. Rev. Genet.* **20**, 417–431 (2019).

[CAS](#) [PubMed](#) [Article](#) [PubMed Central](#) [Google Scholar](#)

37. 37.

Karimi, M. M. et al. DNA methylation and SETDB1/H3K9me3 regulate predominantly distinct sets of genes, retroelements, and chimeric transcripts in mESCs. *Cell Stem Cell* **8**, 676–687 (2011).

[CAS](#) [PubMed](#) [PubMed Central](#) [Article](#) [Google Scholar](#)

38. 38.

Walter, M., Teissandier, A., Pérez-Palacios, R. & Bourc’his, D. An epigenetic switch ensures transposon repression upon dynamic loss of DNA methylation in embryonic stem cells. *eLife* **5**, e11418 (2016).

[PubMed](#) [PubMed Central](#) [Article](#) [Google Scholar](#)

39. 39.

Walsh, C. P., Chaillet, J. R. & Bestor, T. H. Transcription of IAP endogenous retroviruses is constrained by cytosine methylation. *Nat. Genet.* **20**, 116–117 (1998).

[CAS](#) [PubMed](#) [Article](#) [PubMed Central](#) [Google Scholar](#)

40. 40.

Woodcock, D. M., Lawler, C. B., Linsenmeyer, M. E., Doherty, J. P. & Warren, W. D. Asymmetric methylation in the hypermethylated CpG promoter region of the human L1 retrotransposon. *J. Biol. Chem.* **272**, 7810–7816 (1997).

[CAS](#) [PubMed](#) [Article](#) [Google Scholar](#)

41. 41.

Varshney, D. et al. SINE transcription by RNA polymerase III is suppressed by histone methylation but not by DNA methylation. *Nat. Commun.* **6**, 6569 (2015).

[ADS](#) [CAS](#) [PubMed](#) [Article](#) [Google Scholar](#)

42. 42.

Zhang, G. et al. N⁶-methyladenine DNA modification in *Drosophila*. *Cell* **161**, 893–906 (2015).

[CAS](#) [PubMed](#) [Article](#) [Google Scholar](#)

43. 43.

Imbeault, M., Helleboid, P. Y. & Trono, D. KRAB zinc-finger proteins contribute to the evolution of gene regulatory networks. *Nature* **543**, 550–554 (2017).

[ADS](#) [CAS](#) [PubMed](#) [Article](#) [Google Scholar](#)

44. 44.

Wolf, G. et al. KRAB-zinc finger protein gene expansion in response to active retrotransposons in the murine lineage. *eLife* **9**, e56337 (2020).

[CAS](#) [PubMed](#) [PubMed Central](#) [Article](#) [Google Scholar](#)

45. 45.

Rowe, H. M. et al. KAP1 controls endogenous retroviruses in embryonic stem cells. *Nature* **463**, 237–240 (2010).

[ADS](#) [CAS](#) [PubMed](#) [Article](#) [PubMed Central](#) [Google Scholar](#)

46. 46.

Sanchez-Luque, F. J. et al. LINE-1 evasion of epigenetic repression in humans. *Mol. Cell* **75**, 590–604.e12 (2019).

[CAS](#) [PubMed](#) [Article](#) [PubMed Central](#) [Google Scholar](#)

47. 47.

Castel, S. E. & Martienssen, R. A. RNA interference in the nucleus: roles for small RNAs in transcription, epigenetics and beyond. *Nat. Rev. Genet.* **14**, 100–112 (2013).

[CAS](#) [PubMed](#) [PubMed Central](#) [Article](#) [Google Scholar](#)

48. 48.

Goodier, J. L. Restricting retrotransposons: a review. *Mob. DNA* **7**, 16 (2016).

[PubMed](#) [PubMed Central](#) [Article](#) [Google Scholar](#)

49. 49.

Feng, Y., Goubran, M. H., Follack, T. B. & Chelico, L. Deamination-independent restriction of LINE-1 retrotransposition by APOBEC3H. *Sci. Rep.* **7**, 10881 (2017).

[ADS](#) [PubMed](#) [PubMed Central](#) [Article](#) [CAS](#) [Google Scholar](#)

50. 50.

Chung, H. et al. Human ADAR1 prevents endogenous RNA from triggering translational shutdown. *Cell* **172**, 811–824 (2018).

[CAS](#) [PubMed](#) [PubMed Central](#) [Article](#) [Google Scholar](#)

51. 51.

Rice, G. I. et al. Mutations in *ADARI* cause Aicardi-Goutières syndrome associated with a type I interferon signature. *Nat. Genet.* **44**, 1243–1248 (2012).

[CAS](#) [PubMed](#) [PubMed Central](#) [Article](#) [Google Scholar](#)

52. 52.

Zhao, K. et al. Modulation of LINE-1 and Alu/SVA retrotransposition by Aicardi-Goutières syndrome-related SAMHD1. *Cell Rep.* **4**, 1108–1115 (2013).

[CAS](#) [PubMed](#) [PubMed Central](#) [Article](#) [Google Scholar](#)

53. 53.

Stetson, D. B., Ko, J. S., Heidmann, T. & Medzhitov, R. Trex1 prevents cell-intrinsic initiation of autoimmunity. *Cell* **134**, 587–598 (2008). **This work shows that loss of TREX1 in AGS results in accumulation of retrotransposon single-stranded DNA that drives an IFN-I response, and implicates somatic retrotransposon activation as a causal factor in human disease.**

[CAS](#) [PubMed](#) [PubMed Central](#) [Article](#) [Google Scholar](#)

54. 54.

López-Otín, C., Blasco, M. A., Partridge, L., Serrano, M. & Kroemer, G. The hallmarks of aging. *Cell* **153**, 1194–1217 (2013).

[PubMed](#) [PubMed Central](#) [Article](#) [CAS](#) [Google Scholar](#)

55. 55.

Booth, L. N. & Brunet, A. The aging epigenome. *Mol. Cell* **62**, 728–744 (2016).

[CAS](#) [PubMed](#) [PubMed Central](#) [Article](#) [Google Scholar](#)

56. 56.

Pal, S. & Tyler, J. K. Epigenetics and aging. *Sci. Adv.* **2**, e1600584 (2016).

[ADS](#) [PubMed](#) [PubMed Central](#) [Article](#) [CAS](#) [Google Scholar](#)

57. 57.

Sen, P., Shah, P. P., Nativio, R. & Berger, S. L. Epigenetic mechanisms of longevity and aging. *Cell* **166**, 822–839 (2016).

[CAS](#) [PubMed](#) [PubMed Central](#) [Article](#) [Google Scholar](#)

58. 58.

Wood, J. G. et al. Chromatin remodeling in the aging genome of *Drosophila*. *Aging Cell* **9**, 971–978 (2010).

[CAS](#) [PubMed](#) [Article](#) [Google Scholar](#)

59. 59.

Jones, B. C. et al. A somatic piRNA pathway in the *Drosophila* fat body ensures metabolic homeostasis and normal lifespan. *Nat. Commun.* **7**, 13856 (2016).

[ADS](#) [CAS](#) [PubMed](#) [PubMed Central](#) [Article](#) [Google Scholar](#)

60. 60.

Chen, H., Zheng, X., Xiao, D. & Zheng, Y. Age-associated de-repression of retrotransposons in the *Drosophila* fat body, its potential cause and consequence. *Aging Cell* **15**, 542–552 (2016).

[CAS](#) [PubMed](#) [PubMed Central](#) [Article](#) [Google Scholar](#)

61. 61.

Gorgoulis, V. et al. Cellular senescence: defining a path forward. *Cell* **179**, 813–827 (2019).

[CAS](#) [PubMed](#) [Article](#) [Google Scholar](#)

62. 62.

Childs, B. G. et al. Senescent cells: an emerging target for diseases of ageing. *Nat. Rev. Drug Discov.* **16**, 718–735 (2017).

[CAS](#) [PubMed](#) [PubMed Central](#) [Article](#) [Google Scholar](#)

63. 63.

Coppé, J. P. et al. Senescence-associated secretory phenotypes reveal cell-nonautonomous functions of oncogenic RAS and the p53 tumor suppressor. *PLoS Biol.* **6**, 2853–2868 (2008). **This paper reports the discovery of the senescence-associated secretory phenotype (SASP) in senescent cells and implicates its pro-inflammatory effects as the major deleterious consequence of senescent cell accumulation in aging.**

[PubMed](#) [Article](#) [CAS](#) [Google Scholar](#)

64. 64.

Pignolo, R. J., Passos, J. F., Khosla, S., Tchkonia, T. & Kirkland, J. L. Reducing senescent cell burden in aging and disease. *Trends Mol. Med.* **26**, 630–638 (2020).

[CAS](#) [PubMed](#) [PubMed Central](#) [Article](#) [Google Scholar](#)

65. 65.

Chandra, T. & Kirschner, K. Chromosome organisation during ageing and senescence. *Curr. Opin. Cell Biol.* **40**, 161–167 (2016).

[CAS](#) [PubMed](#) [Article](#) [Google Scholar](#)

66. 66.

De Cecco, M. et al. Genomes of replicatively senescent cells undergo global epigenetic changes leading to gene silencing and activation of transposable elements. *Aging Cell* **12**, 247–256 (2013).

[PubMed](#) [Article](#) [CAS](#) [Google Scholar](#)

67. 67.

LaRocca, T. J., Cavalier, A. N. & Wahl, D. Repetitive elements as a transcriptomic marker of aging: evidence in multiple datasets and models. *Aging Cell* **19**, e13167 (2020).

[PubMed](#) [PubMed Central](#) [Article](#) [CAS](#) [Google Scholar](#)

68. 68.

De Cecco, M. et al. Transposable elements become active and mobile in the genomes of aging mammalian somatic tissues. *Aging* **5**, 867–883 (2013).

[PubMed](#) [PubMed Central](#) [Article](#) [Google Scholar](#)

69. 69.

Oberdoerffer, P. et al. SIRT1 redistribution on chromatin promotes genomic stability but alters gene expression during aging. *Cell* **135**, 907–918 (2008).

[CAS](#) [PubMed](#) [PubMed Central](#) [Article](#) [Google Scholar](#)

70. 70.

Issa, J. P. Aging and epigenetic drift: a vicious cycle. *J. Clin. Invest.* **124**, 24–29 (2014).

[CAS](#) [PubMed](#) [PubMed Central](#) [Article](#) [Google Scholar](#)

71. 71.

Klutstein, M., Nejman, D., Greenfield, R. & Cedar, H. DNA methylation in cancer and aging. *Cancer Res.* **76**, 3446–3450 (2016).

[CAS](#) [PubMed](#) [Article](#) [Google Scholar](#)

72. 72.

Horvath, S. & Raj, K. DNA methylation-based biomarkers and the epigenetic clock theory of ageing. *Nat. Rev. Genet.* **19**, 371–384 (2018).

[CAS](#) [PubMed](#) [Article](#) [Google Scholar](#)

73. 73.

Cruickshanks, H. A. et al. Senescent cells harbour features of the cancer epigenome. *Nat. Cell Biol.* **15**, 1495–1506 (2013).

[CAS](#) [PubMed](#) [PubMed Central](#) [Article](#) [Google Scholar](#)

74. 74.

Cole, J. J. et al. Diverse interventions that extend mouse lifespan suppress shared age-associated epigenetic changes at critical gene regulatory regions. *Genome Biol.* **18**, 58 (2017).

[PubMed](#) [PubMed Central](#) [Article](#) [CAS](#) [Google Scholar](#)

75. 75.

Wahl, D., Cavalier, A.N., Smith, M., Seals, D.R. & LaRocca, T.J. Healthy aging interventions reduce repetitive element transcripts. *J. Gerontol. A Biol. Sci. Med. Sci.* **76**, 805–810 (2021).

[PubMed](#) [Article](#) [Google Scholar](#)

76. 76.

Wang, T. et al. Epigenetic aging signatures in mice livers are slowed by dwarfism, calorie restriction and rapamycin treatment. *Genome Biol.* **18**, 57 (2017).

[PubMed](#) [PubMed Central](#) [Article](#) [CAS](#) [Google Scholar](#)

77. 77.

Abe, M. et al. Impact of age-associated increase in 2'-*O*-methylation of miRNAs on aging and neurodegeneration in *Drosophila*. *Genes Dev.* **28**, 44–57 (2014).

1. [CAS](#) [PubMed](#) [PubMed Central](#) [Article](#) [Google Scholar](#)

2. 78.

Hancks, D. C. & Kazazian, H. H., Jr Roles for retrotransposon insertions in human disease. *Mob. DNA* **7**, 9 (2016).

[PubMed](#) [PubMed Central](#) [Article](#) [CAS](#) [Google Scholar](#)

3. 79.

Wimmer, K., Callens, T., Wernstedt, A. & Messiaen, L. The *NF1* gene contains hotspots for L1 endonuclease-dependent de novo insertion. *PLoS Genet.* **7**, e1002371 (2011).

[CAS](#) [PubMed](#) [PubMed Central](#) [Article](#) [Google Scholar](#)

4. 80.

Ervony, G. D. et al. Single-neuron sequencing analysis of L1 retrotransposition and somatic mutation in the human brain. *Cell* **151**, 483–496 (2012).

[CAS](#) [PubMed](#) [PubMed Central](#) [Article](#) [Google Scholar](#)

5. 81.

Upton, K. R. et al. Ubiquitous L1 mosaicism in hippocampal neurons. *Cell* **161**, 228–239 (2015).

[CAS](#) [PubMed](#) [PubMed Central](#) [Article](#) [Google Scholar](#)

6. 82.

Erwin, J. A. et al. L1-associated genomic regions are deleted in somatic cells of the healthy human brain. *Nat. Neurosci.* **19**, 1583–1591 (2016).

[CAS](#) [PubMed](#) [PubMed Central](#) [Article](#) [Google Scholar](#)

7. 83.

Evrony, G. D., Lee, E., Park, P. J. & Walsh, C. A. Resolving rates of mutation in the brain using single-neuron genomics. *eLife* **5**, e12966 (2016).

[PubMed](#) [PubMed Central](#) [Article](#) [CAS](#) [Google Scholar](#)

8. 84.

Zhao, B. et al. Somatic LINE-1 retrotransposition in cortical neurons and non-brain tissues of Rett patients and healthy individuals. *PLoS Genet.* **15**, e1008043 (2019).

[CAS](#) [PubMed](#) [PubMed Central](#) [Article](#) [Google Scholar](#)

9. 85.

Coufal, N. G. et al. L1 retrotransposition in human neural progenitor cells. *Nature* **460**, 1127–1131 (2009). **This study reports an increase in L1 DNA in adult human neurons and hippocampus and implicates the brain as a particularly permissive organ for L1 activation with age.**

[ADS](#) [CAS](#) [PubMed](#) [PubMed Central](#) [Article](#) [Google Scholar](#)

10. 86.

Lee, E. et al. Landscape of somatic retrotransposition in human cancers. *Science* **337**, 967–971 (2012). **This sequencing study from The Cancer Genome Atlas (TCGA) Research Network reveals the profound activation and retrotransposition of L1s in diverse human cancers.**

[ADS](#) [CAS](#) [PubMed](#) [PubMed Central](#) [Article](#) [Google Scholar](#)

11. 87.

Helman, E. et al. Somatic retrotransposition in human cancer revealed by whole-genome and exome sequencing. *Genome Res.* **24**, 1053–1063 (2014).

[CAS](#) [PubMed](#) [PubMed Central](#) [Article](#) [Google Scholar](#)

12. 88.

Tubio, J. M. C. et al. Mobile DNA in cancer. Extensive transduction of nonrepetitive DNA mediated by L1 retrotransposition in cancer genomes. *Science* **345**, 1251343 (2014).

[PubMed](#) [PubMed Central](#) [Article](#) [CAS](#) [Google Scholar](#)

13. 89.

Rodriguez-Martin, B. et al. Pan-cancer analysis of whole genomes identifies driver rearrangements promoted by LINE-1 retrotransposition. *Nat. Genet.* **52**, 306–319 (2020).

[CAS](#) [PubMed](#) [PubMed Central](#) [Article](#) [Google Scholar](#)

14. 90.

Mir, A. A., Philippe, C. & Cristofari, G. euL1db: the European database of L1HS retrotransposon insertions in humans. *Nucleic Acids Res.* **43**, D43–D47 (2015).

[CAS](#) [PubMed](#) [Article](#) [Google Scholar](#)

15. 91.

Hartmann, G. Nucleic acid immunity. *Adv. Immunol.* **133**, 121–169 (2017).

[CAS](#) [PubMed](#) [Article](#) [Google Scholar](#)

16. 92.

Thomas, C. A. et al. Modeling of TREX1-dependent autoimmune disease using human stem cells highlights L1 accumulation as a source of neuroinflammation. *Cell Stem Cell* **21**, 319–331 (2017).

[CAS](#) [PubMed](#) [PubMed Central](#) [Article](#) [Google Scholar](#)

17. 93.

Hopfner, K. P. & Hornung, V. Molecular mechanisms and cellular functions of cGAS–STING signalling. *Nat. Rev. Mol. Cell Biol.* **21**, 501–521 (2020).

[CAS](#) [PubMed](#) [Article](#) [PubMed Central](#) [Google Scholar](#)

18. 94.

Shi, X., Seluanov, A. & Gorbunova, V. Cell divisions are required for L1 retrotransposition. *Mol. Cell. Biol.* **27**, 1264–1270 (2007).

[CAS](#) [PubMed](#) [Article](#) [PubMed Central](#) [Google Scholar](#)

19. 95.

Fukuda, S. et al. Cytoplasmic synthesis of endogenous *Alu* complementary DNA via reverse transcription and implications in age-related macular degeneration. *Proc. Natl Acad. Sci. USA* **118**, e2022751118 (2021).

[CAS](#) [PubMed](#) [PubMed Central](#) [Article](#) [Google Scholar](#)

20. 96.

Roulois, D. et al. DNA-demethylating agents target colorectal cancer cells by inducing viral mimicry by endogenous transcripts. *Cell* **162**, 961–973 (2015).

[CAS](#) [PubMed](#) [PubMed Central](#) [Article](#) [Google Scholar](#)

21. 97.

Chiappinelli, K. B. et al. Inhibiting DNA methylation causes an interferon response in cancer via dsRNA including endogenous retroviruses. *Cell* **162**, 974–986 (2015).

[CAS](#) [PubMed](#) [PubMed Central](#) [Article](#) [Google Scholar](#)

22. 98.

Ahmad, S. et al. Breaching self-tolerance to Alu duplex RNA underlies MDA5-mediated inflammation. *Cell* **172**, 797–810 (2018).

[CAS](#) [PubMed](#) [PubMed Central](#) [Article](#) [Google Scholar](#)

23. 99.

Tunbak, H. et al. The HUSH complex is a gatekeeper of type I interferon through epigenetic regulation of LINE-1s. *Nat. Commun.* **11**, 5387 (2020).

[ADS](#) [CAS](#) [PubMed](#) [PubMed Central](#) [Article](#) [Google Scholar](#)

24. 100.

Zhao, K. et al. LINE1 contributes to autoimmunity through both RIG-I- and MDA5-mediated RNA sensing pathways. *J. Autoimmun.* **90**, 105–115 (2018).

[ADS](#) [CAS](#) [PubMed](#) [Article](#) [Google Scholar](#)

25. 101.

Brisse, M. & Ly, H. Comparative structure and function analysis of the RIG-I-like receptors: RIG-I and MDA5. *Front. Immunol.* **10**, 1586 (2019).

[CAS](#) [PubMed](#) [PubMed Central](#) [Article](#) [Google Scholar](#)

26. 102.

Gasior, S. L., Wakeman, T. P., Xu, B. & Deininger, P. L. The human LINE-1 retrotransposon creates DNA double-strand breaks. *J. Mol. Biol.* **357**, 1383–1393 (2006).

[CAS](#) [PubMed](#) [PubMed Central](#) [Article](#) [Google Scholar](#)

27. 103.

Martin, M., Hiroyasu, A., Guzman, R. M., Roberts, S. A. & Goodman, A. G. Analysis of *Drosophila* STING reveals an evolutionarily conserved antimicrobial function. *Cell Rep.* **23**, 3537–3550.e6 (2018).

[CAS](#) [PubMed](#) [PubMed Central](#) [Article](#) [Google Scholar](#)

28. 104.

Li, W. et al. Activation of transposable elements during aging and neuronal decline in *Drosophila*. *Nat. Neurosci.* **16**, 529–531 (2013).

This works connects the age-associated activation of retrotransposons in *Drosophila* with cognitive decline and proposes the ‘retrotransposon storm’ theory of neurodegeneration.

[CAS](#) [PubMed](#) [PubMed Central](#) [Article](#) [Google Scholar](#)

29. 105.

Hagan, C. R., Sheffield, R. F. & Rudin, C. M. Human Alu element retrotransposition induced by genotoxic stress. *Nat. Genet.* **35**, 219–220 (2003).

[CAS](#) [PubMed](#) [Article](#) [Google Scholar](#)

30. 106.

Yu, Q. et al. Type I interferon controls propagation of long interspersed element-1. *J. Biol. Chem.* **290**, 10191–10199 (2015).

[CAS](#) [PubMed](#) [PubMed Central](#) [Article](#) [Google Scholar](#)

31. 107.

Seluanov, A., Gladyshev, V. N., Vijg, J. & Gorbunova, V. Mechanisms of cancer resistance in long-lived mammals. *Nat. Rev. Cancer* **18**, 433–441 (2018).

[CAS](#) [PubMed](#) [PubMed Central](#) [Article](#) [Google Scholar](#)

32. 108.

Kim, E. B. et al. Genome sequencing reveals insights into physiology and longevity of the naked mole rat. *Nature* **479**, 223–227 (2011).

[ADS](#) [CAS](#) [PubMed](#) [PubMed Central](#) [Article](#) [Google Scholar](#)

33. 109.

Ray, D. A. et al. Multiple waves of recent DNA transposon activity in the bat, *Myotis lucifugus*. *Genome Res.* **18**, 717–728 (2008).

[CAS](#) [PubMed](#) [PubMed Central](#) [Article](#) [Google Scholar](#)

34. 110.

Gorbunova, V., Seluanov, A. & Kennedy, B. K. The world goes bats: living longer and tolerating viruses. *Cell Metab.* **32**, 31–43 (2020).

[CAS](#) [PubMed](#) [PubMed Central](#) [Article](#) [Google Scholar](#)

35. 111.

Franceschi, C., Garagnani, P., Parini, P., Giuliani, C. & Santoro, A. Inflammaging: a new immune-metabolic viewpoint for age-related diseases. *Nat. Rev. Endocrinol.* **14**, 576–590 (2018).

[CAS](#) [PubMed](#) [Article](#) [Google Scholar](#)

36. 112.

Ambati, J. et al. Repurposing anti-inflammasome NRTIs for improving insulin sensitivity and reducing type 2 diabetes development. *Nat. Commun.* **11**, 4737 (2020).

[ADS](#) [CAS](#) [PubMed](#) [PubMed Central](#) [Article](#) [Google Scholar](#)

37. 113.

Neidhart, M. et al. Retrotransposable L1 elements expressed in rheumatoid arthritis synovial tissue: association with genomic DNA hypomethylation and influence on gene expression. *Arthritis Rheum.* **43**, 2634–2647 (2000).

[CAS](#) [PubMed](#) [Article](#) [Google Scholar](#)

38. 114.

Mavragani, C. P. et al. Defective regulation of L1 endogenous retroelements in primary Sjogren's syndrome and systemic lupus erythematosus: role of methylating enzymes. *J. Autoimmun.* **88**, 75–82 (2018).

[CAS](#) [PubMed](#) [Article](#) [Google Scholar](#)

39. 115.

Lee-Kirsch, M. A. et al. Mutations in the gene encoding the 3'-5' DNA exonuclease TREX1 are associated with systemic lupus erythematosus. *Nat. Genet.* **39**, 1065–1067 (2007).

[CAS](#) [PubMed](#) [Article](#) [Google Scholar](#)

40. 116.

Rice, G. et al. Heterozygous mutations in *TREX1* cause familial chilblain lupus and dominant Aicardi-Goutieres syndrome. *Am. J. Hum. Genet.* **80**, 811–815 (2007).

[CAS](#) [PubMed](#) [PubMed Central](#) [Article](#) [Google Scholar](#)

41. 117.

Isenberg, D. A., Manson, J. J., Ehrenstein, M. R. & Rahman, A. Fifty years of anti-ds DNA antibodies: are we approaching journey's end? *Rheumatology* **46**, 1052–1056 (2007).

[CAS](#) [PubMed](#) [Article](#) [Google Scholar](#)

42. 118.

Carter, V. et al. High prevalence and disease correlation of autoantibodies against p40 encoded by long interspersed nuclear elements in systemic lupus erythematosus. *Arthritis Rheumatol.* **72**, 89–99 (2020).

[CAS](#) [PubMed](#) [PubMed Central](#) [Article](#) [Google Scholar](#)

43. 119.

Crow, Y. J. & Manel, N. Aicardi-Goutières syndrome and the type I interferonopathies. *Nat. Rev. Immunol.* **15**, 429–440 (2015).

[CAS](#) [PubMed](#) [Article](#) [Google Scholar](#)

44. 120.

Beck-Engeser, G. B., Eilat, D. & Wabl, M. An autoimmune disease prevented by anti-retroviral drugs. *Retrovirology* **8**, 91 (2011).

[CAS](#) [PubMed](#) [PubMed Central](#) [Article](#) [Google Scholar](#)

45. 121.

Hu, S. et al. SAMHD1 inhibits LINE-1 retrotransposition by promoting stress granule formation. *PLoS Genet.* **11**, e1005367 (2015).

[PubMed](#) [PubMed Central](#) [Article](#) [CAS](#) [Google Scholar](#)

46. 122.

Uehara, R. et al. Two RNase H2 mutants with differential rNMP processing activity reveal a threshold of ribonucleotide tolerance for embryonic development. *Cell Rep.* **25**, 1135–1145 (2018).

[CAS](#) [PubMed](#) [PubMed Central](#) [Article](#) [Google Scholar](#)

47. 123.

Bartsch, K. et al. RNase H2 loss in murine astrocytes results in cellular defects reminiscent of nucleic acid-mediated autoinflammation. *Front. Immunol.* **9**, 587 (2018).

[PubMed](#) [PubMed Central](#) [Article](#) [CAS](#) [Google Scholar](#)

48. 124.

Rice, G. I. et al. Reverse-transcriptase inhibitors in the Aicardi-Goutières syndrome. *N. Engl. J. Med.* **379**, 2275–2277 (2018). **This phase I open-label clinical trial provides evidence that treatment with NRTIs reduces IFN-I activation in patients with AGS.**

[PubMed](#) [Article](#) [PubMed Central](#) [Google Scholar](#)

49. 125.

Kitkumthorn, N. & Mutirangura, A. Long interspersed nuclear element-1 hypomethylation in cancer: biology and clinical applications. *Clin. Epigenetics* **2**, 315–330 (2011).

[CAS](#) [PubMed](#) [PubMed Central](#) [Article](#) [Google Scholar](#)

50. 126.

Benci, J. L. et al. Tumor interferon signaling regulates a multigenic resistance program to immune checkpoint blockade. *Cell* **167**, 1540–1554 (2016).

[CAS](#) [PubMed](#) [PubMed Central](#) [Article](#) [Google Scholar](#)

51. 127.

Terry, D. M. & Devine, S. E. Aberrantly high levels of somatic LINE-1 expression and retrotransposition in human neurological disorders. *Front. Genet.* **10**, 1244 (2020).

[PubMed](#) [PubMed Central](#) [Article](#) [CAS](#) [Google Scholar](#)

52. 128.

Tarallo, V. et al. DICER1 loss and Alu RNA induce age-related macular degeneration via the NLRP3 inflammasome and MyD88. *Cell* **149**, 847–859 (2012).

[CAS](#) [PubMed](#) [PubMed Central](#) [Article](#) [Google Scholar](#)

53. 129.

Fowler, B. J. et al. Nucleoside reverse transcriptase inhibitors possess intrinsic anti-inflammatory activity. *Science* **346**, 1000–1003 (2014).

[ADS](#) [CAS](#) [PubMed](#) [PubMed Central](#) [Article](#) [Google Scholar](#)

54. 130.

Liu, E. Y. et al. Loss of nuclear TDP-43 is associated with decondensation of LINE retrotransposons. *Cell Rep.* **27**, 1409–1421 (2019).

[CAS](#) [PubMed](#) [PubMed Central](#) [Article](#) [Google Scholar](#)

55. 131.

Prudencio, M. et al. Repetitive element transcripts are elevated in the brain of *C9orf72* ALS/FTLD patients. *Hum. Mol. Genet.* **26**, 3421–3431 (2017).

[CAS](#) [PubMed](#) [PubMed Central](#) [Article](#) [Google Scholar](#)

56. 132.

Tam, O. H. et al. Postmortem cortex samples identify distinct molecular subtypes of ALS: retrotransposon activation, oxidative stress, and activated glia. *Cell Rep.* **29**, 1164–1177 (2019).

[CAS](#) [PubMed](#) [PubMed Central](#) [Article](#) [Google Scholar](#)

57. 133.

Hu, Y. et al. Increased peripheral blood inflammatory cytokine levels in amyotrophic lateral sclerosis: a meta-analysis study. *Sci. Rep.* **7**, 9094 (2017).

[ADS](#) [PubMed](#) [PubMed Central](#) [Article](#) [CAS](#) [Google Scholar](#)

58. 134.

Wang, R., Yang, B. & Zhang, D. Activation of interferon signaling pathways in spinal cord astrocytes from an ALS mouse model. *Glia* **59**, 946–958 (2011).

[PubMed](#) [PubMed Central](#) [Article](#) [Google Scholar](#)

59. 135.

Chang, Y. H. & Dubnau, J. The Gypsy endogenous retrovirus drives non-cell-autonomous propagation in a *Drosophila* TDP-43 model of neurodegeneration. *Curr. Biol.* **29**, 3135–3152.e4 (2019).

[CAS](#) [PubMed](#) [PubMed Central](#) [Article](#) [Google Scholar](#)

60. 136.

Krug, L. et al. Retrotransposon activation contributes to neurodegeneration in a *Drosophila* TDP-43 model of ALS. *PLoS Genet.* **13**, e1006635 (2017).

[PubMed](#) [PubMed Central](#) [Article](#) [CAS](#) [Google Scholar](#)

61. 137.

Frost, B., Hemberg, M., Lewis, J. & Feany, M. B. Tau promotes neurodegeneration through global chromatin relaxation. *Nat. Neurosci.* **17**, 357–366 (2014).

[CAS](#) [PubMed](#) [PubMed Central](#) [Article](#) [Google Scholar](#)

62. 138.

Guo, C. et al. Tau activates transposable elements in Alzheimer's disease. *Cell Rep.* **23**, 2874–2880 (2018).

[CAS](#) [PubMed](#) [PubMed Central](#) [Article](#) [Google Scholar](#)

63. 139.

Sun, W., Samimi, H., Gamez, M., Zare, H. & Frost, B. Pathogenic tau-induced piRNA depletion promotes neuronal death through transposable element dysregulation in neurodegenerative tauopathies. *Nat. Neurosci.* **21**, 1038–1048 (2018).

[CAS](#) [PubMed](#) [PubMed Central](#) [Article](#) [Google Scholar](#)

64. 140.

Lee, M. H. et al. Somatic APP gene recombination in Alzheimer's disease and normal neurons. *Nature* **563**, 639–645 (2018).

[ADS](#) [CAS](#) [PubMed](#) [PubMed Central](#) [Article](#) [Google Scholar](#)

65. 141.

Coufal, N. G. et al. Ataxia telangiectasia mutated (ATM) modulates long interspersed element-1 (L1) retrotransposition in human neural stem cells. *Proc. Natl Acad. Sci. USA* **108**, 20382–20387 (2011).

[ADS](#) [CAS](#) [PubMed](#) [PubMed Central](#) [Article](#) [Google Scholar](#)

66. 142.

Petersen, A. J., Rimkus, S. A. & Wassarman, D. A. ATM kinase inhibition in glial cells activates the innate immune response and causes neurodegeneration in *Drosophila*. *Proc. Natl Acad. Sci. USA* **109**, E656–E664 (2012).

[ADS](#) [CAS](#) [PubMed](#) [PubMed Central](#) [Article](#) [Google Scholar](#)

67. 143.

Song, X., Ma, F. & Herrup, K. Accumulation of cytoplasmic DNA due to ATM deficiency activates the microglial viral response system with neurotoxic consequences. *J. Neurosci.* **39**, 6378–6394 (2019).

[CAS](#) [PubMed](#) [PubMed Central](#) [Article](#) [Google Scholar](#)

68. 144.

Haag, S. M. et al. Targeting STING with covalent small-molecule inhibitors. *Nature* **559**, 269–273 (2018).

[ADS](#) [CAS](#) [PubMed](#) [Article](#) [Google Scholar](#)

69. 145.

Lama, L. et al. Development of human cGAS-specific small-molecule inhibitors for repression of dsDNA-triggered interferon expression. *Nat. Commun.* **10**, 2261 (2019).

[ADS](#) [PubMed](#) [PubMed Central](#) [Article](#) [CAS](#) [Google Scholar](#)

70. 146.

Dai, J. et al. Acetylation blocks cGAS activity and inhibits self-DNA-induced autoimmunity. *Cell* **176**, 1447–1460 (2019).

[CAS](#) [PubMed](#) [PubMed Central](#) [Article](#) [Google Scholar](#)

71. 147.

Piscianz, E. et al. Reappraisal of antimalarials in interferonopathies: new perspectives for old drugs. *Curr. Med. Chem.* **25**, 2797–2810 (2018).

[CAS](#) [PubMed](#) [Article](#) [Google Scholar](#)

72. 148.

Kanfi, Y. et al. The sirtuin SIRT6 regulates lifespan in male mice. *Nature* **483**, 218–221 (2012).

[ADS](#) [CAS](#) [PubMed](#) [Article](#) [Google Scholar](#)

73. 149.

Dou, Z. et al. Cytoplasmic chromatin triggers inflammation in senescence and cancer. *Nature* **550**, 402–406 (2017).

[ADS](#) [CAS](#) [PubMed](#) [PubMed Central](#) [Article](#) [Google Scholar](#)

74. 150.

Mackenzie, K. J. et al. cGAS surveillance of micronuclei links genome instability to innate immunity. *Nature* **548**, 461–465 (2017).

[ADS](#) [CAS](#) [PubMed](#) [PubMed Central](#) [Article](#) [Google Scholar](#)

75. 151.

West, A. P. et al. Mitochondrial DNA stress primes the antiviral innate immune response. *Nature* **520**, 553–557 (2015).

[ADS](#) [PubMed](#) [PubMed Central](#) [Article](#) [CAS](#) [Google Scholar](#)

76. 152.

Correia-Melo, C. et al. Mitochondria are required for pro-ageing features of the senescent phenotype. *EMBO J.* **35**, 724–742 (2016).

[CAS](#) [PubMed](#) [PubMed Central](#) [Article](#) [Google Scholar](#)

77. 153.

Vizioli, M. G. et al. Mitochondria-to-nucleus retrograde signaling drives formation of cytoplasmic chromatin and inflammation in senescence. *Genes Dev.* **34**, 428–445 (2020).

[CAS](#) [PubMed](#) [PubMed Central](#) [Article](#) [Google Scholar](#)

[Download references](#)

Acknowledgements

The following funding sources are acknowledged: V.G. and A.S., NIH R37 AG046320, R01 AG027237, P01 AG047200 and P01 AG051449; P.M. and J.D.B., NIH P01 AG051449 and R21 CA235521; F.H.G., NIH R01 AG056306, R01 AG057706, the American Heart Association, Paul G. Allen Frontiers Group Grant no. 19PABHI34610000, the Grace Foundation, the JPB Foundation and A. C. Merle-Smith; J.A.K., NIH P20 GM119943 and P01 AG051449; J.R.T., NIH K99 AG057812; S.L.H., NIH R01 AG024353, P01 AG051449 and R01 AG067306; and J.M.S., NIH R01 AG016694 and P01 AG051449.

Author information

Author notes

1. Paolo Mita

Present address: Pandemic Response Lab, New York, NY, USA

Affiliations

1. Department of Biology, University of Rochester, Rochester, NY, USA

Vera Gorbunova & Andrei Seluanov

2. Department of Medicine, University of Rochester, Rochester, NY, USA

Vera Gorbunova & Andrei Seluanov

3. Institute for Systems Genetics, NYU Langone Health, New York, NY, USA

Paolo Mita, Wilson McKerrow, David Fenyö & Jef D. Boeke

4. Department of Biochemistry and Molecular Pharmacology, NYU Langone Health, New York, NY, USA

Paolo Mita, Wilson McKerrow, David Fenyö & Jef D. Boeke

5. Department of Biomedical Engineering, NYU Tandon School of Engineering, New York, NY, USA

Jef D. Boeke

6. Laboratory of Genetics, The Salk Institute for Biological Studies, La Jolla, CA, USA

Sara B. Linker & Fred H. Gage

7. Center on the Biology of Aging, Brown University, Providence, RI, USA

Jill A. Kreiling, Anna P. Petrashen, Trenton A. Woodham, Jackson R. Taylor, Stephen L. Helfand & John M. Sedivy

8. Department of Molecular Biology, Cell Biology and Biochemistry, Brown University, Providence, RI, USA

Jill A. Kreiling, Anna P. Petrashen, Trenton A. Woodham, Jackson R. Taylor, Stephen L. Helfand & John M. Sedivy

Authors

1. Vera Gorbunova

[View author publications](#)

You can also search for this author in [PubMed](#) [Google Scholar](#)

2. Andrei Seluanov

[View author publications](#)

You can also search for this author in [PubMed](#) [Google Scholar](#)

3. Paolo Mita

[View author publications](#)

You can also search for this author in [PubMed](#) [Google Scholar](#)

4. Wilson McKerrow

[View author publications](#)

You can also search for this author in [PubMed](#) [Google Scholar](#)

5. David Fenyö

[View author publications](#)

You can also search for this author in [PubMed](#) [Google Scholar](#)

6. Jef D. Boeke

[View author publications](#)

You can also search for this author in [PubMed](#) [Google Scholar](#)

7. Sara B. Linker

[View author publications](#)

You can also search for this author in [PubMed](#) [Google Scholar](#)

8. Fred H. Gage

[View author publications](#)

You can also search for this author in [PubMed](#) [Google Scholar](#)

9. Jill A. Kreiling

[View author publications](#)

You can also search for this author in [PubMed](#) [Google Scholar](#)

10. Anna P. Petrashen

[View author publications](#)

You can also search for this author in [PubMed](#) [Google Scholar](#)

11. Trenton A. Woodham

[View author publications](#)

You can also search for this author in [PubMed](#) [Google Scholar](#)

12. Jackson R. Taylor

[View author publications](#)

You can also search for this author in [PubMed](#) [Google Scholar](#)

13. Stephen L. Helfand

[View author publications](#)

You can also search for this author in [PubMed](#) [Google Scholar](#)

14. John M. Sedivy

[View author publications](#)

You can also search for this author in [PubMed](#) [Google Scholar](#)

Contributions

J.M.S. conceived the review. J.M.S., V.G., A.S., P.M., W.M., D.F., J.D.B., S.B.L., F.H.G., J.A.K., A.P.P., T.A.W., J.R.T. and S.L.H. collectively wrote and edited the manuscript.

Corresponding author

Correspondence to [John M. Sedivy](#).

Ethics declarations

Competing interests

V.G. and A.S. are cofounders of Persimmon Bio; V.G. is a member of the scientific advisory board (SAB) of DoNotAge, Centaura and Elysium; J.D.B. is a founder of Neochromosome, founder and director of CDI Labs, and founder and SAB member of ReOpen Diagnostics, and is also an SAB member of Sangamo, Modern Meadow, Sample6 and the Wyss Institute; F.H.G. is an SAB member of Transposon Therapeutics; and J.M.S. is a cofounder and SAB chair of Transposon Therapeutics and consults for Atropos Therapeutics, Gilead Sciences and Oncolinea.

Additional information

Peer review information *Nature* thanks Peter Adams, Jan Vijg and the other, anonymous, reviewer(s) for their contribution to the peer review of this work.

Publisher's note Springer Nature remains neutral with regard to jurisdictional claims in published maps and institutional affiliations.

Rights and permissions

[Reprints and Permissions](#)

About this article



Check for
updates

Cite this article

Gorbunova, V., Seluanov, A., Mita, P. *et al.* The role of retrotransposable elements in ageing and age-associated diseases. *Nature* **596**, 43–53 (2021). <https://doi.org/10.1038/s41586-021-03542-y>

[Download citation](#)

- Received: 16 August 2020
- Accepted: 13 April 2021
- Published: 04 August 2021
- Issue Date: 05 August 2021
- DOI: <https://doi.org/10.1038/s41586-021-03542-y>

Comments

By submitting a comment you agree to abide by our [Terms](#) and [Community Guidelines](#). If you find something abusive or that does not comply with our terms or guidelines please flag it as inappropriate.

[Access through your institution](#)

[Change institution](#)

[Buy or subscribe](#)

Advertisement

This article was downloaded by **calibre** from <https://www.nature.com/articles/s41586-021-03542-y>.

| [Section menu](#) | [Main menu](#) |

Global upper-atmospheric heating on Jupiter by the polar aurorae
[Download PDF](#)

- Article
- Open Access
- [Published: 04 August 2021](#)

Global upper-atmospheric heating on Jupiter by the polar aurorae

- [J. O'Donoghue](#) ORCID: orcid.org/0000-0002-4218-1191^{1,2},
- [L. Moore](#) ORCID: orcid.org/0000-0003-4481-9862³,
- [T. Bhakyaibul](#)³,
- [H. Melin](#) ORCID: orcid.org/0000-0001-5971-2633⁴,
- [T. Stallard](#)⁴,
- [J. E. P. Connerney](#)^{2,5} &
- [C. Tao](#) ORCID: orcid.org/0000-0001-8817-0589⁶

Nature volume 596, pages 54–57 (2021) [Cite this article](#)

- 1288 Accesses
- 793 Altmetric
- [Metrics details](#)

Subjects

- [Atmospheric dynamics](#)
- [Aurora](#)
- [Giant planets](#)
- [Magnetospheric physics](#)

Abstract

Jupiter's upper atmosphere is considerably hotter than expected from the amount of sunlight that it receives^{1,2,3}. Processes that couple the magnetosphere to the atmosphere give rise to intense auroral emissions and enormous deposition of energy

in the magnetic polar regions, so it has been presumed that redistribution of this energy could heat the rest of the planet^{4,5,6}. Instead, most thermospheric global circulation models demonstrate that auroral energy is trapped at high latitudes by the strong winds on this rapidly rotating planet^{3,5,7,8,9,10}. Consequently, other possible heat sources have continued to be studied, such as heating by gravity waves and acoustic waves emanating from the lower atmosphere^{2,11,12,13}. Each mechanism would imprint a unique signature on the global Jovian temperature gradients, thus revealing the dominant heat source, but a lack of planet-wide, high-resolution data has meant that these gradients have not been determined. Here we report infrared spectroscopy of Jupiter with a spatial resolution of 2 degrees in longitude and latitude, extending from pole to equator. We find that temperatures decrease steadily from the auroral polar regions to the equator. Furthermore, during a period of enhanced activity possibly driven by a solar wind compression, a high-temperature planetary-scale structure was observed that may be propagating from the aurora. These observations indicate that Jupiter's upper atmosphere is predominantly heated by the redistribution of auroral energy.

[Download PDF](#)

Main

Jupiter was observed with the 10-m Keck II telescope for five hours on both 14 April 2016 and 25 January 2017 using NIRSPEC (Near-Infrared Spectrometer¹⁴), with the spectral slit aligned north–south along the axis of planetary rotation (Fig. 1a). Spectral images were acquired as Jupiter rotated, as shown in Fig. 1b,c, in which rotational–vibrational (ro-vibrational) emission lines of the H₃⁺ ion can be seen extending from pole to equator. These ions are a major constituent of Jupiter's ionosphere and mainly reside in the altitude range 600–1,000 km above the 1-bar pressure surface¹⁵. The intensity ratio of two or more H₃⁺ lines can be used to derive the column-averaged parameters of that ion: temperature, number density and radiance¹⁶. As H₃⁺ is assumed to be in quasi-local thermodynamic equilibrium with Jupiter's upper atmosphere¹⁶, its derived temperature is representative of the region. Details of the H₃⁺ fitting process and global mapping of parameters are provided in the [Methods](#) and in Extended Data Figs. 1, 2.

Fig. 1: Example set-up showing the acquisition of Jovian spectra on 14 April 2016.

 **figure1**

a, Slit-viewing camera image filtered between 2.134 μm and 4.228 μm wavelength. Guide images such as this are taken every 9 s and indicate the slit's position on the sky relative to Jupiter. In this image, the Great Red Spot (bottom left) and satellite Ganymede (top left) can be seen. **b, c**, Spectral images of Jupiter showing spectral radiance as a function of wavelength and planetocentric latitude. Most emissions seen in **c** are from the reflection of sunlight from hydrocarbons and hazes. Well-defined vertical lines are H_3^+ ro-vibrational emission lines: they are most intense in the polar regions. The R(3,0) and Q(1,0) H_3^+ lines at 3.41277 μm and 3.9529 μm are the focus of this study, as their consistently high signal-to-noise (SNR) at all latitudes allows us to map upper-atmospheric energy balance globally. The SNR of H_3^+ is high at Jupiter owing to the convenient presence of a deep methane absorption band, particularly in **b** (ref. [27](#)).

[Full size image](#)

Global maps of upper-atmospheric temperature have been produced previously^{[17](#)}, but the spatial resolution was such that about two pixels covered 45–90° latitude in each hemisphere, making it difficult to assess how the auroral region was connected to the rest of the planet. In those maps, equatorial temperatures were similar to auroral values, a finding that would indicate that a heat source is active at low latitudes. In Figs. [2](#) and [3](#), we show near-global maps of Jovian column-averaged H_3^+ temperature, density and radiance, which are the product of several thousand individual fits to the spectral data (see [Methods](#)). Using a magnetic field model, we have overlaid oval-shaped lines on the polar regions of Jupiter in both Figs. [2](#) and [3](#), with each representing the footprint of magnetic field lines that trace from the planet out to a particular distance in Jupiter's equatorial plane^{[18](#)}. The main (auroral) oval traces on average to $30R_J$ in Jupiter's equatorial plane (R_J is Jupiter's equatorial radius of 71,492 km at the 1-bar pressure level). The satellite footprints of Io and Amalthea are fiducial markers, mapping out from the planet to $5.9R_J$ and $2.54R_J$ in the equatorial plane, respectively.

Fig. 2: Equirectangular projections of Jupiter's H_3^+ column-integrated temperature, density and radiance.

 figure2

Projections are shown as a function of central meridian longitude (Jovian system III) and planetocentric latitude. Temperature (T) and radiance (E) panels have uncertainties below 5%, while column densities (N) are limited to 20%. Long black-and-white dashed lines show Jupiter's main auroral oval, short black-and-white dashed lines correspond to the magnetic footprint of Io, and the single thick black line corresponds to the magnetic footprint of Amalthea (described in the main text). White indicates regions with no data coverage (or where no results met the uncertainty criteria). Median (and maximum) uncertainty percentiles for 14 April 2016 are: temperature 2.2% (5%), density 9.4% (15%) and radiance 2.2% (5%). Median (and maximum) uncertainties for 25 January 2017 are: temperature 1.6% (5%), density 5.8% (15%) and radiance 1.8% (5%). The [Methods](#) describes the mapping process, and Extended Data Tables 1–3 show the bin sizes that were used in each parameter map.

[Full size image](#)

Fig. 3: Jupiter's column-averaged H_3^+ temperatures on 14 April 2016 and 25 January 2017.

 **figure3**

a, Orthographic projections of uncertainties in temperature are all below 5%. Long black-and-white dashed lines show Jupiter's main auroral oval, short black-and-white dashed lines correspond to the magnetic footprint of Io, and the single thick black line corresponds to the magnetic footprint of Amalthea (as described in the main text). A visible computer-generated globe of Jupiter based on Hubble Space Telescope imagery is shown underneath the H_3^+ temperature projection. Image credit: NASA Goddard Space Flight Center and the Space Telescope Science Institute. Note that Jupiter is tilted differently on each date to reveal different features. The longitude and latitude gridlines shown are spaced in 60° and 10° increments, respectively. Median (and maximum) uncertainty percentiles are 2.2% (5%) for 14 April 2016 and 1.6% (5%) for

25 January 2017. **b**, Median Jovian H_3^+ temperatures found for each latitude across all longitudes. Error bars are 1σ and indicate the variation of temperature over all longitudes. The [Methods](#) describes the mapping process, and Extended Data Table 1 shows the spatial bin sizes that were used in each projection.

[Source data](#).

[Full size image](#)

Temperatures generally decrease from 1,000 K to 600 K between auroral latitudes and the equator, as shown in Figs. 2 and 3. Densities of H_3^+ , which are enhanced by aurorally driven charged-particle precipitation^{19,20}, cut off sharply near the main oval on both dates, indicating that the direct influence of the aurora ends within several degrees of the main oval. At the same time, equatorward of the auroral regions, H_3^+ temperatures do not sharply fall with latitude. In the absence of any known sub-auroral electric current systems (as are common on Earth²¹) provided through magnetosphere–ionosphere coupling that cause planetary-scale ion–neutral collisions, we interpret the observed temperature gradients as strong evidence that the auroral upper atmosphere is migrating away from the auroral region to lower latitudes and adjacent longitudes, transporting its heat signature along with it. This must then be enabled principally by equatorward-propagating meridional winds.

The Jovian magnetosphere, which is subjected to the solar wind, compresses in response to high dynamic pressure exerted by the solar wind²². One model has shown that magnetospheric compression events could lead to propagation of heat away from the main auroral oval towards the equator and polar cap, introducing a temporary local temperature increase of 50–175 K (refs. [10,23](#)). Temperatures were higher planet-wide on 25 January, as were main oval H_3^+ densities, so a solar wind propagation model²⁴ was used to examine the solar wind dynamic pressure and other parameters at Jupiter near the dates of our observations. It was found that dynamic pressures were over an order of magnitude higher within a day of the 25 January observations, relative to quiet conditions, and almost three times higher than conditions on 14 April. This is indicated in Extended Data Figs. 3–5 (along with increased activity in other parameters). Total auroral power has previously been found to correlate positively with the duration of quiet solar wind conditions before a solar wind compression²², so, given the much longer, quieter period of solar wind activity before the 25 January observations reported here (relative to 14 April), we expect that auroral energy deposition was larger on 25 January. Factoring in the uncertainty of the arrival time of the modelled solar wind at Jupiter, ± 1 days on 14 April and ± 1.5 days on 25 January, we conclude that Jupiter was observed to be in the middle of a global heating event owing to solar wind compression of the Jovian magnetosphere on 25 January.

An unusual high-temperature structure was found on 25 January equatorward of the main auroral oval, extending for 160° longitude. Here, relatively cold (~ 800 K) atmosphere is surrounded by hot auroral and sub-auroral atmosphere at $\sim 1,000$ K. The structure appears to straddle the fiducial footprint of Amalthea, a region mapping to Jupiter's equatorial plane at $2.5R_J$ via the magnetic field, but there are no known substantial sources of plasma or current systems linking those regions. It is possible that the structure is a large region of heated upper atmosphere, caught propagating equatorward away from the main auroral oval after a 'pulse' in solar wind pressure was exerted on the magnetosphere¹⁰. If a heated wave of atmosphere propagates equatorward from the main auroral oval at similar velocity over all longitudes, it is likely to retain the main oval shape along the way; thus the apparent alignment of the feature with Amalthea may be circumstantial. Here we provide a simple equatorward velocity estimate to examine whether the feature's propagation is realistic. We use the latitude separation between the structure's centre and the main oval, which grows with longitude and therefore with time, since the data are recorded in order of increasing longitude. Equatorward velocities for the hot feature were evaluated between 180° and 260° longitude in steps of 20° longitude, with ~ 33 min of time elapsing between each step owing to planetary rotation. A median velocity of 620 m s^{-1} was calculated, with minima and maxima of 500 m s^{-1} and $1,500\text{ m s}^{-1}$, respectively. These velocities are similar to equatorward-propagating travelling ionospheric disturbances observed in Earth's ionosphere (300 – $1,000\text{ m s}^{-1}$)²⁵ but much higher than equatorward velocities reported at Saturn (up to 100 m s^{-1})²⁶ and modelled for Jupiter ($\sim 180\text{ m s}^{-1}$)^{6,10}.

In the vicinity of the main oval, H_3^+ temperatures and densities are found to anticorrelate. This may be due to charged particles having higher average precipitation energies here relative to other regions, and so penetrating deeper, producing H_3^+ at lower, colder altitudes, or evidence that H_3^+ is efficiently cooling the atmosphere through infrared emissions^{20,27}. Indeed, this may explain how the main oval appears relatively colder relative to adjacent regions, despite the fact the region may have been recently heated by hot structure as it passed by. Alternatively, the hot structure may have been triggered by an event that lasted a short period of time, sending a single wave of hot atmosphere towards the equator, while the main oval returned to relatively quiet conditions. Morphological differences between the aurorae on each date indicate the location and depth of auroral precipitation, which is reflected in the derived parameters, as reported by previous observations^{19,20}. The median column-integrated H_3^+ densities on 14 April and 25 January between the equator and 30° north were $4 \times 10^{15}\text{ m}^{-2}$ and $2 \times 10^{15}\text{ m}^{-2}$, respectively, with the latter being similar to previous values¹⁷. The $F_{10.7}$ index, an indicator of solar activity via 10.7-cm radio emissions, was 111.8 solar flux units (SFU) and 82.5 SFU on these dates—that is, 36% larger on 14 April, explaining in part this H_3^+ density difference. Note that retrieved H_3^+ column

densities here are expected to be lower by 20% or more of their true value, owing to temperature and density gradients in the upper atmosphere²⁷; thus differences in vertical gradients may also contribute to the measured density difference. Radiance maps indicate the degree to which H₃⁺ radiatively cools the upper atmosphere, and radiance positively correlates with both temperature and density.

Temperature gradients should reveal the dominant heat sources in Jupiter's upper atmosphere, with wave heating showing localized low-latitude peaks¹², and auroral heating showing a monotonic fall from aurora to equator. The gradients presented here are consistent with the latter, at least on these two observed dates. Therefore, the Coriolis forces and other effects that are simulated to confine auroral energy to the magnetic polar regions are evidently overcome at Jupiter. One general circulation model appeared to redistribute auroral heat successfully at Jupiter⁶, but subsequent models did not replicate the finding, so the process that allows meridional transport remains unclear^{9,10}. At Saturn, latitude–altitude temperature profiles also show a negative gradient from the aurora to lower latitudes²⁶, while a recent Saturn model presents a possible mechanism to disrupt the trapping of heat in the polar regions there²⁸. Main auroral oval H₃⁺ densities and global H₃⁺ temperatures were much lower on 14 April than on 25 January, potentially in agreement with model projections²⁴ that the solar wind dynamic pressure on the Jovian magnetosphere was highest on the latter date, increasing the rates of auroral particle precipitation and global heating¹⁰. The observations on 25 January also revealed, by chance, a planetary-scale heated structure, which may be propagating away from the main auroral oval in response to a solar wind compression of the magnetosphere, or may originate in the inner magnetosphere via an unknown mechanism.

Methods

Additional observing details

On 14 April 2016 and 25 January 2017, Jupiter was recorded between 04:53–10:22 UTC and 11:36–16:28 UTC, respectively. The spectrometer slit measured 24" long by 0.432" wide as shown in Fig. 1, and each pixel along the slit had a angular resolution of 0.144" per pixel. The spectral resolution was $\lambda/\delta\lambda \approx 25,000$. On 14 April, each of the 115 recorded spectral images of Jupiter was 30 s long and formed by six integrations each 5 s long. On 25 January, the 80 recorded spectral images of Jupiter were 60 s long and formed by six integrations each 10 s long. The process of saving spectral images and nodding the telescope between positions results in overhead time which led to an average elapsed time between Jupiter spectra of 2.4 min (14 April) and 3.4 min (25 January), so Jupiter rotated a respective 1.4° and 2.3° in longitude during this time.

Absolute calibration

For the spectral images, standard astronomical data reduction techniques were applied such as the subtraction of sky spectra from Jupiter spectra to remove unwanted emissions of the Earth's atmosphere (mainly from water), and the accounting of non-uniformity in the response of the NIRSPEC detector via flat fielding and dark-current subtraction. To convert the photon counts at the detector to units of physical flux, a stellar flux calibration was performed using the A0 stars HR2250 and HR3314 for 14 April and 25 January, respectively. This process is outlined in detail in previous studies¹⁶.

Spatially mapping spectra

Although the width of the slit is 0.432 arcseconds, the longitudes assigned to the slit have a wider range due to atmospheric seeing. The 14 April and 25 January observation nights had clear skies with an atmospheric seeing of 0.61" and 0.81", respectively. The use of multiple guider images within each spectral image allowed for tracking errors to be accounted for, such that the derived position of the slit on Jupiter was from the average position of the slit seen in the guiding images. Owing to the width of the slit, atmospheric seeing and the close distances on the planet between each spectral image, multiple spectra can be ascribed to a single longitude \times latitude cell (spatial bin). In this work, we use five spatial bin sizes: $10^\circ \times 10^\circ$, $8^\circ \times 8^\circ$, $6^\circ \times 6^\circ$, $4^\circ \times 4^\circ$ and $2^\circ \times 2^\circ$ longitude \times latitude. All data were arranged into five four-dimensional (4D) arrays for each observation night of dimensions longitude \times latitude \times spectra \times overlap. The overlap dimension holds the multiple available spectra of each spatial bin, as displayed in Extended Data Fig. 1. Each of the 4D arrays was collapsed into the three dimensions longitude \times latitude \times spectra, by taking the median value of each available spectral element. For example, the spectral dimension has 2,048 elements. For a spatial bin that includes 50 overlapping spectra, that means each of the 2,048 spectral elements has 50 values associated with it. By taking the median of the 50 available values, we ensure each spectral element is not skewed towards outlying data. Larger spatial bin sizes encompass more overlapping data, improving the statistical accuracy of the median value obtained, but at the cost of spatial resolution.

Fitting to H₃⁺

The H₃⁺ ion has millions of ro-vibration transition lines that vary in intensity depending on the ion temperature²⁹, and by finding the ratio between two or more emission lines we can obtain the H₃⁺ temperature. The total number of emitting ions

can then be calculated by dividing the observed emission by that of a single H_3^+ ion emitting at the temperature found above, producing a line-of-sight column-integrated density. A cosine function correction of the planetary emission angle is applied to remove the line-of-sight effects of viewing geometry. The radiance of H_3^+ (also known as the H_3^+ radiative cooling rate) is then found by summing the modelled emission intensities over all wavelengths.

In this work, we used the R(3,0) and Q(1,0) H_3^+ lines at 3.41277 μm and 3.9529 μm (respectively) because of their consistently high SNR at all latitudes. These H_3^+ lines were fitted to and characterized using MPFIT, a least-squares curve-fitting routine³⁰, as shown in the example fits of Extended Data Fig. 2. Non- H_3^+ emissions were found at some latitudes and were subtracted. The data were then passed to a computational model that determines the parameters of H_3^+ based on the line ratios as described by the previous paragraph¹⁶. Uncertainties in MPFIT and the H_3^+ fitting model were propagated through and reflected in the results. Note that these observations are column integrations of the entire path-length of the ionosphere and convolve all vertical structure. Models have demonstrated that these retrieved column-integrated H_3^+ densities represent the lower limits of actual values, while column-averaged H_3^+ temperatures primarily represent the temperature at the altitude peak of H_3^+ density²⁷.

Uncertainty-limited mapping of H_3^+ parameters

The data in every spatial cell of the five data cubes were fitted so as to produce parameter maps of H_3^+ column-integrated temperature, density and radiance, along with corresponding uncertainties. A total of 15 maps were produced for each night: three H_3^+ parameters at the five aforementioned spatial bin sizes. Ideally this study would use only the $2^\circ \times 2^\circ$ maps, but these smaller bins can have lower SNR outside of the hot auroral regions and thus undesirably high uncertainties. In such a case, selecting a larger $4^\circ \times 4^\circ$ bin size to gather more signal and reduce uncertainties is preferable, even though it reduces our ability to see fine detail spatially. To produce a map populated by low-uncertainty data at the smallest bin sizes possible planet-wide, we introduce a technique called uncertainty-limited binning. For example, an H_3^+ temperature map is produced by starting with a blank map, and then all $2^\circ \times 2^\circ$ longitude \times latitude resolution temperatures that have uncertainties under 5% are added. For parts of the map that were not populated by this first pass, data are drawn from the next spatial size up—the $4^\circ \times 4^\circ$ temperature map (again with uncertainties under than 5%)—and this process is then iterated for all remaining larger spatial bin

sizes up to $10^\circ \times 10^\circ$. H_3^+ column-integrated temperature and radiance maps are uncertainty-limited to 5%, while densities are limited to 15%.

Data availability

Observational data that are the basis of this study are publicly available on the Keck telescope observatory archive at <https://koa.ipac.caltech.edu/cgi-bin/KOA/nph-KOAllogin?more> under Semester search terms ‘2016A’ or ‘2017A’ and Principal Investigator ‘ODonoghue’. [Source data](#) are provided with this paper.

Code availability

Open-source computer code used for fitting to H_3^+ and producing temperatures, densities and radiances is available in the Python programming language at <https://pypi.org/project/h3ppy/>. Least-squares curve-fitting routine MPFIT is referenced in the Methods and available as part of the Interactive Data Language (IDL) suite of available programmes at <https://www.13harrisgeospatial.com/docs/mpfit.html>.

References

1. 1.

Strobel, D. F. & Smith, G. R. On the temperature of the Jovian thermosphere. *J. Atmos. Sci.* **30**, 718–725 (1973).

[ADS](#) [CAS](#) [Article](#) [Google Scholar](#)

2. 2.

Yelle, R. V. & Miller, S. *Jupiter’s Thermosphere and Ionosphere* 185–218 (Cambridge Univ. Press, 2004).

3. 3.

Yates, J. N., Ray, L. C., Achilleos, N., Witasse, O. & Altobelli, N. Magnetosphere–ionosphere–thermosphere coupling at Jupiter using a three-dimensional atmospheric general circulation model. *J. Geophys. Res. Space Phys.* **125**, e26792 (2020).

[ADS](#) [Article](#) [Google Scholar](#)

4. 4.

Waite, J. H., Jr. et al. Electron precipitation and related aeronomy of the jovian thermosphere and ionosphere. *J. Geophys. Res.* **88**, A8 (1983).

[Google Scholar](#)

5. 5.

Achilleos, N. et al. JIM: a time-dependent, three-dimensional model of Jupiter's thermosphere and ionosphere. *J. Geophys. Res.* **103**, 20089–20112 (1998).

[ADS](#) [CAS](#) [Article](#) [Google Scholar](#)

6. 6.

Bougher, S. W., Waite, J. H., Majeed, T. & Gladstone, G. R. Jupiter Thermospheric General Circulation Model (JTGCM): global structure and dynamics driven by auroral and Joule heating. *J. Geophys. Res. Planets* **110**, E04008 (2005).

[ADS](#) [Article](#) [Google Scholar](#)

7. 7.

Smith, C. G. A., Aylward, A. D., Millward, G. H., Miller, S. & Moore, L. E. An unexpected cooling effect in Saturn's upper atmosphere. *Nature* **445**, 399–401 (2007).

[ADS](#) [CAS](#) [Article](#) [Google Scholar](#)

8. 8.

Ma, Y. J. et al. Plasma flow and related phenomena in planetary aeronomy. *Space Sci. Rev.* **139**, 311–353 (2008).

[ADS](#) [Article](#) [Google Scholar](#)

9. 9.

Smith, C. G. A. & Aylward, A. D. Coupled rotational dynamics of Jupiter's thermosphere and magnetosphere. *Ann. Geophys.* **27**, 199–230 (2009).

[ADS](#) [Article](#) [Google Scholar](#)

10. 10.

Yates, J. N., Achilleos, N. & Guio, P. Response of the Jovian thermosphere to a transient pulse in solar wind pressure. *Planet. Space Sci.* **91**, 27–44 (2014).

[ADS](#) [Article](#) [Google Scholar](#)

11. 11.

Schubert, G., Hickey, M. P. & Walterscheid, R. L. Heating of Jupiter's thermosphere by the dissipation of upward propagating acoustic waves. *Icarus* **163**, 398–413 (2003).

[ADS](#) [Article](#) [Google Scholar](#)

12. 12.

O'Donoghue, J., Moore, L., Stallard, T. S. & Melin, H. Heating of Jupiter's upper atmosphere above the Great Red Spot. *Nature* **536**, 190–192 (2016).

[ADS](#) [Article](#) [Google Scholar](#)

13. 13.

Lian, Y. & Yelle, R. V. Damping of gravity waves by kinetic processes in Jupiter's thermosphere. *Icarus* **329**, 222–245 (2019).

[ADS](#) [Article](#) [Google Scholar](#)

14. 14.

McLean, I. S. et al. Design and development of NIRSPEC: a near-infrared echelle spectrograph for the Keck II telescope. *SPIE Conf. Series* **3354**, 566–578 (1998).

[ADS](#) [Google Scholar](#)

15. 15.

Uno, T. et al. Vertical emissivity profiles of Jupiter's northern H_3^+ and H_2 infrared auroras observed by Subaru/IRCS. *J. Geophys. Res.* **119**, 10219–10241 (2014).

[Article](#) [Google Scholar](#)

16. 16.

Melin, H. et al. On the anticorrelation between H_3^+ temperature and density in giant planet ionospheres. *Mon. Not. R. Astron. Soc.* **438**, 1611–1617 (2014).

[ADS](#) [CAS](#) [Article](#) [Google Scholar](#)

17. 17.

Lam, H. A. et al. A baseline spectroscopic study of the infrared auroras of Jupiter. *Icarus* **127**, 379–393 (1997).

[ADS](#) [CAS](#) [Article](#) [Google Scholar](#)

18. 18.

Connerney, J. E. P. et al. A new model of Jupiter’s magnetic field from Juno’s first nine orbits. *Geophys. Res. Lett.* **45**, 2590–2596 (2018).

[ADS](#) [Article](#) [Google Scholar](#)

19. 19.

Johnson, R. E. et al. Mapping H_3^+ temperatures in Jupiter’s northern auroral ionosphere using VLT-CRIRES. *J. Geophys. Res. Space Phys.* **123**, 5990–6008 (2018).

[ADS](#) [CAS](#) [Article](#) [Google Scholar](#)

20. 20.

Dinelli, B. M. et al. JUNO/JIRAM’s view of Jupiter’s H_3^+ emissions. *Phil. Trans. R. Soc. Lond. A* **377**, 20180406 (2019).

[ADS](#) [CAS](#) [Article](#) [Google Scholar](#)

21. 21.

Heelis, R. A. & Maute, A. Challenges to understanding the Earth’s ionosphere and thermosphere. *J. Geophys. Res. Space Phys.* **125**, e27497 (2020).

[ADS](#) [Article](#) [Google Scholar](#)

22. 22.

Kita, H. et al. Characteristics of solar wind control on Jovian UV auroral activity deciphered by long-term Hisaki EXCEED observations: evidence of preconditioning of the magnetosphere? *Geophys. Res. Lett.* **43**, 6790–6798 (2016).

[ADS](#) [Article](#) [Google Scholar](#)

23. 23.

Cowley, S. W. H. et al. A simple axisymmetric model of magnetosphere–ionosphere coupling currents in Jupiter’s polar ionosphere. *J. Geophys. Res. Space Phys.* **110**, A11209 (2005).

[ADS](#) [Article](#) [Google Scholar](#)

24. 24.

Tao, C., Kataoka, R., Fukunishi, H., Takahashi, Y. & Yokoyama, T. Magnetic field variations in the jovian magnetotail induced by solar wind dynamic pressure enhancements. *J. Geophys. Res. Space Phys.* **110**, A11208 (2005).

[ADS](#) [Article](#) [Google Scholar](#)

25. 25.

Figueiredo, C. A. O. B. et al. Large-scale traveling ionospheric disturbances observed by GPS dTEC maps over North and South America on Saint Patrick’s Day storm in 2015. *J. Geophys. Res. Space Phys.* **122**, 4755–4763 (2017).

[ADS](#) [Article](#) [Google Scholar](#)

26. 26.

Brown, Z. et al. A pole-to-pole pressure–temperature map of Saturn’s thermosphere from Cassini Grand Finale data. *Nat. Astron.* **4**, 872–879 (2020).

[ADS](#) [Article](#) [Google Scholar](#)

27. 27.

Moore, L. et al. Modelling H_3^+ in planetary atmospheres: effects of vertical gradients on observed quantities. *Phil. Trans. R. Soc. Lond. A* **377**, 20190067 (2019).

[ADS](#) [CAS](#) [Google Scholar](#)

28. 28.

Müller-Wodarg, I. C. F. et al. Atmospheric waves and their possible effect on the thermal structure of Saturn's thermosphere. *Geophys. Res. Lett.* **46**, 2372–2380 (2019).

[ADS](#) [Article](#) [Google Scholar](#)

29. 29.

Neale, L., Miller, S. & Tennyson, J. Spectroscopic properties of the H₃⁺ molecule: a new calculated line list. *Astrophys. J.* **464**, 516–520 (1996).

[ADS](#) [CAS](#) [Article](#) [Google Scholar](#)

30. 30.

Markwardt, C. B. Non-linear least-squares fitting in IDL with MPFIT. In *Astronomical Data Analysis Software and Systems XVIII* Vol. 411 (eds Bohlander, D. A. et al.) (Conference Series no. 251, Astronomical Society of the Pacific, 2009).

[Download references](#)

Acknowledgements

The data presented herein were obtained at the W. M. Keck Observatory, which is operated as a scientific partnership among the California Institute of Technology, the University of California and NASA. The Observatory was made possible by the generous financial support of the W. M. Keck Foundation. The authors wish to recognize and acknowledge the cultural role and reverence that the summit of Maunakea has always had within the indigenous Hawaiian community. We are fortunate to have the opportunity to conduct observations from this mountain. L.M. was supported by NASA under grant no. NNX17AF14G issued through the Solar System Observations Program and grant no. 80NSSC19K0546 issued through the Solar System Workings Program.

Author information

Affiliations

1. Department of Solar System Science, JAXA Institute of Space and Astronautical Science, Sagamihara, Japan

J. O'Donoghue

2. NASA Goddard Space Flight Center, Greenbelt, MD, USA

J. O'Donoghue & J. E. P. Connerney

3. Center for Space Physics, Boston University, Boston, MA, USA

L. Moore & T. Bhakyapaibul

4. Department of Physics and Astronomy, University of Leicester, Leicester, UK

H. Melin & T. Stallard

5. Space Research Corporation, Annapolis, MD, USA

J. E. P. Connerney

6. National Institute of Information and Communications Technology (NICT), Tokyo, Japan

C. Tao

Authors

1. J. O'Donoghue

[View author publications](#)

You can also search for this author in [PubMed](#) [Google Scholar](#)

2. L. Moore

[View author publications](#)

You can also search for this author in [PubMed](#) [Google Scholar](#)

3. T. Bhakyapaibul

[View author publications](#)

You can also search for this author in [PubMed](#) [Google Scholar](#)

4. H. Melin

[View author publications](#)

You can also search for this author in [PubMed](#) [Google Scholar](#)

5. T. Stallard

[View author publications](#)

You can also search for this author in [PubMed](#) [Google Scholar](#)

6. J. E. P. Connerney

[View author publications](#)

You can also search for this author in [PubMed](#) [Google Scholar](#)

7. C. Tao

[View author publications](#)

You can also search for this author in [PubMed](#) [Google Scholar](#)

Contributions

J.O'D. collected, analysed and interpreted the data, and wrote the paper. L.M. greatly assisted in collection and reduction of data and interpretation of the results. T.B. assisted in key data reduction. H.M. provided computer code necessary for the analysis of data. H.M. and T.S. assisted in data collection, analysis and interpretation. J.E.P.C. provided code to map Jupiter's magnetic field and assisted in the interpretation of data. C.T. provided solar wind simulation results. All authors provided comments on the manuscript.

Corresponding author

Correspondence to [J. O'Donoghue](#).

Ethics declarations

Competing interests

The authors declare no competing interests.

Additional information

Peer review information *Nature* thanks George R. Gladstone and the other, anonymous, reviewer(s) for their contribution to the peer review of this work. Peer reviewer reports are available.

Publisher's note Springer Nature remains neutral with regard to jurisdictional claims in published maps and institutional affiliations.

Extended data figures and tables

Extended Data Fig. 1 Data coverage (density) at $4^\circ \times 4^\circ$ longitude \times latitude resolution.

a, 25 January 2017; **b**, 14 April 2016. Each element contains an array of intensities as a function of wavelength, as described in the main text. Data cubes like this also exist for spatial resolutions $2^\circ \times 2^\circ$, $6^\circ \times 6^\circ$, $8^\circ \times 8^\circ$ and $10^\circ \times 10^\circ$.

Extended Data Fig. 2 Selected example fits to data representing multiple days, differing longitudes, latitudes and spatial bin size.

a,b, 14 April 2016; **c,d**, 25 January 2017. Red lines, fits; black crosses, data. Fits to non-H₃⁺ emissions are denoted as noise and 1σ uncertainties to each line are indicated.

Extended Data Fig. 3 A 1D model of solar wind propagation surrounding the dates of the observations reported here.

The orange shaded regions mark the period of ground-based observations. From top to bottom, each panel corresponds to solar wind density, temperature, radial (x ; Jupiter–Sun line) and azimuthal (y ; direction of planetary orbital motion) velocities, magnetic field B_y , dynamic pressure of the solar wind plotted linearly and logarithmically, and the absolute magnetic field magnitude $|B|$ (ref. [24](#)). The 1σ uncertainty in arrival time of the solar wind at Jupiter is denoted by the horizontal, arrowed lines. Produced using Tao–MHD, the magnetohydrodynamic model by Tao et al.[24](#)

[Source data](#).

Extended Data Fig. 4 A 1D model of solar wind propagation surrounding the dates of the observations reported here.

The orange shaded regions mark the period of ground-based observations. From top to bottom, each panel corresponds to solar wind density, temperature, radial (x ; Jupiter–Sun line) and azimuthal (y ; direction of planetary orbital motion) velocities, magnetic field B_y , dynamic pressure of the solar wind plotted linearly and logarithmically and the absolute magnetic field magnitude $|B|$ (ref. [24](#)). The 1σ uncertainty in arrival time of the solar wind at Jupiter is denoted by the horizontal, arrowed lines

[Source data](#)

[Extended Data Fig. 5 A 1D model of solar wind propagation closely surrounding the dates of the observations reported here.](#)

The blue shaded regions mark the periods of ground-based observations. Absolute magnetic field magnitude $|B|$ and dynamic pressure of the solar wind (SW) at Jupiter are shown as a function of date and time²⁴. The 1σ uncertainty in arrival time of the solar wind at Jupiter is denoted by the horizontal arrowed lines.

Extended Data Table 1 Example distribution of 5% uncertainty-limited temperature results in Fig. 2 and Fig. 3a, d by bin size

[Full size table](#)

Extended Data Table 2 Example distribution of 20% uncertainty-limited column-integrated density results in Fig. 2b, e by bin size

[Full size table](#)

Extended Data Table 3 Example distribution of 5% uncertainty-limited radiance results in Fig. 2c, f by bin size

[Full size table](#)

Supplementary information

[Peer Review File](#)

Source data

[Source Data Fig. 3](#)

[Source Data Extended Data Fig. 3](#)

[Source Data Extended Data Fig. 4](#)

Rights and permissions

Open Access This article is licensed under a Creative Commons Attribution 4.0 International License, which permits use, sharing, adaptation, distribution and reproduction in any medium or format, as long as you give appropriate credit to the original author(s) and the source, provide a link to the Creative Commons license, and indicate if changes were made. The images or other third party material in this article are included in the article's Creative Commons license, unless indicated otherwise in a

credit line to the material. If material is not included in the article's Creative Commons license and your intended use is not permitted by statutory regulation or exceeds the permitted use, you will need to obtain permission directly from the copyright holder. To view a copy of this license, visit <http://creativecommons.org/licenses/by/4.0/>.

[Reprints and Permissions](#)

About this article



Check for
updates

Cite this article

O'Donoghue, J., Moore, L., Bhaktyapaibul, T. *et al.* Global upper-atmospheric heating on Jupiter by the polar aurorae. *Nature* **596**, 54–57 (2021).
<https://doi.org/10.1038/s41586-021-03706-w>

[Download citation](#)

- Received: 25 February 2021
- Accepted: 08 June 2021
- Published: 04 August 2021
- Issue Date: 05 August 2021
- DOI: <https://doi.org/10.1038/s41586-021-03706-w>

Comments

By submitting a comment you agree to abide by our [Terms](#) and [Community Guidelines](#). If you find something abusive or that does not comply with our terms or guidelines please flag it as inappropriate.

[Download PDF](#)

Advertisement

| [Section menu](#) | [Main menu](#) |

- Article
- [Published: 04 August 2021](#)

Emergent order in hydrodynamic spin lattices

- [Pedro J. Sáenz](#) [ORCID: orcid.org/0000-0002-0388-9592^{1,2}](#),
- [Giuseppe Pucci](#) [ORCID: orcid.org/0000-0001-6621-3277^{2,3}](#),
- [Sam E. Turton²](#),
- [Alexis Goujon](#) [ORCID: orcid.org/0000-0002-2198-0365^{2,4}](#),
- [Rodolfo R. Rosales²](#),
- [Jörn Dunkel](#) [ORCID: orcid.org/0000-0001-8865-2369²](#) &
- [John W. M. Bush](#) [ORCID: orcid.org/0000-0002-7936-7256²](#)

Nature volume **596**, pages 58–62 (2021) [Cite this article](#)

- 1829 Accesses
- 8 Altmetric
- [Metrics details](#)

Subjects

- [Fluid dynamics](#)
- [Statistical physics, thermodynamics and nonlinear dynamics](#)

Abstract

Macroscale analogues^{1,2,3} of microscopic spin systems offer direct insights into fundamental physical principles, thereby advancing our understanding of synchronization phenomena⁴ and informing the design of novel classes

of chiral metamaterials^{5,6,7}. Here we introduce hydrodynamic spin lattices (HSLs) of ‘walking’ droplets as a class of active spin systems with particle-wave coupling. HSLs reveal various non-equilibrium symmetry-breaking phenomena, including transitions from antiferromagnetic to ferromagnetic order that can be controlled by varying the lattice geometry and system rotation⁸. Theoretical predictions based on a generalized Kuramoto model⁴ derived from first principles rationalize our experimental observations, establishing HSLs as a versatile platform for exploring active phase oscillator dynamics. The tunability of HSLs suggests exciting directions for future research, from active spin–wave dynamics to hydrodynamic analogue computation and droplet-based topological insulators.

Access options

Subscribe to Journal

Get full journal access for 1 year

\$199.00

only \$3.90 per issue

[Subscribe](#)

All prices are NET prices.

VAT will be added later in the checkout.

Tax calculation will be finalised during checkout.

Rent or Buy article

Get time limited or full article access on ReadCube.

from \$8.99

[Rent or Buy](#)

All prices are NET prices.

Additional access options:

- [Log in](#)
- [Access through your institution](#)
- [Learn about institutional subscriptions](#)

Fig. 1: Spontaneous antiferromagnetic order in a 1D HSL.

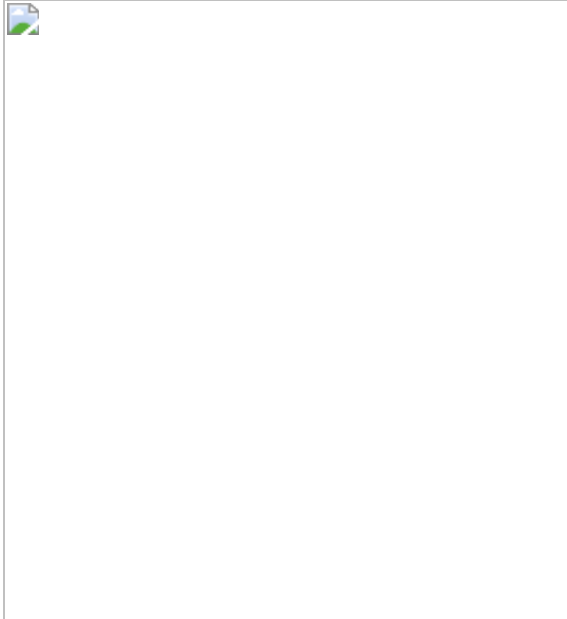


Fig. 2: Tuning collective order through the lattice parameters in experiments and theory.

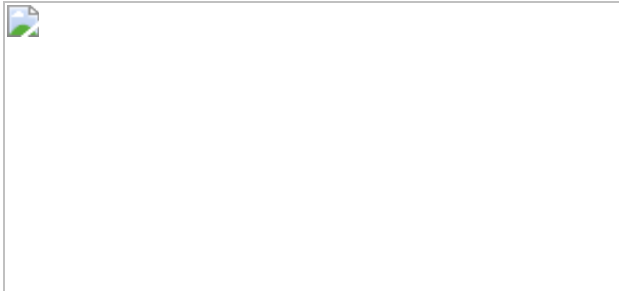


Fig. 3: Inducing global polarization through applied rotation.

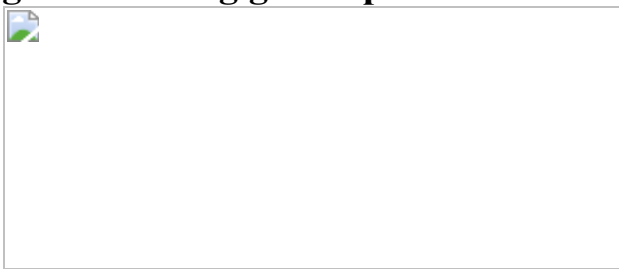
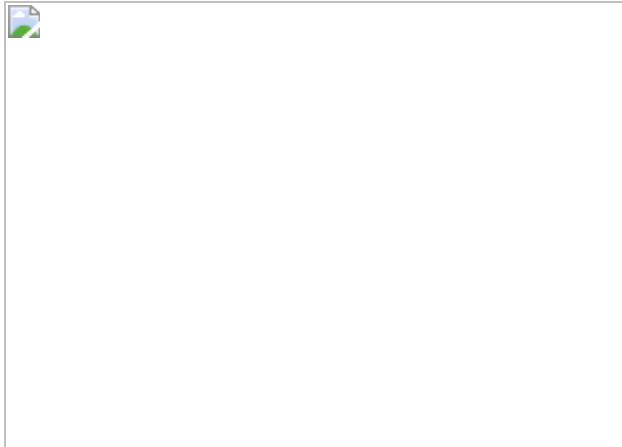


Fig. 4: Rotation-induced polarization transition from antiferromagnetic to ferromagnetic order in 2D square lattices.



Data availability

The data that support the findings of this study are available from the corresponding authors upon reasonable request.

References

1. 1.

Kane, C. L. & Lubensky, T. C. Topological boundary modes in isostatic lattices. *Nat. Phys.* **10**, 39–45 (2014).

[CAS](#) [Article](#) [Google Scholar](#)

2. 2.

Chen, B. G.-g., Upadhyaya, N. & Vitelli, V. Nonlinear conduction via solitons in a topological mechanical insulator. *Proc. Natl Acad. Sci. USA* **111**, 13004–13009 (2014).

[ADS](#) [MathSciNet](#) [PubMed](#) [PubMed Central](#) [MATH](#) [Article](#) [CAS](#) [Google Scholar](#)

3. 3.

Nash, L. M. et al. Topological mechanics of gyroscopic metamaterials. *Proc. Natl Acad. Sci. USA* **112**, 14495–14500 (2015).

[ADS](#) [CAS](#) [PubMed](#) [PubMed Central](#) [Article](#) [Google Scholar](#)

4. 4.

Strogatz, S. H. From Kuramoto to Crawford: exploring the onset of synchronization in populations of coupled oscillators. *Physica D* **143**, 1–20 (2000).

[ADS](#) [MathSciNet](#) [MATH](#) [Article](#) [Google Scholar](#)

5. 5.

Rechtsman, M. C. et al. Optimized structures for photonic quasicrystals. *Phys. Rev. Lett.* **101**, 073902 (2008).

[ADS](#) [PubMed](#) [Article](#) [CAS](#) [Google Scholar](#)

6. 6.

van Zuiden, B. C. et al. Spatiotemporal order and emergent edge currents in active spinner materials. *Proc. Natl Acad. Sci. USA* **113**, 12919–12924 (2016).

[ADS](#) [PubMed](#) [PubMed Central](#) [Article](#) [CAS](#) [Google Scholar](#)

7. 7.

Soni, V. et al. The odd free surface flows of a colloidal chiral fluid. *Nat. Phys.* **15**, 1188–1194 (2019).

[CAS](#) [Article](#) [Google Scholar](#)

8. 8.

Fort, E. et al. Path-memory induced quantization of classical orbits. *Proc. Natl Acad. Sci. USA* **107**, 17515–17520 (2010).

[ADS](#) [CAS](#) [PubMed Central](#) [Article](#) [PubMed](#) [Google Scholar](#)

9. 9.

Coey, J. M. D. *Magnetism and Magnetic Materials* (Cambridge Univ. Press, 2010).

10. 10.

Watson, J. D. & Crick, F. H. C. The structure of DNA. *Cold Spring Harb. Symp. Quant. Biol.* **18**, 123–131 (1953).

[CAS](#) [PubMed](#) [Article](#) [Google Scholar](#)

11. 11.

Weinberg, S. *The Quantum Theory of Fields* Vol. 2 (Cambridge Univ. Press, 1996).

12. 12.

Baltz, V. et al. Antiferromagnetic spintronics. *Rev. Mod. Phys.* **90**, 015005 (2018).

[ADS](#) [MathSciNet](#) [CAS](#) [Article](#) [Google Scholar](#)

13. 13.

Chumak, A. V. et al. Magnon spintronics. *Nat. Phys.* **11**, 453–461 (2015).

[CAS](#) [Article](#) [Google Scholar](#)

14. 14.

Maurer, P. C. et al. Room-temperature quantum bit memory exceeding one second. *Science* **336**, 1283–1286 (2012).

[ADS](#) [CAS](#) [PubMed](#) [Article](#) [Google Scholar](#)

15. 15.

Süsstrunk, R. & Huber, S. D. Observation of phononic helical edge states in a mechanical topological insulator. *Science* **349**, 47–50 (2015).

[ADS](#) [PubMed](#) [Article](#) [CAS](#) [Google Scholar](#)

16. 16.

Schneider, U. et al. Metallic and insulating phases of repulsively interacting fermions in a 3D optical lattice. *Science* **322**, 1520–1525 (2008).

[ADS](#) [CAS](#) [PubMed](#) [Article](#) [Google Scholar](#)

17. 17.

Cheuk, L. W. et al. Quantum-gas microscope for fermionic atoms. *Phys. Rev. Lett.* **114**, 193001 (2015).

[ADS](#) [PubMed](#) [Article](#) [CAS](#) [Google Scholar](#)

18. 18.

Buluta, I., Asshab, S. & Nori, F. Natural and artificial atoms for quantum computation. *Rep. Prog. Phys.* **74**, 104401 (2011).

[ADS](#) [Article](#) [CAS](#) [Google Scholar](#)

19. 19.

Gross, C. & Bloch, I. Quantum simulations with ultracold atoms in optical lattices. *Science* **357**, 995–1001 (2017).

[ADS](#) [CAS](#) [PubMed](#) [Article](#) [Google Scholar](#)

20. 20.

Dieny, B. et al. Opportunities and challenges for spintronics in the microelectronics industry. *Nat. Electron.* **3**, 446–459 (2020).

[Article](#) [Google Scholar](#)

21. 21.

Biktashev, V. N., Barkley, D. & Biktasheva, I. V. Orbital motion of spiral waves in excitable media. *Phys. Rev. Lett.* **104**, 058302 (2010).

[ADS](#) [CAS](#) [PubMed](#) [Article](#) [Google Scholar](#)

22. 22.

Totz, J. F. et al. Spiral wave chimera states in large populations of coupled chemical oscillators. *Nat. Phys.* **14**, 282–285 (2018).

[CAS](#) [Article](#) [Google Scholar](#)

23. 23.

Wioland, H. et al. Ferromagnetic and antiferromagnetic order in bacterial vortex lattices. *Nat. Phys.* **12**, 341–345 (2016).

[CAS](#) [PubMed](#) [PubMed Central](#) [Article](#) [Google Scholar](#)

24. 24.

Nishiguchi, D. et al. Engineering bacterial vortex lattice via direct laser lithography. *Nat. Commun.* **9**, 4486 (2018).

[ADS](#) [PubMed](#) [PubMed Central](#) [Article](#) [CAS](#) [Google Scholar](#)

25. 25.

Riedel, I. H., Kruse, K. & Howard, J. A self-organized vortex array of hydrodynamically entrained sperm cells. *Science* **309**, 300–303 (2005).

[ADS](#) [CAS](#) [PubMed](#) [Article](#) [Google Scholar](#)

26. 26.

Souslov, A. et al. Topological sound in active-liquid metamaterials. *Nat. Phys.* **13**, 1091–1094 (2017).

[CAS](#) [Article](#) [Google Scholar](#)

27. 27.

Sáenz, P. J. et al. Spin lattices of walking droplets. *Phys. Rev. Fluids* **3**, 100508 (2018).

[ADS](#) [CAS](#) [PubMed](#) [Article](#) [Google Scholar](#)

28. 28.

Couder, Y. et al. Dynamical phenomena: walking and orbiting droplets. *Nature* **437**, 208 (2005).

[ADS](#) [CAS](#) [PubMed](#) [Article](#) [Google Scholar](#)

29. 29.

Bush, J. W. M. Pilot-wave hydrodynamics. *Ann. Rev. Fluid Mech.* **47**, 269–292 (2015).

[ADS](#) [MathSciNet](#) [Article](#) [Google Scholar](#)

30. 30.

Lindner, B. et al. Effects of noise in excitable systems. *Phys. Rep.* **392**, 321–424 (2004).

[ADS](#) [Article](#) [Google Scholar](#)

31. 31.

Cumin, D. & Unsworth, C. P. Generalising the Kuramoto model for the study of neuronal synchronization in the brain. *Physica D* **226**,

181–196 (2007).

[ADS](#) [MathSciNet](#) [MATH](#) [Article](#) [Google Scholar](#)

32. 32.

Matheny, M. H. et al. Exotic states in a simple network of nanoelectromechanical oscillators. *Science* **363**, eaav7932 (2019).

[MathSciNet](#) [CAS](#) [PubMed](#) [Article](#) [Google Scholar](#)

33. 33.

Dörfler, F. & Bullo, F. Synchronization in complex networks of phase oscillators: a survey. *Automatica* **50**, 1539–1564 (2014).

[MathSciNet](#) [MATH](#) [Article](#) [Google Scholar](#)

34. 34.

Protière, S., Boudaoud, A. & Couder, Y. Particle-wave association on a fluid interface. *J. Fluid Mech.* **554**, 85–108 (2006).

[ADS](#) [MathSciNet](#) [MATH](#) [Article](#) [Google Scholar](#)

35. 35.

Eddi, A. et al. Information stored in Faraday waves: the origin of a path memory. *J. Fluid Mech.* **674**, 433–463 (2011).

[ADS](#) [MathSciNet](#) [CAS](#) [MATH](#) [Article](#) [Google Scholar](#)

36. 36.

Moláček, J. & Bush, J. W. M. Drops walking on a vibrating bath: towards a hydrodynamic pilot-wave theory. *J. Fluid Mech.* **727**, 612–647 (2013).

[ADS](#) [MATH](#) [Article](#) [Google Scholar](#)

37. 37.

Sáenz, P. J., Cristea-Platon, T. & Bush, J. W. M. A hydrodynamic analog of Friedel oscillations. *Sci. Adv.* **6**, eaay9234 (2020).

[ADS](#) [PubMed](#) [PubMed Central](#) [Article](#) [Google Scholar](#)

38. 38.

Ruderman, M. A. & Kittel, C. Indirect exchange coupling of nuclear magnetic moments by conduction electrons. *Phys. Rev.* **96**, 99–102 (1954).

[ADS](#) [CAS](#) [Article](#) [Google Scholar](#)

39. 39.

Ronellenfitsch, H. et al. Inverse design of discrete mechanical metamaterials. *Phys. Rev. Mater.* **3**, 095201 (2019).

[CAS](#) [Article](#) [Google Scholar](#)

40. 40.

Lagendijk, A., Van Tiggelen, B. & Wiersma, D. S. Fifty years of Anderson localization. *Phys. Today* **62**, 24 (2009).

[CAS](#) [Article](#) [Google Scholar](#)

41. 41.

Oza, A. U., Rosales, R. R. & Bush, J. W. M. Hydrodynamic spin states. *Chaos* **28**, 096106 (2018).

[ADS](#) [PubMed](#) [Article](#) [CAS](#) [Google Scholar](#)

42. 42.

Oza, A. U., Rosales, R. R. & Bush, J. W. M. A trajectory equation for walking droplets: hydrodynamic pilotwave theory. *J. Fluid Mech.* **737**, 552–570 (2013).

[ADS](#) [MathSciNet](#) [CAS](#) [MATH](#) [Article](#) [Google Scholar](#)

43. 43.

Labousse, M. et al. Self-attraction into spinning eigenstates of a mobile wave source by its emission backreaction. *Phys. Rev. E* **94**, 042224 (2016).

[ADS](#) [MathSciNet](#) [PubMed](#) [Article](#) [Google Scholar](#)

44. 44.

Perrard, S. et al. Self-organization into quantized eigenstates of a classical wave-driven particle. *Nat. Commun.* **5**, 3219 (2014).

[ADS](#) [PubMed](#) [Article](#) [CAS](#) [Google Scholar](#)

45. 45.

Eddi, A. et al. Level splitting at macroscopic scale. *Phys. Rev. Lett.* **108**, 264503 (2012).

[ADS](#) [CAS](#) [PubMed](#) [Article](#) [Google Scholar](#)

46. 46.

Harris, D. M. & Bush, J. W. M. Droplets walking in a rotating frame: from quantized orbits to multimodal statistics. *J. Fluid Mech.* **739**, 444–464 (2014).

[ADS](#) [CAS](#) [Article](#) [Google Scholar](#)

47. 47.

Oza, A. U. et al. Pilot-wave dynamics in a rotating frame: on the emergence of orbital quantization. *J. Fluid Mech.* **744**, 404–429 (2014).

[ADS](#) [Article](#) [Google Scholar](#)

48. 48.

Sáenz, P. J., Cristea-Platon, T. & Bush, J. W. M. Statistical projection effects in a hydrodynamic pilot-wave system. *Nat. Phys.* **14**, 315–319 (2018).

[Article](#) [CAS](#) [Google Scholar](#)

49. 49.

Eddi, A. et al. Archimedean lattices in the bound states of wave interacting particles. *Europhys. Lett.* **87**, 56002 (2009).

[ADS](#) [Article](#) [CAS](#) [Google Scholar](#)

50. 50.

Eddi, A., Boudaoud, A. & Couder, Y. Oscillating instability in bouncing droplet crystals. *Europhys. Lett.* **94**, 20004 (2011).

[ADS](#) [Article](#) [CAS](#) [Google Scholar](#)

51. 51.

Thomson, S. J., Couchman, M. M. P. & Bush, J. W. M. Collective vibrations of confined levitating droplets. *Phys. Rev. Fluids* **5**, 083601 (2020).

[ADS](#) [Article](#) [Google Scholar](#)

52. 52.

Thomson, S. J., Durey, M. & Rosales, R. R. Collective vibrations of a hydrodynamic active lattice. *Proc. R. Soc. A* **476**, 20200155 (2020).

[ADS](#) [MathSciNet](#) [CAS](#) [PubMed](#) [PubMed Central](#) [Article](#) [Google Scholar](#)

53. 53.

Couchman, M. M. P. & Bush, J. W. M. Free rings of bouncing droplets: stability and dynamics. *J. Fluid Mech.* **903**, A49 (2020).

[ADS](#) [CAS](#) [MATH](#) [Article](#) [Google Scholar](#)

54. 54.

Nachbin, A. Walking droplets correlated at a distance. *Chaos* **28**, 096110 (2018).

[ADS](#) [MathSciNet](#) [PubMed](#) [Article](#) [CAS](#) [Google Scholar](#)

55. 55.

Nachbin, A. Kuramoto-like synchronization mediated through Faraday surface waves. *Fluids* **5**, 226 (2020).

[CAS](#) [Article](#) [Google Scholar](#)

56. 56.

Whitham, G. B. *Linear and Nonlinear Waves* (Wiley, 1974).

57. 57.

Douady, S. Experimental study of the Faraday instability. *J. Fluid Mech.* **221**, 383–409 (1990).

[ADS](#) [Article](#) [Google Scholar](#)

58. 58.

Harris, D. M. & Bush, J. W. M. Generating uniaxial vibration with an electrodynamic shaker and external air bearing. *J. Sound Vibrat.* **334**, 255–269 (2015).

[ADS](#) [Article](#) [Google Scholar](#)

59. 59.

Faraday, M. On a peculiar class of acoustical figures and on certain forms assumed by groups of particles upon vibrating elastic surfaces. *Philos. Trans. R. Soc. Lond.* **121**, 299–340 (1831).

[ADS](#) [Article](#) [Google Scholar](#)

60. 60.

Harris, D. M., Liu, T. & Bush, J. W. M. A low-cost, precise piezoelectric droplet-on-demand generator. *Exp. Fluids* **56**, 83 (2015).

[Article](#) [Google Scholar](#)

61. 61.

Bush, J. W. M., Oza, A. U. & Moláček, J. The wave-induced added mass of walking droplets. *J. Fluid Mech.* **755**, R7 (2014).

[ADS](#) [Article](#) [Google Scholar](#)

62. 62.

Turton, S. E. *Theoretical Modeling of Pilot-wave Hydrodynamics*. PhD thesis, Massachusetts Institute of Technology (2020).

63. 63.

Labousse, M. & Perrard, S. Non-Hamiltonian features of a classical pilot-wave dynamics. *Phys. Rev. E* **90**, 022913 (2014).

[ADS](#) [CAS](#) [Article](#) [Google Scholar](#)

64. 64.

Cristea-Platon, T., Sáenz, P. J. & Bush, J. W. M. Walking droplets in a circular corral: quantisation and chaos. *Chaos* **28**, 096116 (2018).

[ADS](#) [PubMed](#) [Article](#) [Google Scholar](#)

65. 65.

Tadrist, L. et al. Faraday instability and subthreshold Faraday waves: surface waves emitted by walkers. *J. Fluid Mech.* **848**, 906–945 (2018).

[ADS](#) [MathSciNet](#) [MATH](#) [Article](#) [Google Scholar](#)

66. 66.

Galeano-Rios, C. A. et al. Ratcheting droplet pairs. *Chaos* **28**, 096112 (2018).

[ADS](#) [CAS](#) [PubMed](#) [Article](#) [Google Scholar](#)

67. 67.

Couchman, M. M. P., Turton, S. E. & Bush, J. W. M. Bouncing phase variations in pilot-wave hydrodynamics and the stability of droplet pairs. *J. Fluid Mech.* **871**, 212–243 (2019).

[ADS](#) [CAS](#) [MATH](#) [Article](#) [Google Scholar](#)

68. 68.

Faria, L. M. A model for Faraday pilot waves over variable topography. *J. Fluid Mech.* **811**, 51–66 (2017).

[ADS](#) [MathSciNet](#) [MATH](#) [Article](#) [Google Scholar](#)

69. 69.

Filatrella, G., Nielsen, A. H. & Pedersen, N. F. Analysis of a power grid using a Kuramoto-like model. *Eur. Phys. J. B* **61**, 485–491 (2008).

[ADS](#) [CAS](#) [Article](#) [Google Scholar](#)

70. 70.

Rohden, M. et al. Self-organized synchronization in decentralized power grids. *Phys. Rev. Lett.* **109**, 064101 (2012).

[ADS](#) [PubMed](#) [Article](#) [CAS](#) [Google Scholar](#)

71. 71.

Chen, P. & Wu, K.-A. Subcritical bifurcations and nonlinear balloons in Faraday waves. *Phys. Rev. Lett.* **85**, 3813–3816 (2000).

[ADS](#) [CAS](#) [PubMed](#) [Article](#) [Google Scholar](#)

72. 72.

Périnet, N., Juric, D. & Tuckerman, L. S. Alternating hexagonal and striped patterns in Faraday surface waves. *Phys. Rev. Lett.* **109**, 164501 (2012).

[ADS](#) [PubMed](#) [Article](#) [CAS](#) [PubMed Central](#) [Google Scholar](#)

73. 73.

Pucci, G. et al. Non-specular reflection of walking droplets. *J. Fluid Mech.* **804**, R3 (2016).

[ADS](#) [Article](#) [Google Scholar](#)

74. 74.

Pucci, G. et al. Walking droplets interacting with single and double slits. *J. Fluid Mech.* **835**, 1136–1156 (2018).

[ADS](#) [Article](#) [Google Scholar](#)

75. 75.

Harris, D. M. et al. The interaction of a walking droplet and a submerged pillar: from scattering to the logarithmic spiral. *Chaos* **28**, 096105 (2018).

[ADS](#) [PubMed](#) [Article](#) [CAS](#) [PubMed Central](#) [Google Scholar](#)

76. 76.

Damiano, A. P. et al. Surface topography measurements of the bouncing droplet experiment. *Exp. Fluids* **57**, 163 (2016).

[Article](#) [CAS](#) [Google Scholar](#)

77. 77.

Diep, H. T. *Frustrated Spin Systems* (World Scientific, 2004).

78. 78.

Qi, X.-L. & Zhang, S.-C. Topological insulators and superconductors. *Rev. Mod. Phys.* **83**, 1057–1110 (2011).

[ADS](#) [CAS](#) [Article](#) [Google Scholar](#)

79. 79.

Biktasheva, I. V. & Biktashev, V. N. Wave–particle dualism of spiral waves dynamics. *Phys. Rev. E* **67**, 026221 (2003).

[ADS](#) [CAS](#) [Article](#) [Google Scholar](#)

80. 80.

Biktasheva, I. V. et al. Computation of the drift velocity of spiral waves using response functions. *Phys. Rev. E* **81**, 066202 (2010).

[ADS](#) [MathSciNet](#) [CAS](#) [Article](#) [Google Scholar](#)

81. 81.

Azhand, A., Totz, J. F. & Engel, H. Three-dimensional autonomous pacemaker in the photosensitive Belousov–Zhabotinsky medium. *Europhys. Lett.* **108**, 10004 (2014).

[ADS](#) [Article](#) [CAS](#) [Google Scholar](#)

82. 82.

Totz, J. F., Engel, H. & Steinbock, O. Spatial confinement causes lifetime enhancement and expansion of vortex rings with positive filament tension. *New J. Phys.* **17**, 093043 (2015).

[ADS](#) [Article](#) [Google Scholar](#)

[Download references](#)

Acknowledgements

We gratefully acknowledge financial support from the NSF through CMMI-1727565 (J.W.M.B. and P.J.S.) and DMS-1719637 (R.R.R.), MIT Solomon Buchsbaum Research Fund (J.D.), and CNRS Momentum programme (G.P.).

Author information

Affiliations

1. Department of Mathematics, University of North Carolina, Chapel Hill, NC, USA

Pedro J. Sáenz

2. Department of Mathematics, Massachusetts Institute of Technology,
Cambridge, MA, USA

Pedro J. Sáenz, Giuseppe Pucci, Sam E. Turton, Alexis
Goujon, Rodolfo R. Rosales, Jörn Dunkel & John W. M. Bush

3. Institut de Physique de Rennes, CNRS, Université de Rennes, UMR
6251, Rennes, France

Giuseppe Pucci

4. School of Engineering, École Polytechnique Fédérale de Lausanne,
Lausanne, Switzerland

Alexis Goujon

Authors

1. Pedro J. Sáenz

[View author publications](#)

You can also search for this author in [PubMed](#) [Google Scholar](#)

2. Giuseppe Pucci

[View author publications](#)

You can also search for this author in [PubMed](#) [Google Scholar](#)

3. Sam E. Turton

[View author publications](#)

You can also search for this author in [PubMed](#) [Google Scholar](#)

4. Alexis Goujon

[View author publications](#)

You can also search for this author in [PubMed](#) [Google Scholar](#)

5. Rodolfo R. Rosales

[View author publications](#)

You can also search for this author in [PubMed](#) [Google Scholar](#)

6. Jörn Dunkel

[View author publications](#)

You can also search for this author in [PubMed](#) [Google Scholar](#)

7. John W. M. Bush

[View author publications](#)

You can also search for this author in [PubMed](#) [Google Scholar](#)

Contributions

P.J.S. conceived the study, led the experimental developments and the writing of the paper, and contributed to the theoretical modelling. S.E.T. and R.R.R. contributed to the theoretical modelling. G.P. contributed to the conception and execution of the preliminary experiments. A.G. contributed to the preliminary experiments. J.D. contributed to the theoretical modelling and the writing of the paper. J.W.M.B. contributed to the conception of the experiments and theory, and to writing the paper.

Corresponding authors

Correspondence to [Pedro J. Sáenz](#) or [John W. M. Bush](#).

Ethics declarations

Competing interests

The authors declare no competing interests.

Additional information

Peer review information *Nature* thanks Michael Shats and the other, anonymous, reviewer(s) for their contribution to the peer review of this work.

Publisher's note Springer Nature remains neutral with regard to jurisdictional claims in published maps and institutional affiliations.

Extended data figures and tables

Extended Data Fig. 1 Schematic of the experimental set-up.

The test section was mounted on an optical table and vibrated vertically by an electromagnetic shaker. The shaker was connected to the bath by a thin steel rod coupled with a linear air bearing. The forcing acceleration was monitored by two piezoelectric accelerometers. The bath was enclosed within a transparent acrylic chamber to ensure that ambient air currents did not affect the experiments. A d.c. motor housed inside the hollow air bearing enabled system rotation.

Extended Data Fig. 2 Experimental spin flips.

a–e, Snapshots at different times illustrate a typical spin-flip event arising in a 1D spin lattice (Supplementary Video 6). At each time, the panels at left are colour-coded according to the instantaneous spin S_i (same colour map as in Fig. 1d), while those on the right depict the recent walker trajectories, colour-coded according to the local speed. Perturbed by the wave fields emitted by its neighbours, the middle walker initially follows an elliptical path. The length of the minor axis decreases until the walker trajectory essentially becomes a straight line across the well centre. Subsequently, the process is reversed, resulting in the walker rotating in the opposite sense. The three walkers shown are part of the 1D antiferromagnetic lattice described in Fig. 1h with $\gamma/\gamma_F = 86.0\%$.

Extended Data Fig. 3 Wave coupling.

a, Experimental visualization of the wave field generated by a single walker in a 1D lattice with the same geometry as in Fig. 1h and $\gamma/\gamma_F = 92.0\%$. The submerged wells can be identified as the regions with a different shade of grey. **b**, Superposition of the wave field shown in **a** and the zeros of the drop-centred Bessel function $\langle J_0(k_F |x|) \rangle$. **c**, Wave field of a bouncer computed with the theoretical model developed previously⁶⁸ for walkers over variable topography. The bouncer is located at $(x, y) = (3D/8, 0)$ in a 2D square lattice with the same well diameter D and centre-to-centre separation L as in **a** and $\gamma/\gamma_F = 88.0\%$. Solid blue lines denote the submerged wells and dashed lines the zeros of a Bessel function J_0 centred at the drop position.

Extended Data Fig. 4 Emergent order for varying lattice spacing.

a, b, The dependence of the average spin correlation, $\langle \chi \rangle$ (**a**) and the mean phase difference, $\langle \Delta \phi \rangle$ (**b**) on the lattice spacing, L , as predicted by the Bessel model (equation (16)) with $\tau = 0.4$ s, $\omega_0 = 3.3$ s⁻¹, and $F = 70$ s⁻². The average droplet-induced wave field, which is approximated by a Bessel function $J_0(k_F L)$, centred in the neighbouring well at $L = 0$, is provided for comparison in **a**. **c, d**, Dominant (**c**) and subdominant (**d**) synchronization modes for the corresponding sections (A–D) in **a, b**.

Extended Data Fig. 5 Emergent order for varying bath acceleration.

Comparison of the experimentally observed average spin correlation, $\langle \chi \rangle$, with the predictions of the Bessel model (equation (16)) and the generalized Kuramoto model (equation (23)). Solid lines are fits resulting from smoothing the piecewise linear plot given by connecting the points. Bessel model parameters: $L = 17.7$ mm, $r = 1.8$ mm, $\lambda_F = 2\pi/k_F = 5.1$ mm. The interaction parameter F is varied across the range $70 < F < 130$ s⁻² and transformed back to γ/γ_F using the relation from Extended Data Table 1. To simplify the simulations, we fix the

relaxation time to be $\tau = 0.1$ s and the natural angular frequency to be $\omega_0 = 3.3 \text{ s}^{-1}$, values consistent with experimental observation (Fig. 1c). The effective walker mass is set to $m_w = 1.65m$, in line with prior work⁶¹. GK model parameters: α is varied over the range $8.5 < \alpha < 15 \text{ s}^{-2}$, while maintaining $\beta < 0$ and a constant ratio $|\beta/\alpha| = 0.3$. By dividing the expressions for α and β in equations (25), (26) by a factor of two, in accordance with the mismatch between the GK and Bessel models discussed in Supplementary Fig. 3, the minimum $\langle \chi \rangle$ predicted by the GK model emerged in the vicinity of γ_c .

Extended Data Fig. 6 Emergent order in large 2D square lattices.

Simulations of the Bessel model (equation (16)) and the generalized Kuramoto model (equation (23)) for a 50×50 square lattice demonstrate the emergence of antiferromagnetic and ferromagnetic order in 2D for various lattice spacings and bath accelerations. **a**, The lattice spacing determines the emergent antiferromagnetic (ADM_+) or ferromagnetic (FM_+) order in a manner predicted by our reduced theory (equation (24)). **b**, **c**, Specifically, preferred in-phase rotation between neighbouring pairs can be clearly observed in the antiferromagnetic AFM_+ (**b**), and ferromagnetic FM_+ (**c**) regimes. We note that **b** and **c** correspond to simulations of the Bessel model with the spacings indicated on **a**. **d**, The emergent in-phase antiferromagnetic order (AFM_+) as a function of bath acceleration. Bessel model parameters in **a**: $\tau = 0.1$ s, $\mathcal{F} = 72 \text{ s}^{-2}$, $16.8 \leq L \leq 19$ mm, $\omega_0 = 3.3 \text{ s}^{-1}$, and $\lambda_F = 4.95$ mm. Bessel model parameters in **d** are the same as in **a**, but with $L = 17.1$ mm and the interaction parameter varies across the range $65 \leq \mathcal{F} \leq 85 \text{ s}^{-2}$, which is transformed back to γ/γ_F using the relation from Extended Data Table 1. GK model parameters in **d**: α is varied over the range $9.5 < \alpha < 13 \text{ s}^{-2}$ while maintaining $\beta < 0$ and a constant ratio $|\beta/\alpha| = 0.07$, $\tau = 0.2$ s and $\omega_0 = 3.3 \text{ s}^{-1}$. In all cases, each data point results from averaging 50 simulations of 600 s each, to ensure statistical significance.

Extended Data Fig. 7 Emergent order for different vertical bouncing synchronizations and lattice geometries.

a, Oblique view of a 2D spin lattice where the walker in the centre is bouncing vertically in-phase and out-of-phase with its left and right neighbours, respectively. **b**, Average spin correlation for lattices with the same geometry as those described in Fig. 1 when the walkers all bounce in phase (blue, result presented in text), out of phase (green), or have randomly distributed bouncing phases (red). Vertically in-phase pairs promote in-phase orbital antiferromagnetic order (AFM_+), whereas vertically out-of-phase pairs promote out-of-phase orbital antiferromagnetic order (AFM_-). A random distribution of vertical phases thus leads to competing orbital synchronization modes, which has an effect on the emergent spin correlation. Solid lines are fits resulting from smoothing the piecewise linear plot given by connecting the points. **c**, Triangular HSLs with a lattice spacing tuned to promote antiferromagnetic order can be used to investigate frustration effects.

Extended Data Fig. 8 Emergent collective order in simulations.

Simulations of square HSLs with the theoretical model developed previously⁶⁸ is used to explore collective order in 2D. **a, b**, For appropriate lattice spacings, in-phase ferromagnetic order FM_+ (**a**) and in-phase antiferromagnetic order AFM_+ (**b**) are simulated. Left, schematic; middle, wave field and walker's trajectories; right, time evolution of the orbital phases.

Extended Data Fig. 9 Model tunability.

Proof-of-concept simulations performed with the model developed previously⁶⁸ illustrate the tunability and potential for future research of HSLs. Left, schematic; middle, wave field and drop trajectories; and right, orbital phase evolution. **a**, An HSL tuned to promote FM_+ along the horizontal direction, but AFM_+ across vertical pairs. **b**, FM_+ lattice geometry with a random vertical and horizontal shift $\pm\epsilon$ in the position of

each well. **c**, FM₊ lattice geometry with two drop sizes (and so, two walker speeds). **d**, FM₊ lattice geometry with coupling strength controlled locally through the thickness of the liquid layer.

Extended Data Table 1 Model parameters and physical variables for HSLs

[Full size table](#)

Supplementary information

Supplementary Information

This file contains Supplementary Figures 1-4.

Rights and permissions

[Reprints and Permissions](#)

About this article



Cite this article

Sáenz, P.J., Pucci, G., Turton, S.E. *et al.* Emergent order in hydrodynamic spin lattices. *Nature* **596**, 58–62 (2021). <https://doi.org/10.1038/s41586-021-03682-1>

[Download citation](#)

- Received: 06 July 2020
- Accepted: 01 June 2021

- Published: 04 August 2021
- Issue Date: 05 August 2021
- DOI: <https://doi.org/10.1038/s41586-021-03682-1>

Comments

By submitting a comment you agree to abide by our [Terms](#) and [Community Guidelines](#). If you find something abusive or that does not comply with our terms or guidelines please flag it as inappropriate.

[Access through your institution](#)

[Change institution](#)

[Buy or subscribe](#)

Associated Content

[Bouncing droplets mimic spin systems](#)

- Nicolas Vandewalle

Advertisement

This article was downloaded by **calibre** from <https://www.nature.com/articles/s41586-021-03682-1>

- Article
- [Published: 04 August 2021](#)

Quantized nonlinear Thouless pumping

- [Marius Jürgensen](#) ORCID: [orcid.org/0000-0001-7074-0002¹](https://orcid.org/0000-0001-7074-0002),
- [Seababrata Mukherjee](#) ORCID: [orcid.org/0000-0003-1942-2521¹](https://orcid.org/0000-0003-1942-2521) &
- [Mikael C. Rechtsman](#) ORCID: [orcid.org/0000-0002-6909-8355¹](https://orcid.org/0000-0002-6909-8355)

[Nature](#) volume **596**, pages 63–67 (2021)[Cite this article](#)

- 772 Accesses
- 14 Altmetric
- [Metrics details](#)

Subjects

- [Nonlinear optics](#)
- [Quantum simulation](#)
- [Solitons](#)
- [Topological insulators](#)

Abstract

The topological protection of wave transport, originally observed in the context of the quantum Hall effect in two-dimensional electron gases¹, has been shown to apply broadly to a range of physical platforms, including photonics^{2,3,4,5}, ultracold atoms in optical lattices^{6,7,8} and others^{9,10,11,12}. That said, the behaviour of such systems can be very different from the

electronic case, particularly when interparticle interactions or nonlinearity play a major role^{[13](#),[14](#),[15](#),[16](#),[17](#),[18](#),[19](#),[20](#),[21](#),[22](#)}. A Thouless pump^{[23](#)} is a one-dimensional model that captures the topological quantization of transport in the quantum Hall effect using the notion of dimensional reduction: an adiabatically, time-varying potential mathematically maps onto a momentum coordinate in a conceptual second dimension^{[24](#),[25](#),[26](#),[27](#),[28](#),[29](#),[30](#),[31](#),[32](#),[33](#),[34](#)}. Importantly, quantization assumes uniformly filled electron bands below a Fermi energy, or an equivalent occupation for non-equilibrium bosonic systems. Here we theoretically propose and experimentally demonstrate quantized nonlinear Thouless pumping of photons with a band that is decidedly not uniformly occupied. In our system, nonlinearity acts to quantize transport via soliton formation and spontaneous symmetry-breaking bifurcations. Quantization follows from the fact that the instantaneous soliton solutions centred upon a given unit cell are identical after each pump cycle, up to translation invariance; this is an entirely different mechanism from traditional Thouless pumping. This result shows that nonlinearity and interparticle interactions can induce quantized transport and topological behaviour without a linear counterpart.

Access options

Subscribe to Journal

Get full journal access for 1 year

\$199.00

only \$3.90 per issue

[Subscribe](#)

All prices are NET prices.

VAT will be added later in the checkout.

Tax calculation will be finalised during checkout.

Rent or Buy article

Get time limited or full article access on ReadCube.

from \$8.99

[Rent or Buy](#)

All prices are NET prices.

Additional access options:

- [Log in](#)
- [Access through your institution](#)
- [Learn about institutional subscriptions](#)

Fig. 1: Photonic implementation of a topological Thouless pump.

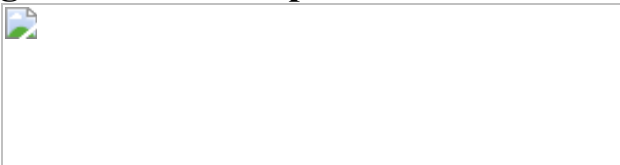


Fig. 2: Linear and nonlinear propagation in topological Thouless pumps.

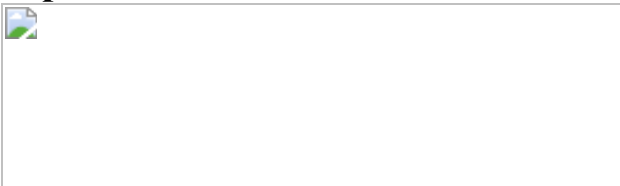
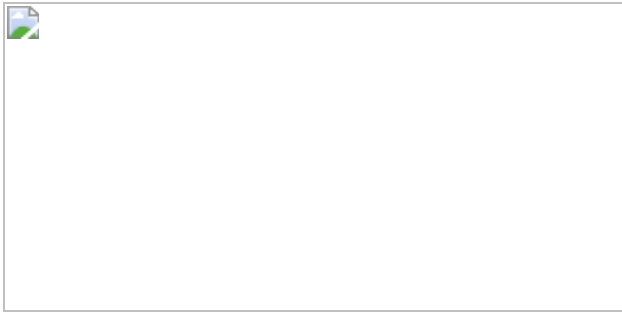


Fig. 3: Mechanism of nonlinear pumping.



Fig. 4: Experimental observation of quantized nonlinear topological pumping.



Data availability

The data that support the findings of this study are available from the corresponding author on reasonable request.

References

1. 1.

Klitzing, K. V., Dorda, G. & Pepper, M. New method for high-accuracy determination of the fine-structure constant based on quantized Hall resistance. *Phys. Rev. Lett.* **45**, 494–497 (1980).

[ADS](#) [Article](#) [Google Scholar](#)

2. 2.

Raghu, S. & Haldane, F. D. M. Analogs of quantum-Hall-effect edge states in photonic crystals. *Phys. Rev. A* **78**, 033834 (2008).

[ADS](#) [Article](#) [CAS](#) [Google Scholar](#)

3. 3.

Wang, Z., Chong, Y., Joannopoulos, J. D. & Soljai, M. Observation of unidirectional backscattering-immune topological electromagnetic states. *Nature* **461**, 772–775 (2009).

[ADS](#) [CAS](#) [PubMed](#) [Article](#) [Google Scholar](#)

4. 4.

Rechtsman, M. C. et al. Photonic Floquet topological insulators. *Nature* **496**, 196 (2013).

[ADS](#) [CAS](#) [PubMed](#) [Article](#) [Google Scholar](#)

5. 5.

Hafezi, M., Mittal, S., Fan, J., Migdall, A. & Taylor, J. M. Imaging topological edge states in silicon photonics. *Nat. Photon.* **7**, 1001 (2013).

[ADS](#) [CAS](#) [Article](#) [Google Scholar](#)

6. 6.

Atala, M. et al. Direct measurement of the Zak phase in topological Bloch bands. *Nat. Phys.* **9**, 795–800 (2013).

[CAS](#) [Article](#) [Google Scholar](#)

7. 7.

Jotzu, G. et al. Experimental realization of the topological Haldane model with ultracold fermions. *Nature* **515**, 237–240 (2014).

[ADS](#) [CAS](#) [PubMed](#) [Article](#) [Google Scholar](#)

8. 8.

Aidelsburger, M. et al. Measuring the Chern number of Hofstadter bands with ultracold bosonic atoms. *Nat. Phys.* **11**, 162–166 (2015).

[CAS](#) [Article](#) [Google Scholar](#)

9. 9.

Ningyuan, J., Owens, C., Sommer, A., Schuster, D. & Simon, J. Time- and site-resolved dynamics in a topological circuit. *Phys. Rev. X* **5**, 021031 (2015).

[Google Scholar](#)

10. 10.

Nalitov, A., Solnyshkov, D. & Malpuech, G. Polariton \mathbb{Z} topological insulator. *Phys. Rev. Lett.* **114**, 116401 (2015).

[ADS](#) [MathSciNet](#) [CAS](#) [PubMed](#) [Article](#) [PubMed Central](#) [Google Scholar](#)

11. 11.

Karzig, T., Bardyn, C.-E., Lindner, N. H. & Refael, G. Topological polaritons. *Phys. Rev. X* **5**, 031001 (2015).

[Google Scholar](#)

12. 12.

Klembt, S. et al. Exciton-polariton topological insulator. *Nature* **562**, 552–556 (2018).

[ADS](#) [CAS](#) [PubMed](#) [Article](#) [Google Scholar](#)

13. 13.

Lumer, Y., Plotnik, Y., Rechtsman, M. C. & Segev, M. Self-localized states in photonic topological insulators. *Phys. Rev. Lett.* **111**, 243905 (2013).

[ADS](#) [PubMed](#) [Article](#) [CAS](#) [Google Scholar](#)

14. 14.

Mukherjee, S. & Rechtsman, M. C. Observation of Floquet solitons in a topological bandgap. *Science* **368**, 856–859 (2020).

[ADS](#) [CAS](#) [PubMed](#) [Article](#) [Google Scholar](#)

15. 15.

Mukherjee, S. & Rechtsman, M. C. Observation of unidirectional soliton-like edge states in nonlinear Floquet topological insulators. Preprint at *arXiv* <https://arxiv.org/abs/2010.11359> (2020).

16. 16.

Maczewsky, L. J. et al. Nonlinearity-induced photonic topological insulator. *Science* **370**, 701–704 (2020).

[ADS](#) [CAS](#) [PubMed](#) [Article](#) [Google Scholar](#)

17. 17.

Smirnova, D., Leykam, D., Chong, Y. & Kivshar, Y. Nonlinear topological photonics. *Appl. Phys. Rev.* **7**, 021306 (2020).

[ADS](#) [CAS](#) [Article](#) [Google Scholar](#)

18. 18.

Xia, S. et al. Nontrivial coupling of light into a defect: the interplay of nonlinearity and topology. *Light Sci. Appl.* **9**, 147 (2020).

[ADS](#) [CAS](#) [PubMed](#) [PubMed Central](#) [Article](#) [Google Scholar](#)

19. 19.

Xia, S. et al. Nonlinear tuning of PT symmetry and non-Hermitian topological states. *Science* **372**, 72–76 (2021).

[ADS](#) [CAS](#) [PubMed](#) [Article](#) [Google Scholar](#)

20. 20.

Tangpanitanon, J. et al. Topological pumping of photons in nonlinear resonator arrays. *Phys. Rev. Lett.* **117**, 213603 (2016).

[ADS](#) [PubMed](#) [Article](#) [Google Scholar](#)

21. 21.

Ke, Y., Qin, X., Kivshar, Y. S. & Lee, C. Multiparticle Wannier states and Thouless pumping of interacting bosons. *Phys. Rev. A* **95**, 063630 (2017).

[ADS](#) [Article](#) [Google Scholar](#)

22. 22.

Hayward, A., Schweizer, C., Lohse, M., Aidelsburger, M. & Heidrich-Meisner, F. Topological charge pumping in the interacting bosonic Rice-Mele model. *Phys. Rev. B* **98**, 245148 (2018).

[ADS](#) [CAS](#) [Article](#) [Google Scholar](#)

23. 23.

Thouless, D. J. Quantization of particle transport. *Phys. Rev. B* **27**, 6083–6087 (1983).

[ADS](#) [MathSciNet](#) [CAS](#) [Article](#) [Google Scholar](#)

24. 24.

Kraus, Y. E., Lahini, Y., Ringel, Z., Verbin, M. & Zilberberg, O. Topological states and adiabatic pumping in quasicrystals. *Phys. Rev. Lett.* **109**, 106402 (2012).

[ADS](#) [PubMed](#) [Article](#) [CAS](#) [Google Scholar](#)

25. 25.

Verbin, M., Zilberberg, O., Kraus, Y. E., Lahini, Y. & Silberberg, Y. Observation of topological phase transitions in photonic quasicrystals. *Phys. Rev. Lett.* **110**, 076403 (2013).

[ADS](#) [PubMed](#) [Article](#) [CAS](#) [Google Scholar](#)

26. 26.

Zilberberg, O. *et al.* Photonic topological boundary pumping as a probe of 4D quantum Hall physics. *Nature* **553**, 59–62 (2018).

[ADS](#) [CAS](#) [PubMed](#) [Article](#) [Google Scholar](#)

27. 27.

Cerjan, A., Wang, M., Huang, S., Chen, K. P. & Rechtsman, M. C. Thouless pumping in disordered photonic systems. *Light Sci. Appl.* **9**, 178 (2020).

[ADS](#) [CAS](#) [PubMed](#) [PubMed Central](#) [Article](#) [Google Scholar](#)

28. 28.

Grinberg, I. H. *et al.* Robust temporal pumping in a magneto-mechanical topological insulator. *Nat. Commun.* **11**, 974 (2020).

[ADS](#) [CAS](#) [PubMed](#) [PubMed Central](#) [Article](#) [Google Scholar](#)

29. 29.

Lohse, M., Schweizer, C., Zilberberg, O., Aidelsburger, M. & Bloch, I. A Thouless quantum pump with ultracold bosonic atoms in an optical superlattice. *Nat. Phys.* **12**, 350–354 (2016).

[CAS](#) [Article](#) [Google Scholar](#)

30. 30.

Lohse, M., Schweizer, C., Price, H. M., Zilberberg, O. & Bloch, I. Exploring 4D quantum Hall physics with a 2D topological charge pump. *Nature* **553**, 55–58 (2018).

[ADS](#) [CAS](#) [PubMed](#) [Article](#) [Google Scholar](#)

31. 31.

Ke, Y. et al. Topological pumping assisted by bloch oscillations. *Phys. Rev. Res.* **2**, 033143 (2020).

[CAS](#) [Article](#) [Google Scholar](#)

32. 32.

Ma, W. et al. Experimental observation of a generalized Thouless pump with a single spin. *Phys. Rev. Lett.* **120**, 120501 (2018).

[ADS](#) [PubMed](#) [Article](#) [Google Scholar](#)

33. 33.

Fedorova, Z., Qiu, H., Linden, S. & Kroha, J. Observation of topological transport quantization by dissipation in fast Thouless pumps. *Nat. Commun.* **11**, 3758 (2020).

[ADS](#) [CAS](#) [PubMed](#) [PubMed Central](#) [Article](#) [Google Scholar](#)

34. 34.

Nakajima, S. et al. Topological Thouless pumping of ultracold fermions. *Nature Phys.* **12**, 296 (2016).

[ADS](#) [Article](#) [CAS](#) [Google Scholar](#)

35. 35.

Aubry, S. & André, G. Analyticity breaking and Anderson localization in incommensurate lattices. *Ann. Israel Phys. Soc.* **3**, 18 (1980).

[MathSciNet](#) [MATH](#) [Google Scholar](#)

36. 36.

Harper, P. G. Single band motion of conduction electrons in a uniform magnetic field. *Proc. Phys. Soc. A* **68**, 874 (1955).

[ADS](#) [MATH](#) [Article](#) [Google Scholar](#)

37. 37.

Thouless, D. J., Kohmoto, M., Nightingale, M. P. & den Nijs, M. Quantized Hall conductance in a two-dimensional periodic potential. *Phys. Rev. Lett.* **49**, 405 (1982).

[ADS](#) [CAS](#) [Article](#) [Google Scholar](#)

38. 38.

Niu, Q. & Thouless, D. Quantised adiabatic charge transport in the presence of substrate disorder and many-body interaction. *J. Phys. Math. Gen.* **17**, 2453 (1984).

[ADS](#) [MathSciNet](#) [MATH](#) [Article](#) [Google Scholar](#)

39. 39.

Pu, H., Maenner, P., Zhang, W. & Ling, H. Y. Adiabatic condition for nonlinear systems. *Phys. Rev. Lett.* **98**, 050406 (2007).

[ADS](#) [MathSciNet](#) [PubMed](#) [MATH](#) [Article](#) [CAS](#) [PubMed Central](#)
[Google Scholar](#)

40. 40.

Wiggins, S. *Introduction to Applied Nonlinear Dynamical Systems and Chaos* Vol. 2 (Springer Science & Business Media, 2003).

41. 41.

Davis, K. M., Miura, K., Sugimoto, N. & Hirao, K. Writing waveguides in glass with a femtosecond laser. *Opt. Lett.* **21**, 1729–1731 (1996).

[ADS](#) [CAS](#) [PubMed](#) [Article](#) [Google Scholar](#)

42. 42.

Szameit, A. & Nolte, S. Discrete optics in femtosecond-laser-written photonic structures. *J. Phys. B* **43**, 163001 (2010).

[ADS](#) [Article](#) [CAS](#) [Google Scholar](#)

43. 43.

Eisenberg, H., Silberberg, Y., Morandotti, R., Boyd, A. & Aitchison, J. Discrete spatial optical solitons in waveguide arrays. *Phys. Rev. Lett.* **81**, 3383 (1998).

[ADS](#) [CAS](#) [Article](#) [Google Scholar](#)

44. 44.

Christodoulides, D. N. & Joseph, R. I. Discrete self-focusing in nonlinear arrays of coupled waveguides. *Opt. Lett.* **13**, 794–796 (1988).

45. 45.

Fleischer, J. W., Segev, M., Efremidis, N. K. & Christodoulides, D. N. Observation of two-dimensional discrete solitons in optically induced nonlinear photonic lattices. *Nature* **422**, 147–150 (2003).

46. 46.

Lederer, F., Stegeman, G. I., Christodoulides, D. N., Assanto, G., Segev, M. & Silberberg, Y. Discrete solitons in optics. *Phys. Rep.* **463**, 1–126 (2008).

47. 47.

Fukui, T., Hatsugai, Y. & Suzuki, H. Chern numbers in discretized Brillouin zone: efficient method of computing (spin) Hall conductances. *J. Phys. Soc. Jpn* **74**, 1674–1677 (2005).

[ADS](#) [CAS](#) [Article](#) [Google Scholar](#)

48. 48.

Ke, Y. et al. Topological phase transitions and Thouless pumping of light in photonic waveguide arrays. *Laser Photon. Rev.* **10**, 995–1001 (2016).

[ADS](#) [CAS](#) [Article](#) [Google Scholar](#)

49. 49.

Wolfram Research, Inc. *Mathematica*. v.12.0. (2019).

50. 50.

Kevrekidis, P. G. *The Discrete Nonlinear Schrödinger Equation: Mathematical Analysis, Numerical Computations and Physical Perspectives* Vol. 232 (Springer Science & Business Media, 2009).

[Download references](#)

Acknowledgements

We acknowledge discussions with A. Cerjan, S. Gopalakrishnan, D. Leykam, O. Zilberberg and P. Kevrekidis. We acknowledge support from the ONR Young Investigator programme under award number N00014-18-1-2595, the ONR-MURI programme N00014-20-1-2325 and the Packard Foundation fellowship, under number 2017-66821. M.J. acknowledges the support of the Verne M. Willaman Distinguished Graduate Fellowship at the Pennsylvania State University. Some numerical calculations were

performed on the Pennsylvania State University's Institute for Computational and Data Sciences' Roar supercomputer.

Author information

Affiliations

1. Department of Physics, The Pennsylvania State University, University Park, PA, USA

Marius Jürgensen, Sebabrata Mukherjee & Mikael C. Rechtsman

Authors

1. Marius Jürgensen

[View author publications](#)

You can also search for this author in [PubMed](#) [Google Scholar](#)

2. Sebabrata Mukherjee

[View author publications](#)

You can also search for this author in [PubMed](#) [Google Scholar](#)

3. Mikael C. Rechtsman

[View author publications](#)

You can also search for this author in [PubMed](#) [Google Scholar](#)

Contributions

M.C.R. initiated and supervised the project; M.J. fabricated and characterized the devices and carried out all measurements, assisted by S.M.; S.M. designed and built the experimental beam shaping and fabrication setup; theoretical investigation was carried out by M.J.; M.J. and M.C.R. wrote the manuscript with input from S.M.

Corresponding authors

Correspondence to [Marius Jürgensen](#) or [Mikael C. Rechtsman](#).

Ethics declarations

Competing interests

The authors declare no competing interests.

Additional information

Peer review information *Nature* thanks the anonymous reviewers for their contribution to the peer review of this work.

Publisher's note Springer Nature remains neutral with regard to jurisdictional claims in published maps and institutional affiliations.

Extended data figures and tables

[Extended Data Fig. 1 Analysis of soliton bifurcation.](#)

a, Energy eigenvalues for the linear eigenstates at $z = 0$ (black) showing three bands. Nonlinear eigenvalues for solitons bifurcating from the upper (middle, lower) band are shown in green (blue, red) and are decreasing with increasing power. **b**, Degree of soliton localization as measured by the Inverse Participation Ratio $\langle \langle \text{IPR} \rangle \rangle = \sum_n |\varphi_n|^4 / (\sum_n |\varphi_n|^2)^2$ for the solitons shown in **a**. **c**, Spectral overlap coefficients between the soliton bifurcating from the lowest band and the linear energy eigenstates are a strong function of power. The two upper panels show the occupation at $(gP/J)^{\max} = 0.2$ and 1.9 (corresponding to Extended Data Fig. 2g and Fig. 2b, respectively). Note the non-uniform occupation of the lowest band (from which the soliton bifurcates), which is particularly pronounced at low power.

Extended Data Fig. 2 Higher Chern number pumping and band occupation.

a–c, Numerically calculated z -evolution for an initial excitation of a maximally localized Wannier state of the upper (middle, lower) band (shown in **a** (**b**, **c**), respectively). The displacement of the centre of mass is dictated by the Chern number of the occupied band. The insets show the projection $\langle\langle \phi(z)|\phi(z)\rangle\rangle^2$ of the propagating wavefunction $\phi(z)$ onto the instantaneous linear Bloch states $\phi_{lin}(z)$ of the lower (middle, upper) band, ordered from left to right by increasing energy eigenvalue. **d**, Band structure of the off-diagonal AAH model, showing three bands with Chern numbers $C = \{-1, 2, -1\}$. End states are shown in red. **e–g**, Similar to **a–c**, but with an initial excitation of a nonlinear eigenstate bifurcated from the upper (middle, lower) band (shown in **e** (**f**, **g**), respectively) with $(gP/J)^{\max} = 0.2$. The displacement of the centre of mass is identical to the Chern number of the band from which the soliton bifurcates. The insets show a strongly non-uniform occupation of the linear Bloch states. Parameters for the system are chosen to be identical to those in Fig. 2, except $L = 4 \times 10^3$ mm with a size of 900 sites for **a–c** and $L = 8 \times 10^5$ mm for **e–g**.

Extended Data Fig. 3 Adiabatic behaviour in the nonlinear system.

Absorbed intensity (relative to the total intensity) during one driving period in relation to the driving frequency. Blue circles are numerical values and the red line has a slope of -2 . The parameters for the simulation are 180 sites with absorbing boundary conditions using 40 sites at each end, $d = 24 \mu\text{m}$, $d = 2 \mu\text{m}$, $\alpha_0 = -2\pi/12$ and $(gP/J)^{\max} = 1.9$.

Extended Data Fig. 4 Calculation of the Chern number for the pumped soliton.

a, Sequence of steps to calculate the Chern number for the nonlinear soliton propagation. **b**, Spatial supercell for a pumped soliton composed of m unit cells with periodic boundary conditions (PBC). **c**, z -evolution of the discrete

soliton wavefunction $\phi_n(z)$ in a supercell with $m = 4$ unit cells and m periods forming a two-dimensional periodic supercell. **d**, Band structure (lower panel) with $3m$ bands calculated using the supercell (upper panel). The eigenstates of one band (here, the lowest) describe the motion of the soliton and its Chern number C can be calculated in the conventional way (here, $C = -1$).

Extended Data Fig. 5 Topological phase transitions.

a, Nonlinearly induced topological phase transition. The Chern number associated with the soliton is calculated for increasing power \((gP/J)^{\max}\). In the grey area, no contiguous path for an adiabatic soliton evolution is found. The red line indicates the Chern number of the lowest band in the linear model from which the soliton bifurcates. **b**, Linearly induced topological phase transition. The Chern number associated with the soliton is calculated as a function of decreasing hopping strength J . The red line indicates the linear Chern number of the band from which the soliton bifurcates. The topological phase transition occurs at $J = 0.25$.

Extended Data Fig. 6 Nonlinear waveguide characterization.

a, Simplified, schematic illustration of the experimental setup, including a half-waveplate (WP) together with a polarizing beam splitter (PBS) to adjust the power of the emitted laser pulses. Two gratings (G_1, G_2) temporally stretch the pulse to 2 ps. Lens L1 focuses the pulses into single waveguides within the waveguide array. Lenses L2 and L3 image the output facet onto a CMOS camera. Simultaneously, using a further beamsplitter (BS), the light is additionally coupled into a fibre and its spectrum is analysed with an optical spectrum analyser (OSA). **b**, Measured input power to output power dependence for two datasets, showing no nonlinear losses due to multi-photon absorption. The black line indicates a linear fit. **c**, Spectral distribution of the pulse after propagation of 76 mm in a lattice of straight waveguides with equal separation of 24 μm . The white lines denote the spectral range in which 76% of the intensity (equivalent to FWHM of a Gaussian) are found. **d**, Theoretical nonlinear parameter $gP(z =$

0) versus the experimental time averaged input power. Depicted are values from five different waveguides in a lattice of straight waveguides with a separation of 24 μm . The black line indicates the value of $g = (0.07 \pm 0.01) \text{ mm}^{-1}$ per mW (time-averaged) input power as the mean value with one standard deviation.

Extended Data Fig. 7 Characterization of the coupling strength.

Coupling constants $J(d, \lambda)$ for wavelength λ , extracted from waveguide lattices with straight waveguides and equal separation, d , between the waveguides. The errorbars show one standard deviation.

Extended Data Fig. 8 Parameter dependence of pitchfork bifurcation.

Input power (relative to the mean input power at modulation $\delta = 1.5 \mu\text{m}$) required for maximum relative intensity in the pumped soliton as a function of spatial modulation strength δ of the waveguides. Dots in colour are measurements, black lines are the respective mean values with one standard deviation. The black dotted line shows the numerically obtained threshold power for the pitchfork bifurcation point.

Supplementary information

Supplementary Video 1

Spatial comparison between linear and nonlinear eigenstates. Spatial shape of the lowest energy eigenstate of each of the three bands (bands are numbered by increasing energy) together with a soliton that bifurcated from that band. The grey vertical line indicates the position of the center of mass of the soliton. We use $gP/J^{\max} = 0.5$. The simulations show that the movement of the soliton's center of mass cannot be simply inferred from the movement of the band edge states, but instead is equal to the (linear) Chern number of the band from which the soliton bifurcated.

Supplementary Video 2

Mechanism of nonlinear pumping. Position of relevant soliton solutions over one period for increasing input power. It is directly related to Fig. 3 in the main text, which only shows the slices at four input power values. The video shows additional unstable eigenstates which are not included in Fig. 3 to keep the figures in the main text uncluttered.

Supplementary Video 3

Nonlinear pumping behavior during a linearly induced topological phase transition. The left panel shows the instantaneous nonlinear eigenstates over one pumping cycle for a soliton that bifurcates from the lowest band, while the underlying model is tuned through a linearly-induced topological phase transition (accompanied by a gap closing). In contrast to a nonlinearly-induced topological phase transition (as described in the main text), the power is kept constant ($\langle\{gP\}/K=0.7\rangle$). Hopping constants are given by Eq. (3) and the topological phase transition occurs at $J=0.25$. During the topological phase transition, the Chern numbers of the bands change from $C=\{-1,2,-1\}$ to $C=\{2,-4,2\}$. The central part shows the position of the center of mass in each unit cell, and the right part shows the corresponding band structure of the model.

Rights and permissions

[Reprints and Permissions](#)

About this article



Check for
updates

Cite this article

Jürgensen, M., Mukherjee, S. & Rechtsman, M.C. Quantized nonlinear Thouless pumping. *Nature* **596**, 63–67 (2021).
<https://doi.org/10.1038/s41586-021-03688-9>

[Download citation](#)

- Received: 04 February 2021
- Accepted: 01 June 2021
- Published: 04 August 2021
- Issue Date: 05 August 2021
- DOI: <https://doi.org/10.1038/s41586-021-03688-9>

Comments

By submitting a comment you agree to abide by our [Terms](#) and [Community Guidelines](#). If you find something abusive or that does not comply with our terms or guidelines please flag it as inappropriate.

[Access through your institution](#)

[Change institution](#)

[Buy or subscribe](#)

Advertisement

This article was downloaded by **calibre** from <https://www.nature.com/articles/s41586-021-03688-9>

- Article
- [Published: 04 August 2021](#)

Pseudogap in a crystalline insulator doped by disordered metals

- [Sae Hee Ryu¹](#) na1,
- [Minjae Huh](#) [ORCID: orcid.org/0000-0002-0362-9205^{1,2}](#) na1,
- [Do Yun Park¹](#) na1,
- [Chris Jozwiak](#) [ORCID: orcid.org/0000-0002-0980-3753³](#),
- [Eli Rotenberg](#) [ORCID: orcid.org/0000-0002-3979-8844³](#),
- [Aaron Bostwick](#) [ORCID: orcid.org/0000-0002-9008-2980³](#) &
- [Keun Su Kim](#) [ORCID: orcid.org/0000-0002-7033-1177¹](#)

[Nature](#) volume **596**, pages 68–73 (2021) [Cite this article](#)

- 1673 Accesses
- 15 Altmetric
- [Metrics details](#)

Subjects

- [Electronic properties and materials](#)
- [Superconducting properties and materials](#)
- [Surfaces, interfaces and thin films](#)
- [Two-dimensional materials](#)

Abstract

Key to our understanding of how electrons behave in crystalline solids is the band structure that connects the energy of electron waves to their wavenumber. Even in phases of matter with only short-range order (liquid or amorphous solid), the coherent part of electron waves still has a band structure. Theoretical models for the band structure of liquid metals were formulated more than five decades ago^{[1](#),^{[2](#)},^{[3](#)},^{[4](#)},^{[5](#)},^{[6](#)},^{[7](#)},^{[8](#)},^{[9](#)},^{[10](#)},^{[11](#)},^{[12](#)},^{[13](#)},^{[14](#)},^{[15](#)}}, but, so far, band-structure renormalization and the pseudogap induced by resonance scattering have remained unobserved. Here we report the observation of the unusual band structure at the interface of a crystalline insulator (black phosphorus) and disordered dopants (alkali metals). We find that a conventional parabolic band structure of free electrons bends back towards zero wavenumber with a pseudogap of 30–240 millielectronvolts from the Fermi level. This is wavenumber renormalization caused by resonance scattering, leading to the formation of quasi-bound states in the scattering potential of alkali-metal ions. The depth of this potential tuned by different kinds of disordered alkali metal (sodium, potassium, rubidium and caesium) allows the classification of the pseudogap of *p*-wave and *d*-wave resonance. Our results may provide a clue to the puzzling spectrum of various crystalline insulators doped by disordered dopants^{[16](#)},^{[17](#)},^{[18](#)},^{[19](#)},^{[20](#)}, such as the waterfall dispersion observed in copper oxides.

Access options

Subscribe to Journal

Get full journal access for 1 year

\$199.00

only \$3.90 per issue

[Subscribe](#)

All prices are NET prices.

VAT will be added later in the checkout.

Tax calculation will be finalised during checkout.

Rent or Buy article

Get time limited or full article access on ReadCube.

from \$8.99

[Rent or Buy](#)

All prices are NET prices.

Additional access options:

- [Log in](#)
- [Access through your institution](#)
- [Learn about institutional subscriptions](#)

Fig. 1: Band structure of liquid metals and experimental systems.

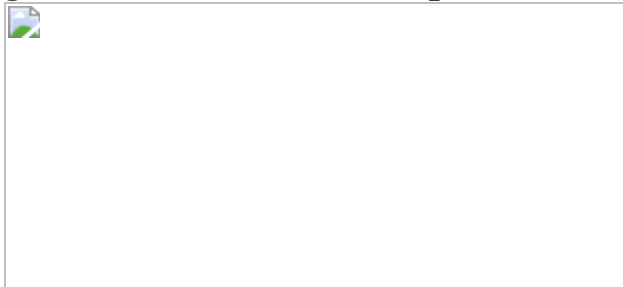


Fig. 2: Electronic structure of black phosphorus doped by disordered alkali metals.

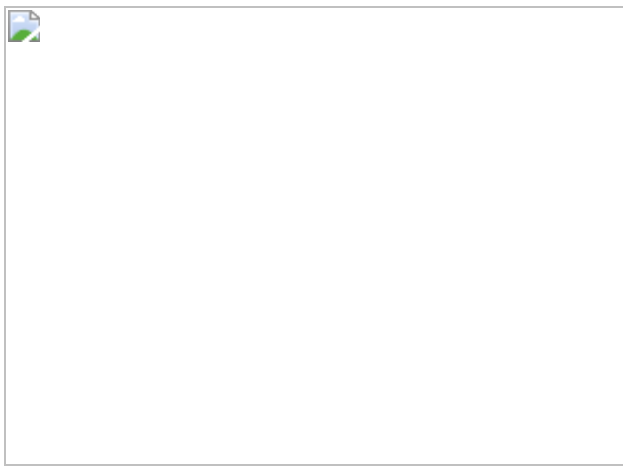


Fig. 3: Resonance scattering in liquid metals and band renormalizations.

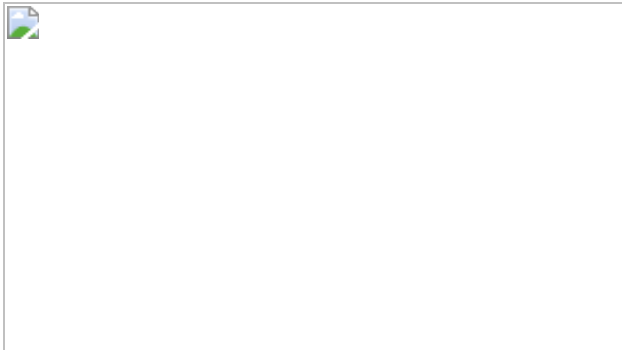


Fig. 4: Density of states in liquid metals and spectral simulations.

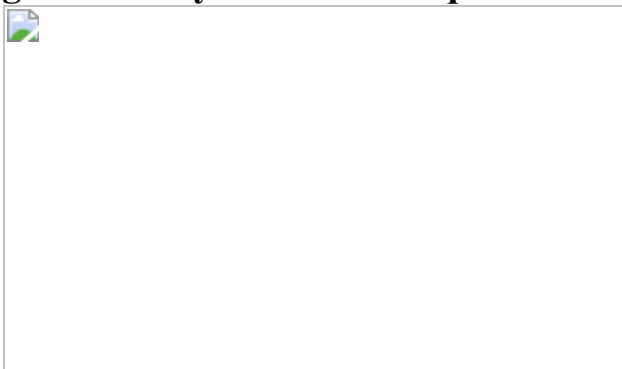


Fig. 5: Magnitude of the pseudogap and phase diagram.

Data availability

The data that support the findings of this study are available within the paper and from the corresponding author upon reasonable request. [Source data](#) are provided with this paper.

References

1. 1.

Edwards, S. F. The electronic structure of disordered systems. *Phil. Mag.* **6**, 617–638 (1961).

[ADS](#) [Article](#) [Google Scholar](#)

2. 2.

Edwards, S. F. The electronic structure of liquid metals. *Proc. R. Soc. Lond. A* **267**, 518–540 (1962).

[ADS](#) [CAS](#) [Article](#) [Google Scholar](#)

3. 3.

Ziman, J. M. A theory of the electrical properties of liquid metals. I: The monovalent metals. *Phil. Mag.* **6**, 1013–1034 (1961).

[ADS](#) [CAS](#) [Article](#) [Google Scholar](#)

4. 4.

Ziman, J. M. The T matrix, the K matrix, d bands and l -dependent pseudo-potentials in the theory of metals. *Proc. Phys. Soc.* **86**, 337–353 (1965).

[ADS](#) [MathSciNet](#) [CAS](#) [Article](#) [Google Scholar](#)

5. 5.

Anderson, P. W. & McMillan, W. L. Multiple-scattering theory and resonances in transition metals. In *Proc. International School of Physics “Enrico Fermi” Course 37* (ed. Marshall, W.) 50–86 (Academic, 1967).

6. 6.

Morgan, G. J. Electron transport in liquid metals II. A model for the wave functions in liquid transition metals. *J. Phys. C* **2**, 1454–1464 (1969).

[ADS](#) [Article](#) [Google Scholar](#)

7. 7.

Gyorffy, B. L. Electronic states in liquid metals: a generalization of the coherent-potential approximation for a system with short-range order. *Phys. Rev. B* **1**, 3290–3299 (1970).

[ADS](#) [Article](#) [Google Scholar](#)

8. 8.

Schwartz, L. & Ehrenreich, H. Single-site approximations in the electronic theory of liquid metals. *Ann. Phys.* **64**, 100–148 (1971).

[ADS](#) [CAS](#) [Article](#) [Google Scholar](#)

9. 9.

Faber, T. E. *An Introduction to the Theory of Liquid Metals* (Cambridge Univ. Press, 1972).

10. 10.

Olson, J. J. Anderson–McMillan prescription for the density of states of liquid iron. *Phys. Rev. B* **12**, 2908–2916 (1975).

[ADS](#) [CAS](#) [Article](#) [Google Scholar](#)

11. 11.

Chang, K. S., Sher, A., Petzinger, K. G. & Weisz, G. Density of states of liquid Cu. *Phys. Rev. B* **12**, 5506–5513 (1975).

[ADS](#) [CAS](#) [Article](#) [Google Scholar](#)

12. 12.

Oglesby, J. & Lloyd, P. Some single-site structure-independent approximations in condensed materials. *J. Phys. C* **9**, 2879–2886 (1976).

[ADS](#) [CAS](#) [Article](#) [Google Scholar](#)

13. 13.

Mott, N. F. Metal–insulator transition. *Rev. Mod. Phys.* **40**, 677–683 (1968).

[ADS](#) [CAS](#) [Article](#) [Google Scholar](#)

14. 14.

Mott, N. F. Conduction in non-crystalline materials: III. Localized states in a pseudogap and near extremities of conduction and valence bands. *Phil. Mag.* **19**, 835–852 (1968).

[ADS](#) [Article](#) [Google Scholar](#)

15. 15.

Anderson, P. W. Absence of diffusion in certain random lattices. *Phys. Rev.* **109**, 1492–1505 (1958).

[ADS](#) [CAS](#) [Article](#) [Google Scholar](#)

16. 16.

Lu, D. et al. Angle-resolved photoemission studies of quantum materials. *Annu. Rev. Condens. Matter Phys.* **3**, 129–167 (2012).

[CAS](#) [Article](#) [Google Scholar](#)

17. 17.

Graf, J. et al. Universal high energy anomaly in the angle-resolved photoemission spectra of high temperature superconductors: possible

evidence of spinon and holon branches. *Phys. Rev. Lett.* **98**, 067004 (2007).

[ADS](#) [CAS](#) [Article](#) [Google Scholar](#)

18. 18.

Inosov, D. S. et al. Momentum and energy dependence of the anomalous high-energy dispersion in the electronic structure of high temperature superconductors. *Phys. Rev. Lett.* **99**, 237002 (2007).

[ADS](#) [CAS](#) [Article](#) [Google Scholar](#)

19. 19.

Kim, Y. K., Sung, N. H., Denlinger, J. D. & Kim, B. J. Observation of a *d*-wave gap in electron-doped Sr₂IrO₄. *Nat. Phys.* **12**, 37–41 (2016).

[CAS](#) [Article](#) [Google Scholar](#)

20. 20.

Uchida, M. et al. Pseudogap of metallic layered nickelate R_{2-x}Sr_xNiO₄ (R = Nd, Eu) crystals measured using angle-resolved photoemission spectroscopy. *Phys. Rev. Lett.* **106**, 027001 (2011).

[ADS](#) [CAS](#) [Article](#) [Google Scholar](#)

21. 21.

Baumberger, F., Auwärter, W., Greber, T. & Osterwalder, J. Electron coherence in a melting lead monolayer. *Science* **306**, 2221–2224 (2004).

[ADS](#) [CAS](#) [Article](#) [Google Scholar](#)

22. 22.

Kim, K. S. & Yeom, H. W. Radial band structure of electrons in liquid metals. *Phys. Rev. Lett.* **107**, 136402 (2011).

[ADS](#) [Article](#) [Google Scholar](#)

23. 23.

Kim, J. et al. Observation of tunable band gap and anisotropic Dirac semimetal state in black phosphorus. *Science* **349**, 723–726 (2015).

[CAS](#) [Article](#) [Google Scholar](#)

24. 24.

Baik, S. S., Kim, K. S., Yi, Y. & Choi, H. J. Emergence of two-dimensional massless Dirac fermions, chiral pseudospins, and Berry's phase in potassium doped few-layer black phosphorus. *Nano Lett.* **15**, 7788–7793 (2015).

[ADS](#) [CAS](#) [Article](#) [Google Scholar](#)

25. 25.

Kiraly, B. et al. Anisotropic two-dimensional screening at the surface of black phosphorus. *Phys. Rev. Lett.* **123**, 216403 (2019).

[ADS](#) [CAS](#) [Article](#) [Google Scholar](#)

26. 26.

Tian, Z. et al. Isotropic charge screening of anisotropic black phosphorus revealed by potassium adatoms. *Phys. Rev. B* **100**, 085440 (2019).

[ADS](#) [CAS](#) [Article](#) [Google Scholar](#)

27. 27.

Negulyaev, N. N. et al. Melting of two-dimensional adatom superlattices stabilized by long-range electronic interactions. *Phys. Rev. Lett.* **102**, 246102 (2009).

[ADS](#) [CAS](#) [Article](#) [Google Scholar](#)

28. 28.

Hirata, A. et al. Direct observation of local atomic order in a metallic glass. *Nat. Mater.* **10**, 28–33 (2011).

[ADS](#) [CAS](#) [Article](#) [Google Scholar](#)

29. 29.

Sakurai, J. J. & Napolitano, J. *Modern Quantum Mechanics* (Cambridge Univ. Press, 2017).

30. 30.

Meyer, A., Nestor, C. W. Jr & Young, W. H. Pseudo-atom phase shifts of liquid metals and alloys. *Adv. Phys.* **16**, 581–590 (1967).

[ADS](#) [CAS](#) [Article](#) [Google Scholar](#)

31. 31.

Kang, M. et al. Evolution of charge order topology across a magnetic phase transition in cuprate superconductors. *Nat. Phys.* **15**, 335–340 (2019); correction **15**, 721 (2019).

[ADS](#) [CAS](#) [Article](#) [Google Scholar](#)

32. 32.

Voit, J. et al. Electronic structure of solids with competing periodic potentials. *Science* **290**, 501–503 (2000).

[ADS](#) [CAS](#) [Article](#) [Google Scholar](#)

33. 33.

Park, S. R. et al. Electronic structure of electron-doped $\text{Sm}_{1.86}\text{Ce}_{0.14}\text{CuO}_4$: strong pseudogap effects, nodeless gap, and signatures of short-range order. *Phys. Rev. B* **75**, 060501 (2007).

[ADS](#) [Article](#) [Google Scholar](#)

34. 34.

Lee, W. S. et al. Abrupt onset of a second energy gap at the superconducting transition of underdoped Bi2212. *Nature* **450**, 81–84 (2007).

[ADS](#) [CAS](#) [Article](#) [Google Scholar](#)

35. 35.

Presland, M. R., Tallon, J. L., Buckley, R. G., Liu, R. S. & Flower, N. E. General trends in oxygen stoichiometry effects on T_c in Bi and Tl superconductors. *Physica C* **176**, 95–105 (1991).

[ADS](#) [CAS](#) [Article](#) [Google Scholar](#)

36. 36.

Fischer, Ø., Kugler, M., Maggio-Aprile, I., Berthod, C. & Renner, C. Scanning tunneling spectroscopy of high-temperature superconductors. *Rev. Mod. Phys.* **79**, 353–419 (2007).

[ADS](#) [CAS](#) [Article](#) [Google Scholar](#)

37. 37.

Jung, S. W. et al. Black phosphorus as a bipolar pseudospin semiconductor. *Nat. Mater.* **19**, 277–281 (2020).

[ADS](#) [CAS](#) [Article](#) [Google Scholar](#)

38. 38.

March, N. H. *Liquid Metals* (Cambridge Univ. Press, 1990).

[Download references](#)

Acknowledgements

We thank S.-S. Baik, Y.-W. Son and E.-G. Moon for helpful discussions; and D. Song and C. Kim for providing samples. This work was supported by National Research Foundation (NRF) of Korea (grant numbers NRF-2020R1A2C2102469, NRF-2017R1A5A1014862, NRF-2020K1A3A7A09080364 and NRF-2021R1A3B1077156), and the Yonsei Signature Research Cluster Program of 2021 (2021-22-0004). This research used resources of the Advanced Light Source, which is a DOE Office of Science User Facility under contract number DE-AC02-05CH11231. The part of this work on copper oxides was carried out with the support of the Diamond Light Source (beamline I05).

Author information

Author notes

1. These authors contributed equally: Sae Hee Ryu, Minjae Huh, Do Yun Park

Affiliations

1. Department of Physics, College of Science, Yonsei University, Seoul, Korea

Sae Hee Ryu, Minjae Huh, Do Yun Park & Keun Su Kim

2. Department of Physics, Pohang University of Science and Technology, Pohang, Korea

Minjae Huh

3. Advanced Light Source, E. O. Lawrence Berkeley National Laboratory, Berkeley, CA, USA

Chris Jozwiak, Eli Rotenberg & Aaron Bostwick

Authors

1. Sae Hee Ryu

[View author publications](#)

You can also search for this author in [PubMed](#) [Google Scholar](#)

2. Minjae Huh

[View author publications](#)

You can also search for this author in [PubMed](#) [Google Scholar](#)

3. Do Yun Park

[View author publications](#)

You can also search for this author in [PubMed](#) [Google Scholar](#)

4. Chris Jozwiak

[View author publications](#)

You can also search for this author in [PubMed](#) [Google Scholar](#)

5. Eli Rotenberg

[View author publications](#)

You can also search for this author in [PubMed](#) [Google Scholar](#)

6. Aaron Bostwick

[View author publications](#)

You can also search for this author in [PubMed](#) [Google Scholar](#)

7. Keun Su Kim

[View author publications](#)

You can also search for this author in [PubMed](#) [Google Scholar](#)

Contributions

S.H.R., M.H. and D.Y.P. performed ARPES experiments with help from C.J., E.R. and A.B. S.H.R. and M.H. performed model calculations and simulations with help from D.Y.P. K.S.K. conceived and directed the project. S.H.R., M.H., D.Y.P. and K.S.K wrote the manuscript with contributions from all other co-authors.

Corresponding author

Correspondence to [Keun Su Kim](#).

Ethics declarations

Competing interests

The authors declare no competing interests.

Additional information

Peer review information *Nature* thanks Andrés Santander and the other, anonymous, reviewer(s) for their contribution to the peer review of this work.

Publisher's note Springer Nature remains neutral with regard to jurisdictional claims in published maps and institutional affiliations.

Extended data figures and tables

[Extended Data Fig. 1 Key assumptions in structural simulations.](#)

a–h, Let us consider the long-range order of dopants whose density is $1 \times 10^{14} \text{ cm}^{-2}$ (**a**). If the position of dopants is fully randomized (**b**), no structure is expected in its FFT (**f**). Considering that each dopant is ionized by donating its valence electron, there should be Coulomb repulsion between the ionized dopants, which prevents them from being located close to each other in a certain range corresponding to the radius of hard spheres. If the position of dopants is randomized under this hard-sphere assumption with no further interactions considered (**c**), one can always find the radial structure factor in its FFT (**g**). The radial shape itself in the structure factor reflects the presence of a mean interatomic distance (or short-range order) generic to ionic dopants randomly distributed under the repulsive interaction. This is the structure factor required for the resonance effect in the theory of liquid metals^{1,2,3,4,5,6,7,8,9,10,11,12}, which is clearly distinguished from both crystalline (**a, e**) and fully random (**b, f**) cases. In the case of monovalent dopants on a crystalline insulator, the area of a circle whose radius is half the radial peak is the same as that enclosed by the Fermi surface in any shape due to charge conservation. To account for the isotropic magnitude of a pseudogap over the anisotropic Fermi surface of C1, the anisotropy of the structure factor is additionally considered based on a recent STM study²⁵, where the radial and anisotropic structure factor was found at the density of $1.8 \times 10^{13} \text{ cm}^{-2}$. When the anisotropy factor of 0.42 taken from the anisotropic k_F values in the Fermi surface is applied to the hard-sphere model (**d**), the radial structure factor becomes anisotropic, as seen in **h**.

Extended Data Fig. 2 Momentum distribution curves.

ARPES data of Na-doped black phosphorus taken along k_s (left) and k_x (right) directions (those in Fig. [2e, f](#)). ARPES intensity is plotted as a function of k at the constant energy shown on the vertical axis. Red dots mark the peak position of k distribution curves to show the backward-bending band dispersion.

Extended Data Fig. 3 Constant-energy map of ARPES spectra.

ARPES intensity maps of bulk black phosphorus whose surface is doped by Na at $n_d = 1.7 \times 10^{14} \text{ cm}^{-2}$ (top row) and K at $n_d = 1.0 \times 10^{14} \text{ cm}^{-2}$ (bottom row). Data are plotted at the constant energy marked on top of each panel as a function of k_x and k_y in the surface Brillouin zone of black phosphorus.

Unlike the pair of C2 bands that cross E_F , the C1 band shows a clear signature of a pseudogap with a magnitude of 235 meV for Na and 65 meV for K. This magnitude of the pseudogap is found to be nearly isotropic with in-plane k directions. The size of the area enclosed by the C1 contour of Na decreases towards E_F , which reflects the backward-bending band dispersion.

Extended Data Fig. 4 Dependence of the pseudogap on photon energy and samples.

a, Photon-energy dependence of ARPES data taken from black phosphorus whose surface is doped by K at $n_d = 1.8 \times 10^{14} \text{ cm}^{-2}$. A pseudogap of 30 meV at this n_d is robustly observed for a photon energy of 106–125 eV (red arrow) in contrast to the C2 band that crosses E_F (blue arrow). **b, c**, Sample dependence of ARPES data taken from black phosphorus doped by Na at $n_d = 1.7 \times 10^{14} \text{ cm}^{-2}$ (**b**) and K at $n_d = 1.0 \times 10^{14} \text{ cm}^{-2}$ (**c**). The pseudogap of 235 meV for Na and 65 meV for K is observed without exception for all of the samples.

Extended Data Fig. 5 Model calculation for partial waves at *d*-wave resonance.

A series of U_l , δ_l , $\text{Re}(\Delta k)$ and $\text{Im}(\Delta k)$ is calculated as described in Methods for the partial waves from $l = 0$ (top row) to $l = 3$ (bottom row). The depth of potential V_0 is set to 16.4 eV, which corresponds to *d*-wave resonance at $k_r = 0.36 \text{ \AA}^{-1}$, as shown in Fig. 4a. The *d*-wave resonance can be identified by δ_2 passing through $\pi/2$, which is accompanied by $\text{Re}(\Delta k)$ and $\text{Im}(\Delta k)$ taking the form of $\sin(2\delta_l)/k^2$ and $\sin^2(\delta_l)/k^2$, respectively. For $l = 0$, there is no potential well, in which electron waves can be trapped, and it is impossible to have *s*-wave resonance.

Extended Data Fig. 6 Comparison of Δk at *p*-wave, *d*-wave and *f*-wave resonances.

A series of U_l , δ_l , $\text{Re}(\Delta k)$ and $\text{Im}(\Delta k)$ is calculated for *p*-wave (top row), *d*-wave (middle row) and *f*-wave (bottom row) resonances (Methods). V_0 was set to 7.4 eV for *p*-wave resonance, 16.4 eV for *d*-wave resonance and 27.8 eV for *f*-wave resonance to have the same k_r of 0.36 \AA^{-1} (dotted line in Fig. 4a). The variation of δ_l , $\text{Re}(\Delta k)$ and $\text{Im}(\Delta k)$ is narrower in k or E width for the higher number of l , which accounts for the smaller magnitude of pseudogap in Fig. 5a.

Extended Data Fig. 7 Spectral simulations compared with experimental ARPES data.

The experimental band structure is taken from black phosphorus whose surface is doped by different kinds of alkali metal (Na, K, Rb and Cs), as marked at the bottom right of each panel. This series of ARPES spectra was taken along k_y (left column), k_s (middle column) and k_x (right column). Each dataset is directly compared with corresponding spectral simulations at *p*-wave resonance for Na and *d*-wave resonance for K, Rb and Cs (Methods). The bottom energy of spectral simulations is limited by that of the non-interacting (bare) band, which is the reason that those for Rb and Cs are slightly cut at a binding energy of 0.42–0.45 eV.

Extended Data Fig. 8 Partial-wave analysis with the screened scattering potential.

a, Phase shift δ_l of the partial waves calculated by the screened scattering potential for the liquid phase of Cs ions, which clearly shows *d*-wave resonance⁹. The dotted line is a fit with that calculated by the spherical step potential at $V_0 = 12.96$ eV and $r_s = 2.1 \text{ \AA}$. **b**, Phase shift δ_l of partial waves calculated by the screened scattering potential of Na, K, Rb and Cs ions³⁰. K, Rb and Cs ions favour *d*-wave resonance, whereas the Na ions favour *p*-wave resonance, which is exactly as observed in our experiments. Our

results reproduce other details as well. (1) δ_l crosses $\pi/2$ clearly for K, Rb and Cs ions, whereas that for Na ions is relatively incomplete. (2) The δ_l values of K and Rb ions are nearly the same. (3) The abruptness of δ_l , which is related to the magnitude of the pseudogap, increases in the order of Na → K/Rb → Cs.

Extended Data Fig. 9 Evolution of pseudogap with surface doping.

A doping series of APRES data are taken from black phosphorus whose surface is doped by Na, K, Rb and Cs, marked at the bottom right of each panel. Shown together in number is the dopant density n_d in units of 10^{14} cm^{-2} . It can be clearly seen that the magnitude of the pseudogap progressively decreases to zero with increasing n_d , as summarized in the phase diagram (Fig. 5b). The hole-like states developing inside of the C1 band (pronounced for Na at $n_d = 3.3 \times 10^{14} \text{ cm}^{-2}$) are the valence band of black phosphorus²³. The additional feature near E_F and at the Γ point (pronounced for K at $n_d = 2.9 \times 10^{14} \text{ cm}^{-2}$) is another conduction band of black phosphorus reproduced in first-principles band calculations²⁴.

Extended Data Fig. 10 Resonance effect for the waterfall dispersion in copper oxides.

a, ARPES data taken from $\text{Bi}_{1.5}\text{Pb}_{0.5}\text{Sr}_2\text{CaCu}_2\text{O}_{8+\delta}$ ($T_c = 88 \text{ K}$) along the nodal direction with a photon energy of 98 eV. n_d is estimated from T_c (88 K)³⁵, pseudogap (32 meV)³⁶ and Luttinger count to be 1.2×10^{14} – $1.4 \times 10^{14} \text{ cm}^{-2}$, corresponding to $k_r = 0.29 \pm 0.01 \text{ \AA}^{-1}$. **b**, Spectral simulations for resonance scattering at $k_r = 0.29 \text{ \AA}^{-1}$ (Methods). The grey curve represents the bare band. The waterfall dispersion in **a** is reproduced remarkably well by our spectral simulations in **b**.

Source data

[**Source Data Fig. 2**](#)

[**Source Data Fig. 4**](#)

[**Source Data Fig. 5**](#)

Rights and permissions

[Reprints and Permissions](#)

About this article



Check for
updates

Cite this article

Ryu, S.H., Huh, M., Park, D.Y. *et al.* Pseudogap in a crystalline insulator doped by disordered metals. *Nature* **596**, 68–73 (2021).
<https://doi.org/10.1038/s41586-021-03683-0>

[Download citation](#)

- Received: 09 September 2020
- Accepted: 28 May 2021
- Published: 04 August 2021
- Issue Date: 05 August 2021
- DOI: <https://doi.org/10.1038/s41586-021-03683-0>

Comments

By submitting a comment you agree to abide by our [Terms](#) and [Community Guidelines](#). If you find something abusive or that does not comply with our terms or guidelines please flag it as inappropriate.

[Access through your institution](#)

[Change institution](#)

[Buy or subscribe](#)

Advertisement

This article was downloaded by **calibre** from <https://www.nature.com/articles/s41586-021-03683-0>

| [Section menu](#) | [Main menu](#) |

- Article
- [Published: 22 June 2021](#)

Aziridine synthesis by coupling amines and alkenes via an electrogenerated dication

- [Dylan E. Holst](#) ORCID: [orcid.org/0000-0001-5218-6642¹](https://orcid.org/0000-0001-5218-6642)
- [Diana J. Wang](#) ORCID: [orcid.org/0000-0003-3790-0240¹](https://orcid.org/0000-0003-3790-0240)
- [Min Ji Kim](#) ORCID: [orcid.org/0000-0002-0542-3577¹](https://orcid.org/0000-0002-0542-3577)
- [Ilia A. Guzei¹](#) &
- [Zachary K. Wickens](#) ORCID: [orcid.org/0000-0002-5733-5288¹](https://orcid.org/0000-0002-5733-5288)

Nature volume **596**, pages 74–79 (2021) [Cite this article](#)

- 10k Accesses
- 134 Altmetric
- [Metrics details](#)

Subjects

- [Synthetic chemistry methodology](#)
- [Reaction mechanisms](#)

Abstract

Aziridines—three-membered nitrogen-containing cyclic molecules—are important synthetic targets. Their substantial ring strain and resultant proclivity towards ring-opening reactions makes them versatile precursors

of diverse amine products^{1,2,3}, and, in some cases, the aziridine functional group itself imbues important biological (for example, anti-tumour) activity^{4,5,6}. Transformation of ubiquitous alkenes into aziridines is an attractive synthetic strategy, but is typically accomplished using electrophilic nitrogen sources rather than widely available amine nucleophiles. Here we show that unactivated alkenes can be electrochemically transformed into a metastable, dicationic intermediate that undergoes aziridination with primary amines under basic conditions. This new approach expands the scope of readily accessible *N*-alkyl aziridine products relative to those obtained through existing state-of-the-art methods. A key strategic advantage of this approach is that oxidative alkene activation is decoupled from the aziridination step, enabling a wide range of commercially available but oxidatively sensitive⁷ amines to act as coupling partners for this strain-inducing transformation. More broadly, our work lays the foundations for a diverse array of difunctionalization reactions using this dication pool approach.

Access options

Subscribe to Journal

Get full journal access for 1 year

\$199.00

only \$3.90 per issue

[Subscribe](#)

All prices are NET prices.

VAT will be added later in the checkout.

Tax calculation will be finalised during checkout.

Rent or Buy article

Get time limited or full article access on ReadCube.

from \$8.99

[Rent or Buy](#)

All prices are NET prices.

Additional access options:

- [Log in](#)
- [Access through your institution](#)
- [Learn about institutional subscriptions](#)

Fig. 1: Development of an oxidative coupling strategy for aziridine synthesis.

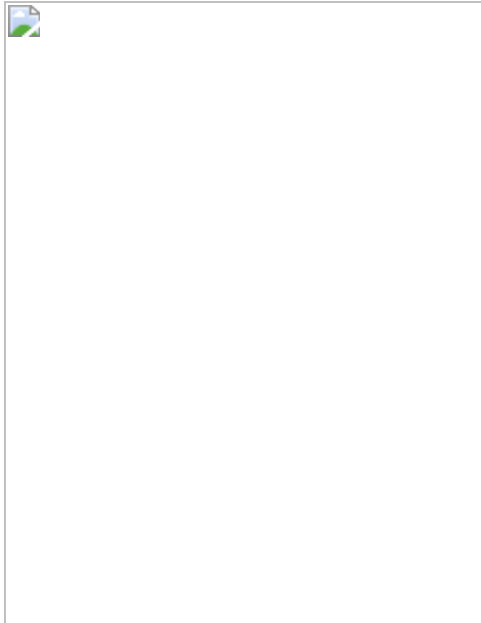


Fig. 2: Scope of the aziridination reaction.

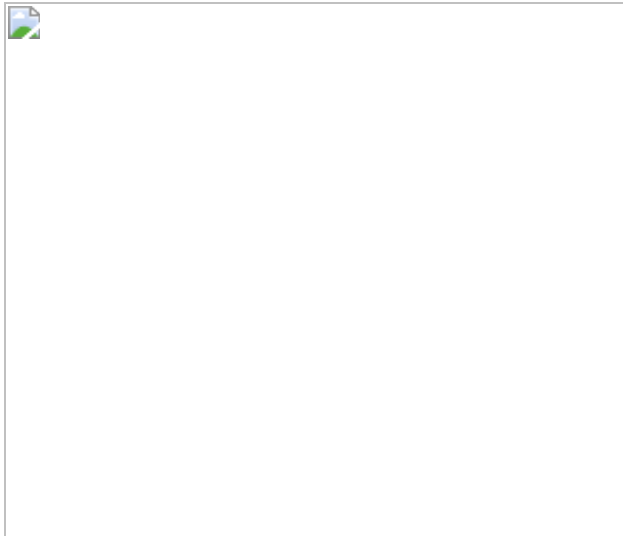


Fig. 3: Synthetic applications of the dication pool strategy.

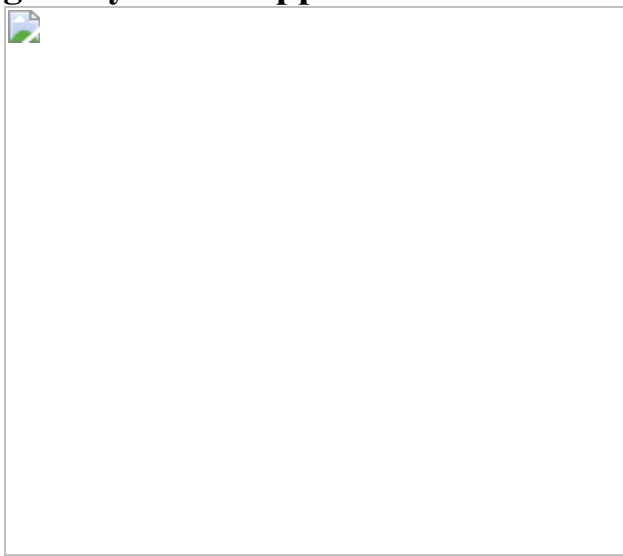


Fig. 4: Mechanistic insight into adduct formation.

Data availability

Crystallographic data for compounds **1** and **2** can be obtained free of charge from the Cambridge Crystallographic Data Centre (<https://www.ccdc.cam.ac.uk>). All data supporting the findings of this paper are available within the paper and its Supplementary Information.

References

1. 1.

Sweeney, J. B. Aziridines: epoxides' ugly cousins? *Chem. Soc. Rev.* **31**, 247–258 (2002).

[CAS](#) [PubMed](#) [Article](#) [Google Scholar](#)

2. 2.

Stanković, S. et al. Regioselectivity in the ring opening of non-activated aziridines. *Chem. Soc. Rev.* **41**, 643–665 (2012).

[PubMed](#) [Article](#) [Google Scholar](#)

3. 3.

Botuha, C., Chemla, F., Ferreira, F. & Pérez-Luna, A. in *Heterocycles in Natural Product Synthesis* 1–39 (John Wiley, 2011).

4. 4.

Ismail, F. M. D., Levitsky, D. O. & Dembitsky, V. M. Aziridine alkaloids as potential therapeutic agents. *Eur. J. Med. Chem.* **44**, 3373–3387 (2009).

[CAS](#) [PubMed](#) [Article](#) [Google Scholar](#)

5. 5.

Thibodeaux, C. J., Chang, W. & Liu, H. Enzymatic chemistry of cyclopropane, epoxide, and aziridine biosynthesis. *Chem. Rev.* **112**,

1681–1709 (2012).

[CAS](#) [PubMed](#) [Article](#) [Google Scholar](#)

6. 6.

Lowden, P. A. S. in *Aziridines and Epoxides in Organic Synthesis* 399–442 (John Wiley, 2006).

7. 7.

Roth, H. G., Romero, N. A. & Nicewicz, D. A. Experimental and calculated electrochemical potentials of common organic molecules for applications to single-electron redox chemistry. *Synlett* **27**, 714–723 (2016).

[CAS](#) [Google Scholar](#)

8. 8.

Evans, D. A., Faul, M. M. & Bilodeau, M. T. Copper-catalyzed aziridination of olefins by (N-(*p*-toluenesulfonyl)imino)phenyliodinane. *J. Org. Chem.* **56**, 6744–6746 (1991).

[CAS](#) [Article](#) [Google Scholar](#)

9. 9.

Sweeney, J. B. in *Aziridines and Epoxides in Organic Synthesis* 117–144 (John Wiley, 2006).

10. 10.

Osborn, H. M. I. & Sweeney, J. The asymmetric synthesis of aziridines. *Tetrahedron Asymmetry* **8**, 1693–1715 (1997).

[CAS](#) [Article](#) [Google Scholar](#)

11. 11.

Wang, H., Yang, J. C. & Buchwald, S. L. CuH-catalyzed regioselective intramolecular hydroamination for the synthesis of alkyl-substituted chiral aziridines. *J. Am. Chem. Soc.* **139**, 8428–8431 (2017).

[CAS](#) [PubMed](#) [PubMed Central](#) [Article](#) [Google Scholar](#)

12. 12.

Legnani, L., Prina-Cerai, G., Delcaillau, T., Willems, S. & Morandi, B. Efficient access to unprotected primary amines by iron-catalyzed aminochlorination of alkenes. *Science* **362**, 434–439 (2018).

[CAS](#) [PubMed](#) [Article](#) [ADS](#) [Google Scholar](#)

13. 13.

Jat, J. L. et al. Direct stereospecific synthesis of unprotected N–H and N–Me aziridines from olefins. *Science* **343**, 61–65 (2014).

[CAS](#) [PubMed](#) [PubMed Central](#) [Article](#) [ADS](#) [Google Scholar](#)

14. 14.

Ma, Z., Zhou, Z. & Kürti, L. Direct and stereospecific synthesis of N–H and N–alkyl aziridines from unactivated olefins using hydroxylamine-O-sulfonic acids. *Angew. Chem. Int. Edn* **56**, 9886–9890 (2017).

[CAS](#) [Article](#) [Google Scholar](#)

15. 15.

Cheng, Q.-Q. et al. Organocatalytic nitrogen transfer to unactivated olefins via transient oxaziridines. *Nat. Catal.* **3**, 386–392 (2020).

[CAS](#) [Article](#) [Google Scholar](#)

16. 16.

Falk, E., Makai, S., Delcaillau, T., Görtler, L. & Morandi, B. Design and scalable synthesis of N-alkylhydroxylamine reagents for the direct iron-catalyzed installation of medicinally relevant amines. *Angew. Chem. Int. Edn* **59**, 21064–21071 (2020).

[CAS](#) [Article](#) [Google Scholar](#)

17. 17.

Munnuri, S., Anugu, R. R. & Falck, J. R. Cu(II)-mediated N–H and N-alkyl aryl amination and olefin aziridination. *Org. Lett.* **21**, 1926–1929 (2019).

[CAS](#) [PubMed](#) [Article](#) [Google Scholar](#)

18. 18.

Govaerts, S. et al. Photoinduced olefin diamination with alkylamines. *Angew. Chem. Int. Edn* **59**, 15021–15028 (2020).

[CAS](#) [Article](#) [Google Scholar](#)

19. 19.

eMolecules (eMolecules Inc, accessed 20 January 2021);
<https://www.emolecules.com>

20. 20.

Lohray, B. B., Gao, Y. & Sharpless, K. B. One pot synthesis of homochiral aziridines and aminoalcohols from homochiral 1,2-cyclic sulfates. *Tetrahedr. Lett.* **30**, 2623–2626 (1989).

[CAS](#) [Article](#) [Google Scholar](#)

21. 21.

Wenker, H. The preparation of ethylene imine from monoethanolamine. *J. Am. Chem. Soc.* **57**, 2328 (1935).

[CAS](#) [Article](#) [Google Scholar](#)

22. 22.

Li, X., Chen, N. & Xu, J. An improved and mild Wenker synthesis of aziridines. *Synthesis* **20**, 3423–3428 (2010).

[Google Scholar](#)

23. 23.

Yan, M., Kawamata, Y. & Baran, P. S. Synthetic organic electrochemical methods since 2000: on the verge of a renaissance. *Chem. Rev.* **117**, 13230–13319 (2017).

[CAS](#) [PubMed](#) [PubMed Central](#) [Article](#) [Google Scholar](#)

24. 24.

Wiebe, A. et al. Electrifying organic synthesis. *Angew. Chem. Int. Edn* **57**, 5594–5619 (2018).

[CAS](#) [Article](#) [Google Scholar](#)

25. 25.

Francke, R. & Little, R. D. Redox catalysis in organic electrosynthesis: basic principles and recent developments. *Chem. Soc. Rev.* **43**, 2492–2521 (2014).

[CAS](#) [PubMed](#) [Article](#) [Google Scholar](#)

26. 26.

Moeller, K. D. Using physical organic chemistry to shape the course of electrochemical reactions. *Chem. Rev.* **118**, 4817–4833 (2018).

[CAS](#) [PubMed](#) [Article](#) [Google Scholar](#)

27. 27.

Yoshida, J., Kataoka, K., Horcajada, R. & Nagaki, A. Modern strategies in electroorganic synthesis. *Chem. Rev.* **108**, 2265–2299 (2008).

[CAS](#) [PubMed](#) [Article](#) [Google Scholar](#)

28. 28.

Sauer, G. S. & Lin, S. An electrocatalytic approach to the radical difunctionalization of alkenes. *ACS Catal.* **8**, 5175–5187 (2018).

[CAS](#) [Article](#) [Google Scholar](#)

29. 29.

Doobary, S., Sedikides, A. T., Caldora, H. P., Poole, D. L. & Lennox, A. J. J. Electrochemical vicinal difluorination of alkenes: scalable and amenable to electron-rich substrates. *Angew. Chem. Int. Edn* **59**, 1155–1160 (2020).

[CAS](#) [Article](#) [Google Scholar](#)

30. 30.

Siu, T. & Yudin, A. K. Practical olefin aziridination with a broad substrate scope. *J. Am. Chem. Soc.* **124**, 530–531 (2002).

[CAS](#) [PubMed](#) [Article](#) [Google Scholar](#)

31. 31.

Oseka, M. et al. Electrochemical aziridination of internal alkenes with primary amines. *Chem* **7**, 255–266 (2021).

[CAS](#) [Article](#) [Google Scholar](#)

32. 32.

Chen, J. et al. Electrocatalytic aziridination of alkenes mediated by n-Bu₄NI: a radical pathway. *Org. Lett.* **17**, 986–989 (2015).

[CAS](#) [PubMed](#) [Article](#) [Google Scholar](#)

33. 33.

Li, J. et al. Electrochemical aziridination by alkene activation using a sulfamate as the nitrogen source. *Angew. Chem. Int. Edn* **57**, 5695–5698 (2018).

[CAS](#) [Article](#) [Google Scholar](#)

34. 34.

Yoshida, J., Shimizu, A. & Hayashi, R. Electrogenerated cationic reactive intermediates: the pool method and further advances. *Chem. Rev.* **118**, 4702–4730 (2018).

[CAS](#) [PubMed](#) [Article](#) [Google Scholar](#)

35. 35.

Hayashi, R., Shimizu, A. & Yoshida, J. The stabilized cation pool method: metal- and oxidant-free benzylic C–H/aromatic C–H cross-coupling. *J. Am. Chem. Soc.* **138**, 8400–8403 (2016).

[CAS](#) [PubMed](#) [Article](#) [Google Scholar](#)

36. 36.

Shine, H. J., Bandlish, B. K., Mani, S. R. & Padilla, A. G. Ion radicals. 43. Addition of thianthrene and phenoxathiin cation radicals to alkenes and alkynes. *J. Org. Chem.* **44**, 915–917 (1979).

[CAS](#) [Article](#) [Google Scholar](#)

37. 37.

Shine, H. J. et al. Adducts of phenoxathiin and thianthrene cation radicals with alkenes and cycloalkenes. *J. Org. Chem.* **68**, 8910–8917 (2003).

[CAS](#) [PubMed](#) [Article](#) [Google Scholar](#)

38. 38.

Rangappa, P. & Shine, H. J. An overview of some reactions of thianthrene cation radical. Products and mechanisms of their formation. *J. Sulfur Chem.* **27**, 617–664 (2006).

[CAS](#) [Article](#) [Google Scholar](#)

39. 39.

Berger, F. et al. Site-selective and versatile aromatic C–H functionalization by thianthrenation. *Nature* **567**, 223–228 (2019).

[CAS](#) [PubMed](#) [Article](#) [ADS](#) [Google Scholar](#)

40. 40.

Engl, P. S. et al. C–N cross-couplings for site-selective late-stage diversification via aryl sulfonium salts. *J. Am. Chem. Soc.* **141**, 13346–13351 (2019).

[CAS](#) [PubMed](#) [Article](#) [Google Scholar](#)

41. 41.

Chen, J., Li, J., Plutschack, M. B., Berger, F. & Ritter, T. Regio- and stereoselective thianthrenation of olefins to access versatile alkenyl electrophiles. *Angew. Chem. Int. Edn* **59**, 5616–5620 (2020).

[CAS](#) [Article](#) [Google Scholar](#)

42. 42.

Houmam, A., Shukla, D., Kraatz, H.-B. & Wayner, D. D. M. Electrosynthesis of mono- and bisthianthrenium salts. *J. Org. Chem.* **64**, 3342–3345 (1999).

[CAS](#) [PubMed](#) [Article](#) [Google Scholar](#)

43. 43.

Iwai, K. & Shine, H. J. Ion radicals. 46. Reactions of the adducts of thianthrene and phenoxathiin cation radicals and cyclohexene with nucleophiles. *J. Org. Chem.* **46**, 271–276 (1981).

[CAS](#) [Article](#) [Google Scholar](#)

44. 44.

Mitchell, S. C. & Waring, R. H. Fate of thianthrene in biological systems. *Xenobiotica* **47**, 731–740 (2017).

[CAS](#) [PubMed](#) [Article](#) [Google Scholar](#)

45. 45.

Kaiser, D., Klose, I., Oost, R., Neuhaus, J. & Maulide, N. Bond-forming and -breaking reactions at sulfur(IV): sulfoxides, sulfonium salts, sulfur ylides, and sulfinate salts. *Chem. Rev.* **119**, 8701–8780 (2019).

[CAS](#) [PubMed](#) [PubMed Central](#) [Article](#) [Google Scholar](#)

46. 46.

Bright, G. M., Brodney, M. A. & Wlodecki, B. Pyridyloxymethyl and benzisoxazole azabicyclic derivatives. International patent WO/2004/081007 (2004).

47. 47.

Qian, D.-Q., Shine, H. J., Guzman-Jimenez, I. Y., Thurston, J. H. & Whitmire, K. H. Mono- and bisadducts from the addition of thianthrene cation radical salts to cycloalkenes and alkenes. *J. Org. Chem.* **67**, 4030–4039 (2002).

[CAS](#) [PubMed](#) [Article](#) [Google Scholar](#)

48. 48.

Speer, M. E. et al. Thianthrene-functionalized polynorbornenes as high-voltage materials for organic cathode-based dual-ion batteries. *Chem. Commun.* **51**, 15261–15264 (2015).

[CAS](#) [Article](#) [Google Scholar](#)

49. 49.

Murata, Y. & Shine, H. J. Ion radicals. XVIII. Reactions of thianthrenium perchlorate and thianthrenium trichlorodiiodide. *J. Org. Chem.* **34**, 3368–3372 (1969).

[CAS](#) [Article](#) [Google Scholar](#)

50. 50.

Sandford, C. et al. A synthetic chemist's guide to electroanalytical tools for studying reaction mechanisms. *Chem. Sci.* **10**, 6404–6422 (2019).

[CAS](#) [PubMed](#) [PubMed Central](#) [Article](#) [Google Scholar](#)

[Download references](#)

Acknowledgements

We thank A. Wendlandt, M. Levin and D. Weix for suggestions and manuscript proofreading. We also acknowledge A. Hoque and F. Wang in the Stahl laboratory for the use of, and technical assistance with, the

electrochemical flow reactor. Additionally, we thank the Weix, Stahl, Yoon and Schomaker groups for sharing their chemical inventories. B. J. Thompson is acknowledged for his assistance with the design and fabrication of the power supply. T. Drier is acknowledged for the fabrication of electrochemical glassware. A. M. Wheaton is acknowledged for assistance with crystallographic studies. We also acknowledge support and suggestions from all members of the Wickens group throughout the investigation of this project. This work was supported financially by the Office of the Vice Chancellor for Research and Graduate Education at the University of Wisconsin–Madison, with funding from the Wisconsin Alumni Research Foundation. Spectroscopic instrumentation was supported by a gift from P. J. and M. M. Bender, by National Science Foundation (NSF) grant CHE-1048642, and by National Institutes of Health (NIH) grants 1S10OD020022-1 and S10 OD01225. This study also made use of the National Magnetic Resonance Facility at Madison, which is supported by NIH grants P41GM136463 (old number P41GM103399 (NIGMS)) and P41RR002301. Equipment was purchased with funds from the University of Wisconsin–Madison, the NIH (grants P41GM103399, S10RR02781, S10RR08438, S10RR023438, S10RR025062 and S10RR029220), the NSF (DMB-8415048, OIA-9977486 and BIR-9214394), and the US Department of Agriculture (USDA). The Bruker D8 VENTURE Photon III X-ray diffractometer was partially funded by NSF award CHE-1919350 to the University of Wisconsin–Madison Department of Chemistry.

Author information

Author notes

1. These authors contributed equally: Dylan E. Holst, Diana J. Wang

Affiliations

1. Department of Chemistry, University of Wisconsin–Madison, Madison, WI, USA

Dylan E. Holst, Diana J. Wang, Min Ji Kim, Ilia A. Guzei & Zachary K. Wickens

Authors

1. Dylan E. Holst

[View author publications](#)

You can also search for this author in [PubMed](#) [Google Scholar](#)

2. Diana J. Wang

[View author publications](#)

You can also search for this author in [PubMed](#) [Google Scholar](#)

3. Min Ji Kim

[View author publications](#)

You can also search for this author in [PubMed](#) [Google Scholar](#)

4. Ilia A. Guzei

[View author publications](#)

You can also search for this author in [PubMed](#) [Google Scholar](#)

5. Zachary K. Wickens

[View author publications](#)

You can also search for this author in [PubMed](#) [Google Scholar](#)

Contributions

Z.K.W., D.E.H. and D.J.W. designed the project. D.E.H., D.J.W. and M.J.K. performed the experiments and collected the data. I.A.G. collected and analysed X-ray data to provide crystal structures. Z.K.W., D.E.H., D.J.W. and M.J.K. analysed the data and contributed to writing the manuscript. D.E.H. and D.J.W. contributed equally.

Corresponding author

Correspondence to [Zachary K. Wickens](#).

Ethics declarations

Competing interests

The authors declare no competing interests.

Additional information

Peer review information *Nature* thanks Louis-Charles Campeau and David Hickey for their contribution to the peer review of this work. Peer reviewer reports are available.

Publisher's note Springer Nature remains neutral with regard to jurisdictional claims in published maps and institutional affiliations.

Supplementary information

Supplementary Information

The file contains the following sections: 1. General Methods and Materials; 2. Supplementary Data; 3. Mechanistic Investigations; 4. Substrate preparation; 5. General Experimental Procedures; 6. Aziridine Product Isolation and Characterization; 7. Scale-Up Flow Electrolysis Set-Up and Procedure; 8. Aziridine Derivatization Reaction Isolation and Characterization; 9. X-Ray Diffraction Data; 10. References; and 11. NMR Spectra.

Peer Review File

Rights and permissions

Reprints and Permissions

About this article



Cite this article

Holst, D.E., Wang, D.J., Kim, M.J. *et al.* Aziridine synthesis by coupling amines and alkenes via an electrogenerated dication. *Nature* **596**, 74–79 (2021). <https://doi.org/10.1038/s41586-021-03717-7>

[Download citation](#)

- Received: 26 January 2021
- Accepted: 11 June 2021
- Published: 22 June 2021
- Issue Date: 05 August 2021
- DOI: <https://doi.org/10.1038/s41586-021-03717-7>

Comments

By submitting a comment you agree to abide by our [Terms](#) and [Community Guidelines](#). If you find something abusive or that does not comply with our terms or guidelines please flag it as inappropriate.

[Access through your institution](#)

[Change institution](#)

[Buy or subscribe](#)

Associated Content

Collection

Synthesis and enabling technologies

Advertisement

This article was downloaded by **calibre** from <https://www.nature.com/articles/s41586-021-03717-7>

| [Section menu](#) | [Main menu](#) |

- Article
- [Published: 04 August 2021](#)

Satellite imaging reveals increased proportion of population exposed to floods

- [B. Tellman](#) [ORCID: orcid.org/0000-0003-3026-6435^{1,2,3}](#) [na1](#),
- [J. A. Sullivan](#) [ORCID: orcid.org/0000-0001-7414-6094^{2,3,4}](#) [na1](#),
- [C. Kuhn](#) [ORCID: orcid.org/0000-0002-9220-630X⁵](#),
- [A. J. Kettner⁶](#),
- [C. S. Doyle](#) [ORCID: orcid.org/0000-0001-6226-2338^{2,7}](#),
- [G. R. Brakenridge](#) [ORCID: orcid.org/0000-0002-3217-4852⁶](#),
- [T. A. Erickson](#) [ORCID: orcid.org/0000-0002-3597-1929⁸](#) &
- [D. A. Slayback](#) [ORCID: orcid.org/0000-0002-4291-843X⁹](#)

[Nature](#) volume 596, pages 80–86 (2021) [Cite this article](#)

- 2978 Accesses
- 1852 Altmetric
- [Metrics details](#)

Subjects

- [Geography](#)
- [Hydrology](#)
- [Natural hazards](#)

Abstract

Flooding affects more people than any other environmental hazard and hinders sustainable development^{1,2}. Investing in flood adaptation strategies may reduce the loss of life and livelihood caused by floods³. Where and how floods occur and who is exposed are changing as a result of rapid urbanization⁴, flood mitigation infrastructure⁵ and increasing settlements in floodplains⁶. Previous estimates of the global flood-exposed population have been limited by a lack of observational data, relying instead on models, which have high uncertainty^{3,7,8,9,10,11}. Here we use daily satellite imagery at 250-metre resolution to estimate flood extent and population exposure for 913 large flood events from 2000 to 2018. We determine a total inundation area of 2.23 million square kilometres, with 255–290 million people directly affected by floods. We estimate that the total population in locations with satellite-observed inundation grew by 58–86 million from 2000 to 2015. This represents an increase of 20 to 24 per cent in the proportion of the global population exposed to floods, ten times higher than previous estimates⁷. Climate change projections for 2030 indicate that the proportion of the population exposed to floods will increase further. The high spatial and temporal resolution of the satellite observations will improve our understanding of where floods are changing and how best to adapt. The global flood database generated from these observations will help to improve vulnerability assessments, the accuracy of global and local flood models, the efficacy of adaptation interventions and our understanding of the interactions between landcover change, climate and floods.

Access options

Subscribe to Journal

Get full journal access for 1 year

\$199.00

only \$3.90 per issue

[Subscribe](#)

All prices are NET prices.
VAT will be added later in the checkout.
Tax calculation will be finalised during checkout.

Rent or Buy article

Get time limited or full article access on ReadCube.

from \$8.99

[Rent or Buy](#)

All prices are NET prices.

Additional access options:

- [Log in](#)
- [Access through your institution](#)
- [Learn about institutional subscriptions](#)

Fig. 1: Summary statistics of the Global Flood Database.

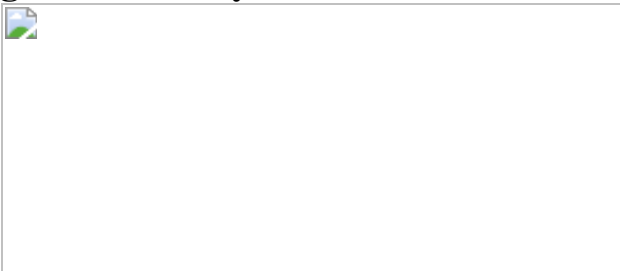


Fig. 2: Observed inundation and flood duration for selected extreme events.

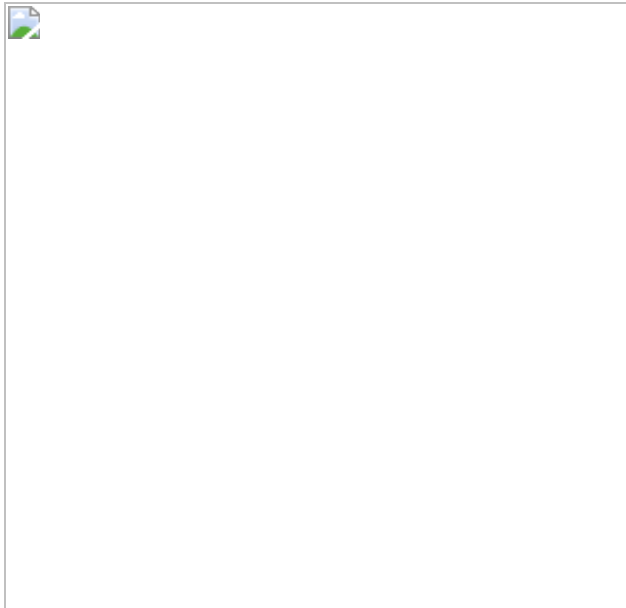


Fig. 3: Population dynamics per pixel (250-m resolution) in observed inundated areas, 2000–2018.

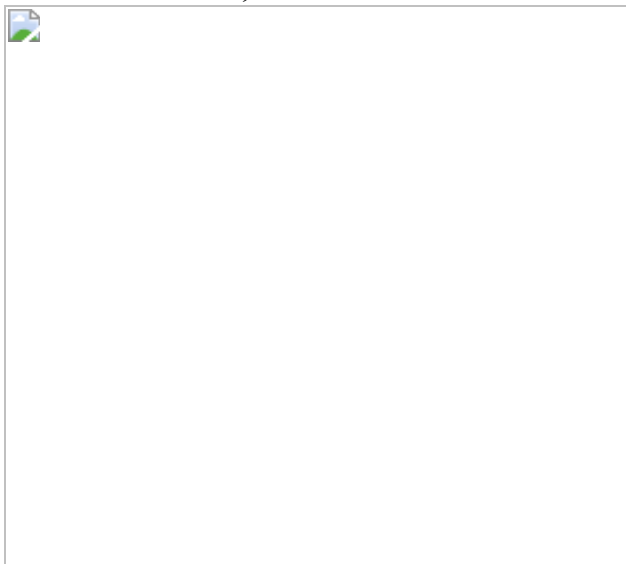
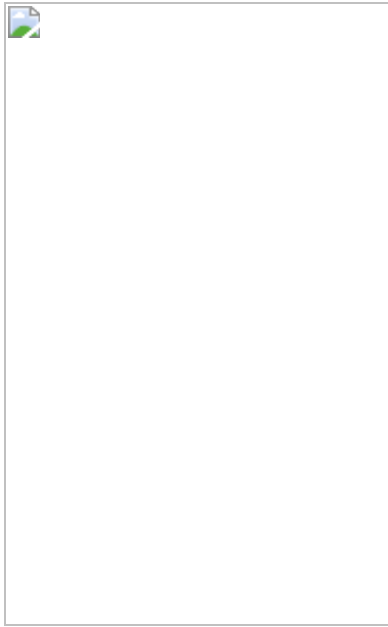


Fig. 4: Change in the proportion of the population exposed to floods observed from 2000 to 2015 and predicted for 2030 per country.



Data availability

The MODIS Collection 6 datasets analysed here are available in the NASA LP DAAC at the USGS EROS Center

(<https://lpdaac.usgs.gov/products/mod09gav006/>,
<https://lpdaac.usgs.gov/products/mod09gqv006/>) and are mirrored in the Google Earth Engine data catalogue (https://developers.google.com/earth-engine/datasets/catalog/MODIS_006_MOD09GA,
https://developers.google.com/earth-engine/datasets/catalog/MODIS_006_MYD09GQ). The MODIS NRT Global Flood Product is available in the NASA LANCE Near Real-Time Data and Imagery service (<https://earthdata.nasa.gov/earth-observation-data/near-real-time/mcdwd-nrt>). The Landsat 5 TM, 7 ETM and 8 OLI surface reflectance products used for the accuracy assessment are available from USGS (<https://earthexplorer.usgs.gov/>) and are mirrored in the Google Earth Engine data catalogue (https://developers.google.com/earth-engine/datasets/catalog/LANDSAT_LT05_C01_T1_SR,
https://developers.google.com/earth-engine/datasets/catalog/LANDSAT_LE07_C01_T1_SR,
https://developers.google.com/earth-engine/datasets/catalog/LANDSAT_LC08_C01_T1_SR) The datasets generated for this study from the Global Flood Database are available on

the Cloud to Street website (<http://global-flood-database.cloudtostreet.ai>) and are mirrored in Google Earth Engine (https://developers.google.com/earth-engine/datasets/catalog/GLOBAL_FLOOD_DB_MODIS_EVENTS_V1). Supplementary Tables provide summary estimates for each event, and all data may be downloaded from <http://global-flood-database.cloudtostreet.ai/>. Source data are provided with this paper.

Code availability

Google Earth Engine's web interface allows the flood mapping algorithm defined in equations (1) and (2) to be applied on any MODIS images. Code to make all figures and flood maps are publicly available at https://github.com/cloudtostreet/MODIS_GlobalFloodDatabase.

References

1. 1.
Hallegatte, S., Vogt-Schilb, A., Bangalore, M. & Rozenberg, J. *Unbreakable: Building the Resilience of the Poor in the Face of Natural Disasters* Ch. 3, 63–77 (The World Bank, 2016).
2. 2.
CRED, UNDRR. *Human Cost of Disasters. An Overview of the last 20 years: 2000–2019*. <https://reliefweb.int/report/world/human-cost-disasters-overview-last-20-years-2000-2019> (UNDRR, 2020).
3. 3.
Jongman, B. et al. Declining vulnerability to river floods and the global benefits of adaptation. *Proc. Natl Acad. Sci. USA* **112**, E2271–E2280 (2015).

4. 4.

Liu, X. et al. High-spatiotemporal-resolution mapping of global urban change from 1985 to 2015. *Nat. Sustain.* **3**, 564–570 (2020).

[Article](#) [Google Scholar](#)

5. 5.

Grill, G. et al. Mapping the world's free-flowing rivers. *Nature* **569**, 215–221 (2019); author correction **572**, E9 (2019).

[CAS](#) [PubMed](#) [Article](#) [ADS](#) [Google Scholar](#)

6. 6.

Ceola, S., Laio, F. & Montanari, A. Satellite nighttime lights reveal increasing human exposure to floods worldwide. *Geophys. Res. Lett.* **41**, 7184–7190 (2014).

[Article](#) [ADS](#) [Google Scholar](#)

7. 7.

Jongman, B., Ward, P. J. & Aerts, J. C. J. H. Global exposure to river and coastal flooding: long term trends and changes. *Glob. Environ. Change* **22**, 823–835 (2012).

[Article](#) [Google Scholar](#)

8. 8.

Winsemius, H. C. et al. Global drivers of future river flood risk. *Nat. Clim. Chang.* **6**, 381–385 (2016).

[Article](#) [ADS](#) [Google Scholar](#)

9. 9.

Trigg, M. A. et al. The credibility challenge for global fluvial flood risk analysis. *Environ. Res. Lett.* **11**, 094014 (2016); corrigendum **13**, 099503 (2018).

[Article](#) [ADS](#) [Google Scholar](#)

10. 10.

Tanoue, M., Hirabayashi, Y. & Ikeuchi, H. Global-scale river flood vulnerability in the last 50 years. *Sci. Rep.* **6**, 36021 (2016).

[CAS](#) [PubMed](#) [PubMed Central](#) [Article](#) [ADS](#) [Google Scholar](#)

11. 11.

Formetta, G. & Feyen, L. Empirical evidence of declining global vulnerability to climate-related hazards. *Glob. Environ. Change* **57**, 101920 (2019).

[PubMed](#) [PubMed Central](#) [Article](#) [Google Scholar](#)

12. 12.

Hoegh-Guldberg, O. et al. in *Global Warming of 1.5 °C. An IPCC Special Report on the Impacts of Global Warming of 1.5 °C Above Pre-industrial Levels and Related Global Greenhouse Gas Emission Pathways, in the Context of Strengthening the Global Response to the Threat of Climate Change, Sustainable Development, and Efforts to Eradicate Poverty* (eds Masson-Delmotte, V. et al.) Ch. 3 (IPCC, 2018).

13. 13.

Alfieri, L. et al. Global projections of river flood risk in a warmer world. *Earth's Futur.* **5**, 171–182 (2017).

[Article](#) [ADS](#) [Google Scholar](#)

14. 14.

Najibi, N. & Devineni, N. Recent trends in the frequency and duration of global floods. *Earth Syst. Dyn.* **9**, 757–783 (2018).

[Article](#) [ADS](#) [Google Scholar](#)

15. 15.

Ward, P. J. et al. A global framework for future costs and benefits of river-flood protection in urban areas. *Nat. Clim. Chang.* **7**, 642–646 (2017).

[Article](#) [ADS](#) [Google Scholar](#)

16. 16.

Kellet, J. & Caravani, A. *Financing Disaster Risk Reduction: A 20 Year Story of International Aid* 60 (GFDRR, ODI, 2013).

17. 17.

IPCC. *Climate Change 2014: Impacts, Adaptation and Vulnerability. Part A: Global and Sectoral Aspects. Contribution of Working Group II to the Fifth Assessment Report of the Intergovernmental Panel on Climate Change* (eds Field, C. B. et al.) (Cambridge Univ. Press, 2014).

18. 18.

Turner, B. L. et al. A framework for vulnerability analysis in sustainability science. *Proc. Natl Acad. Sci. USA* **100**, 8074–8079 (2003).

[CAS](#) [PubMed](#) [PubMed Central](#) [Article](#) [ADS](#) [Google Scholar](#)

19. 19.

Sampson, C. C. et al. A high-resolution global flood hazard model. *Wat. Resour. Res.* **51**, 7358–7381 (2015).

[Article](#) [ADS](#) [Google Scholar](#)

20. 20.

Rufat, S., Tate, E., Burton, C. G. & Maroof, A. S. Social vulnerability to floods: review of case studies and implications for measurement. *Int. J. Disaster Risk Reduct.* **14**, 470–486 (2015).

[Article](#) [Google Scholar](#)

21. 21.

Ward, P. J. et al. Usefulness and limitations of global flood risk models. *Nat. Clim. Chang.* **5**, 712–715 (2015).

[Article](#) [ADS](#) [Google Scholar](#)

22. 22.

Shastry, A. et al. Small-scale anthropogenic changes impact floodplain hydraulics: simulating the effects of fish canals on the Logone floodplain. *J. Hydrol.* **588**, 125035 (2020).

[Article](#) [Google Scholar](#)

23. 23.

Coltin, B., McMichael, S., Smith, T. & Fong, T. Automatic boosted flood mapping from satellite data. *Int. J. Remote Sens.* **37**, 993–1015 (2016).

[PubMed](#) [PubMed Central](#) [Article](#) [ADS](#) [Google Scholar](#)

24. 24.

DeVries, B. et al. Rapid and robust monitoring of flood events using Sentinel-1 and Landsat data on the Google Earth Engine. *Remote Sens. Environ.* **240**, 111664 (2020).

[Article](#) [ADS](#) [Google Scholar](#)

25. 25.

Pekel, J.-F., Cottam, A., Gorelick, N. & Belward, A. S. High-resolution mapping of global surface water and its long-term changes. *Nature* **540**, 418–422 (2016).

[CAS](#) [PubMed](#) [Article](#) [ADS](#) [Google Scholar](#)

26. 26.

Ji, L., Gong, P., Wang, J., Shi, J. & Zhu, Z. Construction of the 500-m resolution daily global surface water change database (2001–2016). *Wat. Resour. Res.* **54**, 10270–10292 (2018).

[Article](#) [ADS](#) [Google Scholar](#)

27. 27.

Bernhofen, M. V. et al. A first collective validation of global fluvial flood models for major floods in Nigeria and Mozambique. *Environ. Res. Lett.* **13**, 104007 (2018).

[Article](#) [ADS](#) [Google Scholar](#)

28. 28.

Policelli, F. et al. in *Remote Sensing of Hydrological Extremes* (ed. Lakshmi, V.) 47 (Springer, 2016).

29. 29.

Smith, A. et al. New estimates of flood exposure in developing countries using high-resolution population data. *Nat. Commun.* **10**, 1814 (2019).

[PubMed](#) [PubMed Central](#) [Article](#) [ADS](#) [CAS](#) [Google Scholar](#)

30. 30.

European Commission, Joint Research Centre & Columbia University, Center for International Earth Science Information Network. *GHS Population Grid, Derived from GPW4, Multitemporal (1975, 1990, 2000, 2015)* https://ghsl.jrc.ec.europa.eu/ghs_pop.php (2015).

31. 31.

Facebook Connectivity Lab and Center for International Earth Science Information Network - CIESIN - Columbia University. *High Resolution Settlement Layer (HDSL)* <https://www.ciesin.columbia.edu/data/hrsl/> (2016).

32. 32.

Riahi, K. et al. RCP 8.5—a scenario of comparatively high greenhouse gas emissions. *Clim. Change* **109**, 33–57 (2011).

[CAS Article](#) [ADS](#) [Google Scholar](#)

33. 33.

Riahi, K. et al. The shared socioeconomic pathways and their energy, land use, and greenhouse gas emissions implications: an overview. *Glob. Environ. Change* **42**, 153–168 (2017).

[Article](#) [Google Scholar](#)

34. 34.

Otsu, N. A threshold selection method from gray-level histograms. *Automatica* **11**, 23–27 (1975).

[Google Scholar](#)

35. 35.

Nigro, J., Slayback, D., Policelli, F. & Brakenridge, G. R. *NASA/DFO MODIS Near Real-Time (NRT) Global Flood Mapping Product Evaluation of Flood and Permanent Water Detection* https://floodmap.modaps.eosdis.nasa.gov/documents/NASAGlobalNREvaluationSummary_v4.pdf (2014).

36. 36.

Centre for Research on the Epidemiology of Disasters. *Em-Dat: the International Disaster Database* <https://public.emdat.be/> (accessed July 2020).

37. 37.

World Resources Institute. *Aqueduct Global Flood Risk Maps* <https://www.wri.org/data/aqueduct-floods-hazard-maps> (2015).

38. 38.

Collenteur, R. A., de Moel, H., Jongman, B. & Di Baldassarre, G. The failed-levee effect: do societies learn from flood disasters? *Nat. Hazards* **76**, 373–388 (2015).

[Article](#) [Google Scholar](#)

39. 39.

Mykhnenko, V. & Turok, I. East European cities — patterns of growth and decline, 1960–2005. *Int. Plann. Stud.* **13**, 311–342 (2008).

[Article](#) [Google Scholar](#)

40. 40.

Zaninetti, J.-M. & Colten, C. E. Shrinking New Orleans: post-Katrina population adjustments. *Urban Geogr.* **33**, 675–699 (2012).

[Article](#) [Google Scholar](#)

41. 41.

Birkmann, J. & Fernando, N. Measuring revealed and emergent vulnerabilities of coastal communities to tsunami in Sri Lanka. *Disasters* **32**, 82–105 (2008).

[PubMed](#) [Article](#) [Google Scholar](#)

42. 42.

United Nations, Department of Economic and Social Affairs, & Population Division. *World Urbanization Prospects: the 2018 Revision*. Report No. ST/ESA/SER.A/420 (United Nations, 2019).

43. 43.

Fiedler, T. et al. Business risk and the emergence of climate analytics. *Nat. Clim. Change* **11**, 87–94 (2021).

44. 44.

Gaillard, J. C. et al. Alternatives for sustained disaster risk reduction. *Human. Geogr.* **3**, 66–88 (2010).

[Article](#) [Google Scholar](#)

45. 45.

de Bruijn, J. A. et al. A global database of historic and real-time flood events based on social media. *Sci. Data* **6**, 311 (2019).

[PubMed](#) [PubMed Central](#) [Article](#) [Google Scholar](#)

46. 46.

Siders, A. R., Hino, M. & Mach, K. J. The case for strategic and managed climate retreat. *Science* **365**, 761–763 (2019).

[CAS](#) [PubMed](#) [Article](#) [ADS](#) [Google Scholar](#)

47. 47.

Painter, M. An inconvenient cost: the effects of climate change on municipal bonds. *J. Financ. Econ.* **135**, 468–482 (2020).

[Article](#) [Google Scholar](#)

48. 48.

Surminski, S. & Oramas-Dorta, D. Flood insurance schemes and climate adaptation in developing countries. *Int. J. Disaster Risk Reduct.* **7**, 154–164 (2014).

[Article](#) [Google Scholar](#)

49. 49.

Blum, A. G., Ferraro, P. J., Archfield, S. A. & Ryberg, K. R. Causal effect of impervious cover on annual flood magnitude for the United States. *Geophys. Res. Lett.* **47**, e2019GL086480 (2020).

[ADS](#) [Google Scholar](#)

50. 50.

Weichselgartner, J. & Kelman, I. Geographies of resilience: challenges and opportunities of a descriptive concept. *Prog. Hum. Geogr.* **39**, 249–267 (2015).

[Article](#) [Google Scholar](#)

51. 51.

Tennekes, M. tmap: thematic maps in R. *J. Stat. Softw.* **84**, 6 (2018).

[Article](#) [Google Scholar](#)

52. 52.

Robinson, D., Bryan, J. & Elias, J. *fuzzyjoin* version 0.1.6,
<https://cran.r-project.org/web/packages/fuzzyjoin/fuzzyjoin.pdf> (2020).

53. 53.

Brakenridge, R. & Anderson, E. in *Transboundary Floods: Reducing Risks Through Flood Management* (eds Marsalek, J. et al.) 1–12 (Springer, 2006).

54. 54.

Sakamoto, T. et al. Detecting temporal changes in the extent of annual flooding within the Cambodia and the Vietnamese Mekong Delta from MODIS time-series imagery. *Remote Sens. Environ.* **109**, 295–313 (2007).

[Article](#) [ADS](#) [Google Scholar](#)

55. 55.

Islam, A. S., Bala, S. K. & Haque, M. A. Flood inundation map of Bangladesh using MODIS time-series images: flood inundation map of Bangladesh. *J. Flood Risk Managem.* **3**, 210–222 (2010).

[Article](#) [Google Scholar](#)

56. 56.

Boschetti, M., Nutini, F., Manfron, G., Brivio, P. A. & Nelson, A. Comparative analysis of normalised difference spectral indices derived from modis for detecting surface water in flooded rice cropping systems. *PLoS One* **9**, e88741 (2014).

[PubMed](#) [PubMed Central](#) [Article](#) [ADS](#) [CAS](#) [Google Scholar](#)

57. 57.

Klein, I., Dietz, A., Gessner, U., Dech, S. & Kuenzer, C. Results of the global WaterPack: a novel product to assess inland water body

dynamics on a daily basis. *Remote Sens. Lett.* **6**, 78–87 (2015).

[Article](#) [Google Scholar](#)

58. 58.

Gorelick, N. et al. Google Earth Engine: planetary-scale geospatial analysis for everyone. *Remote Sens. Environ.* **202**, 18–27 (2017).

[Article](#) [ADS](#) [Google Scholar](#)

59. 59.

Lehner, B. & Grill, G. Global river hydrography and network routing: baseline data and new approaches to study the world's large river systems. *Hydrol. Process.* **27**, 2171–2186 (2013).

[Article](#) [ADS](#) [Google Scholar](#)

60. 60.

Congalton, R. G. A review of assessing the accuracy of classifications of remotely sensed data. *Remote Sens. Environ.* **37**, 35–46 (1991).

[Article](#) [ADS](#) [Google Scholar](#)

61. 61.

Vermote, E. F., El Saleous, N. Z. & Justice, C. O. Atmospheric correction of MODIS data in the visible to middle infrared: first results. *Remote Sens. Environ.* **83**, 97–111 (2002).

[Article](#) [ADS](#) [Google Scholar](#)

62. 62.

Gumley, L., Descloitres, J. & Schmaltz, J. *Creating Reprojected True Color MODIS Images: A Tutorial*
https://ftp.ssec.wisc.edu/pub/willemm/Creating_Reprojected_True_Co

[lor_MODIS_Images_A_Tutorial_process.pdf](#) (Univ. Wisconsin-Madison, 2010).

63. 63.

Donchyts, G., Schellekens, J., Winsemius, H., Eisemann, E. & van de Giesen, N. A. 30 m resolution surface water mask including estimation of positional and thematic differences using Landsat 8, SRTM and OpenStreetMap: a case study in the Murray-Darling Basin, Australia. *Remote Sens.* **8**, 386 (2016).

[Article](#) [ADS](#) [Google Scholar](#)

64. 64.

Verpoorter, C., Kutser, T. & Tranvik, L. Automated mapping of water bodies using Landsat multispectral data: automated mapping of water bodies. *Limnol. Oceanogr. Methods* **10**, 1037–1050 (2012).

[Article](#) [Google Scholar](#)

65. 65.

Danielson, J. J. & Gesch, D. B. *Global Multi-Resolution Terrain Elevation Data 2010 (GMTED2010)*. Report No. OFR 2011-1073 (US Geological Survey, 2011).

66. 66.

Dinerstein, E. et al. An ecoregion-based approach to protecting half the terrestrial realm. *Bioscience* **67**, 534–545 (2017).

[PubMed](#) [PubMed Central](#) [Article](#) [Google Scholar](#)

67. 67.

Xu, H. Modification of normalised difference water index (NDWI) to enhance open water features in remotely sensed imagery. *Int. J. Remote Sens.* **27**, 3025–3033 (2006).

[Article](#) [ADS](#) [Google Scholar](#)

68. 68.

Carroll, M. L., Townshend, J. R., DiMiceli, C. M., Noojipady, P. & Sohlberg, R. A. A new global raster water mask at 250 m resolution. *Int. J. Digit. Earth* **2**, 291–308 (2009).

[Article](#) [ADS](#) [Google Scholar](#)

69. 69.

Ashouri, H. et al. PERSIANN-CDR: daily precipitation climate data record from multisatellite observations for hydrological and climate studies. *Bull. Am. Meteorol. Soc.* **96**, 69–83 (2015).

[Article](#) [ADS](#) [Google Scholar](#)

70. 70.

Chini, M. et al. Sentinel-1 InSAR coherence to detect floodwater in urban areas: Houston and hurricane Harvey as a test case. *Remote Sens.* **11**, 107 (2019).

[Article](#) [ADS](#) [Google Scholar](#)

71. 71.

Hawker, L. et al. Comparing earth observation and inundation models to map flood hazards. *Environ. Res. Lett.* **15**, 124032 (2020).

[Article](#) [ADS](#) [Google Scholar](#)

72. 72.

Leyk, S. et al. The spatial allocation of population: a review of large-scale gridded population data products and their fitness for use. *Earth Syst. Sci. Data* **11**, 1385–1409 (2019).

[Article](#) [ADS](#) [Google Scholar](#)

73. 73.

Archila Bustos, M. F., Hall, O., Niedomysl, T. & Ernstson, U. A pixel level evaluation of five multitemporal global gridded population datasets: a case study in Sweden, 1990–2015. *Popul. Environ.* **42**, 255–277 (2020).

[Article](#) [Google Scholar](#)

74. 74.

Chen, R., Yan, H., Liu, F., Du, W. & Yang, Y. Multiple global population datasets: differences and spatial distribution characteristics. *ISPRS Int. J. Geoinf.* **9**, 637 (2020).

[Article](#) [Google Scholar](#)

75. 75.

Pesaresi, M. et al. *Operating Procedure for the Production of the Global Human Settlement Layer from Landsat Data of the Epochs 1975, 1990, 2000, and 2014*. Report No. JRC97705 (Publications Office of the European Union, 2016).

76. 76.

Bhaduri, B., Bright, E., Coleman, P. & Urban, M. L. LandScan USA: a high-resolution geospatial and temporal modeling approach for population distribution and dynamics. *GeoJournal* **69**, 103–117 (2007).

[Article](#) [Google Scholar](#)

77. 77.

Center for International Earth Science Information Network (CIESIN), Columbia University. *Gridded Population of the World, Version 4*

(GPWv4): Population Density <https://doi.org/10.7927/H4NP22DQ>. (SEDAC, 2016; accessed August 2019).

78. 78.

Ward, P. J. et al. Assessing flood risk at the global scale: model setup, results, and sensitivity. *Environ. Res. Lett.* **8**, 044019 (2013).

[Article](#) [ADS](#) [Google Scholar](#)

79. 79.

Irvine, P. J., Srivari, R. L. & Keller, K. Tension between reducing sea-level rise and global warming through solar-radiation management. *Nat. Clim. Chang.* **2**, 97–100 (2012).

[CAS](#) [Article](#) [ADS](#) [Google Scholar](#)

80. 80.

Ward, P. J. et al. *Aqueduct Floods Methodology* (World Resources Institute, 2020).

81. 81.

Bright, E. A., Coleman, P. R., Rose, A. N. & Urban, M. L. *LandScan 2010* <https://landscan.ornl.gov/landscan-datasets> (2011).

82. 82.

van Huijstee, J., van Bemmel, B., Bouwman, A. & van Rijn, F. *Towards an Urban Preview: Modelling Future Urban Growth With 2UP* <https://www.pbl.nl/en/publications/towards-an-urban-preview> (PBL Netherlands Environmental Assessment Agency, 2018).

83. 83.

UN Habitat. *Informal Settlements* <https://unhabitat.org/habitat-iii-issue-papers-22-informal-settlements> (2016).

[Download references](#)

Acknowledgements

We thank students at the University of Washington for quality checking and validating the Global Flood Database: S. Lau, C. C. Wu, P. K. Kamaluddin, W. Pietsch, S. Lau, G. J. Kim, H. Tran and J. Crinkey. We thank students from the University of Texas at Austin, including C. Norton. We thank the Cloud to Street staff for quality checking additional portions of the database: S. Weber and E. Glinskis. We thank B. L. Turner II, U. Lall, V. Lakshmi, P. Kareiva, C. Tuholkse, J. Doss-Gollin, D. Farnham and A. Massmann for providing comments on the manuscript. Funding for this project was provided by a Google Earth Engine Research Award and NASA award 80NSSC18K0426, 16-GEO16-0068, Integrating Global Remote Sensing and Modeling Systems for Local Flood Prediction and Impact Assessment. This research made use of the LandScan 2010 High Resolution global Population Data Set, copyrighted by UT-Battelle, LLC, operator of Oak Ridge National Laboratory under contract no. DE-AC05-00OR22725 with the United States Department of Energy. The United States Government has certain rights in this dataset. Neither UT-Battelle, LLC nor the United States Department of Energy, nor any of their employees, makes any warranty, express or implied, or assumes any legal liability or responsibility for the accuracy, completeness, or usefulness of the dataset.

Author information

Author notes

1. These authors contributed equally: B. Tellman, J. A. Sullivan

Affiliations

1. Earth Institute, Columbia University, New York, NY, USA

B. Tellman

2. Cloud to Street, Brooklyn, NY, USA
B. Tellman, J. A. Sullivan & C. S. Doyle
3. School of Geography, Development and Environment, University of Arizona, Tucson, AZ, USA
B. Tellman & J. A. Sullivan
4. School for Environment and Sustainability, University of Michigan, Ann Arbor, MI, USA
J. A. Sullivan
5. School of Environmental and Forest Sciences, University of Washington, Seattle, WA, USA
C. Kuhn
6. INSTAAR, Dartmouth Flood Observatory, University of Colorado, Boulder, CO, USA
A. J. Kettner & G. R. Brakenridge
7. Department of Geography and the Environment, University of Texas, Austin, TX, USA
C. S. Doyle
8. Google, Mountain View, CA, USA
T. A. Erickson
9. Science Systems and Applications Inc., Biospheric Sciences Lab, NASA Goddard Space Flight Center, Greenbelt, MD, USA
D. A. Slayback

Authors

1. B. Tellman

[View author publications](#)

You can also search for this author in [PubMed](#) [Google Scholar](#)

2. J. A. Sullivan

[View author publications](#)

You can also search for this author in [PubMed](#) [Google Scholar](#)

3. C. Kuhn

[View author publications](#)

You can also search for this author in [PubMed](#) [Google Scholar](#)

4. A. J. Kettner

[View author publications](#)

You can also search for this author in [PubMed](#) [Google Scholar](#)

5. C. S. Doyle

[View author publications](#)

You can also search for this author in [PubMed](#) [Google Scholar](#)

6. G. R. Brakenridge

[View author publications](#)

You can also search for this author in [PubMed](#) [Google Scholar](#)

7. T. A. Erickson

[View author publications](#)

You can also search for this author in [PubMed](#) [Google Scholar](#)

8. D. A. Slayback

[View author publications](#)

You can also search for this author in [PubMed](#) [Google Scholar](#)

Contributions

B.T. conceived the study and led the population exposure analysis, writing and project administration. J.A.S. conceived the study and algorithm, designed the validation, led the data curation and contributed to writing and editing. C.K. led algorithm accuracy and validation analysis and quality control. C.S.D. contributed to algorithm development and data visualization and curation. A.J.K. contributed to quality control, writing and editing. G.R.B. contributed to editing and data curation of the event database. T.A.E. contributed to data curation. D.A.S. contributed to quality control and data visualization.

Corresponding author

Correspondence to [B. Tellman](#).

Ethics declarations

Competing interests

Two of the authors (B.T. and C.D.) are employed by and hold stock in a company, Cloud to Street, that sells flood observation and satellite monitoring technology. The data in this paper are free and open, and the company expects no direct financial benefit from this study.

Additional information

Peer review information *Nature* thanks Brenden Jongman, Albert van Dijk and the other, anonymous, reviewer(s) for their contribution to the peer review of this work. Peer reviewer reports are available.

Publisher's note Springer Nature remains neutral with regard to jurisdictional claims in published maps and institutional affiliations.

Extended data figures and tables

Extended Data Fig. 1 Global distribution of flood events catalogued by the DFO and the Global Flood Database.

a–c, Flood events in the DFO from 1 January 1985 to 31 December 2018 ($n = 4,712$; **a**), in the DFO and coincident with MODIS imagery ($n = 3,127$; **b**) and that passed the quality control evaluation for the Global Flood Database ($n = 913$; **c**). Base map: US government Large Scale International Boundaries (LSIB) Polygons (2017).

Extended Data Fig. 2 Example of bimodal histograms used to calculate adaptive thresholds for water classifications that approximate, on average, the standard versions of the water classification thresholds.

a, b, Example bimodal histograms (left axes) with interclass variance (ICV; blue lines, right axes) extracted from MODIS imagery used to determine optimal thresholds for $B2B1_{ratio}$ (K_1 ; **a**) and DN_{SWIR} (K_2 ; **b**). The dashed red and black lines reflect the estimated Otsu and standard thresholds, respectively. **c, d**, Distribution of estimated Otsu thresholds calculated for each flood event across the Global Flood Database ($n = 913$), for $B2B1_{ratio}$ (K_1 ; **c**) and DN_{SWIR} (K_2 ; **d**). The average Otsu threshold across the Global Flood Database for $B2B1_{ratio}$ ($K_1 = 0.77$; dashed red line in **c**) and DN_{SWIR} ($K_2 = 599$; dashed red line in **d**) are comparable to the standard thresholds ($K_1 = 0.70$, dashed black line in **a**; $K_2 = 675$, dashed black line in **b**).

Extended Data Fig. 3 Distribution of Landsat 5, 7 and 8 imagery.

The Landsat images used to evaluate 123 flood events in the Global Flood Database are globally distributed, cover 15 biomes⁶⁶ and span 15 years. Flood events for validation were selected on the basis of availability of Landsat imagery. Eligibility of imagery included conditions that Landsat imagery occurred within 24 h of the maximum day of inundation, intersected the flood area and had less than 20% cloud cover. Biome shapefile for the base map (grey shading; <https://ecoregions.appspot.com/>)

indicates varying vegetation patterns that may influence the accuracy of our remote sensing algorithm.

Extended Data Fig. 4 Global Flood Database accuracy metrics.

a, Sensitivity plot of accuracy metrics with random sampling of 500 points for 10 flood events. **b**, Error analysis showing the distribution of true positive (t_p), true negative (t_n), false positive (f_p) and false negative (f_n) rates for each of the four water detection methods, where the centre line represents the median, the hinges represent the 25th and 75th percentiles, the upper whisker extends from the hinge to the largest value no further than 1.5*IQR (interquartile range) and the lower whiskers extends from the hinge to the smallest value no further than 1.5*IQR, and the dots show outlier points outside the whisker range. **c**, Accuracy statistics, given as the mean and standard deviation (s.d), summarized for each thresholding method and image composite choice (metrics per event in Supplementary Table 2).

Extended Data Fig. 5 Global distribution of accuracy metrics based on 123 flood events from the Global Flood Database.

a, b, Overall accuracy (**a**) is consistently distributed across the globe, whereas errors of commission (**b**) are inflated at higher latitudes and errors of omission (**c**) are lower than errors of commission and have no clear spatial pattern. Base maps: GADM (Global Administrative Areas) 2018, version 3.6.

Extended Data Fig. 6 Results of the quality control assessment.

Coverage of the Global Flood Database is well represented in southeast USA, Central America, South America, southeast Asia, Australia, west Africa and east Africa. **a–c**, Counts of flood events that passed (**b**) or failed (**a**) quality control (QC), and the proportion of events that passed as a ratio of total flood events (**c**). Base map: US government LSIB Polygons (2017).

Extended Data Fig. 7 Population uncertainty analysis.

a, Correction factors determined as the ratio of HRSL flood exposure to GHSL flood exposure per continent, where the centre line represents the median, the hinges represent the 25th and 75th percentiles, the upper whisker extends from the hinge to the largest value no further than 1.5*IQR (interquartile range) and the lower whiskers extends from the hinge to the smallest value no further than 1.5*IQR, and the dots show points outside the whisker range. **b**, Uncertainty analysis for each country plotted against flood exposure trends (2000–2015). Countries in the upper right quadrant represent regions with plausibly high uncertainty in population estimates, such that we are not confident in their flood exposure trends (unc., uncertainty; inc., increasing trends; dec., decreasing trends). Countries are labelled by their ISO 1366 standard Alpha-2 two-letter country codes (from LSIB) and coloured by continent.

Extended Data Fig. 8 Sensitivity analysis of return periods to changes in flood exposure, 2010–2030.

a, Change in total population exposed to floods (logarithmic scale; 2030 minus 2010), for each return period, summarized by continent. **b**, Percentage increase in the population exposed to floods from 2010 to 2030, for each return period. **c**, Percentage increase in total population from 2010 to 2030 for each continent. **d**, Multiplicative change in the proportion of the population exposed to floods (equation (7), Methods). For all boxplots (**a–d**), the centre line represents the median, the whiskers represent the 25th and 75th percentile, the upper whisker extends from the hinge to the largest value no further than 1.5*IQR (interquartile range) and the lower whiskers extends from the hinge to the smallest value no further than 1.5*IQR, and the dots show points outside the whisker range.

Extended Data Fig. 9 Comparison of the DFO and Em-Dat databases.

We find moderate temporal correlation, greater representation of events in DFO than in Em-Dat in USA, Australia and Russia, and a smaller catalogue of events in DFO than in Em-Dat in Africa and Latin America. **a**, Annual flood events in DFO and Em-Dat. **b**, Number of flood events in DFO minus

that in Em-Dat for each country. Base map: Natural Earth, tmap R package⁵¹.

Extended Data Fig. 10 Comparison for each country of the population exposed to floods in a 100-year event (using 2010 climate and population) determined from GLOFRIS and an estimate of the total population exposed from the Global Flood Database, 2000–2018.

$r = 0.89$, $P < 0.001$. The blue line represents parity between the population determined from GLOFRIS and from the Global Flood Database line; the black line is the linear regression line. Country names are coloured by continent.

Supplementary information

Supplementary Information

This file contains Supplementary Tables 1-5, 7 and 8, Supplementary Discussion, and Supplementary References.

Supplementary Table 6

Population exposed and area inundation estimated per flood event. *gfd_area_km2* provides area estimates and *gfd_population_exposed* represents population exposure estimates from this study. Other information includes GLIDE numbers, DFO ID numbers, event start and end dates, and other metadata from the DFO for each event.

Supplementary Table 9

Quality control information for the main questions asked in the quality control questionnaire.

Supplementary Data

This file contains 250m-resolution raster .tiff images of observed inundation from satellite data (MODIS) for Figure 2 (a and b) and the duration in days of inundation observed for Figure 2 (c and d).

Supplementary Data

This file contains 250m-resolution raster .tiff images of the population change from 2015 to 2000 in inundated areas observed from satellite data (MODIS) for Figure 3.

Supplementary Data

This file contains the zipped source data (shapefiles) for Figure 4.

Peer Review File

Source data

Source Data Fig. 1

Rights and permissions

Reprints and Permissions

About this article



Check for
updates

Cite this article

Tellman, B., Sullivan, J.A., Kuhn, C. *et al.* Satellite imaging reveals increased proportion of population exposed to floods. *Nature* **596**, 80–86

(2021). <https://doi.org/10.1038/s41586-021-03695-w>

[Download citation](#)

- Received: 25 August 2020
- Accepted: 03 June 2021
- Published: 04 August 2021
- Issue Date: 05 August 2021
- DOI: <https://doi.org/10.1038/s41586-021-03695-w>

Comments

By submitting a comment you agree to abide by our [Terms](#) and [Community Guidelines](#). If you find something abusive or that does not comply with our terms or guidelines please flag it as inappropriate.

[Access through your institution](#)

[Change institution](#)

[Buy or subscribe](#)

Associated Content

[The fraction of the global population at risk of floods is growing](#)

- Brenden Jongman

Advertisement

| [Section menu](#) | [Main menu](#) |

Possible poriferan body fossils in early Neoproterozoic microbial reefs

[Download PDF](#)

- Article
- Open Access
- [Published: 28 July 2021](#)

Possible poriferan body fossils in early Neoproterozoic microbial reefs

- [Elizabeth C. Turner](#) [ORCID: orcid.org/0000-0001-7432-1956¹](#)

[Nature](#) volume **596**, pages 87–91 (2021) [Cite this article](#)

- 22k Accesses
- 1 Citations
- 3729 Altmetric
- [Metrics details](#)

Subjects

- [Marine biology](#)
- [Palaeontology](#)

Abstract

Molecular phylogeny indicates that metazoans (animals) emerged early in the Neoproterozoic era¹, but physical evidence is lacking. The search for animal fossils from the Proterozoic eon is hampered by uncertainty about what physical characteristics to expect. Sponges are the most basic known animal type^{2,3}; it is possible that body fossils of hitherto-undiscovered Proterozoic metazoans might resemble aspect(s) of Phanerozoic fossil sponges. Vermiform microstructure^{4,5}, a complex petrographic feature in Phanerozoic reefal and microbial carbonates, is now known to be the body fossil of nonspicular keratosan demosponges^{6,7,8,9,10}. This Article presents petrographically identical vermiform microstructure from

approximately 890-million-year-old reefs. The millimetric-to-centimetric vermiciform-microstructured organism lived only on, in and immediately beside reefs built by calcifying cyanobacteria (photosynthesizers), and occupied microniches in which these calcimicrobes could not live. If vermiciform microstructure is in fact the fossilized tissue of keratose sponges, the material described here would represent the oldest body-fossil evidence of animals known to date, and would provide the first physical evidence that animals emerged before the Neoproterozoic oxygenation event and survived through the glacial episodes of the Cryogenian period.

[Download PDF](#)

Main

Benthic microbial structures (stromatolites and other microbialites) provide conspicuous evidence of pre-Phanerozoic life, but are difficult to understand because they rarely preserve recognizable evidence of the organisms involved.

Stromatolitologists have struggled for over a century to decipher their microscopic laminae and clots, which are assumed to have been produced or influenced by *in vivo* and/or post-mortem biogeochemical activity, and to formalize the ‘taxony’ of their morphology and microstructure^{5,11}.

The existence of metazoans by the Ediacaran period (the last period of the Neoproterozoic) is indicated by bilaterian ‘body’ and trace fossils¹², and geochemical evidence (biomarkers)¹³ provides disputed^{14,15}, indirect evidence for Cryogenian poriferans. The search for definitive physical evidence of pre-Cryogenian metazoans is confounded by uncertainty about what to look for, but preserved physical evidence should be small, subtle and possibly altogether unfamiliar. Given that sponges are the most basic of known animals^{2,3}, physical evidence of Neoproterozoic sponges could be sought, but effort focused on the characteristics of mineralized sponge skeletons (siliceous or calcareous spicules)^{16,17,18} overlooks sponges with only proteinaceous (spongin or keratin^{19,20}) skeletons. Early metazoan evidence might instead resemble taphonomic (preservational) products of sponge soft tissue^{21,22,23} rather than mineralized sponge skeletal components. Although molecular clock data suggest that sponges emerged in the early Neoproterozoic¹, the oldest undisputed sponge body fossils are from the Cambrian period¹⁵.

Recent work^{6,7} has shown that vermiciform microstructure^{4,5}—an unusual microscopic feature in Phanerozoic reefs and stromatolites that was initially interpreted as being related to algae⁴ or protozoans^{24,25}—is instead a keratose sponge body fossil comprising complexly anastomosing cement-filled microtubules enclosed in carbonate microspar. It is produced taphonomically^{6,10} in nonspicular keratose demosponges

through post-mortem calcification of soft tissue to produce carbonate microspar (automicrite), which surrounds the tough spongin fibres of the ‘skeleton’ of the sponge. Decay of the spongin then produces a network of complexly anastomosing tubular moulds that eventually become passively filled with sparry calcite cement. Although questioned²⁶, the association between vermiform microstructure and sponges has been confirmed in undisputed body fossils of Phanerozoic sponges⁷. Three-dimensional reconstruction of vermiform microstructure has shown that tubule shape and branching configuration are too consistent and complex to be abiogenic (for example, compacted peloids), do not resemble the branching style of other possible organism types (microbial or fungal)⁶ and are identical to the spongin meshworks of keratose sponges⁶. Although the existence of Proterozoic vermiform microstructure has been predicted^{6,10,27}, published examples are rare^{28,29} and difficult to understand.

The calcification of decaying sponge soft tissue has been documented in modern sponges^{21,22}, and produces sponge ‘mummies’²² as well as a range of subtle carbonate sedimentary textures (such as peloid clusters) in living and Phanerozoic fossil sponges^{7,9,21,22}. Taphonomic sediment textures (polymuds) that may be poriferan-related have previously been identified in the reefs that are the subject of this Article²³.

Background

This petrographic study presents possible evidence of sponge body fossils in thin sections (30-µm-thick rock slices, viewed microscopically in transmitted light) from the approximately 890-million-year-old (Ma)^{30,31} Little Dal reefs (Stone Knife Formation³², northwestern Canada) (Fig. 1a, b). These large (about 500 m in thickness, and kilometres in diameter) microbial reefs^{33,34,35,36} were built mainly by variably preserved calcimicrobes that have been interpreted as filamentous cyanobacteria (photosynthesizers)^{33,35,36}, and developed palaeotopographic relief of up to about 100 m above the surrounding subphotic, level-bottom carbonate-mud seafloor. Reef framework, which is generally not discernible in natural exposures, was documented from slabbed hand samples and thin sections³⁵.

Fig. 1: Geographic and stratigraphic location of the study material.

 **figure1**

a, Location of Little Dal reefs in northwestern Canada. Scale bar, 100 km. **b**, Stratigraphic position of the Little Dal reefs in the Stone Knife Formation (Fm)³²; depositional age is known through litho- and chemostratigraphic correlation with the 892 ± 13 -Ma (Re–Os black shale)³⁰ Boot Inlet Formation³¹ (Shaler Supergroup (Sg)), together with other geochronological constraints^{50,51}. Gp, group. **c**, Reef growth stages^{34,35}, simplified summary of framework morphologies³⁵ and off-reef cycles³⁴.

[Full size image](#)

The reefs grew in five stages (Fig. 1c), each with different microbialite morphologies: anastomosing millimetre-to-centimetre-scale masses with no consistent shape (stages I–III); centimetre-scale anastomosing columns and digits (stages II, III and V); and steep sheet-like masses at a scale of decimetres to 10 m (stage IV). Stage V includes cement-rich to micritic, domical, turbinate and columnar stromatolites that generally lack calcimicrobes, with associated ooids and stromaclasts. Microbialites of stage I to IV grew predominantly in moderate-energy, illuminated palaeoenvironments^{33,35,36},

but stage V records a shallow-water, high-energy environment. The microstructure that forms most of the reefal microbialites (especially in stages III and IV) comprises filaments that are about 10 µm in diameter, separated by 10–100-µm masses of marine cement that probably represents the calcified sheath polysaccharide of cyanobacteria^{33,36} that was permineralized during microbialite growth. The reef framework, consisting predominantly of this microstructure and its taphonomically degraded equivalents³⁶, defines primary void networks (millimetres to centimetres in size) that are commonly floored with geopetal carbonate mud and lined by isopachous, fibrous marine calcite cement. The relative timing of void-filling by marine cement precipitation versus geopetal sediment accumulation is variable, attesting to the very early timing of marine cement precipitation.

Results

Vermiform microstructure in samples from stages II, III and V of the Little Dal reefs (Fig. 1c) is identifiable only in rare thin sections, in which it forms millimetre-to-centimetre-scale masses of anastomosing tubes that are filled with calcite spar and surrounded by calcite microspar groundmass (Fig. 2a, b). The approximately 20–30-µm-wide tubules have complex, divergent branching and rejoining at a spacing of about 30–100 µm, form very irregular three-dimensional polygonal meshworks, are defined by enclosing microspar, lack walls, and are filled with clear, equant calcite crystals up to 20 µm wide (Fig. 2b). The homogeneous microspar groundmass that encloses the tubules comprises cloudy, equant, interlocking calcite crystals of about 2–8 µm wide, and differs texturally and compositionally from other fine-grained reefal carbonate in its uniform crystal size, lack of sedimentary texture, and dearth of detrital silicate impurities. Vermiform microstructure preservation is good to barely discernible.

Fig. 2: Characteristics and distribution of Little Dal vermiciform microstructure in stratigraphically oriented 30-µm-thick thin sections.

 **figure2**

a, Well-preserved vermiform microstructure exhibits a polygonal meshwork of anastomosing, slightly curved, approximately 30- μm -diameter tubules embedded in calcite microspar (KEC25). Scale bar, 500 μm . **b**, Enlarged rectangle from **a**, showing branching tubules forming three-dimensional polygons intersected at various angles by the thin section; clear calcite crystals, about 10–20 μm in width, fill tubules in groundmass of more finely crystalline calcite (dark grey). Scale bar, 50 μm . **c**, Three-

dimensional fragment of spongin skeleton from a modern keratosan sponge, illustrating its branching and anastomosing network of fibres (incident light). Scale bars, 100 µm (main panel), 20 µm (inset). **d**, Vermiform microstructure in debris that includes calcimicrobialite and other reef-derived clasts (C) flanking reef stage III (MV63). Scale bars, 1 mm (main panel), 100 µm (inset). **e**, Vermiform microstructure in shelter pore beneath microbialite clast, in detrital sediment occupying a reef-top depression; pore is thinly lined with marine calcite cement (MC) (indicated with an arrow), and partly filled with geopetal carbonate sediment (GCS) (KEC25; stage-III reef core). Rectangle is enlarged in **a**. Scale bar, 1 mm. **f**, Vermiform microstructure in a microbialite (M) framework void is overlain by pore-occluding marine calcite cement; circled area indicates moderately well-preserved tubule meshwork (DL32a; reef stage II; detailed characteristics depicted in Extended Data Fig. 1). Scale bar, 1 mm. **g**, Patches of vermiform microstructure in various relationships with micritic microbialite masses (white dashed outline) and detrital carbonate sediment (CS) (KES23; resedimented stage-II reef clast). Rectangles are enlarged in **i–k**. Scale bar, 1 mm. **h**, Simplified depiction of relationships among vermiform microstructure, microbialite masses and detrital carbonate sediment in **g**. Scale bar, 1 mm. **i**, Vermiform microstructure mingled with microbial micrite within a microbialite digit (enlarged from **g**). Scale bar, 500 µm. **j**, Vermiform-microstructured mass within sediment between microbialite digits; also contains diagenetic dolomite patches (D) (enlarged from **g**). Scale bar, 500 µm. **k**, Vermiform-microstructured mass adhering to the margin of microbialite digit (enlarged from **g**). Scale bar, 500 µm. All images except **c** are in plane-polarized transmitted light. Samples from resedimented reef debris are depicted in depositional orientation based on geopetal structures. Reef locations and abbreviations (such as KEC) are described in a previous publication³⁵. Larger versions of vermiform microstructure photomicrographs are provided in Extended Data Figs. 1–5.

[Full size image](#)

Vermiform microstructure is present in three microfacies (i, ii and iii (the last divided into iiia and iiib subsets)), representing three palaeoenvironments (Figs. 2, 3). It is not present in calcimicrobe-dominated stromatolites or level-bottom carbonate mudstone that is distal to reefs.

Fig. 3: Palaeoenvironments occupied by the Little Dal vermiform microstructure interpreted as possible body fossils of keratose sponges.

 **figure3**

The organism lived (i) on poorly illuminated to non-illuminated carbonate mud surfaces in depressions on the reef surface and on debris aprons mantling reef flanks; (ii) in voids produced by the growth of the complex microbial framework of the reef; and (iii) interlayered with non-calcimicrobial microbialites (cement-rich and muddy-laminated stromatolites in high-energy reef-capping phase V; irregularly muddy-laminated to clotted microbialites in moderate-energy environments of reef stages II and III). Scale bars, 5 mm.

[Full size image](#)

In microfacies i (Fig. [2d,e,g,j](#), Extended Data Figs. [1, 2](#)), veriform microstructure is intercalated with carbonate mud (with or without larger reef-derived clasts and terrigenous impurities) in (1) synsedimentary debris flanking reef stages II and III, and (2) millimetre-to-metre-scale palaeodepressions on reef growth surfaces (stages II and

III). It locally encrusts sides of reef-framework clasts in sediment, extends into crevices, and occupies shelter porosity under clasts (Fig. 2e).

In microfacies ii (Fig. 2f, Extended Data Fig. 3), vermiciform microstructure occupies millimetre-to-centimetre-scale framework voids of reef stages II and III. Void-filling vermiciform microstructure of microfacies i and ii either underlies (Fig. 2f) or overlies (Fig. 2e) isopachous void-lining marine cement.

In rare microfacies iiiia (Fig. 2g–k, Extended Data Fig. 4), vermiciform microstructure encrusts non-calcimicrobial microbialite columns and mingles with irregular muddy microbialite microstructure of reef stages II and III. In rare microfacies iiib (Extended Data Fig. 5), vermiciform microstructure is sub-millimetrically interlayered with stage-V non-calcimicrobial stromatolites where it locally passes laterally to geopetal peloid accumulations in lenticular voids.

Discussion

The shape, size, branching style and polygonal meshworks of the Little Dal vermiciform tubules closely resemble both spongin fibre networks of modern keratosan sponges (Fig. 2a–c) and vermiciform microstructure either demonstrated or interpreted to be sponge-derived in diverse Phanerozoic microbial, reefal and non-reefal carbonate rocks^{6,7,8,10,24,25,27,37}. The compositional and textural homogeneity of the microspar groundmass supports an origin through permineralization of a pre-existing biological substance⁹, rather than incremental accumulation of detrital sediment or microbial carbonate that passively incorporated complexly anastomosing tubular microfossils. Variable preservation and association with geopetal peloid accumulations are familiar aspects of Phanerozoic sponge taphonomy^{9,21,22,38}. In previous work, detailed comparison of the three-dimensional characteristics of vermiciform microstructure with branching cylindrical organism types yielded no convincing alternative to the sponge interpretation⁶.

The preference of Little Dal vermiciform microstructure for environments that were not inhabited by photosynthetic calcimicrobes (reef flanks, depressions on active reef growth surface, and framework and shelter voids), versus its absence from filamentous calcimicrobial reef-framework components, suggests that (1) illumination may not have been a requirement and (2) the organism may have been unable to compete with reef-building photosynthesizers that grew and/or calcified rapidly. The interlayering of vermiciform microstructure with calcimicrobe-free microbialite (microfacies iiib) in the high-energy, well-illuminated reef surfaces of reef stage V supports the interpretation that the vermiciform-microstructured organism was not capable of competing with reef-building filamentous cyanobacteria, but instead occupied niches in which the filamentous calcimicrobes did not live owing to (1) poor illumination or (2) high

hydrodynamic energy. The occupation of cryptic microniches (shelter and reef framework voids) by sponges (for example, microfacies i and ii), is well known in the Phanerozoic^{21,37,39,40}.

The obligatory spatial association of vermicular microstructure with reefs built by oxygen-producing cyanobacteria may indirectly support a metazoan interpretation. Prior to the Neoproterozoic oxygenation event, marine dissolved oxygen was probably low⁴¹ except perhaps in the vicinity of photosynthesizing microbial communities; the metabolic requirements of metazoans may have limited early animals to localized, comparatively well-oxygenated (for the time) environments (oxygen ‘oases’). Given the approximately 890-Ma depositional age^{30,31}, the vermicular-microstructured Little Dal organism may have been tolerant of ‘low’ oxygen (that is, relative to modern levels), which is a characteristic of some modern and fossil sponges⁴².

If the vermicular-microstructured masses in the Little Dal reefs are accepted as early sponge body fossils, their approximately 890-Ma age would imply that (1) the evolutionary emergence of metazoans was decoupled from the Neoproterozoic oxygenation event^{41,42,43,44,45} and (2) early animal life was not catastrophically affected by the Neoproterozoic glacial episodes. If the Little Dal objects are truly sponge body fossils, they are older than the next-youngest undisputed sponge body fossils (Cambrian)¹⁵ by approximately 350 million years.

It would not be surprising to find that the earliest sponges were reef-dwellers; the history of Phanerozoic reefs is rich with reef-building and reef-dwelling sponges⁴⁶. If the masses of vermicular microstructure in the Little Dal reefs were to be accepted as an early Neoproterozoic expression of sponge tissue preservation, their age and proposed identity would be compatible with (1) evidence that the opisthokont (animal + fungus) clade was already established by the time of the Mesoproterozoic–Neoproterozoic transition^{47,48}, (2) possible evidence of 1-billion-year-old multicellular holozoans⁴⁹, (3) molecular clock estimates for the emergence of the Porifera in the early Neoproterozoic¹ and (4) a revised taxonomy of nonspiculate keratose sponges showing that they are a sister group to other demosponges¹⁹. The Little Dal vermicular microstructure is perhaps exactly what should be expected of the earliest metazoan body fossils: preservation through post-mortem calcification of sponge-grade soft tissue in the decaying bodies of small, shapeless, sessile, epibenthic and cryptic animals most closely affiliated with keratose sponges.

Methods

Field work was done on foot from two-person, backpacking-style camps placed at sites that are accessible only by helicopter. Samples were collected at various times

between 1992 and 2018, under all required permits. Recording sample locations using GPS is not possible for most sites owing to the extreme topography of the exposures' cliffs, pinnacles and canyons, and so sample location was documented using photographs and sketches. Several samples are from a mineral-exploration drill-core stored on-site in the field. Owing to the homogeneous grey weathering of reef surfaces, lithofacies cannot be identified in the field. Instead, hand samples were collected and later slabbed and thin-sectioned. Vermiform microstructure was identified in a small proportion of the samples collected. Repeat visits focused primarily on resampling the rare areas in which vermiform microstructure had been identified.

Standard 30- μm -thick thin sections were examined in plane-polarized transmitted light using a Nikon C-Pol binocular microscope fitted with digital camera and Luminera Infinity Analyze software (for lower-magnification images) and an Olympus BX-51 petrographic microscope equipped with Q-Imaging digital capture system (for higher-magnification images).

Reporting summary

Further information on research design is available in the [Nature Research Reporting Summary](#) linked to this paper.

Data availability

All relevant data are contained with the Article and its Supplementary Information, or are available from the author upon reasonable request.

References

1. 1.

Dohrmann, M. & Wörheide, G. Dating early animal evolution using phylogenomic data. *Sci. Rep.* **7**, 3599 (2017).

[PubMed](#) [PubMed Central](#) [Article](#) [ADS](#) [CAS](#) [Google Scholar](#)

2. 2.

Feuda, R. et al. Improved modeling of compositional heterogeneity supports sponges as sister to all other animals. *Curr. Biol.* **27**, 3864–3870.e4 (2017).

[CAS](#) [PubMed](#) [Article](#) [Google Scholar](#)

3. 3.

Simion, P. et al. A large and consistent phylogenomic dataset supports sponges as the sister group to all other animals. *Curr. Biol.* **27**, 958–967 (2017).

[CAS](#) [PubMed](#) [Article](#) [Google Scholar](#)

4. 4.

Walter, M. R. *Stromatolites and the Biostratigraphy of the Australian Precambrian and Cambrian (Special Papers in Palaeontology 11)* (The Palaeontological Association, 1972).

5. 5.

Bertrand-Sarfati, J. in *Stromatolites (Developments in Sedimentology 20)* (ed. Walter, M. R.) 251–259 (Elsevier, 1976).

6. 6.

Luo, C. & Reitner, J. First report of fossil “keratose” demosponges in Phanerozoic carbonates: preservation and 3-D reconstruction. *Naturwissenschaften* **101**, 467–477 (2014).

[CAS](#) [PubMed](#) [Article](#) [ADS](#) [Google Scholar](#)

7. 7.

Lee, J.-H. et al. Furongian (Late Cambrian) sponge-microbial maze-like reefs in the north China platform. *Palaios* **29**, 27–37 (2014).

[Article](#) [ADS](#) [Google Scholar](#)

8. 8.

Luo, C. & Reitner, J. ‘Stromatolites’ built by sponges and microbes - a new type of Phanerozoic bioconstruction. *Lethaia* **49**, 555–570 (2016).

[Article](#) [Google Scholar](#)

9. 9.

Shen, Y. & Neuweiler, F. Questioning the microbial origin of automicrite in Ordovician calathid-demosponge carbonate mounds. *Sedimentology* **65**, 303–333

(2018).

[CAS](#) [Article](#) [Google Scholar](#)

10. 10.

Lee, J.-H. & Riding, R. Keratolite – stromatolite consortia mimic domical and branched columnar stromatolites. *Palaeogeog. Palaeoclimatol. Palaeogeog.* **571**, 110288 (2021).

[Article](#) [ADS](#) [Google Scholar](#)

11. 11.

Grey, K. & Awramik, S. M. *Handbook for the Study and Description of Microbialites (Geological Survey of Western Australia Bulletin 147)* (Geological Survey of Western Australia, 2020)

12. 12.

Chen, Z., Zhou, C., Yuan, X. & Xiao, S. Death march of a segmented and trilobate bilaterian elucidates early animal evolution. *Nature* **573**, 412–415 (2019).

[CAS](#) [PubMed](#) [Article](#) [ADS](#) [Google Scholar](#)

13. 13.

Love, G. D. et al. Fossil steroids record the appearance of Demospongiae during the Cryogenian period. *Nature* **457**, 718–721 (2009).

[CAS](#) [PubMed](#) [Article](#) [ADS](#) [Google Scholar](#)

14. 14.

Antcliffe, J. B. Questioning the evidence of organic compounds called sponge biomarkers. *Palaeontology* **56**, 917–925 (2013).

[Google Scholar](#)

15. 15.

Antcliffe, J. B., Callow, R. H. & Brasier, M. D. Giving the early fossil record of sponges a squeeze. *Biol. Rev. Camb. Philos. Soc.* **89**, 972–1004 (2014).

[PubMed](#) [Article](#) [Google Scholar](#)

16. 16.

Muscente, A. D., Michel, F. M., Dale, J. & Ziao, S. Assessing the veracity of Precambrian ‘sponge’ fossils using in situ nanoscale analytical techniques. *Precambr. Res.* **263**, 142–156 (2015).

[CAS](#) [Article](#) [ADS](#) [Google Scholar](#)

17. 17.

Ma, J.-Y. & Yang, Q. Early divergence dates of demosponges based on mitogenomics and evaluated fossil calibrations. *Palaeoworld* **25**, 292–302 (2016).

[Article](#) [Google Scholar](#)

18. 18.

Botting, J. P. & Muir, L. A. Early sponge evolution: a review and phylogenetic framework. *Palaeoworld* **27**, 1–29 (2018).

[Article](#) [Google Scholar](#)

19. 19.

Erpenbeck, D. et al. Horny sponges and their affairs: on the phylogenetic relationships of keratose sponges. *Mol. Phylogenet. Evol.* **63**, 809–816 (2012).

[PubMed](#) [Article](#) [Google Scholar](#)

20. 20.

Ehrlich, H. et al. Discovery of 505-million-year old chitin in the basal demosponge *Vauxia gracilenta*. *Sci. Rep.* **3**, 3497 (2013).

[CAS](#) [PubMed](#) [PubMed Central](#) [Article](#) [Google Scholar](#)

21. 21.

Reitner, J. Modern cryptic microbialite/metazoan facies from Lizard Island (Great Barrier Reef, Australia) – formation and concepts. *Facies* **29**, 3–39 (1993).

[Article](#) [Google Scholar](#)

22. 22.

Neuveiler, F., Daoust, I., Bourque, P.-A. & Burdige, D. J. Degradative calcification of a modern siliceous sponge from the Great Bahama Bank, The Bahamas: a guide for interpretation of ancient sponge-bearing limestones. *J. Sediment. Res.* **77**, 552–563 (2007).

[CAS](#) [Article](#) [ADS](#) [Google Scholar](#)

23. 23.

Neuveiler, F., Turner, E. C. & Burdige, D. Early Neoproterozoic origin of the metazoan clade recorded in carbonate rock texture. *Geology* **37**, 475–478 (2009).

[Article](#) [ADS](#) [Google Scholar](#)

24. 24.

Gürich, G. Les spongiostromides du Viséen de la Province de Namur. *Mém. Musée R. d'Hist. Nat. Belg.* **3**, 1–55 (1906).

[Google Scholar](#)

25. 25.

Gürich, G. Spongiostromidae – eine neue Familie krustenbildender Organismen aus dem Kohlenkalk von Belgien. *Neues Jahrb. Min. Geol. Paläont.* **1**, 131–138 (1907).

[Google Scholar](#)

26. 26.

Kershaw, S., Li, Q. & Li, Y. Addressing Phanerozoic carbonate facies conundrum – sponges or clotted micrite? Evidence from Early Silurian reefs, South China Block. *The Sed. Record (Washington)* **19**, 3–10 (2021).

[Google Scholar](#)

27. 27.

Lee, J.-H. & Riding, R. The ‘classic stromatolite’ *Cryptozoön* is a keratose sponge-microbial consortium. *Geobiol.* **19**, 189–198 (2021).

[CAS](#) [Article](#) [ADS](#) [Google Scholar](#)

28. 28.

Vologdin, A. G. *The Oldest Algae of the USSR* (in Russian) (USSR Academy of Sciences, 1962).

29. 29.

Shapovalova, I. G. *Stratigraphy and Stromatolites of the Riphean of the Northern Part of the Judomian – Maisk Trough* (in Russian) (Nauka, 1974).

30. 30.

van Acken, D., Thomson, D., Rainbird, R. H. & Creaser, R. A. Constraining the depositional history of the Neoproterozoic Shaler Supergroup, Amundsen Basin, NW Canada: Rhenium–osmium dating of black shales from the Wynnatt and Boot Inlet Formations. *Precambr. Res.* **236**, 124–131 (2013).

[Article](#) [ADS](#) [CAS](#) [Google Scholar](#)

31. 31.

Greenman, W., Rainbird, R. H. & Turner, E. C. High-resolution correlation between contrasting early Tonian carbonate successions in NW Canada highlights pronounced global carbon isotope variations. *Precambr. Res.* **346**, 105816 (2020).

[CAS](#) [Article](#) [ADS](#) [Google Scholar](#)

32. 32.

Turner, E. C. & Long, D. G. F. *Formal definition of the Neoproterozoic Mackenzie Mountains Supergroup (NWT), and formal stratigraphic nomenclature for its carbonate and evaporite formations (Geological Survey of Canada. Open File 7112)* (Geological Survey of Canada, 2012)

33. 33.

Turner, E. C., Narbonne, G. M. & James, N. P. Neoproterozoic reef microstructures from the Little Dal Group, northwestern Canada. *Geology* **21**, 259–262 (1993).

[Article](#) [ADS](#) [Google Scholar](#)

34. 34.
Turner, E. C., James, N. P. & Narbonne, G. M. Growth dynamics of Neoproterozoic calcimicrobial reefs, Mackenzie Mountains, northwest Canada. *J. Sediment. Res.* **67**, 437–450 (1997).
- [CAS](#) [Google Scholar](#)
35. 35.
Turner, E. C., Narbonne, G. M. & James, N. P. Framework composition of early Neoproterozoic calcimicrobial reefs and associated microbialites, Mackenzie Mountains, N.W.T. In *Carbonate Sedimentation and Diagenesis in the Evolving Precambrian World (SEPM Special Publication 67)* (ed. Grotzinger, J. P. & James, N. P.) 179–205 (SEPM, 2000).
36. 36.
Turner, E. C., James, N. P. & Narbonne, G. M. Taphonomic control on microstructure in early Neoproterozoic reefal stromatolites and thrombolites. *Palaios* **15**, 87–111 (2000).
- [Article](#) [ADS](#) [Google Scholar](#)
37. 37.
Park, J. et al. Crouching shells, hidden sponges: unusual Late Ordovician cavities containing sponges. *Sedim. Geol.* **347**, 1–9 (2017).
- [CAS](#) [Article](#) [ADS](#) [Google Scholar](#)
38. 38.
Lee, J.-H., Hong, J., Lee, D.-J. & Choh, S.-J. A new Middle Ordovician bivalve–siliceous sponge–microbe reef-building consortium from north China. *Palaeogeog. Palaeoclim. Palaeoecol.* **457**, 23–30 (2016).
- [Article](#) [ADS](#) [Google Scholar](#)
39. 39.
Kobluk, D. R. & James, N. P. Cavity-dwelling organisms in Lower Cambrian patch reefs from southern Labrador. *Lethaia* **12**, 193–218 (1979).

[Article](#) [Google Scholar](#)

40. 40.

Hong, J., Choh, S.-J. & Lee, D.-J. Tales from the crypt: early adaptation of cryptobiontic sessile metazoans. *Palaios* **29**, 95–100 (2014).

[Article](#) [ADS](#) [Google Scholar](#)

41. 41.

Och, L. M. & Shields-Zhou, G. A. The Neoproterozoic oxygenation event: environmental perturbations and biogeochemical cycling. *Earth Sci. Rev.* **110**, 26–57 (2012).

[CAS Article](#) [ADS](#) [Google Scholar](#)

42. 42.

Mills, D. B. et al. Oxygen requirements of the earliest animals. *Proc. Natl Acad. Sci. USA* **111**, 4168–4172 (2014).

[CAS](#) [PubMed](#) [PubMed Central](#) [Article](#) [ADS](#) [Google Scholar](#)

43. 43.

Turner, E. C. & Bekker, A. Thick sulfate evaporite accumulations marking a mid-Neoproterozoic oxygenation event (Ten Stone Formation, NWT, Canada). *Geol. Soc. Am. Bull.* **128**, 203–222 (2016).

[CAS](#) [Google Scholar](#)

44. 44.

Lenton, T. M., Boyle, R. A., Poulton, S. W., Shields-Zhou, G. A. & Butterfield, N. J. Coevolution of eukaryotes and ocean oxygenation in the Neoproterozoic. *Nat. Geosci.* **7**, 257–265 (2014).

[CAS Article](#) [ADS](#) [Google Scholar](#)

45. 45.

Butterfield, N. J. The Neoproterozoic. *Curr. Biol.* **25**, R859–R863 (2015).

[CAS](#) [PubMed](#) [Article](#) [Google Scholar](#)

46. 46.

Wood, R. *Reef Evolution* (Oxford Univ. Press, 1999).

47. 47.

Loron, C. C., Rainbird, R. H., Turner, E. C., Greenman, W. J. & Javaux, E. J. Organic-walled microfossils from the late Meso- to early Neoproterozoic lower Shaler Supergroup (Arctic Canada): diversity and biostratigraphic significance. *Precambr. Res.* **321**, 349–374 (2019).

[CAS](#) [Article](#) [ADS](#) [Google Scholar](#)

48. 48.

Loron, C. C. et al. Early fungi from the Proterozoic era in Arctic Canada. *Nature* **570**, 232–235 (2019).

[CAS](#) [PubMed](#) [Article](#) [ADS](#) [Google Scholar](#)

49. 49.

Strother, P. K. et al. A possible billion-year-old holozoon with differentiated multicellularity. *Curr. Biol.* **31**, 2658–2665.e2 (2021).

[CAS](#) [PubMed](#) [Article](#) [Google Scholar](#)

50. 50.

Leslie, C. D. *Detrital Zircon Geochronology and Rift Related Magmatism: Central Mackenzie Mountains, Northwest Territories*. Unpublished MSc thesis, Univ. of British Columbia (2009).

51. 51.

Milton, J. E., Hickey, K. A., Gleeson, S. A. & Friedman, R. M. New U-Pb constraints on the age of the Little Dal basalts and Gunbarrel-related volcanism in Rodinia. *Precambr. Res.* **296**, 168–180 (2017).

[CAS](#) [Article](#) [ADS](#) [Google Scholar](#)

[Download references](#)

Acknowledgements

Field work and sample preparation were supported by Natural Sciences and Engineering Research Council (NSERC) Discovery Grants (E.C.T.), and the Agouron Institute (2016), based on locations initially discovered during post-graduate work on microbialites funded through the NSERC grants of G. M. Narbonne and N.P. James.

Author information

Affiliations

1. Harquail School of Earth Sciences, Laurentian University, Sudbury, Ontario, Canada

Elizabeth C. Turner

Authors

1. Elizabeth C. Turner
[View author publications](#)

You can also search for this author in [PubMed](#) [Google Scholar](#)

Contributions

E.C.T. conducted all aspects of the study.

Corresponding author

Correspondence to [Elizabeth C. Turner](#).

Ethics declarations

Competing interests

The author declares no competing interests.

Additional information

Peer review information *Nature* thanks Jeong-Hyun Lee, Joachim Reitner, Robert Riding and the other, anonymous, reviewer(s) for their contribution to the peer review of this work. Peer reviewer reports are available.

Publisher's note Springer Nature remains neutral with regard to jurisdictional claims in published maps and institutional affiliations.

Extended data figures and tables

Extended Data Fig. 1 Vermiform microstructure of microfacies i.

Elaboration of Fig. 2d. **a**, Vermiform microstructure is intercalated with detrital sediment (lower 1/3 of image) that includes calcimicrobialite clasts. **b**, Three-dimensional meshwork of vermiform microstructure transected by the plane of the 30- μm -thick thin section shows anastomosing tubule system; enlarged from **a**. **c**, Anastomosing tubules occluded by clear blocky calcite enclosed by cloudy calcite groundmass of slightly smaller crystals; enlarged from **b**. The tubules have no constructional walls and are defined by the dark enclosing groundmass. Oriented sample MV63 in plane-polarized transmitted light.

Extended Data Fig. 2 Vermiform microstructure of microfacies i.

Elaboration of Fig. 2e. **a**, Vermiform microstructure in a shelter void beneath an irregular microbialite clast and floored by angular reef clasts in carbonate mud, from a reef-top depression. Fibrous isopachous marine calcite cement lined the pore before its occupation by the vermiform mass. **b**, Three-dimensional meshwork of vermiform microstructure transected by the plane of the 30- μm -thick thin section shows anastomosing tubule system; enlarged from **a**. **c**, Anastomosing tubules occluded by clear blocky calcite enclosed by cloudy calcite groundmass of slightly smaller crystals; enlarged from **b**. The tubules have no constructional walls and are defined by the dark enclosing groundmass. Oriented sample KEC25 in plane-polarized transmitted light.

Extended Data Fig. 3 Spatial-temporal relationships among vermiform microstructure, geopetal detrital sediment and marine cement that collectively fill reef framework voids of microfacies ii.

Elaboration of Fig. 2f. **a**, Reef framework void among non-calcimicrobial stromatolites of reef stage II. Detrital sediment (DS) occupies lowest part of the void. Much of the void is occupied by vermiform microstructure (V); uppermost parts of the void are occupied by marine cement (MC) and local burial cement (BC). **b**, Detrital sediment accumulation, which includes quartz silt (transparent white particles); enlarged from **a**. **c**, Upper part of void is lined by isopachous cloudy marine calcite cement (arrow) (MC) and the remaining porosity occluded by burial calcite cement (pale) (BC); enlarged from **a**. **d**, Enlargement from **c** to demonstrate cloudy, isopachous, fibrous nature of the marine calcite cement, versus more transparent,

equant, blocky shape of burial cement that occupies the small amount of pore space remaining after accumulation of geopetal sediment, growth of vermiform microstructure and precipitation of marine cement. **e**, Moderately preserved vermiform microstructure; enlarged from **a**. Oriented sample DL32a from reef stage II, in plane-polarized transmitted light.

Extended Data Fig. 4 Associations of vermiform microstructure, micritic microbialite columns and detrital sediment in microfacies i and iiia.

Elaboration of Fig. 2g–k. **a**, Low-magnification image of two irregular microbialite columns and inter-column sediment (outlined by white dashed line). **b**, Vermiform microstructure is intermingled with muddy microbialite in column interior; enlarged from **a**. **c**, Vermiform microstructure intercalated with inter-column sediment; enlarged from **a**. **d**, Vermiform microstructure encrusting the margin of a microbialite column; enlarged from **a**. Sample KES23, from reef stage II, in plane-polarized transmitted light; sample is from a resedimented reef clast and is oriented on the basis of geopetal structures out of the field of view.

Extended Data Fig. 5 Spatial and textural association of vermiform microstructure and geopetal peloids in microfacies iiib.

This association suggests that geopetal peloid accumulations are a taphonomic product derived through poor preservation of vermiform microstructure. **a**, Poorly preserved vermiform microstructure (arrowed; inset c) adjacent to laminar to lenticular voids containing geopetal peloid accumulations (arrowed; inset b) in cement-rich non-calcimicrobial stromatolites of reef stage V. Oriented IR drillcore sample RT A19-495.4' in plane-polarized transmitted light.

Supplementary information

Reporting Summary

Peer Review File

Rights and permissions

Open Access This article is licensed under a Creative Commons Attribution 4.0 International License, which permits use, sharing, adaptation, distribution and reproduction in any medium or format, as long as you give appropriate credit to the original author(s) and the source, provide a link to the Creative Commons license, and

indicate if changes were made. The images or other third party material in this article are included in the article's Creative Commons license, unless indicated otherwise in a credit line to the material. If material is not included in the article's Creative Commons license and your intended use is not permitted by statutory regulation or exceeds the permitted use, you will need to obtain permission directly from the copyright holder. To view a copy of this license, visit <http://creativecommons.org/licenses/by/4.0/>.

Reprints and Permissions

About this article



Check for
updates

Cite this article

Turner, E.C. Possible poriferan body fossils in early Neoproterozoic microbial reefs. *Nature* **596**, 87–91 (2021). <https://doi.org/10.1038/s41586-021-03773-z>

Download citation

- Received: 30 April 2021
- Accepted: 28 June 2021
- Published: 28 July 2021
- Issue Date: 05 August 2021
- DOI: <https://doi.org/10.1038/s41586-021-03773-z>

Further reading

- [**Sponge-like fossil could be Earth's earliest known animal**](#)

- Max Kozlov

Nature (2021)

Comments

By submitting a comment you agree to abide by our [Terms](#) and [Community Guidelines](#). If you find something abusive or that does not comply with our terms or guidelines please flag it as inappropriate.

[Download PDF](#)

Associated Content

[Strange patterns could be the world's oldest animal fossil](#)

- Nick Petrić Howe

Advertisement

This article was downloaded by **calibre** from <https://www.nature.com/articles/s41586-021-03773-z>

| [Section menu](#) | [Main menu](#) |

- Article
- [Published: 28 July 2021](#)

Molecular architecture of the developing mouse brain

- [Gioele La Manno](#)^{1,2 na1},
- [Kimberly Siletti](#)^{1 na1},
- [Alessandro Furlan](#)^{1 nAff4},
- [Daniel Gyllborg](#) [ORCID: orcid.org/0000-0002-1429-6426](#)³,
- [Elin Vinsland](#)¹,
- [Alejandro Mossi Albiach](#) [ORCID: orcid.org/0000-0001-7009-4901](#)¹,
- [Christoffer Mattsson Langseth](#) [ORCID: orcid.org/0000-0003-2230-8594](#)³,
- [Irina Khven](#)²,
- [Alex R. Lederer](#)²,
- [Lisa M. Dratva](#) [ORCID: orcid.org/0000-0002-2873-6787](#)²,
- [Anna Johnsson](#)¹,
- [Mats Nilsson](#) [ORCID: orcid.org/0000-0001-9985-0387](#)³,
- [Peter Lönnerberg](#)¹ &
- [Sten Linnarsson](#) [ORCID: orcid.org/0000-0002-3491-3444](#)¹

[Nature](#) volume **596**, pages 92–96 (2021) [Cite this article](#)

- 7639 Accesses
- 245 Altmetric
- [Metrics details](#)

Subjects

- [Development of the nervous system](#)
- [Developmental neurogenesis](#)
- [Glial development](#)
- [Transcriptomics](#)

Abstract

The mammalian brain develops through a complex interplay of spatial cues generated by diffusible morphogens, cell–cell interactions and intrinsic genetic programs that result in probably more than a thousand distinct cell types. A complete understanding of this process requires a systematic characterization of cell states over the entire spatiotemporal range of brain development. The ability of single-cell RNA sequencing and spatial transcriptomics to reveal the molecular heterogeneity of complex tissues has therefore been particularly powerful in the nervous system. Previous studies have explored development in specific brain regions^{1,2,3,4,5,6,7,8}, the whole adult brain⁹ and even entire embryos¹⁰. Here we report a comprehensive single-cell transcriptomic atlas of the embryonic mouse brain between gastrulation and birth. We identified almost eight hundred cellular states that describe a developmental program for the functional elements of the brain and its enclosing membranes, including the early neuroepithelium, region-specific secondary organizers, and both neurogenic and gliogenic progenitors. We also used *in situ* mRNA sequencing to map the spatial expression patterns of key developmental genes. Integrating the *in situ* data with our single-cell clusters revealed the precise spatial organization of neural progenitors during the patterning of the nervous system.

Access options

Subscribe to Journal

Get full journal access for 1 year

\$199.00

only \$3.90 per issue

[Subscribe](#)

All prices are NET prices.

VAT will be added later in the checkout.

Tax calculation will be finalised during checkout.

Rent or Buy article

Get time limited or full article access on ReadCube.

from \$8.99

[Rent or Buy](#)

All prices are NET prices.

Additional access options:

- [Log in](#)
- [Access through your institution](#)
- [Learn about institutional subscriptions](#)

Fig. 1: Atlas of the developing mouse brain.

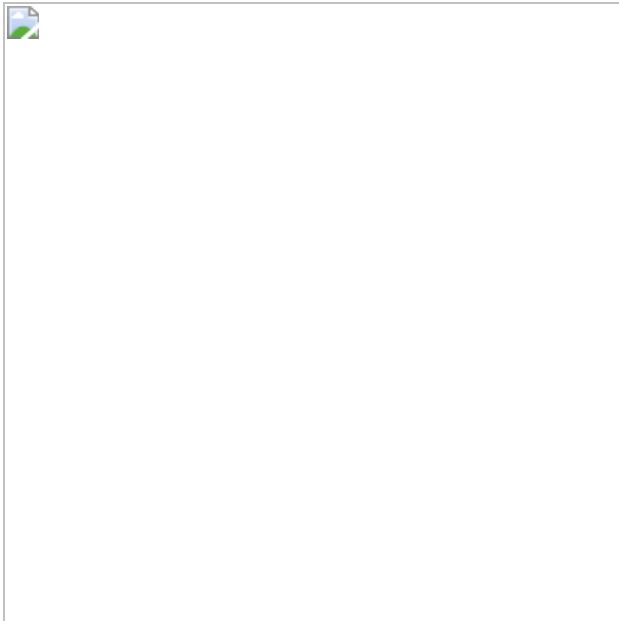


Fig. 2: Molecular diversity of neural tube organizers.

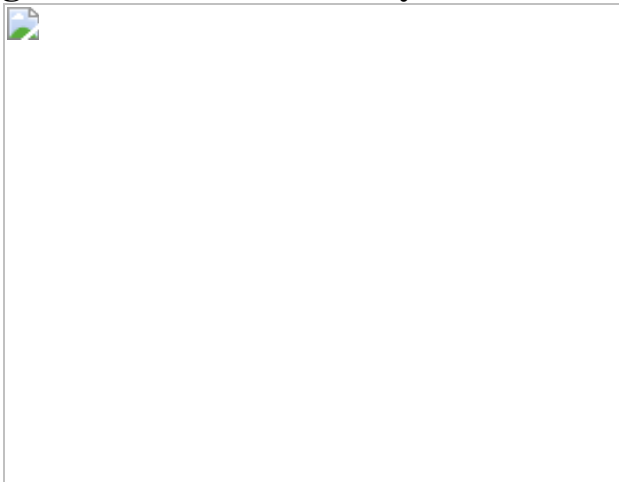
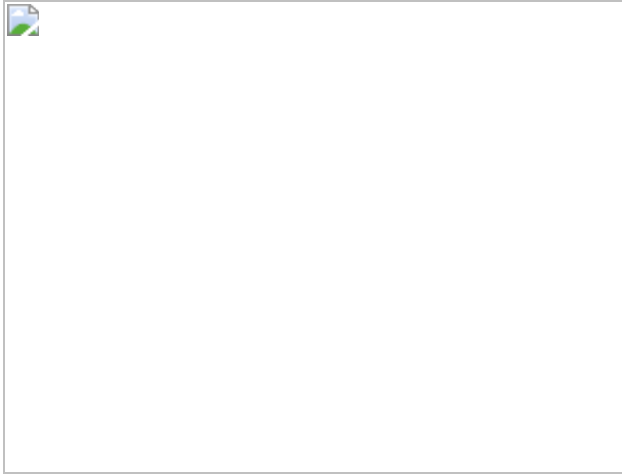


Fig. 3: Non-neuronal cell types.



Fig. 4: Spatial distributions of cell types and states.



Data availability

RNA-seq data are available at the Sequence Read Archive (<https://www.ncbi.nlm.nih.gov/sra>) under accession [PRJNA637987](#). HybISS data are available at <http://mousebrain.org/downloads>. Single-cell gastrulation data were downloaded from <https://github.com/MarioniLab/MouseGastrulationData>.

Code availability

Source code is available at <https://github.com/linnarsson-lab>.

References

1. 1.

Camp, J. G. et al. Human cerebral organoids recapitulate gene expression programs of fetal neocortex development. *Proc. Natl Acad. Sci. USA* **112**, 15672–15677 (2015).

[ADS](#) [CAS](#) [Article](#) [Google Scholar](#)

2. 2.

Pollen, A. A. et al. Molecular identity of human outer radial glia during cortical development. *Cell* **163**, 55–67 (2015).

[CAS](#) [Article](#) [Google Scholar](#)

3. 3.

Nowakowski, T. J. et al. Spatiotemporal gene expression trajectories reveal developmental hierarchies of the human cortex. *Science* **358**, 1318–1323 (2017).

[ADS](#) [CAS](#) [Article](#) [Google Scholar](#)

4. 4.

Zhong, S. et al. A single-cell RNA-seq survey of the developmental landscape of the human prefrontal cortex. *Nature* **555**, 524–528 (2018).

[ADS](#) [CAS](#) [Article](#) [Google Scholar](#)

5. 5.

Telley, L. et al. Temporal patterning of apical progenitors and their daughter neurons in the developing neocortex. *Science* **364**, eaav2522 (2019).

[CAS](#) [Article](#) [Google Scholar](#)

6. 6.

La Manno, G. et al. Molecular diversity of midbrain development in mouse, human, and stem cells. *Cell* **167**, 566–580.e19 (2016).

[Article](#) [Google Scholar](#)

7. 7.

Carter, R. A. et al. A single-cell transcriptional atlas of the developing murine cerebellum. *Curr. Biol.* **28**, 2910–2920.e2 (2018).

[CAS](#) [Article](#) [Google Scholar](#)

8. 8.

Zeisel, A. et al. Molecular architecture of the mouse nervous system. *Cell* **174**, 999–1014.e22 (2018).

[CAS](#) [Article](#) [Google Scholar](#)

9. 9.

Rosenberg, A. B. et al. Single-cell profiling of the developing mouse brain and spinal cord with split-pool barcoding. *Science* **360**, 176–182 (2018).

[ADS](#) [CAS](#) [Article](#) [Google Scholar](#)

10. 10.

Cao, J. et al. The single-cell transcriptional landscape of mammalian organogenesis. *Nature* **566**, 496–502 (2019).

[ADS](#) [CAS](#) [Article](#) [Google Scholar](#)

11. 11.

Siegenthaler, J. A. & Pleasure, S. J. in *Patterning and Cell Type Specification in the Developing CNS and PNS* (eds. Rubenstein, J. L. R. & Rakic, P.) 835–849 (Elsevier, 2013).

12. 12.

Niwa, H., Miyazaki, J. & Smith, A. G. Quantitative expression of Oct-3/4 defines differentiation, dedifferentiation or self-renewal of ES cells. *Nat. Genet.* **24**, 372–376 (2000).

[CAS](#) [Article](#) [Google Scholar](#)

13. 13.

Burtscher, I. & Lickert, H. Foxa2 regulates polarity and epithelialization in the endoderm germ layer of the mouse embryo. *Development* **136**, 1029–1038 (2009).

[CAS](#) [Article](#) [Google Scholar](#)

14. 14.

Li, L. et al. Location of transient ectodermal progenitor potential in mouse development. *Development* **140**, 4533–4543 (2013).

[CAS](#) [Article](#) [Google Scholar](#)

15. 15.

Zhang, X. et al. Pax6 is a human neuroectoderm cell fate determinant. *Cell Stem Cell* **7**, 90–100 (2010).

[CAS](#) [Article](#) [Google Scholar](#)

16. 16.

Hatakeyama, J. et al. Hes genes regulate size, shape and histogenesis of the nervous system by control of the timing of neural stem cell differentiation. *Development* **131**, 5539–5550 (2004).

[CAS](#) [Article](#) [Google Scholar](#)

17. 17.

Pijuan-Sala, B. et al. A single-cell molecular map of mouse gastrulation and early organogenesis. *Nature* **566**, 490–495 (2019).

[ADS](#) [CAS](#) [Article](#) [Google Scholar](#)

18. 18.

Tamai, H. et al. Pax6 transcription factor is required for the interkinetic nuclear movement of neuroepithelial cells. *Genes Cells* **12**, 983–996 (2007).

[CAS](#) [Article](#) [Google Scholar](#)

19. 19.

Alves dos Santos, M. T. M. & Smidt, M. P. En1 and Wnt signaling in midbrain dopaminergic neuronal development. *Neural Dev.* **6**, 23 (2011).

[CAS](#) [Article](#) [Google Scholar](#)

20. 20.

Schwarz, M. et al. Pax2/5 and Pax6 subdivide the early neural tube into three domains. *Mech. Dev.* **82**, 29–39 (1999).

[CAS](#) [Article](#) [Google Scholar](#)

21. 21.

Sato, S. et al. Regulation of Six1 expression by evolutionarily conserved enhancers in tetrapods. *Dev. Biol.* **368**, 95–108 (2012).

[CAS](#) [Article](#) [Google Scholar](#)

22. 22.

Dasgupta, K. & Jeong, J. Developmental biology of the meninges. *Genesis* **57**, e23288 (2019).

[Article](#) [Google Scholar](#)

23. 23.

DeSisto, J. et al. Single-cell transcriptomic analyses of the developing meninges reveal meningeal fibroblast diversity and function. *Dev. Cell* **54**, 43–59.e4 (2020).

[CAS](#) [Article](#) [Google Scholar](#)

24. 24.

Hammond, T. R. et al. Single-cell RNA sequencing of microglia throughout the mouse lifespan and in the injured brain reveals complex cell-state changes. *Immunity* **50**, 253–271.e6 (2019).

[CAS](#) [Article](#) [Google Scholar](#)

25. 25.

Lein, E. S. et al. Genome-wide atlas of gene expression in the adult mouse brain. *Nature* **445**, 168–176 (2007).

[ADS](#) [CAS](#) [Article](#) [Google Scholar](#)

26. 26.

Murdoch, J. N., Eddleston, J., Leblond-Bourget, N., Stanier, P. & Copp, A. J. Sequence and expression analysis of Nhlh1: a basic helix-loop-helix gene implicated in neurogenesis. *Dev. Genet.* **24**, 165–177 (1999).

[CAS](#) [Article](#) [Google Scholar](#)

27. 27.

Gyllborg, D. et al. Hybridization-based *in situ* sequencing (HybISS) for spatially resolved transcriptomics in human and mouse brain tissue. *Nucleic Acids Res.* **48**, e112 (2020).

[CAS](#) [Article](#) [Google Scholar](#)

28. 28.

Biancalani, T. et al. Deep learning and alignment of spatially-resolved whole transcriptomes of single cells in the mouse brain with Tangram. Preprint at <https://doi.org/10.1101/2020.08.29.272831> (2020).

29. 29.

Kinameri, E. et al. Prdm proto-oncogene transcription factor family expression and interaction with the Notch-Hes pathway in mouse neurogenesis. *PLoS ONE* **3**, e3859 (2008).

[ADS](#) [Article](#) [Google Scholar](#)

30. 30.

Sakamoto, T. & Ishibashi, T. Hyalocytes: essential cells of the vitreous cavity in vitreoretinal pathophysiology? *Retina* **31**, 222–228 (2011).

[CAS](#) [Article](#) [Google Scholar](#)

31. 31.

La Manno, G. et al. RNA velocity of single cells. *Nature* **560**, 494–498 (2018).

[ADS](#) [Article](#) [Google Scholar](#)

32. 32.

Gyllborg, D. & Nilsson, M. HybISS: hybridization-based in situ sequencing. *protocols.io.*, <https://doi.org/10.17504/protocols.io.xy4fpyw> (2020).

[Article](#) [Google Scholar](#)

33. 33.

Gopalan, P., Hofman, J. M. & Blei, D. M. Scalable recommendation with Poisson factorization. Preprint at <https://arxiv.org/abs/1311.1704> (2013).

34. 34.

Kobak, D. & Berens, P. The art of using *t*-SNE for single-cell transcriptomics. *Nat. Commun.* **10**, 5416 (2019).

[ADS](#) [Article](#) [Google Scholar](#)

35. 35.

Chalfoun, J. et al. MIST: accurate and scalable microscopy image stitching tool with stage modeling and error minimization. *Sci. Rep.* **7**, 4988 (2017).

[ADS](#) [Article](#) [Google Scholar](#)

[Download references](#)

Acknowledgements

We thank H. Hochgerner and A. Zeisel for advice; E. Arenas for assistance with anatomical annotation; P. Ernfors for supporting the work of A.F.; and the National Genomics Infrastructure for sequencing services. This work was supported by grants from the Knut and Alice Wallenberg Foundation (2015.0041 and 2018.0220 to S.L., and 2018.0172 to S.L. and M.N.), the Erling Persson Family Foundation (HDCA, to S.L. and M.N.), the Chan Zuckerberg Initiative, Torsten Söderberg Foundation and the Swedish Foundation for Strategic Research (RIF 15-0057 and SB16-0065) to S.L., Hjärnfonden (PS2018-0012) to D.G., the Chan Zuckerberg Initiative DAF, an advised fund of Silicon Valley Community Foundation (2018-191929) to M.N., and the Swiss National Science Foundation (CRSK-3_190495 and PZ00P3_193445) and the School of Life Sciences – EPFL to G.L.M. K.S. was supported by the European Molecular Biology Organization (ALTF 1015-2018).

Author information

Author notes

1. Alessandro Furlan

Present address: Cold Spring Harbor Laboratory, Cold Spring Harbor, NY, USA

2. These authors contributed equally: Gioele La Manno, Kimberly Siletti

Affiliations

1. Division of Molecular Neurobiology, Department of Medical Biochemistry and Biophysics, Karolinska Institute, Stockholm, Sweden

Gioele La Manno, Kimberly Siletti, Alessandro Furlan, Elin Vinsland, Alejandro Mossi Albiach, Anna Johnsson, Peter Lönnerberg & Sten Linnarsson

2. Brain Mind Institute, School of Life Sciences, École Polytechnique Fédérale de Lausanne, Lausanne, Switzerland

Gioele La Manno, Irina Khven, Alex R. Lederer & Lisa M. Dratva

3. Science for Life Laboratory, Department of Biochemistry and Biophysics, Stockholm University, Solna, Sweden

Daniel Gyllborg, Christoffer Mattsson Langseth & Mats Nilsson

Authors

1. Gioele La Manno

[View author publications](#)

You can also search for this author in [PubMed](#) [Google Scholar](#)

2. Kimberly Siletti

[View author publications](#)

You can also search for this author in [PubMed](#) [Google Scholar](#)

3. Alessandro Furlan

[View author publications](#)

You can also search for this author in [PubMed](#) [Google Scholar](#)

4. Daniel Gyllborg

[View author publications](#)

You can also search for this author in [PubMed](#) [Google Scholar](#)

5. Elin Vinsland

[View author publications](#)

You can also search for this author in [PubMed](#) [Google Scholar](#)

6. Alejandro Mossi Albiach

[View author publications](#)

You can also search for this author in [PubMed](#) [Google Scholar](#)

7. Christoffer Mattsson Langseth

[View author publications](#)

You can also search for this author in [PubMed](#) [Google Scholar](#)

8. Irina Khven

[View author publications](#)

You can also search for this author in [PubMed](#) [Google Scholar](#)

9. Alex R. Lederer

[View author publications](#)

You can also search for this author in [PubMed](#) [Google Scholar](#)

10. Lisa M. Dratva

[View author publications](#)

You can also search for this author in [PubMed](#) [Google Scholar](#)

11. Anna Johnsson

[View author publications](#)

You can also search for this author in [PubMed](#) [Google Scholar](#)

12. Mats Nilsson

[View author publications](#)

You can also search for this author in [PubMed](#) [Google Scholar](#)

13. Peter Lönnerberg

[View author publications](#)

You can also search for this author in [PubMed](#) [Google Scholar](#)

14. Sten Linnarsson

[View author publications](#)

You can also search for this author in [PubMed](#) [Google Scholar](#)

Contributions

S.L. supervised the project. S.L. and G.L.M. conceived the study design. G.L.M., K.S. and S.L. analysed, annotated and interpreted the single-cell data and wrote the manuscript. G.L.M. and A.F. performed the single-cell experiments. A.F. dissociated embryos. A.J. prepared sequencing libraries. P.L. and S.L. built the companion website. E.V., D.G. and C.M.L. performed *in situ* sequencing experiments. A.M.A. performed and analysed smFISH experiments. E.V. prepared tissue sections and performed anatomical annotation. K.S., I.K., A.R.L., G.L.M. and C.M.L. analysed and interpreted *in situ* sequencing data. L.M.D. performed clustering sensitivity analysis. M.N. supervised *in situ* sequencing experiments. All authors critically reviewed the manuscript and approved the final version.

Corresponding authors

Correspondence to [Gioele La Manno](#) or [Sten Linnarsson](#).

Ethics declarations

Competing interests

M.N. serves as a scientific advisor for 10x Genomics. All other authors declare no competing financial interests.

Additional information

Peer review information *Nature* thanks Jennie Close, Mario Suva and the other, anonymous, reviewer(s) for their contribution to the peer review of this work. Peer reviewer reports are available.

Publisher's note Springer Nature remains neutral with regard to jurisdictional claims in published maps and institutional affiliations.

Extended data figures and tables

[Extended Data Fig. 1 Experimental design and data quality.](#)

a, Stereo microscope photographs illustrating the tissue dissection strategy. **b**, Samples composing the dataset. The area of each circle is proportional to the number of cells sampled. Colour indicates the region dissected. **c**, Histogram showing the distribution of number of UMIs per cell detected across the entire dataset. **d**, Histogram showing the distribution of number of genes detected per cell across the entire dataset. **e**, Distribution of UMIs per cell aggregated per age group. **f**, Distribution of number of genes detected per cell aggregated per age group.

[Extended Data Fig. 2 Global properties of gene expression during brain development.](#)

a, Erythrocyte clusters expressing *Hbb-bhl* (>500 UMIs per cell) (primitive erythropoiesis) or *Hbb-bs* (>5,000 UMIs per cell) (definitive erythropoiesis). **b**, Histogram of cell cycle scores (left) and cell cycle scores

indicated on the main *t*-SNE (right). **c**, Distribution of total UMIs per cell. **d**, Distribution of total number of genes detected per cell. **e**, Distribution of the fraction of unspliced reads detected per cell. **f**, Average *z* score for a set of genes with GO term related to the spliceosome. **g**, Number of clusters observed for each major cell class, as a function of varying hyperparameters of the clustering algorithm (indicated, left). Top row shows the default clustering. Each subsequent row varies one or more hyperparameters (number of genes selected, number of HPF components and the stop condition), resulting in different numbers of clusters per class. Deviations from the default settings are indicated by the colours. **h**, Confusion matrix comparing clustering results for neurons using default settings (vertical axis) and clustering using only 500 genes (horizontal axis). **i**, Same as **h**, but for radial glia. The expression of key marker genes is indicated along the axes to reveal major subclasses. **j**, Distribution of major classes of cells by gestational age.

Extended Data Fig. 3 Computational methods.

a, Illustration of HPF on a small subset of cells using 32 components, showing component loadings across cells for components 4 and 2, illustrating the modularity of components. **b**, Loadings of all components for two single cells, illustrating the sparseness of components; each cell is approximated by a small number of non-negative components. **c**, Scatter plot showing observed expression of all genes in all cells, versus predicted expression based on 96 HPF components. Ninety-three per cent of data points were located inside the 95% confidence intervals of the Poisson distribution, demonstrating the accuracy of the HPF representation. **d**, HPF analysis of all neuronal cells from the full dataset using 32 components, showing that HPF captures essential features of forebrain neurogenesis. Each subplot shows a *t*-SNE coloured by component loading, a list of genes with high loading in the component, and a bar chart and histogram showing the regional distributions of cells. Nine selected components are shown, related to forebrain based on the regional distribution of cells with high loadings. **e**, Example of cells (blue) that fall within a Jensen–Shannon distance of 0.36 of a single cell (black circle), corresponding to 0.5 bits of Shannon entropy. **f**, The relationship between the Kullback–Leibler divergence and the Jensen–Shannon distance, showing that in this case 0.36

JSD corresponds to 0.5 bits. **g**, Two virtual cells (Poisson samples drawn from a single HPF vector), showing the distribution of pure Poisson expression noise. **h**, The effect of switching two HPF components, resulting in a change in expression of many genes and a Jensen–Shannon distance of 0.68 bits. **i**, The ‘curse’ of dimensionality. As the number of HPF components is increased, the difference in Jensen–Shannon distance between nearest-neighbours and far-away cells on the manifold decreases.

Extended Data Fig. 4 Emergence of cell-type heterogeneity from gastrulation to neurulation.

a, Scheme of tissue sampling between E7 and E8.5. **b**, *t*-SNE from Fig. 1 overlaid with cells sampled E7–E8.5 and belonging to dendrogram clades 1–4. **c**, *t*-SNE overlaid with expression of lineage-specific marker genes. **d**, Uniform manifold approximation and projection (UMAP) of the mouse gastrulation single-cell atlas from ref. ¹⁷. **e**, Cells from **b** projected onto the embedding in **d**¹⁷. **f**, Pairwise correlation between neurulation-stage clusters of this Article and those of ref. ¹⁷. **g–i**, UMAP embedding of cells of the first (**g**), second (**h**) and third (**i**) cluster clade of the dendrogram. Cells are coloured and labelled by cluster identity. **j–l**, Heat map showing genes enriched in of the first (**j**), second (**k**) and third (**l**) cluster clade. **m**, UMAP embedding of subclustered neuroepithelial cells obtained from time points E7–E8.5. Cells are coloured by cluster. **n**, Heat map displaying expression of genes enriched in each of the neuroepithelial populations. **o**, Expression of broad neuroepithelial markers overlaid on the UMAP in **m**. **p**, Bar plot reporting the number of E7–E8.5 cells that clustered with the indicated neuroblast clusters. Clusters are sorted by number of cells. Bars are coloured as in **l**. **q**, Bar plots showing the dissection origins of the cells belonging to the clusters in **p**. **r**, UMAP representation of the E8.5 cells belonging to clusters no. 377, no. 366 and no. 338 (top left), and overlaid with expression of enriched transcription factors.

Extended Data Fig. 5 Characterization of molecular identity and signal-receptor repertoire of neural tube organizers.

a, Cell types sorted on the basis of the average Z score of morphogens genes grouped in categories on the basis of gene family and neurulation literature. Hedgehog, *Shh* and *Ptch1*; R-spondins, *Rspo1*, *Rspo2*, *Rspo3* and *Rspo4*; Wnts, *Wnt1*, *Wnt3a*, *Wnt5a* and *Wnt8b*; neuregulins, *Nrg1*, *Nrg3* and *Fgf7*; Fgfs, *Fgf8*, *Fgf15*, *Fgf17* and *Fgf18*; Bmps, *Bmp6*, *Bmp7* and *Gdf7*. Cell types displayed in red were localized and analysed in Fig. 2 and in the panels below. **b**, Summary of the plots in a showing the maximum average z score achieved. **c**, Beeswarm plots showing the expression of a selection of transcription factors that were found to be enriched in the different organizer cell populations. **d**, Beeswarm plots showing the gene expression of enriched receptors and ligands with a distribution in relation to organizers that, to our knowledge, had not previously been described. Genes in c, d were selected for HybISS profiling (Fig. 4).

Extended Data Fig. 6 Glial diversity.

a, Cells from clusters 172 to 320 were pulled from the complete dataset, and a t -SNE embedding was calculated. The dendrogram was cut into 15 metaclusters. Cells are coloured by their original cluster (left) and metacluster cut from the dendrogram (right). **b**, Cells are coloured by their labels for differential gene-expression testing: brown, glioblast; coral, neurogenic; grey, not included in testing. **c**, Select genes are annotated on a volcano plot illustrating differential expression between neurogenic and gliogenic radial glia. The dotted line denotes the significance threshold ($q = 10^{-5}$). The range of the x axis was chosen to capture statistically significant genes. Cell-cycle genes are coloured red. **d**, For each metacluster, the size of the bar indicates the percentage of cells from each tissue (top), each embryonic stage (middle) or that are cycling ($>1\%$ cell-cycle UMIs) (bottom). **e**, Expression dot plots are shown for select genes. The size of the dot represents the fraction of cells expressing a gene. The colour represents normalized mean expression, in which the mean expression for each gene is normalized by the maximum mean expression of the gene across the metaclusters. **f**, Cells selected for region classification are coloured on the t -SNE. Grey cells were not selected. **g**, For a range of parameter values (max_features), a gradient boosting classifier was fit to each training set and tested on the five remaining training sets, coloured as in f. Average precision, recall and F1 scores are plotted for each parameter

value and training set. **h**, F1 scores for each gradient boosting classifier (max_features = 50) are shown for forebrain, midbrain and hindbrain cells. The colour of each line indicates which cells were used to train the classifier (coloured as in **g**). **i**, Feature importance for each gradient boosting classifier was used to rank genes, and the intersection of the 100 most important genes for all 6 classifiers is shown on the *x* axis. Expression dot plots are shown for each of these genes in radial glia, glioblasts and OPCs from the forebrain, midbrain and hindbrain. **j**, Cells are coloured by log-transformed gene expression for the indicated genes. Grey indicates no expression. **k**, Cells that are positive for both *Egfr* and *Dll1* are coloured blue.

Extended Data Fig. 7 Fibroblasts.

Cells from clusters 109 to 125 were pulled from the dataset, and a *t*-SNE embedding was calculated. **a**, Cells are coloured by their clusters. Putative doublets are grey. **b**, Cells are coloured by their tissues of origin. **c**, Cycling cells (>1% cell-cycle UMIs) are coloured blue. **d**, Expression dot plots are shown for select genes. **e**, Cells from the indicated embryonic age are coloured blue on each *t*-SNE. **f**, Cells are coloured if they express the indicated gene. **g**, Multiplexed single-molecule RNA fluorescence *in situ* hybridization for six marker genes (columns) at three different ages (rows). Cartoons on the left indicate the approximate location of each image. Cartoons on the right show an interpretation of the observed gene expression patterns. This experiment was performed once.

Extended Data Fig. 8 Immune cells.

Cells from clusters 157 to 171 were pulled from the dataset, and a *t*-SNE embedding was calculated. **a**, Cells coloured by their clusters. Putative doublets are grey. Infiltrating immune includes six clusters, starred in **d**. ATM, axon tract-associated microglia; MGL, microglia; PVM, perivascular macrophage. **b**, Cells coloured by their tissues of origin. **c**, Cycling cells (>1% cell-cycle UMIs) coloured blue. **d**, Expression dot plots shown for select genes. **e**, Cells from the indicated gestational age coloured blue on each *t*-SNE.

Extended Data Fig. 9 Pseudolineage analysis and neurogenesis.

a, Pseudolineage tree algorithm, computing shortest paths to the root cell passing only through neighbours inside the information radius (that is, neighbours within a fixed maximum Jensen–Shannon distance). **b**, Isolating the pseudolineages terminating in a selected cluster, and projecting to the pseudoage axis. **c**, Ten selected pseudolineages coloured by major class, on the t-SNE of Fig. 1 with grey scale showing the geodesic distance to the root from every cell. **d**, The same ten selected pseudolineages coloured by tissue. **e–i**, Pseudolineages of astrocytes (**e**), OPCs (**f**), fibroblasts (**g**), cortical excitatory neurons (**h**), forebrain GABAergic neurons (**i**), midbrain dopaminergic neurons (**j**) and hindbrain serotonergic neurons (**k**). Each plot shows a randomly selected subset of pseudolineages terminating in the indicated clusters, as well as expression of selected genes in pseudoage bins along the lineage (calculated for all cells in the lineage). The region and class of each cell is indicated at the bottom. **l**, Expression of *Nhlh1* and *Nhlh2*. **m**, In situ hybridization for *Nhlh1* and *Nhlh2* on sagittal sections of the E115 mouse embryo (Allen Brain Atlas). **n**, RNA in situ hybridization of mouse embryonic brain at the indicated time points, showing genes relevant to the cortical lineage (image credit: Allen Institute). Each subpanel shows a strip from ventricular zone to pia at four different ages.

Extended Data Fig. 10 Spatial mapping of single-cell clusters.

a, Expression of *Shh* detected by in situ sequencing on all sections, with close up images showing the detection of individual mRNA molecules. Inset shows the expression of *Shh* by in situ hybridization (Allen Brain Atlas) for reference. **b**, Manually curated anatomical annotation of all tissue sections (coloured as in the Allen Brain Atlas). **c**, Illustration of Tangram (mapping single cells to spatial voxels) and our generalized Tangram (mapping clusters to voxels). **d**, Inferred spatial distribution of roof plate organizers (clusters no. 213, no. 214 and no. 39). **e**, Inferred spatial distribution of cluster no. 206 on all tissue sections. **f**, Imputed expression of *Prdm12*, shown for four informative sections (left) and Allen Brain Atlas ground truth (right). **g**, Spatial gene expression of *Pax6* and imputed gene expression of dorsal (*Mitf* and *Vsx2*) and ventral (*Vax2* and *Pax2*) optic vesicle markers in the left and right eye.

Supplementary information

Reporting Summary

Supplementary Table 1

Sample metadata.

Supplementary Table 2

Cluster annotations and metadata.

Supplementary Table 3

Oligonucleotides used for HybISS.

Peer Review File

Rights and permissions

Reprints and Permissions

About this article



Check for
updates

Cite this article

La Manno, G., Siletti, K., Furlan, A. *et al.* Molecular architecture of the developing mouse brain. *Nature* **596**, 92–96 (2021).
<https://doi.org/10.1038/s41586-021-03775-x>

Download citation

- Received: 01 July 2020
- Accepted: 28 June 2021
- Published: 28 July 2021
- Issue Date: 05 August 2021
- DOI: <https://doi.org/10.1038/s41586-021-03775-x>

Comments

By submitting a comment you agree to abide by our [Terms](#) and [Community Guidelines](#). If you find something abusive or that does not comply with our terms or guidelines please flag it as inappropriate.

[Access through your institution](#)

[Change institution](#)

[Buy or subscribe](#)

Advertisement

This article was downloaded by **calibre** from <https://www.nature.com/articles/s41586-021-03775-x>

- Article
- [Published: 21 July 2021](#)

Gut cytokines modulate olfaction through metabolic reprogramming of glia

- [Xiaoyu Tracy Cai](#)^{1,2,3},
- [Hongjie Li](#)^{4,5,6},
- [Martin Borch Jensen](#)^{2,7},
- [Elie Maksoud](#)²,
- [Jovencio Borneo](#)⁸,
- [Yuxin Liang](#)⁹,
- [Stephen R. Quake](#) [ORCID: orcid.org/0000-0002-1613-0809](#)^{10,11},
- [Liqun Luo](#) [ORCID: orcid.org/0000-0001-5467-9264](#)⁴,
- [Pejmun Haghghi](#)² &
- [Heinrich Jasper](#) [ORCID: orcid.org/0000-0002-6014-4343](#)^{1,2}

[Nature](#) volume **596**, pages 97–102 (2021) [Cite this article](#)

- 6871 Accesses
- 70 Altmetric
- [Metrics details](#)

Subjects

- [Ageing](#)
- [Antimicrobial responses](#)
- [Neurophysiology](#)

Abstract

Infection-induced aversion against enteropathogens is a conserved sickness behaviour that can promote host survival^{1,2}. The aetiology of this behaviour remains poorly understood, but studies in *Drosophila* have linked olfactory and gustatory perception to avoidance behaviours against toxic microorganisms^{3,4,5}. Whether and how enteric infections directly influence sensory perception to induce or modulate such behaviours remains unknown. Here we show that enteropathogen infection in *Drosophila* can modulate olfaction through metabolic reprogramming of ensheathing glia of the antennal lobe. Infection-induced unpaired cytokine expression in the intestine activates JAK–STAT signalling in ensheathing glia, inducing the expression of glial monocarboxylate transporters and the apolipoprotein *glial lazillo* (*GLaz*), and affecting metabolic coupling of glia and neurons at the antennal lobe. This modulates olfactory discrimination, promotes the avoidance of bacteria-laced food and increases fly survival. Although transient in young flies, gut-induced metabolic reprogramming of ensheathing glia becomes constitutive in old flies owing to age-related intestinal inflammation, which contributes to an age-related decline in olfactory discrimination. Our findings identify adaptive glial metabolic reprogramming by gut-derived cytokines as a mechanism that causes lasting changes in a sensory system in ageing flies.

Access options

Subscribe to Journal

Get full journal access for 1 year

\$199.00

only \$3.90 per issue

[Subscribe](#)

All prices are NET prices.

VAT will be added later in the checkout.

Tax calculation will be finalised during checkout.

Rent or Buy article

Get time limited or full article access on ReadCube.

from \$8.99

[Rent or Buy](#)

All prices are NET prices.

Additional access options:

- [Log in](#)
- [Access through your institution](#)
- [Learn about institutional subscriptions](#)

Fig. 1: JAK–STAT signalling in EG after infection transiently inhibits olfactory discrimination, contributing to *Ecc15* aversion, and host survival.

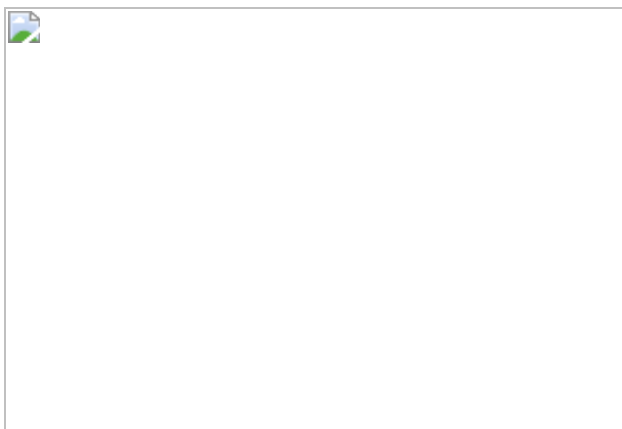


Fig. 2: Chronic activation of JAK–STAT signalling in old EGs causes decline of olfaction sensitivity during ageing.

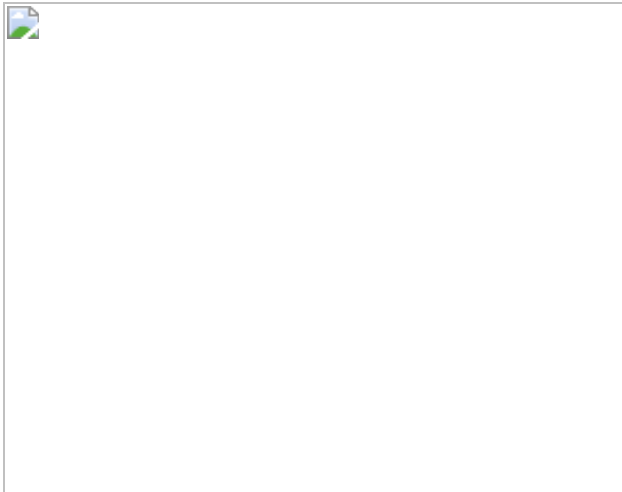
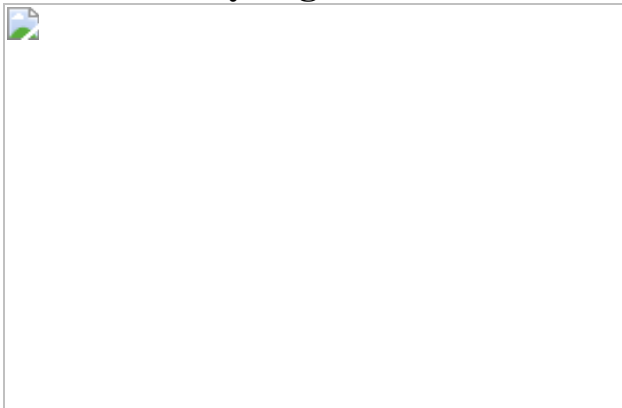


Fig. 3: Disrupting the glia and neuron lactate shuttle in the AL aggravates infection-caused mortality, yet partially alleviates age-related olfactory degeneration.



Data availability

The authors declare that the data supporting the findings of this study are available within the Article and its Supplementary Information. Raw sequencing reads and pre-processed sequence data for bulk RNA-seq files have been deposited in the Gene Expression Omnibus (GEO) under accession code [GSE168530](#). Raw scRNA-seq reads and preprocessed sequence data have been deposited in the GEO under accession code [GSE168572](#). [Source data](#) are provided with this paper.

Code availability

Analysis code for scRNA-seq datasets is available at <https://github.com/Hongjie-Li/flyglia>. *Drosophila* genome (version BDGP6) is available for download at <https://aug2017.archive.ensembl.org/info/data/ftp/index.html>. *Drosophila* genome (r6.10) is available for download at <http://ftp.flybase.net/releases/>. The published scRNA-seq datasets generated by the S. Aerts laboratory are available at <https://scope.aertslab.org>.

References

1. 1.

Wang, A. et al. Opposing effects of fasting metabolism on tissue tolerance in bacterial and viral inflammation. *Cell* **166**, 1512–1525 (2016).

[CAS](#) [Article](#) [Google Scholar](#)

2. 2.

Ayres, J. S. & Schneider, D. S. The role of anorexia in resistance and tolerance to infections in *Drosophila*. *PLoS Biol.* **7**, e1000150 (2009).

[Article](#) [Google Scholar](#)

3. 3.

Kobler, J. M., Rodriguez Jimenez, F. J., Petcu, I. & Grunwald Kadow, I. C. Immune receptor signaling and the mushroom body mediate post-ingestion pathogen avoidance. *Curr. Biol.* **30**, 4693–4709.e3 (2020).

[CAS](#) [Article](#) [Google Scholar](#)

4. 4.

Stensmyr, M. C. et al. A conserved dedicated olfactory circuit for detecting harmful microbes in *Drosophila*. *Cell* **151**, 1345–1357 (2012).

[CAS](#) [Article](#) [Google Scholar](#)

5. 5.

Charroux, B., Daian, F. & Royet, J. *Drosophila* aversive behavior toward erwinia carotovora carotovora is mediated by bitter neurons and leukokinin. *iScience* **23**, 101152 (2020).

[ADS](#) [CAS](#) [Article](#) [Google Scholar](#)

6. 6.

Soria-Gómez, E., Bellocchio, L. & Marsicano, G. New insights on food intake control by olfactory processes: the emerging role of the endocannabinoid system. *Mol. Cell. Endocrinol.* **397**, 59–66 (2014).

[CAS](#) [Article](#) [Google Scholar](#)

7. 7.

Soria-Gómez, E. et al. The endocannabinoid system controls food intake via olfactory processes. *Nat. Neurosci.* **17**, 407–415 (2014).

[Article](#) [Google Scholar](#)

8. 8.

Liang, L. & Luo, L. The olfactory circuit of the fruit fly *Drosophila melanogaster*. *Sci. China Life Sci.* **53**, 472–484 (2010).

[Article](#) [Google Scholar](#)

9. 9.

Liu, H. et al. Astrocyte-like glial cells physiologically regulate olfactory processing through the modification of ORN-PN synaptic strength in *Drosophila*. *Eur. J. Neurosci.* **40**, 2744–2754 (2014).

[Article](#) [Google Scholar](#)

10. 10.

Wu, B., Li, J., Chou, Y. H., Luginbuhl, D. & Luo, L. Fibroblast growth factor signaling instructs ensheathing glia wrapping of *Drosophila* olfactory glomeruli. *Proc. Natl Acad. Sci. USA* **114**, 7505–7512 (2017).

[CAS](#) [Article](#) [Google Scholar](#)

11. 11.

Hussain, A. et al. Inhibition of oxidative stress in cholinergic projection neurons fully rescues aging-associated olfactory circuit degeneration in *Drosophila*. *eLife* **7**, e32018 (2018).

[Article](#) [Google Scholar](#)

12. 12.

Wu, S. C., Cao, Z. S., Chang, K. M. & Juang, J. L. Intestinal microbial dysbiosis aggravates the progression of Alzheimer's disease in *Drosophila*. *Nat. Commun.* **8**, 24 (2017).

[ADS](#) [Article](#) [Google Scholar](#)

13. 13.

Keshavarzian, A., Engen, P., Bonvegna, S. & Cilia, R. The gut microbiome in Parkinson's disease: a culprit or a bystander? *Prog. Brain Res.* **252**, 357–450 (2020).

[Article](#) [Google Scholar](#)

14. 14.

Jiang, H. et al. Cytokine/Jak/Stat signaling mediates regeneration and homeostasis in the *Drosophila* midgut. *Cell* **137**, 1343–1355 (2009).

[Article](#) [Google Scholar](#)

15. 15.

Tracy Cai, X. et al. AWD regulates timed activation of BMP signaling in intestinal stem cells to maintain tissue homeostasis. *Nat. Commun.* **10**, 2988 (2019).

[ADS](#) [Article](#) [Google Scholar](#)

16. 16.

Bach, E. A. et al. GFP reporters detect the activation of the *Drosophila* JAK/STAT pathway in vivo. *Gene Expr. Patterns* **7**, 323–331 (2007).

[CAS](#) [Article](#) [Google Scholar](#)

17. 17.

Freeman, M. R. *Drosophila* central nervous system glia. *Cold Spring Harb. Perspect. Biol.* **7**, a020552 (2015).

[Article](#) [Google Scholar](#)

18. 18.

Chakrabarti, S. et al. Remote control of intestinal stem cell activity by haemocytes in *Drosophila*. *PLoS Genet.* **12**, e1006089 (2016).

[Article](#) [Google Scholar](#)

19. 19.

Rajan, A. & Perrimon, N. *Drosophila* cytokine unpaired 2 regulates physiological homeostasis by remotely controlling insulin secretion. *Cell* **151**, 123–137 (2012).

[CAS](#) [Article](#) [Google Scholar](#)

20. 20.

Doty, R. L. & Kamath, V. The influences of age on olfaction: a review. *Front. Psychol.* **5**, 20 (2014).

[Article](#) [Google Scholar](#)

21. 21.

Li, H., Qi, Y. & Jasper, H. Preventing age-related decline of gut compartmentalization limits microbiota dysbiosis and extends lifespan. *Cell Host Microbe* **19**, 240–253 (2016).

[CAS](#) [Article](#) [Google Scholar](#)

22. 22.

Davie, K. et al. A single-cell transcriptome atlas of the aging *Drosophila* brain. *Cell* **174**, 982–998.e20 (2018).

[CAS](#) [Article](#) [Google Scholar](#)

23. 23.

Liu, L., MacKenzie, K. R., Putluri, N., Maletić-Savatić, M. & Bellen, H. J. The glia-neuron lactate shuttle and elevated ROS promote lipid synthesis in neurons and lipid droplet accumulation in glia via APOE/D. *Cell Metab.* **26**, 719–737.e6 (2017).

[CAS](#) [Article](#) [Google Scholar](#)

24. 24.

Fauny, J. D., Silber, J. & Zider, A. *Drosophila* Lipid Storage Droplet 2 gene (*Lsd-2*) is expressed and controls lipid storage in wing imaginal discs. *Dev. Dyn.* **232**, 725–732 (2005).

[CAS](#) [Article](#) [Google Scholar](#)

25. 25.

Men, T. T., Binh, T. D., Yamaguchi, M., Huy, N. T. & Kamei, K. Function of Lipid storage droplet 1 (Lsd1) in wing development of *Drosophila melanogaster*. *Int. J. Mol. Sci.* **17**, E648 (2016).

[Article](#) [Google Scholar](#)

26. 26.

Kühnlein, R. P. Thematic review series: Lipid droplet synthesis and metabolism: from yeast to man. Lipid droplet-based storage fat metabolism in *Drosophila*. *J. Lipid Res.* **53**, 1430–1436 (2012).

[Article](#) [Google Scholar](#)

27. 27.

Soni, K. G. et al. Coatomer-dependent protein delivery to lipid droplets. *J. Cell Sci.* **122**, 1834–1841 (2009).

[CAS](#) [Article](#) [Google Scholar](#)

28. 28.

Ioannou, M. S. et al. Neuron-astrocyte metabolic coupling protects against activity-induced fatty acid toxicity. *Cell* **177**, 1522–1535 (2019).

[CAS](#) [Article](#) [Google Scholar](#)

29. 29.

Liu, L. et al. Glial lipid droplets and ROS induced by mitochondrial defects promote neurodegeneration. *Cell* **160**, 177–190 (2015).

[CAS](#) [Article](#) [Google Scholar](#)

30. 30.

Rosca, M. G. et al. Oxidation of fatty acids is the source of increased mitochondrial reactive oxygen species production in kidney cortical tubules in early diabetes. *Diabetes* **61**, 2074–2083 (2012).

[CAS](#) [Article](#) [Google Scholar](#)

31. 31.

Brann, D. H. et al. Non-neuronal expression of SARS-CoV-2 entry genes in the olfactory system suggests mechanisms underlying COVID-19-associated anosmia. *Sci. Adv.* **6**, eabc5801 (2020).

[ADS](#) [CAS](#) [Article](#) [Google Scholar](#)

32. 32.

Salmon Ceron, D. et al. Self-reported loss of smell without nasal obstruction to identify COVID-19. The multicenter Coranosmia cohort study. *J. Infect.* **81**, 614–620 (2020).

[CAS](#) [Article](#) [Google Scholar](#)

33. 33.

Hakim-Mishnaevski, K., Flint-Brodsly, N., Shklyar, B., Levy-Adam, F. & Kurant, E. Glial phagocytic receptors promote neuronal loss in adult drosophila brain. *Cell Rep.* **29**, 1438–1448.e3 (2019).

[CAS](#) [Article](#) [Google Scholar](#)

34. 34.

Albrecht, S. C., Barata, A. G., Grosshans, J., Teleman, A. A. & Dick, T. P. In vivo mapping of hydrogen peroxide and oxidized glutathione reveals chemical and regional specificity of redox homeostasis. *Cell Metab.* **14**, 819–829 (2011).

[CAS](#) [Article](#) [Google Scholar](#)

35. 35.

Li, H. et al. Classifying drosophila olfactory projection neuron subtypes by single-cell RNA sequencing. *Cell* **171**, 1206–1220.e22 (2017).

[CAS](#) [Article](#) [Google Scholar](#)

36. 36.

Anders, S. & Huber, W. Differential expression analysis for sequence count data. *Genome Biol.* **11**, R106 (2010).

[CAS](#) [Article](#) [Google Scholar](#)

37. 37.

Picelli, S. et al. Full-length RNA-seq from single cells using Smart-seq2. *Nat. Protocols* **9**, 171–181 (2014).

[CAS](#) [Article](#) [Google Scholar](#)

38. 38.

Dobin, A. et al. STAR: ultrafast universal RNA-seq aligner. *Bioinformatics* **29**, 15–21 (2013).

[CAS](#) [Article](#) [Google Scholar](#)

39. 39.

Anders, S., Pyl, P. T. & Huber, W. HTSeq—a Python framework to work with high-throughput sequencing data. *Bioinformatics* **31**, 166–169 (2015).

[CAS](#) [Article](#) [Google Scholar](#)

40. 40.

Ja, W. W. et al. Prandiology of *Drosophila* and the CAFE assay. *Proc. Natl Acad. Sci. USA* **104**, 8253–8256 (2007).

[ADS](#) [CAS](#) [Article](#) [Google Scholar](#)

[Download references](#)

Acknowledgements

We thank E. Bach, D. Bilder, S. Hou, M. Zeidler, N. Buchon, D. Ferrandon, L. O'Brien, M. A. Welte, M. Miura, C. S. Thummel and T. Dick for flies; M. Sagolla for the training in Yokogawa CSU-W1/Zeiss 3i Marianas spinning disk confocal microscope; the Genentech NGS technology core lab for the support with bulk RNA-seq; and I. C. Grunwald Kadow for the tips in olfactory T-maze assay. We acknowledge funding from the following grants: National Institutes of Health (NIH) R01AG057353 and Genentech, Inc (H.J.) NIH R00AG062746 (H.L.), NIH K99AG056680 (M.B.J.), NIH R56AG057304 (P.H.), NIH R01DC005982 (L.L.), Howard Hughes Medical Institute (L.L.), C. Zuckerberg Biohub (S.R.Q.) Cancer Prevention & Research Institute of Texas (H.L.). The funders had no role in study design, data collection and interpretation, or the decision to submit the work for publication.

Author information

Affiliations

1. Immunology Discovery, Genentech, Inc., South San Francisco, CA, USA

Xiaoyu Tracy Cai & Heinrich Jasper

2. Buck Institute for Research on Aging, Novato, CA, USA

Xiaoyu Tracy Cai, Martin Borch Jensen, Elie Maksoud, Pejmun Haghghi & Heinrich Jasper

3. University of Southern California, Los Angeles, CA, USA

Xiaoyu Tracy Cai

4. Department of Biology and Howard Hughes Medical Institute,
Stanford University, Stanford, CA, USA

Hongjie Li & Liqun Luo

5. Huffington Center on Aging, Baylor College of Medicine, Houston,
TX, USA

Hongjie Li

6. Department of Molecular and Human Genetics, Baylor College of
Medicine, Houston, TX, USA

Hongjie Li

7. Gordian Biotechnology, San Francisco, CA, USA

Martin Borch Jensen

8. FACS lab, Genentech, Inc., South San Francisco, CA, USA

Jovencio Borneo

9. NGS lab, Genentech, Inc., 1 DNA Way, South San Francisco, CA,
USA

Yuxin Liang

10. Department of Bioengineering and Department of Applied Physics,
Stanford University, Stanford, CA, USA

Stephen R. Quake

11. Chan Zuckerberg Biohub, Stanford, CA, USA

Stephen R. Quake

Authors

1. Xiaoyu Tracy Cai

[View author publications](#)

You can also search for this author in [PubMed](#) [Google Scholar](#)

2. Hongjie Li

[View author publications](#)

You can also search for this author in [PubMed](#) [Google Scholar](#)

3. Martin Borch Jensen

[View author publications](#)

You can also search for this author in [PubMed](#) [Google Scholar](#)

4. Elie Maksoud

[View author publications](#)

You can also search for this author in [PubMed](#) [Google Scholar](#)

5. Jovencio Borneo

[View author publications](#)

You can also search for this author in [PubMed](#) [Google Scholar](#)

6. Yuxin Liang

[View author publications](#)

You can also search for this author in [PubMed](#) [Google Scholar](#)

7. Stephen R. Quake

[View author publications](#)

You can also search for this author in [PubMed](#) [Google Scholar](#)

8. Liqun Luo

[View author publications](#)

You can also search for this author in [PubMed](#) [Google Scholar](#)

9. Pejmun Haghghi

[View author publications](#)

You can also search for this author in [PubMed](#) [Google Scholar](#)

10. Heinrich Jasper

[View author publications](#)

You can also search for this author in [PubMed](#) [Google Scholar](#)

Contributions

X.T.C. and H.J. designed all experiments. H.L. performed scRNA-seq experiments and analysis. L.L. and S.R.Q. provided resources and guidance for scRNA-seq experiments. M.B.J., E.M. and P.H. contributed ideas and experiments to Fig. 1g and Extended Data Fig. 4a-d. J.B. contributed to glia sorting in Extended Data Fig. 7g. Y.L. performed bulk RNA sequencing in Extended Data Fig. 7. X.T.C. performed all other experiments and analysed the data. X.T.C. and H.J. wrote the manuscript with input from the other authors.

Corresponding author

Correspondence to [Heinrich Jasper](#).

Ethics declarations

Competing interests

X.T.C. is an employee of Genentech Inc., a Roche subsidiary. H.J., J.B. and Y.L. are employees and shareholders of Genentech Inc., a Roche subsidiary. M.B.J. is employee and shareholder of Gordian Biotechnology.

Additional information

Peer review information *Nature* thanks Matthew Moulton, Scott Pletcher and the other, anonymous, reviewer(s) for their contribution to the peer review of this work. Peer review reports are available.

Publisher's note Springer Nature remains neutral with regard to jurisdictional claims in published maps and institutional affiliations.

Extended data figures and tables

Extended Data Fig. 1 Orco and Gr63 odour receptors are required for infection-induced avoidance behaviours towards enteropathogens.

a, Modified CAFE assay used. **b**, Intake of total food, *Ecc15* containing food and normal food for wild-type flies ($w^{1118} \times OreR$) during homeostasis and 24 h after *Ecc15* infection respectively. **c**, Olfactory T-maze assay and calculation of preference index (P.I.). **d**, Preference index of young flies 24 h (1d) and 5 days (5d) after *Ecc15* infection towards aversive odour, respectively. **e**, Preference index of wild-type flies ($w^{1118} \times OreR$) during homeostasis, infected with heat-killed *Ecc15* or starved on water for 24 h correspondingly. **f**, Intake of total food, *Ecc15*-containing food and normal food for flies in **e**. **g**, Intake of total food, *Ecc15*-containing food and normal food for wild-type flies ($w^{1118} \times OreR$), *Gr63a^l* flies, *Orco^l* flies with or without *Ecc15* infection, respectively. **h, i**, Representative images of 2xSTAT::GFP expression in the central brain 4 h after *Ecc15* infection or *PE* infection, as determined by immunostaining. Anti-GFP antibody amplifies 2xSTAT::GFP signal. Anti-repo immunohistochemistry to label all glia in **i**. Number quantifications of STAT⁺ cells per condition are shown in Fig. [1c](#). Data are mean and s.e.m. The sample size is as follows: $n = 7$ replicates (3 flies per cohort) per condition in **b**, $n = 5$ and 6 independently performed experiments for 1 and 5 days after infection, respectively, in **d**, $n = 7$, 8 and 6 independently performed experiments for mock, starved and infected flies with heat-killed *Ecc15* in **e**, $n = 10$ replicates (3 flies per

cohort) per condition in **f**, $n = 7, 10, 8, 9, 10$ and 10 replicates (3 flies per cohort) for w^{1118} mock, $w^{1118} Ecc15$, $Orco^l$ mock, $Orco^l Ecc15$, $Gr63a^l$ mock, $Gr63a^l Ecc15$ in **g**. Data shown in **f** and **g** are representative of two independently performed experiments, and those shown in **b**, **d**, **h** and **i** are representative of three separate experiments. P values in **b** and **g** from two-tailed Mann–Whitney test; P values in **d** and **f** from Dunn’s multiple comparisons test; other P values from Kruskal–Wallis test. NS, not significant ($P > 0.9999$ in **d**, **f**).

Source data

Extended Data Fig. 2 Infection does not influence numbers and the morphology of EG at the AL.

a, d, Representative images of 2xSTAT::GFP expression in the EG (nls.mCherry⁺ driven by GMR56F03::Gal4) in the central brain during homeostasis and 4 h after *Ecc15* infection. The AL region was magnified in **a** and additional images are shown in **d**. Anti-GFP antibody amplifies the 2xSTAT::GFP signal. Anti-NC82 antibody stained neuropils in **d**. **b**, Quantification of 2xSTAT::GFP reporter activity in the EG (nls.mCherry⁺ in the presence of corresponding Gal4 drivers) during homeostasis and after *Ecc15* infection. Numbers of GFP⁺ mCherry⁺ cells from both ALs were quantified from 30-μm *z*-sections (2 μm each). Four different EG-specific Gal4 drivers were tested correspondingly. **c**, Quantification of EG numbers (nls.mCherry⁺ driven by SPARC::Gal4, GMR10E12::Gal4 or GMR56F03::Gal4 respectively) at both ALs under mock and infected conditions. **e**, Histogram overlay of GFP fluorescence in mCherry⁺ EG in the presence of GMR56F03::Gal4 under conditions as noted, measured by intracellular flow cytometry assay. The GFP fluorescence intensity level (logarithmic scale) is shown in the *x* axis; the number of events (normalized to its peak height, noted as normalized to modal) is shown on the *y* axis. Median fluorescence intensity of GFP in mCherry⁺ EG under these conditions, was computed by FlowJo software and normalized to the median value of mock samples collected on the same day of measurement. mCherry⁺ EG were sorted by the following gates: (1) forward versus side scatter (FSC versus SSC); (2) side scatter height versus width (SSC-H vs

SSC-W); (3) forward scatter height versus width (FSC-H versus FSC-W); (4) fixable viability dye (eFluor 660 to label dead cells before fixation) versus DAPI (labelling nuclei to exclude debris); (5) GFP versus mCherry fluorescence channel (GFP versus mCherry). **f**, Representative images showing EG morphology at the AL from control and infected flies. EG nuclei were labelled by RedStinger, and cellular processes were labelled by CD4::GFP. Neuropils were labelled by an anti-NC82 antibody . Representative images were generated from 7- μm z-sections (1 μm each) after performing maximal intensity projection. Average intensity levels of CD4::GFP were quantified from 20- μm z-stack confocal images after maximal intensity projection. AL sizes were quantified and normalized to the mean value of mock flies. Data are mean and s.e.m. The sample size is as follows: $n = 5, 7, 6, 8, 7, 6, 7$ and 7 brains per condition (from left to right) in **b**, $n = 8, 6, 6, 7, 8$ and 7 brains per condition (from left to right) in **c**, $n = 97, 135$ and 822 mCherry⁺ cells from mock flies and $n = 123, 91, 145$ and 163 mCherry⁺ cells from infected flies in **e**, $n = 9$ and 8 brains for mock and *Ecc15* flies in **f** (left), $n = 9$ brains per condition in **f** (right). Data in **a** and **d** are representative of three independently performed experiments; data shown in **b**, **c**, **e** and **f** are representative of two independently performed experiments. *P* values in **e** from one-tailed Mann–Whitney test; other *P* values from two-tailed Mann–Whitney test.

Source data

Extended Data Fig. 3 JAK–STAT signalling in EG promotes avoidance behaviour against *Ecc15*, yet increasing host survival upon acute infection.

a, Preference index of young flies with indicated JAK–STAT perturbation in the EG. RNAi constructs were expressed in the EG for 7 days by shifting flies to 29 °C (restrictive temperature for Gal80^{ts}). Flies were exposed to *Ecc15* for 24 h. **b**, Preference index of young infected flies expressing *mCherry*^{RNAi}, *dome*^{RNAi} or *stat*^{RNAi} in all glia (repo::Gal4;tubG80^{ts}), measured by T-maze assay. **c**, Quantification of STAT::GFP activity in the glia of flies after *dome*^{RNAi} or *stat*^{RNAi} knockdown in all glia (repo::Gal4; 10xSTAT::GFP), to confirm knockdown efficiency for various RNAi lines

that target Dome or STAT, respectively. **d**, **e**, Total food intake and normal food intake of flies overexpressing *hop*^{tuml} (**d**) and of infected flies after knockdown of *dome* and *stat* (**e**) in EG (driven by GMR56F03::Gal4;tubG80^{ts}), measured by CAFE assay. **f**, Intake of total food, *Ecc15*-containing food and normal food for flies expressing *mCherry*^{RNAi}, *LacZ*^{RNAi} and UAS::LacZ in the EG during homeostasis. **g**, **h**, Survival curve of flies overexpressing *hop*^{tuml} (**g**) or knocking down *dome* (**h**) in the EG after continuous *PE* infection. **i**, Survival curves of wild-type flies (*w¹¹¹⁸ × OreR*), *Gr63a^l* flies, *Orco^l* flies after continuous *PE* infection. Data are mean and s.e.m. The sample size is as follows: $n = 6, 7, 5, 5$ and 5 independently performed experiments per condition (from left to right) in **a**, $n = 4$ independently performed experiments per condition in **b**, $n = 7, 8, 8, 6$ and 7 brains per condition (from left to right) in **c**, $n = 8$ and 9 replicates (3 flies per cohort) for *mCherry*^{RNAi} and *hop*^{tuml}, respectively in **d**, $n = 6, 8$ and 7 replicates (3 flies per cohort) for *mCherry*^{RNAi}, *dome*^{RNAi} and *stat*^{RNAi} in **e**, $n = 8$ replicates per condition (3 flies per cohort) for **f**, $n = 74$ and 96 flies for *mCherry*^{RNAi} and *hop*^{tuml}, respectively, for **g**, $n = 97$ and 118 flies for *mCherry*^{RNAi} and *dome*^{RNAi}, respectively, for **h**, $n = 101, 63$ and 90 flies for wild-type flies (*w¹¹¹⁸ × OreR*), *Orco^l*, *Gr63a^l* flies for **i**. Data in **d**, **e**, **g**, **h** are representative of three independently performed experiments; data shown in **c**, **f** and **i** are representative of two independently performed experiments. *P* values from two-tailed Mann–Whitney test in **a** (*mCherry*^{RNAi} compared with *hop*^{tuml}), **c**, **d**; *P* values from log-rank test in **g–i**; other *P* values from Kruskal–Wallis test.

[Source data](#)

Extended Data Fig. 4 Gut-derived Upd2 and Upd3 are sufficient and required for infection-induced STAT activation in the glia.

a, Gut-derived Upd proteins and their possible effect on the AL. **b**, Glial expression of nuclear mCherry driven by Mex1::Gal4 in the gut and brain of adult flies. **c**, **d**, Activity of 2xSTAT::GFP reporter in the central brain of flies overexpressing *upd2*, *upd3* in enterocytes, driven by Mex1::Gal4;tubG80^{ts}, during homeostasis (**c**) and of infected flies loss of

upd2, *upd3* in enterocytes (**d**). Representative images were generated from 30- μm z-sections, and the AL region was magnified. Numbers of GFP⁺, repo⁺ glia per AL were quantified in Fig. **1g**. **e, f**, Preference index of flies expressing *mCherry*^{RNAi}, UAS::LacZ, *LacZ*^{RNAi}, UAS::*upd2*, UAS::*upd3* and RNAi lines targeting *upd2* or *upd3* in enterocytes with or without *Ecc15* infection. **g**, qPCR analysis confirming the knockdown efficiency of multiple RNAi lines targeting *upd2* or *upd3* correspondingly. **h, j**, Activity of 2xSTAT::GFP reporter in the central brain of flies overexpressing *upd2* or *upd3* in haemocytes (driven by *hm1*::Gal4) during homeostasis and of infected flies loss of *upd3* in haemocytes. Numbers of GFP⁺ repo⁺ cells per AL were quantified from 30- μm z-sections in **j**, and the AL region was magnified. **i, k**, Activity of 2xSTAT::GFP reporter in the central brain of flies overexpressing *upd2* in fatbody (driven by *cg*::Gal4) during homeostasis and of infected flies loss of *upd3* in fatbody. Numbers of GFP⁺ repo⁺ cells per AL were quantified from 30- μm z-sections in **k**, and the AL region was zoomed in. Data are mean and s.e.m. The sample size is as follows: $n = 6, 5, 5, 7, 6$ and 9 independently performed experiments per condition (from left to right) in **e**, $n = 4$ or 5 independently performed experiments per condition in **f**, $n = 3, 4$ and 4 biological replicates per condition (from left to right) in **g** (left), $n = 3, 4$ and 2 biological replicates per condition (from left to right) in **g** (right), $n = 12, 14, 11, 9$ and 11 brains per condition (from left to right) in **j**, $n = 7, 6, 10$ and 13 brains per condition (from left to right) in **k**. Data in **c** and **d** are representative of three independently performed experiments; data shown in **b, g–k** are representative of two independently performed experiments. *P* values from two-tailed Mann–Whitney test in **f, j** and **k** when comparing two groups; other *P* values from Kruskal–Wallis test.

[Source data](#)

Extended Data Fig. 5 Chronic activation of JAK–STAT signalling in EG drives the decline of EG numbers at the AL during ageing.

a, Representative images of glomerular compartments at the AL from young and old flies. Confocal images were generated from 20- μm z-

sections (1 μm each) after performing maximal intensity projection. Neuropils labelled by anti-NC82 antibody. **b**, Representative single z-section images showing EG morphology at the AL from young and old flies. EG nuclei were labelled by RedStinger driven by GMR56F03::Gal4, and cellular processes were labelled by CD4::GFP. Average intensity levels of CD4::GFP and AL sizes were quantified from 20- μm z-stack confocal images after maximal intensity projection. AL sizes were quantified and normalized to the mean values of young flies. **c**, Representative images of 2xSTAT::GFP reporter activity in EG (nls.mCherry⁺ driven by GMR56F03::Gal4) at the AL from young and old flies. Images were generated from 20- μm z-sections (1 μm each) after performing maximal intensity projection. **d**, Preference index of young flies expressing *mCherry*^{RNAi} in EG (GMR56F03::Gal4), old flies expressing *mCherry*^{RNAi}, *dome*^{RNAi} or *stat*^{RNAi} in EG or all glia (repo::Gal4), measured by T-maze assay. **e**, Representative images showing EG morphology at the AL from old flies with or without *dome* knockdown. EG nuclei were labelled by RedStinger in the presence of GMR56F03::Gal4;tubG80^{ts}, while cellular processes were labelled by CD4::GFP. Average intensity levels of CD4::GFP and numbers of RedStinger⁺ cells per AL were quantified. AL sizes were quantified and normalized to the mean value of old control flies. Flies were aged at 25 °C for 14 days followed by 29 °C for 14 days to induce *dome*^{RNAi} expression. **f**, Representative images showing the activity of 2xSTAT::GFP reporter in the central brain of old flies knocking down *upd2* or *upd3* in enterocytes, driven by Mex1::Gal4;tubG80^{ts}. Representative images were generated from 30- μm z-sections, and the AL region was magnified. **g**, Preference index of young flies expressing *mCherry*^{RNAi} and old flies expressing *mCherry*^{RNAi}, *Upd2*^{RNAi} or *Upd3*^{RNAi} in enterocytes, driven by Mex1::Gal4;tubG80^{ts}. Data are mean and s.e.m. The sample size is as follows: $n = 8$ and 6 brains for young and old conditions, respectively, in **b**, $n = 6, 7, 8$ and 7 independently performed experiments for young *mCherry*^{RNAi}, old *mCherry*^{RNAi}, *dome*^{RNAi} and *stat*^{RNAi} correspondingly in **d** (left), $n = 4, 3$ and 3 independently performed experiments for old *mCherry*^{RNAi}, *dome*^{RNAi} and *stat*^{RNAi} correspondingly in **d** (middle and right), $n = 7$ and 10 brains for *mCherry*^{RNAi}, *dome*^{RNAi}, respectively, in **e**, $n = 5, 7, 7$ and 7 independently performed experiments for young *mCherry*^{RNAi}, old *mCherry*^{RNAi}, *Upd2*^{RNAi} and *Upd3*^{RNAi},

respectively, in **g**. Data in **a–c, f** are representative of two independently performed experiments; data in **e** are representative of three independently performed experiments. *P* values from two-tailed Mann–Whitney test in **b, d** (when comparing young and old *mCherry*^{RNAi}), **e, g** (when comparing young and old *mCherry*^{RNAi}); *P* values from Dunn’s multiple comparisons test in **d** (right); other *P* values from Kruskal–Wallis test.

Source data

Extended Data Fig. 6 Age-related decline of olfaction sensitivity and morphological decays of EG are independent from microbiota.

a, Preference index of germ-free wild-type flies (*w¹¹¹⁸ × OreR*) during ageing, measured by T-maze assay. **b**, Representative images of 2xSTAT::GFP reporter activity in the EG at the AL from conventionally-reared or germ-free old flies. EG nuclei were labelled by nls.mCherry in the presence of GMR56F03::Gal4 driver. Anti-GFP antibody amplified 2xSTAT::GFP signal. Anti-NC82 antibody labelled neuropils. Confocal images were generated from 20-μm *z*-sections after performing maximal intensity projection. Flies were aged at room temperature. **c, d**, Representative images showing EG morphology at the AL from young and old flies that were conventionally reared and from old germ-free flies, respectively. EG nuclei were labelled by RedStinger in the presence of GMR56F03::Gal4, and cellular processes were labelled by CD4::GFP. Neuropils were labelled by anti-NC82 antibody. Images were generated from 20-μm *z*-sections after performing maximal intensity projection. Average intensity levels of CD4::GFP and numbers of RedStinger⁺ cells per AL were quantified in **d**. AL sizes were quantified and normalized to the mean value of young conventionally reared animals in **d**. Flies were aged at room temperature. Data are mean and s.e.m. The sample size is as follows: *n* = 6, 4, 4, 7 and 2 independently performed experiments per condition (from left to right) in **a**, *n* = 7 and 8 brains for 30-day conventional and 30-day sterile conditions, respectively, in **b**, *n* = 6, 8 and 5 brains per condition (from left to right) in **d** (left), *n* = 6, 7 and 5 brains per condition (from left to right) in **d** (middle and right). Data in **b–d** are representative of two

independently performed experiments. *P* values from Kruskal–Wallis test in **a**; other *P* values from two-tailed Mann–Whitney test.

[Source data](#)

Extended Data Figure 7 JAK–STAT signalling regulates glial lipid metabolism.

a, Workflow of scRNA-seq using plate-based Smart-seq2. FACS, fluorescence-activated cell sorting. Four groups of glia were sequenced: 5 and 50 day all glia (GFP^+ , driven by $\text{rep}::\text{Gal4}$); 5 and 50 day EG (GFP^+ , driven by $\text{GMR56F03}::\text{Gal4}$). **b**, Visualization of glial cells using *t*-SNE plots. Cells were coloured according to cell types, ages and Louvain clusters with default resolution. Non-EG were curated from all repo^+ glia with EG ($\text{GMR56F03}::\text{Gal4}^+$) removed (Methods). EG and non-EG were readily separated into different clusters (left and middle). In total, 10 clusters were formed from these glia (right), suggesting the heterogeneity of glial population. **c**, Violin plot showing expression levels of *dome* in non-EG and EG. For both EG and non-EG, cells were combined from young and old flies. In non-EG, *dome* expression was barely detected except in one cell. In EG, a subset of cells showed high expression of *dome*. **d**, Violin plots showing expression levels of *Socs36E* in young and old non-EG (left) and EG (right) respectively. **e**, Visualization of all annotated glial cells from a previously published whole fly brain scRNA-seq dataset²² using a *t*-SNE plot. scRNA-seq was performed using droplet-based 10x Genomics platform. Glia are in red (repo^+), and neurons are in grey. Two subsets of EG (in orange box) and six subsets of non-EG (in blue box) are annotated. **f**, Violin plots showing expression levels of *Socs36E* in non-EG and EG at eight different ages. Cells from 3-, 6- and 9-day-old flies were combined as young samples, and compared with cells from 50-day-old flies (old). **g**, Gating strategy for sorting STAT::GFP $^+$ glia and STAT::GFP $^-$ glia from the central brain of young mock or young infected (4-h *Ecc15* infection) flies overexpressing *tdTomato* in all glia ($\text{repo}::\text{Gal4}$) while expressing 10xSTAT::GFP reporter. **h**, Visualization of gene expression variation between STAT::GFP $^+$ glia and STAT::GFP $^-$ glia by PCA plot. Each dot represents a sample replicate independently collected from a cohort of 100

flies. Samples with the same genotype were grouped together, and samples with different treatments were coloured separately. **i**, Volcano plot displaying differentially expressed genes between STAT::GFP⁺ glia and STAT::GFP⁻ glia (highlighted in red) under homeostatic conditions, using a cut-off of twofold change, $P < 0.001$, FDR < 0.01 . **j**, Gene Ontology analysis of significantly upregulated genes in STAT::GFP⁺ glia during homeostasis. **k**, Lipid storage-associated genes were significantly upregulated in STAT::GFP⁺ glia during homeostasis. Reads per kilobase per normalized million mapped reads (nRPKM) values of each gene in STAT::GFP⁺ glia and STAT::GFP⁻ glia are shown correspondingly. **l**, Genes involved in monocarboxylate transport were significantly upregulated in STAT::GFP⁺ glia during homeostasis. nRPKM values of each gene in STAT::GFP⁺ glia and STAT::GFP⁻ glia are shown correspondingly. **m**, Schematic demonstrating mitochondrial fatty acid β-oxidation. **n**, Genes involved in fatty acid β-oxidation that were significantly upregulated in STAT::GFP⁺ glia during homeostasis. nRPKM values of each gene in STAT::GFP⁺ glia and STAT::GFP⁻ glia are shown correspondingly. Data are mean and s.e.m. The sample size is as follows: $n = 4$ replicates per condition (each replicate was independently pooled from 100 flies on different days) in **g–n**. P values in **k**, **l** and **n** were calculated by Partek Flow; P values in **c**, **d** and **f** from one-tailed Student's *t*-test.

Source data

Extended Data Fig. 8 JAK–STAT signalling regulates LD accumulation via *GLaz* and *out* after infection, with no influence on lipid peroxidation.

a, Immunostaining detecting LDs at the AL from young flies during homeostasis, 24 h after *Ecc15* infection, or 4 days after infection, using LipidTox deep red probes. LD numbers per AL were quantified. **b**, **c**, Immunostaining detecting LDs at the AL from young flies overexpressing *mCherry*^{RNAi} or *hop*^{tuml} in EG (driven by GMR56F03::Gal4;tubG80^{ts}) during homeostasis (**b**), and from infected flies knocking down *dome*, *stat*, *GLaz* or *out* in EG (**c**). LD numbers per AL were quantified. **d**, Immunostaining detecting LDs at the AL from young flies overexpressing

Upd cytokines in enterocytes, driven by Mex1::Gal4;tubG80^{ts}, during homeostasis, and from infected flies knocking down Upd cytokines in enterocytes. LD numbers per AL were quantified. **e, f**, qPCR analysis confirming the knockdown efficiency of several RNAi lines targeting *out*, *GLaz*, *NLaz* and *Ldh*, respectively. **g, h**, Representative images showing lipid peroxidation in LDs at the AL from young flies expressing *mCherry*^{RNAi} or *hop*^{tuml} in the EG (driven by GMR56F03::Gal4;tubG80^{ts}) during homeostasis (**g**), from young mock flies, infected flies or 4 days after *Ecc15* infection (**h**), and from infected flies knocking down *dome* or *stat* in the EG (**h**). Lipid peroxidation levels of LDs for each sample were measured as the mean 488/561 nm intensity ratios in LDs. The ratios were normalized to the mean value of corresponding control samples. Data are mean and s.e.m. The sample size is as follows: $n = 10, 7$ and 7 brains per condition (from left to right) in **a**, $n = 7$ and 5 brains for *mCherry*^{RNAi} and *hop*^{tuml}, respectively, in **b**, $n = 13, 7, 7, 9$ and 7 brains per condition for *mCherry*^{RNAi}, *dome*^{RNAi}, *stat*^{RNAi}, *GLaz*^{RNAi} and *out*^{RNAi} in **c**, $n = 8, 7, 5, 6, 8$ and 8 brains per condition (from left to right) in **d**, $n = 4$ and 3 biological replicates for *mCherry*^{RNAi} and *out*^{RNAi} in **e** (left), $n = 3$ biological replicates for *mCherry*^{RNAi} and *Ldh*^{RNAi} in **e** (right), $n = 4, 3, 4, 4, 4$ and 3 biological replicates per condition (from left to right) in **f**, $n = 6$ and 5 brains *mCherry*^{RNAi} and *hop*^{tuml} in **g**, $n = 10, 7, 7, 7$ and 7 brains per condition (from left to right) in **h**. Images in **a–e, h** were generated from 20-μm z-sections (1-μm each) after performing maximal intensity projection. Data in **a–d, g, h** are representative of three independently performed experiments; data shown in **e** and **f** are representative of two separate experiments. *P* values in **a, b, e–g** from two-tailed Mann–Whitney test; other *P* values from Kruskal–Wallis test. NS, not significant ($P > 0.9999$ in **g**).

[Source data](#)

Extended Data Fig. 9 Deactivation of JAK–STAT signalling alleviates lipid toxicity during ageing, thus rescuing the age-related decline of ensheathing glia numbers.

a, Immunostaining detecting LDs in EG (RedStinger^+ , $\text{CD4}::\text{GFP}^+$) at the AL of young (5–7 day old) and old (51–54 day old) flies, using LipidTox deep red probes. LD numbers per glia were quantified. **b**, Cytosolic H_2O_2 levels in EG at the AL from young (7 day old) and old (50 day old) flies, measured as the mean 405/488 nm intensity ratio. The ratios for old flies were normalized to the mean value for young flies. **c–e**, Levels of cytosolic H_2O_2 (**c**), cytosolic glutathione redox potential (**d**) and mitochondrial H_2O_2 (**e**) in all glia (driven by $\text{repo}::\text{Gal4}$) from young and old flies, measured as the mean 405/488 nm intensity ratios for corresponding ROS sensors. **f**, Representative images showing lipid peroxidation in LDs at the AL from young flies expressing $m\text{Cherry}^{\text{RNAi}}$ in the EG (driven by $\text{GMR56F03}::\text{Gal4};\text{tubG80}^{\text{ts}}$) and from old flies expressing $m\text{Cherry}^{\text{RNAi}}$ or $\text{stat}^{\text{RNAi}}$ in the EG. LD numbers per AL were quantified. Lipid peroxidation levels of LDs for each sample were measured as the mean 488/561 nm intensity ratio. The ratios were normalized to the mean value of young control samples. Flies were aged at room temperature before being transferred to 29 °C for 7 days. **g**, Representative images showing lipid peroxidation in LDs at the AL from old flies after loss of $upd2$ or $upd3$ in enterocytes driven by $\text{Mex1}::\text{Gal4};\text{tubG80}^{\text{ts}}$. LD numbers per AL were quantified. Lipid peroxidation levels of LDs for each sample were measured as the mean 488/561 nm intensity ratio. The ratios were normalized to the mean value of old control samples. Data are mean and s.e.m. The sample size is as follows: $n = 8$ and 6 brains for young and old conditions correspondingly in **a** and **b**, $n = 6$ brains per condition in **c**, $n = 6$ and 7 brains for young and old conditions correspondingly in **d**, $n = 7$, 7 and 6 brains per condition (from left to right) in **e**, $n = 8$, 11 and 8 brains per condition (from left to right) correspondingly in **f** (left), $n = 9$, 11 and 8 brains per condition (from left to right) correspondingly in **f** (right), $n = 4$, 4 and 6 brains per condition (from left to right) in **g** (left), $n = 5$, 5 and 6 brains per condition (from left to right) in **g** (right). Images in **a–g** were generated from 20-μm z-sections (1-μm each) after performing maximal intensity projection. Data in **a–e** are representative of two independently performed experiments, and those in **f** and **g** are representative of three separate experiments. P values in **a–d**, **f** from two-tailed Mann–Whitney test; other P values from Kruskal–Wallis test.

Source data

Extended Data Fig. 10 Inhibiting lipid export or lactate intake in projection neurons partially rescues the decline of olfaction sensitivity upon infection and during ageing.

a, Preference index of young infected flies after knockdown of *dome*, *stat*, *GLaz* or *out* in the EG with additional RNAi lines. **b**, **c**, Intake of total food, *Ecc15⁺* food and normal food for mock flies during homeostasis and for infected flies after the loss of *dome*, *stat*, *GLaz* or *out*, measured by CAFE assay. The *GLaz*^{RNAi} and *out*^{RNAi} lines in **b** and **c** are different. **d**, Survival curve of young flies after loss of *GLaz* or *out* upon continuous *PE* infection. The *GLaz*^{RNAi} and *out*^{RNAi} lines are as in **b**. **e**, Representative images showing LD accumulation and lipid peroxidation at the AL from old flies after knockdown of *GLaz* or *out* in EG driven by GMR56F03::Gal4;tubG80^{ts}. LD numbers per AL were quantified. Lipid peroxidation levels of LDs for each sample were measured as the mean 488/561 nm intensity ratio. The ratios were normalized to the mean value of old control samples. Flies were aged at 25 °C for 14 days followed by 29 °C for 14 days to induce expression of RNAi lines. **f**, Preference index values of old flies overexpressing Lip-4, or knockdown of *NLaz*, *Ldh* or *out* in projection neurons using the GH146::Gal4 driver. **g**, Intake of total food, *Ecc15⁺* food and normal food for young infected flies after knockdown of *NLaz* or *out* in projection neurons. **h**, Survival curve of flies after knockdown of *NLaz* or *out* in projection neurons upon continuous *PE* infection. **i**, Intake of total food and normal food for young infected flies overexpressing Lip-4 in projection neurons. Data are mean and s.e.m. The sample size is as follows: $n = 5, 5, 5, 5, 5, 5$ and 4 independently performed experiments per condition (from left to right) in **a**, $n = 6, 6, 5$ and 7 replicates (3 flies per cohort) for mock *mCherry*^{RNAi}, *Ecc15 mCherry*^{RNAi}, *Ecc15 GLaz*^{RNAi} and *Ecc15 out*^{RNAi} correspondingly in **b**, $n = 8, 8, 8, 7$ and 6 replicates (3 flies per cohort) for *mCherry*^{RNAi}, *dome*^{RNAi}, *stat*^{RNAi}, *GLaz*^{RNAi} and *out*^{RNAi} correspondingly in **c**, $n = 100, 59$ and 85 flies for *mCherry*^{RNAi}, *GLaz*^{RNAi} and *out*^{RNAi} respectively in **d**, $n = 15, 7$ and 7 brains per condition (from left to right) in **e**, $n = 13, 8, 7, 8$ and 7 independently performed experiments per condition (from left to right) in **f**,

n = 6, 7, 8 and 7 replicates for *mCherry*^{RNAi}, *NLaz*^{RNAi}, *out*^{RNAi}(v51157) and *out*^{RNAi}(BL67858) correspondingly in **g**, *n* = 49, 86, 87 and 53 flies for *mCherry*^{RNAi}, *NLaz*^{RNAi}, *out*^{RNAi}(v51157) and *out*^{RNAi}(BL67858), respectively, in **h**, *n* = 8 replicates (3 flies per cohort) per condition in **i**. Data in **b–d**, **g** and **h** are representative of two independently performed experiments, and those shown in **e** and **i** are representative of three separate experiments. *P* values in **d** and **h** from log-rank test; *P* values in **a** (when comparing *mCherry*^{RNAi}, *LacZ*^{RNAi} and UAS::LacZ), **c** (top: when comparing *mCherry*^{RNAi}, *dome*^{RNAi} and *GLaz*^{RNAi}; bottom) and **g** from Kruskal–Wallis test; other *P* values from two-tailed Mann–Whitney test.

[Source data](#)

Supplementary information

[Supplementary Figure 1](#)

Example of gating strategy for FACs sorting used in Extended Data Fig. 7g.

[Reporting Summary](#)

[Supplemental Table 1](#)

Genotypes, genders and ages of flies used in each figure.

[Supplemental Table 2](#)

List of differentially expressed genes in STAT::GFP⁺ glia compared to STAT::GFP⁻ glia under homeostatic conditions, shown in Extended Data Fig. 7i.

[Peer Review File](#)

Source data

[**Source Data Fig. 1**](#)

[**Source Data Fig. 2**](#)

[**Source Data Fig. 3**](#)

[**Source Data Extended Data Fig. 1**](#)

[**Source Data Extended Data Fig. 2**](#)

[**Source Data Extended Data Fig. 3**](#)

[**Source Data Extended Data Fig. 4**](#)

[**Source Data Extended Data Fig. 5**](#)

[**Source Data Extended Data Fig. 6**](#)

[**Source Data Extended Data Fig. 7**](#)

[**Source Data Extended Data Fig. 8**](#)

[**Source Data Extended Data Fig. 9**](#)

[**Source Data Extended Data Fig. 10**](#)

Rights and permissions

[**Reprints and Permissions**](#)

About this article



Check for
updates

Cite this article

Cai, X.T., Li, H., Borch Jensen, M. *et al.* Gut cytokines modulate olfaction through metabolic reprogramming of glia. *Nature* **596**, 97–102 (2021).
<https://doi.org/10.1038/s41586-021-03756-0>

[Download citation](#)

- Received: 13 October 2020
- Accepted: 22 June 2021
- Published: 21 July 2021
- Issue Date: 05 August 2021
- DOI: <https://doi.org/10.1038/s41586-021-03756-0>

Comments

By submitting a comment you agree to abide by our [Terms](#) and [Community Guidelines](#). If you find something abusive or that does not comply with our terms or guidelines please flag it as inappropriate.

[Access through your institution](#)

[Change institution](#)

[Buy or subscribe](#)

Advertisement

| [Section menu](#) | [Main menu](#) |

In vivo monoclonal antibody efficacy against SARS-CoV-2 variant strains

[Download PDF](#)

- Article
- [Published: 21 June 2021](#)

In vivo monoclonal antibody efficacy against SARS-CoV-2 variant strains

- [Rita E. Chen](#)^{1,2} na1,
- [Emma S. Winkler](#)^{1,2} na1,
- [James Brett Case](#) [ORCID: orcid.org/0000-0001-7331-5511](#)¹ na1,
- [Ishmael D. Aziati](#)¹,
- [Traci L. Bricker](#)¹,
- [Astha Joshi](#) [ORCID: orcid.org/0000-0003-4914-8228](#)¹,
- [Tamarand L. Darling](#)¹,
- [Baoling Ying](#)¹,
- [John M. Errico](#) [ORCID: orcid.org/0000-0002-4452-8152](#)²,
- [Swathi Shrihari](#)¹,
- [Laura A. VanBlargan](#)¹,
- [Xuping Xie](#) [ORCID: orcid.org/0000-0003-0918-016X](#)³,
- [Pavlo Gilchuk](#)⁴,
- [Seth J. Zost](#) [ORCID: orcid.org/0000-0001-6712-5076](#)⁴,
- [Lindsay Droit](#)⁵,
- [Zhuoming Liu](#) [ORCID: orcid.org/0000-0001-8198-0976](#)⁵,
- [Spencer Stumpf](#)⁵,
- [David Wang](#)⁵,
- [Scott A. Handley](#)²,
- [W. Blaine Stine Jr](#)⁶,
- [Pei-Yong Shi](#) [ORCID: orcid.org/0000-0001-5553-1616](#)^{3,7,8},
- [Meredith E. Davis-Gardner](#)⁹,
- [Mehul S. Suthar](#)⁹,
- [Miguel Garcia Knight](#)¹⁰,
- [Raul Andino](#) [ORCID: orcid.org/0000-0001-5503-9349](#)¹⁰,
- [Charles Y. Chiu](#) [ORCID: orcid.org/0000-0003-2915-2094](#)^{11,12},
- [Ali H. Ellebedy](#) [ORCID: orcid.org/0000-0002-6129-2532](#)^{2,13,14},

- [Dave H. Fremont](#) ORCID: [orcid.org/0000-0002-8544-2689^{2,5,15}](https://orcid.org/0000-0002-8544-2689),
- [Sean P. J. Whelan](#) ORCID: [orcid.org/0000-0003-1564-8590⁵](https://orcid.org/0000-0003-1564-8590),
- [James E. Crowe Jr](#) ORCID: [orcid.org/0000-0002-0049-1079^{4,16,17}](https://orcid.org/0000-0002-0049-1079),
- [Lisa Purcell¹⁸](#),
- [Davide Corti](#) ORCID: [orcid.org/0000-0002-5797-1364¹⁹](https://orcid.org/0000-0002-5797-1364),
- [Adrianus C. M. Boon](#) ORCID: [orcid.org/0000-0002-4700-8224^{1,2,5}](https://orcid.org/0000-0002-4700-8224) &
- [Michael S. Diamond](#) ORCID: [orcid.org/0000-0002-8791-3165^{1,2,5,13,14}](https://orcid.org/0000-0002-8791-3165)

Nature volume 596, pages 103–108 (2021) [Cite this article](#)

- 43k Accesses
- 504 Altmetric
- [Metrics details](#)

Subjects

- [Antibodies](#)
- [SARS-CoV-2](#)

Abstract

Rapidly emerging SARS-CoV-2 variants jeopardize antibody-based countermeasures. Although cell culture experiments have demonstrated a loss of potency of several anti-spike neutralizing antibodies against variant strains of SARS-CoV-2^{1,2,3}, the *in vivo* importance of these results remains uncertain. Here we report the *in vitro* and *in vivo* activity of a panel of monoclonal antibodies (mAbs), which correspond to many in advanced clinical development by Vir Biotechnology, AbbVie, AstraZeneca, Regeneron and Lilly, against SARS-CoV-2 variant viruses. Although some individual mAbs showed reduced or abrogated neutralizing activity in cell culture against B.1.351, B.1.1.28, B.1.617.1 and B.1.526 viruses with mutations at residue E484 of the spike protein, low prophylactic doses of mAb combinations protected against infection by many variants in K18-hACE2 transgenic mice, 129S2 immunocompetent mice and hamsters, without the emergence of resistance. Exceptions were LY-CoV555 monotherapy and LY-CoV555 and LY-CoV016 combination therapy, both of which lost all protective activity, and the combination of AbbVie 2B04 and 47D11, which showed a partial loss of activity. When administered after infection, higher doses of several mAb cocktails protected *in vivo* against viruses with a B.1.351 spike gene. Therefore, many—but not all—of the antibody products with Emergency Use

Authorization should retain substantial efficacy against the prevailing variant strains of SARS-CoV-2.

[Download PDF](#)

Main

Variant strains of SARS-CoV-2 have been detected in the UK (B.1.1.7, also known as Alpha), South Africa (B.1.351, also known as Beta), Brazil (B.1.1.28 (also known as P.1, also known as Gamma)) and elsewhere that contain substitutions in the N-terminal domain and the receptor-binding motif of the receptor-binding domain (RBD). Cell-based assays suggest that neutralization by many antibodies may be diminished against variants that express spike mutations, especially at position E484^{1,2,3,4,5}. However, the *in vivo* implications of this loss of mAb neutralizing activity remains uncertain, particularly for combination mAb therapies.

To evaluate the effects of SARS-CoV-2 strain variation on mAb protection, we assembled a panel of infectious SARS-CoV-2 strains with sequence substitutions in the spike gene (Fig. 1a, b) including a B.1.1.7 isolate from the UK, a B.1.429 isolate from California (USA), a B.1.617.1 isolate (of a clade identified in India) and two B.1.526 isolates from New York (USA). We also used SARS-CoV-2 strains from Washington (USA) with a D614G substitution (WA1/2020 D614G) or with both N501Y and D614G substitutions (WA1/2020 N501Y/D614G) as well as chimeric SARS-CoV-2 strains with B.1.351 or B.1.1.28 spike genes in the Washington strain background (denoted Wash-B.1.351 and Wash-B.1.1.28, respectively)^{1,6}. All viruses were propagated in Vero cells expressing transmembrane protease serine 2 (Vero-TMPRSS2 cells) to prevent the emergence of mutations at or near the furin cleavage site in the spike protein that affect virulence⁷. All viruses were deep-sequenced to confirm the presence of expected mutations before use (Supplementary Table 1).

Fig. 1: Neutralization of SARS-CoV-2 variant strains by clinically relevant mAbs.

 **figure1**

a, b, Amino acid substitutions in SARS-CoV-2 variants mapped onto the structure of the spike protein. Schematic layout of the spike protein monomer is depicted at the top. Structure of spike monomer (Protein Data Bank code (PDB) 7C2L, with RBD from PDB 6W41) is depicted as a cartoon, with the N-terminal domain (NTD), RBD, receptor-binding motif (RBM) and S2 coloured in orange, green, magenta and light blue, respectively. Substitutions for each variant are shown as spheres and coloured according to the legend. Substitutions shown in black are shared between several variants. The purple triangle, pink square, purple hexagon and black pentagon represent approximate locations of L5, S13, D253 and P681, respectively, which were not modelled in the original structures. CH, central helix; FP, fusion peptide; HR, heptad repeat; TM, transmembrane domain. The structural figure in **a** was generated using UCSF ChimeraX³³. **b**, Viruses used with indicated coloured mutations in the spike protein. **c**, Summary of EC₅₀ values (ng ml⁻¹) of neutralization of SARS-CoV-2 viruses performed in Vero-TMPRSS2 cells. Blue shading of cells indicates a partial (EC₅₀ > 1,000 ng ml⁻¹) or complete (EC₅₀ > 10,000 ng ml⁻¹) loss of neutralizing activity. **d**, Neutralization curves comparing the sensitivity of SARS-CoV-2 strains to

the indicated individual or combinations of mAbs. Data are representative of two to five experiments, each performed in technical duplicate.

[Source data](#)

[Full size image](#)

We first assessed the effect of SARS-CoV-2 spike variation on antibody neutralization (Fig. [1c, d](#)). We tested individual mAbs and cocktails of mAbs in clinical development that target the RBD, including 2B04 and 47D11 (AbbVie), S309 and S2E12 (Vir Biotechnology), COV2-2130 and COV2-2196 (Vanderbilt University Medical Center, with derivatives being evaluated by AstraZeneca), REGN10933 and REGN10987 (synthesized on the basis of casirivimab and imdevimab sequences from Regeneron), and LY-CoV555 (synthesized on the basis of bamlanivimab sequences from Lilly). All individual mAbs tested efficiently neutralized the WA1/2020 D614G, WA1/2020 N501Y/D614G and B.1.1.7 strains, and several mAbs (COV2-2130, COV2-2196, S309, S2E12 and 47D11) showed little change in potency against the Wash-B.1.351, Wash-B.1.1.28, B.1.429 and B.1.526 strains (Fig. [1c, d](#)). By comparison, REGN10987 and LY-CoV555 showed an approximately 10-fold and complete loss, respectively, in inhibitory activity against the B.1.429 and B.1.617.1 strains, which is consistent with previous studies that have identified L452 and adjacent residues as interaction sites for these mAbs⁸ (Supplementary Table [2](#)). Moreover, REGN10933, LY-CoV555 and 2B04 exhibited a substantial or complete loss of neutralizing activity against Wash-B.1.351, Wash-B.1.1.28, B.1.617.1 and B.1.526 (E484K) viruses that contain mutations at residue E484 (Fig. [1c, d](#), Extended Data Fig. [1](#)), which corresponds with structural and mapping studies (Supplementary Table [2](#)). Analysis of mAb cocktails showed that COV2-2130 in combination with COV2-2196 (COV2-2130/COV2-2196), S309/S2E12 and REGN10933/REGN10987 neutralized all of the virus strains we tested; the last of these combinations retained potency corresponding to the mAb with inhibitory activity in the cocktail for a given virus. The 2B04/47D11 mAb combination efficiently neutralized WA1/2020 D614G, WA1/2020 N501Y/D614G, B.1.1.7 and B.1.429 strains, whereas the activity of this combination against Wash-B.1.351, Wash-B.1.1.28, B.1.617.1 and B.1.526 (E484K) reflected the less-potent 47D11 mAb component (half-maximal effective concentration (EC_{50}) of 384–2,187 ng ml⁻¹) (Fig. [1c, d](#)). Additional mutations in B.1.617.1 decreased the potency of the 2B04/47D11 combination further. By contrast, almost all of the mAbs retained neutralizing potency against B.1.526 (S477N).

Prophylactic efficacy against variants

To evaluate the efficacy of the mAb combinations *in vivo*, we initially used K18-hACE2 mice in which human ACE2 expression is driven by the cytokeratin 18 gene

promoter^{9,10}. In previous studies it was established that low (2 mg per kg body weight (mg kg^{-1})) doses of several anti-RBD neutralizing human mAbs provide a threshold of protection when administered as prophylaxis¹¹. Accordingly, we gave K18-hACE2 mice a single 40-μg (about 2 mg kg^{-1} total) dose of the mAb combinations (2B04/47D11, S309/S2E12, COV2-2130/COV2-2196 or REGN10933/REGN10987) or LY-CoV555 as monotherapy by intraperitoneal injection one day before intranasal inoculation with SARS-CoV-2 (WA1/2020 N501Y/D614G, B.1.1.7, Wash-B.1.351 or Wash-B.1.1.28). For these in vivo studies, we used a recombinant version of WA1/2020 that encodes N501Y for direct comparison to B.1.1.7, Wash-B.1.351 or Wash-B.1.1.28 (all of which contain this residue). This substitution increases infection in mice^{12,13}, but did not substantively affect neutralization of the mAbs we tested (Fig. 1c).

Compared to a control human mAb, a single 40-μg prophylaxis dose of the anti-SARS-CoV-2 mAbs conferred substantial protection against WA1/2020-N501Y/D614G-induced weight loss and viral burden in the lungs, nasal washes, brain, spleen and heart in the K18-hACE2 mice at 6 days after infection (Fig. 2a–c, Extended Data Figs. 2, 3a). Although all of the anti-SARS-CoV-2 mAb cocktails protected against weight loss caused by B.1.1.7 (Fig. 2d), Wash-B.1.351 (Fig. 2g) or Wash-B.1.1.28 (Fig. 2j), LY-CoV555 monotherapy protected only against the B.1.1.7 strain (Fig. 2d,g,j). Some of the antibodies provided less virological protection against the B.1.1.7 (Fig. 2e,f), Wash-B.1.351(Fig. 2h,i) or Wash-B.1.1.28 (Fig. 2k,l) strains in specific tissues. Whereas all mAb groups protected against B.1.1.7 infection in the lung (Fig. 2e), 2B04/47D11 or LY-CoV555 did not perform as well in nasal washes (Fig. 2f), and LY-CoV555 showed reduced protection in the brain (Extended Data Fig. 2). Sanger sequencing analysis of the RBD region of viral RNA of brain, nasal wash and lung samples from mice treated with these mAbs did not show evidence of neutralization escape (Supplementary Table 3). Mice treated with 2B04/47D11 or LY-CoV555 also showed greater virus breakthrough than those treated with the other tested antibodies when challenged with Wash-B.1.351 (Fig. 2h,i) or Wash-B.1.1.28 (Fig. 2k,l) viruses: 2B04/47D11 reduced viral burden in the lungs, nasal washes and brain much less efficiently than the other mAb cocktails, and LY-CoV555 mAb treatment conferred virtually no protection in any tissue analysed (Fig. 2h,i,k,l, Extended Data Figs. 2, 3b). Compared to COV2-2130/COV2-2196 and S309/S2E12, REGN10933/REGN10987 also showed less ability to reduce viral RNA levels in nasal washes of mice infected with Wash-B.1.351 (Fig. 2i) or Wash-B.1.1.28 (Fig. 2l) viruses. To confirm that our findings with Wash-B.1.351 are similar to a bona fide B.1.351 strain, we tested mAbs from each cocktail for neutralization and the COV2-2130/COV2-2196 cocktail for protection in K18-hACE2 mice. Equivalent levels of neutralization and viral burden reduction were seen with B.1.351 and Wash-B.1.351 viruses (Extended Data Fig. 4).

Fig. 2: Antibody prophylaxis against SARS-CoV-2 variants in K18-hACE2 mice.

 figure2

a–l, Eight-to-ten-week-old female and male K18-hACE2 transgenic mice received 40 µg (about 2 mg kg⁻¹) of the indicated mAb treatment by intraperitoneal injection one day before intranasal inoculation with 10³ FFU of the SARS-CoV-2 N501Y/D614G

(**a–c**), B.1.1.7 (**d–f**), Wash-B.1.351 (**g–i**) or Wash-B.1.1.28 (**j–l**) strains. Tissues were collected at six days after infection. **a, d, g, j**, Weight change after infection with SARS-CoV-2 (mean \pm s.e.m.; $n = 6$ –12 mice per group, two experiments; one-way analysis of variance (ANOVA) with Dunnett's test of area under the curve. NS, not significant; **** $P < 0.0001$). Viral RNA levels in the lung (**b, e, h, k**) and nasal washes (**c, f, i, l**) were measured (line indicates median; in order from left to right, $n = 9, 6, 7, 6, 6$ and 6 (**a**); $n = 11, 5, 5, 6, 6$ and 6 (**b**); $n = 9, 5, 5, 6, 6$ and 6 (**c**); $n = 12, 6, 6, 6, 5$ and 6 (**d–f**); $n = 12, 6, 6, 6, 6$ and 6 (**g, h, j, k**); $n = 12, 6, 6, 6, 6$ and 5 (**i**); $n = 10, 6, 6, 6, 6$ and 5 (**l**) mice per group, two experiments; one-way ANOVA with Dunnett's test with comparison to control mAb. NS, not significant, **** $P < 0.0001$; * $P = 0.026$ (**c**); ** $P = 0.0016$, *** $P = 0.0002$ (**l**)). Dotted line indicates the limit of detection of the assay.

[Source data](#)

[Full size image](#)

To evaluate further the extent of protection conferred by the different mAb groups against the SARS-CoV-2 variant viruses, we measured pro-inflammatory cytokine and chemokines in lung homogenates collected at six days after infection (Extended Data Figs. [5](#), [6](#)). This analysis showed a strong correspondence with viral RNA levels in the lung: (1) compared to the control mAb, S309/S2E12, COV2-2130/COV2-2196 and REGN10933/REGN10987 combinations showed markedly reduced levels of pro-inflammatory cytokines and chemokines (G-CSF, IFN γ , IL-6, CXCL10, LIF, CCL2, CXCL9, CCL3 and CCL4) after infection with WA1/2020 N501Y/D614G, B.1.1.7, Wash-B.1.351 or Wash-B.1.1.28; and (2) prophylaxis with 2B04/47D11 or LY-CoV555 resulted in reduced inflammatory cytokine and chemokine levels in mice infected with WA1/2020 N501Y/D614G and B.1.1.7, with less improvement in mice infected with Wash-B.1.351 or Wash-B.1.1.28.

Given that a 40- μ g dose of the S309/S2E12, COV2-2130/COV2-2196 and REGN10933/REGN10987 combinations prevented infection and inflammation caused by the different SARS-CoV-2 strains, we tested a tenfold-lower (4 μ g) dose (about 0.2 mg kg $^{-1}$) to assess for possible differences in protection. Prophylaxis with COV2-2130/COV2-2196, S309/S2E12, REGN10933/REGN10987 or 2B04/47D11 protected K18-hACE2 mice against weight loss caused by all four viruses (Extended Data Fig. [7a–d](#)). Whereas the COV2-2130/COV2-2196, S309/S2E12 and REGN10933/REGN10987 mAb combinations reduced viral RNA levels in the lung at six days after infection in K18-hACE2 mice infected with WA1/2020 N501Y/D614G, B.1.1.7, Wash-B.1.351 or Wash-B.1.1.28, the 2B04/47D11 treatment conferred protection against B.1.1.7 and WA1/2020 N501Y/D614G but not against Wash-B.1.351 or Wash-B.1.1.28 viruses at this lower dose (Extended Data Fig. [7e–h](#)). By comparison, in nasal washes, all four mAb cocktails resulted in relatively similar

reductions in viral RNA levels at six days after infection of mice inoculated with WA1/2020 N501Y/D614G, B.1.1.7, Wash-B.1.351 or Wash-B.1.1.28 (Extended Data Fig. 7*i–l*). Even at this low treatment dose, with the exception of some breakthrough events ($>6 \log_{10}$ (copies of N per mg): COV2-2130/COV2-2196 (2 of 24 mice); S309/S2E12 (6 of 24 mice); REGN10933/REGN10987 (1 of 24 mice); and 2B04/47D11 (6 of 24 mice)), the mAb combinations generally prevented infection of the brain (Extended Data Fig. 7*m–p*, Supplementary Table 3). Overall, the neutralization activity of mAbs in vitro against SARS-CoV-2 variants correlated with lung viral burden after prophylactic administration (Extended Data Fig. 8).

As an alternative model for evaluating mAb efficacy, we tested immunocompetent, inbred 129S2 mice, which are permissive to infection by SARS-CoV-2 strains that encode an N501Y substitution without human ACE2 expression^{12,13}; presumably, the N501Y adaptive mutation enables engagement of mouse ACE2. We administered a single 40- μ g (about 2 mg kg⁻¹) dose of mAb cocktails (COV2-2130/COV2-2196, S309/S2E12 or REGN10933/REGN10987) or a control mAb via intraperitoneal injection one day before intranasal inoculation with 10³ focus-forming units (FFU) of WA1/2020 N501Y/D614G, Wash-B.1.351 or Wash-B.1.1.28, and 10⁵ FFU of B.1.1.7 (Extended Data Fig. 9). A higher inoculating dose of B.1.1.7 was required to obtain equivalent levels of viral RNA in the lung compared to the other three viruses. At three days after infection, we collected tissues for viral burden analyses; at this time point, reproducible weight loss was not observed. All three mAb cocktails tested (COV2-2130/COV2-2196, S309/S2E12 and REGN10933/REGN10987) protected 129S2 mice against infection in the lung by all of the SARS-CoV-2 strains (Extended Data Fig. 9*a–d*); despite some variability, we observed a trend towards less complete protection in mice infected with Wash-B.1.351 and Wash-B.1.1.28 strains (Extended Data Fig. 3*c–f*). When we evaluated the nasal washes, reductions in viral RNA levels were diminished with the Wash-B.1.351 virus, especially for the COV2-2130/COV2-2196 and REGN10933/REGN10987 combinations (Extended Data Fig. 9*e–h*). Sequencing analysis of lung samples from the infected 129S2 mice also did not reveal evidence of acquisition of mutations in the RBD (Supplementary Table 3).

The immunocompetent Syrian golden hamster has previously been used to evaluate mAb activity against SARS-CoV-2 infection^{14,15}. We used this model to assess independently the inhibitory activity and possible emergence of resistance of one of the mAb combinations (COV2-2130/COV2-2196) against viruses containing the B.1.351 spike protein. One day before intranasal inoculation with 5 × 10⁵ FFU of Wash-B.1.351 or WA1/2020 D614G, we treated hamsters with a single 800- μ g (about 10 mg kg⁻¹) or 320- μ g (about 4 mg kg⁻¹) dose of the COV2-2130/COV2-2196 cocktail or isotype control mAb by intraperitoneal injection (Extended Data Fig. 10). Weights were followed for four days, and tissues were collected for virological and cytokine analysis. At the 800- μ g mAb cocktail dose, hamsters treated with COV2-

2130/COV2-2196 and infected with WA1/2020 D614G or Wash-B.1.351 showed protection against weight loss and reduced viral burden levels in the lungs, but not nasal swabs, compared to the isotype control mAb (Extended Data Fig. 10a–d). Correspondingly, quantitative PCR with reverse transcription analysis of a previously described set of cytokines and inflammatory genes¹¹ showed reduced mRNA expression in the lungs of hamsters treated with COV2-2130/COV2-2196 (Extended Data Fig. 10e–h). Consensus sequencing of the RBD region of viral RNA samples from the lungs of hamsters treated with COV2-2130/COV2-2196 did not show evidence of mutation or escape (Supplementary Table 3). When the lower 320-μg dose of COV2-2130/COV2-2196 was administered, we observed a trend towards protection against weight loss in hamsters infected with WA1/2020 D614G and Wash-B.1.351. Consistent with a partially protective phenotype, hamsters treated with the lower 320-μg dose of COV2-2130/COV2-2196 and inoculated with either WA1/2020 D614G or Wash-B.1.351 showed a trend towards reduced viral RNA in the lungs at 4 days after infection and markedly diminished (about 10⁴- to 10⁵-fold) levels of infectious virus as determined by plaque assay (Extended Data Fig. 10j, k). The reduction in lung viral load conferred by the lower dose of COV2-2130/COV2-2196 corresponded with diminished inflammatory gene expression after infection with either WA1/2020 D614G or Wash-B.1.351 (Extended Data Fig. 10m–p). In contrast to the protection seen in the lung, differences in viral RNA were not observed in nasal washes between COV2-2130/COV2-2196 and isotype control mAb-treated hamsters, regardless of the infecting strain (Extended Data Fig. 10l). Sequencing of the RBD of viral RNA from the lungs of COV2-2130/COV2-2196 or isotype mAb-treated hamsters also did not detect evidence of escape mutation selection after infection (Supplementary Table 3). Overall, these studies in hamsters with near-threshold dosing of the COV2-2130/COV2-2196 mAb cocktail establish protection and an absence of rapid escape against SARS-CoV-2 containing spike proteins from historical or variant strains.

Therapeutic efficacy against variants

As mAbs are being developed clinically as therapeutic agents, we assessed their post-exposure efficacy against the SARS-CoV-2 strain expressing the B.1.351 spike protein using K18-hACE2 mice. We administered a single, higher (200-μg; about 10 mg kg⁻¹) dose of COV2-2130/COV2-2196, S309/S2E12, REGN10933/REGN10987 or 2B04/47D11 by intraperitoneal injection one day after inoculation with WA1/2020 N501Y/D614G (Fig. 3a–c) or Wash-B.1.351 (Fig. 3d–f). Compared to the control mAb-treated mice, which lost at least 15% of their starting weight over the 6 days of the experiment, each of these mAb cocktails prevented weight loss induced by WA1/2020 N501Y/D614G or Wash-B.1.351 infection (Fig. 3a, d). Histopathological analysis of lung sections from control mAb-treated mice showed interstitial oedema, immune cell infiltration and collapsed alveolar spaces, consistent with the

inflammation induced by SARS-CoV-2 infection (Extended Data Fig. 11). By contrast, COV2-2130/COV2-2196-, S309/S2E12-, REGN10933/REGN10987- and 2B04/47D11-treated mice showed reduced or minimal lung pathology. COV2-2130/COV2-2196, S309/S2E12 and REGN10933/REGN10987 mAb cocktail treatments resulted in reduced infectious virus and viral RNA levels in lung homogenates, and viral RNA levels in nasal washes and brain homogenates from mice infected with either WA1/2020 N501Y/D614G or Wash-B.1.351 (Fig. 3b, c, e, f, Extended Data Figs. 3g, h, 12). By comparison, although the 2B04/47D11 mAb cocktail reduced viral RNA levels in the lungs, it showed less protection in the nasal washes of WA1/2020-N501Y/D614G- or Wash-B.1.351-infected mice. Although neutralizing capacity correlated with lung viral burden when mAbs were administered as prophylaxis, this association was less direct when mAbs were given in the post-exposure setting (Extended Data Fig. 8). This result was not entirely unexpected, as effector functions of some mAbs are required for optimal activity when given as post-exposure therapy^{11,16}. Indeed, recent studies with influenza and SARS-CoV-2 neutralizing antibodies suggest that Fc engagement mitigates inflammation, improves respiratory mechanics and promotes viral clearance in the lung^{11,17}.

Fig. 3: Post-exposure antibody therapy against SARS-CoV-2 variants in K18-hACE2 mice.



a–f, Eight-to-ten-week-old female and male K18-hACE2 transgenic mice were administered 10^3 FFU of the SARS-CoV-2 N501Y/D614G (**a–c**) or Wash-B.1.351 (**d–f**) strains by intranasal inoculation. One day later, mice received 200 μ g (about 10 mg kg $^{-1}$) of the indicated mAb treatment by intraperitoneal injection. Tissues were collected at six days after infection. **a, d**, Weight change after infection with SARS-CoV-2 (mean \pm s.e.m.; in order from left to right $n = 15, 6, 6, 6, 6, 7$ and 7 (**a, d**) mice per group, two experiments; one-way ANOVA with Dunnett's test of area under the curve. NS, not significant, *** $P < 0.0001$). Viral RNA levels in the lung (**b, e**) and nasal wash (**c, f**) (line indicates median; in order from left to right $n = 7, 6, 6, 6, 6, 7$ and 7 (**b**); $n = 9, 6, 6, 6, 6, 7$ and 7 (**c, e, f**) mice per group, 2 experiments; one-way ANOVA with Dunnett's test with comparison to control mAb. NS, not significant, *** $P < 0.0001$; ** $P = 0.0014$ (left) and 0.0088 (right), *** $P = 0.0007$ (left) and 0.0003 (right) (**b**); ** $P = 0.0026$ (left), 0.0041 (middle) and 0.0049 (right) (**c**); ** $P = 0.0049$, *** $P = 0.0004$ (**e**); ** $P = 0.0094$, *** $P = 0.0005$, * $P = 0.0442$ (**f**)). Dotted line indicates the limit of detection of the assay.

[Source data](#)

[Full size image](#)

With the emergence of several SARS-CoV-2 variants, it remains uncertain whether vaccines and antibody-based therapies will lose efficacy¹⁸. Cell-culture-based studies have shown that several of the mutations in variant strains (especially those at positions 452 and 484) result in reduced neutralization by antibodies derived from infected or vaccinated individuals^{1,2,3,19,20}. Here we evaluated antibodies forming the basis of five mAb therapies in clinical development for in vivo efficacy against infection by SARS-CoV-2 variants. Monotherapy with LY-CoV555, an antibody that corresponds to bamlanivimab²¹, showed complete neutralization escape in cell culture and did not confer protection against viruses containing E484 substitutions. By contrast, all cocktails of two neutralizing mAbs conferred protection to varying degrees, even if one of the constituent mAbs showed reduced activity owing to resistance. Moreover, the higher doses of mAbs used in patients (for example, about 35 mg kg $^{-1}$ for casirivimab and imdevimab (corresponding to the REGN mAbs)) could compensate for loss in neutralization potency. Generally, in mice and hamsters, mAb-mediated protection was better in the lung than in nasal washes, possibly because IgG levels in the respiratory mucosa are lower than in plasma^{22,23}.

In our study, combination therapy with several mAbs was protective in mice and hamsters against variant strains, which highlights the importance of using multiple mAbs that recognize distinct epitopes (rather than monotherapy) to control SARS-CoV-2 infection. Indeed, the Emergency Use Authorization for bamlanivimab (LY-CoV555) as monotherapy was revoked, as the antibody does not reduce SARS-CoV-2

infection of several variants of concern^{2,24,25}; instead, a combination of bamlanivimab (LY-CoV555) and etesevimab (LY-CoV016) is recommended, even though strains that contain E484 and K417 mutations (such as B.1.351, B.1.1.28, B.1.617.1 and B.1.526) will probably have resistance to both mAb components^{2,26} (Extended Data Fig. 13). Indeed, in K18-hACE2 mice, we found that LY-CoV555/LY-CoV016 had therapeutic activity against WA1/2020 N501Y/D614G (Fig. 3a–c) but not against Wash-B.1.351 (Fig. 3d–f). This failure of protection occurred because both of the mAbs in the cocktail lost neutralizing activity. Other cocktails may fare better against variants of concern as long as one of the mAbs in each pair retains substantial inhibitory activity. Beyond a loss of potency against already circulating resistant variants, antibody monotherapy can be compromised within an individual by rapid selection of escape mutations. Consistent with this idea, in other animal experiments with SARS-CoV-2, we observed the emergence of resistance against antibody monotherapy, resulting in the accumulation of mutations at RBD residues 476, 477, 484, or 487 (ref. 27, and M.S.D., unpublished data). Despite amplifying sequences from 99 brain, nasal wash and lung samples from mice and hamsters treated with the different mAb combinations in this study, we did not detect a single escape mutant. Combination mAb treatment may prevent escape through synergistic interactions *in vivo* or by driving selection of mutants with compromised fitness.

At the lower doses of the mAbs we tested, we observed some differences in mAb cocktail efficacy between rodent models, which could be due to host variation, viral variation or small differences in antibody levels. For example, mutations in the RBD can affect mAb binding as well as ACE2 binding²⁸. Mutation at position 501 of the spike is of particular interest, as it enables mouse adaptation^{12,13} and is present in several variants of concern. The N501Y change associated with infection of conventional laboratory mice could facilitate virus engagement with mouse ACE2 or possibly other putative receptors. Beyond this, polymorphisms in or differences of expression of host receptors on key target cells also could affect SARS-CoV-2 infection in different hosts and the inhibitory effects of neutralizing antibodies. This complexity of antibody–spike protein–receptor interactions probably explains some of the variation in protection between K18-hACE2 mice, 129S2 mice and hamsters. Alternatively, the pharmacokinetics of human antibodies could vary between animals and affect efficacy. We observed small differences in serum antibody levels in the context of viral challenge that could affect relative protection (Supplementary Table 4).

Previous studies with pseudoviruses and authentic SARS-CoV-2 containing variant substitutions have suggested that adjustments to therapeutic antibody regimens might be necessary^{1,2,29,30,31}. Although our studies with variant strains *in vivo* suggest that this conclusion probably holds for mAb monotherapy, four different mAb combinations performed well even when a virus was fully resistant to one mAb

component. Thus, our results suggest that—as previously described for the historical WA1/2020 strain³²—many, but not all, combination therapies with neutralizing mAbs should retain efficacy against emerging SARS-CoV-2 variants.

Methods

No statistical methods were used to predetermine sample size. The experiments were not randomized, and investigators were not blinded to allocation during experiments and outcome assessment.

Cells

Vero-TMPRSS2³⁴ and Vero cells expressing human ACE2 and TMPRSS2 (Vero-hACE2-TMPRSS2)¹ cells were cultured at 37 °C in Dulbecco’s modified Eagle medium (DMEM) supplemented with 10% fetal bovine serum (FBS), 10 mM HEPES pH 7.3, 1 mM sodium pyruvate, 1× non-essential amino acids and 100 U ml⁻¹ of penicillin–streptomycin. Vero-TMPRSS2 cells were supplemented with 5 µg ml⁻¹ of blasticidin. Vero-hACE2-TMPRSS2 cells were supplemented with 10 µg ml⁻¹ of puromycin. All cells routinely tested negative for mycoplasma using a PCR-based assay.

Viruses

The WA1/2020 recombinant strains with substitutions (D614G or N501Y/D614G) were obtained from an infectious cDNA clone of the 2019n-CoV/USA_WA1/2020 strain, as previously described³⁵. The B.1.351- and B.1.1.28-variant spike genes were introduced into the WA1/2020 backbone as previously described to create chimeric SARS-CoV-2¹. The B.1.1.7, B.1.429, B.1.351 and B.1.526 (S477N or E484K variant) isolates were obtained from nasopharyngeal isolates. The B.1.617.1 variant was plaque-purified from a midturbinate nasal swab and passaged twice on Vero-TMPRSS2 cells, as previously described³⁶. All viruses were passaged once in Vero-TMPRSS2 cells and subjected to next-generation sequencing as previously described¹ to confirm the introduction and stability of substitutions (Supplementary Table 1). Substitutions for each variant were as follows: B.1.1.7: deletion of 69 and 70 and 144 and 145, N501Y, A570D, D614G, P681H, T716I, S982A, and D1118H; B.1.351: D80A, T95I, D215G, deletion of 242-244, K417N, E484K, N501Y, D614G, and A701V; B.1.1.28: L18F, T20N, P26S, D138Y, R190S, K417T, E484K, N501Y, D614G, H655Y, and T1027I; B.1.429: S13I, W152C, L452R, and D614G; B.1.617.1: G142D, E154K, L452R, E484Q, D614G, P681R, Q1071H, and H1101D; and B.1.526 (S477N or E484K variant): L5F, T95I, D253G, S477N, E484K, D614G, and A701V

or Q957R. All virus experiments were performed in an approved biosafety level 3 facility.

mAb purification

The mAbs studied in this paper (COV2-2196, COV2-2130, S309, S2E12, 2B04, 47D11, REGN10933, REGN10987, LY-CoV555 and LY-CoV016) have previously been described^{[32](#),[37](#),[38](#),[39](#),[40](#),[41](#),[42](#),[43](#)}. COV2-2196 and COV2-2130 mAbs were produced after transient transfection using the Gibco ExpiCHO Expression System (ThermoFisher Scientific) following the manufacturer's protocol. Culture supernatants were purified using HiTrap MabSelect SuRe columns (Cytiva, (formerly GE Healthcare Life Sciences)) on an AKTA Pure chromatographer (GE Healthcare Life Sciences). Purified mAbs were buffer-exchanged into PBS, concentrated using Amicon Ultra-4 50-kDa centrifugal filter units (Millipore Sigma) and stored at -80 °C until use. Purified mAbs were tested for endotoxin levels (found to be less than 30 EU per mg IgG). Endotoxin testing was performed using the PTS201F cartridge (Charles River), with a sensitivity range from 10 to 0.1 EU per ml, and an Endosafe Nexgen-MCS instrument (Charles River). S309, S2E12, REGN10933, REGN10987, LY-CoV016 and LY-CoV555 mAb proteins were produced in CHOEXPI cells and affinity-purified using HiTrap Protein A columns (GE Healthcare, HiTrap mAb select Xtra no. 28-4082-61). Purified mAbs were suspended into 20 mM histidine, 8% sucrose, pH 6.0. The final products were sterilized by filtration through 0.22-μm filters and stored at 4 °C.

Mouse experiments

Animal studies were carried out in accordance with the recommendations in the Guide for the Care and Use of Laboratory Animals of the National Institutes of Health. The protocols were approved by the Institutional Animal Care and Use Committee at the Washington University School of Medicine (assurance number A3381–01). Virus inoculations were performed under anaesthesia that was induced and maintained with ketamine hydrochloride and xylazine, and all efforts were made to minimize animal suffering.

Heterozygous K18-hACE2 C57BL/6J mice (strain: 2B6.Cg-Tg(K18-ACE2)2PrIrn/J) and 129 mice (strain: 129S2/SvPasCrl) were obtained from The Jackson Laboratory and Charles River Laboratories, respectively. Mice were housed in groups and fed standard chow diets. Six-to-ten-week-old mice of both sexes were administered 10³ or 10⁵ FFU of the respective SARS-CoV-2 strain by intranasal administration. In vivo studies were not blinded, and mice were randomly assigned to treatment groups. No sample-size calculations were performed to power each study. Instead, sample sizes were determined on the basis of previous in vivo virus challenge experiments.

For antibody prophylaxis and therapeutic experiments, mice were administered the indicated mAb dose by intraperitoneal injection one day before or after intranasal inoculation with the indicated SARS-CoV-2 strain.

Hamster experiments

Six-month-old male Syrian hamsters were purchased from Charles River Laboratories and housed in microisolator units. All hamsters were allowed free access to food and water and cared for under United States Department of Agriculture (USDA) guidelines for laboratory animals. Hamsters were administered by intraperitoneal injection mAbs COV2-2130 and COV2-2196 or isotype control (4 or 10 mg kg⁻¹, depending on the experiment). One day later, hamsters were given 5 × 10⁵ FFU of indicated SARS-CoV-2 strain by the intranasal route in a final volume of 100 µl. All hamsters were monitored for body weight loss until being humanely euthanized at four days after infection. Nasal swabs were collected at three days after infection. All procedures were approved by the Washington University School of Medicine (assurance number A3381–01). Virus inoculations and antibody transfers were performed under anaesthesia that was induced and maintained with 5% isoflurane. All efforts were made to minimize animal suffering.

Focus reduction neutralization test

Serial dilutions of mAbs (starting at 10 µg ml⁻¹ dilution) were incubated with 10² FFU of different strains or variants of SARS-CoV-2 for 1 h at 37 °C. Antibody–virus complexes were added to Vero-TMPRSS2 cell monolayers in 96-well plates and incubated at 37 °C for 1 h. Subsequently, cells were overlaid with 1% (w/v) methylcellulose in MEM. Plates were collected 30 h later by removing overlays and fixed with 4% PFA in PBS for 20 min at room temperature. Plates were washed and sequentially incubated with an oligoclonal pool of SARS2-2, SARS2-11, SARS2-16, SARS2-31, SARS2-38, SARS2-57 and SARS2-71⁴⁴ anti-S antibodies and HRP-conjugated goat anti-mouse IgG (Sigma, 12-349) in PBS supplemented with 0.1% saponin and 0.1% bovine serum albumin. SARS-CoV-2-infected cell foci were visualized using TrueBlue peroxidase substrate (KPL) and quantitated on an ImmunoSpot microanalyzer (Cellular Technologies).

Measurement of viral burden

Tissues were weighed and homogenized with zirconia beads in a MagNA Lyser instrument (Roche Life Science) in 1000 µl of DMEM medium supplemented with 2% heat-inactivated FBS. Tissue homogenates were clarified by centrifugation at 10,000 rpm for 5 min and stored at –80 °C. RNA was extracted using the MagMax mirVana Total RNA isolation kit (Thermo Fisher Scientific) on the Kingfisher Flex extraction

robot (Thermo Fisher Scientific). RNA was reverse-transcribed and amplified using the TaqMan RNA-to-CT 1-Step Kit (Thermo Fisher Scientific). Reverse transcription was carried out at 48 °C for 15 min followed by 2 min at 95 °C. Amplification was accomplished over 50 cycles as follows: 95 °C for 15 s and 60 °C for 1 min. Copies of SARS-CoV-2 *N* gene RNA in samples were determined using a previously published assay⁴⁵. In brief, a TaqMan assay was designed to target a highly conserved region of the *N* gene (forward primer: ATGCTGCAATCGTGCTACAA; reverse primer: GACTGCCGCCTCTGCTC; probe: /56-FAM/TCAAGGAAC/ZEN/AACATTGCCAA/3IABkFQ/). This region was included in an RNA standard to allow for copy number determination down to 10 copies per reaction. The reaction mixture contained final concentrations of primers and probe of 500 and 100 nM, respectively.

Plaque assay

Vero-hACE2-TMPRSS2 cells were seeded at a density of 1×10^5 cells per well in 24-well tissue culture plates. The following day, medium was removed and replaced with 200 µl of material to be titrated diluted serially in DMEM supplemented with 2% FBS. One hour later, 1 ml of methylcellulose overlay was added. Plates were incubated for 72 h, then fixed with 4% paraformaldehyde (final concentration) in PBS for 20 min. Plates were stained with 0.05% (w/v) crystal violet in 20% methanol and washed twice with distilled, deionized water.

Cytokine and chemokine protein measurements

Lung homogenates were incubated with Triton-X-100 (1% final concentration) for 1 h at room temperature to inactivate SARS-CoV-2. Homogenates then were analysed for cytokines and chemokines by Eve Technologies using their Mouse Cytokine Array/Chemokine Array 31-Plex (MD31) platform.

Lung histology

Animals were euthanized before harvest and fixation of tissues. Lungs were inflated with about 2 ml of 10% neutral buffered formalin using a 3-ml syringe and catheter inserted into the trachea and kept in fixative for 7 days. Tissues were embedded in paraffin, and sections were stained with haematoxylin and eosin. Images were captured using the Nanozoomer (Hamamatsu) at the Alafi Neuroimaging Core at Washington University.

Statistical analysis

All statistical tests were performed as described in the indicated figure legends using Prism 8.0. Statistical significance was determined using an ordinary one-way ANOVA with Dunnett's post-test when comparing three or more groups. The number of independent experiments used are indicated in the relevant figure legends.

Reporting summary

Further information on research design is available in the [Nature Research Reporting Summary](#) linked to this paper.

Data availability

All data supporting the findings of this study are available within the paper and are available from the corresponding author upon request. [Source data](#) are provided with this paper.

References

1. 1.

Chen, R. E. et al. Resistance of SARS-CoV-2 variants to neutralization by monoclonal and serum-derived polyclonal antibodies. *Nat. Med.* **27**, 717–726 (2021).

[CAS](#) [Article](#) [Google Scholar](#)

2. 2.

Wang, P. et al. Antibody resistance of SARS-CoV-2 variants B.1.351 and B.1.1.7. *Nature* **593**, 130–135 (2021).

[ADS](#) [CAS](#) [Article](#) [Google Scholar](#)

3. 3.

Wang, Z. et al. mRNA vaccine-elicited antibodies to SARS-CoV-2 and circulating variants. *Nature* **592**, 616–622 (2021).

[ADS](#) [CAS](#) [Article](#) [Google Scholar](#)

4. 4.

Wibmer, C. K. et al. SARS-CoV-2 501Y.V2 escapes neutralization by South African COVID-19 donor plasma. *Nat. Med.* **27**, 622–625 (2021).

[CAS Article](#) [Google Scholar](#)

5. 5.

Tada, T. et al. Convalescent-phase sera and vaccine-elicited antibodies largely maintain neutralizing titer against global SARS-CoV-2 variant spikes. *mBio* **12**, <https://doi.org/10.1128/mBio.00696-21> (2021).

6. 6.

Xie, X. et al. Neutralization of SARS-CoV-2 spike 69/70 deletion, E484K and N501Y variants by BNT162b2 vaccine-elicited sera. *Nat. Med.* **27**, 620–621 (2021).

[CAS Article](#) [Google Scholar](#)

7. 7.

Johnson, B. A. et al. Loss of furin cleavage site attenuates SARS-CoV-2 pathogenesis. *Nature* **591**, 293–299 (2021).

[ADS](#) [CAS Article](#) [Google Scholar](#)

8. 8.

Deng X. et al. Transmission, infectivity, and neutralization of a spike L452R SARS-CoV-2 variant. *Cell* **184**, 3426–3437 (2021).

9. 9.

Winkler, E. S. et al. SARS-CoV-2 infection of human ACE2-transgenic mice causes severe lung inflammation and impaired function. *Nat. Immunol.* **21**, 1327–1335 (2020).

[CAS Article](#) [Google Scholar](#)

10. 10.

McCray, P. B. Jr et al. Lethal infection of K18-hACE2 mice infected with severe acute respiratory syndrome coronavirus. *J. Virol.* **81**, 813–821 (2007).

[CAS Article](#) [Google Scholar](#)

11. 11.

Winkler, E. S. et al. Human neutralizing antibodies against SARS-CoV-2 require intact Fc effector functions for optimal therapeutic protection. *Cell* **184**, 1804–1820 (2021).

[CAS Article](#) [Google Scholar](#)

12. 12.

Rathnasinghe, R. et al. The N501Y mutation in SARS-CoV-2 spike leads to morbidity in obese and aged mice and is neutralized by convalescent and post-vaccination human sera. Preprint at <https://doi.org/10.1101/2021.01.19.21249592> (2021).

13. 13.

Gu, H. et al. Adaptation of SARS-CoV-2 in BALB/c mice for testing vaccine efficacy. *Science* **369**, 1603–1607 (2020).

[ADS](#) [CAS Article](#) [Google Scholar](#)

14. 14.

Zhou, D. et al. Robust SARS-CoV-2 infection in nasal turbinates after treatment with systemic neutralizing antibodies. *Cell Host Microbe* **29**, 551–563 (2021).

[CAS Article](#) [Google Scholar](#)

15. 15.

Andreano, E. et al. Extremely potent human monoclonal antibodies from COVID-19 convalescent patients. *Cell* **184**, 1821–1835 (2021).

[CAS Article](#) [Google Scholar](#)

16. 16.

Schäfer, A. et al. Antibody potency, effector function, and combinations in protection and therapy for SARS-CoV-2 infection in vivo. *J. Exp. Med.* **218**, e20201993 (2021).

[Article](#) [Google Scholar](#)

17. 17.

Bournazos, S., Corti, D., Virgin, H. W. & Ravetch, J. V. Fc-optimized antibodies elicit CD8 immunity to viral respiratory infection. *Nature* **588**, 485–490 (2020).

[ADS](#) [CAS](#) [Article](#) [Google Scholar](#)

18. 18.

Cobey, S., Larremore, D. B., Grad, Y. H. & Lipsitch, M. Concerns about SARS-CoV-2 evolution should not hold back efforts to expand vaccination. *Nat. Rev. Immunol.* **21**, 330–335 (2021).

[CAS](#) [Article](#) [Google Scholar](#)

19. 19.

Shen, X. et al. Neutralization of SARS-CoV-2 variants B.1.429 and B.1.351. *N. Engl. J. Med.* (2021).

20. 20.

.McCallum, M. et al. SARS-CoV-2 immune evasion by variant B.1.427/B.1.429. Preprint at <https://doi.org/10.1101/2021.03.31.437925> (2021).

21. 21.

ACTIV-3/TICO LY-CoV555 Study Group. A neutralizing monoclonal antibody for hospitalized patients with Covid-19. *N. Engl. J. Med.* **384**, 905–914 (2021).

[Article](#) [Google Scholar](#)

22. 22.

Reynolds, H. Y. Immunoglobulin G and its function in the human respiratory tract. *Mayo Clin. Proc.* **63**, 161–174 (1988).

[CAS](#) [Article](#) [Google Scholar](#)

23. 23.

Borrok, M. J. et al. Enhancing IgG distribution to lung mucosal tissue improves protective effect of anti-*Pseudomonas aeruginosa* antibodies. *JCI Insight* **3**,

e97844 (2018).

[Article](#) [Google Scholar](#)

24. 24.

Gottlieb, R. L. et al. Effect of bamlanivimab as monotherapy or in combination with etesevimab on viral load in patients with mild to moderate COVID-19: a randomized clinical trial. *J. Am. Med. Assoc.* **325**, 632–644 (2021).

[CAS](#) [Article](#) [Google Scholar](#)

25. 25.

Wang, P. et al. Increased resistance of SARS-CoV-2 variant P.1 to antibody neutralization. *Cell Host Microbe* **29**, 747–751 (2021).

[CAS](#) [Article](#) [Google Scholar](#)

26. 26.

Starr, T. N., Greaney, A. J., Dingens, A. S. & Bloom, J. D. Complete map of SARS-CoV-2 RBD mutations that escape the monoclonal antibody LY-CoV555 and its cocktail with LY-CoV016. *Cell Rep. Med.* **2**, 100255 (2021).

[Article](#) [Google Scholar](#)

27. 27.

Schmitz, A. J. et al. A public vaccine-induced human antibody protects against SARS-CoV-2 and emerging variants. Preprint at <https://doi.org/10.1101/2021.03.24.436864> (2021).

28. 28.

Tian, F. et al. Mutation N501Y in RBD of spike protein strengthens the interaction between COVID-19 and its receptor ACE2. Preprint at <https://doi.org/10.1101/2021.02.14.431117> (2021).

29. 29.

Graham, C. et al. Neutralization potency of monoclonal antibodies recognizing dominant and subdominant epitopes on SARS-CoV-2 spike is impacted by the B.1.1.7 variant. *Immunity* **54**, 1276–1289 (2021).

[CAS](#) [Article](#) [Google Scholar](#)

30. 30.

Rees-Spear, C. et al. The effect of spike mutations on SARS-CoV-2 neutralization. *Cell Rep.* **34**, 108890 (2021).

[CAS](#) [Article](#) [Google Scholar](#)

31. 31.

Zhou, D. et al. Evidence of escape of SARS-CoV-2 variant B.1.351 from natural and vaccine-induced sera. *Cell* **184**, 2348–2361 (2021).

[CAS](#) [Article](#) [Google Scholar](#)

32. 32.

Baum, A. et al. Antibody cocktail to SARS-CoV-2 spike protein prevents rapid mutational escape seen with individual antibodies. *Science* **369**, 1014–1018 (2020).

[ADS](#) [CAS](#) [Article](#) [Google Scholar](#)

33. 33.

Goddard, T. D. et al. UCSF ChimeraX: meeting modern challenges in visualization and analysis. *Protein Sci.* **27**, 14–25 (2018).

[CAS](#) [Article](#) [Google Scholar](#)

34. 34.

Zang, R. et al. TMPRSS2 and TMPRSS4 promote SARS-CoV-2 infection of human small intestinal enterocytes. *Sci. Immunol.* **5**, eabc3582 (2020).

[CAS](#) [Article](#) [Google Scholar](#)

35. 35.

Plante, J. A. et al. Spike mutation D614G alters SARS-CoV-2 fitness. *Nature* **592**, 116–121 (2021).

[ADS](#) [CAS](#) [Article](#) [Google Scholar](#)

36. 36.

Edara, V.-V. et al. Infection and vaccine-induced neutralizing antibody responses to the SARS-CoV-2 B.1.617.1 variant. Preprint at <https://doi.org/10.1101/2021.05.09.443299> (2021).

37. 37.

Zost, S. J. et al. Rapid isolation and profiling of a diverse panel of human monoclonal antibodies targeting the SARS-CoV-2 spike protein. *Nat. Med.* **26**, 1422–1427 (2020).

[CAS](#) [Article](#) [Google Scholar](#)

38. 38.

Pinto, D. et al. Cross-neutralization of SARS-CoV-2 by a human monoclonal SARS-CoV antibody. *Nature* **583**, 290–295 (2020).

[ADS](#) [CAS](#) [Article](#) [Google Scholar](#)

39. 39.

Tortorici, M. A. et al. Ultrapotent human antibodies protect against SARS-CoV-2 challenge via multiple mechanisms. *Science* **370**, 950–957 (2020).

[ADS](#) [CAS](#) [Article](#) [Google Scholar](#)

40. 40.

Alsoussi, W. B. et al. A potently neutralizing antibody protects mice against SARS-CoV-2 infection. *J. Immunol.* **205**, 915–922 (2020).

[CAS](#) [Article](#) [Google Scholar](#)

41. 41.

Baum, A. et al. REGN-COV2 antibodies prevent and treat SARS-CoV-2 infection in rhesus macaques and hamsters. *Science* **370**, 1110–1115 (2020).

[ADS](#) [CAS](#) [Article](#) [Google Scholar](#)

42. 42.

Jones, B. E. et al. The neutralizing antibody, LY-CoV555, protects against SARS-CoV-2 infection in nonhuman primates. *Sci. Transl. Med.* **13**, eabf1906 (2020).

[Article](#) [Google Scholar](#)

43. 43.

Shi, R. et al. A human neutralizing antibody targets the receptor-binding site of SARS-CoV-2. *Nature* **584**, 120–124 (2020).

[ADS](#) [CAS](#) [Article](#) [Google Scholar](#)

44. 44.

Liu, Z. et al. Identification of SARS-CoV-2 spike mutations that attenuate monoclonal and serum antibody neutralization. *Cell Host Microbe* **29**, 477–488 (2021).

[CAS](#) [Article](#) [Google Scholar](#)

45. 45.

Case, J. B., Bailey, A. L., Kim, A. S., Chen, R. E. & Diamond, M. S. Growth, detection, quantification, and inactivation of SARS-CoV-2. *Virology* **548**, 39–48 (2020).

[CAS](#) [Article](#) [Google Scholar](#)

[Download references](#)

Acknowledgements

This study was supported by grants and contracts from NIH (R01 AI157155, U01 AI151810, U01 AI141990, R01 AI118938, 75N93019C00051, HHSN272201400006C, HHSN272201400008C, HHSN75N93019C00074 and HHSN272201400006C), the Children’s Discovery Institute (PDII2018702), the Defense Advanced Research Project Agency (HR0011-18-2-0001), the Dolly Parton COVID-19 Research Fund at Vanderbilt University, a grant from Fast Grants, Mercatus Center, George Mason University and the Future Insight Prize (Merck KGaA; to J.E.C. Jr). J.B.C. is supported by a Helen Hay Whitney Foundation postdoctoral fellowship, E.S.W. is supported by F30 AI152327 and S.J.Z. is supported by NIH grant T32 AI095202. P.-Y.S. is supported by the Sealy & Smith Foundation, the Kleberg Foundation, the John S. Dunn Foundation, the Amon G. Carter

Foundation, the Gilson Longenbaugh Foundation and the Summerfield Robert Foundation. We thank R. Nargi, R. Carnahan, T. Tan and L. Schimanski for assistance and generosity with mAb generation and purification; S. Tahan for some of the deep sequencing analysis; and the Pulmonary Morphology Core at Washington University School of Medicine for tissue sectioning and slide imaging.

Author information

Author notes

1. These authors contributed equally: Rita E. Chen, Emma S. Winkler, James Brett Case

Affiliations

1. Department of Medicine, Washington University School of Medicine, St Louis, MO, USA

Rita E. Chen, Emma S. Winkler, James Brett Case, Ishmael D. Aziati, Traci L. Bricker, Astha Joshi, Tamarand L. Darling, Baoling Ying, Swathi Shrihari, Laura A. VanBlargan, Adrianus C. M. Boon & Michael S. Diamond

2. Department of Pathology and Immunology, Washington University School of Medicine, St Louis, MO, USA

Rita E. Chen, Emma S. Winkler, John M. Errico, Scott A. Handley, Ali H. Ellebedy, Daved H. Fremont, Adrianus C. M. Boon & Michael S. Diamond

3. Department of Biochemistry and Molecular Biology, University of Texas Medical Branch, Galveston, TX, USA

Xuping Xie & Pei-Yong Shi

4. Vanderbilt Vaccine Center, Vanderbilt University Medical Center, Nashville, TN, USA

Pavlo Gilchuk, Seth J. Zost & James E. Crowe Jr

5. Department of Molecular Microbiology, Washington University School of Medicine, St Louis, MO, USA

Lindsay Droit, Zhuoming Liu, Spencer Stumpf, David Wang, Daved H. Fremont, Sean P. J. Whelan, Adrianus C. M. Boon & Michael S. Diamond

6. AbbVie Bioresearch Center, Worcester, MA, USA

W. Blaine Stine Jr

7. Department of Microbiology and Immunology, University of Texas Medical Branch, Galveston, TX, USA

Pei-Yong Shi

8. Sealy Institute for Vaccine Sciences, University of Texas Medical Branch, Galveston, TX, USA

Pei-Yong Shi

9. Center for Childhood Infections and Vaccines of Children's Healthcare of Atlanta, Department of Pediatrics, Emory Vaccine Center, Emory University School of Medicine, Atlanta, GA, USA

Meredith E. Davis-Gardner & Mehul S. Suthar

10. Department of Microbiology and Immunology, University of California San Francisco, San Francisco, CA, USA

Miguel Garcia Knight & Raul Andino

11. Department of Laboratory Medicine, University of California San Francisco, San Francisco, CA, USA

Charles Y. Chiu

12. Department of Medicine, University of California San Francisco, San Francisco, CA, USA

Charles Y. Chiu

13. Andrew M. and Jane M. Bursky Center for Human Immunology and Immunotherapy Programs, Washington University School of Medicine, St Louis, MO, USA

Ali H. Ellebedy & Michael S. Diamond

14. Center for Vaccines and Immunity to Microbial Pathogens, Washington University School of Medicine, St Louis, MO, USA

Ali H. Ellebedy & Michael S. Diamond

15. Department of Biochemistry and Molecular Biophysics, Washington University School of Medicine, St Louis, MO, USA

Daved H. Fremont

16. Department of Pediatrics, Vanderbilt University Medical Center, Nashville, TN, USA

James E. Crowe Jr

17. Department of Pathology, Microbiology and Immunology, Vanderbilt University Medical Center, Nashville, TN, USA

James E. Crowe Jr

18. Vir Biotechnology, St Louis, MO, USA

Lisa Purcell

19. Humabs BioMed SA, a subsidiary of Vir Biotechnology, Bellinzona, Switzerland

Davide Corti

Authors

1. Rita E. Chen

[View author publications](#)

You can also search for this author in [PubMed](#) [Google Scholar](#)

2. Emma S. Winkler

[View author publications](#)

You can also search for this author in [PubMed](#) [Google Scholar](#)

3. James Brett Case

[View author publications](#)

You can also search for this author in [PubMed](#) [Google Scholar](#)

4. Ishmael D. Aziati

[View author publications](#)

You can also search for this author in [PubMed](#) [Google Scholar](#)

5. Traci L. Bricker

[View author publications](#)

You can also search for this author in [PubMed](#) [Google Scholar](#)

6. Astha Joshi

[View author publications](#)

You can also search for this author in [PubMed](#) [Google Scholar](#)

7. Tamarand L. Darling

[View author publications](#)

You can also search for this author in [PubMed](#) [Google Scholar](#)

8. Baoling Ying

[View author publications](#)

You can also search for this author in [PubMed](#) [Google Scholar](#)

9. John M. Errico

[View author publications](#)

You can also search for this author in [PubMed](#) [Google Scholar](#)

10. Swathi Shrihari

[View author publications](#)

You can also search for this author in [PubMed](#) [Google Scholar](#)

11. Laura A. VanBlargan

[View author publications](#)

You can also search for this author in [PubMed](#) [Google Scholar](#)

12. Xuping Xie

[View author publications](#)

You can also search for this author in [PubMed](#) [Google Scholar](#)

13. Pavlo Gilchuk

[View author publications](#)

You can also search for this author in [PubMed](#) [Google Scholar](#)

14. Seth J. Zost

[View author publications](#)

You can also search for this author in [PubMed](#) [Google Scholar](#)

15. Lindsay Droit

[View author publications](#)

You can also search for this author in [PubMed](#) [Google Scholar](#)

16. Zhuoming Liu

[View author publications](#)

You can also search for this author in [PubMed](#) [Google Scholar](#)

17. Spencer Stumpf

[View author publications](#)

You can also search for this author in [PubMed](#) [Google Scholar](#)

18. David Wang

[View author publications](#)

You can also search for this author in [PubMed](#) [Google Scholar](#)

19. Scott A. Handley

[View author publications](#)

You can also search for this author in [PubMed](#) [Google Scholar](#)

20. W. Blaine Stine Jr

[View author publications](#)

You can also search for this author in [PubMed](#) [Google Scholar](#)

21. Pei-Yong Shi

[View author publications](#)

You can also search for this author in [PubMed](#) [Google Scholar](#)

22. Meredith E. Davis-Gardner

[View author publications](#)

You can also search for this author in [PubMed](#) [Google Scholar](#)

23. Mehul S. Suthar

[View author publications](#)

You can also search for this author in [PubMed](#) [Google Scholar](#)

24. Miguel Garcia Knight

[View author publications](#)

You can also search for this author in [PubMed](#) [Google Scholar](#)

25. Raul Andino

[View author publications](#)

You can also search for this author in [PubMed](#) [Google Scholar](#)

26. Charles Y. Chiu

[View author publications](#)

You can also search for this author in [PubMed](#) [Google Scholar](#)

27. Ali H. Ellebedy

[View author publications](#)

You can also search for this author in [PubMed](#) [Google Scholar](#)

28. Daved H. Fremont

[View author publications](#)

You can also search for this author in [PubMed](#) [Google Scholar](#)

29. Sean P. J. Whelan

[View author publications](#)

You can also search for this author in [PubMed](#) [Google Scholar](#)

30. James E. Crowe Jr

[View author publications](#)

You can also search for this author in [PubMed](#) [Google Scholar](#)

31. Lisa Purcell

[View author publications](#)

You can also search for this author in [PubMed](#) [Google Scholar](#)

32. Davide Corti

[View author publications](#)

You can also search for this author in [PubMed](#) [Google Scholar](#)

33. Adrianus C. M. Boon

[View author publications](#)

You can also search for this author in [PubMed](#) [Google Scholar](#)

34. Michael S. Diamond

[View author publications](#)

You can also search for this author in [PubMed](#) [Google Scholar](#)

Contributions

R.E.C. performed and analysed neutralization assays. R.E.C., E.S.W. and J.B.C. performed mouse experiments. R.E.C., E.S.W., J.B.C., B.Y. and S. Shrihari performed viral burden analyses. X.X. generated the recombinant SARS-CoV-2 viruses. R.E.C. and L.A.V. propagated and validated SARS-CoV-2 viruses. L.D., S.A.H. and D.W. performed deep sequencing analysis. I.D.A. and S. Stumpf performed Sanger sequencing analyses. T.L.D., T.L.B. and A.C.M.B. performed the hamster studies. T.L.D. and A.J. performed viral burden and inflammatory gene analysis. J.M.E. and D.H.F. performed structural analysis. Z.L. generated escape mutants. E.S.W. quantified serum antibody concentrations. J.B.C. and T.L.B. performed plaque assays. D.C., P.G., S.J.Z., W.B.S. Jr, J.E.C. Jr, A.H.E. and L.P. provided mAbs. M.S.S., M.E.D.-G., P.-Y.S., M.G.K., R.A. and C.Y.C. provided SARS-CoV-2 strains. P.-Y.S., A.H.E., D.C., S.P.J.W., A.C.M.B. and M.S.D. obtained funding and supervised the research. R.E.C., E.S.W., J.B.C. and M.S.D. wrote the initial draft, with the other authors providing editorial comments.

Corresponding author

Correspondence to [Michael S. Diamond](#).

Ethics declarations

Competing interests

M.S.D. is a consultant for Inbios, Vir Biotechnology, Fortress Biotech and Carnival Corporation, and on the Scientific Advisory Boards of Moderna and Immunome. The laboratory of M.S.D. has received funding support in sponsored research agreements from Moderna, Vir Biotechnology, Kaleido and Emergent BioSolutions. M.S.S. is on the Advisory Board of Moderna. J.E.C. Jr has served as a consultant for Eli Lilly and Luna Biologics, is a member of the Scientific Advisory Boards of CompuVax and Meissa Vaccines, and is Founder of IDBiologics. The laboratory of J.E.C. Jr has received sponsored research agreements from Takeda, AstraZeneca and IDBiologics. Vanderbilt University (J.E.C. Jr) and Washington University (A.H.E., D.H.F., J.B.C., A.C.M.B. and M.S.D.) have applied for patents related to antibodies in this paper. The laboratory of A.H.E. has received funding support in sponsored research agreements from AbbVie Inc. and Emergent BioSolutions. The laboratory of A.C.M.B. has received funding support in sponsored research agreements from AI Therapeutics, GreenLight Biosciences, AbbVie, and Nano Targeting & Therapy Biopharma. The laboratory of P.-Y.S. has received sponsored research agreements from Pfizer, Gilead, Merck and IGM Sciences Inc. D.C. and L.P. are employees of Vir Biotechnology and may hold equity in Vir Biotechnology. L.P. is a former employee and may hold equity in Regeneron Pharmaceuticals. W.B.S. Jr is an employee of AbbVie and may hold equity.

Additional information

Peer review information *Nature* thanks the anonymous reviewers for their contribution to the peer review of this work. Peer reviewer reports are available.

Publisher's note Springer Nature remains neutral with regard to jurisdictional claims in published maps and institutional affiliations.

Extended data figures and tables

[Extended Data Fig. 1 Neutralization curves with mAbs and variant SARS-CoV-2 strains.](#)

Anti-SARS-CoV-2 human mAbs were tested for inhibition of infection of the indicated viruses on Vero-TMPRSS2 cells using a focus reduction neutralization test. One representative experiment of two performed in duplicate is shown.

[Source data](#)

[Extended Data Fig. 2 SARS-CoV-2 variant infection after antibody prophylaxis of K18-hACE2 mice.](#)

a–l, Eight-to-ten-week-old female and male K18-hACE2 transgenic mice received 40 µg of the indicated mAb treatment by intraperitoneal injection one day before intranasal challenge with 10^3 FFU of the indicated SARS-CoV-2 strain. At 6 days after infection, viral RNA levels in the heart (**a–d**), spleen (**e–h**) and brain (**i–l**) were measured (line indicates median; in order from left to right $n = 9, 5, 5, 6, 6$ and 6 (**a**); $n = 12, 6, 6, 6, 5$, and 6 (**b, c, f, g, j, k**); $n = 10, 6, 6, 6, 6$ and 5 (**d, h**); $n = 6, 5, 5, 3, 3$ and 3 (**e**); $n = 9, 4, 4, 6, 6$ and 6 (**i**); $n = 11, 6, 6, 6, 6$ and 5 (**l**) mice per group, two experiments; one-way ANOVA with Dunnett's test with comparison to control mAb: ns, not significant, $****P < 0.0001$; in order from left to right $**P = 0.0066, 0.0032, 0.0080, 0.0016$ and 0.0052 (**a**); $***P = 0.0002, **P = 0.0017$ and 0.0052 (**b**); $***P = 0.0004$ and $0.0004, *P = 0.0140, **P = 0.0043$ (**c**); $**P = 0.0080$ and $0.0080, *P = 0.0226$ (**d**); $***P = 0.0001, 0.0001, 0.0008, 0.0008$ and 0.0008 (**e**); $***P = 0.0008$ (**h**); $**P = 0.0014, 0.0014, 0.0029$ and 0.0032 (**j**); $***P = 0.0002$ and $0.0002, **P = 0.0061$ and 0.0028 (**k**); $*P = 0.0371$ (**l**)). Dotted line indicates the limit of detection of the assay.

[Source data](#)

Extended Data Fig. 3 Reduced infectious virus in the lungs of antibody-treated mice.

a, b, Eight-to-ten-week-old female and male K18-hACE2 transgenic mice received 40 µg (about 2 mg kg^{-1}) of the indicated mAb treatment by intraperitoneal injection one day before intranasal inoculation with 10^3 FFU of the indicated SARS-CoV-2 strain. Tissues were collected at six days after infection. **c–f**, Six-to-seven-week-old female and male immunocompetent 129S2 mice received 40 µg (about 2 mg kg^{-1}) of the indicated mAb treatment by intraperitoneal injection one day before intranasal inoculation with 10^3 FFU of WA1/2020 N501Y/D614G, Wash-B.1.351 or Wash-B.1.1.28 and 10^5 FFU of B.1.1.7. Tissues were collected at three days after infection. **g, h**, Eight-to-ten-week-old female and male K18-hACE2 transgenic mice were administered 10^3 FFU of the indicated SARS-CoV-2 strain by intranasal inoculation. One day later, mice received 200 µg (about 10 mg kg^{-1}) of the indicated mAb treatment by intraperitoneal injection. Tissues were collected at six days after infection. For all panels, infectious virus in lung homogenates was determined by plaque assay using Vero-hACE2-TMPRSS2 cells (line indicates median; in order from left to right $n = 5, 5, 5, 6, 6$ and 6 (**a**); $n = 6, 6, 6, 6, 6$ and 6 (**b–h**) mice per group, one-way ANOVA with Dunnett's test with comparison to control mAb: ns, not significant, $****P < 0.0001, **P = 0.0012, ***P = 0.0003$ (**c**); $**P = 0.0048, ***P = 0.0005$ (**e**); $**P = 0.0031, 0.0019$ and 0.0020 (**f**, from left to right)). Dotted lines indicate the limit of detection of the assay.

[Source data](#)

Extended Data Fig. 4 Antibody neutralization and protection against a natural B.1.351 isolate.

a, Selected anti-SARS-CoV-2 mAbs (one from each cocktail) were tested for neutralization of infection by WA1/2020 D614G, Wash-B.1.351 or B.1.351 on Vero-TMPRSS2 cells using an focus reduction neutralization test (FRNT). One representative experiment of two performed in duplicate is shown. **b–e**, Eight-to-ten-week-old female K18-hACE2 transgenic mice received 40 µg (about 2 mg kg⁻¹) of control mAb or COV2-2130/COV2-2196 by intraperitoneal injection one day before intranasal inoculation with 10³ FFU of B.1.351. **b**, Weight change following infection (mean ± s.e.m.; *n* = 6 mice per group, two experiments; one-way ANOVA with Dunnett's test of area under the curve: ns, not significant, ****P* < 0.0001). Viral RNA levels in the lung (**c**), nasal wash (**d**) and brain (**e**) (line indicates median; *n* = 6 mice per group, two experiments; Mann–Whitney test: ***P* = 0.002 (**c–e**)). Dotted line indicates the limit of detection of the assay.

[Source data](#)

Extended Data Fig. 5 Antibody-mediated protection against SARS-CoV-2-induced inflammation.

Eight-to-ten-week-old female and male K18-hACE2 transgenic mice received 40 µg (about 2 mg kg⁻¹) of the indicated mAb treatment by intraperitoneal injection one day before intranasal inoculation with 10³ FFU of the indicated SARS-CoV-2 strain. Heat map of cytokine and chemokine protein expression levels in lung homogenates collected at six days after infection from the indicated groups. Data are presented as log₂-transformed fold change over naive mice. Blue, reduction; red, increase.

[Source data](#)

Extended Data Fig. 6 Cytokine and chemokine induction following SARS-CoV-2 infection.

Individual plots for cytokine and chemokine protein levels in the lungs of antibody-treated K18-hACE2 transgenic mice at 6 days after infection with the indicated SARS-CoV-2 strain (line indicates mean; $n = 3$ naive, $n = 5$ for all other groups of B.1.1.7- and N501Y-infected mice; $n = 3$ naive, 10 control, 5 for all other groups of Wash-B.1.351- and Wash-B.1.1.28-infected mice; one-way ANOVA with Dunnett's test with comparison to control mAb: ns, not significant, $****P < 0.0001$; all other P values are listed in Supplementary Table 5). Select cytokines and chemokines were used to generate the heat map in Extended Data Fig. 5.

Source data

Extended Data Fig. 7 Low-dose antibody prophylaxis against SARS-CoV-2 variants in K18-hACE2 mice.

a–p, Eight-to-ten-week-old female and male K18-hACE2 transgenic mice received 4 µg (about 0.2 mg kg⁻¹) of the indicated mAb treatment by intraperitoneal injection one day before intranasal inoculation with 10³ FFU of the indicated SARS-CoV-2 strain. Tissues were collected at six days after infection. **a–d**, Weight change following infection with SARS-CoV-2 (mean ± s.e.m.; in order from left to right $n = 11, 6, 6$ and 7, 7 (**a**); $n = 10, 6, 6, 5$ and 7 (**b**); $n = 10, 6, 6, 7$ and 7 (**c, d**) mice per group, two experiments; one-way ANOVA with Dunnett's test of area under the curve with comparison to control mAb: $****P < 0.0001$). Viral RNA levels in the lung (**e–h**), nasal wash (**i–l**) or brain (**m–p**) were measured (line indicates median; in order from left to right $n = 11, 6, 6, 6$ and 7 (**e**); $n = 10, 6, 6, 5$ and 7 (**f, n**); $n = 10, 6, 6, 7$ and 7 (**g–i, k, m, o**); $n = 8, 6, 6, 5$ and 6 (**j**); $n = 10, 6, 6, 6$ and 7 (**l, p**) mice per group, two experiments; one-way ANOVA with Dunnett's test with comparison to isotype control mAb: ns, not significant, $****P < 0.0001$); * $P = 0.034$ (**e**); * $P = 0.0422$, $***P = 0.0004$ (**g**); ** $P = 0.0080$ (**h**); * $P = 0.0209$ (left), 0.0365 (right) (**j**); * $P = 0.0124$ (left), 0.0497 (right), $***P = 0.0001$ (**k**); ** $P = 0.0069$ (**l**);

$**P = 0.0087$ (left), 0.0061 (right), $*P = 0.0264$ (**n**); $*P = 0.0378$ (left), 0.0446 (right), $***P = 0.0004$ (**o**); $**P = 0.0045$ (left), 0.0035 (right), $***P = 0.0002$, $*P = 0.0107$ (**p**)). Dotted line indicates the limit of detection of the assay.

[Source data](#)

[Extended Data Fig. 8 In vivo correlation of antibody-mediated protection against SARS-CoV-2.](#)

For each panel, the fold change in the EC₅₀ values of the indicated mAb or mAb cocktails between the N501Y/D614G strain and one or more variants of concern (B.1.1.7, Wash-B.1.351 or Wash-B.1.1.28) were plotted on the *x* axis. Next, the fold change in lung viral RNA titre corresponding to the indicated treatment group (top labels) between the N501Y/D614G strain and one or more variants of concern (B.1.1.7, Wash-B.1.351 or Wash-B.1.1.28) were plotted on the *y* axis. Best-fit lines were calculated using a simple linear regression. Two-tailed Pearson correlation was used to calculate R² and *P* values indicated within each panel.

[Source data](#)

[Extended Data Fig. 9 Antibody-mediated protection against SARS-CoV-2 variants in 129S2 mice.](#)

a–h, Six-to-seven-week-old female and male immunocompetent 129S2 mice received 40 µg (about 2 mg kg⁻¹) of the indicated mAb treatment by intraperitoneal injection one day before intranasal inoculation with 10³ FFU of WA1/2020 N501Y/D614G, Wash-B.1.351 or Wash-B.1.1.28 or 10⁵ FFU of B.1.1.7. Tissues were collected at three days after infection. Viral RNA levels in the lung (**a–d**) or nasal washes (**e–h**) were determined (line indicates median; in order from left to right *n* = 12, 8, 6 and 5 (**a**); *n* = 12, 7, 9 and 10 (**b**); *n* = 11, 9, 8 and 10 (**c**); *n* = 14, 9, 6 and 5 (**d**); *n* = 14, 5, 9 and 9 (**e**); *n* = 11, 7, 9 and 10 (**f**); *n* = 10, 9, 8 and 10 (**g**); *n* = 15, 9, 7 and 10 (**h**) mice per group, pooled from two to three experiments; one-way ANOVA with Dunnett's test with comparison to control mAb: ns, not significant,

$***P < 0.001$; $***P = 0.0009$, $*P = 0.0176$, $**P = 0.0077$ (**c**);
 $**P = 0.0042$, $***P = 0.0001$ (left), 0.0010 (right) (**d**); $*P = 0.0467$ (left),
 0.0188 (right) (**e**); $**P = 0.0059$, $***P = 0.0002$ (left), 0.0004 (right) (**f**);
 $*P = 0.0184$ (**g**), $*P = 0.0129$, $**P = 0.0090$ (**h**)). Dotted line indicates the limit of detection of the assay.

[Source data](#)

[Extended Data Fig. 10 COV2-2130/COV2-2196 antibody cocktail protects hamsters against historical and variant SARS-CoV-2 strains.](#)

Six-week-old male Syrian golden hamsters received a single $800\text{ }\mu\text{g}$ (about 10 mg kg^{-1}) (**a–h**) or $320\text{ }\mu\text{g}$ (about 4 mg kg^{-1}) dose (**i–p**) of COV2-2130/COV2196 mAb cocktail or control mAb by intraperitoneal injection one day before intranasal inoculation with 5×10^5 FFU of WA1/2020 D614G or Wash-B.1.351 viruses. Nasal swabs and lung tissues were collected at three and four days after infection, respectively. **a, i**, Weight change following infection with SARS-CoV-2 (line indicates mean; $n = 5$ hamsters per group, one experiment). Infectious virus in the lung (**b, j**) or viral RNA levels in the lung (**c, k**) and nasal swabs (**d, l**) were determined (line indicates median; $n = 5$ hamsters per group, one experiment). Dotted line indicates the limit of detection of the assay. **e–h, m–p**, Cytokine and inflammatory gene expression in lung homogenates collected at 6 days after infection from indicated groups (line indicates mean; $n = 5$ hamsters per group). Values were calculated using the $\Delta\Delta C_t$ method compared to a naive control group. Because data were obtained from a single experiment (even with multiple hamsters), statistical analysis was not performed.

[Source data](#)

[Extended Data Fig. 11 Antibody protection against SARS-CoV-2 induced lung pathology.](#)

Eight-to-ten-week-old female K18-hACE2 transgenic mice received $200\text{ }\mu\text{g}$ (about 10 mg kg^{-1}) of the indicated mAb treatment or isotype control by

intraperitoneal injection one day after intranasal inoculation with 10^3 FFU of Wash-B.1.351 SARS-CoV-2. At six days after infection, mice were killed and lungs fixed for sectioning before staining with haematoxylin and eosin. A lung section from a naive, uninfected mouse is shown (top panels) as a reference control. Images show low (left panels for each treatment) and high (right panels for each treatment; boxed region from left) resolution. Scale bars, 100 μm . Representative images from $n = 3$ mice per group.

Extended Data Fig. 12 Post-exposure antibody therapy against SARS-CoV-2 variants in K18-hACE2 mice.

a, b, Eight-to-ten-week-old female and male K18-hACE2 transgenic mice were administered 10^3 FFU of the indicated SARS-CoV-2 strain by intranasal inoculation. One day later, mice received 200 μg (about 10 mg kg^{-1}) of the indicated mAb treatment by intraperitoneal injection. Brain tissues were collected at six days after infection. Viral RNA levels are shown (**a, b**) (line indicates median; in order from left to right $n = 9, 6, 6, 6, 6, 6$ and 6 (**a**); $n = 7, 6, 6, 6, 6, 5$ and 7 (**b**) mice per group, two experiments; one-way ANOVA with Dunnett's test with comparison to control mAb: ns, not significant, **** $P < 0.0001$). Dotted line indicates the limit of detection of the assay.

[Source data](#)

Extended Data Fig. 13 Neutralization curves with mAb LY-CoV016 as monotherapy and combination with variant SARS-CoV-2 strains.

a, b, Anti-SARS-CoV-2 human mAb LY-CoV016 and combination LY-CoV555/LY-CoV016 (parental mAbs of bamlanivimab and etesevimab, respectively) were tested for inhibition of infection of the indicated SARS-CoV-2 viruses using a FRNT. EC₅₀ values (ng ml⁻¹) (**a**) and one representative experiment of two performed in duplicate is shown (**b**).

[Source data](#)

Supplementary information

Reporting Summary

Supplementary Table 1

Deep sequencing of viral strains.

Supplementary Table 2

Neutralizing monoclonal antibodies.

Supplementary Table 3

Sequencing of RBD from virally-infected tissue homogenates.

Supplementary Table 4

Serum mAb concentrations.

Supplementary Table 5

Cytokine and Chemokine *P*-Values.

Peer Review File

Source data

Source Data Fig. 1

Source Data Fig. 2

Source Data Fig. 3

Source Data Extended Data Fig. 1

[Source Data Extended Data Fig. 2](#)

[Source Data Extended Data Fig. 3](#)

[Source Data Extended Data Fig. 4](#)

[Source Data Extended Data Fig. 5](#)

[Source Data Extended Data Fig. 6](#)

[Source Data Extended Data Fig. 7](#)

[Source Data Extended Data Fig. 8](#)

[Source Data Extended Data Fig. 9](#)

[Source Data Extended Data Fig. 10](#)

[Source Data Extended Data Fig. 12](#)

[Source Data Extended Data Fig. 13](#)

Rights and permissions

[Reprints and Permissions](#)

About this article



Check for
updates

[**Cite this article**](#)

Chen, R.E., Winkler, E.S., Case, J.B. *et al.* In vivo monoclonal antibody efficacy against SARS-CoV-2 variant strains. *Nature* **596**, 103–108 (2021). <https://doi.org/10.1038/s41586-021-03720-y>

[Download citation](#)

- Received: 21 April 2021
- Accepted: 11 June 2021
- Published: 21 June 2021
- Issue Date: 05 August 2021
- DOI: <https://doi.org/10.1038/s41586-021-03720-y>

Comments

By submitting a comment you agree to abide by our [Terms](#) and [Community Guidelines](#). If you find something abusive or that does not comply with our terms or guidelines please flag it as inappropriate.

[Download PDF](#)

Advertisement

This article was downloaded by **calibre** from <https://www.nature.com/articles/s41586-021-03720-y>.

SARS-CoV-2 mRNA vaccines induce persistent human germinal centre responses
[Download PDF](#)

- Article
- [Published: 28 June 2021](#)

SARS-CoV-2 mRNA vaccines induce persistent human germinal centre responses

- [Jackson S. Turner](#)^{1,na1},
- [Jane A. O'Halloran](#) [ORCID: orcid.org/0000-0001-8265-9471](#)^{2,na1},
- [Elizaveta Kalaidina](#)³,
- [Wooseob Kim](#) [ORCID: orcid.org/0000-0002-9199-1000](#)¹,
- [Aaron J. Schmitz](#) [ORCID: orcid.org/0000-0002-8077-6751](#)¹,
- [Julian Q. Zhou](#) [ORCID: orcid.org/0000-0001-9602-2092](#)¹,
- [Tingting Lei](#)¹,
- [Mahima Thapa](#)¹,
- [Rita E. Chen](#)^{1,4},
- [James Brett Case](#) [ORCID: orcid.org/0000-0001-7331-5511](#)⁴,
- [Fatima Amanat](#) [ORCID: orcid.org/0000-0002-8029-8227](#)^{5,6},
- [Adriana M. Rauseo](#)²,
- [Alem Haile](#)⁷,
- [Xuping Xie](#) [ORCID: orcid.org/0000-0003-0918-016X](#)⁸,
- [Michael K. Klebert](#)⁷,
- [Teresa Suessen](#)⁹,
- [William D. Middleton](#)⁹,
- [Pei-Yong Shi](#) [ORCID: orcid.org/0000-0001-5553-1616](#)⁸,
- [Florian Krammer](#) [ORCID: orcid.org/0000-0003-4121-776X](#)⁵,
- [Sharlene A. Teeffey](#)⁹,
- [Michael S. Diamond](#) [ORCID: orcid.org/0000-0002-8791-3165](#)^{4,10,11},
- [Rachel M. Presti](#) [ORCID: orcid.org/0000-0002-5469-0727](#)^{2,10} &
- [Ali H. Ellebedy](#) [ORCID: orcid.org/0000-0002-6129-2532](#)^{1,10,11}

- 301k Accesses
- 6386 Altmetric
- [Metrics details](#)

Subjects

- [B cells](#)
- [Germinal centres](#)
- [RNA vaccines](#)
- [SARS-CoV-2](#)

Abstract

SARS-CoV-2 mRNA-based vaccines are about 95% effective in preventing COVID-19^{[1,2,3,4,5](#)}. The dynamics of antibody-secreting plasmablasts and germinal centre B cells induced by these vaccines in humans remain unclear. Here we examined antigen-specific B cell responses in peripheral blood ($n = 41$) and draining lymph nodes in 14 individuals who had received 2 doses of BNT162b2, an mRNA-based vaccine that encodes the full-length SARS-CoV-2 spike (*S*) gene^{[1](#)}. Circulating IgG and IgA-secreting plasmablasts that target the *S* protein peaked one week after the second immunization and then declined, becoming undetectable three weeks later. These plasmablast responses preceded maximal levels of serum anti-*S* binding and neutralizing antibodies to an early circulating SARS-CoV-2 strain as well as emerging variants, especially in individuals who had previously been infected with SARS-CoV-2 (who produced the most robust serological responses). By examining fine needle aspirates of draining axillary lymph nodes, we identified germinal centre B cells that bound *S* protein in all participants who were sampled after primary immunization. High frequencies of *S*-binding germinal centre B cells and plasmablasts were sustained in these draining lymph nodes for at least 12 weeks after the booster immunization. *S*-binding monoclonal antibodies derived from germinal centre B cells predominantly targeted the receptor-binding domain of the *S* protein, and fewer clones bound to the N-terminal domain or to epitopes shared with the *S* proteins of the human betacoronaviruses OC43 and HKU1. These latter cross-reactive B cell clones had higher levels of somatic hypermutation as compared to those that recognized only the SARS-CoV-2 *S* protein, which suggests a memory B cell origin. Our studies demonstrate that SARS-CoV-2 mRNA-based vaccination of humans induces a persistent germinal centre B cell response, which enables the generation of robust humoral immunity.

[Download PDF](#)

Main

The concept of using mRNAs as vaccines was introduced over 30 years ago^{6,7}. Key refinements that improved the biological stability and translation capacity of exogenous mRNA enabled development of these molecules as vaccines^{8,9}. The emergence of SARS-CoV-2 in December 2019, and the ensuing pandemic, has revealed the potential of this platform^{9,10,11}. Hundreds of millions of people have received one of the two SARS-CoV-2 mRNA-based vaccines that were granted emergency use authorization by the US Food and Drug Administration in December 2020. Both of these vaccines demonstrated notable immunogenicity in phase-I/II studies and efficacy in phase-III studies^{1,2,3,4,12,13,14}. Whether these vaccines induce the robust and persistent germinal centre reactions that are critical for generating high-affinity and durable antibody responses has not been examined in humans. To address this question, we conducted an observational study of 41 healthy adults (8 of whom had a history of confirmed SARS-CoV-2 infection) who received the Pfizer–BioNTech SARS-CoV-2 mRNA vaccine BNT162b2 (Extended Data Tables 1, 2). Blood samples were collected at baseline, and at weeks 3 (pre-boost), 4, 5, 7 and 15 after the first immunization. Fine needle aspirates (FNAs) of the draining axillary lymph nodes were collected from 14 participants (none with history of SARS-CoV-2 infection) at weeks 3 (pre-boost), 4, 5, 7, and 15 after the first immunization (Fig. 1a).

Fig. 1: Plasmablast and antibody response to SARS-CoV-2 immunization.

 **figure1**

a, Study design. Forty-one healthy adult volunteers (ages 28–73, 8 with a history of SARS-CoV-2 infection) were enrolled and received the BNT162b2 mRNA SARS-CoV-2 vaccine. Blood was collected before immunization, and at 3, 4, 5, 7 and 15 weeks after immunization. For 14 participants (ages 28–52, none with a history of SARS-CoV-2 infection), FNAs of ipsilateral axillary lymph nodes (LNs) were collected at 3, 4, 5, 7 and 15 weeks after immunization. **b**, **c**, ELISpot quantification of S-binding IgG- (**b**) and IgA- (**c**) secreting plasmablasts (PBs) in blood at baseline, and at 3, 4, 5 and 7 weeks after immunization in participants without (red) and with (black) a history of SARS-CoV-2 infection. **d**, Plasma IgG titres against SARS-CoV-2 S (left) and the RBD of S (right) measured by ELISA in participants without (red) and with (black) a history of SARS-CoV-2 infection at baseline, and at 3, 4, 5, 7 and 15 weeks after immunization. Dotted lines indicate limits of detection. Symbols at each time

point in **b–d** represent one sample ($n = 41$). Results are from one experiment performed in duplicate.

[Full size image](#)

We used an enzyme-linked immune absorbent spot (ELISpot) assay to measure antibody-secreting plasmablasts in blood that bound SARS-CoV-2 S protein. We detected SARS-CoV-2-S-specific IgG- and IgA-secreting plasmablasts 3 weeks after primary immunization in 24 of 33 participants with no history of SARS-CoV-2 infection, but in 0 of 8 participants who had previously been infected with SARS-CoV-2. Plasmablasts peaked in blood during the first week after boosting (week 4 after primary immunization), with frequencies that varied widely from 3 to 4,100 S-binding plasmablasts per 10^6 peripheral blood mononuclear cells (PBMCs) (Fig. [1b, c](#)). We found that plasma IgG antibody titres against S, measured by enzyme-linked immunosorbent assay (ELISA), increased in all participants over time, and reached peak geometric mean half-maximal binding titres of 5,567 and 15,850 at 5 weeks after immunization among participants without and with history of SARS-CoV-2 infection, respectively, with a subsequent decline by 15 weeks after immunization. Anti-S IgA titres and IgG titres against the receptor-binding domain (RBD) of S showed similar kinetics, and reached peak geometric mean half-maximal binding titres of 172 and 739 for anti-S IgA and 4,501 and 7,965 for anti-RBD IgG among participants without and with history of SARS-CoV-2 infection, respectively, before declining. IgM responses were weaker and more transient, peaking 4 weeks after immunization among participants without history of SARS-CoV-2 infection with a geometric mean half-maximal binding titre of 78 and were undetectable in all but 2 previously infected participants (Fig. [1d](#), Extended Data Fig. [1a](#)).

The functional quality of serum antibody was measured using high-throughput focus reduction neutralization tests^{[15](#)} on Vero cells expressing TMPRSS2 against three authentic infectious SARS-CoV-2 strains with sequence variations in the S gene^{[16,17](#)}: (1) a Washington strain (2019n-CoV/USA) with a prevailing D614G substitution (WA1/2020 D614G); (2) a B.1.1.7 isolate with signature changes in the S gene^{[18](#)}, including mutations resulting in the deletion of residues 69, 70, 144 and 145 as well as N501Y, A570D, D614G and P681H substitutions; and (3) a chimeric SARS-CoV-2 with a B.1.351 S gene in the Washington strain background (Wash-B.1.351) that contained the following changes: D80A, deletion of residues 242–244, R246I, K417N, E484K, N501Y, D614G and A701V. Serum neutralizing titres increased markedly in participants without a history of SARS-CoV-2 infection after boosting, with geometric mean neutralization titres against WA1/2020 D614G of 58 at 3 weeks after primary immunization and 572 at 2 or 4 weeks after boost (5 or 7 weeks after primary immunization). Neutralizing titres against the B.1.1.7 and B.1.351 variants were lower, with geometric mean neutralization titres of 49 and 373 against B.1.1.7 and 36 and

137 against B.1.351 after primary and secondary immunization, respectively. In participants with a history of previous SARS-CoV-2 infection, neutralizing titres against all three viruses were detected at baseline (geometric mean neutralization titres of 241.8, 201.8 and 136.7 against WA1/2020 D614G, B.1.1.7 and B.1.351, respectively). In these participants, neutralizing titres increased more rapidly and to higher levels after immunization, with geometric mean neutralization titres of 4,544, 3,584 and 1,897 against WA1/2020 D614G, B.1.1.7 and B.1.351, respectively, after primary immunization, and 9,381, 9,351 and 2,749 against WA1/2020 D614G, B.1.1.7 and B.1.351, respectively, after secondary immunization. These geometric mean neutralization titres were 78-, 73- and 53-fold higher after primary immunization and 16-, 25- and 20-fold higher after boosting against WA1/2020 D614G, B.1.1.7 and B.1.351, respectively, than in participants without a history of SARS-CoV-2 infection (Extended Data Fig. [1b](#)).

The BNT162b2 vaccine is injected into the deltoid muscle, which drains primarily to the lateral axillary lymph nodes. We used ultrasonography to identify and guide FNA of accessible axillary nodes on the side of immunization approximately 3 weeks after primary immunization. In 5 of the 14 participants, a second draining lymph node was identified and sampled after secondary immunization (Fig. [2a](#)). Germinal centre B cells (defined as $CD19^+CD3^-IgD^{low}BCL6^+CD38^{int}$ lymphocytes) were detected in all lymph nodes (Fig. [2b, d](#), Extended Data Fig. [2a](#), Extended Data Table [3](#)). We co-stained FNA samples with two fluorescently labelled S probes to detect S-binding germinal centre B cells. A control tonsillectomy sample with a high frequency of germinal centre B cells that was collected before the COVID-19 pandemic from an unrelated donor was stained as a negative control. S-binding germinal centre B cells were detected in FNAs from all 14 participants following primary immunization. The kinetics of the germinal centre response varied among participants, but S-binding germinal centre B cell frequencies increased at least transiently in all participants after boosting and persisted at high frequency in most individuals for at least 7 weeks. Notably, S-binding germinal centre B cells remained at or near their peak frequency 15 weeks after immunization in 8 of the 10 participants sampled at that time point, and these prolonged germinal centre responses had high proportions of S-binding cells (Fig. [2c–e](#), Extended Data Fig. [2b](#)).

Fig. 2: Germinal centre B cell response to SARS-CoV-2 immunization.

 **figure2**

a, Representative colour Doppler ultrasound image of two draining lymph nodes ('1' and '2') adjacent to the axillary vein 'LAX V' 5 weeks after immunization. **b, c**, Representative flow cytometry plots of BCL6 and CD38 staining on IgD^{low}CD19⁺CD3⁻ live singlet lymphocytes in FNA samples (**b**; LN1, top row; LN2, bottom row) and S staining on BCL6⁺CD38^{int} germinal centre B cells in tonsil and FNA samples (**c**) at the indicated times after immunization. **d, e**, Kinetics of total (blue) and S⁺ (white) germinal centre (GC) B cells as gated in **b** and **c** (**d**) and S-binding per cent of germinal centre B cells (**e**) from FNA of draining lymph nodes. Symbols at each time point represent one FNA sample; square symbols denote the second lymph node sampled ($n = 14$). Horizontal lines indicate the median.

[Full size image](#)

To evaluate the domains targeted by the S-protein-specific germinal centre response after vaccination, we generated recombinant monoclonal antibodies from single-cell-sorted S-binding germinal centre B cells (defined by the surface-marker phenotype

$\text{CD19}^+\text{CD3}^-\text{IgD}^{\text{low}}\text{CD20}^{\text{high}}\text{CD38}^{\text{int}}\text{CD71}^+\text{CXCR5}^+$ lymphocytes) from three of the participants one week after boosting (Extended Data Fig. 2a). Fifteen, five and seventeen S-binding, clonally distinct monoclonal antibodies were generated from participants 07, 20 (lymph node 1) and 22, respectively (Extended Data Table 4). Of the 37 S-binding monoclonal antibodies, 17 bound the RBD, 6 recognized the N-terminal domain and 3 were cross-reactive with S proteins from seasonal betacoronavirus OC43; 2 of these monoclonal antibodies also bound S from seasonal betacoronavirus HKU1 (Fig. 3a). Clonal relatives of 14 out of 15, 1 out of 5 and 12 out of 17 of the S-binding monoclonal antibodies were identified among bulk-sorted total plasmablasts from PBMCs and germinal centre B cells at 4 weeks after immunization from participants 07, 20 and 22, respectively (Fig. 3b, Extended Data Figs. 2c, 3a, b, Extended Data Tables 5, 6). Clones related to S-binding monoclonal antibodies had significantly increased mutation frequencies in their immunoglobulin heavy chain variable region (*IGHV*) genes compared to previously published naive B cells¹⁹, particularly those related to monoclonal antibodies that cross-reacted with seasonal betacoronaviruses (Fig. 3c, d).

Fig. 3: Clonal analysis of germinal centre response to SARS-CoV-2 immunization.

 **figure3**

a, Binding of monoclonal antibodies (mAbs) generated from germinal centre B cells to SARS-CoV-2 S, N-terminal domain (NTD) of S, RBD, or S proteins of betacoronavirus OC43 or HKU1, measured by ELISA. Results are from one experiment performed in duplicate. Baseline for area under the curve was set to the mean + three times the s.d. of background binding to bovine serum albumin. **b**, Clonal relationship of sequences from S-binding germinal centre-derived monoclonal antibodies (cyan) to sequences from bulk repertoire analysis of plasmablasts from PBMCs (red) and germinal centre B cells (blue) sorted 4 weeks after immunization. Each clone is visualized as a network in which each node represents a sequence and sequences are linked as a minimum spanning tree of the network. Symbol shape indicates sequence isotype: IgG (circle), IgA (star) and IgM (square); symbol size corresponds to sequence count. **c, d**, Comparison of nucleotide mutation frequency

in *IGHV* genes of naive B cells sorted from individuals vaccinated with influenza virus vaccine¹⁹ (grey) to clonal relatives of S-binding monoclonal antibodies among plasmablasts sorted from PBMCs and germinal centre B cells 4 weeks after immunization (green) in indicated participants (c) and between clonal relatives of S-binding monoclonal antibodies cross-reactive (purple) or not (teal) to seasonal coronavirus S proteins among plasmablasts sorted from PBMCs and germinal centre B cells 4 weeks after immunization (d). Horizontal lines and error bars indicate the median and interquartile range. Sequence counts were 2,553 (naive), 199 (participant 07), 6 (participant 20), 240 (participant 22), 54 (cross-reactive) and 391 (not cross-reactive). *P* values from two-sided Kruskal–Wallis test with Dunn’s post-test between naive B cells and S-binding clones (c) or two-sided Mann–Whitney *U* test (d).

[Full size image](#)

In addition to germinal centre B cells, we detected robust plasmablast responses in the draining lymph nodes of all 14 participants in the FNA cohort. S-binding plasmablasts (defined as CD19⁺CD3⁻IgD^{low}CD20^{low}CD38⁺CD71⁺BLIMP1⁺ lymphocytes) were detected in all of the lymph nodes that we sampled, and increased in frequency after boosting (Extended Data Fig. 4a,b). The detected plasmablasts were unlikely to be a contaminant of blood, because CD14⁺ monocyte and/or granulocyte frequencies were below 1% in all FNA samples (well below the 10% threshold that was previously established¹⁹) (Extended Data Table 3). Moreover, S-binding plasmablasts were detected in FNA samples at 5, 7 and 15 weeks after immunization, when they had become undetectable in blood from all participants in the cohort. The vast majority of S-binding lymph node plasmablasts were isotype-switched at 4 weeks after primary immunization, and IgA-switched cells accounted for 25% or more of the plasmablasts in 6 out of 14 participants (Extended Data Fig. 4c,d).

This study evaluated whether SARS-CoV-2 mRNA-based vaccines induce antigen-specific plasmablast and germinal centre B cell responses in humans. The vaccine induced a strong IgG-dominated plasmablast response in blood that peaked one week after the booster immunization. In the draining lymph nodes, we detected robust SARS-CoV-2 S-binding germinal centre B cell and plasmablast responses in aspirates from all 14 of the participants. These responses were detectable after the first immunization but greatly expanded after the booster injection. Notably, S-binding germinal centre B cells and plasmablasts persisted for at least 15 weeks after the first immunization (12 weeks after secondary immunization) in 8 of the 10 participants who were sampled at that time point. These responses to mRNA vaccination are superior to those seen after seasonal influenza virus vaccination in humans¹⁹, in whom haemagglutinin-binding germinal centre B cells were detected in only three out of eight participants. More robust germinal centre responses are consistent with antigen dissemination to multiple lymph nodes and the self-adjuvating characteristics of the

mRNA–lipid nanoparticle vaccine platform compared to nonadjuvanted inactivated vaccines used for seasonal influenza virus vaccination^{7,20,21}. Our data in humans corroborate reports that demonstrate the induction of potent germinal centre responses by SARS-CoV-2 mRNA-based vaccines in mice^{22,23}.

To our knowledge, this is the first study to provide direct evidence for the induction of a persistent antigen-specific germinal centre B cell response after vaccination in humans. Dynamics of germinal centre B cell responses vary widely depending on the model system in which they are studied, although the most active period of the response usually occurs over the course of a few weeks. Primary alum-adjuvanted protein immunization of mice typically leads to germinal centre responses that peak 1–2 weeks after immunization and contract at least 10-fold within 5–7 weeks^{24,25,26}. Germinal centre responses induced by immunization with more robust adjuvants such as sheep red blood cells, complete Freund's adjuvant or saponin-based adjuvants tend to peak slightly later, at 2–4 weeks after vaccination, and can persist at low frequencies for several months^{27,28,29,30,31,32,33}. Although studies of extended durability are rare, antigen-specific germinal centre B cells have been found to persist for at least one year, albeit at very low levels^{28,30}. In this study, we show SARS-CoV-2 mRNA vaccine-induced germinal centre B cells are maintained at or near peak frequencies for at least 12 weeks after secondary immunization.

The persistence of S-binding germinal centre B cells and plasmablasts in draining lymph nodes is a positive indicator for induction of long-lived plasma cell responses²⁵. Future studies will be needed to examine whether mRNA vaccination induces a robust S-specific long-lived plasma cell compartment in the bone marrow. As part of such studies, it will be critical to generate a comprehensive set of monoclonal antibodies derived from plasmablasts and germinal centre B cells isolated from several time points to define the breadth of the B cell response elicited by this vaccine. None of the 14 participants in our study who underwent FNA of draining lymph nodes had a history of SARS-CoV-2 infection. Thus, further comparison of vaccine-induced germinal centre responses from naive and previously infected individuals will be informative. Finally, the work presented here focuses on the B cell component of the germinal centre reaction. A robust T follicular helper response sustains the germinal centre reaction^{34,35}. As such, studies are planned to investigate the magnitude, specificity and durability of the T follicular helper cell response after SARS-CoV-2 mRNA vaccination in humans.

A preliminary observation from our study is the dominance of RBD-targeting clones among responding germinal centre B cells. A more detailed analysis³⁶ of these RBD-binding monoclonal antibodies assessed their in vitro inhibitory capacity against the WA1/2020 D614G strain using an authentic SARS-CoV-2 neutralization assay: five showed high neutralization potency, with 80% neutralization values of less than

100 ng ml⁻¹. For the most part, RBD-binding clones contained few (<3) nonsynonymous nucleotide substitutions in their *IGHV* genes, which indicates that they originated from recently engaged naive B cells. This contrasts with the three cross-reactive germinal centre B cell clones that recognized conserved epitopes within the S proteins of betacoronaviruses. These cross-reactive clones had significantly higher mutation frequencies, which suggests a memory B cell origin. These data are consistent with previous findings from seasonal influenza virus vaccination in humans that show that the germinal centre reaction can engage pre-existing memory B cells directed against conserved epitopes as well as naive clones targeting novel epitopes¹⁹. However, these cross-reactive clones were not identified in all individuals and comprised a small fraction of responding B cells, consistent with a similar analysis of SARS-CoV-2 mRNA vaccine-induced plasmablasts³⁷. Overall, our data demonstrate the capacity of SARS-CoV-2 mRNA-based vaccines to induce robust and prolonged germinal centre reactions. The induced germinal centre reaction recruited cross-reactive memory B cells as well as newly engaged clones that target unique epitopes within SARS-CoV-2 S protein. Elicitation of high affinity and durable protective antibody responses is a hallmark of a successful humoral immune response to vaccination. By inducing robust germinal centre reactions, SARS-CoV-2 mRNA-based vaccines are on track for achieving this outcome.

Methods

No statistical methods were used to predetermine sample size.

Sample collection, preparation, and storage

All studies were approved by the Institutional Review Board of Washington University in St Louis. Written consent was obtained from all participants. Forty-one healthy volunteers were enrolled, of whom 14 provided axillary lymph node samples (Extended Data Table 1). In 5 of the 14 participants, a second draining lymph node was identified and sampled following secondary immunization. One participant (15) received the second immunization in the contralateral arm; draining lymph nodes were identified and sampled on both sides. Blood samples were collected in EDTA tubes, and PBMCs were enriched by density gradient centrifugation over Ficoll 1077 (GE) or Lymphopure (BioLegend). The residual red blood cells were lysed with ammonium chloride lysis buffer, and cells were immediately used or cryopreserved in 10% dimethylsulfoxide in fetal bovine serum (FBS). Ultrasound-guided FNA of axillary lymph nodes was performed by a radiologist or a qualified physician's assistant under the supervision of a radiologist. Lymph node dimensions and cortical thickness were measured, and the presence and degree of cortical vascularity and location of the lymph node relative to the axillary vein were determined before each FNA. For each

FNA sample, six passes were made under continuous real-time ultrasound guidance using 25-gauge needles, each of which was flushed with 3 ml of RPMI 1640 supplemented with 10% FBS and 100 U ml⁻¹ penicillin–streptomycin, followed by three 1-ml rinses. Red blood cells were lysed with ammonium chloride buffer (Lonza), washed with phosphate-buffered saline (PBS) supplemented with 2% FBS and 2 mM EDTA, and immediately used or cryopreserved in 10% dimethylsulfoxide in FBS. Participants reported no adverse effects from phlebotomies or serial FNAs.

Cell lines

Expi293F cells were cultured in Expi293 Expression Medium (Gibco). Vero E6 (CRL-1586, American Type Culture Collection), Vero cells expressing TMPRSS2 (Vero-TMPRSS2 cells)³⁸ (a gift from S. Ding), and Vero cells expressing human ACE2 and TMPRSS2 (Vero-hACE2-TMPRSS2) (a gift of A. Creanga and B. Graham) cells were cultured at 37 °C in Dulbecco’s modified Eagle medium (DMEM) supplemented with 10% FBS, 10 mM HEPES (pH 7.3), 1 mM sodium pyruvate, 1× nonessential amino acids and 100 U ml⁻¹ of penicillin–streptomycin. Vero-TMPRSS2 cell cultures were supplemented with 5 µg ml⁻¹ of blasticidin. Vero-hACE2-TMPRSS2 cell cultures were supplemented with 10 µg ml⁻¹ of puromycin.

Viruses

The 2019n-CoV/USA_WA1/2020 isolate of SARS-CoV-2 was obtained from the US Centers for Disease Control. The B.1.1.7 isolate from the UK was obtained from an infected individual. The point mutation D614G in the *S* gene was introduced into an infectious complementary DNA clone of the 2019n-CoV/USA_WA1/2020 strain as previously described³⁹. Nucleotide substitutions were introduced into a subclone puc57-CoV-2-F5-7 containing the *S* gene of the SARS-CoV-2 wild-type infectious clone⁴⁰. The *S* gene of the B.1.351 variant (first identified in South Africa) was produced synthetically by Gibson assembly. The full-length infectious cDNA clones of the variant SARS-CoV-2 viruses were assembled by in vitro ligation of seven contiguous cDNA fragments following a previously described protocol⁴⁰. In vitro transcription was then performed to synthesize full-length genomic RNA. To recover the mutant viruses, the RNA transcripts were electroporated into Vero E6 cells. The viruses from the supernatant of cells were collected 40 h later and served as p0 stocks. All viruses were passaged once in Vero-hACE2-TMPRSS2 cells and subjected to deep sequencing after RNA extraction to confirm the introduction and stability of substitutions¹⁷. All virus preparation and experiments were performed in an approved biosafety level 3 facility.

Antigens

Recombinant soluble SARS-CoV-2 S protein, recombinant RBD of S, human coronavirus OC43 S, and human coronavirus HKU1 S were expressed as previously described⁴¹. In brief, mammalian cell codon-optimized nucleotide sequences coding for the soluble ectodomain of the S protein of SARS-CoV-2 (GenBank: MN908947.3, amino acids 1–1213) including a C-terminal thrombin cleavage site, T4 foldon trimerization domain and hexahistidine tag, and for the RBD (amino acids 319–541) along with the signal peptide (amino acids 1–14) plus a hexahistidine tag were cloned into mammalian expression vector pCAGGS. The S protein sequence was modified to remove the polybasic cleavage site (RRAR to A), and two pre-fusion stabilizing proline mutations were introduced (K986P and V987P, wild-type numbering). Expression plasmids encoding for the S of common human coronaviruses OC43 and HKU1 were provided by B. Graham⁴². Recombinant proteins were produced in Expi293F cells (ThermoFisher) by transfection with purified DNA using the ExpiFectamine 293 Transfection Kit (ThermoFisher). Supernatants from transfected cells were collected 3 days after transfection, and recombinant proteins were purified using Ni-NTA agarose (ThermoFisher), then buffer-exchanged into PBS and concentrated using Amicon Ultracel centrifugal filters (EMD Millipore). For flow cytometry staining, recombinant S was labelled with Alexa Fluor 647–NHS ester or biotinylated using the EZ-Link Micro NHS-PEG4-Biotinylation Kit (Thermo Fisher); excess Alexa Fluor 647 and biotin were removed using 7-kDa Zeba desalting columns (Pierce).

ELISpot assay

Plates were coated with Flucelvax Quadrivalent 2019/2020 seasonal influenza virus vaccine (Sequiris), S or RBD. A direct ex vivo ELISpot assay was performed to determine the number of total, vaccine-binding or recombinant S-binding IgG- and IgA-secreting cells present in PBMC samples using IgG/IgA double-colour ELISpot Kits (Cellular Technology) according to the manufacturer's instructions. ELISpot plates were analysed using an ELISpot counter (Cellular Technology).

ELISAs

Assays were performed in 96-well plates (MaxiSorp; Thermo) coated with 100 µl of recombinant S, RBD, N-terminal domain of S (SinoBiological), OC43 S, HKU1 S or bovine serum albumin diluted to 1 µg ml⁻¹ in PBS, and plates were incubated at 4 °C overnight. Plates then were blocked with 10% FBS and 0.05% Tween 20 in PBS. Plasma or purified monoclonal antibodies were serially diluted in blocking buffer and added to the plates. Plates were incubated for 90 min at room temperature and then washed 3 times with 0.05% Tween 20 in PBS. Goat anti-human IgG-HRP (goat polyclonal, Jackson ImmunoResearch, 1:2,500), IgA (goat polyclonal, Jackson ImmunoResearch, 1:2,500) or IgM (goat polyclonal, Caltag, 1:4,000) were diluted in

blocking buffer before adding to wells and incubating for 60 min at room temperature. Plates were washed 3 times with 0.05% Tween 20 in PBS and 3 times with PBS before the addition of *o*-phenylenediamine dihydrochloride peroxidase substrate (Sigma-Aldrich). Reactions were stopped by the addition of 1 M hydrochloric acid. Optical density measurements were taken at 490 nm. The area under the curve for each monoclonal antibody and half-maximal binding dilution for each plasma sample were calculated using Graphpad Prism v.8.

Focus reduction neutralization test

Plasma samples were declotted by diluting 1:10 in DMEM supplemented with 2% FBS, 10 mM HEPES and 100 U ml⁻¹ penicillin–streptomycin and incubating for 3 h at 37 °C. Serial dilutions of resulting serum were incubated with 10² focus-forming units of different strains or variants of SARS-CoV-2 for 1 h at 37 °C. Antibody–virus complexes were added to Vero-TMPRSS2 cell monolayers in 96-well plates and incubated at 37 °C for 1 h. Subsequently, cells were overlaid with 1% (w/v) methylcellulose in MEM supplemented with 2% FBS. Plates were collected 30 h later by removing overlays and fixed with 4% PFA in PBS for 20 min at room temperature. Plates were washed and sequentially incubated with an oligoclonal pool of mouse anti-S monoclonal antibodies (SARS2-2, SARS2-11, SARS2-16, SARS2-31, SARS2-38, SARS2-57 and SARS2-71) (ref. [43](#)) and HRP-conjugated goat anti-mouse IgG (polyclonal, Sigma, 1:500) in PBS supplemented with 0.1% saponin and 0.1% bovine serum albumin. SARS-CoV-2-infected cell foci were visualized using TrueBlue peroxidase substrate (KPL) and quantified on an ImmunoSpot microanalyser (Cellular Technology).

Flow cytometry and cell sorting

Staining for flow cytometry analysis and sorting was performed using freshly isolated or cryo-preserved FNA, PBMC or tonsil samples. For analysis, cells were incubated for 30 min on ice with biotinylated and Alexa Fluor 647 conjugated recombinant soluble S and PD-1-BB515 (EH12.1, BD Horizon, 1:100) in 2% FBS and 2 mM EDTA in PBS (P2), washed twice, then stained for 30 min on ice with IgG–BV480 (goat polyclonal, Jackson ImmunoResearch, 1:100), IgA–FITC (M24A, Millipore, 1:500), CD45–A532 (HI30, Thermo, 1:50), CD38–BB700 (HIT2, BD Horizon, 1:500), CD20–Pacific Blue (2H7, 1:400), CD27–BV510 (O323, 1:50), CD8–BV570 (RPA-T8, 1:200), IgM–BV605 (MHM-88, 1:100), HLA-DR–BV650 (L243, 1:100), CD19–BV750 (HIB19, 1:100), CXCR5–PE–Dazzle 594 (J252D4, 1:50), IgD–PE–Cy5 (IA6-2, 1:200), CD14–PerCP (HCD14, 1:50), CD71–PE–Cy7 (CY1G4, 1:400), CD4–Spark685 (SK3, 1:200), streptavidin–APC–Fire750, CD3–APC–Fire810 (SK7, 1:50) and Zombie NIR (all BioLegend) diluted in Brilliant Staining buffer (BD Horizon). Cells were washed twice with P2, fixed for 1 h at 25 °C using the True Nuclear

fixation kit (BioLegend), washed twice with True Nuclear Permeabilization/Wash buffer, stained with FOXP3–BV421 (206D, BioLegend, 1:15), Ki-67–BV711 (Ki-67, BioLegend, 1:200), Tbet–BV785 (4B10, BioLegend, 1:400), BCL6–PE (K112-91, BD Pharmingen, 1:25), and BLIMP1–A700 (646702, R&D, 1:50) for 1 h at 25 °C, washed twice with True Nuclear Permeabilization/Wash buffer, and acquired on an Aurora using SpectroFlo v.2.2 (Cytek). Flow cytometry data were analysed using FlowJo v.10 (Treestar).

For sorting germinal centre B cells, FNA single-cell suspensions were stained for 30 min on ice with CD19–BV421 (HIB19, 1:100), CD3–FITC (HIT3a, 1:200), IgD–PerCP–Cy5.5 (IA6-2, 1:200), CD71–PE (CY1G4, 1:400), CXCR5–PE–Dazzle 594 (J252D4, 1:50), CD38–PE–Cy7 (HIT2, 1:200), CD20–APC–Fire750 (2H7, 1:100), Zombie Aqua (all BioLegend), and Alexa Fluor 647 conjugated recombinant soluble S. For sorting plasmablasts, PBMCs were stained for 30 min on ice with CD20–PB (2H7, 1:400), CD71–FITC (CY1G4, 1:200), CD4–PerCP (OKT4, 1:100), IgD–PE (IA6-2, 1:200), CD38–PE–Cy7 (HIT2, 1:200), CD19–APC (HIB19, 1:200) and Zombie Aqua (all BioLegend). Cells were washed twice, and single S-binding germinal centre B cells (live singlet CD3⁻CD19⁺IgD^{low}CD20^{high}CD38^{int}CD71⁺CXCR5^{+S⁺}) were sorted using a FACSAria II into 96-well plates containing 2 µl Lysis Buffer (Clontech) supplemented with 1 U µl⁻¹ RNase inhibitor (NEB), or total germinal centre B cells or plasmablasts (live singlet CD3⁻CD19⁺IgD^{low}CD20^{low}CD38⁺CD71⁺) were bulk-sorted into buffer RLT Plus (Qiagen) and immediately frozen on dry ice.

Monoclonal antibody generation

Antibodies were cloned as previously described⁴⁴. In brief, VH, V κ and V λ genes were amplified by reverse transcription PCR and nested PCR reactions from singly sorted germinal centre B cells using primer combinations specific for IgG, IgM, IgA, Ig κ and Ig λ from previously described primer sets⁴⁵, and then sequenced. To generate recombinant antibodies, restriction sites were incorporated via PCR with primers to the corresponding heavy and light chain V and J genes. The amplified VH, V κ and V λ genes were cloned into IgG1 and Ig κ or Ig λ expression vectors, respectively, as previously described^{45,46,47}. Heavy and light chain plasmids were co-transfected into Expi293F cells (Gibco) for expression, and antibody was purified using protein A agarose chromatography (Goldbio). Sequences were obtained from PCR reaction products and annotated using the ImMunoGeneTics (IMGT)/V-QUEST database (http://www.imgt.org/IMGT_vquest/)^{48,49}. Mutation frequency was calculated by counting the number of nonsynonymous nucleotide mismatches from the germline sequence in the heavy chain variable segment leading up to the CDR3, while excluding the 5' primer sequences that could be error-prone.

Bulk B cell receptor sequencing

RNA was purified from sorted plasmablasts from PBMCs and germinal centre B cells from lymph nodes from participants 07, 20 (lymph node 1) and 22 using the RNeasy Plus Micro kit (Qiagen). Reverse transcription, unique molecular identifier (UMI) barcoding, cDNA amplification, and Illumina linker addition to B cell heavy chain transcripts were performed using the human NEBNext Immune Sequencing Kit (New England Biolabs) according to the manufacturer's instructions. High-throughput 2× 300-bp paired-end sequencing was performed on the Illumina MiSeq platform with a 30% PhiX spike-in according to manufacturer's recommendations, except for performing 325 cycles for read 1 and 275 cycles for read 2.

Processing of B cell receptor bulk-sequencing reads

Demultiplexed pair-end reads were BLAST'ed using blastn v.2.11.0 (ref. [50](#)) for PhiX removal and subsequently preprocessed using pRESTO v.0.6.2 (ref. [51](#)) as follows. (1) Reads with a mean Phred quality score below 20 were filtered. (2) Reads were aligned against template switch sequences and constant region primers (Extended Data Table [5](#)), with a maximum mismatch rate of 0.5 and 0.2 respectively. (3) A UMI was assigned to each read by extracting the first 17 nucleotides preceding the template switch site. (4) Sequencing and multiplexing errors in the UMI region were then corrected using a previously published approach^{[52](#)}. In brief, reads with similar UMIs were clustered using cd-hit-est v.4.8.1 (ref. [53](#)) on the basis of the pairwise distance of their UMIs with a similarity threshold of 0.83 that was estimated from 10,000 reads. The UMI-based read groups were further clustered within themselves on the basis of the pairwise distance of the non-UMI region of their reads with a similarity threshold of 0.8. Read clusters spanning multiple multiplexed samples were assigned to the majority sample. (5) Separate consensus sequences for the forward and reverse reads within each read cluster were constructed with a maximum error score of 0.1 and minimum constant region primer frequency of 0.6. If multiple constant region primers were associated with a particular read cluster, the majority primer was used. (6) Forward and reverse consensus sequence pairs were assembled by first attempting de novo assembly with a minimum overlap of 8 nucleotides and a maximum mismatch rate of 0.3. If unsuccessful, this was followed by reference-guided assembly using blastn v.2.11.0 (ref. [50](#)) with a minimum identity of 0.5 and an *E*-value threshold of 1×10^{-5} . (7) Isotypes were assigned by local alignment of the 3' end of each consensus sequence to isotype-specific internal constant region sequences (Extended Data Table [5](#)) with a maximum mismatch rate of 0.3. Sequences with inconsistent isotype assignment and constant region primer alignment were removed. (8) Duplicate consensus sequences, except those with different isotype assignments, were collapsed

into unique sequences. Only unique consensus sequences with at least two contributing reads were used subsequently (Extended Data Table 6).

B cell receptor genotyping

Initial germline V(D)J gene annotation was performed using IgBLAST v.1.17.1 (ref. 54) with IMGT/GENE-DB release 202113-2 (ref. 55). IgBLAST output was parsed using Change-O v.1.0.2 (ref. 56). Quality control was performed, requiring each sequence to have non-empty V and J gene annotations; exhibit chain consistency in all annotations; bear fewer than 10 non-informative (non-A/T/G/C, such as N or –) positions; and carry a CDR3 with no N and a nucleotide length that is a multiple of 3. Individualized genotypes were inferred using TIgGER v.1.0.0 (ref. 57) and used to finalize V(D)J annotations. Sequences annotated as non-productively rearranged by IgBLAST were removed from further analysis.

Clonal lineage analysis

B cell clonal lineages were inferred on the basis of productively rearranged heavy chain sequences using hierarchical clustering with single linkage^{58,59}. Sequences were first partitioned based on common V and J gene annotations and CDR3 lengths. Within each partition, sequences with CDR3s that were within 0.15 normalized Hamming distance from each other were clustered as clones. This distance threshold was determined by manual inspection in conjunction with kernel density estimates to identify the local minimum between the two modes of the within-participant bimodal distance-to-nearest distribution (Extended Data Fig. 3a). Following clonal clustering, full-length clonal consensus germline sequences were reconstructed for each clone with D-segment and N/P regions masked with Ns, resolving any ambiguous gene assignments by majority rule. Within each clone, duplicate IMGT-aligned V(D)J sequences from bulk sequencing were collapsed with the exception of duplicates derived from different B cell compartments or isotypes. Clones were visualized as networks⁶⁰ using igraph v.1.2.5 (ref. 61). First, a full network was calculated for each clone, in which an edge was drawn between every pair of sequences with CDR3s that were within 0.15 normalized Hamming distance from each other. Then, a minimum spanning tree was derived from the full network, in which only edges essential for ensuring that all sequences connected in the full network remain connected in the minimum spanning tree either directly or indirectly were retained. The minimum spanning tree was then visualized for each clone.

Calculation of somatic hypermutation frequency

Mutation frequency was calculated by counting the number of nucleotide mismatches from the germline sequence in the observed heavy chain variable segment leading up to the CDR3, while excluding the first 18 positions that could be error-prone owing to the primers used for generating the monoclonal antibody sequences. Calculation was performed using the calcObservedMutations function from SHazaM v.1.0.2 (ref. [56](#)).

Reporting summary

Further information on research design is available in the [Nature Research Reporting Summary](#) linked to this paper.

Data availability

Antibody sequences are deposited on GenBank under the following accession numbers: MW926396–MW926407, MW926409–MW926430, MW926432–MW926441 and MZ292481–MZ292510, available from GenBank/EMBL/DDBJ. Bulk sequencing reads are deposited on Sequence Read Archive under BioProject [PRJNA731610](#). Processed B cell receptor data are deposited at <https://doi.org/10.5281/zenodo.5042252>. The IMGT/V-QUEST database is accessible at http://www.imgt.org/IMGT_vquest/. Other relevant data are available from the corresponding authors upon request.

References

1. 1.

Mulligan, M. J. et al. Phase I/II study of COVID-19 RNA vaccine BNT162b1 in adults. *Nature* **586**, 589–593 (2020).

[ADS](#) [CAS](#) [Article](#) [Google Scholar](#)

2. 2.

Jackson, L. A. et al. An mRNA vaccine against SARS-CoV-2 – preliminary report. *N. Engl. J. Med.* **383**, 1920–1931 (2020).

[CAS](#) [PubMed](#) [Article](#) [Google Scholar](#)

3. 3.

Sahin, U. et al. COVID-19 vaccine BNT162b1 elicits human antibody and T_H1 T cell responses. *Nature* **586**, 594–599 (2020).

[ADS](#) [CAS](#) [Article](#) [Google Scholar](#)

4. 4.

Polack, F. P. et al. Safety and efficacy of the BNT162b2 mRNA Covid-19 vaccine. *N. Engl. J. Med.* **383**, 2603–2615 (2020).

[CAS](#) [Article](#) [Google Scholar](#)

5. 5.

Baden, L. R. et al. Efficacy and safety of the mRNA-1273 SARS-CoV-2 vaccine. *N. Engl. J. Med.* **384**, 403–416 (2021).

[CAS](#) [PubMed](#) [Article](#) [Google Scholar](#)

6. 6.

Zhou, X. et al. Self-replicating Semliki forest virus RNA as recombinant vaccine. *Vaccine* **12**, 1510–1514 (1994).

[CAS](#) [PubMed](#) [Article](#) [Google Scholar](#)

7. 7.

Cagigi, A. & Loré, K. Immune responses induced by mRNA vaccination in mice, monkeys and humans. *Vaccines* **9**, 61 (2021).

[CAS](#) [PubMed](#) [PubMed Central](#) [Article](#) [Google Scholar](#)

8. 8.

Karikó, K. et al. Incorporation of pseudouridine into mRNA yields superior nonimmunogenic vector with increased translational capacity and biological stability. *Mol. Ther.* **16**, 1833–1840 (2008).

[PubMed](#) [Article](#) [CAS](#) [Google Scholar](#)

9. 9.

Schlake, T., Thess, A., Fotin-Mleczek, M. & Kallen, K.-J. Developing mRNA-vaccine technologies. *RNA Biol.* **9**, 1319–1330 (2012).

[CAS](#) [PubMed](#) [PubMed Central](#) [Article](#) [Google Scholar](#)

10. 10.

Graham, B. S., Mascola, J. R. & Fauci, A. S. Novel vaccine technologies: essential components of an adequate response to emerging viral diseases. *J. Am. Med. Assoc.* **319**, 1431–1432 (2018).

[Article](#) [Google Scholar](#)

11. 11.

Bettini, E. & Locci, M. SARS-CoV-2 mRNA vaccines: immunological mechanism and beyond. *Vaccines* **9**, 147 (2021).

[PubMed](#) [PubMed Central](#) [Article](#) [Google Scholar](#)

12. 12.

Amit, S., Regev-Yochay, G., Afek, A., Kreiss, Y. & Leshem, E. Early rate reductions of SARS-CoV-2 infection and COVID-19 in BNT162b2 vaccine recipients. *Lancet* **397**, 875–877 (2021).

[CAS](#) [PubMed](#) [PubMed Central](#) [Article](#) [Google Scholar](#)

13. 13.

Dagan, N. et al. BNT162b2 mRNA Covid-19 vaccine in a nationwide mass vaccination setting. *N. Engl. J. Med.* **384**, 1412–1423 (2021).

[CAS](#) [PubMed](#) [Article](#) [Google Scholar](#)

14. 14.

Vasileiou, E. et al. Interim findings from first-dose mass COVID-19 vaccination roll-out and COVID-19 hospital admissions in Scotland: a national prospective cohort study. *Lancet* **397**, 1646–1657 (2021).

[CAS](#) [PubMed](#) [PubMed Central](#) [Article](#) [Google Scholar](#)

15. 15.

Case, J. B. et al. Neutralizing antibody and soluble ACE2 inhibition of a replication-competent VSV-SARS-CoV-2 and a clinical isolate of SARS-CoV-2. *Cell Host Microbe* **28**, 475–485.e5 (2020).

[CAS](#) [PubMed](#) [PubMed Central](#) [Article](#) [Google Scholar](#)

16. 16.

Liu, Y. et al. Neutralizing activity of BNT162b2-elicited serum. *N. Engl. J. Med.* **384**, 1466–1468 (2021).

[Article](#) [Google Scholar](#)

17. 17.

Chen, R. E. et al. Resistance of SARS-CoV-2 variants to neutralization by monoclonal and serum-derived polyclonal antibodies. *Nat. Med.* **27**, 717–726 (2021).

[CAS](#) [PubMed](#) [Article](#) [Google Scholar](#)

18. 18.

Leung, K., Shum, M. H., Leung, G. M., Lam, T. T. & Wu, J. T. Early transmissibility assessment of the N501Y mutant strains of SARS-CoV-2 in the United Kingdom, October to November 2020. *Euro Surveill.* **26**, 2002106 (2021).

[PubMed Central](#) [Article](#) [PubMed](#) [Google Scholar](#)

19. 19.

Turner, J. S. et al. Human germinal centres engage memory and naive B cells after influenza vaccination. *Nature* **586**, 127–132 (2020).

[ADS](#) [CAS](#) [PubMed](#) [PubMed Central](#) [Article](#) [Google Scholar](#)

20. 20.

Pardi, N. et al. Expression kinetics of nucleoside-modified mRNA delivered in lipid nanoparticles to mice by various routes. *J. Control. Release* **217**, 345–351 (2015).

[CAS](#) [PubMed](#) [PubMed Central](#) [Article](#) [Google Scholar](#)

21. 21.

Liang, F. et al. Efficient targeting and activation of antigen-presenting cells in vivo after modified mRNA vaccine administration in rhesus macaques. *Mol. Ther.* **25**, 2635–2647 (2017).

[CAS](#) [PubMed](#) [PubMed Central](#) [Article](#) [Google Scholar](#)

22. 22.

Tai, W. et al. A novel receptor-binding domain (RBD)-based mRNA vaccine against SARS-CoV-2. *Cell Res.* **30**, 932–935 (2020).

[CAS](#) [PubMed](#) [Article](#) [Google Scholar](#)

23. 23.

Lederer, K. et al. SARS-CoV-2 mRNA vaccines foster potent antigen-specific germinal center responses associated with neutralizing antibody generation. *Immunity* **53**, 1281–1295.e5 (2020).

[CAS](#) [PubMed](#) [PubMed Central](#) [Article](#) [Google Scholar](#)

24. 24.

Kaji, T. et al. Distinct cellular pathways select germline-encoded and somatically mutated antibodies into immunological memory. *J. Exp. Med.* **209**, 2079–2097 (2012).

[CAS](#) [PubMed](#) [PubMed Central](#) [Article](#) [Google Scholar](#)

25. 25.

Weisel, F. J., Zuccarino-Catania, G. V., Chikina, M. & Shlomchik, M. J. A Temporal switch in the germinal center determines differential output of memory B and plasma cells. *Immunity* **44**, 116–130 (2016).

[CAS](#) [PubMed](#) [PubMed Central](#) [Article](#) [Google Scholar](#)

26. 26.

Good-Jacobson, K. L. et al. Regulation of germinal center responses and B-cell memory by the chromatin modifier MOZ. *Proc. Natl Acad. Sci. USA* **111**, 9585–9590 (2014).

[ADS](#) [CAS](#) [PubMed](#) [PubMed Central](#) [Article](#) [Google Scholar](#)

27. 27.

Bachmann, M. F., Odermatt, B., Hengartner, H. & Zinkernagel, R. M. Induction of long-lived germinal centers associated with persisting antigen after viral infection. *J. Exp. Med.* **183**, 2259–2269 (1996).

[CAS](#) [PubMed](#) [Article](#) [Google Scholar](#)

28. 28.

Dogan, I. et al. Multiple layers of B cell memory with different effector functions. *Nat. Immunol.* **10**, 1292–1299 (2009).

[CAS](#) [PubMed](#) [Article](#) [Google Scholar](#)

29. 29.

Rothaeusler, K. & Baumgarth, N. B-cell fate decisions following influenza virus infection. *Eur. J. Immunol.* **40**, 366–377 (2010).

[CAS](#) [PubMed](#) [PubMed Central](#) [Article](#) [Google Scholar](#)

30. 30.

Pape, K. A., Taylor, J. J., Maul, R. W., Gearhart, P. J. & Jenkins, M. K. Different B cell populations mediate early and late memory during an endogenous immune response. *Science* **331**, 1203–1207 (2011).

[ADS](#) [CAS](#) [PubMed](#) [PubMed Central](#) [Article](#) [Google Scholar](#)

31. 31.

Turner, J. S., Benet, Z. L. & Grigorova, I. Transiently antigen primed B cells can generate multiple subsets of memory cells. *PLoS ONE* **12**, e0183877 (2017).

[PubMed](#) [PubMed Central](#) [Article](#) [CAS](#) [Google Scholar](#)

32. 32.

Havenar-Daughton, C. et al. Rapid germinal center and antibody responses in non-human primates after a single nanoparticle vaccine immunization. *Cell Rep.* **29**, 1756–1766.e8 (2019).

[CAS](#) [PubMed](#) [PubMed Central](#) [Article](#) [Google Scholar](#)

33. 33.

Cirelli, K. M. et al. Slow delivery immunization enhances HIV neutralizing antibody and germinal center responses via modulation of immunodominance. *Cell* **177**, 1153–1171.e28 (2019).

[CAS](#) [PubMed](#) [PubMed Central](#) [Article](#) [Google Scholar](#)

34. 34.

Qi, H., Cannons, J. L., Klauschen, F., Schwartzberg, P. L. & Germain, R. N. SAP-controlled T-B cell interactions underlie germinal centre formation. *Nature* **455**, 764–769 (2008).

[ADS](#) [CAS](#) [PubMed](#) [PubMed Central](#) [Article](#) [Google Scholar](#)

35. 35.

Johnston, R. J. et al. Bcl6 and Blimp-1 are reciprocal and antagonistic regulators of T follicular helper cell differentiation. *Science* **325**, 1006–1010 (2009).

[ADS](#) [CAS](#) [PubMed](#) [PubMed Central](#) [Article](#) [Google Scholar](#)

36. 36.

Schmitz, A. J. et al. A public vaccine-induced human antibody protects against SARS-CoV-2 and emerging variants. Preprint at <https://doi.org/10.1101/2021.03.24.436864> (2021).

37. 37.

Amanat, F. et al. SARS-CoV-2 mRNA vaccination induces functionally diverse antibodies to NTD, RBD and S2. *Cell* <https://doi.org/10.1016/j.cell.2021.06.005> (2021).

38. 38.

Zang, R. et al. TMPRSS2 and TMPRSS4 promote SARS-CoV-2 infection of human small intestinal enterocytes. *Sci. Immunol.* **5**, eabc3582 (2020).

[CAS](#) [PubMed](#) [PubMed Central](#) [Article](#) [Google Scholar](#)

39. 39.

Plante, J. A. et al. Spike mutation D614G alters SARS-CoV-2 fitness. *Nature* **592**, 116–121 (2021).

[ADS](#) [CAS](#) [PubMed](#) [Article](#) [Google Scholar](#)

40. 40.

Xie, X. et al. An infectious cDNA clone of SARS-CoV-2. *Cell Host Microbe* **27**, 841–848.e3 (2020).

[CAS](#) [PubMed](#) [PubMed Central](#) [Article](#) [Google Scholar](#)

41. 41.

Stadlbauer, D. et al. SARS-CoV-2 seroconversion in humans: a detailed protocol for a serological assay, antigen production, and test setup. *Curr. Protoc. Microbiol.* **57**, e100 (2020).

[CAS](#) [PubMed](#) [PubMed Central](#) [Article](#) [Google Scholar](#)

42. 42.

Pallesen, J. et al. Immunogenicity and structures of a rationally designed prefusion MERS-CoV spike antigen. *Proc. Natl Acad. Sci. USA* **114**, E7348–E7357 (2017).

[CAS](#) [PubMed](#) [PubMed Central](#) [Article](#) [Google Scholar](#)

43. 43.

Liu, Z. et al. Identification of SARS-CoV-2 spike mutations that attenuate monoclonal and serum antibody neutralization. *Cell Host Microbe* **29**, 477–488.e4 (2021).

[CAS](#) [PubMed](#) [PubMed Central](#) [Article](#) [Google Scholar](#)

44. 44.

Wrammert, J. et al. Broadly cross-reactive antibodies dominate the human B cell response against 2009 pandemic H1N1 influenza virus infection. *J. Exp. Med.* **208**, 181–193 (2011).

[CAS](#) [PubMed](#) [PubMed Central](#) [Article](#) [Google Scholar](#)

45. 45.

Smith, K. et al. Rapid generation of fully human monoclonal antibodies specific to a vaccinating antigen. *Nat. Protoc.* **4**, 372–384 (2009).

[ADS](#) [CAS](#) [PubMed](#) [PubMed Central](#) [Article](#) [Google Scholar](#)

46. 46.

Wrammert, J. et al. Rapid cloning of high-affinity human monoclonal antibodies against influenza virus. *Nature* **453**, 667–671 (2008).

[ADS](#) [CAS](#) [PubMed](#) [PubMed Central](#) [Article](#) [Google Scholar](#)

47. 47.

Nachbagauer, R. et al. broadly reactive human monoclonal antibodies elicited following pandemic H1N1 influenza virus exposure protect mice against highly pathogenic H5N1 challenge. *J. Virol.* **92**, 1–17 (2018).

[Article](#) [Google Scholar](#)

48. 48.

Brochet, X., Lefranc, M.-P. & Giudicelli, V. IMGT/V-QUEST: the highly customized and integrated system for IG and TR standardized V-J and V-D-J sequence analysis. *Nucleic Acids Res.* **36**, W503–W508 (2008).

[CAS](#) [PubMed](#) [PubMed Central](#) [Article](#) [Google Scholar](#)

49. 49.

Giudicelli, V., Brochet, X. & Lefranc, M.-P. IMGT/V-QUEST: IMGT standardized analysis of the immunoglobulin (IG) and T cell receptor (TR) nucleotide sequences. *Cold Spring Harb. Protoc.* **2011**, pdb.prot5633 (2011).

[PubMed](#) [Google Scholar](#)

50. 50.

Camacho, C. et al. BLAST+: architecture and applications. *BMC Bioinformatics* **10**, 421 (2009).

[PubMed](#) [PubMed Central](#) [Article](#) [CAS](#) [Google Scholar](#)

51. 51.

Vander Heiden, J. A. et al. pRESTO: a toolkit for processing high-throughput sequencing raw reads of lymphocyte receptor repertoires. *Bioinformatics* **30**, 1930–1932 (2014).

[Article](#) [CAS](#) [Google Scholar](#)

52. 52.

Jiang, R. et al. Thymus-derived B cell clones persist in the circulation after thymectomy in myasthenia gravis. *Proc. Natl Acad. Sci. USA* **117**, 30649–30660 (2020).

[CAS](#) [PubMed](#) [PubMed Central](#) [Article](#) [Google Scholar](#)

53. 53.

Li, W. & Godzik, A. Cd-hit: a fast program for clustering and comparing large sets of protein or nucleotide sequences. *Bioinformatics* **22**, 1658–1659 (2006).

[CAS](#) [PubMed](#) [Article](#) [Google Scholar](#)

54. 54.

Ye, J., Ma, N., Madden, T. L. & Ostell, J. M. IgBLAST: an immunoglobulin variable domain sequence analysis tool. *Nucleic Acids Res.* **41**, W34–W40 (2013).

[PubMed](#) [PubMed Central](#) [Article](#) [Google Scholar](#)

55. 55.

Giudicelli, V., Chaume, D. & Lefranc, M. P. IMGT/GENE-DB: a comprehensive database for human and mouse immunoglobulin and T cell receptor genes. *Nucleic Acids Res.* **33**, D256–D261 (2005).

[CAS](#) [PubMed](#) [Article](#) [Google Scholar](#)

56. 56.

Gupta, N. T. et al. Change-O: a toolkit for analyzing large-scale B cell immunoglobulin repertoire sequencing data. *Bioinformatics* **31**, 3356–3358 (2015).

[CAS](#) [PubMed](#) [PubMed Central](#) [Article](#) [Google Scholar](#)

57. 57.

Gadala-Maria, D., Yaari, G., Uduman, M. & Kleinstein, S. H. Automated analysis of high-throughput B-cell sequencing data reveals a high frequency of novel immunoglobulin V gene segment alleles. *Proc. Natl Acad. Sci. USA* **112**, E862–E870 (2015).

[ADS](#) [CAS](#) [PubMed](#) [PubMed Central](#) [Article](#) [Google Scholar](#)

58. 58.

Gupta, N. T. et al. Hierarchical clustering can identify B cell clones with high confidence in Ig repertoire sequencing data. *J. Immunol.* **198**, 2489–2499 (2017).

[CAS](#) [PubMed](#) [Article](#) [Google Scholar](#)

59. 59.

Zhou, J. Q. & Kleinstein, S. H. Cutting edge: Ig H chains are sufficient to determine most B cell clonal relationships. *J. Immunol.* **203**, 1687–1692 (2019).

[CAS](#) [PubMed](#) [Article](#) [Google Scholar](#)

60. 60.

Bashford-Rogers, R. J. M. et al. Network properties derived from deep sequencing of human B-cell receptor repertoires delineate B-cell populations. *Genome Res.* **23**, 1874–1884 (2013).

[CAS](#) [PubMed](#) [PubMed Central](#) [Article](#) [Google Scholar](#)

61. 61.

Csardi, G. & Nepusz, T. The igraph software package for complex network research. *InterJournal Complex Syst.* **1695**, 1–9 (2006).

[Google Scholar](#)

[Download references](#)

Acknowledgements

We thank the donors for providing specimens, L. Kessels, A. J. Winingham, K. Safi and the staff of the Infectious Diseases Clinical Research Unit at Washington University School of Medicine for assistance with scheduling participants and sample collection, and E. Lantelme for facilitating sorting. The Vero-TMPRSS2 cells were provided by S. Ding. The expression plasmids encoding the S of coronaviruses OC43 and HKU1 were provided by K. Corbett and B. Graham. The laboratory of A.H.E. was supported by National Institute of Allergy and Infectious Diseases (NIAID) grants U01AI141990 and 1U01AI150747 and NIAID Centers of Excellence for Influenza Research and Surveillance (CEIRS) contract HHSN272201400006C. The laboratories of A.H.E. and F.K. were supported by NIAID CEIRS contract HHSN272201400008C and NIAID Collaborative Influenza Vaccine Innovation Centers contract 75N93019C00051. The laboratory of M.S.D. was supported by R01 AI157155. The laboratory of P.Y.-S. was supported by NIH grants AI134907 and UL1TR001439, and awards from the Sealy & Smith Foundation, Kleberg Foundation, the John S. Dunn Foundation, the Amon G. Carter Foundation, the Gilson Longenbaugh Foundation and the Summerfield Robert Foundation. J.S.T. was supported by NIAID 5T32CA009547. J.B.C. was supported by a Helen Hay Whitney Foundation postdoctoral fellowship. The WU368 study was reviewed and approved by the Washington University Institutional Review Board (approval no. 202012081).

Author information

Author notes

1. These authors contributed equally: Jackson S. Turner, Jane A. O'Halloran

Affiliations

1. Department of Pathology and Immunology, Washington University School of Medicine, St Louis, MO, USA

Jackson S. Turner, Wooseob Kim, Aaron J. Schmitz, Julian Q. Zhou, Tingting Lei, Mahima Thapa, Rita E. Chen & Ali H. Ellebedy

2. Division of Infectious Diseases, Department of Internal Medicine, Washington University School of Medicine, St Louis, MO, USA

Jane A. O'Halloran, Adriana M. Rauseo & Rachel M. Presti

3. Division of Allergy and Immunology, Department of Internal Medicine, Washington University School of Medicine, St Louis, MO, USA

Elizaveta Kalaidina

4. Department of Medicine, Washington University School of Medicine, St Louis, MO, USA

Rita E. Chen, James Brett Case & Michael S. Diamond

5. Department of Microbiology, Icahn School of Medicine at Mount Sinai, New York, NY, USA

Fatima Amanat & Florian Krammer

6. Graduate School of Biomedical Sciences, Icahn School of Medicine at Mount Sinai, New York, NY, USA

Fatima Amanat

7. Clinical Trials Unit, Washington University School of Medicine, St Louis, MO, USA

Alem Haile & Michael K. Klebert

8. University of Texas Medical Branch, Galveston, TX, USA

Xuping Xie & Pei-Yong Shi

9. Mallinckrodt Institute of Radiology, Washington University School of Medicine, St Louis, MO, USA

Teresa Suessen, William D. Middleton & Sharlene A. Teeffey

10. Center for Vaccines and Immunity to Microbial Pathogens, Washington University School of Medicine, St Louis, MO, USA

Michael S. Diamond, Rachel M. Presti & Ali H. Ellebedy

11. The Andrew M. and Jane M. Bursky Center for Human Immunology & Immunotherapy Programs, Washington University School of Medicine, St Louis, MO, USA

Michael S. Diamond & Ali H. Ellebedy

Authors

1. Jackson S. Turner

[View author publications](#)

You can also search for this author in [PubMed](#) [Google Scholar](#)

2. Jane A. O'Halloran

[View author publications](#)

You can also search for this author in [PubMed](#) [Google Scholar](#)

3. Elizaveta Kalaidina

[View author publications](#)

You can also search for this author in [PubMed](#) [Google Scholar](#)

4. Wooseob Kim

[View author publications](#)

You can also search for this author in [PubMed](#) [Google Scholar](#)

5. Aaron J. Schmitz

[View author publications](#)

You can also search for this author in [PubMed](#) [Google Scholar](#)

6. Julian Q. Zhou

[View author publications](#)

You can also search for this author in [PubMed](#) [Google Scholar](#)

7. Tingting Lei

[View author publications](#)

You can also search for this author in [PubMed](#) [Google Scholar](#)

8. Mahima Thapa

[View author publications](#)

You can also search for this author in [PubMed](#) [Google Scholar](#)

9. Rita E. Chen

[View author publications](#)

You can also search for this author in [PubMed](#) [Google Scholar](#)

10. James Brett Case

[View author publications](#)

You can also search for this author in [PubMed](#) [Google Scholar](#)

11. Fatima Amanat

[View author publications](#)

You can also search for this author in [PubMed](#) [Google Scholar](#)

12. Adriana M. Rauseo

[View author publications](#)

You can also search for this author in [PubMed](#) [Google Scholar](#)

13. Alem Haile

[View author publications](#)

You can also search for this author in [PubMed](#) [Google Scholar](#)

14. Xuping Xie

[View author publications](#)

You can also search for this author in [PubMed](#) [Google Scholar](#)

15. Michael K. Klebert

[View author publications](#)

You can also search for this author in [PubMed](#) [Google Scholar](#)

16. Teresa Suessen

[View author publications](#)

You can also search for this author in [PubMed](#) [Google Scholar](#)

17. William D. Middleton

[View author publications](#)

You can also search for this author in [PubMed](#) [Google Scholar](#)

18. Pei-Yong Shi

[View author publications](#)

You can also search for this author in [PubMed](#) [Google Scholar](#)

19. Florian Krammer

[View author publications](#)

You can also search for this author in [PubMed](#) [Google Scholar](#)

20. Sharlene A. Teeffey

[View author publications](#)

You can also search for this author in [PubMed](#) [Google Scholar](#)

21. Michael S. Diamond

[View author publications](#)

You can also search for this author in [PubMed](#) [Google Scholar](#)

22. Rachel M. Presti

[View author publications](#)

You can also search for this author in [PubMed](#) [Google Scholar](#)

23. Ali H. Ellebedy

[View author publications](#)

You can also search for this author in [PubMed](#) [Google Scholar](#)

Contributions

A.H.E., J.A.O. and R.M.P. conceived and designed the study. J.A.O., A.H., M.K.K. and R.M.P. wrote and maintained the Institutional Review Board protocol, recruited and phlebotomized participants, and coordinated sample collection. J.S.T., E.K., W.K., A.J.S. and T.L. processed specimens. J.S.T., E.K., W.K. and A.J.S. performed ELISA and ELISpot. R.E.C. and J.B.C. performed neutralization assays. J.S.T., E.K., W.K., A.J.S., T.L. and M.T. generated and characterized monoclonal antibodies. A.J.S. performed RNA extractions and library preparation for B cell receptor bulk sequencing. J.Q.Z. analysed B cell receptor repertoire data. T.S. and W.D.M. performed FNA. W.D.M. and S.A.T. supervised lymph node evaluation prior to FNA and specimen collection and evaluated lymph node ultrasound data. A.J.S. expressed SARS-CoV-2 S and RBD proteins. F.A. and F.K. expressed coronavirus S proteins. J.S.T. sorted cells and collected and analysed the flow cytometry data. X.X. and P.-Y.S. prepared the SARS-CoV-2 with variant S mutations. J.S.T., A.M.R. and A.H.E. analysed the data. M.S.D. and A.H.E. supervised experiments and obtained funding. J.S.T. and A.H.E. composed the manuscript. All authors reviewed the manuscript.

Corresponding authors

Correspondence to [Rachel M. Presti](#) or [Ali H. Ellebedy](#).

Ethics declarations

Competing interests

The laboratory of A.H.E. received funding under sponsored research agreements that are unrelated to the data presented in the current study from Emergent BioSolutions and from AbbVie. A.H.E. is a consultant for Mubadala Investment Company and the founder of ImmuneBio Consulting. J.S.T., A.J.S., M.S.D. and A.H.E. are recipients of a licensing agreement with Abbvie that is unrelated to the data presented in the current study. M.S.D. is a consultant for Inbios, Vir Biotechnology, Fortress Biotech and Carnival Corporation, and on the Scientific Advisory Boards of Moderna and Immunome. The laboratory of M.S.D. has received unrelated funding support in sponsored research agreements from Moderna, Vir Biotechnology and Emergent BioSolutions. A patent application related to this work has been filed by Washington University School of Medicine. The Icahn School of Medicine at Mount Sinai has filed patent applications relating to SARS-CoV-2 serological assays and NDV-based SARS-CoV-2 vaccines which list F.K. as co-inventor. Mount Sinai has spun out a company, Kantaro, to market serological tests for SARS-CoV-2. F.K. has consulted for Merck and Pfizer (before 2020), and is currently consulting for Pfizer, Seqirus and Avimex. The laboratory of F.K. is also collaborating with Pfizer on animal models of SARS-CoV-2. The laboratory of P.-Y.S. has received sponsored research agreements from Pfizer, Gilead, Merck and IGM Sciences Inc. The content of this manuscript is solely the responsibility of the authors and does not necessarily represent the official view of NIAID or NIH.

Additional information

Peer review information *Nature* thanks the anonymous reviewers for their contribution to the peer review of this work. Peer reviewer reports are available.

Publisher's note Springer Nature remains neutral with regard to jurisdictional claims in published maps and institutional affiliations.

Extended data figures and tables

Extended Data Fig. 1 Antibody response to SARS-CoV-2 immunization.

a, Plasma IgA (left) and IgM (right) titres against SARS-CoV-2 S measured by ELISA in participants without (red) and with (black) a history of SARS-CoV-2 infection at baseline, and 3, 4, 5, 7 and 15 weeks after immunization. **b**, Neutralizing activity of serum against WA1/2020 D614G (left), B.1.1.7 (middle) and a chimeric virus expressing B.1.351 S (right) in Vero-TMPRSS2 cells at baseline, 3, and 5 or 7 weeks after immunization in participants without (red) and with (black) a history of SARS-CoV-2 infection. *P* values from two-sided Mann–Whitney tests. Dotted lines indicate limits of detection. Horizontal lines indicate the geometric mean. Symbols at each time point represent one sample ($n = 41$). Results are from one experiment performed in duplicate.

Extended Data Fig. 2 Gating strategies for analysis of germinal centre response to SARS-CoV-2 immunization.

a, c, Sorting gating strategies for S-binding germinal centre B cells from FNAs (**a**) and total plasmablasts from PBMCs (**c**). **b**, Representative plot of germinal centre B cells in tonsil.

Extended Data Fig. 3 Clonal analysis of germinal centre response to SARS-CoV-2 immunization.

a, Distance-to-nearest-neighbour plots for choosing a distance threshold for inferring clones via hierarchical clustering. After partitioning sequences based on common V and J genes and CDR3 length, the nucleotide Hamming distance of a CDR3 to its nearest nonidentical neighbour from the same participant within its partition was calculated and normalized by CDR3 length (blue histogram). For reference, the distance to the nearest

nonidentical neighbour from other participants was calculated (green histogram). A clustering threshold of 0.15 (dashed black line) was chosen via manual inspection and kernel density estimate (dashed purple line) to separate the two modes of the within-participant distance distribution representing, respectively, sequences that were probably clonally related and unrelated. **b**, Clonal relationship of sequences from S-binding germinal centre-derived monoclonal antibodies (cyan) to sequences from bulk repertoire analysis of plasmablasts sorted from PBMCs (red) and germinal centre B cells (blue) 4 weeks after immunization. Each clone is visualized as a network in which each node represents a sequence and sequences are linked as a minimum spanning tree of the network. Symbol shape indicates sequence isotype: IgG (circle), IgA (star) and IgM (square); symbol size corresponds to sequence count.

[Extended Data Fig. 4 Lymph node plasmablast response to SARS-CoV-2 immunization.](#)

a, c, Representative flow cytometry plots showing gating of $CD20^{\text{low}}CD38^+$ $CD71^+BLIMP1^+S^+$ plasmablasts from $IgD^{\text{low}}CD19^+CD3^-$ live singlet lymphocytes (**a**) and IgA and IgM staining on S^+ plasmablasts (**c**) in FNA samples. **b**, Kinetics of S^+ plasmablasts gated as in **a** from FNA of draining lymph nodes. Symbols at each time point represent one FNA sample; square symbols denote second lymph node sampled ($n = 14$). Horizontal lines indicate the median. **d**, Percentages of IgM^+ (teal), IgA^+ (yellow) or IgM^-IgA^- (purple) S^+ plasmablasts gated as in **c** in FNA of draining lymph nodes 4 weeks after primary immunization. Each bar represents one sample ($n = 14$).

Extended Data Table 1 Participant demographics

[Full size table](#)

Extended Data Table 2 Vaccine side effects

[Full size table](#)

Extended Data Table 3 Lymph node population frequencies

[Full size table](#)

Extended Data Table 4 Immunoglobulin gene usage of S-binding monoclonal antibodies

[Full size table](#)

Extended Data Table 5 Template switch sequences, constant region primers and isotype-specific internal constant region sequences for bulk BCR sequencing and processing

[Full size table](#)

Extended Data Table 6 Processing of bulk sequencing BCR reads

[Full size table](#)

Supplementary information

[Reporting Summary](#)

[Peer Review File](#)

Rights and permissions

[Reprints and Permissions](#)

About this article



Check for
updates

Cite this article

Turner, J.S., O'Halloran, J.A., Kalaidina, E. *et al.* SARS-CoV-2 mRNA vaccines induce persistent human germinal centre responses. *Nature* **596**, 109–113 (2021). <https://doi.org/10.1038/s41586-021-03738-2>

[Download citation](#)

- Received: 08 March 2021
- Accepted: 18 June 2021

- Published: 28 June 2021
- Issue Date: 05 August 2021
- DOI: <https://doi.org/10.1038/s41586-021-03738-2>

Comments

By submitting a comment you agree to abide by our [Terms](#) and [Community Guidelines](#). If you find something abusive or that does not comply with our terms or guidelines please flag it as inappropriate.

[Download PDF](#)

Advertisement

This article was downloaded by **calibre** from <https://www.nature.com/articles/s41586-021-03738-2>

| [Section menu](#) | [Main menu](#) |

- Article
- [Published: 14 July 2021](#)

Adaptive immunity induces mutualism between commensal eukaryotes

- [Kyla S. Ost](#) ORCID: orcid.org/0000-0003-4101-2836^{1,2},
- [Teresa R. O'Meara](#) ORCID: orcid.org/0000-0002-8901-0154³,
- [W. Zac Stephens](#) ORCID: orcid.org/0000-0002-8072-9023^{1,2},
- [Tyson Chiaro](#)^{1,2},
- [Haoyang Zhou](#)^{1,2},
- [Jourdan Penman](#)^{1,2},
- [Rickesha Bell](#) ORCID: orcid.org/0000-0002-0554-0730^{1,2},
- [Jason R. Catanzaro](#)⁴,
- [Deguang Song](#)⁵,
- [Shakti Singh](#)⁶,
- [Daniel H. Call](#)⁷,
- [Elizabeth Hwang-Wong](#)⁸,
- [Kimberly E. Hanson](#)⁹,
- [John F. Valentine](#)¹⁰,
- [Kenneth A. Christensen](#) ORCID: orcid.org/0000-0002-3736-5500⁷,
- [Ryan M. O'Connell](#) ORCID: orcid.org/0000-0003-0860-1401^{1,2},
- [Brendan Cormack](#) ORCID: orcid.org/0000-0002-2554-9345⁸,
- [Ashraf S. Ibrahim](#)^{6,11},
- [Noah W. Palm](#)⁵,
- [Suzanne M. Noble](#)¹² &
- [June L. Round](#) ^{1,2}

- 5276 Accesses
- 225 Altmetric
- [Metrics details](#)

Subjects

- [Fungal host response](#)
- [Mucosal immunology](#)

Abstract

Pathogenic fungi reside in the intestinal microbiota but rarely cause disease. Little is known about the interactions between fungi and the immune system that promote commensalism. Here we investigate the role of adaptive immunity in promoting mutual interactions between fungi and host. We find that potentially pathogenic *Candida* species induce and are targeted by intestinal immunoglobulin A (IgA) responses. Focused studies on *Candida albicans* reveal that the pathogenic hyphal morphotype, which is specialized for adhesion and invasion, is preferentially targeted and suppressed by intestinal IgA responses. IgA from mice and humans directly targets hyphal-enriched cell-surface adhesins. Although typically required for pathogenesis, *C. albicans* hyphae are less fit for gut colonization^{1,2} and we show that immune selection against hyphae improves the competitive fitness of *C. albicans*. *C. albicans* exacerbates intestinal colitis³ and we demonstrate that hyphae and an IgA-targeted adhesin exacerbate intestinal damage. Finally, using a clinically relevant vaccine to induce an adhesin-specific immune response protects mice from *C. albicans*-associated damage during colitis. Together, our findings show that adaptive immunity suppresses harmful fungal effectors, with benefits to both *C. albicans* and its host. Thus, IgA uniquely uncouples colonization from pathogenesis in commensal fungi to promote homeostasis.

Access options

[Subscribe to Journal](#)

Get full journal access for 1 year

\$199.00

only \$3.90 per issue

[Subscribe](#)

All prices are NET prices.

VAT will be added later in the checkout.

Tax calculation will be finalised during checkout.

Rent or Buy article

Get time limited or full article access on ReadCube.

from \$8.99

[Rent or Buy](#)

All prices are NET prices.

Additional access options:

- [Log in](#)
- [Access through your institution](#)
- [Learn about institutional subscriptions](#)

Fig. 1: Adaptive immune responses target and suppress *C. albicans* hyphae in the gut.

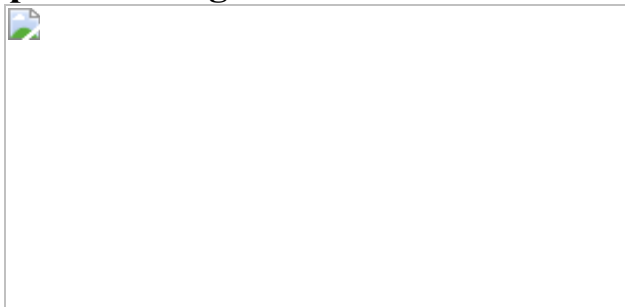


Fig. 2: IgA targets *C. albicans* adhesins.

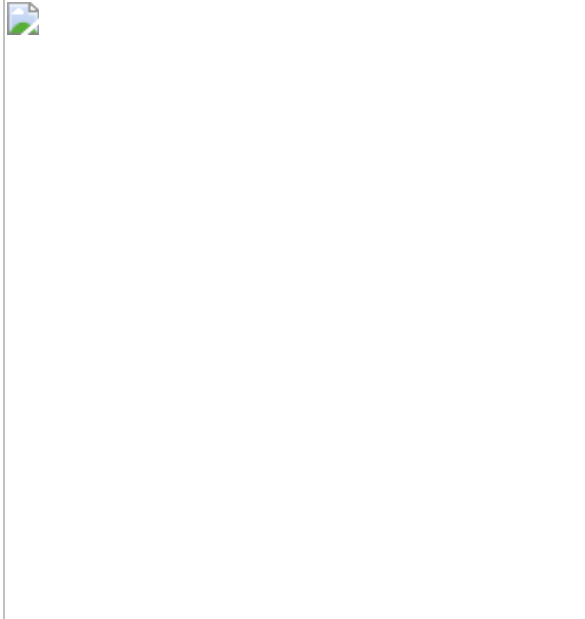


Fig. 3: Adaptive immunity enhances the competitive fitness of *C. albicans*.

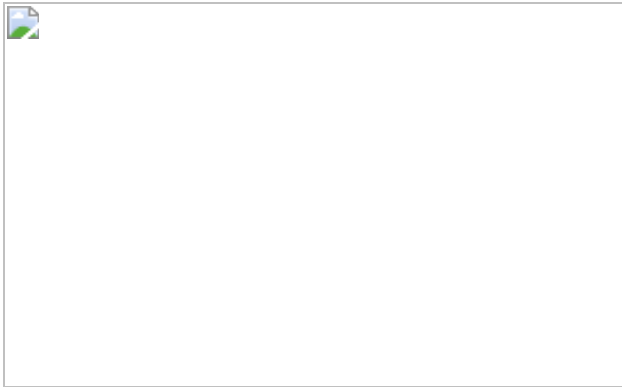
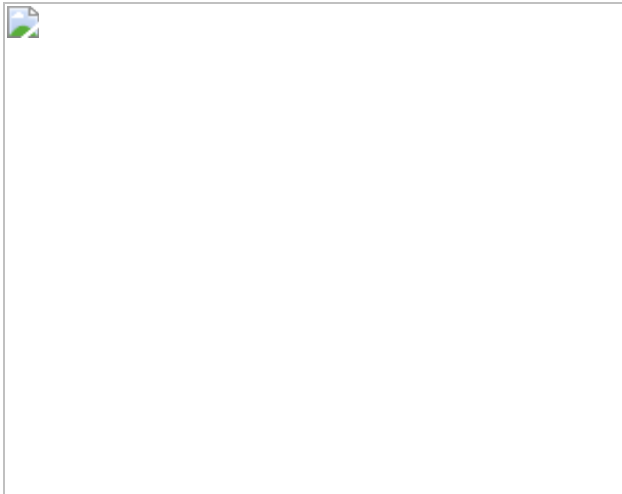


Fig. 4: Vaccination against *C. albicans* adhesin prevents damage during colitis.



Data availability

Raw *C. albicans* RNA-seq reads have been deposited at the NCBI Sequence Read Archive under the BioProject accession number [PRJNA728116](#). All other data needed to evaluate the conclusions in the paper are available within the Article or its [Supplementary Information](#). [Source data](#) are provided with this paper.

Code availability

All code used for processing and mapping RNA-seq reads is available at https://github.com/RoundLab/Ost_CandidaRNASEq.

References

1. 1.

Witchley, J. N. et al. *Candida albicans* morphogenesis programs control the balance between gut commensalism and invasive infection. *Cell Host Microbe* **25**, 432–443 (2019).

[CAS Article](#) [PubMed Central](#) [Google Scholar](#)

2. 2.

Tso, G. H. W. et al. Experimental evolution of a fungal pathogen into a gut symbiont. *Science* **362**, 589–595 (2018).

[ADS](#) [CAS](#) [Article](#) [PubMed Central](#) [Google Scholar](#)

3. 3.

Leonardi, I. et al. CX3CR1⁺ mononuclear phagocytes control immunity to intestinal fungi. *Science* **359**, 232–236 (2018).

[ADS](#) [CAS](#) [Article](#) [PubMed Central](#) [Google Scholar](#)

4. 4.

Zhai, B. et al. High-resolution mycobiota analysis reveals dynamic intestinal translocation preceding invasive candidiasis. *Nat. Med.* **26**, 59–64 (2020).

[CAS](#) [Article](#) [PubMed Central](#) [Google Scholar](#)

5. 5.

Jain, U. et al. *Debaryomyces* is enriched in Crohn's disease intestinal tissue and impairs healing in mice. *Science* **371**, 1154–1159 (2021).

[ADS](#) [CAS](#) [Article](#) [PubMed Central](#) [Google Scholar](#)

6. 6.

Li, X. V., Leonardi, I. & Iliev, I. D. Gut mycobiota in immunity and inflammatory disease. *Immunity* **50**, 1365–1379 (2019).

[CAS](#) [Article](#) [PubMed Central](#) [Google Scholar](#)

7. 7.

Weis, A. M. & Round, J. L. Microbiota–antibody interactions that regulate gut homeostasis. *Cell Host Microbe* **29**, 334–346 (2021).

[CAS](#) [Article](#) [PubMed Central](#) [Google Scholar](#)

8. 8.

Huertas, B. et al. Serum antibody profile during colonization of the mouse gut by *Candida albicans*: relevance for protection during systemic infection. *J. Proteome Res.* **16**, 335–345 (2017).

[CAS](#) [Article](#) [PubMed Central](#) [Google Scholar](#)

9. 9.

Doron, I. et al. Human gut mycobiota tune immunity via CARD9-dependent induction of anti-fungal IgG antibodies. *Cell* **184**, 1017–1031 (2021).

[CAS](#) [Article](#) [PubMed Central](#) [Google Scholar](#)

10. 10.

Bai, X.-D., Liu, X.-H. & Tong, Q.-Y. Intestinal colonization with *Candida albicans* and mucosal immunity. *World J. Gastroenterol.* **10**, 2124–2126 (2004).

[Article](#) [PubMed Central](#) [Google Scholar](#)

11. 11.

Millet, N., Solis, N. V. & Swidergall, M. Mucosal IgA prevents commensal *Candida albicans* dysbiosis in the oral cavity. *Front. Immunol.* **11**, 555363 (2020).

[CAS](#) [Article](#) [PubMed Central](#) [Google Scholar](#)

12. 12.

Standaert-Vitse, A. et al. *Candida albicans* is an immunogen for anti-*Saccharomyces cerevisiae* antibody markers of Crohn's disease. *Gastroenterology* **130**, 1764–1775 (2006).

[CAS](#) [Article](#) [PubMed Central](#) [Google Scholar](#)

13. 13.

Strope, P. K. et al. The 100-genomes strains, an *S. cerevisiae* resource that illuminates its natural phenotypic and genotypic variation and emergence as an opportunistic pathogen. *Genome Res.* **25**, 762–774 (2015).

[CAS](#) [Article](#) [PubMed Central](#) [Google Scholar](#)

14. 14.

Richardson, J. P., Ho, J. & Naglik, J. R. *Candida*–epithelial interactions. *J. Fungi* **4**, 22 (2018).

[Article](#) [Google Scholar](#)

15. 15.

Noble, S. M., Gianetti, B. A. & Witchley, J. N. *Candida albicans* cell-type switching and functional plasticity in the mammalian host. *Nat. Rev. Microbiol.* **15**, 96–108 (2017).

[CAS](#) [Article](#) [PubMed Central](#) [Google Scholar](#)

16. 16.

Noble, S. M., French, S., Kohn, L. A., Chen, V. & Johnson, A. D. Systematic screens of a *Candida albicans* homozygous deletion library decouple morphogenetic switching and pathogenicity. *Nat. Genet.* **42**, 590–598 (2010).

[CAS](#) [Article](#) [PubMed Central](#) [Google Scholar](#)

17. 17.

Homann, O. R., Dea, J., Noble, S. M. & Johnson, A. D. A phenotypic profile of the *Candida albicans* regulatory network. *PLoS Genet.* **5**,

e1000783 (2009).

[Article](#) [PubMed Central](#) [Google Scholar](#)

18. 18.

Lohse, M. B., Gulati, M., Johnson, A. D. & Nobile, C. J. Development and regulation of single- and multi-species *Candida albicans* biofilms. *Nat. Rev. Microbiol.* **16**, 19–31 (2018).

[CAS](#) [Article](#) [PubMed Central](#) [Google Scholar](#)

19. 19.

Braun, B. R., Kadosh, D. & Johnson, A. D. *NRG1*, a repressor of filamentous growth in *C. albicans*, is down-regulated during filament induction. *EMBO J.* **20**, 4753–4761 (2001).

[CAS](#) [Article](#) [PubMed Central](#) [Google Scholar](#)

20. 20.

Ruben, S. et al. Ahr1 and Tup1 contribute to the transcriptional control of virulence-associated genes in *Candida albicans*. *MBio* **11**, e00206-20 (2020).

[Article](#) [PubMed Central](#) [Google Scholar](#)

21. 21.

De Groot, P. W. J., Bader, O., De Boer, A. D., Weig, M. & Chauhan, N. Adhesins in human fungal pathogens: glue with plenty of stick. *Eukaryot. Cell* **12**, 470–481 (2013).

[Article](#) [PubMed Central](#) [Google Scholar](#)

22. 22.

Askew, C. et al. The zinc cluster transcription factor Ahr1p directs Mcm1p regulation of *Candida albicans* adhesion. *Mol. Microbiol.* **79**, 940–953 (2011).

[CAS](#) [Article](#) [PubMed Central](#) [Google Scholar](#)

23. 23.

Carreté, L. et al. Patterns of genomic variation in the opportunistic pathogen *Candida glabrata* suggest the existence of mating and a secondary association with humans. *Curr. Biol.* **28**, 15–27 (2018).

[Article](#) [PubMed Central](#) [Google Scholar](#)

24. 24.

Nobbs, A. H., Vickerman, M. M. & Jenkinson, H. F. Heterologous expression of *Candida albicans* cell wall-associated adhesins in *Saccharomyces cerevisiae* reveals differential specificities in adherence and biofilm formation and in binding oral *Streptococcus gordonii*. *Eukaryot. Cell* **9**, 1622–1634 (2010).

[CAS](#) [Article](#) [PubMed Central](#) [Google Scholar](#)

25. 25.

Edwards, J. E. Jr et al. A fungal immunotherapeutic vaccine (NDV-3A) for treatment of recurrent vulvovaginal candidiasis—a phase 2 randomized, double-blind, placebo-controlled trial. *Clin. Infect. Dis.* **66**, 1928–1936 (2018).

[CAS](#) [Article](#) [PubMed Central](#) [Google Scholar](#)

26. 26.

Fiedorová, K. et al. Bacterial but not fungal gut microbiota alterations are associated with common variable immunodeficiency (CVID) phenotype. *Front. Immunol.* **10**, 1914 (2019).

[Article](#) [PubMed Central](#) [Google Scholar](#)

27. 27.

Spellberg, B. J. et al. Efficacy of the anti-*Candida* rAls3p-N or rAls1p-N vaccines against disseminated and mucosal candidiasis. *J. Infect. Dis.* **194**, 256–260 (2006).

[CAS](#) [Article](#) [PubMed Central](#) [Google Scholar](#)

28. 28.

Ibrahim, A. S. et al. Vaccination with recombinant N-terminal domain of Als1p improves survival during murine disseminated candidiasis by enhancing cell-mediated, not humoral, immunity. *Infect. Immun.* **73**, 999–1005 (2005).

[CAS](#) [Article](#) [PubMed Central](#) [Google Scholar](#)

29. 29.

Voth, W. P., Richards, J. D., Shaw, J. M. & Stillman, D. J. Yeast vectors for integration at the *HO* locus. *Nucleic Acids Res.* **29**, e59 (2001).

[CAS](#) [Article](#) [PubMed Central](#) [Google Scholar](#)

30. 30.

Igyártó, B. Z. et al. Skin-resident murine dendritic cell subsets promote distinct and opposing antigen-specific T helper cell responses. *Immunity* **35**, 260–272 (2011).

[Article](#) [PubMed Central](#) [Google Scholar](#)

31. 31.

Basso, L. R., Jr et al. Transformation of *Candida albicans* with a synthetic hygromycin B resistance gene. *Yeast* **27**, 1039–1048 (2010).

[CAS](#) [Article](#) [PubMed Central](#) [Google Scholar](#)

32. 32.

Seman, B. G. et al. Yeast and filaments have specialized, independent activities in a zebrafish model of *Candida albicans* infection. *Infect. Immun.* **86**, e00415-18 (2018).

[Article](#) [PubMed Central](#) [Google Scholar](#)

33. 33.

Schindelin, J. et al. Fiji: an open-source platform for biological-image analysis. *Nat. Methods* **9**, 676–682 (2012).

[CAS](#) [Article](#) [Google Scholar](#)

34. 34.

Martin, M. Cutadapt removes adapter sequences from high-throughput sequencing reads. *EMBnet J.* **17**, 10–12 (2011).

[Article](#) [Google Scholar](#)

35. 35.

Bray, N. L., Pimentel, H., Melsted, P. & Pachter, L. Near-optimal probabilistic RNA-seq quantification. *Nat. Biotechnol.* **34**, 525–527 (2016).

[CAS](#) [Article](#) [PubMed Central](#) [Google Scholar](#)

36. 36.

Pimentel, H., Bray, N. L., Puente, S., Melsted, P. & Pachter, L. Differential analysis of RNA-seq incorporating quantification uncertainty. *Nat. Methods* **14**, 687–690 (2017).

[CAS](#) [Article](#) [PubMed Central](#) [Google Scholar](#)

37. 37.

Yu, G., Wang, L. G., Han, Y. & He, Q. Y. clusterProfiler: an R package for comparing biological themes among gene clusters. *OMICS* **16**, 284–287 (2012).

[CAS](#) [Article](#) [PubMed Central](#) [Google Scholar](#)

38. 38.

Sergushichev, A. A. An algorithm for fast preranked gene set enrichment analysis using cumulative statistic calculation. Preprint at <https://doi.org/10.1101/060012> (2016).

39. 39.

Blighe, K., Rana S. & Lewis, M. EnhancedVolcano: publication-ready volcano plots with enhanced colouring and labeling.
<https://github.com/kevinblighe/EnhancedVolcano> (2018).

40. 40.

Kubinak, J. L. et al. MyD88 signaling in T cells directs IgA-mediated control of the microbiota to promote health. *Cell Host Microbe* **17**, 153–163 (2015).

[CAS](#) [Article](#) [PubMed Central](#) [Google Scholar](#)

41. 41.

Plaine, A. et al. Functional analysis of *Candida albicans* GPI-anchored proteins: roles in cell wall integrity and caspofungin sensitivity. *Fungal Genet. Biol.* **45**, 1404–1414 (2008).

[CAS](#) [Article](#) [PubMed Central](#) [Google Scholar](#)

42. 42.

Singh, S. et al. The NDV-3A vaccine protects mice from multidrug resistant *Candida auris* infection. *PLoS Pathog.* **15**, e1007460 (2019).

[CAS Article](#) [PubMed Central](#) [Google Scholar](#)

[Download references](#)

Acknowledgements

We thank A. Weis and J. Hill for their edits of this manuscript; R. Wheeler for providing the pENO1-iRFP and pENO1-Neon *C. albicans* constructs; L. Cowen for the pLC605 TetO construct; J. Berman for the YJM11522 *C. albicans* strain; A. Nobbs for the *S. cerevisiae* strains expressing *C. albicans* adhesins; D. Stillman for *S. cerevisiae* strains and reagents; and the ULAM GF Mouse Facility at the University of Michigan for the GF *Rag1*^{-/-} mice. Proteomics mass spectrometry analysis was performed at the Mass Spectrometry and Proteomics Core Facility at the University of Utah. Mass spectrometry equipment was obtained through a Shared Instrumentation Grant 1 S10 OD018210 01A1. This work was supported by the Helen Hay Whitney Foundation (K.S.O.), a University of Utah NRSA Microbial Pathogenesis T32 Training Grant (K.S.O.), a CCFA Senior Research Award (J.L.R.), NIDDK R01DK124336 (J.L.R.), the Edward Mallinckrodt Jr. Foundation (J.L.R.), a NSF CAREER award (IOS-1253278) (J.L.R.), a Packard Fellowship in Science and Engineering (J.L.R.), a Burroughs Welcome Investigator in Pathogenesis Award (J.L.R), the American Asthma Foundation (J.L.R.), the Margolis Foundation (J.L.R.), an MS Society Center grant (J.L.R.), NIAID R01046223 (B.C.), an NIH New Innovator Award DP2GM111099-01 (R.M.O.), NHLBI R00HL102228-05 (R.M.O.), an American Cancer Society Research Grant (R.M.O.), a Kimmel Scholar Award (R.M.O.), R01AG047956 (R.M.O.) and NIAID R01AI141202 (A.S.I.). This work was supported by the University of Utah Flow Cytometry Facility in addition to the National Cancer Institute through award number 5P30CA042014-24. The support and resources from the Center for High Performance Computing at the University of Utah are gratefully acknowledged.

Author information

Affiliations

1. Department of Pathology, Division of Microbiology and Immunology, University of Utah School of Medicine, Salt Lake City, UT, USA

Kyla S. Ost, W. Zac Stephens, Tyson Chiaro, Haoyang Zhou, Jourdan Penman, Rickesha Bell, Ryan M. O'Connell & June L. Round

2. Huntsman Cancer Institute, University of Utah, Salt Lake City, UT, USA

Kyla S. Ost, W. Zac Stephens, Tyson Chiaro, Haoyang Zhou, Jourdan Penman, Rickesha Bell, Ryan M. O'Connell & June L. Round

3. Department of Microbiology and Immunology, University of Michigan Medical School, Ann Arbor, MI, USA

Teresa R. O'Meara

4. Section of Pulmonology, Allergy, Immunology and Sleep Medicine, Department of Pediatrics, Yale University School of Medicine, New Haven, CT, USA

Jason R. Catanzaro

5. Department of Immunobiology, Yale University School of Medicine, New Haven, CT, USA

Deguang Song & Noah W. Palm

6. The Lundquist Institute of Biomedical Innovation, Harbor–UCLA Medical Center, Torrance, CA, USA

Shakti Singh & Ashraf S. Ibrahim

7. Department of Chemistry and Biochemistry, Brigham Young University, Provo, UT, USA

Daniel H. Call & Kenneth A. Christensen

8. Department of Molecular Biology and Genetics, Johns Hopkins University School of Medicine, Baltimore, MD, USA

Elizabeth Hwang-Wong & Brendan Cormack

9. Department of Pathology, Division of Clinical Microbiology, University of Utah, Salt Lake City, UT, USA

Kimberly E. Hanson

10. Department of Internal Medicine, Division of Gastroenterology, University of Utah School of Medicine, Salt Lake City, UT, USA

John F. Valentine

11. David Geffen School of Medicine at UCLA, Los Angeles, CA, USA

Ashraf S. Ibrahim

12. Department of Microbiology and Immunology, UCSF School of Medicine, San Francisco, CA, USA

Suzanne M. Noble

Authors

1. Kyla S. Ost

[View author publications](#)

You can also search for this author in [PubMed](#) [Google Scholar](#)

2. Teresa R. O'Meara

[View author publications](#)

You can also search for this author in [PubMed](#) [Google Scholar](#)

3. W. Zac Stephens

[View author publications](#)

You can also search for this author in [PubMed](#) [Google Scholar](#)

4. Tyson Chiaro

[View author publications](#)

You can also search for this author in [PubMed](#) [Google Scholar](#)

5. Haoyang Zhou

[View author publications](#)

You can also search for this author in [PubMed](#) [Google Scholar](#)

6. Jourdan Penman

[View author publications](#)

You can also search for this author in [PubMed](#) [Google Scholar](#)

7. Rickesha Bell

[View author publications](#)

You can also search for this author in [PubMed](#) [Google Scholar](#)

8. Jason R. Catanzaro

[View author publications](#)

You can also search for this author in [PubMed](#) [Google Scholar](#)

9. Deguang Song

[View author publications](#)

You can also search for this author in [PubMed](#) [Google Scholar](#)

10. Shakti Singh

[View author publications](#)

You can also search for this author in [PubMed](#) [Google Scholar](#)

11. Daniel H. Call

[View author publications](#)

You can also search for this author in [PubMed](#) [Google Scholar](#)

12. Elizabeth Hwang-Wong

[View author publications](#)

You can also search for this author in [PubMed](#) [Google Scholar](#)

13. Kimberly E. Hanson

[View author publications](#)

You can also search for this author in [PubMed](#) [Google Scholar](#)

14. John F. Valentine

[View author publications](#)

You can also search for this author in [PubMed](#) [Google Scholar](#)

15. Kenneth A. Christensen

[View author publications](#)

You can also search for this author in [PubMed](#) [Google Scholar](#)

16. Ryan M. O'Connell

[View author publications](#)

You can also search for this author in [PubMed](#) [Google Scholar](#)

17. Brendan Cormack

[View author publications](#)

You can also search for this author in [PubMed](#) [Google Scholar](#)

18. Ashraf S. Ibrahim

[View author publications](#)

You can also search for this author in [PubMed](#) [Google Scholar](#)

19. Noah W. Palm

[View author publications](#)

You can also search for this author in [PubMed](#) [Google Scholar](#)

20. Suzanne M. Noble

[View author publications](#)

You can also search for this author in [PubMed](#) [Google Scholar](#)

21. June L. Round

[View author publications](#)

You can also search for this author in [PubMed](#) [Google Scholar](#)

Contributions

K.S.O. conceived the study, performed most experiments and helped to write the manuscript. T.R.O. helped with experimental design and fungal strain creation, and edited the manuscript. W.Z.S. analysed the RNA-seq data, helped with experimental design and edited the manuscript. T.C. helped with the immune profiling experiments and edited the manuscript. H.Z. helped to perform the *C. albicans* IgA screens and edited the manuscript. J.P. helped with fungal IgA-binding assays and edited the manuscript. R.B. managed the GF mouse experiments, helped with the immune profiling experiments and edited the manuscript. J.R.C., D.S. and N.W.P. provided the collection of human faecal samples, provided guidance on human antibody experiments and edited the manuscript. D.H.C. and K.A.C. guided the imaging flow cytometry experiments and edited the manuscript. E.H.-W. and B.C. created the *S. cerevisiae* strains expressing the *C. glabrata* adhesin-like proteins and edited the manuscript. K.E.H. edited the manuscript and provided the clinical *C. glabrata* strains. R.M.O. provided guidance on immunological experiments. S.M.N. provided *C. albicans* strains, provided guidance on fungal genetics experiments and edited the manuscript. A.S.I. and S.S. provided the NDV-3A vaccine and edited the manuscript. J.F.V. provided the human serum samples. J.L.R

conceived the study, guided the experiments, analysed data and helped to write the manuscript.

Corresponding author

Correspondence to [June L. Round](#).

Ethics declarations

Competing interests

The authors declare no competing interests.

Additional information

Peer review information *Nature* thanks Gordon Brown and the other, anonymous, reviewer(s) for their contribution to the peer review of this work.

Publisher's note Springer Nature remains neutral with regard to jurisdictional claims in published maps and institutional affiliations.

Extended data figures and tables

[Extended Data Fig. 1 Human faecal and serum anti-fungal antibodies.](#)

a, Human faecal antibody binding to cultured fungi and quantified by flow cytometry after staining with fluorescent secondary antibodies ($n = 70$). Staining intensity normalized to fungi stained with secondary antibodies but without human faecal wash. Box plots show minimum 25% quartile and maximum 75% quartile around the median and whiskers show range. **b**, IgA binding to cultured fungi from serial dilutions of human faecal wash ($n = 30$ healthy, $n = 23$ Crohn's disease and $n = 17$ UC). Geometric mean with 95% CI **c**, **d**, Human serum antibody binding to cultured fungi. Serum

diluted 1:75. ($n = 12$, $n = 4$ healthy and $n = 8$ Crohn's disease). Mean \pm s.d. **e**, Faecal ASCA IgA levels from undiluted faecal wash ($n = 30$ healthy, $n = 18$ Crohn's disease and $n = 14$ UC). Median with 95% CI **f**, Serum ASCA IgA levels from human serum samples diluted 1:100 ($n = 4$ healthy and $n = 8$ Crohn's disease). Median with 95% CI. P values calculated using two-way ANOVA with Tukey's test (**a**), one-way ANOVA with Dunn's test (**c**) or two-sided Mann–Whitney U -test (**f, d**).

[Source data](#)

[Extended Data Fig. 2 IgA targets *Candida* species but not *S. cerevisiae*.](#)

a, IgA-bound faecal fungi gating strategy. **b**, Peyer's patch GC B cell and T_{FH} cell gating strategy. **c**, Colon LP IgA plasma cell gating strategy ($n = 4$ mice per group 30 days after inoculation; representative of two experiments for **b, c**). **d**, IgA binding to faecal GFP⁺ *S. cerevisiae* and GFP⁺ *C. albicans* in monocolonized SW mice. **e**, Total IgA levels from monocolonized SW mice. **f**, Flow cytometry quantification of SW IgA binding to cultured *S. cerevisiae* and *C. albicans* ($n = 4$ *C. albicans*-colonized and $n = 5$ *S. cerevisiae*-colonized, one experiment for **d–f**). **g, h**, Serum antibody binding to cultured *C. albicans* or *S. cerevisiae* from SW (**g**) or B6 (**h**) GF or monocolonized mice. Antibody quantified by flow cytometry from serum diluted 1:25 (SW: GF $n = 4$, Sc-colonized $n = 5$, Ca-colonized $n = 5$; B6: GF $n = 3$, Sc $n = 5$, Ca-colonized $n = 3$). **i**, Lumen and tissue-associated fungal burden in monocolonized B6 mice 30 days after inoculation ($n = 4$ mice per group; one experiment; representative of two experiments). **j**, Whole-intestinal IgA four weeks after inoculation. **k**, Caecal wash IgA binding to cultured *C. glabrata* measured by flow cytometry. **l**, Peyer's patch T_{FH} cells four weeks after inoculation. **m**, Peyer's patch GC B cells ($n = 4$ mice per group; one experiment for **j–m**). **n**, IgA binding to cultured *C. glabrata*, *S. cerevisiae* and *C. albicans* from faecal wash from GF, *C. albicans*-monocolonized or *C. glabrata*-monocolonized intestinal wash ($n = 2$ *C. albicans*, $n = 3$ *C. glabrata* and $n = 3$ *S. cerevisiae* faecal washes) **o**, Percentage of IgA binding and binding intensity of faecal *C. albicans* during colonization of antibiotic-treated wild-type and *Tcrb*^{−/−} mice ($n = 6$

Tcrb^{-/-} and *n* = 8 wild-type mice from two experiments). *P* values calculated using two-way ANOVA (**d**, **o**), with Sidak's test (**b**, **e**, **f**, **g**, **h**, **n**), or two-sided unpaired *t*-test (**j**, **k**, **l**, **m**). Mean values ± s.d. for **b**, **d–o**.

[Source data](#)

Extended Data Fig. 3 An IgA response is not induced by 124 distinct *S. cerevisiae* strains.

a, IgA binding to the 20–24 strains from each pool was assessed by flow cytometry. Mice were gavaged weekly with the indicated pool for three weeks and caecal wash from mice was used as a source of IgA. *C. albicans* bound by IgA from *C. albicans*-monocolonized mice is shown in red. **b**, Total IgA in caecum contents quantified by ELISA. Mean values ± s.d. **c**, IgA binding to *S. cerevisiae* (pre-gated on CFW intermediate) populations from caecal material. (*n* = 3 mice per group representative of two experiments).

[Source data](#)

Extended Data Fig. 4 Fungal burden and GO term enrichment analysis of RNA-seq comparison of *C. albicans* in monocolonized wild-type and *Rag1*^{-/-} mice.

a, Fungal burden in wild-type and *Rag1*^{-/-} mice monocolonized with *C. albicans* four weeks after inoculation. Mean values ± s.d. **b**, **c**, Biological process (**b**) or molecular function (**c**) GO term enrichment in genes with *q* ≤ 0.05 and log₂-transformed fold change ≥ 1 or ≤ -1. **d**, Volcano plot of the ratio of *C. albicans* transcripts in wild-type and *Rag1*^{-/-} mice with active transmembrane transporter activity genes labelled in red (*n* = 5 wild type and 4 *Rag1*^{-/-} mice for **a–d**; one experiment). **e**, *C. albicans* morphology in colon contents from monocolonized wild-type or *Rag1*^{-/-} mice four weeks after colonization. Mean values ± s.d. (*n* = 3 mice per group; one experiment). **f**, IgA binding to *C. albicans* in the faeces of antibiotic-treated wild-type and *μMT*^{-/-} mice four weeks after inoculation. Mean values ± s.d. (*n* = 5 mice per group; one experiment). *P* values

calculated using two-way ANOVA with Sidak's multiple comparisons test (**a, f**) or two-sided unpaired *t*-test (**e**).

[Source data](#)

Extended Data Fig. 5 Filamentation and Ahr1 promote intestinal IgA responses.

a, Morphology of indicated *C. albicans* strains incubated for 4 h in RPMI with 10% FBS, YPD or YPD + 5 µg ml⁻¹ aTC). TetO-*NRG1* constitutively expresses *NRG1* when untreated (TetOn), but aTC repressed *NRG1* expression (TetOff). **b**, *C. albicans* in caecum contents stained with AF488 anti-*Candida* antibody. **c**, Intestinal fungal burden (mean values ± s.d.). **d**, Peyer's patch T_{FH} cells (ICOS⁺PD-1⁺CD4⁺CD3⁺ live cells) (mean values ± s.d.). **e**, Peyer's patch GC B cells (GL-7⁺Fas⁺IgD⁻CD19⁺ live cells) (mean values ± s.d.). **f**, Colon LP IgA⁺ plasma cells (IgA⁺CD138⁺CD45⁺CD3⁻CD19⁻ live cells) (mean values ± s.d.) quantified from mice monocolonized for four weeks (for **c–f**, *n* = 4 mice per group; one experiment). **g**, Faecal *AHRI* qPCR in aTC-treated mice monocolonized with wild-type or TetO-*AHRI* (TetOff-*AHRI*) (wild type *n* = 3 and TetOff-*ALSI* *n* = 5; one experiment). Mean values ± s.d. **h**, Fungal burden of wild-type- and TetOff-*AHRI*-monocolonized mice. **i**, IgA from wild-type- or TetOff-*AHRI*-monocolonized mice, **j**, **k**, Peyer's patch T_{FH} cells (**j**) and Peyer's patch GC B cells (**k**) from mice monocolonized with wild type or TetOff-*AHRI*. **l**, qRT-PCR from the small intestinal contents of monocolonized mice (for **h–l**, wild type *n* = 8 and TetOff-*ALSI* *n* = 10 mice per group from two experiments). **m**, Intestinal IgA (from *C. albicans*-monocolonized mice) binding to strains that were cultured untreated or were treated with aTC. **n**, Human IgA binding to indicated strains cultured without aTC (wild type, *ahrl*Δ/Δ, *ahrl*Δ/Δ TetOn-*ALSI*) or with 5 µg ml⁻¹ aTC (*ahrl*Δ/Δ TetOff-*ALSI*). IgA binding quantified by flow cytometry (healthy *n* = 13 and IBD *n* = 22; one experiment. Samples chosen had enough *C. albicans*-reactive IgA to bind at least 10% of cultured wild-type *C. albicans*). *P* values calculated using one-way ANOVA with Tukey's test (**c–f**), two-way ANOVA with Sidak's test (**i**),

two-sided unpaired *t*-test (**j**, **k**, **l**), two-sided Mann–Whitney *U*-test (**g**) or Friedman test with Dunn’s test (**n**).

[Source data](#)

Extended Data Fig. 6 *C. albicans-* and *C. glabrata-*induced IgA targets adhesins or adhesin-like proteins.

a, Anti-HA staining of the control *S. cerevisiae* expressing the Cwp1 scaffold control and the *S. cerevisiae* strains expressing HA-tagged *C. albicans* adhesins. **b**, Anti-HA and IgA binding to *S. cerevisiae* strains expressing HA-tagged *C. glabrata* adhesins after incubation in caecal wash from mice monocolonized with *C. glabrata*. SC104, SC106, SC97 and SC27 express adhesins not tagged by HA. HA and IgA binding quantified by flow cytometry.

[Source data](#)

Extended Data Fig. 7 Antibody induction by *S. cerevisiae* strains expressing *Candida* adhesins.

GF SW mice were monocolonized with the indicated strains or left GF. Colonized mice were gavaged three times per week with cultured strains. The control *S. cerevisiae* expresses the *CWP1* cell surface scaffold but not an adhesin. **a**, Weekly faecal IgA levels normalized by faecal weight. **b**, **c**, Intestinal IgA (**b**) and IgG (**c**) levels at day 28 normalized by material weight. **d**, Colon lamina propria IgG1 plasma cells (live IgG1⁺IgA⁻CD138⁺CD19⁻CD3⁻CD45⁺ live cells). **e**, Colon lamina propria IgA plasma cells (live IgA⁺IgG1⁻CD138⁺CD19⁻CD3⁻CD45⁺ live cells) (for **a–e**, GF *n* = 6, control Sc *n* = 4, Sc + Als1 *n* = 5, Sc + Als3 *n* = 5, Sc + Hwp1 *n* = 4, Sc + CAGL0B00154g *n* = 5 mice per group; one experiment). *P* values calculated using one-way ANOVA with Tukey’s test (**d**, **e**) or two-way ANOVA with Tukey’s test (**a–c**). All data are mean ± s.d.

[Source data](#)

Extended Data Fig. 8 Immune-enhanced fitness diminishes after 14 days.

Competitive index (CI) of *C. albicans* conditioned for four weeks in indicated GF recipient mice. B6-conditioned *C. albicans* was iRFP⁺ and *Rag1*^{-/-}-conditioned *C. albicans* was Neon⁺. CI normalized to the CI when strains were competed in wild-type and *Rag1*^{-/-} mice directly from culture (competition mice, $n = 3$ B6 and $n = 4$ *Rag1*^{-/-} mice from one experiment). P values calculated using two-way ANOVA with Sidak's test. Data are mean \pm s.d.

[Source data](#)

Extended Data Fig. 9 *AHRI* exacerbates DSS colitis.

a, Schematic of DSS colitis experiments. **b**, Histology images and scores for mice treated with no *C. albicans* or with TetO-*AHRI* with and without aTC (no-Ca UT, no-Ca aTC and TetOn-*AHRI* UT $n = 7$ mice per group, TetOff-*AHRI* aTC $n = 8$ mice per group from two independent experiments). Data are mean \pm s.d. **c**, DSS histology images for mice treated with no *C. albicans* or with wild-type *C. albicans*, *ahr1* Δ/Δ *C. albicans*, TetOn-*ALS1* *ahr1* Δ/Δ *C. albicans* and TetOff-*ALS1* *ahr1* Δ/Δ *C. albicans* (aTC-treated). P values calculated using two-way ANOVA with Tukey's test (**b**).

[Source data](#)

Extended Data Fig. 10 NDV-3A induces an intestinal anti-Als3 antibody response.

a, model of monocolonization and DSS experiment in vaccinated mice. **b**, **c**, ELISA quantification of Als3-specific IgA (**b**) and IgG (**c**) from the faeces of GF mice one week after boost with alum of NDV-3A vaccine. **d**, **e**, Faecal (**d**) and intestinal (**e**) lumen CFU of *C. albicans* in monocolonized alum or NDV-3A vaccinated mice. Intestinal CFU quantified 12 days after colonization. **f**, Imaging flow cytometry images of IgA⁺ *C. albicans* from

caecum of NDV-3A vaccinated mice. **g**, Percentage of hyphae quantified using an AF488 anti-*Candida* antibody to visualize morphology from indicated intestinal region 12 days after monocolonization. **h**, *HWPI* and *HYRI* transcripts quantified by qRT–PCR from colon *C. albicans* 12 days after monocolonization. (for **b–h**, $n = 5$ mice per group; one experiment). **i**, **j**, ELISA quantification of Als3-specific IgA (**i**) and IgG (**j**) in the faeces of conventionally colonized mice used for the DSS experiment. **k**, *C. albicans* CFU in colon contents after DSS treatment (for **i–k**, $n = 10$ mice per group, one experiment). **l**, Example H&E-stained histology images from the NDV-3A DSS experiment. *P* values calculated using two-way ANOVA with Sidak's test (**b**, **c**, **i**, **j**). All data are mean \pm s.d. Silhouettes in **a** were created using BioRender.

[Source data](#)

Supplementary information

[Supplementary Information](#)

This file contains Supplementary Figure 1.

[Reporting Summary](#)

[Supplementary Table 1](#)

RNAseq differential gene expression analysis.

[Supplementary Table 2](#)

IgA binding screen of Noble and Homann knock-out collections.

[Supplementary Table 3](#)

IgA targeted hyphae vs. yeast cell wall proteomics analysis.

[Supplementary Table 4](#)

Fungal strains used in this study.

Supplementary Table 5

S. cerevisiae strains expressing *C. albicans* or *C. glabrata* adhesins or adhesin-like domains.

Supplementary Table 6

Primers used for this study.

Supplementary Table 7

Plasmids used in this study.

Supplementary Table 8

Flow cytometry antibodies used in this study.

Supplementary Table 9

Human fecal and serum metadata.

Source data

Source Data Fig. 1

Source Data Fig. 2

Source Data Fig. 3

Source Data Extended Data Fig. 1

Source Data Extended Data Fig. 2

[**Source Data Extended Data Fig. 3**](#)

[**Source Data Extended Data Fig. 4**](#)

[**Source Data Extended Data Fig. 5**](#)

[**Source Data Extended Data Fig. 6**](#)

[**Source Data Extended Data Fig. 7**](#)

[**Source Data Extended Data Fig. 8**](#)

[**Source Data Extended Data Fig. 9**](#)

[**Source Data Extended Data Fig. 10**](#)

Rights and permissions

[Reprints and Permissions](#)

About this article



Check for
updates

Cite this article

Ost, K.S., O'Meara, T.R., Stephens, W.Z. *et al.* Adaptive immunity induces mutualism between commensal eukaryotes. *Nature* **596**, 114–118 (2021).
<https://doi.org/10.1038/s41586-021-03722-w>

[Download citation](#)

- Received: 24 June 2020
- Accepted: 14 June 2021
- Published: 14 July 2021
- Issue Date: 05 August 2021
- DOI: <https://doi.org/10.1038/s41586-021-03722-w>

Comments

By submitting a comment you agree to abide by our [Terms](#) and [Community Guidelines](#). If you find something abusive or that does not comply with our terms or guidelines please flag it as inappropriate.

[Access through your institution](#)

[Change institution](#)

[Buy or subscribe](#)

Advertisement

This article was downloaded by **calibre** from <https://www.nature.com/articles/s41586-021-03722-w>

| [Section menu](#) | [Main menu](#) |

- Article
- [Published: 21 July 2021](#)

Phenotype, specificity and avidity of antitumour CD8⁺ T cells in melanoma

- [Giacomo Oliveira](#) ORCID: orcid.org/0000-0001-7435-5603^{1,2},
- [Kari Stromhaug](#)¹,
- [Susan Klaeger](#) ORCID: orcid.org/0000-0002-0074-5163³,
- [Tomasz Kula](#)⁴ nAff10,
- [Dennie T. Frederick](#)⁵,
- [Phuong M. Le](#)⁶,
- [Juliet Forman](#)⁶,
- [Teddy Huang](#)⁶,
- [Shuqiang Li](#)^{3,6},
- [Wandi Zhang](#)¹,
- [Qikai Xu](#)⁴,
- [Nicoletta Cieri](#) ORCID: orcid.org/0000-0003-1340-6272¹,
- [Karl R. Clauiser](#)³,
- [Sachet A. Shukla](#)^{3,6},
- [Donna Neuberg](#) ORCID: orcid.org/0000-0003-2566-3145⁷,
- [Sune Justesen](#)⁸,
- [Gavin MacBeath](#) ORCID: orcid.org/0000-0003-2585-6772⁴,
- [Steven A. Carr](#)³,
- [Edward F. Fritsch](#)^{1,3},
- [Nir Hacohen](#) ORCID: orcid.org/0000-0002-2349-2656^{2,3,5},
- [Moshe Sade-Feldman](#) ORCID: orcid.org/0000-0002-0022-0287^{3,5},
- [Kenneth J. Livak](#) ORCID: orcid.org/0000-0001-9105-5856^{1,6},

- [Genevieve M. Boland^{2,3,5}](#),
- [Patrick A. Ott ORCID: orcid.org/0000-0002-4253-943X^{1,2,3,9}](#),
- [Derin B. Keskin^{1,6}](#) &
- [Catherine J. Wu ORCID: orcid.org/0000-0002-3348-5054^{1,2,3,9}](#)

[Nature](#) volume **596**, pages 119–125 (2021) [Cite this article](#)

- 8875 Accesses
- 81 Altmetric
- [Metrics details](#)

Subjects

- [CD8-positive T cells](#)
- [Melanoma](#)
- [T-cell receptor](#)
- [Tumour immunology](#)

Abstract

Interactions between T cell receptors (TCRs) and their cognate tumour antigens are central to antitumour immune responses^{1,2,3}; however, the relationship between phenotypic characteristics and TCR properties is not well elucidated. Here we show, by linking the antigenic specificity of TCRs and the cellular phenotype of melanoma-infiltrating lymphocytes at single-cell resolution, that tumour specificity shapes the expression state of intratumoural CD8⁺ T cells. Non-tumour-reactive T cells were enriched for viral specificities and exhibited a non-exhausted memory phenotype, whereas melanoma-reactive lymphocytes predominantly displayed an exhausted state that encompassed diverse levels of differentiation but rarely acquired memory properties. These exhausted phenotypes were observed both among clonotypes specific for public overexpressed melanoma antigens (shared across different tumours) or personal neoantigens (specific for each tumour). The recognition of such tumour antigens was provided by

TCRs with avidities inversely related to the abundance of cognate targets in melanoma cells and proportional to the binding affinity of peptide–human leukocyte antigen (HLA) complexes. The persistence of TCR clonotypes in peripheral blood was negatively affected by the level of intratumoural exhaustion, and increased in patients with a poor response to immune checkpoint blockade, consistent with chronic stimulation mediated by residual tumour antigens. By revealing how the quality and quantity of tumour antigens drive the features of T cell responses within the tumour microenvironment, we gain insights into the properties of the anti-melanoma TCR repertoire.

Access options

Subscribe to Journal

Get full journal access for 1 year

\$199.00

only \$3.90 per issue

[Subscribe](#)

All prices are NET prices.

VAT will be added later in the checkout.

Tax calculation will be finalised during checkout.

Rent or Buy article

Get time limited or full article access on ReadCube.

from \$8.99

[Rent or Buy](#)

All prices are NET prices.

Additional access options:

- [Log in](#)
- [Access through your institution](#)
- [Learn about institutional subscriptions](#)

Fig. 1: Distinct cell states among CD8⁺ TCR clonotype families in melanoma.



Fig. 2: Target specificity and phenotype of tumour-specific CD8⁺ TCRs.



Fig. 3: Antigenic specificity and avidity of tumour-specific TCRs.

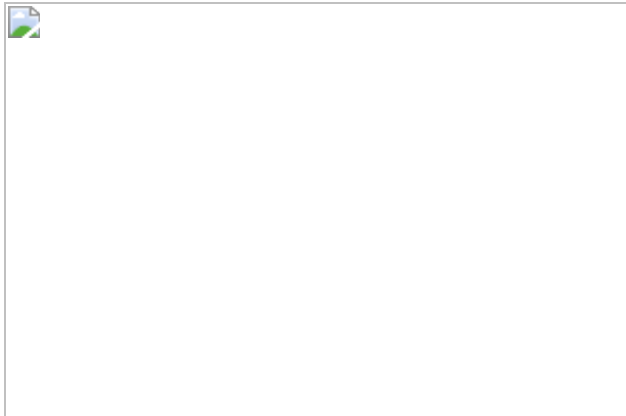
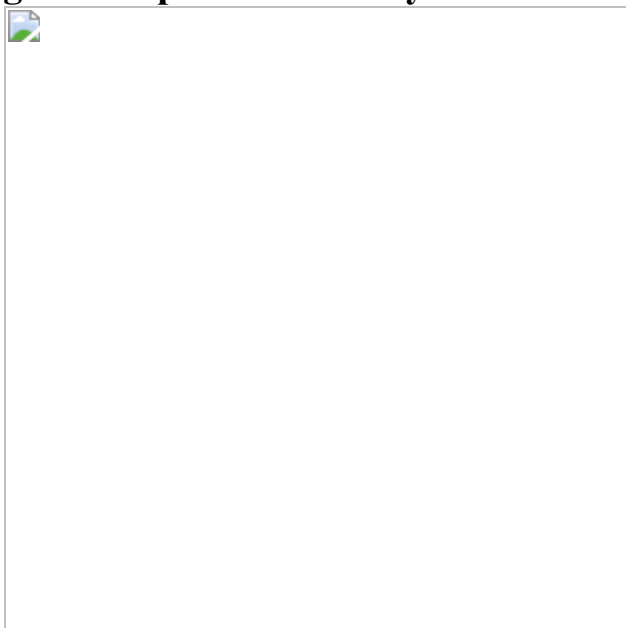


Fig. 4: Peripheral blood dynamics of CD8⁺ TIL-TCRs.



Data availability

scRNA-seq, scTCR-seq and CITE-seq data are available through the dbGaP portal (study ID: 26121, accession number: [phs001451.v3.p1](#)). All other data are available from the corresponding author on reasonable request.

Code availability

The code used for data analysis included the Broad Institute Picard Pipeline (for whole-exome sequencing/RNA-seq), GATK4 v4.0, Mutect2 v2.7.0 (for single-nucleotide variant and indel identification), NetMHCpan 4.0 (for

NeoAg-binding prediction), ContEst (for contamination estimation), ABSOLUTE v1.1 (for purity/ploidy estimation), STAR v2.6.1c (for sequencing alignment), RSEM v1.3.1 (for gene expression quantification), Seurat v3.2.0 (for single-cell sequencing analysis), Harmony v1.0 (for single-cell data normalization), SingleR v3.22, Scanpy v1.5.1 and Python v3.7.4 (for comparison with other single-cell datasets), which are each publicly available. The computer code used to generate the analyses is available at <https://github.com/kstromhaug/oliveira-stromhaug-melanoma-tcrs-phenotypes>.

References

1. 1.

van der Leun, A. M., Thommen, D. S. & Schumacher, T. N. CD8⁺ T cell states in human cancer: insights from single-cell analysis. *Nat. Rev. Cancer* **20**, 218–232 (2020).

[Article](#) [Google Scholar](#)

2. 2.

Scheper, W. et al. Low and variable tumor reactivity of the intratumoral TCR repertoire in human cancers. *Nat. Med.* **25**, 89–94 (2019).

[CAS](#) [Article](#) [Google Scholar](#)

3. 3.

Simoni, Y. et al. Bystander CD8⁺ T cells are abundant and phenotypically distinct in human tumour infiltrates. *Nature* **557**, 575–579 (2018).

[ADS](#) [CAS](#) [Article](#) [Google Scholar](#)

4. 4.

Ott, P. A. et al. An immunogenic personal neoantigen vaccine for patients with melanoma. *Nature* **547**, 217–221 (2017).

[ADS](#) [CAS](#) [Article](#) [Google Scholar](#)

5. 5.

Sarkizova, S. et al. A large peptidome dataset improves HLA class I epitope prediction across most of the human population. *Nat. Biotechnol.* **38**, 199–209 (2020).

[CAS](#) [Article](#) [Google Scholar](#)

6. 6.

Hu, Z. et al. Personal neoantigen vaccines induce persistent memory T cell responses and epitope spreading in patients with melanoma. *Nat. Med.* **27**, 515–525 (2021).

[CAS](#) [Article](#) [Google Scholar](#)

7. 7.

Stoeckius, M. et al. Simultaneous epitope and transcriptome measurement in single cells. *Nat. Methods* **14**, 865–868 (2017).

[CAS](#) [Article](#) [Google Scholar](#)

8. 8.

Sade-Feldman, M. et al. Defining T cell states associated with response to checkpoint immunotherapy in melanoma. *Cell* **175**, 998–1013.e20 (2018).

[CAS](#) [Article](#) [Google Scholar](#)

9. 9.

Yost, K. E. et al. Clonal replacement of tumor-specific T cells following PD-1 blockade. *Nat. Med.* **25**, 1251–1259 (2019).

[CAS](#) [Article](#) [Google Scholar](#)

10. 10.

Oh, D. Y. et al. Intratumoral CD4⁺ T cells mediate anti-tumor cytotoxicity in human bladder cancer. *Cell* **181**, 1612–1625.e13 (2020).

[CAS](#) [Article](#) [Google Scholar](#)

11. 11.

Wolfl, M. et al. Activation-induced expression of CD137 permits detection, isolation, and expansion of the full repertoire of CD8⁺ T cells responding to antigen without requiring knowledge of epitope specificities. *Blood* **110**, 201–210 (2007).

[CAS](#) [Article](#) [Google Scholar](#)

12. 12.

Chen, S.-Y., Yue, T., Lei, Q. & Guo, A.-Y. TCRdb: a comprehensive database for T-cell receptor sequences with powerful search function. *Nucleic Acids Res.* **49**, D468–D474 (2021).

[CAS](#) [Article](#) [Google Scholar](#)

13. 13.

Gros, A. et al. PD-1 identifies the patient-specific CD8⁺ tumor-reactive repertoire infiltrating human tumors. *J. Clin. Invest.* **124**, 2246–2259 (2014).

[CAS](#) [Article](#) [Google Scholar](#)

14. 14.

Krishna, S. et al. Human papilloma virus specific immunogenicity and dysfunction of CD8⁺ T cells in head and neck cancer. *Cancer Res.* **78**, 6159–6170 (2018).

[CAS](#) [Article](#) [Google Scholar](#)

15. 15.

Duhen, T. et al. Co-expression of CD39 and CD103 identifies tumor-reactive CD8 T cells in human solid tumors. *Nat. Commun.* **9**, 2724 (2018).

[ADS](#) [Article](#) [Google Scholar](#)

16. 16.

Miller, B. C. et al. Subsets of exhausted CD8⁺ T cells differentially mediate tumor control and respond to checkpoint blockade. *Nat. Immunol.* **20**, 326–336 (2019).

[CAS](#) [Article](#) [Google Scholar](#)

17. 17.

Utzschneider, D. T. et al. T cell factor 1-expressing memory-like CD8⁺ T cells sustain the immune response to chronic viral infections. *Immunity* **45**, 415–427 (2016).

[CAS](#) [Article](#) [Google Scholar](#)

18. 18.

Im, S. J. et al. Defining CD8⁺ T cells that provide the proliferative burst after PD-1 therapy. *Nature* **537**, 417–421 (2016).

[ADS](#) [CAS](#) [Article](#) [Google Scholar](#)

19. 19.

Siddiqui, I. et al. Intratumoral Tcf1⁺PD-1⁺CD8⁺ T cells with stem-like properties promote tumor control in response to vaccination and checkpoint blockade immunotherapy. *Immunity* **50**, 195–211.e10 (2019).

[CAS Article](#) [Google Scholar](#)

20. 20.

Milner, J. J. et al. Runx3 programs CD8⁺ T cell residency in non-lymphoid tissues and tumours. *Nature* **552**, 253–257 (2017).

[ADS](#) [CAS Article](#) [Google Scholar](#)

21. 21.

Joshi, N. S. et al. Inflammation directs memory precursor and short-lived effector CD8⁺ T cell fates via the graded expression of T-bet transcription factor. *Immunity* **27**, 281–295 (2007).

[CAS Article](#) [Google Scholar](#)

22. 22.

Jansen, C. S. et al. An intra-tumoral niche maintains and differentiates stem-like CD8 T cells. *Nature* **576**, 465–470 (2019).

[ADS](#) [CAS Article](#) [Google Scholar](#)

23. 23.

Krishna, S. et al. Stem-like CD8 T cells mediate response of adoptive cell immunotherapy against human cancer. *Science* **370**, 1328–1334 (2020).

[ADS](#) [CAS Article](#) [Google Scholar](#)

24. 24.

Wells, D. K. et al. Key parameters of tumor epitope immunogenicity revealed through a consortium approach improve neoantigen prediction. *Cell* **183**, 818–834.e13 (2020).

[CAS](#) [Article](#) [Google Scholar](#)

25. 25.

Wu, T. D. et al. Peripheral T cell expansion predicts tumour infiltration and clinical response. *Nature* **579**, 274–278 (2020).

[ADS](#) [CAS](#) [Article](#) [Google Scholar](#)

26. 26.

Leon, E., Ranganathan, R. & Savoldo, B. Adoptive T cell therapy: boosting the immune system to fight cancer. *Semin. Immunol.* **49**, 101437 (2020).

[CAS](#) [Article](#) [Google Scholar](#)

27. 27.

Hu, Z., Ott, P. A. & Wu, C. J. Towards personalized, tumour-specific, therapeutic, therapeutic vaccines for cancer. *Nat. Rev. Immunol.* **18**, 168–182 (2018).

[CAS](#) [Article](#) [Google Scholar](#)

28. 28.

Stuart, T. et al. Comprehensive integration of single-cell data. *Cell* **177**, 1888–1902.e21 (2019).

[CAS](#) [Article](#) [Google Scholar](#)

29. 29.

Korsunsky, I. et al. Fast, sensitive and accurate integration of single-cell data with Harmony. *Nat. Methods* **16**, 1289–1296 (2019).

[CAS](#) [Article](#) [Google Scholar](#)

30. 30.

Cohen, C. J., Zhao, Y., Zheng, Z., Rosenberg, S. A. & Morgan, R. A. Enhanced antitumor activity of murine–human hybrid T-cell receptor (TCR) in human lymphocytes is associated with improved pairing and TCR/CD3 stability. *Cancer Res.* **66**, 8878–8886 (2006).

[CAS](#) [Article](#) [Google Scholar](#)

31. 31.

Haga-Friedman, A., Horovitz-Fried, M. & Cohen, C. J. Incorporation of transmembrane hydrophobic mutations in the TCR enhance its surface expression and T cell functional avidity. *J. Immunol.* **188**, 5538–5546 (2012).

[CAS](#) [Article](#) [Google Scholar](#)

32. 32.

Bialer, G., Horovitz-Fried, M., Ya'acobi, S., Morgan, R. A. & Cohen, C. J. Selected murine residues endow human TCR with enhanced tumor recognition. *J. Immunol.* **184**, 6232–6241 (2010).

[CAS](#) [Article](#) [Google Scholar](#)

33. 33.

Hu, Z. et al. A cloning and expression system to probe T-cell receptor specificity and assess functional avidity to neoantigens. *Blood* **132**, 1911–1921 (2018).

[CAS](#) [Article](#) [Google Scholar](#)

34. 34.

Kawakami, Y. et al. Identification of the immunodominant peptides of the MART-1 human melanoma antigen recognized by the majority of HLA-A2-restricted tumor infiltrating lymphocytes. *J. Exp. Med.* **180**, 347–352 (1994).

[CAS](#) [Article](#) [Google Scholar](#)

35. 35.

Abelin, J. G. et al. Mass spectrometry profiling of HLA-associated peptidomes in mono-allelic cells enables more accurate epitope prediction. *Immunity* **46**, 315–326 (2017).

[CAS](#) [Article](#) [Google Scholar](#)

36. 36.

Campoli, M. R. et al. Human high molecular weight-melanoma-associated antigen (HMW-MAA): a melanoma cell surface chondroitin sulfate proteoglycan (MSCP) with biological and clinical significance. *Crit. Rev. Immunol.* **24**, 267–296 (2004).

[CAS](#) [Article](#) [Google Scholar](#)

37. 37.

Harndahl, M. et al. Peptide binding to HLA class I molecules: homogenous, high-throughput screening, and affinity assays. *J. Biomol. Screen.* **14**, 173–180 (2009).

[CAS](#) [Article](#) [Google Scholar](#)

[Download references](#)

Acknowledgements

We are grateful for expert assistance from O. Olive and K. Shetty from the DFCI Center for Personal Cancer Vaccines; M. Manos and M. Severgnini and the staff of the DFCI Center for Immuno-Oncology (CIO); S. Pollock and C. Patterson (the Broad Institute's Biological Samples, Genetic Analysis, and Genome Sequencing Platform) for their help in sample collection and management; and D. Braun, S. Gohil, S. Sarkizova and all of the members of the Wu laboratory for productive discussions and critical reading of the manuscript. This research was made possible by a generous gift from the Blavatnik Family Foundation, and was supported by grants from the US National Institutes of Health (NCI-1R01CA155010 and NCI-U24CA224331 to C.J.W.; NIH/NCI R21 CA216772-01A1 and NCI-SPORE-2P50CA101942-11A1 to D.B.K.; NCI-1R01CA229261-01 to P.A.O.; NIH/NCI P01CA229092 and NIH/NIAID U19 AI082630 to K.J.L.; NCI R50CA211482-01 to S.A.S.; NCI R50CA251956 to S.L.; and R01 CA208756 to N.H.) and a Team Science Award from the Melanoma Research Alliance (to C.J.W., P.A.O. and K.J.L.). G.O. was supported by the American Italian Cancer Foundation fellowship. This work was further supported by The G. Harold and Leila Y. Mathers Foundation, and the Bridge Project, a partnership between the Koch Institute for Integrative Cancer Research at MIT and the Dana-Farber/Harvard Cancer Center.

Author information

Author notes

1. Tomasz Kula

Present address: Society of Fellows, Harvard University, Cambridge, MA, USA

Affiliations

1. Department of Medical Oncology, Dana-Farber Cancer Institute, Boston, MA, USA

Giacomo Oliveira, Kari Stromhaug, Wandi Zhang, Nicoletta Cieri, Edward F. Fritsch, Kenneth J. Livak, Patrick A. Ott, Derin B.

Keskin & Catherine J. Wu

2. Harvard Medical School, Boston, MA, USA

Giacomo Oliveira, Nir Hacohen, Genevieve M. Boland, Patrick A. Ott & Catherine J. Wu

3. Broad Institute of MIT and Harvard, Cambridge, MA, USA

Susan Klaeger, Shuqiang Li, Karl R. Clauser, Sachet A. Shukla, Steven A. Carr, Edward F. Fritsch, Nir Hacohen, Moshe Sade-Feldman, Genevieve M. Boland, Patrick A. Ott & Catherine J. Wu

4. TScan Therapeutics, Waltham, MA, USA

Tomasz Kula, Qikai Xu & Gavin MacBeath

5. Center for Cancer Research, Massachusetts General Hospital, Boston, MA, USA

Dennie T. Frederick, Nir Hacohen, Moshe Sade-Feldman & Genevieve M. Boland

6. Translational Immunogenomics Laboratory, Dana-Farber Cancer Institute, Boston, MA, USA

Phuong M. Le, Juliet Forman, Teddy Huang, Shuqiang Li, Sachet A. Shukla, Kenneth J. Livak & Derin B. Keskin

7. Department of Data Science, Dana-Farber Cancer Institute, Boston, MA, USA

Donna Neuberg

8. Immunitrack, Copenhagen, Denmark

Sune Justesen

9. Department of Medicine, Brigham and Women's Hospital, Boston, MA, USA

Patrick A. Ott & Catherine J. Wu

Authors

1. Giacomo Oliveira

[View author publications](#)

You can also search for this author in [PubMed](#) [Google Scholar](#)

2. Kari Stromhaug

[View author publications](#)

You can also search for this author in [PubMed](#) [Google Scholar](#)

3. Susan Klaeger

[View author publications](#)

You can also search for this author in [PubMed](#) [Google Scholar](#)

4. Tomasz Kula

[View author publications](#)

You can also search for this author in [PubMed](#) [Google Scholar](#)

5. Dennie T. Frederick

[View author publications](#)

You can also search for this author in [PubMed](#) [Google Scholar](#)

6. Phuong M. Le

[View author publications](#)

You can also search for this author in [PubMed](#) [Google Scholar](#)

7. Juliet Forman

[View author publications](#)

You can also search for this author in [PubMed](#) [Google Scholar](#)

8. Teddy Huang

[View author publications](#)

You can also search for this author in [PubMed](#) [Google Scholar](#)

9. Shuqiang Li

[View author publications](#)

You can also search for this author in [PubMed](#) [Google Scholar](#)

10. Wandi Zhang

[View author publications](#)

You can also search for this author in [PubMed](#) [Google Scholar](#)

11. Qikai Xu

[View author publications](#)

You can also search for this author in [PubMed](#) [Google Scholar](#)

12. Nicoletta Cieri

[View author publications](#)

You can also search for this author in [PubMed](#) [Google Scholar](#)

13. Karl R. Clauser

[View author publications](#)

You can also search for this author in [PubMed](#) [Google Scholar](#)

14. Sachet A. Shukla

[View author publications](#)

You can also search for this author in [PubMed](#) [Google Scholar](#)

15. Donna Neuberg

[View author publications](#)

You can also search for this author in [PubMed](#) [Google Scholar](#)

16. Sune Justesen

[View author publications](#)

You can also search for this author in [PubMed](#) [Google Scholar](#)

17. Gavin MacBeath

[View author publications](#)

You can also search for this author in [PubMed](#) [Google Scholar](#)

18. Steven A. Carr

[View author publications](#)

You can also search for this author in [PubMed](#) [Google Scholar](#)

19. Edward F. Fritsch

[View author publications](#)

You can also search for this author in [PubMed](#) [Google Scholar](#)

20. Nir Hacohen

[View author publications](#)

You can also search for this author in [PubMed](#) [Google Scholar](#)

21. Moshe Sade-Feldman

[View author publications](#)

You can also search for this author in [PubMed](#) [Google Scholar](#)

22. Kenneth J. Livak

[View author publications](#)

You can also search for this author in [PubMed](#) [Google Scholar](#)

23. Genevieve M. Boland

[View author publications](#)

You can also search for this author in [PubMed](#) [Google Scholar](#)

24. Patrick A. Ott

[View author publications](#)

You can also search for this author in [PubMed](#) [Google Scholar](#)

25. Derin B. Keskin

[View author publications](#)

You can also search for this author in [PubMed](#) [Google Scholar](#)

26. Catherine J. Wu

[View author publications](#)

You can also search for this author in [PubMed](#) [Google Scholar](#)

Contributions

G.O. and C.J.W. conceived the project and directed the overall study. G.O. designed and performed the experimental and data analysis together with K.S., S.K., P.M.L., W.Z., J.F., T.H., S.L., K.J.L., N.C. and D.B.K. G.O. and K.S. analysed the single-cell sequencing data. J.F., S.A.S. and K.J.L. analysed the bulk sequencing data. K.S. and D.N. designed and performed the statistical analyses. S.K., D.B.K., K.R.C. and S.A.C. generated and analysed the mass spectrometry results. S.J. provided the peptide-stability measurements. T.K., Q.X. and G.M. supported TCR cloning and screening. D.F.T., G.M.B., M.S.-F. and P.A.O. provided patient samples and clinical information. N.C., M.S.-F., E.F.F. and N.H. contributed to data discussion and interpretation. G.O. and C.J.W. wrote the manuscript. All authors discussed the results and read the manuscript.

Corresponding author

Correspondence to [Catherine J. Wu](#).

Ethics declarations

Competing interests

E.F.F. is an equity holder and consultant for BioNTech, and equity holder and SAB member of BioEntre. N.H. and C.J.W. are equity holders of BioNTech. N.H. is an advisor and equity holder for Related Sciences, and receives research funding from Bristol-Myers Squibb. P.A.O. has received research funding from and has advised Neon Therapeutics, Bristol-Myers Squibb, Merck, CytomX, Pfizer, Novartis, Celldex, Amgen, Array, AstraZeneca/MedImmune, Armo BioSciences and Roche/Genentech. C.J.W. is subject to a conflict of interest management plan for the reported studies because of her former competing financial interests in Neon Therapeutics, which was acquired by BioNTech. Under this plan, C.J.W. may not access identifiable data for human participants or otherwise participate directly in the IRB-approved protocol reported herein; the contributions by C.J.W. to the overall strategy and data analyses occurred on a de-identified basis. Patent applications have been filed on aspects of the described work entitled as follows: ‘Compositions and methods for personalized neoplasia vaccines’ (N.H., E.F.F. and C.J.W.), ‘Methods for identifying tumour specific neo-antigens’ (N.H. and C.J.W.), ‘Formulations for neoplasia vaccines’ (E.F.F.) and ‘Combination therapy for neoantigen vaccine’ (N.H., C.J.W. and E.F.F.). The Dana-Farber Cancer Institute has a proprietary and financial interest in the personalized NeoAg vaccine. S.J. is chief scientific officer of Immunitrack. S.A.S. reported non-financial support from Bristol-Myers Squibb outside the submitted work, previously advised and has received consulting fees from Neon Therapeutics, and reported non-financial support from Bristol-Myers Squibb and equity in Agenus Inc., Agios Pharmaceuticals, Breakbio Corp., Bristol-Myers Squibb and Lumos Pharma, outside the submitted work. T.K. and G.M. are employees of TScan Therapeutics and hold equity in TScan Therapeutics. T.K. is a founder of TScan Therapeutics. D.B.K. has previously advised Neon Therapeutics and has received consulting fees from Neon Therapeutics, and owns equity in Aduro Biotech, Agenus, Armata Pharmaceuticals, Breakbio, BioMarin Pharmaceutical, Bristol-Myers Squibb, Celldex Therapeutics, Editas Medicine, Exelixis, Gilead Sciences, IMV, Lexicon Pharmaceuticals, Moderna and Regeneron Pharmaceuticals. BeiGene, a Chinese biotech company, supports unrelated research at the DFCI Translational Immunogenomics Laboratory (TIGL). S.A.C. is a

member of the scientific advisory boards of Kymera, PTM BioLabs and Seer, and a scientific advisor to Pfizer and Biogen. The remaining authors declare no competing interests.

Additional information

Peer review information *Nature* thanks Benny Chain, Aude Chapuis and the other, anonymous, reviewer(s) for their contribution to the peer review of this work.

Publisher's note Springer Nature remains neutral with regard to jurisdictional claims in published maps and institutional affiliations.

Extended data figures and tables

[Extended Data Fig. 1 Clinical course of patients with melanoma analysed for single-cell sequencing and TCR specificity.](#)

Schematic representation of the clinical histories of the four patients with melanoma profiled in this study. Triangles indicate the time of collection of tumour biopsies (red) analysed with single-cell sequencing or of peripheral blood samples (blue) used for isolation of tumour-reactive T cells at serial time points (TP). NED, no evidence of disease.

[Extended Data Fig. 2 Single-cell profiling of CD8⁺ TILs.](#)

a, Flow-cytometry plots quantifying the proportion of T lymphocytes (defined as CD45⁺CD3⁺) infiltrating five tumour biopsies subjected to single-cell sequencing. Tissue origin for each tumour sample is indicated. **b**, Density plots identifying CD8⁺ TILs through CITE-seq antibody signals for CD4⁺ (orange) and CD8⁺ (blue). Data are reported as CD4 and CD8 CITE-seq signals relative to isotype controls for all sequenced cells that were identified as T cells after flow sorting and computational filtering. **c**, Size and patient distribution of the 13 clusters identified from CD8⁺ TIL

scRNA-seq. Left: per cluster, sample origin is denoted by colour. The analysed CD8⁺ dataset is predominantly composed by cells from three patients (Pt-A (green), Pt-C (red) and Pt-D (blue)). Two clusters were found to be patient-specific (clusters 8 and 11). Right: UMAPs depicting cluster distribution of patient-specific CD8⁺ TILs. **d**, Heatmaps depicting the mean cluster expression of a panel of T cell-related genes, measured by scRNA-seq (left panel) and the mean surface expression of the corresponding proteins measured through CITE-seq (right panel). Clusters (columns) are labelled using the annotation provided in Fig. 1b; markers (rows) are grouped based on their biological function. Grey, unevaluable markers (CD45 isoforms for scRNA-seq) or those that were not assessed (for CITE-seq). CITE-seq CD3 surface expression was poorly detected because of the presence of competing CD3 sorting antibody. **e**, Violin plots quantifying relative transcriptional expression of genes (columns) with high differential expression among CD8⁺ TIL clusters (rows). **f**, UMAPs depicting the single-cell expression of representative T cell markers among CD8⁺ TILs either through detection of surface protein expression with CITE-seq (Ab) or through scRNA-seq (RNA). **g**, Characterization of the CD8⁺ TIL clusters using independent reference gene signatures^{8,9,10}. Heatmaps show cross-labelling of T cell clusters defined in the present study (columns, reported as in Fig. 1b) versus reference gene signatures (rows) derived from the analyses in Sade-Feldman et al.⁸, Yost et al.⁹ and Oh et al.¹⁰, with intensities indicating normalized frequency.

Extended Data Fig. 3 Clonality of CD8⁺ TILs and cell states of TCR clonotypes.

a, Histograms depicting the number (bottom panel) and overall frequency (top panel) of patients' TCR clonotype families divided in categories based on their size (*x* axis). **b**, Histograms showing the intracluster TCR clonality, calculated for CD8⁺ T cells in each cluster (*x* axis) using normalized Shannon index. The symbols indicate individual TCR clonality for the three patients with high numbers of TILs (Pt-A, Pt-C and Pt-D). The bars indicate the overall TCR clonality measured within each cluster. **c**, UMAPs of the cluster distribution of representative dominant TCR clonotype families among CD8⁺ TILs from TIL-rich patients (*n* = 3). For each patient, the

numbers denote the ranking of each TCR clonotype (Fig. 1c), while colours identify their primary cluster (Fig. 1b).

Extended Data Fig. 4 Characterization of patient-derived melanoma cell lines.

a, Purity of tumour cultures, originating from patient biopsies, was assessed by flow cytometry by staining cells with isotype controls (top panels) or surface markers (bottom panels) identifying melanoma (using melanoma chondroitin sulfate proteoglycan (MCSP); *y* axis) or fibroblast lineages (fibroblast antigen; *x* axis). Consistent with previous reports³⁶, MCSP was expressed in three of four tumour cultures, with each lacking substantive fibroblast contamination. **b**, Flow-cytometric assessment of HLA class I surface expression on the established melanoma cell lines. Surface expression was measured with a pan-HLA class I antibody (top panels) or with an HLA-A:02-specific antibody (bottom panels) at basal culture conditions (magenta) or upon exposure to IFN γ for 72 h (purple), compared with isotype control (grey). **c**, Comparison of the mutation burden of patient-derived melanoma cell lines versus corresponding parental tumours. For all patients, mutation calling from whole-exome sequencing (WES) of tumour biopsies and cell lines was performed through comparison with autologous PBMCs serving as germline controls. Venn diagrams show the numbers and frequencies of mutations unique to parental tumours (red) or melanoma cell lines (blue) or shared between the two (black).

Corresponding dot plots, using the same colour code, show the variant allele frequencies (VAF) of mutations detected in the parental tumours (*x* axis) and derived cell lines (*y* axis). For both, tumour purity inferred from single-cell data (parental tumours) or detected by flow cytometry (cell lines) is indicated. The high concordance between the genomic mutations detected in paired specimens demonstrates that the melanoma cell lines are reflective of the corresponding parental tumours. **d**, Gene expression profiles of HLA class I genes and MAA genes in pdMel-CLs (columns, black) or in matched parental tumours (columns, white), compared with control tumour-derived fibroblast cell lines ($n = 3$) originating from unrelated melanoma biopsies (right columns). Tumour purity is reported in red. Gene expression was measured by RNA-seq and normalized as logarithmic transcripts per million mapped reads (TPM). **e**, HLA class I

immunopeptidome of patient-derived melanoma cell lines cultured with or without IFN γ . Bars indicate the numbers of unique peptides detected by mass spectrometry (MS) after immunoprecipitation of peptide–HLA class I complexes (bottom panel) and of unique genes from which the detected peptides were derived (top panel), and are grouped based on their origin from MAAs or NeoAgs and coloured by patient. The number of MS acquisitions for each condition is indicated.

Extended Data Fig. 5 Antitumour reactivity of in vitro-reconstructed TCRs.

a, Schema for classification of TCR reactivities based on CD137 upregulation of TCR-transduced T cell lines upon challenge with patient-derived melanoma cells (pdMel-CLs; with or without IFN γ pre-treatment (red)) or controls (PBMCs, B cells and EBV-LCLs (blue)). A TCR was defined as tumour-specific if it recognized only the autologous melanoma cell line, but did not upregulate CD137 when challenged with autologous controls. **b**, Representative flow cytometry plots depicting CD137 upregulation measured on CD8 $^+$ T cells transduced with TCRs isolated from Pt-A and cultured with melanoma or control targets. Background reactivity was estimated by measuring CD137 upregulation on CD8 $^+$ T cells transduced with an irrelevant TCR. **c**, Cytotoxic potential provided by TCRs with exhausted (left) or non-exhausted (right) primary clusters isolated from all four studied patients. Degranulation (CD107a/b $^+$) and concomitant production of cytokines (IFN γ , TNF and IL-2) were assessed through intracellular staining, gating on TCR-transduced (mTRBC $^+$) CD8 $^+$ T cells cultured alone or in the presence of autologous pdMel-CLs. Each dot represents the result for a single TCR isolated from CD8 $^+$ TILs, colour-coded based on its primary phenotypic cluster (as defined in Fig. [1b](#)). For each analysed TCR, background cytotoxicity from CD8 $^+$ T cells transduced with an irrelevant TCR was subtracted. White dots depict the basal level of activation of untransduced cells. Overall, these data indicate that antitumour cytotoxicity mainly resides among TCR clonotypes with exhausted primary clusters.

Extended Data Fig. 6 Isolation, single-cell sequencing and screening of tumour-reactive TCRs from peripheral blood samples.

a, b, PBMCs collected at serial time points (TP1, TP2 and TP3; Extended Data Fig. 1) were cultured with autologous melanoma cell lines to enrich for antitumour TCRs. After two rounds of stimulation, the reactivity of effector CD8⁺ T cells was assessed by measuring: degranulation and cytokine production (**a**) or CD137 upregulation upon re-challenge with melanoma (blue line) (**b**). The specificity of the response was supported by the low recognition of HLA-mismatched unrelated melanoma (grey dashed line). Negative controls (cultured in the absence of target cells) and positive controls (polyclonal stimulators, PHA or PMA-ionomycin) are displayed as solid grey and black lines, respectively. **c**, FACS sorting strategy for the isolation of tumour-reactive T cells. CD8⁺ effectors with active degranulation and concomitant cytokine production were identified using cytokine secretion assays (Supplementary Methods) upon stimulation without any target (top panel) or in the presence of autologous melanoma (bottom panels). CD107a/b⁺ cells secreting at least one of the measured cytokines (IFN γ , TNF and IL-2) were single-cell sorted and sequenced. Gates depict the detection and quantification of reactive (black) or sorted cells (magenta) from a representative sample (TP3 PBMCs from Pt-A). **d**, TCR clonotypes identified upon single-cell sorting and scTCR-seq of melanoma-reactive CD8⁺ T cells from the four studied patients. Bars indicate cell counts of clonotype families, defined as CD8⁺ cells bearing identical TCR α and TCR β chains, divided on the basis of their detection at specific time points (TP1, TP2 and TP3) or across multiple time points (shared). The presence of multiple TCR α or TCR β chains is indicated with black or orange borders, respectively. **e–h**, TCRs isolated and sequenced from anti-melanoma cultures were reconstructed, expressed in CD8⁺ T cells and screened against melanoma (pdMel-CL; with or without IFN γ pre-treatment in red) or controls (PBMCs, B cells and EBV-LCLs in blue). TCRs were classified as reported in Extended Data Fig. 5a, to identify: tumour-specific TCRs (**e**), non-tumour-reactive TCRs (**f**) and tumour/control reactive TCRs (**g**). Reactivity was calculated by subtracting the background of lymphocytes transduced with an irrelevant TCR from

CD137 expression of CD8⁺ cells transduced with the reconstructed TCR. Floating boxes show minimum to maximum measurements, with mean values depicted as horizontal lines; white dots denote the basal level of activation measured on untransduced cells. The pie charts in **h** summarize the classification of TCR reactivity for all reconstructed TCRs. **i**, Cytotoxicity mediated by TCRs classified as tumour-specific (left panel), non-tumour-reactive (middle panel) or tumour/control-reactive (right panel). Degranulation (CD107a/b⁺) and concomitant production of cytokines (IFN γ , TNF and IL-2) were measured through intracellular flow cytometry on TCR transduced (mTRBC⁺) CD8⁺ T cells cultured alone or in the presence of autologous pdMel-CLs. Each dot represents the results of a single TCR isolated from CD8⁺ TILs (upon subtraction of background activation measured on CD8⁺ lymphocytes transduced with an irrelevant TCR). White dots denote the basal level of cytotoxicity of untransduced cells. **j**, Bar plots showing intratumoural cluster distribution of cells bearing tumour-specific (left) or non-tumour-reactive (right) TCRs isolated from blood and traced within the tumour microenvironment (Fig. [2e](#)). For each patient, the numbers denote the ranking of each TCR among the top 100 clonotype families (Fig. [1c](#)), while the colours identify their primary cluster (Fig. [1b](#)).

[Extended Data Fig. 7 Cell states of tumour-specific CD8⁺ TILs.](#)

a–c, Antigen specificity screening of 94 TCRs sequenced from clonally expanded CD8⁺ T cells isolated from tumour biopsies of 7 patients with metastatic melanoma from Sade-Feldman et al.⁸. **a**, After TCR reconstruction and expression in T cells, reactivity was measured as CD137 upregulation on TCR-transduced (mTRBC⁺) CD8⁺ cells upon culture with autologous EBV-LCLs pulsed with peptide pools covering immunogenic viral epitopes (CEF). Unstimulated cells were analysed as negative control. Results are reported after subtraction of background CD137 expression on T cells transduced with an irrelevant TCR. Five TCRs (black dots) recognized unpulsed EBV-LCLs, thereby documenting specificity for EBV epitopes. **b**, TCR antitumour reactivity, evaluated upon culture with autologous EBV-LCLs pulsed with peptide pools derived from 12 known MAAs. Background detected upon culture with DMSO-pulsed EBV-LCLs

was subtracted. Additional negative and positive controls were an irrelevant peptide (Ova) and polyclonal stimulators (PHA or PMA/ionomycin), respectively. Coloured dots denote MAA-reactive TCRs. **c**, Table summarizing patient distribution of TCR specificities either discovered from reconstruction and screening of 94 TCRs or present within a database of human TCRs with known specificities (TCRdb¹²). **d–f**, Single-cell phenotype of TILs with antiviral or anti-MAA TCRs identified in the validation cohort from Sade-Feldman et al.⁸. **d**, t-SNE plot of CD8⁺ TILs highlighting the spatial distribution of cells containing TCRs with identified antigen specificity. Each colour denotes a distinct specificity, with crosses representing two cells with identical spatial coordinates. **e**, Pie charts summarizing the assignment of single cells containing antiviral (top) or anti-MAA (bottom) TCRs to one of the previously reported six clusters⁸. **f**, RNA transcripts differentially expressed between antiviral and anti-MAA T cells ($\log_2\text{FC} > 1.5$, adj. P value < 0.05). The heatmap reports Z scores, calculated from average gene expression of each TCR clonotype family (columns). Antigen specificity is reported on top with the same colour code as in **d**. **g, h**, Analysis of deregulated genes in exhausted clusters (T_{Ex}), enriched in tumour-reactive T cells, from the discovery cohort. **g**, Average gene expression, reported as Z scores, for each TCR clonotype family (columns) validated in vitro as tumour-specific (orange, 134 TCRs) or defined as virus-specific (black, 17 TCRs). The heatmap reports 98 RNA transcripts (adj. $P < 0.0001$, $\log_2\text{FC} > 1$) and 6 surface proteins (bottom rows, adj. $P < 0.0001$, $\log_2\text{FC} > 0.4$) detected through scRNA-seq and CITE-seq, respectively. **h**, Plots depicting expression of representative RNA transcripts (top) or surface proteins (bottom) in each TCR clonotype family with antiviral (black) or antitumour (orange) specificity. Dots depict the average gene expression in each TCR clonotype, with size proportional to the frequency of the TCR clonotype within patient-specific CD8⁺ TILs. **i**, Heatmap depicting the top 20 overexpressed genes in each tumour-specific (TS) cluster of TS CD8⁺ cells (columns). Z scores of gene expression among five subpopulations are shown (Z score colour legend as in panel **j**). Genes important for the classification of each subset are highlighted in blue. **j**, Heatmaps depicting the expression of a panel of T cell-related transcripts detected through scRNA-seq (left) or surface proteins detected through CITE-seq (right). Z scores document the trends in expression among

subpopulations of TS CD8⁺ cells (columns). **k**, Enrichment in expression of gene signatures among identified clusters of TS CD8⁺ cells (columns). Single cells with TS TCRs were divided in clusters as reported in Fig. 2f and scored for the expression of gene signatures defined from analysis of CD8 TILs of the discovery cohort (left), reported in external datasets of sequenced human CD8⁺ TILs (middle), or defined from published mouse studies (right) ([Methods](#); Supplementary Table 8). The average enrichment score was calculated for each cluster and reported as the Z score.

Extended Data Fig. 8 Antigen specificity of tumour-reactive TCRs.

a, Antitumour TCRs isolated from patients positive for HLA-A*02:01 (Pt-A, Pt-B and Pt-D) were tested for the ability to cross-recognize allogeneic HLA-A*02:01⁺ melanomas. Melanoma reactivity was measured as CD137 upregulation on TCR-transduced (mTRBC⁺) CD8⁺ cells upon culture with autologous or allogeneic HLA-A*02:01-matched melanomas. Tumour specificity was ruled out through parallel detection of CD137 upregulation upon challenge with matched non-tumour controls (PBMCs). The floating boxes show minimum to maximum measurements, with mean values denoted by horizontal lines. All results are shown after subtraction of background CD137 expression on T cells transduced with an irrelevant TCR; the white dots denote the basal level of activation of untransduced CD8⁺ T cells. Pt-A and Pt-B displayed high melanoma-specific (that is, lack of recognition of autologous PBMCs) cross-reactivity indicating that a substantial proportion of antitumour TCRs recognize public HLA-A*02:01-restricted melanoma antigens. **b, c**, Antigen specificity screening of 299 antitumour TCRs. Upregulation of CD137 was assessed by flow cytometry on CD8⁺ T cells transduced with previously identified tumour-specific TCRs upon culture with autologous EBV-LCLs. Background, assessed using DMSO-pulsed target cells, was subtracted from each condition. **b**, Antigen recognition tested with pools of peptides corresponding to predicted immunogenic NeoAgs (Supplementary Table 9), known MAAs (Supplementary Table 10) or immunogenic viral epitopes. Reactivity was also assessed against an irrelevant peptide (Ova) or in the presence of polyclonal stimulators (PHA or PMA/ionomycin) as negative and positive

controls, respectively. The black dots show the activation levels of a control Flu-specific HLA-A*02:01-restricted TCR. The coloured dots show confirmed antigen-reactive TCRs, coloured on the basis of the highest reactivity against a particular antigen, as per the legend, compared with the other tested antigens; white dots indicate TCRs reactive against an antigen that was not the highest of the panel of antigens tested, and hence considered a cross-reactive response; grey dots show negative responses. Deconvolution of antigen specificity of TCRs reactive to NeoAg peptide pools is reported in Supplementary Information—‘Flow-cytometry data’. **c**, Antigen specificity tested using NeoAg or MAA peptides detected by HLA class I mass spectrometry (MS) immunopeptidome of melanoma cell lines (Supplementary Tables 9, 10) with the addition of the MLANA protein (not retrieved by MS but known as highly immunogenic³⁴). The coloured dots indicate confirmed antigen-reactive TCRs, coloured on the basis of the highest reactivity against a particular antigen (colour legend reported in **d**), compared with the other tested antigens; the white dots denote TCRs reactive against an antigen that was not the highest of the panel of antigens tested, and hence considered a cross-reactive response. **d**, Distribution of antigen specificities of antitumour TCRs per patient successfully deorphanized after screening. Colours denote the distinct peptides recognized by individual antitumour TCRs. Note that TCRs classified as specific for antigenic pools ($n = 11$) represent CD8-restricted specificities showing reactivity against peptide pools (**b**), but not towards single peptides (**c**), probably due to the absence of the specific cognate antigen within the tested panels of epitopes in **c**.

Extended Data Fig. 9 Phenotype of MAA/NeoAg-TCRs and parameters affecting their avidity.

a, Heatmap showing genes differentially expressed between CD8⁺ TILs with identified MAA-specific, NeoAg-specific or virus-specific TCRs. Comparisons were performed independently for each patient, and only significantly deregulated genes (adj. $P < 0.05$, $\log_2\text{FC} > 1$ for scRNA-seq data; $\log_2\text{FC} > 0.4$ for CITE-seq data) in at least two out of four patients were selected. No deregulated gene was found upon comparison of single cells with MAA-TCRs versus NeoAg-TCRs; 60 RNA transcripts and 2

surface proteins resulted from comparison of MAA and/or NeoAg cells versus viral cells. Heatmap colours depict Z scores of average gene expression within a TCR clonotype (columns). Top tracks: annotations of antigen specificity (colour legend reported in panel **b**), normalized antitumour TCR reactivity, TCR avidity and patient of origin. **b**, To define the avidity of antitumour TCRs, TCR-dependent CD137 upregulation was measured on TCR-transduced (mTRBC^+) CD8^+ cells upon culture with patient-derived EBV-LCLs pulsed with increasing concentrations of the cognate antigen (MAAs in the top panel; NeoAgs in bottom panels). Reactivity to DMSO-pulsed targets (0) and autologous melanoma (pdMel-LCLs) are reported on the left; for NeoAg-specific TCRs, the dashed lines report reactivity against wild-type peptides. A colour legend depicts the different cognate antigens targeted by the deorphanized TCRs and report the number of TCRs for each antigenic specificity. **c**, EC_{50} calculated from titration curves; note that high EC_{50} values correspond to low TCR avidities. Means with s.d. are reported, with TCR numbers corresponding to that reported in the legend of **b**. Most of the NeoAg-specific TCRs display higher avidities than MAA-specific TCRs. **d**, Expression levels of MAA or NeoAg transcripts (from bulk RNA-seq data) from which the analysed epitopes are generated, as a measure of cognate peptide abundance in tumour cells, as analysed from four patient-derived cell lines (symbols). Columns show means values with s.d. **e**, Assessment of the affinity (left) and stability (right) of peptide–HLA complexes. The interactions between reported MAA or NeoAg peptides and their HLA restriction (assessed *in vitro* as shown in Supplementary Information—‘Flow-cytometry data’) were measured as previously described³⁷. Note that high values correspond to low affinity (left) or to stable interactions (right). Columns report mean affinity/stability with standard deviations from repeated measurements; the number of replicates is indicated at the base of the columns. The horizontal grey lines denote affinity levels of reference peptides reported to be strong binders for the analysed HLA alleles that were tested in parallel. In all NeoAg panels, comparisons of mutant (Mut, coloured bars) versus wild-type (WT, white bars) peptides were performed using two-tailed ratio-paired parametric *t*-tests, and *P* values are reported. na, not assessed; NB, non-binding; ND, not detectable; ne, not evaluable.

Extended Data Fig. 10 Peripheral blood dynamics of intratumoural T cell specificities.

a, Peripheral blood dynamics of T cells containing TCRs with in vitro-defined antigen specificity (black: virus-specific TCRs; red: MAA-specific TCRs; green: NeoAg-specific TCRs). TCRs were quantified through bulk sequencing of TCR β chains of sorted CD3 $^{+}$ T cells from serial peripheral blood sampling of the four patients with melanoma within the discovery cohort. The numbers report the median number of TCRs detected longitudinally out of the total number of TCRs within each category. **b-d**, CD8 $^{+}$ TCR clonotypes identified in CD8 $^{+}$ TILs were traced within serial peripheral blood samples collected from an independent cohort of patients with melanoma ($n = 14$) treated with immune checkpoint blockade therapies and with available scRNA-seq data generated from TILs⁸. TCRs were classified as exhausted (red) or non-exhausted (blue) based on their phenotypic primary cluster assessed by scRNA-seq. Quantification of circulating TCR clonotypes was performed through bulk sequencing of TCR β chains on circulating CD3 $^{+}$ cells and reported as percentage of total TCR sequences detected. Patient clinical outcomes were grouped as: survivors who did not experienced post-therapy disease recurrence (panel **b**, $n = 4$); survivors who experienced disease progression after immunotherapy (panel **c**, $n = 3$); and deceased patients (panel **d**, $n = 7$). Per patient, a schematic of the clinical timeline and sample collection is depicted above each panel. ND, not detected; NED, no evidence of disease.

Supplementary information

Supplementary Information

This file contains supplementary methods, sorting strategies, Gating strategies for analysis of flow-cytometry data, Flow-cytometry data and supplementary references.

Reporting Summary

Supplementary Tables

This file contains Supplementary Tables 1 – 11. Supplementary Table 1. Characteristics of discovery cohort. Supplementary Table 2. List of CITEseq Ab used for single cell sequencing. Supplementary Table 3. Metrics of single-cell RNAseq, TCRseq and TCR clonotype information. Supplementary Table 4. Differentially expressed genes among the 12 clusters of CD8+ TILs identified by scRNA-seq. Supplementary Table 5. Characteristics of validation cohort. Supplementary Table 6. Differentially expressed genes in tumor-specific CD8 TILS compared to virus-specific CD8 TILs. Supplementary Table 7. Differentially expressed genes among the 5 clusters of CD8+ TILs with in vitro verified tumor-specific TCRs. Supplementary Table 8. Gene-signature from internal or external datasets. Supplementary Table 9. Neoantigen peptides tested for TCR recognition. Supplementary Table 10. MAA peptides tested for TCR recognition. Supplementary Table 11. Summary of cognate antigens recognized by antitumor deorphanized TCRs.

Rights and permissions

Reprints and Permissions

About this article



Check for
updates

Cite this article

Oliveira, G., Stromhaug, K., Klaeger, S. *et al.* Phenotype, specificity and avidity of antitumour CD8⁺ T cells in melanoma. *Nature* **596**, 119–125 (2021). <https://doi.org/10.1038/s41586-021-03704-y>

Download citation

- Received: 21 December 2020
- Accepted: 08 June 2021
- Published: 21 July 2021
- Issue Date: 05 August 2021
- DOI: <https://doi.org/10.1038/s41586-021-03704-y>

Comments

By submitting a comment you agree to abide by our [Terms](#) and [Community Guidelines](#). If you find something abusive or that does not comply with our terms or guidelines please flag it as inappropriate.

[Access through your institution](#)

[Change institution](#)

[Buy or subscribe](#)

Advertisement

This article was downloaded by **calibre** from <https://www.nature.com/articles/s41586-021-03704-y>.

| [Section menu](#) | [Main menu](#) |

Transcriptional programs of neoantigen-specific TIL in anti-PD-1-treated lung cancers
[Download PDF](#)

- Article
- Open Access
- [Published: 21 July 2021](#)

Transcriptional programs of neoantigen-specific TIL in anti-PD-1-treated lung cancers

- [Justina X. Caushi](#)^{1,2,3 na1},
- [Jiajia Zhang](#)^{1,2,3 na1},
- [Zhicheng Ji](#)^{4 nAff11},
- [Ajay Vaghasia](#)³,
- [Boyang Zhang](#)⁴,
- [Emily Han-Chung Hsue](#)^{3,5,6},
- [Brian J. Mog](#) ORCID: orcid.org/0000-0001-9988-7147^{3,5,6},
- [Wenpin Hou](#) ORCID: orcid.org/0000-0003-0972-2192⁴,
- [Sune Justesen](#)⁷,
- [Richard Blosser](#)^{1,3},
- [Ada Tam](#)^{1,3},
- [Valsamo Anagnostou](#) ORCID: orcid.org/0000-0001-9480-3047^{1,3},
- [Tricia R. Cottrell](#) ORCID: orcid.org/0000-0003-2952-1830^{1,2,3 nAff12},
- [Haidan Guo](#)^{1,2,3},
- [Hok Yee Chan](#)^{1,2,3},
- [Dipika Singh](#)^{1,2,3},
- [Sampriti Thapa](#)^{1,2,3},
- [Arbor G. Dykema](#)^{1,2,3},
- [Poromendro Burman](#)^{1,2,3},
- [Begum Choudhury](#)^{1,2,3},
- [Luis Aparicio](#)^{1,2,3},
- [Laurene S. Cheung](#)^{1,2,3},
- [Mara Lanis](#)^{1,3},
- [Zineb Belcaid](#)^{1,3},

- [Margueritta El Asmar](#)^{1,3},
- [Peter B. Illei](#)³,
- [Rulin Wang](#)³,
- [Jennifer Meyers](#)³,
- [Kornel Schuebel](#)³,
- [Anuj Gupta](#)³,
- [Alyza Skaist](#)³,
- [Sarah Wheelan](#) [ORCID: orcid.org/0000-0002-9002-0800](#)³,
- [Jarushka Naidoo](#)^{1,3 nAff13},
- [Kristen A. Marrone](#)^{1,3},
- [Malcolm Brock](#)³,
- [Jinny Ha](#)³,
- [Errol L. Bush](#)³,
- [Bernard J. Park](#)⁸,
- [Matthew Bott](#)⁸,
- [David R. Jones](#)⁸,
- [Joshua E. Reuss](#)^{3 nAff14},
- [Victor E. Velculescu](#) [ORCID: orcid.org/0000-0003-1195-438X](#)^{1,3},
- [Jamie E. Chaft](#) [ORCID: orcid.org/0000-0002-5838-9982](#)⁸,
- [Kenneth W. Kinzler](#)^{3,5,6},
- [Shibin Zhou](#) [ORCID: orcid.org/0000-0003-1941-4425](#)^{3,5,6},
- [Bert Vogelstein](#)^{3,5,6},
- [Janis M. Taube](#)^{1,2,3},
- [Matthew D. Hellmann](#)⁸,
- [Julie R. Brahmer](#)^{1,3},
- [Taha Merghoub](#) [ORCID: orcid.org/0000-0002-1518-5111](#)^{8,9,10},
- [Patrick M. Forde](#)^{1,3},
- [Srinivasan Yegnasubramanian](#) [ORCID: orcid.org/0000-0003-0744-6606](#)^{1,2,3},
- [Hongkai Ji](#) [ORCID: orcid.org/0000-0002-6480-0141](#)⁴,
- [Drew M. Pardoll](#) ^{1,2,3} &
- [Kellie N. Smith](#) [ORCID: orcid.org/0000-0002-6295-8930](#)^{1,2,3}

[Nature](#) volume **596**, pages 126–132 (2021) [Cite this article](#)

- 22k Accesses
- 215 Altmetric
- [Metrics details](#)

Subjects

- [CD8-positive T cells](#)
- [Cellular immunity](#)
- [Immunotherapy](#)
- [T-cell receptor](#)
- [Tumour immunology](#)

Abstract

PD-1 blockade unleashes CD8 T cells¹, including those specific for mutation-associated neoantigens (MANA), but factors in the tumour microenvironment can inhibit these T cell responses. Single-cell transcriptomics have revealed global T cell dysfunction programs in tumour-infiltrating lymphocytes (TIL). However, the majority of TIL do not recognize tumour antigens², and little is known about transcriptional programs of MANA-specific TIL. Here, we identify MANA-specific T cell clones using the MANA functional expansion of specific T cells assay³ in neoadjuvant anti-PD-1-treated non-small cell lung cancers (NSCLC). We use their T cell receptors as a ‘barcode’ to track and analyse their transcriptional programs in the tumour microenvironment using coupled single-cell RNA sequencing and T cell receptor sequencing. We find both MANA- and virus-specific clones in TIL, regardless of response, and MANA-, influenza- and Epstein–Barr virus-specific TIL each have unique transcriptional programs. Despite exposure to cognate antigen, MANA-specific TIL express an incompletely activated cytolytic program. MANA-specific CD8 T cells have hallmark transcriptional programs of tissue-resident memory (TRM) cells, but low levels of interleukin-7 receptor (IL-7R) and are functionally less responsive to interleukin-7 (IL-7) compared with influenza-specific TRM cells. Compared with those from responding tumours, MANA-specific clones from non-responding tumours express T cell receptors with markedly lower ligand-dependent signalling, are largely confined to HOBIT^{high} TRM subsets, and coordinately upregulate checkpoints, killer inhibitory receptors and inhibitors of T cell activation. These findings provide important insights for overcoming resistance to PD-1 blockade.

[Download PDF](#)

Main

The efficacy of PD-1- and PD-L1-blocking agents is predicated upon CD8 T cell-mediated anti-tumour immunity¹. Early studies focused on tumour-associated antigens, whereas recent work has shifted attention to T cell recognition of mutation-associated neoantigens (MANA), owing to the large numbers of somatic mutations

acquired by many cancers during their development⁴. The association of improved anti-PD-1 and anti-PD-L1 clinical responses with high tumour mutational burden⁵ strongly suggests that MANA are important targets of anti-tumour immunity induced by PD-1 blockade.

Despite the success of immune checkpoint blockade (ICB) in improving clinical outcomes, most cancers still do not respond⁶. Improving response rates to ICB will require an understanding of the functional state of tumour-specific T cells, particularly in the tumour microenvironment. However, a fundamental limitation in the current understanding of the T cell functional programs that underpin the response to ICB has been the absence of transcriptional profiling of true MANA-specific TIL. A related problem is the paucity of information regarding the differences between MANA-specific TIL in ICB-responsive versus resistant tumours. Indeed, MANA-specific T cells represent a small fraction of total TIL^{2,7}, particularly in lung cancer, in which they have been shown to selectively upregulate CD39. This highlights the challenges confronting characterization of the cells responsible for the activity of T cell-targeting immunotherapies.

Global gene expression of NSCLC TIL

For this study, we used peripheral blood and tissue biospecimens obtained from the first-in-human clinical trial of neoadjuvant anti-PD-1 (nivolumab) in resectable non-small cell lung cancer⁸ (NSCLC; ClinicalTrials.gov identifier: NCT02259621; Fig. 1a, top) to study the transcriptional programs of MANA-specific TIL. Nine out of 20 patients with NSCLC (45%) treated in this trial had a major pathologic response (MPR) at the time of resection, defined as no more than 10% viable tumour at the time of surgery; previous studies have established an association between MPR and improved overall survival^{9,10,11,12}. A schematic of the study design and experimental approach is shown in Fig. 1a, bottom. Combined single-cell RNA sequencing (scRNA-seq) and T cell receptor sequencing (TCR-seq) was performed on TIL ($n = 15$), paired adjacent normal lung ($n = 12$), tumour-draining lymph nodes (TDLN, $n = 3$) and a distant metastasis (Extended Data Fig. 1a, Supplementary Tables 1–3). In total, 560,916 T cells passed quality control (Fig. 1b, Supplementary Table 3) and were carried forward for analyses.

Fig. 1: Profiling single T cells in NSCLC treated with neoadjuvant PD-1 blockade.

 **figure1**

Twenty patients with resectable NSCLC were treated with two doses of PD-1 blockade before surgical resection. **a**, An overall schematic of the clinical trial, biospecimen collection (top) and study design (bottom). scRNA-seq–TCR-seq was performed on T cells isolated from resected tumour ($n = 15$), adjacent normal lung (NL; $n = 12$), TDLN ($n = 3$), and a resected brain metastasis ($n = 1$) from patients with NSCLC treated with two doses of neoadjuvant anti-PD-1 (bottom). The MANAFEST and ViraFEST assays were used to identify MANA- and viral (EBV and influenza)-specific TCRs, respectively. WES, whole-exome sequencing. **b**, UMAP projection of the expression profiles of the 560,916 T cells that passed quality control. Immune cell subsets, defined by 15 unique clusters, are annotated and marked by colour code. **c**, Relative expression of the top-5 most differentially expressed genes. Five-thousand cells (or all cells in the cluster if the cluster size was fewer than 5,000 cells) were randomly sampled from each cluster for visualization. MAIT, mucosal-associated

invariant T cells; T_{FH} , T follicular helper cells; T_{reg} , regulatory T cells. **d**, Expression of T cell subset-defining genes, T cell subset-selective genes and major T cell checkpoint genes. *CD39* is also known as *ENTPD1*. **e**, PCA of cell-cluster-level pseudobulk gene expression for individual samples for tumour (yellow, $n = 15$) and adjacent normal lung (dark blue, $n = 12$). One-sided permutation test. **f**, PCA of cell-cluster-level pseudobulk gene expression for non-MPR (red, $n = 9$) and MPR (light blue, $n = 6$) tumours. One-sided permutation test.

[Full size image](#)

Uniform manifold approximation and projection (UMAP) analysis of cells from all samples on the basis of filtered and normalized transcript counts defined 15 T cell clusters (Fig. 1b, c, Extended Data Fig. 1b–e, Supplementary Data 1, 1). Expression of subset-defining markers and T cell checkpoints was visualized in red scale on the UMAP (Fig. 1d). The two clusters designated as TRM had the highest expression of the canonical TRM genes, *ZNF683* (also known as *HOBIT*) and *ITGAE* (also known as *CD103*), and the highest expression of a TRM gene set¹³ (Extended Data Fig. 1f, Supplementary Data 2, 1). Principal component analysis (PCA) of samples based on concatenated cell-cluster-level pseudobulk profiles distinguished adjacent normal-lung T cells from TIL (Fig. 1e), but did not distinguish MPR from non-MPR TIL (Fig. 1f). We did not observe notable differentially expressed gene programs between MPR and non-MPR TIL (Supplementary Data 3), indicating that gene expression profiling of total TIL has limited sensitivity in distinguishing the pathologic response to PD-1 blockade.

Expression programs of MANA-specific TIL

We next performed the MANA functional expansion of specific T cells assay (MANAFEST)³ on 9 of the 16 individuals on whom scRNA-seq–TCR-seq was conducted. This assay detects *in vivo* antigen-experienced T cell responses and identifies the clonal identity of the T cell receptor (TCR) corresponding to these cells. Of these nine, four were classed as MPR and five were non-MPR (results from one individual have been previously described⁸). Putative MANA (Supplementary Tables 4–6), peptide pools representing influenza matrix and nucleoproteins, and a pool of major histocompatibility complex (MHC) class I-restricted cytomegalovirus (CMV), Epstein–Barr virus (EBV) and influenza virus epitopes (CEF) were queried for CD8⁺ T cell reactivity in parallel (Supplementary Tables 6, 7). From 7 (3 with MPR and 4 without MPR) of the 9 individuals, 72 total unique MANA-specific TCRs, 33 unique CEF-specific TCRs, and 52 unique influenza-specific TCRs were identified (Extended Data Fig. 2, Supplementary Tables 8, 9, Supplementary Data 4, 5). Out of 33 CEF-specific TCRs, 6 matched known public EBV-specific TCRs and 3 matched known

public influenza-specific TCRs¹⁴. No CMV-reactive TCRs were mapped from our CEF-specific TCRs. Notably, 4 of the 41 MANA-specific TCRV β complementarity-determining region 3 (CDR3) clonotypes identified in a patient without MPR (patient ID MD01-004) (Extended Data Fig. 2) were specific for a MANA (MD01-004-MANA12) derived from a p53 R248L hotspot mutation, and were found at appreciable frequency in the pre- and post-treatment tumour (Extended Data Fig. 3), despite the tumour not attaining MPR. Most MANA-specific clones were detected at very low frequency (median: 0.001%) in the peripheral blood across all available time points (Fig. 2a, Extended Data Fig. 3). Overall, pathologic response was not associated with the prevalence, frequency or intratumoral representation of MANA-specific T cells (Extended Data Figs. 2, 3 Supplementary Table 9). In fact, more MANA-specific TIL were observed among non-MPR TIL than among MPR TIL. No consistent pattern was observed for the frequency of viral-specific T cells in the tissue or peripheral blood (Extended Data Figs. 2, 3).

Fig. 2: Characterization of antigen-specific T cells in NSCLC treated with neoadjuvant PD-1 blockade.

 **figure2**

The MANIFEST assay was performed on four patients with MPR and five patients without MPR. Results are shown in Extended Data Fig. 2 and Supplementary Data 5. **a**, Four TCRs recognizing p53(R248L)-derived MD01-004-MANA12 were identified in patient without MPR MD01-004. Their frequency was tracked in serial peripheral blood. Mut, mutant. **b**, Refined clustering was performed on 235,851 CD8⁺ T cells from tumour ($n = 15$), adjacent normal lung ($n = 12$), TDLN ($n = 3$) and one resected brain metastasis (MD043-011). Fourteen unique clusters were visualized and were using T cell gene programs described in previous studies¹⁶. Cluster-defining genes are shown in Extended Data Fig. 5a. **c**, MANA-specific (red), influenza-specific (blue)

and EBV-specific (purple) clonotypes were visualized on the CD8 UMAP. **d**, Antigen-specific gene programs in the TIL were visualized as a heat map. Comparisons were performed at the individual cell level using a two-sided Wilcoxon rank-sum test with *P*-value adjustment using Bonferroni correction. **e**, Expression levels of key markers are shown. *TBET* is also known as *TBX21*; *4-1BB* is also known as *TNFRSF9*. **f**, Transcriptional programs of influenza-specific and MANA-specific TIL were compared. The top-15 significantly upregulated genes in influenza -specific T cells (blue) and in MANA-specific T cells (yellow) are shown. **g**, TIL from MD01-004 were cultured with MD01-004-MANA-12 or influenza peptide and titrating concentrations of IL-7, followed by scRNA-seq–TCR-seq. In total, 814 influenza-specific TIL (410 co-cultured with influenza peptide and 404 co-cultured with MANA peptide) and 581 MANA-specific TIL (366 co-cultured with influenza peptide and 215 co-cultured with MANA peptide) were detected from a single experiment and were analysed. Composite expression of an IL-7 gene set by influenza-specific and MANA-specific TIL (as determined by their TCRV β CDR3) was analysed. Dose-response curve of the IL-7-upregulated gene set-score is shown (mean \pm s.e.m.). **h**, TCRs corresponding to seven MANA-specific clonotypes from two patients without MPR (red lines), three MANA-specific clonotypes from a patient with MPR (yellow lines), two influenza-specific TCRs, and one EBV-specific TCR (orange lines) were tested for ligand-dependent TCR-signalling capacity. Ctrl, control; RLU, relative luminescence units.

[Full size image](#)

Ten MANA-specific clonotypes, for which the TCR α could be confidently identified from the single-cell analysis, were selected for validation of MANA recognition via TCR cloning and introduction into a Jurkat–NFAT luciferase reporter system¹⁵. Seventy per cent of tested clonotypes (representing 95.2% of total cells bearing TCRs identified by MANAFEST) were validated as MANA-specific (Extended Data Fig. [4a–c](#)). Peptide–human leukocyte antigen (HLA) binding assays demonstrated that two MANA peptides—MD01-005-MANA7 and MD01-004-MANA12—displayed comparably high MHC class I affinity (measured dissociation constants (K_d) = 5.1 nM and 17.5 nM, respectively) and stability (Extended Data Fig. [4d, e](#)).

We next evaluated the transcriptional programming of MANA- and viral-specific CD8 $^+$ T cells. Refined clustering of all CD8 $^+$ T cells ($n = 235,851$) identified 15 unique clusters (Fig. [2b](#), Extended Data Fig. [5a](#), [Supplementary Data 1.2](#)). Clusters were named on the basis of previously defined T cell states from single-cell transcriptomic studies¹⁶. Six clusters had gene expression programs consistent with TRM T cells, characterized by high expression of *HOBIT*, *LINC02246*, *CD103* and a previously published TRM gene set (Extended Data Fig. [5b](#)). Selective genes and linkage to the global CD3 T cell clusters shown in Fig. [1](#) were visualized (Extended

Data Figs. 5c, d). The six TRM subsets were heterogeneous in their expression of an exhaustion gene set described previously in NSCLC¹⁷ (Extended Data Fig. 5e, Supplementary Data 2.2). None of the most frequent tumour-infiltrating clonotypes were restricted to a single cluster (Extended Data Fig. 5f). Among all tested individuals, a total of 28 MANA-specific CD8 clonotypes (1,350 total cells from 3 patients with MPR and 3 patients without MPR) as identified by MANAFEST were detected in the single-cell data, of which 20 clonotypes (890 cells) were in the tumour (Fig. 2c, Supplementary Table 8). Of the viral-specific T cell clonotypes, 23 influenza-specific (866 cells) and 2 EBV-specific (281 cells) clones were found in the CD8 single-cell analysis.

Overlay of these clonotypes onto the CD8⁺ T cell UMAP demonstrated a marked distinction between the clonotypes with different antigen specificities (Fig. 2c, Extended Data Fig. 6a–c). EBV-reactive T cells primarily resided in effector T (T_{eff}) cell clusters, whereas influenza- and MANA-specific T cells largely occupied distinct TRM clusters. Notably, because influenza is a respiratory virus, influenza-specific T cells may be considered the archetypal lung-resident memory T cells¹⁸. None of the patients in our study were symptomatic for influenza in the six weeks preceding surgery. It is therefore not surprising that influenza-specific CD8 cells were TRM rather than T_{eff} cells. By contrast, EBV-specific T cells exclusively occupied T_{eff} clusters, consistent with periodic acute stimulation upon latent EBV reactivation. Whereas influenza-specific cells were the most abundant in normal lung, MANA-specific CD8 cells were more numerous in the tumour (Extended Data Fig. 6d, e).

There was considerable shared expression of selective cytotoxic T lymphocyte (CTL) activation genes between MANA- and EBV-specific T cells, in particular genes encoding T cell activation and CTL activity, such as *HLA-DRA*, *GZMH*, *IFNG* and *NKG7* (Fig. 2d, Supplementary Data 1.3). However, genes encoding certain canonical cytolytic molecules, such as *GZMK*, were expressed at low levels in MANA-specific TIL. Most notably, *EOMES*, which encodes a transcription factor that is critical for CTL activity¹⁹, was expressed in EBV-specific CD8 cells but was minimally expressed in most MANA-specific cells. Multiple checkpoints were significantly upregulated in MANA-specific TIL compared with EBV-specific TIL. Notably, MANA-specific cells expressed higher levels of *PRDM1*, which encodes BLIMP-1 and has been reported to participate in coordinated transcriptional activation of multiple checkpoint genes, including *PD-1* (also known as *PDCD1*), *LAG3*, *TIGIT* and *HAVCR2*²⁰. *TOX*, which encodes a chromatin modifier important for exhaustion programs of chronic virus-specific and tumour-specific T cells in mouse models^{21,22}, was only marginally increased in MANA-specific cells, whereas its homologue, *TOX2*, which has also been reported to drive T cell exhaustion²³, showed much higher upregulation in MANA-specific versus EBV-specific CD8 TIL. *HOBIT*, which is

selectively upregulated in TRM T cells²⁴, was also upregulated in MANA-specific TIL, even relative to influenza-specific TRM (Fig. 2e). Indeed, MANA-specific T cells demonstrated the highest immune checkpoint and exhaustion signatures¹⁷ (Extended Data Fig. 6f). These findings demonstrate that MANA-specific CD8 T cells in the tumour have an unconventional hybrid transcriptional program characterized by incomplete activation of effector programs and significant upregulation of checkpoint molecules such as PD-1, CTLA-4, TIM3, TIGIT and CD39. Genes encoding each of these checkpoint molecules were more highly expressed among MANA-specific CD8 cells than either influenza- or EBV-specific CD8 cells, with *CD39* being the most highly differentially expressed (Fig. 2d,e), congruent with previous flow cytometry findings on MANA-specific lung cancer TIL².

Influenza-specific TRM were distinguished from MANA-specific TRM by low levels of both activation and effector CTL programs and had lower expression of multiple checkpoint molecules, but had the highest levels of genes associated with T memory stem cells, such as TCF7 and IL-7R (Fig. 2e,f). Indeed, IL-7R expression was 4.6-fold higher on influenza-specific TIL relative to MANA-specific TIL. In TIL obtained from patient without MPR MD01-004, culture with titrating concentrations of IL-7 in vitro induced much higher levels of IL-7R-regulated genes ([Supplementary Data 2.3](#)) in influenza-specific TIL than in MANA-specific TIL (Fig. 2g, Extended Data Fig. 7). Nonetheless, supraphysiological levels of IL-7 induced appreciable upregulation of IL-7R-induced genes in MANA-specific TIL. Given the distinct transcriptional programs of the identified MANA-specific CD8 cells, we hypothesized that other CD8 T cells in the same TRM cluster showing differential expression relative to influenza-specific T cells (Fig. 2g) may also recognize MANA that were not detected by the MANAFEST assay. We cloned seven TCRs corresponding to CD8⁺ T cells with highly differential gene expression relative to influenza-specific T cells. We screened each TCR with a library of candidate MANA ([Supplementary Table 6](#)) and confirmed MANA recognition in three of these TCRs, one TCR each from patients MD01-004, MD01-005 and MD043-011 (Extended Data Fig. 8a-d).

To next investigate the ligand-dependent TCR signalling capacity of antigen-specific T cells, we performed a dose-response curve with cognate peptides matched to the ten total Jurkat-validated MANA-specific TCR α -TCR β pairs ([Supplementary Table 10](#)). Peptide dose-response curves of MPR-derived TCRs were comparable to those of EBV- and influenza-specific TCRs, suggesting that these TCRs were capable of strong ligand-dependent signalling (sometimes referred to as functional avidity). However, the peptide dose-response curves of TCRs derived from patients without MPR were markedly lower (approximately 2 log₁₀ leftward shift in peptide dose-response curve) (Fig. 2h, Extended Data Fig. 8e). Together, our data show that despite similar measured MANA-HLA binding affinities (Extended Data Fig. 4c,d), TCR from

expandable MANA-specific clones from the patient with MPR had significantly higher functional avidity than MANA-specific clones from patients without MPR.

MANA-specific TIL programs correlate with MPR

To explore determinants of ICB sensitivity, we examined differences in gene expression patterns between MPR and non-MPR MANA-specific TIL. The neoadjuvant clinical trial format enabled us to make this distinction through pathological analysis of surgically resected tissue. In total, we compared 45 MPR TIL transcriptomes (39 from MD01-005, 2 from MD043-003 and 4 from NY016-025) with 885 non-MPR TIL transcriptomes (782 from MD043-011, 62 from MD01-004 and 22 from NY016-014; Extended Data Fig. 9, Supplementary Table 8). We observed highly significant differences between pathologic MPR and non-MPR tumours (Fig. 3a, [Supplementary Data 1.4](#)). Significantly higher levels of genes associated with T cell dysfunction such as *TOX2*, *CTLA4*, *HAVCR2* and *ENTPD1* were observed for non-MPR MANA-specific T cells, whereas MPR MANA-specific T cells had higher expression of genes associated with memory (*IL7R* and *TCF7*) and effector function (*GZMK*) (Fig. 3a–c). Both the checkpoint score and exhaustion score were higher in MANA-specific TIL from patients without MPR (Fig. 3d, Extended Data Fig. 10a, b). Of note, *CXCL13* is one of the genes most highly correlated with checkpoint-associated genes in non-MPR MANA-specific TIL, and was also found to be highly expressed in MANA-specific cells relative to virus-specific cells among CD8 TIL (Fig. 2d–f).

Fig. 3: Differential gene expression programs of MANA-specific CD8 T cells in MPR versus non-MPR tumours.

 **figure3**

Seven unique MANA-specific clonotypes, representing 45 total transcriptomes, were identified in MPR TIL: 39 from MD01-005, 2 from MD043-003 and 4 from NY016-025. In non-MPR TIL, 16 unique clonotypes, representing 885 total transcriptomes, were identified: 782 from MD043-011, 62 from MD01-004 and 22 from NY016-014 (Supplementary Table 8). Differential gene expression analysis was performed on the MANA-specific T cells detected in MPR ($n = 3$) and non-MPR ($n = 3$) tumours. **a**, The top differential genes and selective immune markers of tumour-infiltrating MANA-specific T cells from MPR and non-MPR tumours. Comparisons were performed at the individual cell level using two-sided Wilcoxon rank sum test. P -value adjustment was performed using Bonferroni correction. Side bar shows the adjusted P value (green scale) and response status (red, TIL from MPR; light blue, TIL from non-MPR). **b**, Histograms show the expression of key genes among MANA-specific T cells from MPR (light blue) and non-MPR (red) tumours. **c**, A violin plot shows IL-7R

expression by each MANA-specific CD8 T cell in MPR (red) and non-MPR (light blue) tumours. Comparisons were performed at the individual cell level using two-sided Wilcoxon rank-sum test. **d**, A T cell immune checkpoint score was calculated for each MANA-specific CD8 T cell detected in MPR (red) and non-MPR (light blue) tumours. This checkpoint score was compared between MPR and non-MPR using two-sided Wilcoxon rank-sum test. **e**, The relative correlation coefficient (MPR MANA-specific TIL versus non-MPR MANA-specific TIL) with the immune checkpoint score is shown for genes more highly correlated in non-MPR (yellow) and MPR (blue) TIL.

[Full size image](#)

A number of genes encoding T cell inhibitory molecules were more highly correlated with a composite immune checkpoint score of MANA-specific TIL from patients without MPR than those from patients with MPR (Fig. 3e, Extended Data Fig. 10c). In two patients without MPR (MD01-004 and MD043-011) and one patient with MPR (MD01-005), we also detected MANA-specific cells upon single-cell profiling of CD8 T cells from TDLN (Extended Data Fig. 10d, e). Tracking the MANA-specific CD8 clonotypes from the primary tumour, we detected those clones among TIL from a brain metastasis resected from patient MD043-011 24 months after primary tumour resection (Extended Data Fig. 10f). Relative to the primary tumour, even-higher levels of three checkpoints—LAG3, TIGIT and HAVCR2—were expressed on MANA-specific TIL in the metastasis (Extended Data Fig. 10g, [Supplementary Data 1.5](#)).

Going back to overall TIL transcriptomic patterns, we hypothesized that MANA-specific T cells and/or a MANA-specific T cell-like signature might correlate with response to ICB, even though total TIL single-cell transcriptomic patterns did not (Fig. 1e). Among CD8 TIL from six MPR tumours and nine non-MPR tumours, the greatest correlation with pathologic response status was observed by combining four TIL clusters most highly enriched in MANA-specific cells, whereas the expression profile of total CD8 TIL did not distinguish MPR from non-MPR (Extended Data Fig. 11). These data suggest that additional T cells with this profile may contribute to the anti-tumour response.

Systemic reprogramming of MANA-specific T cells

We next performed scRNA-seq–TCR-seq of serial peripheral blood T cells from patient with MPR MD01-005 after enriching for expression of the TCR-V β genes corresponding to this patient's MANA-specific TCRs using fluorescence-activated cell sorting (FACS) (Fig. 4a–c, Extended Data Fig. 12a). Nine out of ten MANA-specific clones mapped to a TRM-like cluster ($T_{mem}(3)$; T_{mem} , memory T cell), with some transcriptional features of TRM, such as expression of *HOBIT* two weeks after

the initiation of anti-PD-1 treatment (Fig. 4d). By four weeks (time of tumour resection), a significant diversification of phenotype was observed ($P \leq 0.021$; Methods). Half of the MANA-specific cells were in T_{eff} clusters (Fig. 4e). By 11 weeks (7 weeks after tumour resection), the MANA-specific cells were below the limit of detection in the blood, consistent with known TRM patterns in the peripheral blood²⁵. Using RNA velocity, we observed a clear bidirectional flow of TRM-like memory MANA-specific T cells in the $T_{\text{mem}}(3)$ cluster towards either an activated effector ($T_{\text{eff}}(3)$) or a $T_{\text{mem}}(2)$ transcriptional profile (Fig. 4f). Genes associated with T_{eff} cell function and activation, T cell homing and migration, and tissue retention were upregulated along the pseudotime from $T_{\text{mem}}(3)$ to $T_{\text{eff}}(3)$, whereas there was a decrease in genes associated with resting memory T cells (Fig. 4g, h). Gene Ontology (GO) analysis revealed significant enrichment of an IFN γ -mediated signalling pathway along the differentiation trajectory (Extended Data Fig. 12b–f). Although all these tissue compartments were only available for one MPR, these findings are consistent with our hypothesis that, upon activation, functional effector MANA-specific T cells enter the blood and traffic into tissues, including normal lung, in search of micro-metastatic tumour²⁶, and are compatible with a previous study showing that TRM cell plasticity can influence systemic memory T cell responses²⁷.

Fig. 4: Neoadjuvant PD-1 blockade promotes systemic transcriptional reprogramming in MANA-specific T cells from a patient with complete pathologic response.

 **figure4**

a, Longitudinal peripheral blood mononuclear cells were collected from complete pathologic responder MD01-005 (0% residual tumour) during treatment and in post-surgery follow up. Peripheral blood CD8⁺ T cells were sorted using FACS on the basis of expression of TCRVβ2, which corresponds to the MANA-specific CDR3 CASNKLGYQPQHF, as identified by the MANAFEST assay (Extended Data Fig. 2a). scRNA-seq–TCR-seq was performed on the sorted population from each time point. **b**, UMAP projection of expression profiles of 4,409 peripheral blood CD8⁺TCRVβ2⁺ T cells. **c**, Heat map of the top-5 differential genes, ranked by average fold change, for each T cell cluster. **d**, UMAP projection of MANA-specific T cells, identified via the CASNKLGYQPQHF or CASSLLENQPQHF TCRVβ CDR3, is shown for each time point. Clusters were coloured using the same colour scheme as in **b**. MANA-specific T cells are highlighted as triangles. **e**, The proportions of cells in each T cell cluster among all MANA-specific cells identified at week 2 and week 4

were compared (two-sided Fisher's exact test and a two-sided test accounting for background cell proportion, both smaller than 0.021; Methods). **f**, Diffusion plot with RNA velocity for clusters in which MANA-specific T cells were detected. Cells were randomly downsampled to 100 cells (or all cells in the cluster if cluster size was smaller than 100 cells) for each cluster for visualization. **g**, Heat map of the top differential genes along the pseudotime trajectory from $T_{\text{mem}}(3)$ to $T_{\text{eff}}(3)$. **h**, Pseudotemporal expression of genes that significantly change along the pseudotime from $T_{\text{mem}}(3)$ to $T_{\text{eff}}(3)$. Red curves represent the mean temporal function estimates of the three samples from this individual (Methods). Cells with gene expression levels above the top one percentile were removed as outliers.

[Full size image](#)

Discussion

Here we describe the transcriptional programming of MANA-specific TIL after ICB in lung cancer, and further, differential gene programs between patients whose tumours show MPR versus those that do not. Using the MANAFEST platform, MANA-specific CD8 T cells in peripheral blood were detected in the majority of patients who were treated with anti-PD-1; these were also found among TIL in roughly a third of these individuals. Detection of these T cells was independent of tumour response, suggesting that factors in the tumour microenvironment affecting T cell function probably contribute to anti-tumour responsiveness. Indeed, the most frequent MANA-specific clonotype, representing 782 TIL, was observed in a patient with no MPR. This tumour had dual *KRAS* and *STK11* oncogenic mutations, which are known to be highly associated with non-response to PD-1 blockade²⁸. Consistent with an earlier study², *CD39* expression was a key difference between MANA-specific and viral-specific T cells. Among MANA-specific CD8 TIL, roughly 90% were TRM with high expression of *HOBIT* that also displayed a partial but incompletely activated T_{eff} program, along with upregulation of several targetable checkpoints in non-MPR tumours. MANA-specific T cells also express far less IL-7R relative to influenza TRM, translating functionally into poor IL-7 responsiveness. These features may all contribute to their limited tumour-specific responsiveness in contrast to anti-viral responses. Future studies are warranted to assess the diminished functional capacity of MANA-specific T cells that was suggested by the transcriptomic profiles observed in our study.

One hypothesis for the lack of ICB response in some patients is that tumour-specific T cells exhibit low activity owing to poor avidity or affinity of their TCR for its cognate peptide MHC. Our finding comparing the ligand-induced TCR signalling of three MANA-specific TCRs from MPR TIL with seven from patients without MPR

supports this notion, although additional studies of this type are necessary to definitively test the hypothesis. An overall limitation of these studies is the modest number of MANA-specific cells among TIL that we were able to detect, representing three responders and three non-responders. Indeed, identification of MANA-specific cells is experimentally challenging, and only a few studies have successfully identified these cells in NSCLC^{2,3,8,29,30}, yet none of these profiled the transcriptome of MANA-specific T cells at single-cell resolution. Among the 930 MANA-specific transcriptomes that we identified in TIL, there was high consistency among cells from each response group in highly differential expression of key genes known to regulate T cell function. These findings inform on potential ICB combination therapies to overcome anti-PD-1 resistance that occurs even in the presence of potent MANA-specific T cells. For example, our data demonstrated reduced activation of transcriptional programs downstream of IL-7 ligation in MANA-specific TIL relative to influenza-specific TIL, but the MANA-specific TIL retain their ability to respond to supraphysiological levels of IL-7. Because IL-7 signalling is a requisite for maintenance of T cell homeostasis and long-lived memory, it is conceivable that targeting the IL-7 pathway could enhance ICB response. Our findings thus provide a platform for follow-up studies to more rigorously test the generalizability of our conclusions in the setting of resectable and metastatic NSCLC.

Methods

No statistical methods were used to predetermine sample size. The experiments were not randomized. The investigators were not blinded to allocation during experiments and outcome assessment.

Patients and biospecimens

This study was approved by the Institutional Review Boards (IRB) at Johns Hopkins University (JHU) and Memorial Sloan Kettering Cancer Center and was conducted in accordance with the Declaration of Helsinki and the International Conference on Harmonization Good Clinical Practice guidelines. The patients described in this study provided written informed consent. All biospecimens were obtained from patients with stage I-IIIA NSCLC who were enrolled to a phase II clinical trial evaluating the safety and feasibility of administering two doses of anti-PD-1 (nivolumab) before surgical resection. Pathological response assessments of primary tumours were reported previously^{8,31}. Tumours with no more than 10% residual viable tumour cells were considered to have a MPR.

scRNA-seq–TCR-seq

Cryobanked T cells were thawed and washed twice with pre-warmed RPMI with 20% FBS and gentamicin. Cells were resuspended in PBS and stained with a viability marker (LIVE/DEAD Fixable Near-IR; ThermoFisher) for 15 min at room temperature in the dark. Cells were incubated with Fc block for 15 min on ice and stained with antibody against CD3 (BV421, clone SK7) for 30 min on ice. After staining, highly viable CD3⁺ T cells were sorted into 0.04% BSA in PBS using a BD FACSAria II Cell Sorter. Sorted cells were manually counted using a hemocytometer and prepared at the desired cell concentration (1,000 cells per μ l), when possible. The Single Cell 5' V(D)J and 5' DGE kits (10X Genomics) were used to capture immune repertoire information and gene expression from the same cell in an emulsion-based protocol at the single-cell level. Cells and barcoded gel beads were partitioned into nanolitre-scale droplets using the 10X Genomics Chromium platform to partition up to 10,000 cells per sample followed by RNA capture and cell-barcoded cDNA synthesis using the manufacturer's standard protocols. Libraries were generated and sequenced on an Illumina NovaSeq instrument using 2 \times 150-bp paired end sequencing. 5' VDJ libraries were sequenced to a depth of ~5,000 reads per cell, for a total of 5 million to 25 million reads. The 5' DGE libraries were sequenced to a target depth of ~50,000 reads per cell.

Whole-exome sequencing, mutation calling and neoantigen prediction

Genomic data for most individuals in our study were reported previously⁸, and whole-exome sequencing, variant calling and neoantigen predictions for individuals MD043-003 and NY016-025 were performed prospectively for the present study. Whole-exome sequencing was performed on pre-treatment tumours unless otherwise noted (Supplementary Table 4) and matched normal samples. DNA was extracted from tumours and matched peripheral blood using the Qiagen DNA kit (Qiagen). Fragmented genomic DNA from tumour and normal samples was used for Illumina TruSeq library construction (Illumina) and exonic regions were captured in solution using the Agilent SureSelect v.4 kit (Agilent,) according to the manufacturers' instructions as previously described³². Paired-end sequencing, resulting in 100 bases from each end of the fragments for the exome libraries was performed using Illumina HiSeq 2000/2500 instrumentation (Illumina). The depth of total and distinct coverage is shown in Supplementary Table 4. Somatic mutations, consisting of point mutations, insertions, and deletions across the whole exome were identified using the VariantDx custom software for identifying mutations in matched tumour and normal samples as previously described^{32,33}. Somatic mutations, consisting of nonsynonymous single base substitutions, insertions and deletions, were evaluated for putative MHC class I neoantigens using the ImmunoSelect-R pipeline (Personal Genome Diagnostics) as previously described³⁰. Somatic sequence alterations are listed in Supplementary Table 5.

Identification of neoantigen-specific TCRV β CDR3 clonotypes

We used the MANAFEST assay³ to evaluate T cell responsiveness to MANA and viral antigens. In brief, pools of MHC class I-restricted CMV, EBV and influenza peptide epitopes (CEFX, jpt Peptide Technologies), pools representing the matrix protein and nucleoprotein from H1N1 and H3N2 (jpt Peptide Technologies), and putative neoantigenic peptides defined by the ImmunoSelect-R pipeline (jpt Peptide Technologies; Supplementary Table 6) were each used to stimulate 250,000 T cells in vitro for 10 days as previously described³. The time point of peripheral blood collection used for each MANAFEST assay is described in Supplementary Tables 2, 7. In brief, on day 0, T cells were isolated from PBMC by negative selection (EasySep; STEMCELL Technologies). The T cell-negative fraction was co-cultured with an equal number of selected T cells in culture medium (IMDM/5% human serum with 50 $\mu\text{g ml}^{-1}$ gentamicin) with 1 $\mu\text{g ml}^{-1}$ relevant neoantigenic peptide, 1 $\mu\text{g ml}^{-1}$ of an MHC class I-restricted CMV, EBV, and influenza peptide epitope pool (CEFX, jpt Peptide Technologies), 1 $\mu\text{g ml}^{-1}$ of pools representing the matrix protein and nucleoprotein from H1N1 and H3N2 (jpt Peptide Technologies), or no peptide (to use as a reference for non-specific or background clonotypic expansion). On day 3, half the medium was replaced with fresh medium containing cytokines for a final concentration of 50 IU ml^{-1} IL-2 (Chiron), 25 ng ml^{-1} IL-7 (Miltenyi) and 25 ng ml^{-1} IL-15 (PeproTech). On day 7, half the medium was replaced with fresh culture medium containing cytokines for a final concentration of 100 IU ml^{-1} IL-2 and 25 ng ml^{-1} IL-7 and IL-15. On day 10, cells were harvested, washed twice with PBS, and the CD8 $^{+}$ fraction was isolated using a CD8 $^{+}$ negative enrichment kit (EasySep; STEMCELL Technologies). DNA was extracted from each CD8-enriched culture condition using the Qiamp micro-DNA kit according to the manufacturer's instructions. TCR sequencing was performed on each individual peptide-stimulated T cell culture using survey-level sequencing (max depth ~60,000 reads) by Adaptive Biotechnologies using their established platform³⁴ or by the Sidney Kimmel Comprehensive Cancer Center FEST and TCR Immunogenomics Core (FTIC) facility using the Oncomine TCR Beta short-read assay (Illumina) and sequenced on an Illumina iSeq 100 using unique dual indexes, for a maximum of ~40,000 reads per sample.

Data pre-processing was performed to eliminate non-productive TCR sequences and to align and trim the nucleotide sequences to obtain only the CDR3 region. Sequences not beginning with C or ending with F or W and having less than seven amino acids in the CDR3 were eliminated. TCR sequencing samples with less than 1,000 productive reads were excluded from downstream analysis. MD043-011-MANA_22 was the only such sample in the present study (see Supplementary Table 7). Resultant processed data files were uploaded to our publicly available MANAFEST analysis web app

(<http://www.stat-apps.onc.jhmi.edu/FEST>) to bioinformatically identify antigen-specific T cell clonotypes.

Bioinformatic analysis of productive clones was performed to identify antigen-specific T cell clonotypes meeting the following criteria: (1) significant expansion (Fisher's exact test with Benjamini–Hochberg correction for false discovery rate (FDR), $P < 0.05$) compared to T cells cultured without peptide, (2) significant expansion compared to every other peptide-stimulated culture (FDR <0.05) except for conditions stimulated with similar neoantigens derived from the same mutation, (3) an odds ratio >5 compared to the no peptide control, and (4) present in at least 10% of the cultured wells to ensure adequate distribution among culture wells. A lower read threshold of 300 was used for assays sequenced by the FTIC and a lower threshold of 30 was used for samples sequenced by Adaptive Biotechnologies. In MANIFEST assays testing less than 10 peptides or peptide pools, cultures were performed in triplicate and reactive clonotypes were defined as being significantly expanded relative to T cells cultured without peptide (FDR <0.05) in two out of three triplicates, and not significantly expanded in any other well tested. When available, TCRseq was also performed on DNA extracted from tumour, normal lung, and lymph node tissue obtained before treatment and at the time of surgical resection, as well as serial peripheral blood samples. The assays performed on each biospecimen are outlined in Supplementary Table 2.

Peptide affinity and stability measurements

Peptide affinity for cognate HLA molecules was assessed using a luminescent oxygen channeling immunoassay (LOCI; AlphaScreen, Perkin Elmer) as previously described³⁵. This is a proximity-based system using a donor and acceptor bead, each conjugated with an epitope tag. When the donor bead is excited with light at 650 nm and can activate an acceptor bead, resulting in a signal at 520–620 nm, which can be quantified per second as a surrogate of affinity. A higher number of counts per second indicates higher affinity of the peptide:HLA pair. The stability of peptide loaded complexes was measured by refolding MHC with peptide and subsequently challenging complexes with a titration of urea. The denaturation of MHC was monitored by ELISA as described previously³⁶.

TCR reconstruction and cloning

Ten MANIFEST+ TCR sequences for which the TCR α chain could be enumerated (>3 cells in single-cell data with the same TCR α –TCR β pair) were selected for cloning. In addition, seven clones (from three individuals: MD01-004, MD01-005 and MD043-011) that have high composite signature (using the AddModuleScore function) consisting of differential gene programs of MANA-specific T cell relative to

influenza-specific T cells in the TRM were selected for cloning. Relevant TCRs were analysed with the IMGT/V-Quest database (<http://www.imgt.org>). The database allows us to identify the TRAV and TRBV families with the highest likelihood to contain the identified segments which match the sequencing data. To generate the TCRs, the identified TCRA V-J region sequences were fused to the human TRA constant chain, and the TCRB V-D-J regions to the human TRB constant chain. The full-length TCRA and TCRB chains were then synthesized as individual gene blocks (IDT) and cloned into the pCI mammalian expression vector, containing a CMV promoter, and transformed into competent *Escherichia coli* cells according to the manufacturer's instructions (NEBuilder HiFi DNA Assembly, NEB). Post transformation and plasmid miniprep, the plasmids were sent for Sanger sequencing to ensure no mutations were introduced (Genewiz).

T cell transfection, transient TCR expression and MANA-recognition assays

To generate a Jurkat reporter cell in which we could transfer our TCRs of interest, the endogenous TCR α- and β-chains were knocked out of a specific Jurkat line that contains a luciferase reporter driven by an NFAT response element (Promega) using the Alt-R CRISPR system (Integrated DNA Technologies, IDT). Two sequential rounds of CRISPR knockout were performed using crDNA targeting the TCRα constant region (AGAGTCTCTCAGCTGGTACA) and the TCRβ constant region (AGAAGGTGGCCGAGACCCTC). Limiting dilution was then used to acquire single cell clones and clones with both TCRα and TCRβ knocked out, as confirmed by Sanger sequencing and restoration of CD3 expression only by the co-transfection of TCRα or TCRβ chains, were chose. CD8α and CD8β chains were then transduced into the TCRα⁻TCRβ⁻ Jurkat reporter cells using the MSCV retroviral expression system (Clontech). Jurkat reporter cells were then co-electroporated with the pCI vector encoding the TCRB and TCRA gene blocks, respectively, using ECM830 Square wave electroporation system (BTX) at 275 V for 10 ms in OptiMem media in a 4-mm cuvette. Post electroporation, cells were rested overnight by incubating in RPMI 10% FBS at 37 °C, 5% CO₂. TCR expression was confirmed by flow cytometric staining for CD3 on a BD FACSCelesta and 50,000 CD3⁺ T cells were plated in each well of a 96-well plate. Reactivity of the TCR-transduced Jurkat cells was assessed by co-culturing with 1 × 10⁵ autologous EBV-transformed B cells, loaded with titrating concentrations of MANA peptides, viral peptide pools or negative controls. After overnight incubation, activation of the NFAT reporter gene was measured by the Bio-Glo Luciferase Assay per manufacturer's instructions (Promega). Jurkat cells were routinely tested for mycoplasma contamination. No cell line authentication was performed.

COS-7 transfection with HLA allele and p53 plasmids

gBlocks (IDT) encoding HLA A*68:01, p53(R248L) and wild-type p53 were cloned into pcDNA3.4 vector (Thermo Fisher Scientific, A14697).

COS-7 cells were transfected with plasmids at 70–80% confluency using Lipofectamine 3000 (Thermo Fisher Scientific, L3000015) and incubated at 37 °C overnight in T75 flasks. A total of 30 µg plasmid (1:1 ratio of HLA plasmid per target protein plasmid in co-transfections) was used. Post transfection, COS-7 cells were plated with TCR $\alpha\beta$ -transfected JurkaT cells containing NFAT reporter gene at a 1:1 ratio. After overnight incubation, activation of the NFAT reporter gene was measured by the Bio-Glo Luciferase Assay per manufacturer's instructions (Promega).

Single-cell data pre-processing and quality control

Cell Ranger v3.1.0 was used to demultiplex the FASTQ reads, align them to the GRCh38 human transcriptome, and extract their cell and unique molecular identifier (UMI) barcodes. The output of this pipeline is a digital gene expression (DGE) matrix for each sample, which records the number of UMIs for each gene that are associated with each cell barcode. The quality of cells was then assessed based on (1) the number of genes detected per cell and (2) the proportion of mitochondrial gene/ribosomal gene counts. Low-quality cells were filtered if the number of detected genes was below 250 or above 3 \times the median absolute deviation away from the median gene number of all cells. Cells were filtered out if the proportion of mitochondrial gene counts was higher than 10% or the proportion of ribosomal genes was less than 10%. For single-cell VDJ sequencing, only cells with full-length sequences were retained. Dissociation/stress associated genes^{37,38}, mitochondrial genes (annotated with the prefix 'MT-'), high abundance lincRNA genes, genes linked with poorly supported transcriptional models (annotated with the prefix 'RP-')³⁹ and TCR (TR) genes (TRA/TRB/TRD/TRG, to avoid clonotype bias) were removed from further analysis. In addition, genes that were expressed in less than five cells were excluded.

Single-cell data integration and clustering

Seurat⁴⁰ (3.1.5) was used to normalize the raw count data, identify highly variable features, scale features, and integrate samples. PCA was performed based on the 3,000 most variable features identified using the vst method implemented in Seurat. Gene features associated with type I Interferon

(IFN) response, immunoglobulin genes and specific mitochondrial related genes were excluded from clustering to avoid cell subsets driven by the above genes³⁹. Dimension reduction was done using the RunUMAP function. Cell markers were identified by using a two-sided Wilcoxon rank sum test. Genes with adjusted $P < 0.05$ were retained. Clusters were labelled based on the expression of the top differential gene in each cluster as well as canonical immune cell markers. Global clustering on all CD3 T cells and refined clustering on CD8 T cells were performed using same procedure. To select for CD8⁺ T cells, SAVER⁴¹ was used to impute dropouts by borrowing information across similar genes and cells. A density curve was fitted to the log₂-transformed SAVER imputed CD8A expression values (using the ‘density’ function in R) of all cells from all samples. A cut-off is determined as the trough of the bimodal density curve (that is, the first location where the first derivative is zero and the second derivative is positive). All cells with log₂-transformed SAVER imputed CD8A expression larger than the cut-off are defined as CD8⁺ T cells. TRB amino acid sequences were used as a biological barcode to match MANA, EBV or influenza A-specific T cell clonotypes identified from the FEST assay with single-cell VDJ profile and were projected onto CD8⁺ T cell refined UMAP.

Single-cell subset pseudobulk gene expression analysis

PCA was performed on a standardized pseudobulk gene expression profile, where each feature was standardized to have a mean of zero and unit variance. In global CD3 and CD8 TIL PCA, for each cell cluster we first aggregated read counts across cells within the cluster to produce a pseudobulk expression profile for each sample and normalized these pseudobulk expression profiles across samples by library size. Combat function in the sva R package^{42,43} was applied to address potential batch effects on the normalized pseudobulk profile. Highly variable genes (HVGs) were selected for each cell cluster by fitting a locally weighted scatterplot smoothing (LOESS) regression of standard deviation against the mean for each gene and identifying genes with positive residuals. For each sample, all cell clusters were then concatenated by retaining each cluster’s HVGs to construct a concatenated gene expression vector consisting of all highly variable features identified from different cell clusters. Each element

in this vector represents the pseudobulk expression of a HVG in a cell cluster. Samples were embedded into the PCA space based on these concatenated gene expression vectors. Canonical correlation^{44,45} between the first two PCs (that is, PC1 and PC2) and a covariate of interest (that is, tissue type or response status) was calculated. Permutation test was used to assess the significance by randomly permuting the sample labels 10,000 times. In the MANA-specific PCA (Extended Data Fig. 11), MANA-enriched cell clusters, defined by clusters with MANA-specific T cell frequency at least two fold higher than randomly expected, were aggregated as one combined cell cluster. Then, a similar procedure by first identifying HVGs, computing the first 2 PCs and then calculating the canonical correlation was repeated for the combined MANA-enriched cell cluster and each of the other CD8 clusters.

Differential analysis comparing MPR and non-MPR by total CD8 or CD4 TIL and by cell cluster

The gene expression read counts were adjusted by library size. SAVER⁴¹ was used to impute the dropouts, and further log2-transformed the imputed values after adding a pseudocount of 1. A linear mixed-effect model⁴⁶ was constructed to identify genes that are significantly differential between MPR and non-MPR among total CD8/CD4 TIL and by each cell cluster, respectively. The B-H procedure⁴⁷ was used to adjust the *P* values for multiple testing, and the statistical significance is determined using a cut-off of FDR <0.05.

Differential-expression tests and antigen-specific T cell marker genes

Differential-expression tests for antigen-specific T cells were performed using FindAllMarkers functions in Seurat with Wilcoxon rank-sum test on SAVER imputed expression values. Genes with >0.25 log₂-fold changes, at least 25% expressed in tested groups, and Bonferroni-corrected p values <0.05 were regarded as significantly differentially expressed genes (DEGs). Antigen-specific (MANA versus influenza versus EBV) T cell marker genes were identified by applying the differential expression tests for

upregulated genes between cells of one antigen specificity to all other antigen-specific T cells in the dataset. MANA-specific T cell genes associated with response to ICB were identified by applying the differential expression tests comparing MANA-specific T cells from MPR versus those from non-MPR. Top ranked DEGs (by log-fold changes) with a \log_2 -fold changes >0.8 and DEGs relating to T cell function were extracted for further visualization in a heat map using pheatmap package. SAVER-imputed expression values of selective marker genes (transcriptional regulators, memory markers, tissue-resident markers, T cell checkpoints, effector and activation markers) were plotted using the RidgePlot function in Seurat.

In vitro short-term TIL stimulation with IL-7

Cryopreserved TIL from patient MD01-004 were thawed, counted, and stained with the LIVE/DEAD Fixable Aqua (ThermoFisher) viability marker and antibodies specific for CD3 (PE, clone SK1) and CD8 (BV786, clone RPA-T8). Thirty-thousand CD8⁺ T cells per condition were sorted on a BD FACSAria II Cell Sorter into a 96-well plate. Autologous T cell-depleted PBMC were added as antigen presenting cells (APC) at 1:1 ratio. The cells were stimulated with either influenza A or MD01-004-MANA 12 peptide and titrating concentrations of recombinant human IL-7 (Miltenyi) for 12 h in a round-bottomed 96-well plate.

Gene expression analysis of IL-7-stimulated MANA- and influenza-specific TIL

Following 12 h of antigen and IL-7 stimulation, cells were spun down, counted and re-suspended in 1% BSA at desired concentration. scRNA-seq and VDJ libraries were prepared using 10X Chromium single cell platform using 5' DGE library preparation reagents and kits according to manufacturer's protocols (10X Genomics) and as described above. MANA- or influenza-specific T cell clonotypes from the single-cell dataset were identified by using the TRB amino acid sequences as a biological barcode. SAVER imputed gene expression was scaled and centred using the ScaleData function in Seurat. A composite score for the IL-7-upregulated

gene set⁴⁸ ([Supplementary Data 2.3](#)) expression was computed using the AddModuleScore function and subsequently visualized using ridgeplot. Mean \pm standard error was used to show the dose–response curve of the IL-7-upregulated gene-set score by antigen-specific T cells and peptide-stimulation groups.

Immune checkpoint and exhaustion score generation and highly correlated genes

To characterize dysfunctional CD8 MANA TIL, six best-characterized (and clinically targeted) checkpoints: CTLA4, PDCD1, LAG3, HAVCR2, TIGIT and ENTPD1, were used to compute the T cell checkpoint score, and a published gene list from exhausted T cells was used to compute the T cell exhaustion score, using AddModuleScore function in Seurat. Applying T cell checkpoint score as an anchor, genes that were maximally correlated to the score were identified using linear correlation in MANA-specific TIL from MPR and non-MPR, respectively. Top-30 genes (from HVG selected using FindVariableGenes function in Seurat and excluded the 6 genes included in immune checkpoint score generation) with the highest correlation coefficients were plotted as a bar plot. The difference of correlation coefficients of the above genes was additionally computed between MPR and non-MPR and visualized using waterfall plot.

Evaluation of peripheral MANA-specific T cell transcriptome changes during treatment

Peripheral blood T cells from patient MD01-005 were sorted based on expression of CD8 and TCRV β 2, followed by scRNA-seq–TCR-seq and clustering on conventional CD8 $^+$ T cells (MAIT cells excluded). To evaluate whether there was a statistically significant change in the cell types of MANA cells between week 2 (W2) and week 4 (W4) samples in Fig. [4d](#), [e](#), we first conducted a Fisher’s exact test, which yields a $P = 0.021$, indicating a statistically significant phenotype change in MANA-specific cells (Fig. [4e](#)). We also conducted a more sophisticated test that adjust for potential background differences in cell type abundance between W2 and W4 samples. In this test, we let $m_{c,t}$ denote the probability that a MANA-

specific T cell collected at time point t (W2 or W4) comes from cell type c , and let $p_{c,t}$ denote the proportion of all cells in time point t that come from cell type c . We evaluated the ratio $R_{c,t} = m_{c,t}/p_{c,t}$, which characterizes the relative abundance of MANA-specific T cells in each cell type. We compared the null model where this ratio does not change over time (H_0 : $R_{c,W2} = R_{c,W4}$ for all cell type c) versus the alternative model where W2 and W4 T cells have different ratios (H_1 : $R_{c,W2} \neq R_{c,W4}$). To do this, we computed the test statistic $\langle S = \sum_c \{(\{R\}_{c,W2} - \{R\}_{c,W4})\}^2 \rangle$ using the observed data and compared it to its null distribution obtained using Monte Carlo simulations. To construct the null distribution for $\langle S \rangle$, we pooled cells from W2 and W4 together and treated them as one sample to estimate the common ratio $R_{c,W2} = R_{c,W4} = R_c$ shared by W2 and W4, and then derived the probability that a MANA-specific T cell collected at time point t comes from cell type c under the null model H_0 , which is proportional to $p_{c,t} R_c$ (that is, the product of the sample-specific background cell type proportion $p_{c,t}$ and the common MANA-abundance ratio R_c shared between samples). The MANA-specific T cells at time point t were then redistributed to different cell types randomly based on a multinomial distribution with this expected MANA-specific T cell type proportion (that is, the expected probability that a MANA-specific T cell at time point t comes from cell type c under H_0 is $\langle \{p\}_{c,t} \{R\}_c \rangle / (\sum_c \{p\}_{c,t} \{R\}_c)$), while keeping the total number of MANA-specific T cells at each time point the same as the observed MANA-specific T cell number at that time point. The test statistic S was then computed using this simulated sample. We repeated this simulation 10,000 times to derive the null distribution of S . Comparing the observed S to its null distribution yields a $P < 10^{-4}$.

RNA velocity-based differentiation-trajectory tracing

The RNA velocity analysis was performed by first recounting the spliced reads and unspliced reads based on aligned bam files of scRNA-seq data using the *velocyto* Python package. The calculation of RNA velocity values for each gene in each cell and embedding RNA velocity vector to low-dimension space were done using the SeuratWapper workflow for

estimating RNA velocity using Seurat (<https://github.com/satijalab/seurat-wrappers/blob/master/docs/velocity.md>). The first two diffusion components from Diffusion map were used to construct the coordinates along with velocity. TSCAN (v.1.7.0) was used to reconstruct the cellular pseudotime on diffusion maps space for the PBMC T cells from three time points (samples) of one patient (MD01-005). Based on velocity analysis, the $T_{mem}(3)$ cluster was specified as the starting cluster for the pseudotemporal trajectory which has branches. For each branch, \log_2 -transformed and library size-normalized SAVER-imputed gene expression values were used for analysing gene expression dynamics along the pseudotime. 10,325 genes with normalized expression ≥ 0.01 in at least 1% of cells were retained. For each gene g , the gene expression along pseudotime t in each sample s was described as a function $\langle\{f\}_s(g_s(t))\rangle$ which was obtained by fitting B-spline regression to the gene's normalized expression values in single cells. The red curves in Fig. 4h are the mean of the function $\langle\{f\}_s(g_s(t))\rangle$ of the three samples. In order to test whether the gene expression shows a significant change along pseudotime, we compared the above model with a null model in which $\langle\{f\}_s(g_s(t))\rangle$ is assumed to be a constant over time. The likelihood ratio statistic between the two models was computed. To determine the P value, the null distribution of the likelihood ratio statistic was constructed by permuting the pseudotime of cells in each sample, refitting the models and recomputing the likelihood ratio statistic. The P value was calculated as the number of permutations out of a total of 1,000 permutations that produce a likelihood ratio statistic larger than the observed one. The P values from all genes were converted to FDR by Benjamini–Hochberg procedure to adjust for multiple testing. Genes with $FDR < 0.05$ were considered as dynamic genes with statistical significance. k -Means clustering was applied to group genes with similar dynamic expression patterns into clusters. topGO (v.2.42.0) was used to identify the enriched Gene Ontology terms by comparing the genes in each cluster to all 10,325 genes as background.

Reporting summary

Further information on research design is available in the [Nature Research Reporting Summary](#) linked to this paper.

Data availability

Bulk TCRV β sequencing data generated by Adaptive Biotechnologies are available in the Adaptive Biotechnologies ImmuneACCESS repository under DOI 10.21417/JC2021N, at

<https://clients.adaptivebiotech.com/pub/caushi-2021-n>. Bulk TCRV β raw and processed sequencing data generated by the Sidney Kimmel Comprehensive Cancer Center FTIC are available in the Gene Expression Omnibus with accession number [GSE173351](#). Raw scRNA-seq–TCR-seq data reported in this paper are available in the European Genome-phenome Archive under controlled access with accession number [EGAS00001005343](#). Owing to the personal, sensitive and inherently identifying nature of raw genomic data, access to raw RNA-seq–TCR-seq data is controlled and full instructions to apply for data access can be found at <https://ega-archive.org/access/data-access>. Approvals will be granted immediately upon confirmation that all requirements are met. Processed and de-identified single-cell data are available in the Gene Expression Omnibus with accession number [GSE176022](#).

Code availability

Scripts to reproduce the analyses used in this study are available at <https://github.com/BKI-immuno/neoantigen-specific-T-cells-NSCLC>.

References

1. 1.

Tumeh, P. C. et al. PD-1 blockade induces responses by inhibiting adaptive immune resistance. *Nature* **515**, 568–571 (2014).

[ADS](#) [CAS](#) [PubMed](#) [PubMed Central](#) [Article](#) [Google Scholar](#)

2. 2.

Simoni, Y. et al. Bystander CD8⁺ T cells are abundant and phenotypically distinct in human tumour infiltrates. *Nature* **557**, 575–579 (2018).

[ADS](#) [CAS](#) [PubMed](#) [Article](#) [Google Scholar](#)

3. 3.

Danilova, L. et al. The mutation-associated neoantigen functional expansion of specific T Cells (MANIFEST) assay: a sensitive platform for monitoring antitumor immunity. *Cancer Immunol. Res.* **6**, 888–899 (2018).

[CAS](#) [PubMed](#) [PubMed Central](#) [Article](#) [Google Scholar](#)

4. 4.

Vogelstein, B. et al. Cancer genome landscapes. *Science* **339**, 1546–1558 (2013).

[ADS](#) [CAS](#) [PubMed](#) [PubMed Central](#) [Article](#) [Google Scholar](#)

5. 5.

Yarchoan, M., Hopkins, A. & Jaffee, E. M. Tumor mutational burden and response rate to PD-1 inhibition. *N. Engl. J. Med.* **377**, 2500–2501 (2017).

[PubMed](#) [PubMed Central](#) [Article](#) [Google Scholar](#)

6. 6.

Yarchoan, M., Johnson, B. A., III, Lutz, E. R., Laheru, D. A. & Jaffee, E. M. Targeting neoantigens to augment antitumour immunity. *Nat. Rev. Cancer* **17**, 209–222 (2017).

[CAS](#) [PubMed](#) [PubMed Central](#) [Article](#) [Google Scholar](#)

7. 7.

Scheper, W. et al. Low and variable tumor reactivity of the intratumoral TCR repertoire in human cancers. *Nat. Med.* **25**, 89–94 (2019).

[CAS](#) [PubMed](#) [Article](#) [Google Scholar](#)

8. 8.

Forde, P. M. et al. Neoadjuvant PD-1 blockade in resectable lung cancer. *N. Engl. J. Med.* **378**, 1976–1986 (2018).

[CAS](#) [PubMed](#) [PubMed Central](#) [Article](#) [Google Scholar](#)

9. 9.

Blank, C. U. et al. Neoadjuvant versus adjuvant ipilimumab plus nivolumab in macroscopic stage III melanoma. *Nat. Med.* **24**, 1655–1661 (2018).

[CAS](#) [PubMed](#) [Article](#) [Google Scholar](#)

10. 10.

Huang, A. C. et al. A single dose of neoadjuvant PD-1 blockade predicts clinical outcomes in resectable melanoma. *Nat. Med.* **25**, 454–461 (2019).

[CAS](#) [PubMed](#) [PubMed Central](#) [Article](#) [Google Scholar](#)

11. 11.

Kaunitz, G. J. et al. Melanoma subtypes demonstrate distinct PD-L1 expression profiles. *Lab. Invest.* **97**, 1063–1071 (2017).

[CAS](#) [PubMed](#) [PubMed Central](#) [Article](#) [Google Scholar](#)

12. 12.

Topalian, S. L. et al. Neoadjuvant nivolumab for patients with resectable Merkel cell carcinoma in the CheckMate 358 Trial. *J. Clin. Oncol.* **38**, 2476–2487 (2020).

[CAS](#) [PubMed](#) [PubMed Central](#) [Article](#) [Google Scholar](#)

13. 13.

Clarke, J. et al. Single-cell transcriptomic analysis of tissue-resident memory T cells in human lung cancer. *J. Exp. Med.* **216**, 2128–2149 (2019).

[CAS](#) [PubMed](#) [PubMed Central](#) [Article](#) [Google Scholar](#)

14. 14.

Bagayev, D. V. et al. VDJdb in 2019: database extension, new analysis infrastructure and a T-cell receptor motif compendium. *Nucleic Acids Res.* **48**, D1057–D1062 (2020).

15. 15.

Dykema, A. G. et al. Functional characterization of CD4⁺ T cell receptors crossreactive for SARS-CoV-2 and endemic coronaviruses. *J. Clin. Invest.* **131**, 146922 (2021).

[PubMed](#) [Article](#) [Google Scholar](#)

16. 16.

van der Leun, A. M., Thommen, D. S. & Schumacher, T. N. CD8⁺ T cell states in human cancer: insights from single-cell analysis. *Nat. Rev. Cancer* **20**, 218–232 (2020).

[PubMed](#) [PubMed Central](#) [Article](#) [CAS](#) [Google Scholar](#)

17. 17.

Guo, X. et al. Global characterization of T cells in non-small-cell lung cancer by single-cell sequencing. *Nat. Med.* **24**, 978–985 (2018).

[CAS](#) [PubMed](#) [Article](#) [Google Scholar](#)

18. 18.

Pizzolla, A. et al. Influenza-specific lung-resident memory T cells are proliferative and polyfunctional and maintain diverse TCR profiles. *J. Clin. Invest.* **128**, 721–733 (2018).

[PubMed](#) [PubMed Central](#) [Article](#) [Google Scholar](#)

19. 19.

Pearce, E. L. et al. Control of effector CD8⁺ T cell function by the transcription factor eomesodermin. *Science* **302**, 1041–1043 (2003).

[ADS](#) [CAS](#) [PubMed](#) [Article](#) [Google Scholar](#)

20. 20.

Chihara, N. et al. Induction and transcriptional regulation of the co-inhibitory gene module in T cells. *Nature* **558**, 454–459 (2018).

[ADS](#) [CAS](#) [PubMed](#) [PubMed Central](#) [Article](#) [Google Scholar](#)

21. 21.

Scott, A. C. et al. TOX is a critical regulator of tumour-specific T cell differentiation. *Nature* **571**, 270–274 (2019).

[CAS](#) [PubMed](#) [PubMed Central](#) [Article](#) [Google Scholar](#)

22. 22.

Yao, C. et al. Single-cell RNA-seq reveals TOX as a key regulator of CD8⁺ T cell persistence in chronic infection. *Nat. Immunol.* **20**, 890–901 (2019).

[CAS](#) [PubMed](#) [PubMed Central](#) [Article](#) [Google Scholar](#)

23. 23.

Seo, H. et al. TOX and TOX2 transcription factors cooperate with NR4A transcription factors to impose CD8⁺ T cell exhaustion. *Proc. Natl Acad. Sci. USA* **116**, 12410–12415 (2019).

[CAS](#) [PubMed](#) [PubMed Central](#) [Article](#) [Google Scholar](#)

24. 24.

Mackay, L. K. et al. Hobit and Blimp1 instruct a universal transcriptional program of tissue residency in lymphocytes. *Science* **352**, 459–463 (2016).

[ADS](#) [CAS](#) [PubMed](#) [Article](#) [Google Scholar](#)

25. 25.

Kok, L. et al. A committed tissue-resident memory T cell precursor within the circulating CD8⁺ effector T cell pool. *J. Exp. Med.* **217**, e20191711 (2020).

[CAS](#) [PubMed](#) [PubMed Central](#) [Article](#) [Google Scholar](#)

26. 26.

Topalian, S. L., Taube, J. M. & Pardoll, D. M. Neoadjuvant checkpoint blockade for cancer immunotherapy. *Science* **367**, eaax0182 (2020).

[CAS](#) [PubMed](#) [PubMed Central](#) [Article](#) [Google Scholar](#)

27. 27.

Behr, F. M. et al. Tissue-resident memory CD8⁺ T cells shape local and systemic secondary T cell responses. *Nat. Immunol.* **21**, 1070–1081 (2020).

[CAS](#) [PubMed](#) [Article](#) [Google Scholar](#)

28. 28.

Skoulidis, F. et al. *STK11/LKB1* mutations and PD-1 inhibitor resistance in *KRAS*-mutant lung adenocarcinoma. *Cancer Discov.* **8**, 822–835 (2018).

[CAS](#) [PubMed](#) [PubMed Central](#) [Article](#) [Google Scholar](#)

29. 29.

Smith, K. N. et al. Persistent mutant oncogene specific T cells in two patients benefitting from anti-PD-1. *J. Immunother. Cancer* **7**, 40 (2019).

[PubMed](#) [PubMed Central](#) [Article](#) [Google Scholar](#)

30. 30.

Anagnostou, V. et al. Evolution of neoantigen landscape during immune checkpoint blockade in non-small cell lung cancer. *Cancer Discov.* **7**, 264–276 (2017).

[CAS](#) [PubMed](#) [Article](#) [Google Scholar](#)

31. 31.

Cottrell, T. R. et al. Pathologic features of response to neoadjuvant anti-PD-1 in resected non-small-cell lung carcinoma: a proposal for quantitative immune-related pathologic response criteria (irPRC). *Ann. Oncol.* **29**, 1853–1860 (2018).

[CAS](#) [PubMed](#) [PubMed Central](#) [Article](#) [Google Scholar](#)

32. 32.

Anagnostou, V. et al. Multimodal genomic features predict outcome of immune checkpoint blockade in non-small-cell lung cancer. *Nat.*

Cancer **1**, 99–111 (2020).

[PubMed](#) [PubMed Central](#) [Article](#) [Google Scholar](#)

33. 33.

Jones, S. et al. Personalized genomic analyses for cancer mutation discovery and interpretation. *Sci. Transl. Med.* **7**, 283ra53 (2015).

[PubMed](#) [PubMed Central](#) [Article](#) [CAS](#) [Google Scholar](#)

34. 34.

Carlson, C. S. et al. Using synthetic templates to design an unbiased multiplex PCR assay. *Nat. Commun.* **4**, 2680 (2013).

[ADS](#) [PubMed](#) [PubMed Central](#) [Article](#) [CAS](#) [Google Scholar](#)

35. 35.

Harndahl, M. et al. Peptide binding to HLA class I molecules: homogenous, high-throughput screening, and affinity assays. *J. Biomol. Screen.* **14**, 173–180 (2009).

[CAS](#) [PubMed](#) [Article](#) [Google Scholar](#)

36. 36.

Sylvester-Hvid, C. et al. Establishment of a quantitative ELISA capable of determining peptide - MHC class I interaction. *Tissue Antigens* **59**, 251–258 (2002).

[CAS](#) [PubMed](#) [Article](#) [Google Scholar](#)

37. 37.

O'Flanagan, C. H. et al. Dissociation of solid tumor tissues with cold active protease for single-cell RNA-seq minimizes conserved collagenase-associated stress responses. *Genome Biol.* **20**, 210 (2019).

[PubMed](#) [PubMed Central](#) [Article](#) [CAS](#) [Google Scholar](#)

38. 38.

van den Brink, S. C. et al. Single-cell sequencing reveals dissociation-induced gene expression in tissue subpopulations. *Nat. Methods* **14**, 935–936 (2017).

[Article](#) [CAS](#) [Google Scholar](#)

39. 39.

Li, H. et al. Dysfunctional CD8 T cells form a proliferative, dynamically regulated compartment within human melanoma. *Cell* **181**, 747 (2020).

[CAS](#) [PubMed](#) [Article](#) [Google Scholar](#)

40. 40.

Stuart, T. et al. Comprehensive integration of single-cell data. *Cell* **177**, 747–1902 (2019).

[Article](#) [CAS](#) [Google Scholar](#)

41. 41.

Huang, M. et al. SAVER: gene expression recovery for single-cell RNA sequencing. *Nat. Methods* **15**, 539–542 (2018).

[CAS](#) [PubMed](#) [PubMed Central](#) [Article](#) [Google Scholar](#)

42. 42.

Leek, J. T., Johnson, W. E., Parker, H. S., Jaffe, A. E. & Storey, J. D. The sva package for removing batch effects and other unwanted variation in high-throughput experiments. *Bioinformatics* **28**, 882–883 (2012).

[CAS](#) [PubMed](#) [PubMed Central](#) [Article](#) [Google Scholar](#)

43. 43.

Johnson, W. E., Li, C. & Rabinovic, A. Adjusting batch effects in microarray expression data using empirical Bayes methods. *Biostatistics* **8**, 118–127 (2007).

[PubMed](#) [MATH](#) [Article](#) [Google Scholar](#)

44. 44.

Hotelling, H. *Relations Between Two Sets of Variates* Vol. 28, 321–377 (Biometrika, 1936).

45. 45.

Härdle, W. K. & Simar, L. *Applied Multivariate Statistical Analysis* 1st edn (Springer-Verlag, 2003).

46. 46.

McCulloch, C. E., Searle, S. R. & Neuhaus, J. M. *Generalized, Linear and Mixed Models* 2nd edn (Wiley, 2008).

47. 47.

Benjamini, Y. & Hochberg, Y. Controlling the false discovery rate: a practical and powerful approach to multiple testing. *J. R. Stat. Soc. B* **57**, 289–300 (1995).

[MathSciNet](#) [MATH](#) [Google Scholar](#)

48. 48.

Belarif, L. et al. IL-7 receptor blockade blunts antigen-specific memory T cell responses and chronic inflammation in primates. *Nat. Commun.* **9**, 4483 (2018). 10.1038/s41467-018-06804-y

[ADS](#) [PubMed](#) [PubMed Central](#) [Article](#) [CAS](#) [Google Scholar](#)

[Download references](#)

Acknowledgements

We thank the FEST and TCR Immunogenomics Core (FTIC) and the Experimental and Computational Genomics Core (ECGC) at the Sidney Kimmel Comprehensive Cancer Center; P. F. Robbins and R. Yossef for assistance with developing TCR cloning methods; G. Pereira and A. Curry from the Johns Hopkins Upper Aerodigestive Biorepository; the Melanoma DMT Tissue Repository Team and Memorial Sloan Kettering; I. Beadles and C. Barkley for clinical support; and K. Maly, L. Hartman, R. Carlson and our respective administrative teams. Graphical images were created by BioRender.com. This work was funded by grants from the Lung Cancer Foundation of America (K.N.S.), The Mark Foundation for Cancer Research (D.M.P., J.M.T., V.E.V. and V.A.), The SU2C/Mark Foundation Lung Cancer Dream Team Convergence Award (D.M.P.), the SU2C INTIME and SU2C-LUNGevity-American Lung Association Lung Cancer Interception Dream Team (J.R.B. and V.E.V.), Bristol-Myers Squibb, the SU2C DCS International Translational Cancer Research Dream Team (SU2C-AACR-DT1415, V.E.V.), The IASLC Foundation (K.N.S.), Swim Across America (K.N.S. and V.A.), The LUNGevity Foundation (K.N.S. and V.A.), The Commonwealth Foundation (K.N.S., S.Z., D.M.P. and S.Y.), The Banks Family Foundation (M. Brock), Subsidies for Current Expenditures to Private Institutions of Higher Education from the PMAC, through a sub-award from Juntendo University (M. Brock), the Dr. Miriam and Sheldon G. Adelson Medical Research Foundation (V.E.V.), The Virginia and D.K. Ludwig Fund for Cancer Research (B.V., K.W.K. and S.Z.), the Ludwig Center for Cancer Immunotherapy at Memorial Sloan Kettering (T.M.), the Cancer Research Institute (T.M.), the Parker Institute for Cancer Immunotherapy (T.M.), The Lustgarten Foundation for Pancreatic Cancer Research (B.V., K.W.K. and S.Z.), The Conquer Cancer Foundation of ASCO (K.A.M. and J.E.R.), Bloomberg Philanthropies, the Maryland Cigarette Restitution Fund (S.Y.), the V Foundation (V.A. and V.E.V.), the Allegheny Health Network–Johns Hopkins Research Fund (V.A. and V.E.V.), the Damon Runyon Cancer Research Foundation (CI-98-

18, M.D.H.), US NIH grants R37CA251447 (K.N.S.), R01HG010889 (H.J.), R01HG009518 (H.J.), R01CA121113 (V.A. and V.E.V.), R01CA217169 (J.E.C.), R01CA240472 (J.E.C.), CA62924 (B.V. and K.W.K.), T32 CA193145 (T.R.C.), T32 CA009110 (J.X.C.) and T32 GM136577 (B.V. and K.W.K.), and NIH Cancer Center Support Grants (P30 CA008748 and P30 CA006973). Stand Up To Cancer is a programme of the Entertainment Industry Foundation administered by the American Association for Cancer Research.

Author information

Author notes

1. Zhicheng Ji

Present address: Department of Biostatistics and Bioinformatics, Duke University School of Medicine, Durham, NC, USA

2. Tricia R. Cottrell

Present address: Ontario Institute for Cancer Research, Queens University, Kingston, Ontario, Canada

3. Jarushka Naidoo

Present address: Beaumont Hospital Dublin, RCSI University of Medicine and Health Science, Dublin, Ireland

4. Joshua E. Reuss

Present address: Georgetown Lombardi Comprehensive Cancer Center at Georgetown University, Washington, DC, USA

5. These authors contributed equally: Justina X. Caushi, Jiajia Zhang

Affiliations

1. Bloomberg~Kimmel Institute for Cancer Immunotherapy at Johns Hopkins, Baltimore, MD, USA

Justina X. Caushi, Jiajia Zhang, Richard Blosser, Ada Tam, Valsamo Anagnostou, Tricia R. Cottrell, Haidan Guo, Hok Yee Chan, Dipika Singh, Sampriti Thapa, Arbor G. Dykema, Poromendro Burman, Begum Choudhury, Luis Aparicio, Laurene S. Cheung, Mara Lanis, Zineb Belcaid, Margueritta El Asmar, Jarushka Naidoo, Kristen A. Marrone, Victor E. Velculescu, Janis M. Taube, Julie R.

Brahmer, Patrick M. Forde, Srinivasan Yegnasubramanian, Drew M. Pardoll & Kellie N. Smith

2. The Mark Center for Advanced Genomics and Imaging at Johns Hopkins, Baltimore, MD, USA

Justina X. Caushi, Jiajia Zhang, Tricia R. Cottrell, Haidan Guo, Hok Yee Chan, Dipika Singh, Sampriti Thapa, Arbor G. Dykema, Poromendro Burman, Begum Choudhury, Luis Aparicio, Laurene S. Cheung, Janis M. Taube, Srinivasan Yegnasubramanian, Drew M. Pardoll & Kellie N. Smith

3. Sidney Kimmel Comprehensive Cancer Center at Johns Hopkins, Baltimore, MD, USA

Justina X. Caushi, Jiajia Zhang, Ajay Vaghasia, Emily Han-Chung Hsiue, Brian J. Mog, Richard Blosser, Ada Tam, Valsamo Anagnostou, Tricia R. Cottrell, Haidan Guo, Hok Yee Chan, Dipika Singh, Sampriti Thapa, Arbor G. Dykema, Poromendro Burman, Begum Choudhury, Luis Aparicio, Laurene S. Cheung, Mara Lanis, Zineb Belcaid, Margueritta El Asmar, Peter B. Illei, Rulin Wang, Jennifer Meyers, Kornel Schuebel, Anuj Gupta, Alyza Skaist, Sarah Wheelan, Jarushka Naidoo, Kristen A. Marrone, Malcolm Brock, Jinny Ha, Errol L. Bush, Joshua E. Reuss, Victor E. Velculescu, Kenneth W. Kinzler, Shabin Zhou, Bert Vogelstein, Janis M. Taube, Julie R. Brahmer, Patrick M. Forde, Srinivasan Yegnasubramanian, Drew M. Pardoll & Kellie N. Smith

4. Department of Biostatistics, Bloomberg School of Public Health, Johns Hopkins University, Baltimore, MD, USA

Zhicheng Ji, Boyang Zhang, Wenpin Hou & Hongkai Ji

5. Ludwig Center and Howard Hughes Medical Institute at Johns Hopkins, Baltimore, MD, USA

Emily Han-Chung Hsiue, Brian J. Mog, Kenneth W. Kinzler, Shabin Zhou & Bert Vogelstein

6. Lustgarten Pancreatic Cancer Research Laboratory, Sidney Kimmel Comprehensive Cancer Center, Johns Hopkins University, Baltimore, MD, USA

Emily Han-Chung Hsiue, Brian J. Mog, Kenneth W. Kinzler, Shabin Zhou & Bert Vogelstein

7. Immunitrack, Copenhagen, Denmark

Sune Justesen

8. Department of Medicine, Memorial Sloan Kettering Cancer Center and Weill Cornell Medicine, New York, NY, USA

Bernard J. Park, Matthew Bott, David R. Jones, Jamie E. Chaft, Matthew D. Hellmann & Taha Merghoub

9. The Swim Across America and Ludwig Collaborative Laboratory, Immunology Program, Parker Institute for Cancer Immunotherapy at Memorial Sloan Kettering Cancer Center, New York, NY, USA

Taha Merghoub

10. Human Oncology and Pathogenesis Program, Memorial Sloan Kettering Cancer Center, New York, NY, USA

Taha Merghoub

Authors

1. Justina X. Caushi
[View author publications](#)

You can also search for this author in [PubMed](#) [Google Scholar](#)

2. Jiajia Zhang

[View author publications](#)

You can also search for this author in [PubMed](#) [Google Scholar](#)

3. Zhicheng Ji

[View author publications](#)

You can also search for this author in [PubMed](#) [Google Scholar](#)

4. Ajay Vaghasia

[View author publications](#)

You can also search for this author in [PubMed](#) [Google Scholar](#)

5. Boyang Zhang

[View author publications](#)

You can also search for this author in [PubMed](#) [Google Scholar](#)

6. Emily Han-Chung Hsieue

[View author publications](#)

You can also search for this author in [PubMed](#) [Google Scholar](#)

7. Brian J. Mog

[View author publications](#)

You can also search for this author in [PubMed](#) [Google Scholar](#)

8. Wenpin Hou

[View author publications](#)

You can also search for this author in [PubMed](#) [Google Scholar](#)

9. Sune Justesen

[View author publications](#)

You can also search for this author in [PubMed](#) [Google Scholar](#)

10. Richard Blosser

[View author publications](#)

You can also search for this author in [PubMed](#) [Google Scholar](#)

11. Ada Tam

[View author publications](#)

You can also search for this author in [PubMed](#) [Google Scholar](#)

12. Valsamo Anagnostou

[View author publications](#)

You can also search for this author in [PubMed](#) [Google Scholar](#)

13. Tricia R. Cottrell

[View author publications](#)

You can also search for this author in [PubMed](#) [Google Scholar](#)

14. Haidan Guo

[View author publications](#)

You can also search for this author in [PubMed](#) [Google Scholar](#)

15. Hok Yee Chan

[View author publications](#)

You can also search for this author in [PubMed](#) [Google Scholar](#)

16. Dipika Singh

[View author publications](#)

You can also search for this author in [PubMed](#) [Google Scholar](#)

17. Sampriti Thapa

[View author publications](#)

You can also search for this author in [PubMed](#) [Google Scholar](#)

18. Arbor G. Dykema

[View author publications](#)

You can also search for this author in [PubMed](#) [Google Scholar](#)

19. Poromendro Burman

[View author publications](#)

You can also search for this author in [PubMed](#) [Google Scholar](#)

20. Begum Choudhury

[View author publications](#)

You can also search for this author in [PubMed](#) [Google Scholar](#)

21. Luis Aparicio

[View author publications](#)

You can also search for this author in [PubMed](#) [Google Scholar](#)

22. Laurene S. Cheung

[View author publications](#)

You can also search for this author in [PubMed](#) [Google Scholar](#)

23. Mara Lanis

[View author publications](#)

You can also search for this author in [PubMed](#) [Google Scholar](#)

24. Zineb Belcaid

[View author publications](#)

You can also search for this author in [PubMed](#) [Google Scholar](#)

25. Margueritta El Asmar

[View author publications](#)

You can also search for this author in [PubMed](#) [Google Scholar](#)

26. Peter B. Illei

[View author publications](#)

You can also search for this author in [PubMed](#) [Google Scholar](#)

27. Rulin Wang

[View author publications](#)

You can also search for this author in [PubMed](#) [Google Scholar](#)

28. Jennifer Meyers

[View author publications](#)

You can also search for this author in [PubMed](#) [Google Scholar](#)

29. Kornel Schuebel

[View author publications](#)

You can also search for this author in [PubMed](#) [Google Scholar](#)

30. Anuj Gupta

[View author publications](#)

You can also search for this author in [PubMed](#) [Google Scholar](#)

31. Alyza Skaist

[View author publications](#)

You can also search for this author in [PubMed](#) [Google Scholar](#)

32. Sarah Wheelan

[View author publications](#)

You can also search for this author in [PubMed](#) [Google Scholar](#)

33. Jarushka Naidoo

[View author publications](#)

You can also search for this author in [PubMed](#) [Google Scholar](#)

34. Kristen A. Marrone

[View author publications](#)

You can also search for this author in [PubMed](#) [Google Scholar](#)

35. Malcolm Brock

[View author publications](#)

You can also search for this author in [PubMed](#) [Google Scholar](#)

36. Jinny Ha

[View author publications](#)

You can also search for this author in [PubMed](#) [Google Scholar](#)

37. Errol L. Bush

[View author publications](#)

You can also search for this author in [PubMed](#) [Google Scholar](#)

38. Bernard J. Park

[View author publications](#)

You can also search for this author in [PubMed](#) [Google Scholar](#)

39. Matthew Bott

[View author publications](#)

You can also search for this author in [PubMed](#) [Google Scholar](#)

40. David R. Jones

[View author publications](#)

You can also search for this author in [PubMed](#) [Google Scholar](#)

41. Joshua E. Reuss

[View author publications](#)

You can also search for this author in [PubMed](#) [Google Scholar](#)

42. Victor E. Velculescu

[View author publications](#)

You can also search for this author in [PubMed](#) [Google Scholar](#)

43. Jamie E. Chaft

[View author publications](#)

You can also search for this author in [PubMed](#) [Google Scholar](#)

44. Kenneth W. Kinzler

[View author publications](#)

You can also search for this author in [PubMed](#) [Google Scholar](#)

45. Shibin Zhou

[View author publications](#)

You can also search for this author in [PubMed](#) [Google Scholar](#)

46. Bert Vogelstein

[View author publications](#)

You can also search for this author in [PubMed](#) [Google Scholar](#)

47. Janis M. Taube

[View author publications](#)

You can also search for this author in [PubMed](#) [Google Scholar](#)

48. Matthew D. Hellmann

[View author publications](#)

You can also search for this author in [PubMed](#) [Google Scholar](#)

49. Julie R. Brahmer

[View author publications](#)

You can also search for this author in [PubMed](#) [Google Scholar](#)

50. Taha Merghoub

[View author publications](#)

You can also search for this author in [PubMed](#) [Google Scholar](#)

51. Patrick M. Forde

[View author publications](#)

You can also search for this author in [PubMed](#) [Google Scholar](#)

52. Srinivasan Yegnasubramanian

[View author publications](#)

You can also search for this author in [PubMed](#) [Google Scholar](#)

53. Hongkai Ji

[View author publications](#)

You can also search for this author in [PubMed](#) [Google Scholar](#)

54. Drew M. Pardoll

[View author publications](#)

You can also search for this author in [PubMed](#) [Google Scholar](#)

55. Kellie N. Smith

[View author publications](#)

You can also search for this author in [PubMed](#) [Google Scholar](#)

Contributions

A.V. and Z.J. contributed equally to this work. J.X.C., J.Z., S.Y., H.J., D.M.P. and K.N.S. conceived the project and wrote the manuscript. J.X.C., A.V., R.B., A.T., H.G., H.Y.C., D.S., M.E.A., S.T., A.G.D., B.C., L.S.C., R.W., J.M., K.S., A.G. and A.S. designed and performed functional T cell and single-cell experiments. T.R.C., J.M.T., P.B.I., E.L.B., J.H., M. Brock, J.E.R., P.M.F., J.R.B., K.A.M., J.N., B.J.P., D.R.J., M.D.H., J.E.C. and M.

Bott. provided pathologic assessments, response classifications and clinical annotation. E.H.-C.H., B.J.M., K.W.K., S.Z. and B.V. designed and optimized the CD8⁺ Jurkat cell line. V.A., V.E.V., M.L. and Z.B. performed whole-exome sequencing, mutation calls, neoantigen prediction and interpretation of genetic data. S.J. performed peptide–MHC binding and stability assays. J.Z., Z.J., B.Z., P.B., S.W., W.H., L.A., S.Y. and H.J. performed computational, bioinformatic and biostatistical analyses. T.M., D.M.P. and K.N.S. led analysis and interpretation of immunological experiments. All authors provided input on the manuscript. S.Y., H.J., D.M.P. and K.N.S. supervised all aspects of this work.

Corresponding authors

Correspondence to [Srinivasan Yegnasubramanian](#) or [Hongkai Ji](#) or [Drew M. Pardoll](#) or [Kellie N. Smith](#).

Ethics declarations

Competing interests

V.A. receives research funding from Bristol-Myers Squibb and Astra Zeneca. J.M.T. receives research funding from Bristol-Myers Squibb and serves a consulting/advisory role for Bristol-Myers Squibb, Merck, and AstraZeneca. P.B.I. receives research funding from Bristol-Myers Squibb and Erbe Elektromedizin GmbH and serves a consulting/advisory role for AstraZeneca and Veran Medical Technologies. J.N. receives research funding from AstraZeneca, Bristol-Myers Squibb, and Merck, and serves a consulting/advisory role for AstraZeneca, Daiichi Sankyo, Bristol-Myers Squibb, Merck, and Roche/Genentech. K.A.M. is a consultant for Amgen and AstraZeneca. D.R.J. is a consultant for More Health and AstraZeneca and a Steering Committee Member for Merck. B.J.P. is a consultant for AstraZeneca and Regeneron and has received honoraria from Intuitive Surgical. J.E.C. is a consultant for AstraZeneca, Genentech, Merck, Flame Bioscience, and Novartis. V.E.V. is a founder of Delfi Diagnostics and Personal Genome Diagnostics, serves on the Board of Directors and as a consultant for both organizations, and owns Delfi Diagnostics and Personal

Genome Diagnostics stock, which are subject to certain restrictions under university policy. Additionally, Johns Hopkins University owns equity in Delfi Diagnostics and Personal Genome Diagnostics. V.E.V. is an advisor to Bristol-Myers Squibb, Genentech, Merck, and Takeda Pharmaceuticals. Within the last five years, V.E.V. has been an advisor to Daiichi Sankyo, Janssen Diagnostics, and Ignyta. M.D.H. receives research support from Bristol-Myers Squibb; has been a compensated consultant for Merck, Bristol-Myers Squibb, AstraZeneca, Genentech/Roche, Nektar, Syndax, Mirati, Shattuck Labs, Immunai, Blueprint Medicines, Achilles, Arcus, and Natera; received travel support/honoraria from AstraZeneca, Eli Lilly, and Bristol-Myers Squibb; has options from Shattuck Labs, Immunai, and Arcus; and has a patent filed by his institution related to the use of tumor mutation burden to predict response to immunotherapy (PCT/US2015/062208), which has received licensing fees from PGDx. The Johns Hopkins University is in the process of filing patent applications related to technologies described in this paper on which E.H.-C.H., B.V., K.W.K. and S.Z. are listed as inventors. B.V. and K.W.K. are founders of Thrive Earlier Detection. K.W.K. is a consultant to and was on the Board of Directors of Thrive Earlier Detection. B.V., K.W.K. and S.Z. own equity in Exact Sciences. B.V., K.W.K. and S.Z. are founders of, hold or may hold equity in, and serve or may serve as consultants to manaT Bio, and hold or may hold equity in manaT Holdings, LLC. B.V., K.W.K., and S.Z. are founders of, hold equity in, and serve as consultants to Personal Genome Diagnostics. S.Z. has a research agreement with BioMed Valley Discoveries. K.W.K. and B.V. are consultants to Sysmex, Eisai, and CAGE Pharma and hold equity in CAGE Pharma. B.V. is a consultant to and holds equity in Catalio. K.W.K., B.V. and S.Z. are consultants to and hold equity in NeoPhore. The companies named above, as well as other companies, have licensed previously described technologies related to the work from this lab at Johns Hopkins University. Licenses to these technologies are or will be associated with equity or royalty payments to the inventors as well as to Johns Hopkins University. T.M. is a cofounder and holds equity in IMVAQ Therapeutics, is a consultant for Immunos Therapeutics, ImmunoGenesis, and Pfizer, receives research funding from Bristol-Myers Squibb, Surface Oncology, Kyn Therapeutics, Infinity Pharmaceuticals, Inc., Peregrine Pharmaceuticals, Inc., Adaptive Biotechnologies, Leap Therapeutics, Inc., and Aprea, and holds patents on applications related to

work on oncolytic viral therapy, alpha virus-based vaccines, neoantigen modeling, CD40, GITR, OX40, PD-1, and CTLA-4. J.R.B. serves an advisory/consulting role for Amgen, AstraZeneca, Bristol-Myers Squibb, Genentech/Roche, Eli Lilly, GlaxoSmithKline, Merck, Sanofi, and Regeneron, receives research funding from AstraZeneca, Bristol-Myers Squibb, Genentech/Roche, Merck, RAPT Therapeutics, Inc., and Revolution Medicines, and is on the Data and Safety Monitoring Board of GlaxoSmithKline, Janssen, and Sanofi. P.M.F. receives research support from AstraZeneca, Bristol-Myers Squibb, Novartis, and Kyowa, and has been a consultant for AstraZeneca, Amgen, Bristol-Myers Squibb, Daichii Sankyo, and Janssen and serves on a data safety and monitoring board for Polaris. S.Y. receives research funding from Bristol-Myers Squibb/Celgene, Janssen, and Cepheid, has served as a consultant for Cepheid, and owns founder's equity in Astra Therapeutics and Digital Harmonic. K.N.S., D.M.P., B.V. and K.W.K. have filed for patent protection on the MANAFEST technology described herein (serial no. 16/341,862). K.N.S., D.M.P., J.E.C., B.V., E.H.-C.H. D.M.P., K.W.K. and S.Z. have filed for patent protection on the p53 R248L mutation-specific TCR described herein (serial no. 63/168,878). D.M.P. is a consultant for Compugen, Shattuck Labs, WindMIL, Tempest, Immunai, Bristol-Myers Squibb, Amgen, Janssen, Astellas, Rockspring Capital, Immunomic, Dracen and owns founder's equity in manaT Holdings, LLC, WindMIL, Trex, Jounce, Anara, Tizona, Tieza, RAPT and receives research funding from Compugen, Bristol-Myers Squibb, and Anara. K.N.S. has received travel support/honoraria from Illumina, Inc., receives research funding from Bristol-Myers Squibb, Anara, and Astra Zeneca, and owns founder's equity in manaT Holdings, LLC. The terms of all these arrangements are being managed by the respective institutions in accordance with their conflict-of-interest policies.

Additional information

Peer review information *Nature* thanks Benny Chain, Aude Chapuis, Evan Newell and the other, anonymous, reviewer(s) for their contribution to the peer review of this work.

Publisher's note Springer Nature remains neutral with regard to jurisdictional claims in published maps and institutional affiliations.

Extended data figures and tables

Extended Data Fig. 1 Defining CD3⁺ T cell subsets in patients with non-small cell cancer treated with anti-PD-1.

a, FACS gating strategy for sorting CD3⁺ T cells. The gating strategy is shown for sorting live CD3⁺ T cells from tumour, normal lung, lymph node, or metastasis, when available, on a BD FACSaria. **b**, Patient and tissue compartment variability across clusters on UMAP. scRNA-seq–TCR-seq was performed on available resected biospecimens (tumour, adjacent NL, TDNL, and a brain metastasis) from 16 patients treated with neoadjuvant PD-1 blockade. CD3⁺ T cells stratified by patient are visualized using UMAP. Each cluster is annotated and marked by colour code. **c**, Barplots show the proportion of each T cell cluster in the TDNL, brain metastasis, tumour, and adjacent NL of each patient. Each cluster as shown on the UMAP is denoted by colour code. No clusters were driven by a particular patient based. **d**, A density plot of all CD3⁺ T cells on the UMAP, stratified by tissue compartment, is shown. Cells were obtained from 15 tumours, 12 adjacent NL specimens, and 3 TDNL. Because a metastasis was sequenced in only one patient, this specimen is not included in this analysis. **e**, The proportion (%) of total CD3⁺ T cells made up by each T cell cluster was compared between tumour ($n = 15$ biologically independent samples), adjacent NL ($n = 12$ biologically independent samples), and TDNL ($n = 3$ biologically independent samples). P values were obtained using Kruskal–Wallis Test and were adjusted for multiple comparisons using Benjamini–Hochberg method. Each dot represents a patient and all data points are shown. Individual data points are superimposed over a Box and Whiskers plot summarizing the data. The middle bar shows the median, with the lower and upper hinges corresponding to the 25th and 75th percentiles, respectively (interquartile range, IQR). The upper whisker extends from the hinge to the largest value no further than 1.5 * IQR from the hinge. The lower whisker extends from the hinge to the smallest value at most 1.5 * IQR of the hinge. **f**, Tissue-resident defining genes and core TRM gene set

signature on different T cell cluster. The top and middle violin plots show the expression of TRM-defining genes (ITGAE, ZNF683) by each cell in each cluster. The dashed line indicates the mean expression of the respective gene among all CD3⁺ T cells. Expression values were log₁₀ transformed for visualization. The bottom violin plot shows the TRM gene-set score for each cluster. This gene-set is comprised of TRM-associated genes as published previously ([Supplementary Data 2.1](#)). The dashed line shows the mean TRM gene-set score among all T cells. Because the proliferating cluster is driven by proliferation-associated genes and is comprised of mixed cell types, this cluster was not shown in the violin plots.

Extended Data Fig. 2 MANA-specific TCRs detected in patient without MPR MD01-004 using MANAFEST and ViraFEST assays.

Antigen-specific responses identified using the MANAFEST assay are shown for patient without MPR MD01-004. MANAFEST assays for all other patients are shown in Supplementary Data [5](#). Each antigen-specific clonotypic expansion is colour coded to indicate if the clone was not detected in the single-cell data (blue), detected in the single-cell data but not tested via TCR cloning (green), or detected in the single-cell data and validated with TCR cloning (red). Data are shown as the percent of MANAFEST+ clonotypes among CD8⁺ T cells after 10 day culture.

Extended Data Fig. 3 Peripheral dynamics and cross-compartment representation of antigen-specific T cells.

Bulk TCRseq was performed on pre- and post-treatment tissue (left panels) and peripheral blood (right panels) for each patient in whom antigen-specific TCRs were identified by ViraFEST/MANAFEST (as shown in Extended Data Fig. [2](#) and Supplementary Data [5](#)). Data are shown as the frequency of each influenza-, CEF-, and MANA-specific TCR clonotype among all TCRs detected by bulk TCR sequencing of the indicated tissue or peripheral blood time point. Antigen-specific clonotypes were not detected by bulk TCRseq of any available tissue/peripheral blood time point in

patient NY016-025. TDLN, tumour draining lymph node; DLN, draining lymph node.

Extended Data Fig. 4 TCR cloning validation of MANA-specific TCRs and MANA binding kinetics.

Ten TCRs identified via the MANAFEST assay were selected for TCR cloning and transfer into our NFAT/luciferase Jurkat reporter system. Seven of these TCRs recognized the cognate MANA. **a**, In MD01-005, three TCR V β clonotypes recognizing the ARVCF H497L-derived EVIVPLSGW MANA were identified by MANAFEST. Single-cell analysis determined that the V β CDR3 s CASNKLGYQPQHF and CASSLLENQPQHF were consistently detected in the same cell and paired with the same V α CDR3, CALSMGGNEKLT, likely the result of incomplete allelic exclusive at the beta locus. To validate that these TCRs recognized MD01-005-MANA7, and to determine which V β CDR3 was responsible for recognition in the case of incomplete allelic exclusion, all three TCRs were cloned into the Jurkat NFAT luciferase reporter system and tested against autologous LCL loaded with titrating concentrations of MD01-005-MANA7. Data are shown as relative luminescence units (RLU) for MD01-005-MANA7 (solid red square), the cognate wild-type peptide (open red square), or MD01-005-MANA8, which was predicted to bind A*25:01, for each individual TCR. **b**, In patient without MPR MD01-004, four TCRs recognizing the p53 R248L-derived NSSCMGGMNL R MANA (MD01-004-MANA12) were identified by MANAFEST and were detected in the single-cell data. Each V β chain paired exclusively with a single V α chain. These four TCRs were cloned into the Jurkat NFAT/luciferase reporter system and tested against autologous LCL loaded with titrating concentrations of MD01-004-MANA12. Data are shown as relatively luminescence units (RLU) in response to MD01-004-MANA12 (solid blue square) or the cognate wild-type peptide (open blue square). **c**, In patient without MPR MD043-011, a TCR recognizing the CARM1 R208W-derived FAAQAGAWKIY MANA (MD043-011-MANA36) was a candidate for positivity by MANAFEST and was detected in the single-cell data. This V β chain paired exclusively with a single V α chain. This TCR was cloned into the Jurkat NFAT/luciferase reporter system and tested against autologous LCL loaded with titrating concentrations of MD043-011-MANA36. Data are shown as

relatively luminescence units (RLU) in response to MD01-004-MANA12 (solid green square) or the cognate wild-type peptide (open green square). **d**, The affinity of MD01-005-MANA7 for HLA A*25:01 was assessed using a luminescent oxygen channeling immunoassay (LOCI, left). This is a proximity-based system using a “donor” and “acceptor” bead, each conjugated with an epitope tag. When the donor bead is excited with light at 650nm and can activate an acceptor bead, resulting in a signal at 520-620nm, which can be quantified per second as a surrogate of affinity. A higher number of counts per second indicates higher affinity of the peptide:HLA pair. Data are shown as the number of counts per second for titrating concentrations of MD01-005-MANA7 (solid blue square), the cognate wild-type (open blue square), MD01-005-MANA8, which is predicted to bind HLA A*68:01 (black circle), or no peptide (star). Stability of these same peptides in the HLA A*68:01 complex was also evaluated using a urea-based assay, whereby the stability of the peptide:HLA complex is measured at increasing concentrations of urea (right). Data are shown as the absorbance at 450nm. Data points represent the mean +/- s.d. of two independent experiments. **e**, Binding (top left) and stability (top right) assays were conducted as in (b) for the p53 R248L-derived MD01-004-MANA12 (solid green square), the cognate wild-type peptide (open green square), a positive control peptide for HLA A*68:01 (orange diamond), the YTAVPLVYV peptide which is predicted to bind A*68:01 (black circle), or no peptide (black star). Data points represent the mean +/- s.d. of two independent experiments. To determine if MD01-004-MANA12 is endogenously processed and presented by HLA A*68:01, COS-7 cells were transfected with HLA-A*68:01 plasmid and p53 R248L mutant plasmid or p53 wild type plasmid. HLA- and p53-transfected COS-7 cells, autologous APC loaded with MD01-004-MANA12, and HLA-A*68:01-transfected COS-7 were co-cultured with CD8+ Jurkat reporter cells expressing the MD01-004-MANA12-reactive TCR, V β : CATTGGQNTEAFF, V α : CILSGANNLFF. Data are shown as relative luminescence units (RLU) for each condition (bottom).

Extended Data Fig. 5 Refined clustering on CD8 T cells.

a, A heat map shows the top differential genes, ranked by average fold change, for each refined CD8 T cell cluster. 5,000 cells (or all cells in the

cluster if cluster size <5000 cells) were randomly sampled from each cluster for visualization ($n = 16$ patients). **b**, Violin plots show the log₁₀ expression of the TRM-defining genes, ITGAE (top) and ZNF683 (HOBIT, middle), and a TRM gene-set score (bottom) for each CD8 T cell cluster. The dashed line indicates the mean expression of the respective gene or gene-set score among all CD8 T cells. Because the proliferating cluster is driven by proliferation-associated genes and represents mixed cell types, this cluster was not shown in the plot. **c**, 2D UMAP red-scale projection of canonical T cell subset marker genes, cell subset selective genes, and immune checkpoints on CD8 T cell subsets. **d**, A heat map shows the proportion of each refined CD8 T cell cluster (Fig. 2b) that is found within each global UMAP T cell cluster (Fig. 1b). This enables visualization of the “parent” cluster for the refined CD8 T cell clusters. **e**, A violin plot shows the exhaustion gene-set score, comprised of a published exhaustion gene list ([Supplementary Data 2.2](#)), for each refined CD8 T cell cluster. The dashed line shows the mean exhaustion gene-set score among all CD8 T cells. Because the proliferating cluster is driven by proliferation-associated genes and represents mixed cell types, this cluster was not shown in the plot. **f**, CD8⁺ T cell clonotypic cluster composition. The top 50 CD8⁺ TCR clonotypes in the tumour are shown for each patient, and the proportion of each clonotype that was found within each cluster is designated by the colour code.

[Extended Data Fig. 6 Distinct phenotype of antigen-specific T cells.](#)

a, Distribution of MANA-specific T cells on UMAP. Individual MANA-specific clonotypes are shown on the UMAP, stratified by tissue compartment and patient ID. Each colour represents a unique MANA-specific clonotype, and each symbol represents a patient. **b**, Distribution of EBV-specific T cells on UMAP. Individual EBV-specific clonotypes are shown on the UMAP, stratified by tissue compartment. Each colour represents a unique EBV-specific clonotype and each symbol represents a patient. **c**, Distribution of influenza-specific T cells on UMAP. Individual influenza-specific clonotypes are shown on the UMAP, stratified by tissue compartment and patient ID. Each colour represents a unique influenza-specific clonotype, and each symbol represents a patient. The CD8 T cell

clusters are annotated according to the designation in Fig. 2b. **d**, The barplot (upper) shows the proportion of antigen-specific T cells among total CD8 T cells by tissue compartment (blue bar, adjacent NL; yellow bar, tumour). The dotplot (bottom) shows the proportion of antigen-specific T cells stratified by subset, with the size of the dot representing the proportion among total CD8 T cells (blue dot, adjacent NL; yellow dot, tumour). **e**, TIL and adjacent NL CD8 T cells were downsampled to equal numbers of cells on UMAP before visualization of antigen-specific clonotypes in tumour (left) and adjacent normal lung (right). **f**, The immune checkpoint score and exhaustion score of antigen-specific T cells. A violin plot shows a composite immune checkpoint score (left) and exhaustion score (right) for EBV(purple)-, influenza (blue)-, and MANA (red)-specific T cells.

Extended Data Fig. 7 IL-7-induced gene signature between MANA-specific and influenza-specific TIL.

TIL from patient MD01-004 were cultured with MD01-004-MANA-12 or influenza A peptide and titrating concentrations of recombinant human IL-7, followed by coupled scRNA-seq–TCR-seq. A total of 814 influenza-specific (410 co-cultured with influenza peptide, 404 co-cultured with MANA peptide) and 581 MANA-specific TIL (366 co-cultured with influenza peptide, 215 co-cultured with MANA peptide) were detected in the single-cell data from a single experiment and were analysed. **a**, Composite expression of an IL-7 gene set by influenza-specific and MANA-specific TIL (as determined by their TCR V β CDR3) stimulated with cognate or non-cognate antigen is shown. **b**, Dose–response curve showing the fold change of averaged expression of IL-7-induced genes ([Supplementary Data 2.3](#)) that significantly changed from baseline (no IL-7 vs 0.1 ng/ml) in influenza-specific (red) or MANA-specific (blue) T cells. Comparisons were performed using two-sided Wilcoxon rank sum test and adjusted for multiple comparisons using BH method.

Extended Data Fig. 8 Cloning and dose response of antigen-specific T cells.

a–c, Cloning and screening of TCRs corresponding to CD8 T cells with highly differential gene expression relative to influenza-specific T cells. Seven TCRs were selected from the refined CD8 sc data based on highly differential gene expression relative to influenza-specific T cells. These TCRs were cloned into the Jurkat/NFAT luciferase reporter system and first screened against autologous LCL pre-loaded with pools of putative MANA peptides (10 μ g/ml) based on the respective patient's WES and MANA predictions. Three TCRs recognized a MANA peptide pool, one each from patients MD01-005 (**a**), MD01-004 (**b**), and MD043-011 (**c**). The reactive MANA was then mapped from the reactive peptide pool by stimulating the TCR-transfected Jurkat cell with autologous LCL pre-loaded with 10 μ g/ml of each individual MANA within the reactive pool (centre). Dose–response curves were then generated for each MANA-specific TCR (right). Data are shown as relative luminescence units. A (+) sign indicates the positive response. **d**, Functional characterization of MANAFEST-identified and screening-identified TCRs. 2D projection of clones identified from the MANAFEST assay (red) and clones identified via cloning of TCRs corresponding to T cells with differential gene expression relative to influenza-specific T cells (green) is shown for patients MD01-004, MD01-005, and MD043-011. CD8 T cell clusters are marked with the same colour code as Fig. [2b](#). **e**, Viral-specific TCRs and MANA-specific TCRs from one patient with MPR and two patients without MPR were cloned into the Jurkat reporter system and tested against titrating concentrations of relevant peptide. The average log₁₀ relative luminescence of viral-specific TCRs (blue, 3 clonotypes from 3 different patients), MANA-specific MPR TCRs (green, 3 clonotypes from 1 patient with MPR), and MANA-specific non-MPR TCRs (red, 7 clonotypes from 2 patients without MPR) was compared at each peptide titration. Data are shown as a Box and Whiskers plot. The middle bar shows the median, with the lower and upper hinges corresponding to the 25th and 75th percentiles, respectively (interquartile range, IQR). The upper whisker extends from the hinge to the largest value no further than 1.5 * IQR from the hinge. The lower whisker extends from the hinge to the smallest value at most 1.5 * IQR of the hinge. Comparisons of relative luminescence units for viral-specific vs MANA-specific T cell clonotypes at different titrations were performed using two-sided Wilcoxon rank sum test. ns: $P > 0.05$; *, $0.01 < P < 0.05$.

Extended Data Fig. 9 Patient representation of antigen-specific clonotypes.

a, b, Barplots summarize the total number of unique tumour-infiltrating clonotypes (**a**) and cells (**b**), stratified by antigen specificity and method of detection (MANAFEST or based on the TRM gene signature and cloning/peptide screen). Different colours represent the patient identity. **c**, Visualization of clonotypes included in the MANA-specific analysis. The individual UMAP projections of clonotypes that were validated (left) and were not validated (right) by TCR cloning are shown. Of the cells that corresponded to a MANAFEST-identified, MANA-specific clonotype that was detected in the single-cell data, >94% were validated by the jurkat/luciferase TCR cloning system.

Extended Data Fig. 10 Signatures of MANA-specific T cells according to response and tissue compartment.

a, Exhaustion score and co-expression of immune checkpoints/effectector/memory function gene on MANA-specific TIL. Violin plot shows the exhaustion gene-set score ([Supplementary Data 2.2](#)) of MANA-specific TIL of non-MPR (red, $n = 3$) and MPR (light blue, $n = 3$) tumours. Comparisons were performed at the individual cell level using two-sided Wilcoxon rank sum test without multiple comparison adjustment. **b**, Heat map shows co-expression of immune checkpoints and effector/memory genes on MANA-specific TIL. Each column represent a cell. The exhaustion score, response status, and patient IDs are designated by the relevant colour bar. For visualization, MANA-specific T cells were downsampled to the same number of cells from MPR ($n = 3$) and non-MPR ($n = 3$). **c**, Top ranked genes correlated with the immune checkpoint score in MANA-specific TIL. Barplots show the correlation coefficients of the top ranked genes highly correlated with the immune checkpoint score in MPR (left) and non-MPR (right) MANA-specific TIL. **d**, MANA-specific T cells found in the tumour (red triangles) and TD LN (blue triangles) of patients MD01-004, MD01-005, and MD043-011 were projected on the refined CD8 UMAP. **e**, Expression of selective genes is shown for MANA-specific T cells in the tumour and TD LN ($n = 3$). **f**, MANA-specific T cells found in

the tumour (red triangle) and brain metastasis (purple triangle) are shown on the UMAP for patient MD043-011. **g**, The scatterplot shows the average expression of genes comparing all refined CD8 T cells from the primary tumour and metastatic brain resection in patient MD043-011. The top differential genes enriched in the brain metastasis are labelled in red. Comparisons were performed at the individual cell level using two-sided Wilcoxon rank sum test. *P*-value adjustment was performed using bonferroni correction. A complete list of differential genes comparing primary tumour at resection vs. the distant brain metastasis is shown in [Supplementary Data 1.5](#). CD8 T cell clusters are marked by the same colour code as Fig. 2b.

Extended Data Fig. 11 Canonical correlations of CD8 T cell clusters with pathologic response.

The canonical correlation between pathologic response status and CD8 T cell clusters vs. a MANA-specific T cell-enriched cluster was evaluated. **a**, Selection of MANA-specific T cell enriched clusters (Proliferating, TRM(IV), TRM (V) and TRM (II)) based on >2 fold change (red dotted line) of MANA-specific T cell frequency relative to random expectation. The above 4 clusters were combined as a ‘MANA-combined’ cluster. **b**, Combined MANA-specific T cell enriched clusters showed the highest canonical correlation with pathologic response. **c**, PCA of pseudobulk gene expression from all CD8 T cell clusters for individual tumour samples ($n = 15$, 6 MPRs and 9 non-MPRs), coloured by response status (MPR as blue dots, non-MPR as red dots). **d**, PCA of pseudobulk gene expression from combined MANA enriched T cell cluster for individual tumour samples ($n = 15$, 6 MPRs and 9 non-MPRs), coloured by response status (MPR as light blue dots, non-MPR as red dots). *P* values were obtained using a one-sided permutation test, without correction for multiple comparisons.

Extended Data Fig. 12 Phenotypic characteristics of FACS-sorted peripheral blood CD8+/V β 2+ T cells from MPR MD01-005.

a, Selective gene expression of 2D UMAP red-scale projection is shown of canonical T cell subset marker genes, cell subset selective genes, and immune checkpoints on CD8 T cell subsets sorted from longitudinal peripheral blood of one patient (MD01-005) with complete pathologic response. **b-d**, Pseudotime reconstruction and pseudo-temporal dynamic gene identification in peripheral blood CD8 T cells from a complete pathologic responder. Longitudinal PBMC were collected from complete pathologic responder MD01-005 (0% residual tumour) during treatment and in post-surgery follow up. Peripheral blood CD8⁺ T cells were FACS sorted based on expression of TCR V β 2, which corresponds to the MANA-specific CDR3 CASNKLGYQPQHF as identified previously via the MANAFEST assay (Extended Data Fig. [2a](#)). scRNA-seq–TCR-seq was performed on the sorted population from each time point. **b**, Constructing the pseudotime axis on the diffusion map from $T_{\text{mem}}(3)$ to $T_{\text{eff}}(3)$ as trajectory 1. **c**, GO analysis for genes that significantly change along trajectory 1, ranked by FDR. **d**, Constructing the pseudotime axis on the diffusion map from $T_{\text{mem}}(3)$ to $T_{\text{mem}}(2)$ as trajectory 2. **e**, GO analysis for genes that significantly change along trajectory 2, ranked by FDR. **f**, Heat map showing genes that significantly change along trajectory 2 (FDR < 0.05).

Supplementary information

Supplementary Information

This file contains the full descriptions for Supplementary Data files 1-5, and the titles for Supplementary Tables 1-10.

Reporting Summary

Supplementary Data 1

This file contains differential gene lists in global CD3+ and refined CD8+ T cell UMAP clusters. See Supplementary Information PDF for full file description.

Supplementary Data 2

This file contains gene sets used to study transcriptional programs. See Supplementary Information PDF for full file description.

Supplementary Data 3

This file contains differential gene expression analysis comparing MPR (n=6) vs. non-MPR (n=9) by cell cluster and total CD4/CD8 TIL. See Supplementary Information PDF for full file description.

Supplementary Data 4

This file contains MANAFEST and ViraFEST assay results for each patient. See Supplementary Information PDF for full file description.

Supplementary Data 5

This file contains MANAFEST and ViraFEST assay graphs. See Supplementary Information PDF for full file description.

Supplementary Tables

This file contains Supplementary Tables 1-10. See Supplementary Information PDF for descriptions.

Rights and permissions

Open Access This article is licensed under a Creative Commons Attribution 4.0 International License, which permits use, sharing, adaptation, distribution and reproduction in any medium or format, as long as you give appropriate credit to the original author(s) and the source, provide a link to the Creative Commons license, and indicate if changes were made. The images or other third party material in this article are included in the article's Creative Commons license, unless indicated otherwise in a credit line to the material. If material is not included in the

article's Creative Commons license and your intended use is not permitted by statutory regulation or exceeds the permitted use, you will need to obtain permission directly from the copyright holder. To view a copy of this license, visit <http://creativecommons.org/licenses/by/4.0/>.

Reprints and Permissions

About this article



Check for
updates

Cite this article

Caushi, J.X., Zhang, J., Ji, Z. *et al.* Transcriptional programs of neoantigen-specific TIL in anti-PD-1-treated lung cancers. *Nature* **596**, 126–132 (2021). <https://doi.org/10.1038/s41586-021-03752-4>

Download citation

- Received: 08 January 2021
- Accepted: 18 June 2021
- Published: 21 July 2021
- Issue Date: 05 August 2021
- DOI: <https://doi.org/10.1038/s41586-021-03752-4>

Comments

By submitting a comment you agree to abide by our [Terms](#) and [Community Guidelines](#). If you find something abusive or that does not comply with our terms or guidelines please flag it as inappropriate.

[Download PDF](#)

Advertisement

This article was downloaded by **calibre** from <https://www.nature.com/articles/s41586-021-03752-4>

| [Section menu](#) | [Main menu](#) |

- Article
- [Published: 07 July 2021](#)

BANP opens chromatin and activates CpG-island-regulated genes

- [Ralph S. Grand](#)¹ na1,
- [Lukas Burger](#) [ORCID: orcid.org/0000-0001-5596-7567](#)^{1,2} na1,
- [Cathrin Gräwe](#)³,
- [Alicia K. Michael](#)¹,
- [Luke Isbel](#) [ORCID: orcid.org/0000-0002-5270-4347](#)^{1,4},
- [Daniel Hess](#) [ORCID: orcid.org/0000-0002-1642-5404](#)¹,
- [Leslie Hoerner](#)¹,
- [Vytautas Iesmantavicius](#)¹,
- [Sevi Durdu](#) [ORCID: orcid.org/0000-0001-9746-6779](#)¹,
- [Marco Pregnolato](#)^{1,5},
- [Arnaud R. Krebs](#)¹ nAff6,
- [Sébastien A. Smallwood](#)¹,
- [Nicolas Thomä](#) [ORCID: orcid.org/0000-0003-2685-906X](#)¹,
- [Michiel Vermeulen](#) [ORCID: orcid.org/0000-0003-0836-6894](#)³ &
- [Dirk Schübeler](#) [ORCID: orcid.org/0000-0002-9229-2228](#)^{1,5}

[Nature](#) volume **596**, pages 133–137 (2021) [Cite this article](#)

- 8628 Accesses
- 175 Altmetric
- [Metrics details](#)

Subjects

- [Chromatin](#)
- [DNA methylation](#)
- [Gene regulation](#)
- [Transcription](#)

Abstract

The majority of gene transcripts generated by RNA polymerase II in mammalian genomes initiate at CpG island (CGI) promoters^{1,2}, yet our understanding of their regulation remains limited. This is in part due to the incomplete information that we have on transcription factors, their DNA-binding motifs and which genomic binding sites are functional in any given cell type^{3,4,5}. In addition, there are orphan motifs without known binders, such as the CGCG element, which is associated with highly expressed genes across human tissues and enriched near the transcription start site of a subset of CGI promoters^{6,7,8}. Here we combine single-molecule footprinting with interaction proteomics to identify BTG3-associated nuclear protein (BANP) as the transcription factor that binds this element in the mouse and human genome. We show that BANP is a strong CGI activator that controls essential metabolic genes in pluripotent stem and terminally differentiated neuronal cells. BANP binding is repelled by DNA methylation of its motif in vitro and in vivo, which epigenetically restricts most binding to CGIs and accounts for differential binding at aberrantly methylated CGI promoters in cancer cells. Upon binding to an unmethylated motif, BANP opens chromatin and phases nucleosomes. These findings establish BANP as a critical activator of a set of essential genes and suggest a model in which the activity of CGI promoters relies on methylation-sensitive transcription factors that are capable of chromatin opening.

Access options

Subscribe to Journal

Get full journal access for 1 year

\$199.00

only \$3.90 per issue

[Subscribe](#)

All prices are NET prices.

VAT will be added later in the checkout.

Tax calculation will be finalised during checkout.

Rent or Buy article

Get time limited or full article access on ReadCube.

from \$8.99

[Rent or Buy](#)

All prices are NET prices.

Additional access options:

- [Log in](#)
- [Access through your institution](#)
- [Learn about institutional subscriptions](#)

Fig. 1: BANP binds the CGCG element in vivo.

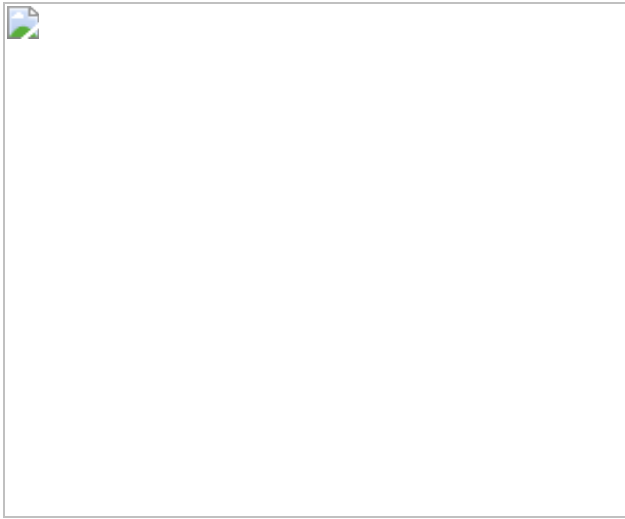


Fig. 2: BANP is sensitive to DNA methylation.

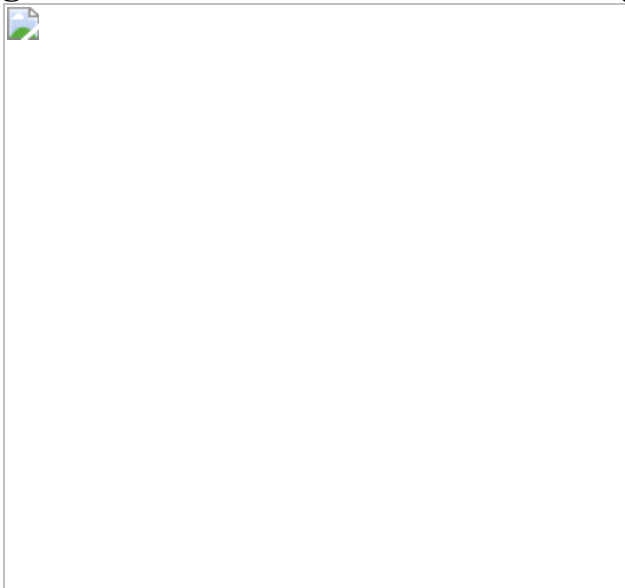


Fig. 3: BANP drives the expression of essential genes.

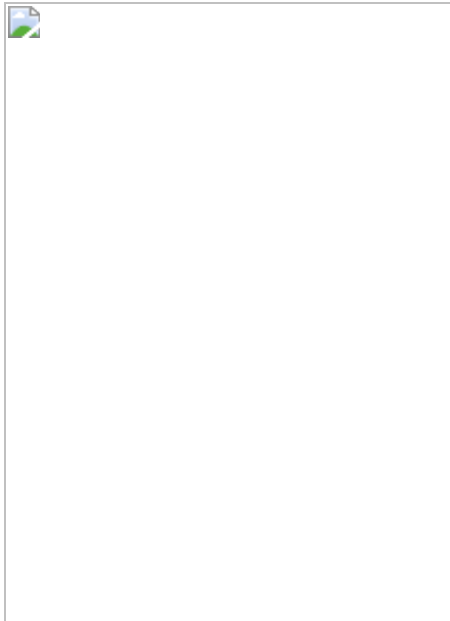
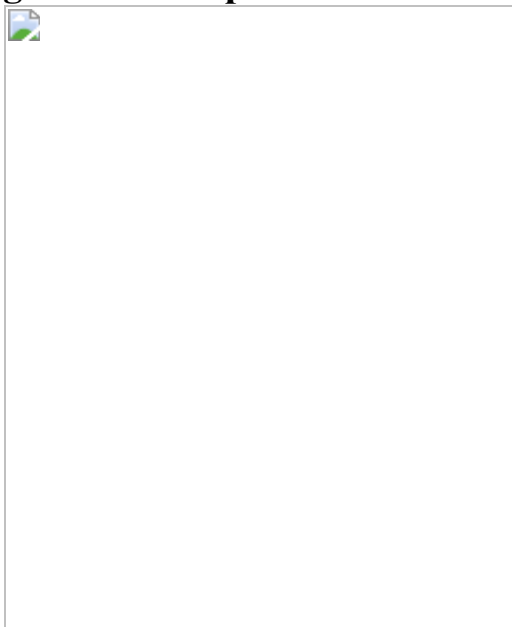


Fig. 4: BANP opens chromatin at CGIs.



Data availability

Next-generation sequencing data have been deposited at the Gene Expression Omnibus with accession number [GSE155604](#). Mass spectrometry data have been deposited at the ProteomeXchange Consortium through the PRIDE partner repository with the identifier [PXD024794](#).

References

1. 1.

Mohn, F. & Schübeler, D. Genetics and epigenetics: stability and plasticity during cellular differentiation. *Trends Genet.* **25**, 129–136 (2009).

[CAS](#) [PubMed](#) [Article](#) [Google Scholar](#)

2. 2.

Deaton, A. M. & Bird, A. CpG islands and the regulation of transcription. *Genes Dev.* **25**, 1010–1022 (2011).

[CAS](#) [PubMed](#) [PubMed Central](#) [Article](#) [Google Scholar](#)

3. 3.

Lambert, S. A. et al. The human transcription factors. *Cell* **172**, 650–665 (2018).

[CAS](#) [PubMed](#) [Article](#) [Google Scholar](#)

4. 4.

Vaquerizas, J. M., Kummerfeld, S. K., Teichmann, S. A. & Luscombe, N. M. A census of human transcription factors: function, expression and evolution. *Nat. Rev. Genet.* **10**, 252–263 (2009).

[CAS](#) [PubMed](#) [Article](#) [Google Scholar](#)

5. 5.

Slattery, M. et al. Absence of a simple code: how transcription factors read the genome. *Trends Biochem. Sci.* **39**, 381–399 (2014).

[CAS](#) [PubMed](#) [PubMed Central](#) [Article](#) [Google Scholar](#)

6. 6.

Ernst, J. et al. Genome-scale high-resolution mapping of activating and repressive nucleotides in regulatory regions. *Nat. Biotechnol.* **34**, 1180–1190 (2016).

[CAS](#) [PubMed](#) [PubMed Central](#) [Article](#) [Google Scholar](#)

7. 7.

FitzGerald, P. C., Shlyakhtenko, A., Mir, A. A. & Vinson, C. Clustering of DNA sequences in human promoters. *Genome Res.* **14**, 1562–1574 (2004).

[CAS](#) [PubMed](#) [PubMed Central](#) [Article](#) [Google Scholar](#)

8. 8.

Pique-Regi, R. et al. Accurate inference of transcription factor binding from DNA sequence and chromatin accessibility data. *Genome Res.* **21**, 447–455 (2011).

[CAS](#) [PubMed](#) [PubMed Central](#) [Article](#) [Google Scholar](#)

9. 9.

Yang, J. G., Madrid, T. S., Sevastopoulos, E. & Narlikar, G. J. The chromatin-remodeling enzyme ACF is an ATP-dependent DNA length sensor that regulates nucleosome spacing. *Nat. Struct. Mol. Biol.* **13**, 1078–1083 (2006).

[CAS](#) [PubMed](#) [Article](#) [Google Scholar](#)

10. 10.

Lienert, F. et al. Identification of genetic elements that autonomously determine DNA methylation states. *Nat. Genet.* **43**, 1091–1097 (2011).

[CAS](#) [PubMed](#) [Article](#) [Google Scholar](#)

11. 11.

Pardo, C. E., Darst, R. P., Nabilsi, N. H., Delmas, A. L. & Kladde, M. P. Simultaneous single-molecule mapping of protein–DNA interactions and DNA methylation by MAPit. *Curr. Protoc. Mol. Biol.* **95**, 21.22.1–21.22.18 (2011).

[Article](#) [Google Scholar](#)

12. 12.

Sönmezer, C. et al. Molecular co-occupancy identifies transcription factor binding cooperativity in vivo. *Mol. Cell* **81**, 255–267 (2021).

[PubMed](#) [Article](#) [CAS](#) [Google Scholar](#)

13. 13.

Makowski, M. M. et al. Global profiling of protein–DNA and protein–nucleosome binding affinities using quantitative mass spectrometry. *Nat. Commun.* **9**, 1653 (2018).

[ADS](#) [PubMed](#) [PubMed Central](#) [Article](#) [CAS](#) [Google Scholar](#)

14. 14.

Saksouk, N. et al. Redundant mechanisms to form silent chromatin at pericentromeric regions rely on BEND3 and DNA methylation. *Mol. Cell* **56**, 580–594 (2014).

[CAS](#) [PubMed](#) [Article](#) [Google Scholar](#)

15. 15.

Dai, Q. et al. The BEN domain is a novel sequence-specific DNA-binding domain conserved in neural transcriptional repressors. *Genes Dev.* **27**, 602–614 (2013).

[CAS](#) [PubMed](#) [PubMed Central](#) [Article](#) [Google Scholar](#)

16. 16.

Dai, Q. et al. Common and distinct DNA-binding and regulatory activities of the BEN-solo transcription factor family. *Genes Dev.* **29**, 48–62 (2015).

[PubMed](#) [PubMed Central](#) [Article](#) [CAS](#) [Google Scholar](#)

17. 17.

Khan, A. & Prasanth, S. G. BEND3 mediates transcriptional repression and heterochromatin organization. *Transcription* **6**, 102–105 (2015).

[CAS](#) [PubMed](#) [PubMed Central](#) [Article](#) [Google Scholar](#)

18. 18.

Sathyan, K. M., Shen, Z., Tripathi, V., Prasanth, K. V. & Prasanth, S. G. A BEN-domain-containing protein associates with heterochromatin and represses transcription. *J. Cell Sci.* **124**, 3149–3163 (2011).

[CAS](#) [PubMed](#) [PubMed Central](#) [Article](#) [Google Scholar](#)

19. 19.

Rampalli, S., Pavithra, L., Bhatt, A., Kundu, T. K. & Chattopadhyay, S. Tumor suppressor SMAR1 mediates cyclin D1 repression by recruitment of the SIN3/histone deacetylase 1 complex. *Mol. Cell. Biol.* **25**, 8415–8429 (2005).

[CAS](#) [PubMed](#) [PubMed Central](#) [Article](#) [Google Scholar](#)

20. 20.

Sreenath, K. et al. Nuclear matrix protein SMAR1 represses HIV-1 LTR mediated transcription through chromatin remodeling. *Virology* **400**, 76–85 (2010).

[CAS](#) [PubMed](#) [Article](#) [Google Scholar](#)

21. 21.

Domcke, S. et al. Competition between DNA methylation and transcription factors determines binding of NRF1. *Nature* **528**, 575–579 (2015).

[ADS](#) [CAS](#) [PubMed](#) [Article](#) [Google Scholar](#)

22. 22.

Baylin, S. B. & Jones, P. A. Epigenetic determinants of cancer. *Cold Spring Harb. Perspect. Biol.* **8**, a019505 (2016).

[PubMed](#) [PubMed Central](#) [Article](#) [CAS](#) [Google Scholar](#)

23. 23.

Berman, B. P. et al. Regions of focal DNA hypermethylation and long-range hypomethylation in colorectal cancer coincide with nuclear lamina-associated domains. *Nat. Genet.* **44**, 40–46 (2011).

[PubMed](#) [PubMed Central](#) [Article](#) [CAS](#) [Google Scholar](#)

24. 24.

Mahpour, A., Scruggs, B. S., Smiraglia, D., Ouchi, T. & Gelman, I. H. A methyl-sensitive element induces bidirectional transcription in TATA-less CpG island-associated promoters. *PLoS ONE* **13**, e0205608 (2018).

[PubMed](#) [PubMed Central](#) [Article](#) [CAS](#) [Google Scholar](#)

25. 25.

Wang, T. et al. Identification and characterization of essential genes in the human genome. *Science* **350**, 1096–1101 (2015).

[ADS](#) [CAS](#) [PubMed](#) [PubMed Central](#) [Article](#) [Google Scholar](#)

26. 26.

McDonald, E. R., III et al. Project DRIVE: a compendium of cancer dependencies and synthetic lethal relationships uncovered by large-scale, deep RNAi screening. *Cell* **170**, 577–592 (2017).

[CAS](#) [PubMed](#) [Article](#) [Google Scholar](#)

27. 27.

Nabet, B. et al. The dTAG system for immediate and target-specific protein degradation. *Nat. Chem. Biol.* **14**, 431–441 (2018).

[CAS](#) [PubMed](#) [PubMed Central](#) [Article](#) [Google Scholar](#)

28. 28.

Muhar, M. et al. SLAM-seq defines direct gene-regulatory functions of the BRD4–MYC axis. *Science* **360**, 800–805 (2018).

[CAS](#) [PubMed](#) [PubMed Central](#) [Article](#) [Google Scholar](#)

29. 29.

Gaidatzis, D., Burger, L., Florescu, M. & Stadler, M. B. Analysis of intronic and exonic reads in RNA-seq data characterizes transcriptional and post-transcriptional regulation. *Nat. Biotechnol.* **33**, 722–729 (2015).

[CAS](#) [PubMed](#) [Article](#) [Google Scholar](#)

30. 30.

Dahlet, T. et al. Genome-wide analysis in the mouse embryo reveals the importance of DNA methylation for transcription integrity. *Nat. Commun.* **11**, 3153 (2020).

[ADS](#) [CAS](#) [PubMed](#) [PubMed Central](#) [Article](#) [Google Scholar](#)

31. 31.

Thoma, E. C. et al. Ectopic expression of neurogenin 2 alone is sufficient to induce differentiation of embryonic stem cells into mature neurons. *PLoS ONE* **7**, e38651 (2012).

[ADS](#) [CAS](#) [PubMed](#) [PubMed Central](#) [Article](#) [Google Scholar](#)

32. 32.

Buenrostro, J. D., Wu, B., Chang, H. Y. & Greenleaf, W. J. ATAC-seq: a method for assaying chromatin accessibility genome-wide. *Curr. Protoc. Mol. Biol.* **109**, 21.29.1–21.29.9 (2015).

[Article](#) [Google Scholar](#)

33. 33.

Fu, Y., Sinha, M., Peterson, C. L. & Weng, Z. The insulator binding protein CTCF positions 20 nucleosomes around its binding sites across the human genome. *PLoS Genet.* **4**, e1000138 (2008).

[PubMed](#) [PubMed Central](#) [Article](#) [CAS](#) [Google Scholar](#)

34. 34.

Vierstra, J. et al. Global reference mapping of human transcription factor footprints. *Nature* **583**, 729–736 (2020).

[ADS](#) [CAS](#) [PubMed](#) [PubMed Central](#) [Article](#) [Google Scholar](#)

35. 35.

Wilson, B. C. et al. Intellectual disability-associated factor Zbtb11 cooperates with NRF-2/GABP to control mitochondrial function. *Nat. Commun.* **11**, 5469 (2020).

[ADS](#) [CAS](#) [PubMed](#) [PubMed Central](#) [Article](#) [Google Scholar](#)

36. 36.

Stielow, B. et al. The SAM domain-containing protein 1 (SAMD1) acts as a repressive chromatin regulator at unmethylated CpG islands. *Sci. Adv.* **7**, eabf2229 (2021).

[CAS](#) [PubMed](#) [PubMed Central](#) [Article](#) [Google Scholar](#)

37. 37.

Weber, M. et al. Distribution, silencing potential and evolutionary impact of promoter DNA methylation in the human genome. *Nat. Genet.* **39**, 457–466 (2007).

[CAS](#) [PubMed](#) [Article](#) [Google Scholar](#)

38. 38.

Iurlaro, M. et al. Mammalian SWI/SNF continuously restores local accessibility to chromatin. *Nat. Genet.* **53**, 279–287 (2021).

[CAS](#) [PubMed](#) [Article](#) [Google Scholar](#)

39. 39.

Schick, S. et al. Acute BAF perturbation causes immediate changes in chromatin accessibility. *Nat. Genet.* **53**, 269–278 (2021).

[CAS](#) [PubMed](#) [Article](#) [Google Scholar](#)

40. 40.

Hartl, D. et al. CG dinucleotides enhance promoter activity independent of DNA methylation. *Genome Res.* **29**, 554–563 (2019).

[CAS](#) [PubMed](#) [PubMed Central](#) [Article](#) [Google Scholar](#)

41. 41.

Mohn, F. et al. Lineage-specific polycomb targets and de novo DNA methylation define restriction and potential of neuronal progenitors. *Mol. Cell* **30**, 755–766 (2008).

[CAS](#) [PubMed](#) [Article](#) [Google Scholar](#)

42. 42.

Zhang, Y. et al. Rapid single-step induction of functional neurons from human pluripotent stem cells. *Neuron* **78**, 785–798 (2013).

[CAS](#) [PubMed](#) [PubMed Central](#) [Article](#) [Google Scholar](#)

43. 43.

Lowary, P. T. & Widom, J. New DNA sequence rules for high affinity binding to histone octamer and sequence-directed nucleosome positioning. *J. Mol. Biol.* **276**, 19–42 (1998).

[CAS](#) [PubMed](#) [Article](#) [Google Scholar](#)

44. 44.

Khan, A. et al. JASPAR 2018: update of the open-access database of transcription factor binding profiles and its web framework. *Nucleic Acids Res.* **46**, D260–D266 (2018).

[CAS](#) [PubMed](#) [PubMed Central](#) [Article](#) [Google Scholar](#)

45. 45.

Feng, Y. Q. et al. Site-specific chromosomal integration in mammalian cells: highly efficient CRE recombinase-mediated cassette exchange. *J. Mol. Biol.* **292**, 779–785 (1999).

[CAS](#) [PubMed](#) [Article](#) [Google Scholar](#)

46. 46.

Gaidatzis, D., Lerch, A., Hahne, F. & Stadler, M. B. QuasR: quantification and annotation of short reads in R. *Bioinformatics* **31**, 1130–1132 (2015).

[CAS](#) [PubMed](#) [Article](#) [Google Scholar](#)

47. 47.

Ostapcuk, V. et al. Activity-dependent neuroprotective protein recruits HP1 and CHD4 to control lineage-specifying genes. *Nature* **557**, 739–743 (2018).

[ADS](#) [CAS](#) [PubMed](#) [Article](#) [Google Scholar](#)

48. 48.

Cox, J. et al. Andromeda: a peptide search engine integrated into the MaxQuant environment. *J. Proteome Res.* **10**, 1794–1805 (2011).

[ADS](#) [CAS](#) [Article](#) [Google Scholar](#)

49. 49.

Cox, J. et al. Accurate proteome-wide label-free quantification by delayed normalization and maximal peptide ratio extraction, termed MaxLFQ. *Mol. Cell. Proteomics* **13**, 2513–2526 (2014).

[CAS](#) [PubMed](#) [PubMed Central](#) [Article](#) [Google Scholar](#)

50. 50.

Hubner, N. C. et al. Quantitative proteomics combined with BAC TransgeneOmics reveals in vivo protein interactions. *J. Cell Biol.* **189**, 739–754 (2010).

[CAS](#) [PubMed](#) [PubMed Central](#) [Article](#) [Google Scholar](#)

51. 51.

Tyanova, S. et al. The Perseus computational platform for comprehensive analysis of (prote)omics data. *Nat. Methods* **13**, 731–740 (2016).

[CAS](#) [PubMed](#) [Article](#) [Google Scholar](#)

52. 52.

Tusher, V. G., Tibshirani, R. & Chu, G. Significance analysis of microarrays applied to the ionizing radiation response. *Proc. Natl Acad. Sci. USA* **98**, 5116–5121 (2001).

[ADS](#) [CAS](#) [PubMed](#) [PubMed Central](#) [MATH](#) [Article](#) [Google Scholar](#)

53. 53.

Wang, Y. et al. Reversed-phase chromatography with multiple fraction concatenation strategy for proteome profiling of human MCF10A cells. *Proteomics* **11**, 2019–2026 (2011).

[CAS](#) [PubMed](#) [PubMed Central](#) [Article](#) [Google Scholar](#)

54. 54.

Perez-Riverol, Y. et al. The PRIDE database and related tools and resources in 2019: improving support for quantification data. *Nucleic Acids Res.* **47**, D442–D450 (2019).

[CAS](#) [Article](#) [Google Scholar](#)

55. 55.

Gräwe, C., Makowski, M. M. & Vermeulen, M. PAQMAN: protein-nucleic acid affinity quantification by mass spectrometry in nuclear extracts. *Methods* **184**, 70–77 (2020).

[PubMed](#) [Article](#) [CAS](#) [Google Scholar](#)

56. 56.

Corces, M. R. et al. An improved ATAC-seq protocol reduces background and enables interrogation of frozen tissues. *Nat. Methods* **14**, 959–962 (2017).

[CAS](#) [PubMed](#) [PubMed Central](#) [Article](#) [Google Scholar](#)

57. 57.

Cui, K. & Zhao, K. Genome-wide approaches to determining nucleosome occupancy in metazoans using MNase-seq. *Methods Mol. Biol.* **833**, 413–419 (2012).

[CAS](#) [PubMed](#) [PubMed Central](#) [Article](#) [Google Scholar](#)

58. 58.

Gaidatzis, D. et al. DNA sequence explains seemingly disordered methylation levels in partially methylated domains of mammalian genomes. *PLoS Genet.* **10**, e1004143 (2014).

[PubMed](#) [PubMed Central](#) [Article](#) [CAS](#) [Google Scholar](#)

59. 59.

Barisic, D., Stadler, M. B., Iurlaro, M. & Schübeler, D. Mammalian ISWI and SWI/SNF selectively mediate binding of distinct transcription factors. *Nature* **569**, 136–140 (2019).

[ADS](#) [CAS](#) [PubMed](#) [PubMed Central](#) [Article](#) [Google Scholar](#)

60. 60.

Abdulrahman, W. et al. A set of baculovirus transfer vectors for screening of affinity tags and parallel expression strategies. *Anal. Biochem.* **385**, 383–385 (2009).

[CAS](#) [PubMed](#) [Article](#) [Google Scholar](#)

61. 61.

Huber, W. et al. Orchestrating high-throughput genomic analysis with Bioconductor. *Nat. Methods* **12**, 115–121 (2015).

[CAS](#) [PubMed](#) [PubMed Central](#) [Article](#) [Google Scholar](#)

62. 62.

Lawrence, M., Gentleman, R. & Carey, V. rtracklayer: an R package for interfacing with genome browsers. *Bioinformatics* **25**, 1841–1842 (2009).

[CAS](#) [PubMed](#) [PubMed Central](#) [Article](#) [Google Scholar](#)

63. 63.

Ginno, P. A. et al. A genome-scale map of DNA methylation turnover identifies site-specific dependencies of DNMT and TET activity. *Nat. Commun.* **11**, 2680 (2020).

[ADS](#) [CAS](#) [PubMed](#) [PubMed Central](#) [Article](#) [Google Scholar](#)

64. 64.

Langmead, B., Trapnell, C., Pop, M. & Salzberg, S. L. Ultrafast and memory-efficient alignment of short DNA sequences to the human genome. *Genome Biol.* **10**, R25 (2009).

[PubMed](#) [PubMed Central](#) [Article](#) [CAS](#) [Google Scholar](#)

65. 65.

Zhang, Y. et al. Model-based analysis of ChIP-seq (MACS). *Genome Biol.* **9**, R137 (2008).

[PubMed](#) [PubMed Central](#) [Article](#) [CAS](#) [Google Scholar](#)

66. 66.

Heinz, S. et al. Simple combinations of lineage-determining transcription factors prime *cis*-regulatory elements required for macrophage and B cell identities. *Mol. Cell* **38**, 576–589 (2010).

[CAS](#) [PubMed](#) [PubMed Central](#) [Article](#) [Google Scholar](#)

67. 67.

Héberlé, É. & Bardet, A. F. Sensitivity of transcription factors to DNA methylation. *Essays Biochem.* **63**, 727–741 (2019).

[PubMed](#) [PubMed Central](#) [Article](#) [Google Scholar](#)

68. 68.

Buck-Kohntop, B. A. et al. Molecular basis for recognition of methylated and specific DNA sequences by the zinc finger protein Kaiso. *Proc. Natl Acad. Sci. USA* **109**, 15229–15234 (2012).

[ADS](#) [CAS](#) [PubMed](#) [PubMed Central](#) [Article](#) [Google Scholar](#)

69. 69.

Ritchie, M. E. et al. limma powers differential expression analyses for RNA-sequencing and microarray studies. *Nucleic Acids Res.* **43**, e47 (2015).

[PubMed](#) [PubMed Central](#) [Article](#) [CAS](#) [Google Scholar](#)

70. 70.

Arnold, P. et al. Modeling of epigenome dynamics identifies transcription factors that mediate Polycomb targeting. *Genome Res.* **23**, 60–73 (2013).

[CAS](#) [PubMed](#) [PubMed Central](#) [Article](#) [Google Scholar](#)

71. 71.

Kim, D., Paggi, J. M., Park, C., Bennett, C. & Salzberg, S. L. Graph-based genome alignment and genotyping with HISAT2 and HISAT-genotype. *Nat. Biotechnol.* **37**, 907–915 (2019).

[CAS](#) [PubMed](#) [PubMed Central](#) [Article](#) [Google Scholar](#)

72. 72.

Neumann, T. et al. Quantification of experimentally induced nucleotide conversions in high-throughput sequencing datasets. *BMC Bioinformatics* **20**, 258 (2019).

[PubMed](#) [PubMed Central](#) [Article](#) [CAS](#) [Google Scholar](#)

73. 73.

Danecek, P. et al. The variant call format and VCFtools. *Bioinformatics* **27**, 2156–2158 (2011).

[CAS](#) [PubMed](#) [PubMed Central](#) [Article](#) [Google Scholar](#)

74. 74.

Martin, M. Cutadapt removes adapter sequences from high-throughput sequencing reads. *EMBnet. J.* **17**, 10 (2011).

[Article](#) [Google Scholar](#)

75. 75.

Stadler, M. B. et al. DNA-binding factors shape the mouse methylome at distal regulatory regions. *Nature* **480**, 490–495 (2011).

[ADS](#) [CAS](#) [PubMed](#) [Article](#) [Google Scholar](#)

76. 76.

Blattler, A. et al. Global loss of DNA methylation uncovers intronic enhancers in genes showing expression changes. *Genome Biol.* **15**, 469 (2014).

[PubMed](#) [PubMed Central](#) [Article](#) [CAS](#) [Google Scholar](#)

77. 77.

Xuan Lin, Q. X. et al. MethMotif: an integrative cell specific database of transcription factor binding motifs coupled with DNA methylation profiles. *Nucleic Acids Res.* **47**, D145–D154 (2019).

[PubMed](#) [Article](#) [CAS](#) [Google Scholar](#)

78. 78.

Hon, G. C. et al. Global DNA hypomethylation coupled to repressive chromatin domain formation and gene silencing in breast cancer. *Genome Res.* **22**, 246–258 (2012).

[CAS](#) [PubMed](#) [PubMed Central](#) [Article](#) [Google Scholar](#)

79. 79.

The ENCODE Project Consortium. An integrated encyclopedia of DNA elements in the human genome. *Nature* **489**, 57–74 (2012).

[ADS](#) [PubMed Central](#) [Article](#) [CAS](#) [PubMed](#) [Google Scholar](#)

80. 80.

Venables, W. N. & Ripley, B. D. *Modern Applied Statistics with S* 4th edn (Springer, 2002).

81. 81.

Hahne, F. & Ivanek, R. Visualizing genomic data using Gviz and Bioconductor. *Methods Mol Biol.* **1418**, 335–351 (2016).

[PubMed](#) [Article](#) [Google Scholar](#)

82. 82.

Alexa, A., Rahnenführer, J. & Lengauer, T. Improved scoring of functional groups from gene expression data by decorrelating GO graph structure. *Bioinformatics* **22**, 1600–1607 (2006).

[CAS](#) [PubMed](#) [PubMed Central](#) [Article](#) [Google Scholar](#)

83. 83.

Lawrence, M. et al. Software for computing and annotating genomic ranges. *PLoS Comput. Biol.* **9**, e1003118 (2013).

[CAS](#) [PubMed](#) [PubMed Central](#) [Article](#) [Google Scholar](#)

84. 84.

Fenouil, R. et al. CpG islands and GC content dictate nucleosome depletion in a transcription-independent manner at mammalian promoters. *Genome Res.* **22**, 2399–2408 (2012).

[CAS](#) [PubMed](#) [PubMed Central](#) [Article](#) [Google Scholar](#)

[Download references](#)

Acknowledgements

We thank P. Papasaikas for help with the SLAM-seq analysis; M. Frederiksen and N. Leroy from the Novartis Institutes of Biomedical Research for providing the dTAG13 compound; and M. Lorincz and members of the D.S. laboratory for critical feedback on the manuscript. D.S. and N.T. acknowledge support from the Novartis Research Foundation, the Swiss National Science Foundation (310030B_176394 to D.S. and 31003A_179541 to N.T.) and the European Research Council under the European Union's (EU) Horizon 2020 research and innovation programme grant agreements (ReadMe-667951 and DNAaccess-884664 to

D.S. and CsnCRL-666068 and NucEM-884331 to N.T.). M.V. is part of the Oncode Institute, which is partly funded by the Dutch Cancer Society. R.S.G., A.K.M. and S.D. acknowledge EMBO Long-Term Fellowships. R.S.G and L.I. acknowledge the EU Horizon 2020 Research and Innovation Program under the Marie Skłodowska-Curie grant (705354 to R.S.G. and 748760 to L.I.). A.K.M. acknowledges the Human Frontier Science Program. L.I. acknowledges the National Health and Medical Research Council CJ Martin Fellowship APP1148380. A.R.K. acknowledges support from the European Molecular Biology Laboratory, Deutsche Forschungsgemeinschaft (KR 5247/1-1) and a Swiss National Fund Ambizione grant (PZOOP3_161493).

Author information

Author notes

1. Arnaud R. Krebs

Present address: Genome Biology Unit, European Molecular Biology Laboratory, Heidelberg, Germany

2. These authors contributed equally: Ralph S. Grand, Lukas Burger

Affiliations

1. Friedrich Miescher Institute for Biomedical Research, Basel, Switzerland

Ralph S. Grand, Lukas Burger, Alicia K. Michael, Luke Isbel, Daniel Hess, Leslie Hoerner, Vytautas Iesmantavicius, Sevi Durdu, Marco Pagnolato, Arnaud R. Krebs, Sébastien A. Smallwood, Nicolas Thomä & Dirk Schübeler

2. Swiss Institute of Bioinformatics, Basel, Switzerland

Lukas Burger

3. Department of Molecular Biology, Faculty of Science, Radboud Institute for Molecular Life Sciences, Oncode Institute, Radboud University Nijmegen, Nijmegen, The Netherlands

Cathrin Gräwe & Michiel Vermeulen

4. School of Biotechnology and Biomolecular Sciences, University of New South Wales, Sydney, New South Wales, Australia

Luke Isbel

5. Faculty of Science, University of Basel, Basel, Switzerland

Marco Pregnolato & Dirk Schübeler

Authors

1. Ralph S. Grand

[View author publications](#)

You can also search for this author in [PubMed](#) [Google Scholar](#)

2. Lukas Burger

[View author publications](#)

You can also search for this author in [PubMed](#) [Google Scholar](#)

3. Cathrin Gräwe

[View author publications](#)

You can also search for this author in [PubMed](#) [Google Scholar](#)

4. Alicia K. Michael

[View author publications](#)

You can also search for this author in [PubMed](#) [Google Scholar](#)

5. Luke Isbel

[View author publications](#)

You can also search for this author in [PubMed](#) [Google Scholar](#)

6. Daniel Hess

[View author publications](#)

You can also search for this author in [PubMed](#) [Google Scholar](#)

7. Leslie Hoerner

[View author publications](#)

You can also search for this author in [PubMed](#) [Google Scholar](#)

8. Vytautas Iesmantavicius

[View author publications](#)

You can also search for this author in [PubMed](#) [Google Scholar](#)

9. Sevi Durdu

[View author publications](#)

You can also search for this author in [PubMed](#) [Google Scholar](#)

10. Marco Pregnolato

[View author publications](#)

You can also search for this author in [PubMed](#) [Google Scholar](#)

11. Arnaud R. Krebs

[View author publications](#)

You can also search for this author in [PubMed](#) [Google Scholar](#)

12. Sébastien A. Smallwood

[View author publications](#)

You can also search for this author in [PubMed](#) [Google Scholar](#)

13. Nicolas Thomä

[View author publications](#)

You can also search for this author in [PubMed](#) [Google Scholar](#)

14. Michiel Vermeulen

[View author publications](#)

You can also search for this author in [PubMed](#) [Google Scholar](#)

15. Dirk Schübeler

[View author publications](#)

You can also search for this author in [PubMed](#) [Google Scholar](#)

Contributions

R.S.G., L.B. and D.S. conceived and planned the experiments. R.S.G. performed all experiments, performed SMF analysis and contributed to initial data analysis. L.B. performed comprehensive computational data analysis. C.G. and M.V. validated the affinity purification and performed PAQMAN analysis. A.K.M. performed and N.T. supervised protein purification and biochemistry assays. L.I. assisted with genomics and biochemistry assays. D.H. and V.I. performed mass spectrometry quantification and initial data processing. L.H. assisted with western blots, MNase-seq and cell line maintenance. S.D. performed and analysed the immunofluorescence experiments. M.P. and A.R.K. assisted in the establishment of the SMF method. S.A.S. advised on and oversaw the generation of next-generation-sequencing data. D.S. supervised the project. R.S.G., L.B. and D.S. interpreted the results and wrote the manuscript.

Corresponding author

Correspondence to [Dirk Schübeler](#).

Ethics declarations

Competing interests

The authors declare no competing interests.

Additional information

Peer review information *Nature* thanks Eric Mendenhall and the other, anonymous, reviewer(s) for their contribution to the peer review of this work. Peer reviewer reports are available.

Publisher's note Springer Nature remains neutral with regard to jurisdictional claims in published maps and institutional affiliations.

Extended data figures and tables

Extended Data Fig. 1 BANP binds the orphan CGCG element in the mouse genome.

a, Footprint created by REST bound to its motif (red) and CpG methylation around the bound motif (black). Motif indicated by grey rectangle in the middle. **b**, No footprint over the scrambled REST motif (red) and corresponding CpG methylation at this inserted construct (black). Individual biological replicates are shown ($n = 2$). Red line is the mean. **c**, ChIP-seq read counts for REST at two genomic loci with a REST motif (top and middle) and one without (bottom). SMF amplicon indicated in blue, REST motif in grey¹². **d**, Footprinting of the corresponding loci in **c**. A footprint of around 30 bp was detected over the REST motif (top and middle) compared to a site without a motif. The transcription factor footprint is distinguishable from the neighbouring nucleosome footprint by size—around 30 bp compared to around 150 bp in width. Individual biological replicates are shown ($n = 4$). Red line is the mean. **e, f**, Same as Fig. **1b** but including CpG methylation. Individual biological replicates are shown ($n = 2$). Red line is the mean. **g**, Quantitative mass spectrometry (PAQMAN) determines affinity of BANP for the CGCG element to be around 18.5 nM. Binding curves were generated by fitting the parameters of the Hill equation to determine the relative equilibrium dissociation constant (K_d^{app}). Data are the mean of three experiments ($n = 3$), error bars represent standard error of the mean. **h**, Reproducibility of enrichments at peaks ($n = 1302$) for three independent BANP ChIP-seq replicates (R1–R3) from wild-type mouse ES cells. Pearson correlation coefficients are indicated. **i**,

Top motif found by de novo motif search in the top 500 peaks of each ChIP-seq replicate (R1–R3) using HOMER. **j**, 6mer enrichments as measured by Pearson residuals (Methods) at the top 500 peaks inside CpG islands (CGIs) and outside of CGIs (nonCGI). The five sub-6mers of the highest-scoring motif in **i** (TCTCGCGAGA), TCTCGC, CTCGCG, TCGCGA, CGCGAG and GCGAGA are marked in red. R1–R3 indicate biological replicates. **k**, BANP motif instances of varying motif scores were predicted genome-wide (Methods) and the fraction of predicted motifs that overlap common peaks (peaks identified in all three replicates, Methods) was determined for equally spaced bins of motif scores (missing bins do not contain any predicted sites). The chosen cut-off of 12.5 is indicated by a dashed line. **l**, The fraction of common BANP peaks in varying bins of BANP enrichment that contain a predicted BANP motif using the cut-off of 12.5 defined in **k**. **m**, Reproducibility of BANP enrichments at predicted BANP motifs ($n = 1207$) as defined in **k**. Pearson correlation coefficients are indicated. R1–R3 indicate biological replicates. **n**, GO enrichment of genes that contain a bound BANP motif. The top 30 most significant GO categories are shown.

Extended Data Fig. 2 BANP is methylation-sensitive in mouse and human cells.

a, BANP binding versus percentage methylation of the CpGs in the BANP motif. n indicates the number of motifs per bin. R indicates Pearson correlation coefficient. Black lines correspond to median, boxes to first and third quartile and whiskers to the maximum and minimum values of the distribution after removal of outliers, in which outliers are defined as more than $1.5 \times$ (interquartile range) away from the box ([Methods](#)). **b**, Fraction of variance in BANP binding explained by a linear model that incorporates either motif score or methylation of the motif, or both ([Methods](#)). **c**, True versus predicted BANP ChIP–seq enrichments at predicted motifs (as defined in Extended Data Fig. [1k](#)) for a linear model that uses motif score (left), methylation (middle) or both motif score and methylation (right) as predictors. Fraction of variance explained is indicated as R^2 . **d**, PAQMAN using a methylated (Meth.) BANP motif reduces affinity by more than 16-fold compared to an unmethylated (unmeth.) motif. Binding curves were generated by fitting the parameters of the Hill equation to determine the relative equilibrium dissociation constant (K_d^{app}). Data are the mean of three experiments ($n = 3$), error bars represent standard error of the mean. **e**, Top motif found by HOMER in the top 500 peaks of each replicate (R1–R3) in DNMT TKO cells. **f**, Reproducibility of changes in BANP binding in DNMT TKO versus wild-type ES cells at predicted BANP motifs ($n = 1,207$). Pearson correlation coefficient is indicated. R1–R3 indicate biological replicates. **g**, Change in BANP binding in DNMT TKO versus wild-type ES cells compared to the methylation level of the motif (WGBS) in wild-type ES cells at predicted BANP motifs ($n = 1,207$). **h**, Distribution of motif scores as a function of change in BANP binding in DNMT TKO versus wild-type ES cells. Box plots as in **a**. Notches extend to $\pm 1.58 \times$ (interquartile range/sqrt(n)). **i**, Single-locus examples of BANP binding in wild-type ES cells and DNMT TKO cells at promoters with a methylated BANP motif. Methylation of the CpGs in the motif is indicated by the colour of the circles above the motif. Colour range from white (0% methylation) to black (100% methylation). For *Tex13b*, the circle represents the average methylation of both CpGs as the coverage was too low to

quantify each CpG separately. **j**, Expression changes versus changes in BANP binding between wild-type ES cells and DNMT TKO cells at genes with a predicted BANP motif in their promoter. For the definition of gene-motif pairings, see [Methods](#). **k**, Superose 6 increase 10/300 GL size exclusion chromatography profile of full-length (FL) BANP protein. Peak fractions were analysed by SDS-PAGE and stained by Coomassie (inset) showing protein size and high purity. **l**, Electrophoretic mobility shift assay of full-length BANP binding to the unmethylated (left), methylated (middle) or scrambled (right) BANP motif ($n = 2$ replicates). **m**, Reproducibility of changes in BANP binding at peaks between the human cancer cell line HCT116 and HCC1954. R indicates the Pearson correlation coefficient. **n**, Top motif found by de novo motif search (HOMER) in the top 500 peaks of the first replicate of both cell types. Motifs found for the remaining replicates are very similar (data not shown). **o**, The fraction of peaks that contain a BANP motif as a function of peak strength in the first replicate of both cell types. Peaks were sorted by read counts and binned into groups of 250 peaks (each bar representing one group). Although we identified between around 14,000–24,000 peaks, only the top bins show a high fraction of peaks with motif (results very similar for the remaining replicates, data not shown). The additional peaks are likely to be false positives owing to an open chromatin bias in the ChIP-seq data as shown for HCT116 in **p**. **p**, BANP binding versus DNaseI in HCT116 cells in 1-kb tiling windows of chromosome 1. There is a global correlation of ChIP-seq and DNaseI signal, which probably explains the large number of peaks without a BANP motif. **q**, GO enrichment of genes that contain a bound BANP motif. The 30 most significant GO categories are shown and GO categories were grouped as in Extended Data Fig. [1n](#). Similarities to the mouse GO analysis are indicated by coloured bars and arrows (Extended Data Fig. [1n](#)). **r**, Differential methylation versus differential binding at BANP motifs bound in at least one of the two cell types. Single locus displayed in Fig. [2d](#) is circled. R indicates Pearson correlation coefficient. **s**, **t**, BANP binding and DNA methylation in HCT116 and HCC1954 cells at a BANP motif at a differentially methylated CGI shore (**s**) or in a CGI that lies in a partially methylated domain (**t**). Methylation of the CpGs in the motif is indicated by the colour of the circles above the motif. Colour range from white (0% methylation) to black (100% methylation). **u**, Negative correlation between methylation in the BANP motif and BANP binding at

CGI promoter sites in several human cancer cell lines of different origin, using DNaseI hypersensitivity as an indicator of BANP binding. Both methylation and DNaseI are shown relative to the average level across all cell types. Only sites that are bound in at least one cell line are shown (Methods). Pearson correlation coefficients are indicated.

Extended Data Fig. 3 Inducible BANP depletion by targeted degradation allows the loss of function of this essential gene to be studied.

a, Activation of a luciferase reporter gene by one, two or three copies of the BANP motif after transient transfection into mouse ES cells. **b**, BANP lethality score from genome wide CRISPR screens across more than 500 cell lines. A gene with a score below -0.5 is considered a common essential gene (Broad Institute (<https://depmap.org/portal/>)). Black lines correspond to median, boxes to first and third quartile and whiskers to the maximum and minimum values of the distribution. **c**, Full sized western blot of BANP in wild-type and DNMT TKO cell lines before and after addition of the dTAG demonstrates the reduced level of BANP due to tagging, and the absence of protein following induced degradation by the addition of the dTAG13 compound to the medium ($n = 3$ replicates). Arrowhead on right indicates the target protein. **d**, The cell-cycle phase distribution determined by BrdU incorporation followed by flow cytometry analysis of wild-type and DNMT TKO cells before and after endogenous tagging of the *Banp* gene ($n = 2$ replicates). **e**, Immunofluorescence visualizes BANP degradation in mouse ES cells ($n = 2$ replicates). a.u., arbitrary units. **f**, Quantification of cell death in wild-type and TKO cells after inducing BANP depletion by the addition of the dTAG13 compound. Individual data points are shown and the bars represent the mean of three biological replicates. **g**, Level of s4U incorporation at different time points of a BANP degradation time course, in which D stands for the time of induced BANP degradation and T for the time of incorporation. Percentage refers to the fraction of Ts converted to Cs. Although cells untreated with s4U show very low percentages (wild-type untreated R1–R3), the percentages increase with increasing incorporation time. Only genes with at least a total count of 50 reads overlapping Ts in all replicates are shown. R1–R3 indicate biological replicates. Black lines correspond to median, boxes to first and third

quartile and whiskers to the maximum and minimum values of the distribution after removal of outliers, in which outliers are defined as more than $1.5 \times$ (interquartile range) away from the box. $n = 13,801$ genes. **h**, Change in gene expression level of BANP-bound and unbound genes between wild-type and BANP degron-tagged cells. There is no consistent global difference between BANP bound and unbound genes. Same y range as Fig. [3c](#) for comparison. Box plots as in **g**. Notches extend to $\pm 1.58 \times$ (interquartile range/sqrt(n)). **i**, Change in RNA across a BANP degradation time course showing the response of unbound genes. Same y range as Fig. [3c](#) for comparison. Box plots as in **g**. **j**, Beeswarm plot of expression changes (\log_2) after 6 h of dTAG treatment (versus untreated) for all genes with a bound BANP motif belonging to one of the groups of GO categories as defined in Extended Data Fig. [1n](#).

Extended Data Fig. 4 Correlation heat maps for the wild-type ES cell RNA-seq time course.

a–f, Pearson correlations between samples for all quantifiable genes on exon level (**a**), intron level (**b**) and in SLAM-seq (**c**). **d–f**, Same as **a–c** but for all quantifiable genes with a BANP motif in their promoter. To remove correlations due to varying gene lengths, counts in all three measures were converted to \log_2 RPKM values before determining the correlation coefficients. r1–r3 indicate biological replicates. Samples named as in Extended Data Fig. [3g](#). **a–f** illustrate high reproducibility between replicates. **d–f** indicate that changes on the transcriptional level at BANP target genes occur fast whereas changes on the mRNA level are delayed. Note that the correlation structure in SLAM-seq is also influenced by the varying incorporation times.

Extended Data Fig. 5 Reproducibility and comparison of exonic, intronic and SLAM-seq signal during a time course of BANP degradation.

Top three rows show reproducibility of \log_2 changes relative to untreated for exonic, intronic and SLAM-seq, respectively. The first two replicates are shown in each case (R1 and R2). Bottom three rows show the same

changes comparing SLAM-seq to intronic, intronic to exonic and SLAM-seq to exonic signal, respectively. Average of all replicates is shown.

Comparisons indicate a high degree of similarity between intronic and SLAM-seq signal and a delayed exonic response. In all figures, Pearson correlations were calculated on all genes with a promoter that overlaps a bound BANP motif, highlighted in red.

Extended Data Fig. 6 The downregulation of BANP target genes is also detected at the protein level.

a, Pearson correlations of \log_2 changes in protein levels at different time points relative to untreated for all quantifiable genes (left) or for all quantifiable genes with a BANP motif in their promoter (right). Reproducible changes can be clearly observed after 10 h. R1–R3 indicate biological replicates. **b**, Scatter plots showing the correlation between RNA (exonic) and protein levels across a BANP degradation time course ($n = 8,128$ genes). In all panels, Pearson correlations were calculated on all genes with a promoter that overlaps a bound BANP motif ($n = 357$ genes), shown in red. As the aim of these comparisons is to see how mRNA changes of BANP targets are reflected at the protein level, but BANP itself, which has a BANP motif in its promoter, has been degraded at the protein level, it was removed from the comparisons. Its protein level changes are shown in **c** (top). The 10-h time point is missing as it was not measured in RNA. **c**, Depletion of BANP (top) and an essential BANP target gene, TUBGCP5 (bottom), relative to untreated cells across the BANP degradation time course. **d**, Total proteome showing the downregulation of BANP target genes at the protein level over a BANP degradation time course. BANP itself was removed as in **b**. Black lines correspond to median, boxes to first and third quartile and whiskers to the maximum and minimum values of the distribution after removal of outliers, in which outliers are defined as more than $1.5 \times$ (interquartile range) away from the box. Notches extend to $\pm 1.58 \times$ (interquartile range/sqrt(n)). Bound: $n = 357$ genes, unbound: $n = 7,861$ genes. **e**, Western blot for the essential BANP target gene TUBGCP5 over a degradation time course ($n = 2$ replicates). Arrowhead on right indicates the target protein. **f**, Quantification of the TUBGCP5 protein level in **e** normalized to the loading control. Individual replicates are shown, and the bars represent the mean.

Extended Data Fig. 7 BANP regulates a similar set of genes in DNMT TKO cells and is necessary and sufficient to drive expression of TKO-specific bound genes.

a–d, Same as Extended Data Fig. 4a, b, d, e, but for a DNMT TKO RNA-seq time course. **e, f**, Same as top two rows in Extended Data Fig. 5, but for a DNMT TKO RNA-seq time course. **g**, Comparison of the RNA response (exonic level) to BANP removal in wild-type versus TKO cell lines. In all panels, Pearson correlations were calculated on all genes with a promoter that overlaps a bound (bound in either wild-type or DNMT TKO) BANP motif, which are shown in red. All annotated promoters were used in order not to bias the analysis towards promoters with Pol II signal in wild-type (Methods, ‘Annotations’). **h**, Expression changes (relative to wild-type cells) in the DNMT TKO degron cell line across a BANP degradation time course for the genes that gain binding and increase expression in DNMT TKO cells (Extended Data Fig. 2i, j). The three genes are inactivated in response to BANP removal in DNMT TKO cells, which is a combination of reduced BANP levels in the dTAG line (dTAG untreated) and induced degradation by the addition of the dTAG13 compound (dTAG 1–6 h). Initial expression levels of these genes in wild-type ES cells are below 0.1 RPKM and can thus be considered inactive. Bars show means of $n = 6$ for TKO, $n = 2$ for TKO dTAG 1h and otherwise $n = 3$ biological replicates. Individual replicates are shown as dots. Error bars denote ± 1 standard deviation.

Extended Data Fig. 8 BANP binding in neurons is mostly conserved compared to ES cells but also shows cell-type-specific binding.

a, Immunofluorescence of mouse ES cells and derived neurons stained with Hoechst and calcein-AM ($n = 3$ replicates). **b**, Reproducibility of BANP enrichments at predicted BANP motifs ($n = 1,207$) as defined in Extended Data Fig. 1k. Pearson correlation coefficients are indicated. R1–R3 indicate biological replicates. UI, ES cells with uninduced *Ngn2* construct. **c**, Scatter plot of the change in BANP binding from ES cells to neurons at predicted BANP-binding sites. R1 and R2 indicate biological replicates. **d**, Change in

RNA compared to the change in BANP binding between mouse ES cells and neurons at predicted BANP motifs ($n = 1,207$). The Pearson correlation coefficient is indicated.

Extended Data Fig. 9 BANP-bound genes are rapidly downregulated in neurons.

a, Western blot of BANP in neurons demonstrates absence of protein following induced degradation by the addition of the dTAG13 compound to the medium ($n = 3$ replicates, replicate 1 shown). Arrowhead on right indicates the target protein. **b, c**, Same as Extended Data Fig. 4a, b, d, e, but for a neuron RNA-seq time course. Ey wt, wild-type ES cells. wtBANP, wild-type ES cells with the BANP dTAG. UI, uninduced, I, induced. D, dTAG-treated. **d, e**, Same as top two rows in Extended Data Fig. 5, but for a neuron RNA-seq time course. **f**, Scatter plots of the change in gene expression after BANP degradation in ES cells versus neurons. R indicates Pearson correlation coefficient. Bound BANP motifs are shown in red.

Extended Data Fig. 10 Open chromatin and phased nucleosomes around BANP-bound motifs in CGIs is linked to gene activity.

a, Hierarchically clustered correlation heat map of ATAC-seq signal at predicted BANP motifs across a BANP degradation time course. The main change in signal occurs already in the first hour of degradation. **b**, Average ATAC-seq profiles around bound BANP motifs across the time course, illustrating (as in **a**) that the main change occurs within the first hour. For each time point, there are two replicates shown in the same colour. Signal smoothed over 51 nt. **c**, Accessibility change relative to untreated at bound BANP motifs after removal of BANP. Same as inset in Fig. 4b, but for all time points. Dots represent individual replicates, bars the mean of the two replicates. **d**, Scatter plots of MNase-seq signal at predicted BANP motifs in untreated, 1-h-BANP-degraded (1 h) and 4-h-BANP-degraded (4 h) cells ($n = 2$ replicates combined per condition). The main change occurs within the first hour (see also **e**). The Pearson correlation coefficient is indicated. **e**, Scatter plot comparing changes in MNase-seq signal at predicted BANP

motifs after 1 h and 4 h of BANP degradation relative to untreated, indicating little change from 1 h to 4 h. Pearson correlation coefficient indicated. **f**, Nucleosome phasing around the top 100 BANP or CTCF-bound motifs in CGI promoters. Profiles are oriented in the 5' to 3' direction to the corresponding genes. This highly organized chromatin is at odds with previous suggestions of low nucleosomal density at CGIs⁸⁴, which we speculate reflects inefficient amplification of GC rich sequences in first-generation sequencing reagents. **g**, Changes in MNase-seq versus changes in ATAC-seq signal after 1h of BANP degradation at BANP motifs. Sites that lose accessibility tend to gain nucleosome signal. Pearson correlation coefficient indicated. **h, i**, Changes in ATAC-seq (**h**) and MNase-seq (**i**) after 1h of BANP degradation versus BANP binding strength. Loss in accessibility and gain in nucleosomal signal occurs mostly at bound sites. Pearson correlation coefficient indicated. **j–l**, Change in expression at 6h versus untreated (exonic) compared to BANP binding (**j**), change in accessibility (**k**) or nucleosomal signal (**l**) after 1 h of BANP degradation at predicted BANP motifs. For the definition of gene–motif pairings, see [Methods](#). Exonic changes at 6 h were used as they are similar to intronic changes at 1 h (Extended Data Fig. [5](#)), but allow for the quantification of a larger number of genes. Accessibility and expression changes are positively correlated, whereas nucleosomal signal and expression changes are negatively correlated. *P* values were determined via an approximate permutation test (two-sided, $n = 458$ in all cases, [Methods](#)). **m**, The changes in expression (RNA, $P = 2.5 \cdot 10^{-16}$, robust *F* test, two-sided), accessibility (ATAC-seq, $P = 0.015$, robust *F* test, two-sided) and nucleosome positioning (MNase-seq, $P = 1.3 \cdot 10^{-10}$, robust *F* test, two-sided) after removal of BANP increase significantly with increasing binding strength ([Methods](#)). Unbound, below twofold enriched (IP/IgG). Weak, \log_2 enrichment (IP/IgG) between 1 and 4. Strong, \log_2 enrichment larger than 4. Box plots as in Extended Data Fig. [6d](#). **n**, Linear model to predict changes in expression (exonic) after 6 h of BANP degradation versus untreated cells using BANP binding, ATAC-seq changes after 1 h of BANP degradation (ATAC-seq), MNase-seq changes after 1 h of BANP degradation (MNase-seq) and distance of the BANP motif to TSS, a binary variable that indicates whether the motif lies within 100 nt upstream of the TSS ([Methods](#)). Only bound motifs were used ($\log_2(\text{IP/IgG}) \geq 1$) and, to be able

to cleanly assign motifs to genes, only genes with promoters that contained one bound motif and for which the motif did not overlap with any other promoter were used ($n = 321$). The models were evaluated via fivefold crossvalidation (Methods). Left, fraction of variance explained using only BANP binding (binding), binding and distance to TSS (binding + TSSdist) or BANP binding, distance to TSS, MNase-seq and ATAC-seq signal (binding + TSSdist + chromatin). Coloured dots refer to the performance of each model in each partition of the cross-validation. Chromatin information increases the predictive power of the model as is evident by the larger average fraction of explained variance of ‘Binding + TSS + chromatin’ (averaged over all five partitions) as well as the fact that ‘Binding + TSSdist + chromatin’ outperforms ‘Binding’ in all partitions and ‘Binding + TSSdist’ in 4 out of 5 partitions. Middle, inferred coefficients for the full model. Colours refer to the different partitions. Right, true expression changes versus predicted expression changes when using the average coefficients (averaged over all partitions) for prediction. In all panels, ATAC-seq, MNase-seq and ChIP-seq signal are quantified in a 201-bp window centred around the motif.

Supplementary information

Supplementary Tables

This file contains Supplementary Tables 1-6. Supplementary Table 1: Antibodies and dilutions used in this study. Supplementary Table 2: Motif sequences used for RMCE insertion and footprinting. A footprintable GpC was added to both ends of each motif to maximize the ability to detect a footprint (red). Supplementary Table 3: Oligonucleotide sequences used for affinity purification. Supplementary Table 4: Oligonucleotides used for PAQMAN assay. Supplementary Table 5: Motif sequences used for RMCE insertion and luciferase assays. Supplementary Table 6: BANP degradation time and s4U incorporation time for the SLAM-seq time course.

Reporting Summary

Peer Review File

Rights and permissions

[Reprints and Permissions](#)

About this article



Check for
updates

Cite this article

Grand, R.S., Burger, L., Gräwe, C. *et al.* BANP opens chromatin and activates CpG-island-regulated genes. *Nature* **596**, 133–137 (2021).
<https://doi.org/10.1038/s41586-021-03689-8>

[Download citation](#)

- Received: 22 August 2020
- Accepted: 03 June 2021
- Published: 07 July 2021
- Issue Date: 05 August 2021
- DOI: <https://doi.org/10.1038/s41586-021-03689-8>

Comments

By submitting a comment you agree to abide by our [Terms](#) and [Community Guidelines](#). If you find something abusive or that does not comply with our terms or guidelines please flag it as inappropriate.

[Access through your institution](#)

[Change institution](#)

[Buy or subscribe](#)

Advertisement

This article was downloaded by **calibre** from <https://www.nature.com/articles/s41586-021-03689-8>

| [Section menu](#) | [Main menu](#) |

- Article
- [Published: 21 July 2021](#)

Structural basis of human separase regulation by securin and CDK1–cyclin B1

- [Jun Yu](#) [ORCID: orcid.org/0000-0001-5642-3991¹](#),
- [Pierre Raia](#) [ORCID: orcid.org/0000-0003-3469-1922¹](#) na1,
- [Chloe M. Ghent²](#) na1,
- [Tobias Raisch](#) [ORCID: orcid.org/0000-0002-6531-3812³](#) na1,
- [Yashar Sadian⁴](#),
- [Simone Cavadini⁵](#),
- [Pramod M. Sabale](#) [ORCID: orcid.org/0000-0002-7291-6697⁶](#),
- [David Barford](#) [ORCID: orcid.org/0000-0001-8810-950X⁷](#),
- [Stefan Raunser](#) [ORCID: orcid.org/0000-0001-9373-3016³](#),
- [David O. Morgan](#) [ORCID: orcid.org/0000-0001-8753-4416²](#) &
- [Andreas Boland](#) [ORCID: orcid.org/0000-0003-1218-6714¹](#)

[Nature](#) volume 596, pages 138–142 (2021) [Cite this article](#)

- 4256 Accesses
- 137 Altmetric
- [Metrics details](#)

Subjects

- [Chromosome segregation](#)
- [Cryoelectron microscopy](#)

- [Enzyme mechanisms](#)
- [Mitosis](#)
- [Proteases](#)

This article has been [updated](#)

Abstract

In early mitosis, the duplicated chromosomes are held together by the ring-shaped cohesin complex¹. Separation of chromosomes during anaphase is triggered by separase—a large cysteine endopeptidase that cleaves the cohesin subunit SCC1 (also known as RAD21^{2,3,4}). Separase is activated by degradation of its inhibitors, securin⁵ and cyclin B⁶, but the molecular mechanisms of separase regulation are not clear. Here we used cryogenic electron microscopy to determine the structures of human separase in complex with either securin or CDK1–cyclin B1–CKS1. In both complexes, separase is inhibited by pseudosubstrate motifs that block substrate binding at the catalytic site and at nearby docking sites. As in *Caenorhabditis elegans*⁷ and yeast⁸, human securin contains its own pseudosubstrate motifs. By contrast, CDK1–cyclin B1 inhibits separase by deploying pseudosubstrate motifs from intrinsically disordered loops in separase itself. One autoinhibitory loop is oriented by CDK1–cyclin B1 to block the catalytic sites of both separase and CDK1^{9,10}. Another autoinhibitory loop blocks substrate docking in a cleft adjacent to the separase catalytic site. A third separase loop contains a phosphoserine⁶ that promotes complex assembly by binding to a conserved phosphate-binding pocket in cyclin B1. Our study reveals the diverse array of mechanisms by which securin and CDK1–cyclin B1 bind and inhibit separase, providing the molecular basis for the robust control of chromosome segregation.

Access options

Subscribe to Journal

Get full journal access for 1 year

\$199.00

only \$3.90 per issue

[Subscribe](#)

All prices are NET prices.

VAT will be added later in the checkout.

Tax calculation will be finalised during checkout.

Rent or Buy article

Get time limited or full article access on ReadCube.

from \$8.99

[Rent or Buy](#)

All prices are NET prices.

Additional access options:

- [Log in](#)
- [Access through your institution](#)
- [Learn about institutional subscriptions](#)

Fig. 1: Domain organization of *Homo sapiens* (*Hs*) separase–securin and separase–CDK1–cyclin B1–CKS1 (CCC) complexes.

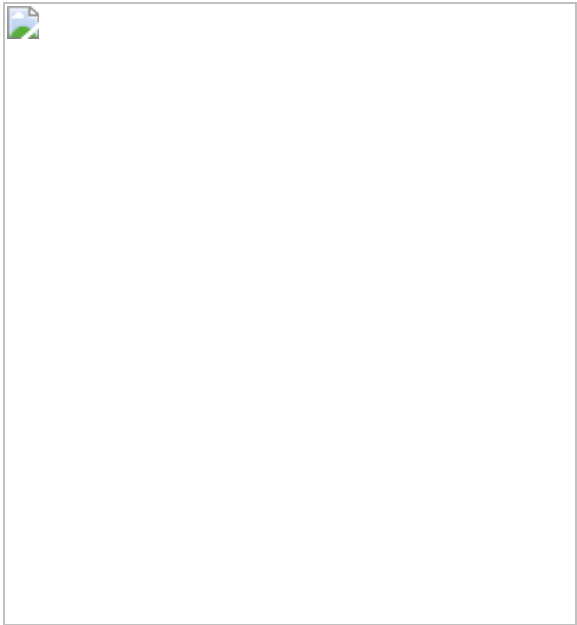


Fig. 2: Binding modes of an SCC1 peptide substrate, securin and the CCC complex to separase.

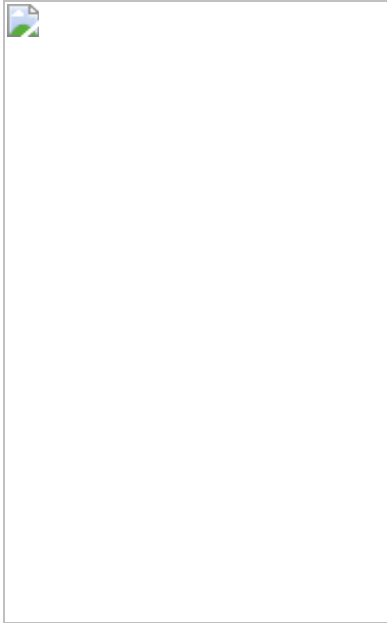
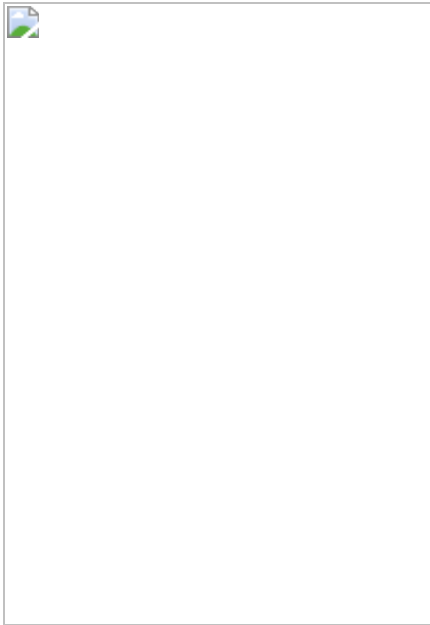


Fig. 3: Assembly of the separase-CDK1-cyclin B1-CKS1 complex and structural basis of inhibition of CDK1 by separase.



Data availability

The EM maps have been deposited in the Electron Microscopy Data Bank (EMDB) under accession codes [EMD-12368](#) and [EMD-12369](#) for the separase–CCC and separase–securin complexes, respectively. Protein coordinates for separase–CCC and separase–securin have been deposited in the Protein Data Bank (PDB) under accession codes [7NJ0](#) and [7NJ1](#), respectively. [Source data](#) are provided with this paper.

Change history

- [30 July 2021](#)

This Article was amended to correct the linking to Supplementary Videos 1-3

References

1. 1.

Gruber, S., Haering, C. H. & Nasmyth, K. Chromosomal cohesin forms a ring. *Cell* **112**, 765–777 (2003).

[CAS](#) [PubMed](#) [Article](#) [Google Scholar](#)

2. 2.

Uhlmann, F., Wernic, D., Poupart, M. A., Koonin, E. V. & Nasmyth, K. Cleavage of cohesin by the CD clan protease separin triggers anaphase in yeast. *Cell* **103**, 375–386 (2000).

[CAS](#) [PubMed](#) [Article](#) [Google Scholar](#)

3. 3.

Hauf, S., Waizenegger, I. C. & Peters, J. M. Cohesin cleavage by separase required for anaphase and cytokinesis in human cells. *Science* **293**, 1320–1323 (2001).

[ADS](#) [CAS](#) [PubMed](#) [Article](#) [Google Scholar](#)

4. 4.

Waizenegger, I. C., Hauf, S., Meinke, A. & Peters, J. M. Two distinct pathways remove mammalian cohesin from chromosome arms in prophase and from centromeres in anaphase. *Cell* **103**, 399–410 (2000).

[CAS](#) [PubMed](#) [Article](#) [Google Scholar](#)

5. 5.

Ciosk, R. et al. An ESP1/PDS1 complex regulates loss of sister chromatid cohesion at the metaphase to anaphase transition in yeast. *Cell* **93**, 1067–1076 (1998).

[CAS](#) [PubMed](#) [Article](#) [Google Scholar](#)

6. 6.

Stemmann, O., Zou, H., Gerber, S. A., Gygi, S. P. & Kirschner, M. W. Dual inhibition of sister chromatid separation at metaphase. *Cell* **107**, 715–726 (2001).

[CAS](#) [PubMed](#) [Article](#) [Google Scholar](#)

7. 7.

Boland, A. et al. Cryo-EM structure of a metazoan separase-securin complex at near-atomic resolution. *Nat. Struct. Mol. Biol.* **24**, 414–418 (2017).

[CAS](#) [PubMed](#) [PubMed Central](#) [Article](#) [Google Scholar](#)

8. 8.

Luo, S. & Tong, L. Molecular mechanism for the regulation of yeast separase by securin. *Nature* **542**, 255–259 (2017).

[ADS](#) [CAS](#) [PubMed](#) [PubMed Central](#) [Article](#) [Google Scholar](#)

9. 9.

Gorr, I. H. et al. Essential CDK1-inhibitory role for separase during meiosis I in vertebrate oocytes. *Nat. Cell Biol.* **8**, 1035–1037 (2006).

[CAS](#) [PubMed](#) [PubMed Central](#) [Article](#) [Google Scholar](#)

10. 10.

Gorr, I. H., Boos, D. & Stemmann, O. Mutual inhibition of separase and Cdk1 by two-step complex formation. *Mol. Cell* **19**, 135–141 (2005).

[CAS](#) [PubMed](#) [Article](#) [Google Scholar](#)

11. 11.

Santaguida, S. & Amon, A. Short- and long-term effects of chromosome mis-segregation and aneuploidy. *Nat. Rev. Mol. Cell Biol.* **16**, 473–485 (2015).

[CAS](#) [PubMed](#) [Article](#) [Google Scholar](#)

12. 12.

Kamenz, J. & Hauf, S. Time to split up: dynamics of chromosome separation. *Trends Cell Biol.* **27**, 42–54 (2017).

[CAS](#) [PubMed](#) [Article](#) [Google Scholar](#)

13. 13.

Rosen, L. E. et al. Cohesin cleavage by separase is enhanced by a substrate motif distinct from the cleavage site. *Nat. Commun.* **10**, 5189 (2019).

[ADS](#) [PubMed](#) [PubMed Central](#) [Article](#) [CAS](#) [Google Scholar](#)

14. 14.

Zou, H., McGarry, T. J., Bernal, T. & Kirschner, M. W. Identification of a vertebrate sister-chromatid separation inhibitor involved in transformation and tumorigenesis. *Science* **285**, 418–422 (1999).

[CAS](#) [PubMed](#) [Article](#) [Google Scholar](#)

15. 15.

Li, J., Ouyang, Y. C., Zhang, C. H., Qian, W. P. & Sun, Q. Y. The cyclin B2/CDK1 complex inhibits separase activity in mouse oocyte meiosis I. *Development* **146**, dev182519 (2019).

[CAS](#) [PubMed](#) [Article](#) [Google Scholar](#)

16. 16.

Hellmuth, S., Gómez-H, L., Pendás, A. M. & Stemmann, O. Securin-independent regulation of separase by checkpoint-induced shugoshin–MAD2. *Nature* **580**, 536–541 (2020).

[ADS](#) [CAS](#) [PubMed](#) [Article](#) [Google Scholar](#)

17. 17.

Hellmuth, S. et al. Human chromosome segregation involves multi-layered regulation of separase by the peptidyl-prolyl-isomerase Pin1. *Mol. Cell* **58**, 495–506 (2015).

[CAS](#) [PubMed](#) [Article](#) [Google Scholar](#)

18. 18.

Shindo, N., Kumada, K. & Hirota, T. Separase sensor reveals dual roles for separase coordinating cohesin cleavage and cdk1 inhibition. *Dev. Cell* **23**, 112–123 (2012).

[CAS](#) [PubMed](#) [Article](#) [Google Scholar](#)

19. 19.

Lin, Z., Luo, X. & Yu, H. Structural basis of cohesin cleavage by separase. *Nature* **532**, 131–134 (2016).

[ADS](#) [CAS](#) [PubMed](#) [PubMed Central](#) [Article](#) [Google Scholar](#)

20. 20.

Sullivan, M., Hornig, N. C. D., Porstmann, T. & Uhlmann, F. Studies on substrate recognition by the budding yeast separase. *J. Biol. Chem.* **279**, 1191–1196 (2004).

[CAS](#) [PubMed](#) [Article](#) [Google Scholar](#)

21. 21.

Nagao, K. & Yanagida, M. Securin can have a separase cleavage site by substitution mutations in the domain required for stabilization and inhibition of separase. *Genes Cells* **11**, 247–260 (2006).

[CAS](#) [PubMed](#) [Article](#) [Google Scholar](#)

22. 22.

Alexandru, G., Uhlmann, F., Mechtler, K., Poupart, M. A. & Nasmyth, K. Phosphorylation of the cohesin subunit Scc1 by Polo/Cdc5 kinase regulates sister chromatid separation in yeast. *Cell* **105**, 459–472 (2001).

[CAS](#) [PubMed](#) [Article](#) [Google Scholar](#)

23. 23.

Boos, D., Kuffer, C., Lenobel, R., Körner, R. & Stemmann, O. Phosphorylation-dependent binding of cyclin B1 to a Cdc6-like domain of human separase. *J. Biol. Chem.* **283**, 816–823 (2008).

[CAS](#) [PubMed](#) [Article](#) [Google Scholar](#)

24. 24.

Kõivomägi, M. et al. Multisite phosphorylation networks as signal processors for Cdk1. *Nat. Struct. Mol. Biol.* **20**, 1415–1424 (2013).

[PubMed](#) [Article](#) [CAS](#) [Google Scholar](#)

25. 25.

McGrath, D. A. et al. Cks confers specificity to phosphorylation-dependent CDK signaling pathways. *Nat. Struct. Mol. Biol.* **20**, 1407–1414 (2013).

[CAS](#) [PubMed](#) [PubMed Central](#) [Article](#) [Google Scholar](#)

26. 26.

Holland, A. J., Böttger, F., Stemmann, O. & Taylor, S. S. Protein phosphatase 2A and separase form a complex regulated by separase autocleavage. *J. Biol. Chem.* **282**, 24623–24632 (2007).

[CAS](#) [PubMed](#) [Article](#) [Google Scholar](#)

27. 27.

Zou, H., Stemman, O., Anderson, J. S., Mann, M. & Kirschner, M. W. Anaphase specific auto-cleavage of separase. *FEBS Lett.* **528**, 246–250 (2002).

[CAS](#) [PubMed](#) [Article](#) [Google Scholar](#)

28. 28.

Luo, S. & Tong, L. in *Macromolecular Protein Complexes III: Structure and Function*. (eds. Harris, J. R. & Marles-Wright, J.) 217–232 (Springer, 2021).

29. 29.

Bachmann, G. et al. A closed conformation of the *Caenorhabditis elegans* separase-securin complex. *Open Biol.* **6**, 160032 (2016).

[PubMed](#) [PubMed Central](#) [Article](#) [CAS](#) [Google Scholar](#)

30. 30.

Dephoure, N. et al. A quantitative atlas of mitotic phosphorylation. *Proc. Natl Acad. Sci. USA* **105**, 10762–10767 (2008).

[ADS](#) [CAS](#) [PubMed](#) [PubMed Central](#) [Article](#) [Google Scholar](#)

31. 31.

Cheng, K. Y. et al. The role of the phospho-CDK2/cyclin A recruitment site in substrate recognition. *J. Biol. Chem.* **281**, 23167–23179 (2006).

[CAS](#) [PubMed](#) [Article](#) [Google Scholar](#)

32. 32.

Russo, A. A., Jeffrey, P. D., Patten, A. K., Massagué, J. & Pavletich, N. P. Crystal structure of the p27Kip1 cyclin-dependent-kinase inhibitor bound to the cyclin A-Cdk2 complex. *Nature* **382**, 325–331 (1996).

[ADS](#) [CAS](#) [PubMed](#) [Article](#) [Google Scholar](#)

33. 33.

Melesse, M., Bembeneck, J. N. & Zhulin, I. B. Conservation of the separase regulatory domain. *Biol. Direct* **13**, 7 (2018).

[PubMed](#) [PubMed Central](#) [Article](#) [CAS](#) [Google Scholar](#)

34. 34.

Goda, T., Ishii, T., Nakajo, N., Sagata, N. & Kobayashi, H. The RRASK motif in Xenopus cyclin B2 is required for the substrate recognition of Cdc25C by the cyclin B-Cdc2 complex. *J. Biol. Chem.* **278**, 19032–19037 (2003).

[CAS](#) [PubMed](#) [Article](#) [Google Scholar](#)

35. 35.

Zhang, Z., Yang, J. & Barford, D. Recombinant expression and reconstitution of multiprotein complexes by the USER cloning method in the insect cell-baculovirus expression system. *Methods* **95**, 13–25 (2016).

[CAS](#) [PubMed](#) [Article](#) [Google Scholar](#)

36. 36.

Zhang, S. et al. Molecular mechanism of APC/C activation by mitotic phosphorylation. *Nature* **533**, 260–264 (2016).

[ADS](#) [CAS](#) [PubMed](#) [PubMed Central](#) [Article](#) [Google Scholar](#)

37. 37.

Martin, T. G., Boland, A., Fitzpatrick, A. W. P. & Scheres, S. H. W. *Graphene Oxide Grid Preparation*.
https://figshare.com/articles/Graphene_Oxide_Grid_Preparation/3178669 (2016).

38. 38.

Stabrin, M. et al. TranSPHIRE: automated and feedback-optimized on-the-fly processing for cryo-EM. *Nat. Commun.* **11**, 5716 (2020).

[ADS](#) [CAS](#) [PubMed](#) [PubMed Central](#) [Article](#) [Google Scholar](#)

39. 39.

Zheng, S. Q. et al. MotionCor2: anisotropic correction of beam-induced motion for improved cryo-electron microscopy. *Nat. Methods* **14**, 331–332 (2017).

[CAS](#) [PubMed](#) [PubMed Central](#) [Article](#) [Google Scholar](#)

40. 40.

Rohou, A. & Grigorieff, N. CTFFIND4: fast and accurate defocus estimation from electron micrographs. *J. Struct. Biol.* **192**, 216–221 (2015).

[PubMed](#) [PubMed Central](#) [Article](#) [Google Scholar](#)

41. 41.

Wagner, T. et al. SPHIRE-crYOLO is a fast and accurate fully automated particle picker for cryo-EM. *Commun. Biol.* **2**, 218 (2019).

[PubMed](#) [PubMed Central](#) [Article](#) [Google Scholar](#)

42. 42.

Yang, Z., Fang, J., Chittuluru, J., Asturias, F. J. & Penczek, P. A. Iterative stable alignment and clustering of 2D transmission electron microscope images. *Structure* **20**, 237–247 (2012).

[CAS](#) [PubMed](#) [PubMed Central](#) [Article](#) [Google Scholar](#)

43. 43.

Wilkinson, M. E., Kumar, A. & Casañal, A. Methods for merging data sets in electron cryo-microscopy. *Acta Crystallogr. D* **75**, 782–791 (2019).

[CAS](#) [Article](#) [Google Scholar](#)

44. 44.

Punjani, A., Rubinstein, J. L., Fleet, D. J. & Brubaker, M. A. cryoSPARC: algorithms for rapid unsupervised cryo-EM structure determination. *Nat. Methods* **14**, 290–296 (2017).

[CAS](#) [Article](#) [Google Scholar](#)

45. 45.

Bepler, T. et al. Positive-unlabeled convolutional neural networks for particle picking in cryo-electron micrographs. *Nat. Methods* **16**, 1153–1160 (2019).

[CAS](#) [PubMed](#) [PubMed Central](#) [Article](#) [Google Scholar](#)

46. 46.

Zivanov, J., Nakane, T. & Scheres, S. H. W. Estimation of high-order aberrations and anisotropic magnification from cryo-EM data sets in RELION-3.1. *IUCrJ* **7**, 253–267 (2020).

[CAS](#) [PubMed](#) [PubMed Central](#) [Article](#) [Google Scholar](#)

47. 47.

Sanchez-Garcia, R. et al. DeepEMhancer: a deep learning solution for cryo-EM volume post-processing. Preprint at <https://doi.org/10.1101/2020.06.12.148296> (2020).

48. 48.

Kucukelbir, A., Sigworth, F. J. & Tagare, H. D. Quantifying the local resolution of cryo-EM density maps. *Nat. Methods* **11**, 63–65 (2014).

[CAS](#) [PubMed](#) [Article](#) [Google Scholar](#)

49. 49.

Adams, P. D. et al. PHENIX: a comprehensive Python-based system for macromolecular structure solution. *Acta Crystallogr. D* **66**, 213–221 (2010).

[CAS](#) [PubMed](#) [PubMed Central](#) [Article](#) [Google Scholar](#)

50. 50.

Emsley, P., Lohkamp, B., Scott, W. G. & Cowtan, K. Features and development of Coot. *Acta Crystallogr. D* **66**, 486–501 (2010).

[CAS](#) [PubMed](#) [PubMed Central](#) [Article](#) [Google Scholar](#)

51. 51.

Brown, N. R. et al. CDK1 structures reveal conserved and unique features of the essential cell cycle CDK. *Nat. Commun.* **6**, 6769 (2015).

[ADS](#) [CAS](#) [PubMed](#) [PubMed Central](#) [Article](#) [Google Scholar](#)

52. 52.

Topf, M. et al. Protein structure fitting and refinement guided by cryo-EM density. *Structure* **16**, 295–307 (2008).

[CAS](#) [PubMed](#) [PubMed Central](#) [Article](#) [Google Scholar](#)

53. 53.

Afonine, P. V. et al. New tools for the analysis and validation of cryo-EM maps and atomic models. *Acta Crystallogr. D* **74**, 814–840 (2018).

[CAS](#) [Article](#) [Google Scholar](#)

54. 54.

Williams, C. J. et al. MolProbity: More and better reference data for improved all-atom structure validation. *Protein Sci.* **27**, 293–315 (2018).

[CAS](#) [PubMed](#) [Article](#) [Google Scholar](#)

55. 55.

Yang, Z. et al. UCSF Chimera, MODELLER, and IMP: an integrated modeling system. *J. Struct. Biol.* **179**, 269–278 (2012).

[CAS](#) [PubMed](#) [Article](#) [Google Scholar](#)

56. 56.

Goddard, T. D. et al. UCSF ChimeraX: meeting modern challenges in visualization and analysis. *Protein Sci.* **27**, 14–25 (2018).

[CAS](#) [PubMed](#) [Article](#) [Google Scholar](#)

[Download references](#)

Acknowledgements

We thank Y. Pfister and I. Flückinger for technical assistance; A. K. Höfler and L. Poulain for input and discussion; J. Kamenz, R. Loewith and F. Steiner for critical reading of the manuscript; J. Yang and Z. Zhang for assistance in the early stages of this project; O. Hofnagel and D. Prumbaum for assistance with EM data collection at the Max Planck Institute of Molecular Physiology; C. Alfieri for sharing his PLK1 plasmid; the computing department of the University of Geneva for providing an infrastructure to perform cryo-EM analysis; N. Roggli for maintaining computing in the Molecular Biology department; C. Bauer for his contributions to the cryo-EM facility in Geneva (cryoGENic); O. Barabas for critical input; and the Metabolomics Core Facility at EMBL Heidelberg for mass spectrometry analysis. We acknowledge Diamond for access and support of the cryo-EM facilities at the UK national electron bio-imaging centre (eBIC), proposal EM13708, funded by the Wellcome Trust, MRC and BBSRC. This work was supported by the Swiss National Science Foundation (310030_185235), the Schmidheiny Foundation, a Novartis Research grant (all awarded to A.B.), a grant from the US National Institute of General Medical Sciences (R35-GM118053) to D.O.M., and an MRC grant (MC_UP_1201/6) to D.B.

Author information

Author notes

1. These authors contributed equally: Pierre Raia, Chloe M. Ghent, Tobias Raisch

Affiliations

1. Department of Molecular Biology, University of Geneva, Geneva, Switzerland

Jun Yu, Pierre Raia & Andreas Boland

2. Department of Physiology, University of California, San Francisco, San Francisco, CA, USA

Chloe M. Ghent & David O. Morgan

3. Department of Structural Biochemistry, Max Planck Institute of Molecular Physiology, Dortmund, Germany

Tobias Raisch & Stefan Raunser

4. Bioimaging Center, University of Geneva, Geneva, Switzerland

Yashar Sadian

5. Friedrich Miescher Institute for Biomedical Research, Basel, Switzerland

Simone Cavadini

6. Department of Organic Chemistry, NCCR Chemical Biology, University of Geneva, Geneva, Switzerland

Pramod M. Sabale

7. MRC Laboratory of Molecular Biology, Cambridge, UK

David Barford

Authors

1. Jun Yu

[View author publications](#)

You can also search for this author in [PubMed](#) [Google Scholar](#)

2. Pierre Raia

[View author publications](#)

You can also search for this author in [PubMed](#) [Google Scholar](#)

3. Chloe M. Ghent

[View author publications](#)

You can also search for this author in [PubMed](#) [Google Scholar](#)

4. Tobias Raisch

[View author publications](#)

You can also search for this author in [PubMed](#) [Google Scholar](#)

5. Yashar Sadian

[View author publications](#)

You can also search for this author in [PubMed](#) [Google Scholar](#)

6. Simone Cavadini

[View author publications](#)

You can also search for this author in [PubMed](#) [Google Scholar](#)

7. Pramod M. Sabale

[View author publications](#)

You can also search for this author in [PubMed](#) [Google Scholar](#)

8. David Barford

[View author publications](#)

You can also search for this author in [PubMed](#) [Google Scholar](#)

9. Stefan Raunser

[View author publications](#)

You can also search for this author in [PubMed](#) [Google Scholar](#)

10. David O. Morgan

[View author publications](#)

You can also search for this author in [PubMed](#) [Google Scholar](#)

11. Andreas Boland

[View author publications](#)

You can also search for this author in [PubMed](#) [Google Scholar](#)

Contributions

J.Y. expressed and purified the securin(Δ 160)–separase complexes, the MBP–securin fusions and the CDK1–cyclin B1–CKS1 complexes. C.M.G. purified securin(Δ 138)–separase fusion protein. P.R. and C.M.G. performed separase cleavage activity assays. J.Y. and Y.S. prepared grids and T.R. collected EM data with contributions from S.C. and A.B. J.Y. and P.R. analysed EM data and J.Y. determined the 3D reconstructions. J.Y. and Y.S. built the model ab initio and P.R. made the figures. A.B. directed the project and designed experiments together with D.O.M. A.B. and D.O.M. wrote the manuscript with contributions and discussions from J.Y., P.R., C.M.G., T.R., Y.S., P.M.S., D.B. and S.R.

Corresponding author

Correspondence to [Andreas Boland](#).

Ethics declarations

Competing interests

The authors declare no competing interests.

Additional information

Peer review information *Nature* thanks Silke Hauf, Frank Uhlmann and the other, anonymous, reviewer(s) for their contribution to the peer review of this work. Peer reviewer reports are available.

Publisher's note Springer Nature remains neutral with regard to jurisdictional claims in published maps and institutional affiliations.

Extended data figures and tables

Extended Data Fig. 1 Preparations and EM images of the human separase–securin and separase–CCC complexes.

a, SDS-PAGE gels of wild-type *Hs* separase–securin and *Hs* securin(Δ 160)–separase(C2029S)–CDK1–cyclin B1–CKS1. **b**, Representative cryo-electron micrographs of *Hs* separase–securin (left), *Hs* securin(Δ 160)–separase(C2029S)–CCC (middle), and *Hs* securin(Δ 138)–separase(C2029S) (right) collected on graphene oxide-coated EM grids. Scale bars, 500 Å. **c**, Gallery of two-dimensional class averages of *Hs* separase–securin (left), *Hs* securin(Δ 160)–separase(C2029S)–CCC (middle) and *Hs* securin(Δ 138)–separase(C2029S) (right) showing typical classes. White arrow, flexible N-terminal HEAT-repeat domain. Scale bars, 100 Å. To increase the number of views of separase in complex with either securin or the CCC complex, we used graphene oxide-coated electron microscopy (EM) grids as described^{7,37}. We used the deep-learning software packages TOPAZ⁴⁵ and crYOLO⁴¹ to establish reliable particle picking conditions that allowed the identification of rare particle projections. **d**, Gold standard FSC curve for full-length separase–securin, focused refined separase–securin C-terminal domains (TPR-like and protease domains) and securin(Δ 160)–separase(C2029S)–CCC complexes. **e**, EM density maps colour-coded according to local resolution ranging from 2.8 Å to 6 Å

Source data.

Extended Data Fig. 2 Evaluation of complex formation by size-exclusion chromatography (SEC).

a, SEC runs on the isolated PIN1, securin(Δ 160)–separase(C2029S) and CDK1–cyclin B1–CKS1 complexes resulted in elution volumes of approximately 1.9 ml, 1.5 ml and 1.6 ml, respectively (green, blue and red dashed lines). Adding the CDK1–cyclin B1–CKS1 complex (CCC) to securin(Δ 160)–separase(C2029S) did not yield a stable interaction between these two complexes under these conditions (solid red line). Adding PIN1 to the securin(Δ 160)–separase(C2029S) complex in the presence of CCC did not result in a detectable interaction of these two complexes (solid yellow line). However, a shoulder at high molecular weight can be

observed, indicating partial phosphorylation in insect cells, in accordance with our mass spectrometry results in **c**. Adding ATP to securin(Δ 160)–separase(C2029S), PIN1 and CCC resulted in a clear shift to a 1.35-ml elution volume (solid purple line). A clear shift was also observed when we added ATP to securin(Δ 160)–separase(C2029S) and CCC, indicating that PIN1 is dispensable for complex formation in vitro (solid blue line). **b**, Coomassie blue-stained polyacrylamide gels of fractions from the SEC runs. **c**, Mass spectrometry analysis of human separase, without the CCC complex, shows phosphorylation of numerous sites in separase, including Ser1126. Each vertical bar indicates the number of times a peptide containing that site was identified, coloured to indicate the presence of phosphorylation: for Ser1126, blue segments indicate high-confidence assignment of phosphorylation (Mascot peptide score >32) at three peptides, and red segments indicate lower scores at two peptides. The colour of the amino acid label indicates the Mascot maximum delta mod score; a score of 10 for Ser1126 indicates high-confidence assignment of phosphorylation to that residue. **d**, Mass spectrometry analysis of human separase after incubation with 5 mM ATP, 10 mM Mg²⁺ and the CCC complex also shows phosphorylation of separase Ser1126, with three high-confidence peptides (score >32) and a maximum delta mod score of 8, also indicating a high-confidence assignment. Note that this analysis does not allow a rigorous quantitative comparison of Ser1126 phosphorylation in the two preparations

[Source data](#).

Extended Data Fig. 3 Representative EM density for ab initio model building.

a, Securin density at different threshold levels (stronger information at the N terminus of securin). Side-chain density is clearly visible. **b**, Density of AIL1 located in a cleft between the TPR-like and protease domains (left) and the CDC6-like domain of insert 2 (right). EM density allows the unambiguous placement of side chains in both loop segments. **c**, Density of the TPR-like domain of human separase. **d**, Examples of EM map quality for the separase protease domain. **e**, Strong density of phosphothreonine 161 in CDK1 (left) and the separase phosphoserine 1126 of the cyclin B1-

binding loop (right). **f**, Extra density of human CKS1, possibly due to binding of phosphorylated threonine 1346 of separase.

Extended Data Fig. 4 Data-processing flowchart for the two datasets of the human separase–securin complex.

See [Methods](#). 3D classification of separase–securin complexes resulted in about 55% of particles with strong density for the N-terminal HEAT-repeat domain. These particles were subjected to CTF refinement and classified on either the N or C terminus. We used particle subtraction for further classification. Classification on the N-terminal domain was executed without alignment (in contrast to the larger C-terminal part) and resulted in approximately 200,000 particles that were used for a final 3D reconstruction. In both cases, DeepEMhancer⁴⁷ was used for post-processing.

Extended Data Fig. 5 Data-processing flowchart for the human separase–CCC complex.

See [Methods](#). 3D classification of securin(Δ 160)–separase(C2029S)–CCC complexes resulted in approximately 312,000 particles subjected to CTF refinement and Bayesian polishing. The final reconstruction refined to roughly 3.6 Å resolution and was post-processed in RELION.

Extended Data Fig. 6 Comparison of flexible elements in separase proteins.

a, Comparison of human separase in complex with securin or CCC to budding yeast (*Sc*) and *C. elegans* (*Ce*) separase. The loops—AIL1, AIL2, AIL3 (highlighted in blue) and the cyclin B-binding loop (highlighted in purple)—become ordered upon binding of CCC. The N-terminal domain adopts an elongated shape in human separase (two left structures) but in yeast this N-terminal domain is kinked. This domain is lost in *C. elegans* separase. **b**, Comparison of the N-terminal domains of human and yeast separases, with EM density for the first approximately 250 residues of human separase indicated as blue cartoon. The yeast N-terminal domain

adopts a much more compact fold, with the N terminus of the yeast protein folding back in close proximity to the TPR-like domain. This folded architecture may be an intrinsic feature of the yeast N-terminal domain or due to crystal packing constraints. **c**, EM density of human separase–securin at low-threshold rendering allows a full representation of the enzyme (grey envelope). A predicted model of the N-terminal 250 residues is shown in yellow, and the EM-derived structure of separase–securin is shown in blue and orange, respectively.

Extended Data Fig. 7 Multiple sequence alignments of conserved docking motifs in SCC1, securin and AILs of separase.

a, Sequence comparison of the catalytic site binding motif in SCC1 (purple), securin (orange) and the AIL3 of separase (grey) in different species. Key residues are boxed. The invariant arginine residue involved in substrate catalysis (SCC1) is replaced by a large hydrophobic residue in securin. **b**, Sequence comparison of the NXLXΦE binding motif in SCC1, securin and AIL1 of separase. A phenylalanine three amino acids upstream of the docking motif might correspond to the P1 position in SCC1 (arginine) or securin (hydrophobic residue). **c**, Sequence comparison of the LPE docking motif in SCC1 and securin. **d**, Residues in securin and AIL2 of separase that bind to a hydrophobic cleft situated in the TPR-like domain of separase. See also Extended Data Fig. [11a](#).

Extended Data Fig. 8 Molecular surface charge representation of the separase–securin and separase–CDK1–cyclin B1 complexes.

Surface charge of separase reveals a basic groove near the catalytic site that facilitates binding of AIL3 (top) and securin (bottom). Note that AIL3 binds in an inverted orientation to separase when compared to SCC1 or securin. SCC1 phosphorylation at a nearby serine residue stimulates binding to this basic groove in yeast separase²³. Phosphorylation of serine residues in AIL3 has been detected in other studies^{19,30}. Sequence alignment (below)

of the separase protease domain reveals conservation of residues that are critical for substrate or inhibitor recognition (boxed in grey).

Extended Data Fig. 9 SCC1 cleavage is enhanced by the NHLEYE motif downstream of the cleavage site.

a, SCC1 deletion mutants (left gel) were constructed to test the function of the 82-amino-acid region between the cleavage site (¹⁶⁹EIMR) and the ²⁵⁵LPE docking site. Constructs were made in an internal SCC1 fragment (residues 142–300). Each construct removed from 22 to 82 residues around the centre of the intervening region, as indicated in the diagrams. In another series of constructs (right gel), different amounts of the intervening sequence were replaced with random linker sequence (G, S, A, and T). ³⁵S-labelled SCC1 fragments were incubated with or without separase, and reaction products were analysed by SDS–PAGE and phosphorimaging. The central 22-amino acid region contains the conserved ²⁰⁷NHLEYE sequence. Results are representative of four independent experiments. **b**, The indicated amino acids were replaced with alanine in SCC1 (residues 142–300). ³⁵S-labelled SCC1 mutants were incubated with or without separase, and reaction products were analysed by SDS–PAGE and phosphorimaging. Results are representative of four independent experiments. **c**, In SCC1, 30–40-residue spacers separate the cleavage site (¹⁶⁹EIMR) and two docking sites (²⁰⁷NHLEYE and ²⁵⁵LPE). The importance of the spacer regions was tested with various mutations in an internal SCC1 fragment (residues 90–300). In the SCC1(ΔS) mutant, both spacers were deleted. In the three linker mutants, the two intervening spacers were replaced, together or one at a time, with random linker sequence (G, S, A, and T). Results are representative of four independent experiments. The reaction on the far right demonstrates cleavage of the securin(RE) mutant (residues 93–150), in which the pseudosubstrate motif ¹¹⁵EKFFP is converted to EKFRE¹³. Thus, closely spaced docking motifs allow cleavage of securin but not of SCC1.

Extended Data Fig. 10 Loop deletions of AIL1 and AIL3 enhance separase cleavage activity.

a, Separase mutants carrying deletions of AIL1 and/or AIL3 were purified to analyse the effect of these loop segments on separase cleavage activity. The results are representative of three independent experiments. Regions deleted in each mutant as follows (see Extended Data Table 2 for sequence details): AIL1 Δ , deletion of AIL1, which harbours the NDLNYE motif; AIL3 Δ 1, deletion of CDC6-like domain and NFS motif; AIL3 Δ 2, deletion of entire insert 2; AIL3 Δ 3, deletion of NFS motif. 35 S-labelled full-length SCC1 was incubated with either wild-type (WT) separase, an inactive separase mutant (C2029S), or separase loop deletions as indicated. Reaction products were analysed by SDS-PAGE and phosphorimaging. All loop deletions show enhanced SCC1 cleavage activity, with the exception of a mutant carrying a deletion of the entire insert 2, which exhibits cleavage activity comparable to that of the wild-type protein. Quantification of three independent experiments shown in Fig. 2g. **b**, Full-length SCC1 cleavage assays as described in **a** in the presence or absence of the CCC complex. Results are representative of three independent experiments. While SCC1 cleavage by wild-type separase is fully repressed by the CCC complex (lane 3), mutant proteins with deletions of AIL1 and/or AIL3 show partial cleavage activity in the presence of the CCC complex. Deletion of insert 2 (AIL3 Δ 2) leads to lower cleavage activity compared to other loop deletions. The reduction in inhibition by the CCC complex can be partially explained through reduced complex affinity, as demonstrated by SEC runs in **c**. Only wild-type separase (solid blue line) shows a clear shift towards a higher molecular weight elution volume after incubation with 5 mM ATP, 10 mM Mg $^{2+}$ and the CCC complex. **d**, Schematic diagram of the loop mutants analysed in these experiments

[Source data](#).

[Extended Data Fig. 11 A hydrophobic cleft in separase promotes securin binding and correlates directly with substrate cleavage efficiency.](#)

a, Close-up of the binding interface of the hydrophobic cleft of separase interacting with securin (top left, orange) or the AIL2 of separase (top right, grey). The molecular surface representation (below) highlights the hydrophobic nature of the binding cleft in separase. **b**, Schematic

representation of constructs used in binding and cleavage assays. **c**, In vitro pull-down assays using maltose binding protein (MBP)–securin fusions as bait demonstrates the importance of a stretch of hydrophobic amino acids in securin. A construct including residues 1–157 or wild-type securin (1–202) can bind to separase (lanes 9 and 10), whereas two C-terminal truncations (securin(Δ 127) and securin(Δ 138)) do not bind separase under these conditions (lanes 7 and 8). Purified MBP serves as negative control (lane 6). Lanes 1–5 are 10% of the input. Pull-down experiments have been repeated in three independent experiments. **d**, 35 S-labelled full-length SCC1 proteins were incubated with or without separase, and reaction products were analysed by SDS–PAGE and phosphorimaging. SCC1 cleavage by separase is inhibited by addition of full-length securin 1–202 or truncated securin 1–157 (lanes 5 and 6). Shorter securin constructs (1–127 and 1–138), which lack a stretch of hydrophobic residues, do not inhibit cleavage under these conditions (lanes 3 and 4).

Extended Data Fig. 12 The CDK1–cyclin B1–CKS1 complex binds to a clearly defined cleft in separase.

a, The separase–securin complex has a clearly defined cleft between the TPR-like and protease domains. **b**, The separase–CCC complex in four orientations (each rotated by 90°). The HEAT-repeat domain is omitted for clarity.

Extended Data Fig. 13 Molecular surface charge representation of cyclins.

a, The cyclin B-binding loop of separase binds inverted to the substrate-docking hydrophobic patch of cyclin B1 when compared to common substrates. **b**, Sequence alignment of the cyclin B-binding loop docking site motif. **c**, Calculating the surface charge of A- and B-type cyclins illustrates the existence of a phosphate-binding pocket in cyclin B1 but not cyclin A (compare top left versus top right). The cyclin B-binding loop also binds to the substrate-docking hydrophobic patch of cyclin B1, comparable to a typical cyclin B1-binding partner. Multiple sequence alignment of residues lining the phosphate-binding pocket shows conservation of Arg307, His320

and Lys324 in B-type cyclins (bottom left) but not in cyclin A (bottom right).

Extended Data Fig. 14 Binding of separase to CDK1–cyclin B is mediated through two distinct loops.

a, Comparison of human CDK1 in a chemical inhibitor-bound state (green) and the separase–CCC complex (pale red) with the CDC6-like domain of separase (AIL3; cyan). In the separase–CCC complex, the activation loop is in its active conformation (downwards) and allows substrate and separase binding. In the inhibitor-bound structure, the activation loop conformation is incompatible with substrate binding. **b**, The CDC6-like domain of separase binds to the active site of CDK1, while the cyclin B-binding loop (purple) of separase wraps around cyclin B1 with pSer1126 in its centre and hydrophobic patch interactions nearby. In common cyclin B substrates, these interactions are mediated through one continuous polypeptide (red). **c**, A kink in AIL3 is formed at the interface of cyclin B1 and the separase protease domain, with Thr1389, Arg1390 and Leu1391 being key residues for binding of AIL3 to cyclin B1.

Extended Data Table 1 Cryo-EM data collection, refinement and validation statistics

[Full size table](#)

Extended Data Table 2 List of proteins used in this study

[Full size table](#)

Supplementary information

Supplementary Figure 1

This file includes the uncropped gels and blots for Fig. 2f, and Extended Data Figs. 1a, 2b, 9a-c, 10a, b and 11c, d.

Reporting Summary

Video 1

Overall structure of inhibitory separase complexes This video shows the overall architecture of the human separase-securin and the separase- Cdk1-cyclin B1-Cks1 complexes as electron density and ribbon representation while rotating around the X-axis.

[Video 2](#)

Autoinhibitory loops mimic securin binding This video shows a superposition of the autoinhibitory loop 1 and 3 with securin and highlights common binding motifs that recognise structural elements in separase adjacent to the catalytic site.

[Video 3](#)

Separase and Cdk1-cyclin B1-Cks1 complex assembly This video describes the structural assembly of the separase-Cdk1-cyclin B1-Cks1 complex. The phosphate-binding pocket in cyclin B1 and the Cdc6-like domain are highlighted. A superposition between a Cdk1 structure bound to a substrate peptide and the separase Cdc6- like domain bound to the catalytic site of Cdk1 illustrates the structural similarities between these two binding partners.

[Peer Review File](#)

Source data

[Source Data Fig. 2](#)

[Source Data Extended Data Fig. 1](#)

[Source Data Extended Data Fig. 2](#)

[Source Data Extended Data Fig. 10](#)

Rights and permissions

[Reprints and Permissions](#)

About this article



Check for
updates

Cite this article

Yu, J., Raia, P., Ghent, C.M. *et al.* Structural basis of human separase regulation by securin and CDK1–cyclin B1. *Nature* **596**, 138–142 (2021). <https://doi.org/10.1038/s41586-021-03764-0>

[Download citation](#)

- Received: 14 February 2021
- Accepted: 23 June 2021
- Published: 21 July 2021
- Issue Date: 05 August 2021
- DOI: <https://doi.org/10.1038/s41586-021-03764-0>

Comments

By submitting a comment you agree to abide by our [Terms](#) and [Community Guidelines](#). If you find something abusive or that does not comply with our terms or guidelines please flag it as inappropriate.

[Access through your institution](#)

[Change institution](#)

[Buy or subscribe](#)

Associated Content

[Two giants of cell division in an oppressive embrace](#)

- Silke Hauf

Advertisement

This article was downloaded by **calibre** from <https://www.nature.com/articles/s41586-021-03764-0>

| [Section menu](#) | [Main menu](#) |

- Article
- [Published: 07 July 2021](#)

Structure of human Ca_v2.2 channel blocked by the painkiller ziconotide

- [Shuai Gao ORCID: orcid.org/0000-0002-8734-2489¹](#) na1,
- [Xia Yao ORCID: orcid.org/0000-0003-2406-268X¹](#) na1 &
- [Nieng Yan ORCID: orcid.org/0000-0003-4829-7416¹](#)

[Nature](#) volume 596, pages 143–147 (2021) [Cite this article](#)

- 5665 Accesses
- 62 Altmetric
- [Metrics details](#)

Subjects

- [Cryoelectron microscopy](#)
- [Ion channels in the nervous system](#)

Abstract

The neuronal-type (N-type) voltage-gated calcium (Ca_v) channels, which are designated Ca_v2.2, have an important role in the release of neurotransmitters^{1,2,3}. Ziconotide is a Ca_v2.2-specific peptide pore blocker that has been clinically used for treating intractable pain^{4,5,6}. Here we present cryo-electron microscopy structures of human Ca_v2.2 (comprising the core α1 and the ancillary α2δ-1 and β3 subunits) in the presence or

absence of ziconotide. Ziconotide is thoroughly coordinated by helices P1 and P2, which support the selectivity filter, and the extracellular loops (ECLs) in repeats II, III and IV of $\alpha 1$. To accommodate ziconotide, the ECL of repeat III and $\alpha 2\delta-1$ have to tilt upward concertedly. Three of the voltage-sensing domains (VSDs) are in a depolarized state, whereas the VSD of repeat II exhibits a down conformation that is stabilized by Ca_v2 -unique intracellular segments and a phosphatidylinositol 4,5-bisphosphate molecule. Our studies reveal the molecular basis for $\text{Ca}_v2.2$ -specific pore blocking by ziconotide and establish the framework for investigating electromechanical coupling in Ca_v channels.

Access options

Subscribe to Journal

Get full journal access for 1 year

\$199.00

only \$3.90 per issue

[Subscribe](#)

All prices are NET prices.

VAT will be added later in the checkout.

Tax calculation will be finalised during checkout.

Rent or Buy article

Get time limited or full article access on ReadCube.

from \$8.99

[Rent or Buy](#)

All prices are NET prices.

Additional access options:

- [Log in](#)
- [Access through your institution](#)
- [Learn about institutional subscriptions](#)

Fig. 1: Specific pore blockade of $\text{Ca}_v2.2$ by ziconotide.

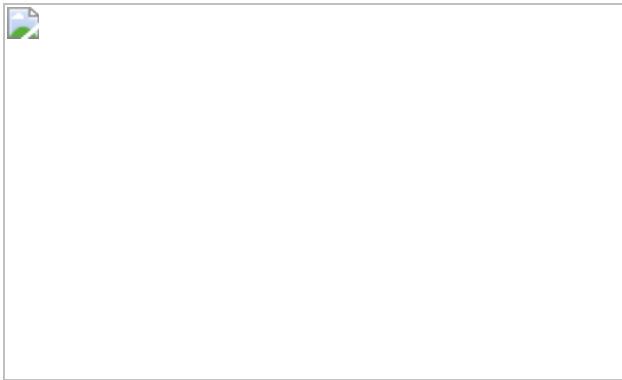


Fig. 2: Cytosolic segments unique to Ca_v2 in the II–III linker.

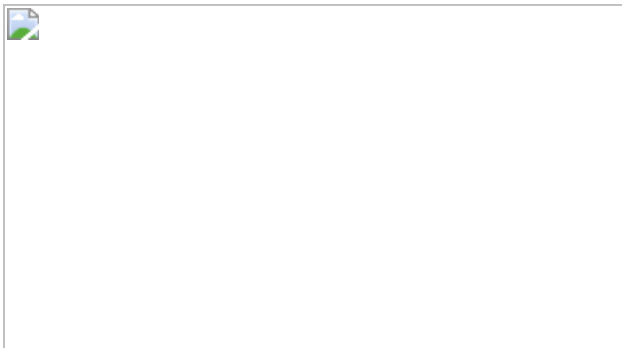
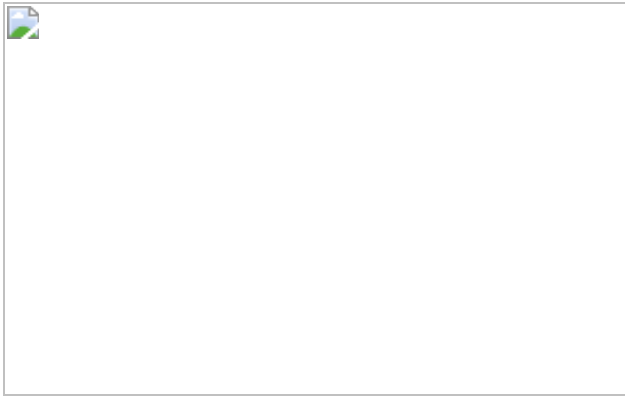


Fig. 3: VSD_{II} in a down state.



Fig. 4: The down conformation of VSD_{II} is stabilized by several intracellular segments and a bound PIP₂.



Data availability

The atomic coordinates and electron microscopy maps for Ca_v2.2 in complex with ziconotide and alone have been deposited in the PDB with the accession codes [7MIX](#) (with ziconotide) and [7MIY](#) (without ziconotide) and in the Electron Microscopy Data Bank with the codes [EMD-23867](#) (with ziconotide) and [EMD-23868](#) (without ziconotide), respectively. The atomic coordinates of the proteins for structural comparison in this study can be found in the PDB: rabbit Ca_v1.1 ([5GJW](#)), toxin-bound human Na_v1.2 ([6J8E](#)), toxin-bound Na_vPaS-1.7 chimera ([6NT4](#)), toxin-bound rat Na_v1.5 ([7K18](#)), Ci-VSP ([4G80](#)), HCN1 ([6UQF](#)) and KCNQ1 ([6V01](#)). Expression plasmids for the Ca_v2.2 subunits are available from the corresponding author upon reasonable request.

References

1. 1.

Dubel, S. J. et al. Molecular cloning of the α -1 subunit of an ω -conotoxin-sensitive calcium channel. *Proc. Natl Acad. Sci. USA* **89**, 5058–5062 (1992).

[ADS](#) [CAS](#) [PubMed](#) [PubMed Central](#) [Article](#) [Google Scholar](#)

2. 2.

Komuro, H. & Rakic, P. Selective role of N-type calcium channels in neuronal migration. *Science* **257**, 806–809 (1992).

[ADS](#) [CAS](#) [PubMed](#) [Article](#) [Google Scholar](#)

3. 3.

Zamponi, G. W., Striessnig, J., Koschak, A. & Dolphin, A. C. The physiology, pathology, and pharmacology of voltage-gated calcium channels and their future therapeutic potential. *Pharmacol. Rev.* **67**, 821–870 (2015).

[CAS](#) [PubMed](#) [PubMed Central](#) [Article](#) [Google Scholar](#)

4. 4.

Bowersox, S. S. & Luther, R. Pharmacotherapeutic potential of omega-conotoxin MVIIA (SNX-111), an N-type neuronal calcium channel blocker found in the venom of *Conus magus*. *Toxicon* **36**, 1651–1658 (1998).

[CAS](#) [PubMed](#) [Article](#) [Google Scholar](#)

5. 5.

Miljanich, G. P. Ziconotide: neuronal calcium channel blocker for treating severe chronic pain. *Curr. Med. Chem.* **11**, 3029–3040 (2004).

[CAS](#) [PubMed](#) [Article](#) [Google Scholar](#)

6. 6.

Schmidtko, A., Lötsch, J., Freyhagen, R. & Geisslinger, G. Ziconotide for treatment of severe chronic pain. *Lancet* **375**, 1569–1577 (2010).

[CAS](#) [PubMed](#) [Article](#) [Google Scholar](#)

7. 7.

Lin, Y., McDonough, S. I. & Lipscombe, D. Alternative splicing in the voltage-sensing region of N-type CaV2.2 channels modulates channel kinetics. *J. Neurophysiol.* **92**, 2820–2830 (2004).

[CAS](#) [PubMed](#) [Article](#) [Google Scholar](#)

8. 8.

Dolphin, A. C. Voltage-gated calcium channels and their auxiliary subunits: physiology and pathophysiology and pharmacology. *J. Physiol.* **594**, 5369–5390 (2016).

[CAS](#) [PubMed](#) [PubMed Central](#) [Article](#) [Google Scholar](#)

9. 9.

Saegusa, H. et al. Suppression of inflammatory and neuropathic pain symptoms in mice lacking the N-type Ca^{2+} channel. *EMBO J.* **20**, 2349–2356 (2001).

[CAS](#) [PubMed](#) [PubMed Central](#) [Article](#) [Google Scholar](#)

10. 10.

Snutch, T. P. Targeting chronic and neuropathic pain: the N-type calcium channel comes of age. *NeuroRx* **2**, 662–670 (2005).

[PubMed](#) [PubMed Central](#) [Article](#) [Google Scholar](#)

11. 11.

McGivern, J. G. Targeting N-type and T-type calcium channels for the treatment of pain. *Drug Discov. Today* **11**, 245–253 (2006).

[CAS](#) [PubMed](#) [Article](#) [Google Scholar](#)

12. 12.

McCleskey, E. W. et al. Omega-conotoxin: direct and persistent blockade of specific types of calcium channels in neurons but not muscle. *Proc. Natl Acad. Sci. USA* **84**, 4327–4331 (1987).

[ADS](#) [CAS](#) [PubMed](#) [PubMed Central](#) [Article](#) [Google Scholar](#)

13. 13.

Ellinor, P. T., Zhang, J. F., Horne, W. A. & Tsien, R. W. Structural determinants of the blockade of N-type calcium channels by a peptide neurotoxin. *Nature* **372**, 272–275 (1994).

[ADS](#) [CAS](#) [PubMed](#) [Article](#) [Google Scholar](#)

14. 14.

Stocker, J. W., Nadasdi, L., Aldrich, R. W. & Tsien, R. W. Preferential interaction of ω -conotoxins with inactivated N-type Ca^{2+} channels. *J. Neurosci.* **17**, 3002–3013 (1997).

[CAS](#) [PubMed](#) [PubMed Central](#) [Article](#) [Google Scholar](#)

15. 15.

Deer, T. et al. Effectiveness and safety of intrathecal ziconotide: interim analysis of the patient registry of intrathecal ziconotide management (PRIZM). *Pain Pract.* **18**, 230–238 (2018).

[PubMed](#) [Article](#) [Google Scholar](#)

16. 16.

Nair, A. S., Poornachand, A. & Kodisharapu, P. K. Ziconotide: indications, adverse effects, and limitations in managing refractory chronic pain. *Indian J. Palliat. Care* **24**, 118–119 (2018).

[PubMed](#) [PubMed Central](#) [Article](#) [Google Scholar](#)

17. 17.

Wu, J. et al. Structure of the voltage-gated calcium channel Ca_v 1.1 complex. *Science* **350**, aad2395 (2015).

[PubMed](#) [Article](#) [CAS](#) [Google Scholar](#)

18. 18.

Wu, J. et al. Structure of the voltage-gated calcium channel Ca_v 1.1 at 3.6 Å resolution. *Nature* **537**, 191–196 (2016).

[ADS](#) [CAS](#) [Article](#) [Google Scholar](#)

19. 19.

Zhao, Y. et al. Molecular basis for ligand modulation of a mammalian voltage-gated Ca^{2+} channel. *Cell* **177**, 1495–1506.e12 (2019).

[CAS](#) [PubMed](#) [Article](#) [Google Scholar](#)

20. 20.

Zhao, Y. et al. Cryo-EM structures of apo and antagonist-bound human Ca_v 3.1. *Nature* **576**, 492–497 (2019).

[ADS](#) [CAS](#) [PubMed](#) [Article](#) [Google Scholar](#)

21. 21.

Gao, S. & Yan, N. Structural basis of the modulation of the voltage-gated calcium ion channel Ca_v 1.1 by dihydropyridine compounds. *Angew. Chem. Int. Ed. Engl.* **60**, 3131–3137 (2021).

[CAS](#) [PubMed](#) [Article](#) [Google Scholar](#)

22. 22.

Yang, J., Ellinor, P. T., Sather, W. A., Zhang, J. F. & Tsien, R. W. Molecular determinants of Ca^{2+} selectivity and ion permeation in L-

type Ca^{2+} channels. *Nature* **366**, 158–161 (1993).

[ADS](#) [CAS](#) [PubMed](#) [Article](#) [Google Scholar](#)

23. 23.

Pragnell, M. et al. Calcium channel β -subunit binds to a conserved motif in the I-II cytoplasmic linker of the $\alpha 1$ -subunit. *Nature* **368**, 67–70 (1994).

[ADS](#) [CAS](#) [PubMed](#) [Article](#) [Google Scholar](#)

24. 24.

Kim, J. I., Takahashi, M., Otake, A., Wakamiya, A. & Sato, K. Tyr¹³ is essential for the activity of ω -conotoxin MVIIA and GVIA, specific N-type calcium channel blockers. *Biochem. Biophys. Res. Commun.* **206**, 449–454 (1995).

[CAS](#) [PubMed](#) [Article](#) [Google Scholar](#)

25. 25.

Benjamin, E. R. et al. Pharmacological characterization of recombinant N-type calcium channel ($\text{Ca}_v2.2$) mediated calcium mobilization using FLIPR. *Biochem. Pharmacol.* **72**, 770–782 (2006).

[CAS](#) [PubMed](#) [Article](#) [Google Scholar](#)

26. 26.

Pan, X. et al. Molecular basis for pore blockade of human Na^+ channel $\text{Na}_v1.2$ by the μ -conotoxin KIIIA. *Science* **363**, 1309–1313 (2019).

[ADS](#) [CAS](#) [PubMed](#) [Article](#) [Google Scholar](#)

27. 27.

Sousa, S. R. et al. Novel analgesic ω -conotoxins from the vermivorous cone snail *Conus moncuri* provide new insights into the evolution of conopeptides. *Sci. Rep.* **8**, 13397 (2018).

[ADS](#) [PubMed](#) [PubMed Central](#) [Article](#) [CAS](#) [Google Scholar](#)

28. 28.

Nadasdi, L. et al. Structure-activity analysis of a *Conus* peptide blocker of N-type neuronal calcium channels. *Biochemistry* **34**, 8076–8081 (1995).

[CAS](#) [PubMed](#) [Article](#) [Google Scholar](#)

29. 29.

Mould, J. et al. The $\alpha 2\delta$ auxiliary subunit reduces affinity of ω -conotoxins for recombinant N-type ($\text{Ca}_v 2.2$) calcium channels. *J. Biol. Chem.* **279**, 34705–34714 (2004).

[CAS](#) [PubMed](#) [Article](#) [Google Scholar](#)

30. 30.

Chen, Y. H. et al. Structural basis of the $\alpha_1-\beta$ subunit interaction of voltage-gated Ca^{2+} channels. *Nature* **429**, 675–680 (2004).

[ADS](#) [CAS](#) [PubMed](#) [Article](#) [Google Scholar](#)

31. 31.

Van Petegem, F., Clark, K. A., Chatelain, F. C. & Minor, D. L., Jr. Structure of a complex between a voltage-gated calcium channel β -subunit and an α -subunit domain. *Nature* **429**, 671–675 (2004).

[ADS](#) [PubMed](#) [PubMed Central](#) [Article](#) [CAS](#) [Google Scholar](#)

32. 32.

Opatowsky, Y., Chen, C. C., Campbell, K. P. & Hirsch, J. A. Structural analysis of the voltage-dependent calcium channel β subunit functional core and its complex with the $\alpha 1$ interaction domain. *Neuron* **42**, 387–399 (2004).

[CAS](#) [PubMed](#) [Article](#) [Google Scholar](#)

33. 33.

Clairfeuille, T. et al. Structural basis of α -scorpion toxin action on Na_v channels. *Science* **363**, eaav8573 (2019).

[CAS](#) [PubMed](#) [Article](#) [Google Scholar](#)

34. 34.

Jiang, D. et al. Structural basis for voltage-sensor trapping of the cardiac sodium channel by a deathstalker scorpion toxin. *Nat. Commun.* **12**, 128 (2021).

[ADS](#) [CAS](#) [PubMed](#) [PubMed Central](#) [Article](#) [Google Scholar](#)

35. 35.

Sun, J. & MacKinnon, R. Structural basis of human KCNQ1 modulation and gating. *Cell* **180**, 340–347.e9 (2020).

[CAS](#) [PubMed](#) [Article](#) [Google Scholar](#)

36. 36.

Wu, L., Bauer, C. S., Zhen, X. G., Xie, C. & Yang, J. Dual regulation of voltage-gated calcium channels by PtdIns(4,5)P₂. *Nature* **419**, 947–952 (2002).

[ADS](#) [CAS](#) [PubMed](#) [Article](#) [Google Scholar](#)

37. 37.

Rodríguez-Menchaca, A. A., Adney, S. K., Zhou, L. & Logothetis, D. E. Dual regulation of voltage-sensitive ion channels by PIP₂. *Front. Pharmacol.* **3**, 170 (2012).

[PubMed](#) [PubMed Central](#) [Article](#) [CAS](#) [Google Scholar](#)

38. 38.

Mastronarde, D. N. Automated electron microscope tomography using robust prediction of specimen movements. *J. Struct. Biol.* **152**, 36–51 (2005).

[PubMed](#) [PubMed Central](#) [Article](#) [Google Scholar](#)

39. 39.

Zheng, S. Q. et al. MotionCor2: anisotropic correction of beam-induced motion for improved cryo-electron microscopy. *Nat. Methods* **14**, 331–332 (2017).

[CAS](#) [PubMed](#) [PubMed Central](#) [Article](#) [Google Scholar](#)

40. 40.

Zhang, K. Gctf: real-time CTF determination and correction. *J. Struct. Biol.* **193**, 1–12 (2016).

[ADS](#) [CAS](#) [PubMed](#) [PubMed Central](#) [Article](#) [Google Scholar](#)

41. 41.

Zivanov, J. et al. New tools for automated high-resolution cryo-EM structure determination in RELION-3. *eLife* **7**, e42166 (2018).

[PubMed](#) [PubMed Central](#) [Google Scholar](#)

42. 42.

Rosenthal, P. B. & Henderson, R. Optimal determination of particle orientation, absolute hand, and contrast loss in single-particle electron cryomicroscopy. *J. Mol. Biol.* **333**, 721–745 (2003).

[CAS](#) [Article](#) [Google Scholar](#)

43. 43.

Chen, S. et al. High-resolution noise substitution to measure overfitting and validate resolution in 3D structure determination by single particle electron cryomicroscopy. *Ultramicroscopy* **135**, 24–35 (2013).

[CAS](#) [PubMed](#) [PubMed Central](#) [Article](#) [Google Scholar](#)

44. 44.

Nowycky, M. C., Fox, A. P. & Tsien, R. W. Three types of neuronal calcium channel with different calcium agonist sensitivity. *Nature* **316**, 440–443 (1985).

[ADS](#) [CAS](#) [PubMed](#) [Article](#) [Google Scholar](#)

45. 45.

Waterhouse, A. et al. SWISS-MODEL: homology modelling of protein structures and complexes. *Nucleic Acids Res.* **46**, W296–W303 (2018).

[CAS](#) [PubMed](#) [PubMed Central](#) [Article](#) [Google Scholar](#)

46. 46.

Pettersen, E. F. et al. UCSF Chimera—a visualization system for exploratory research and analysis. *J. Comput. Chem.* **25**, 1605–1612 (2004).

[CAS](#) [Article](#) [Google Scholar](#)

47. 47.

Emsley, P., Lohkamp, B., Scott, W. G. & Cowtan, K. Features and development of Coot. *Acta Crystallogr. D* **66**, 486–501 (2010).

[CAS](#) [PubMed](#) [PubMed Central](#) [Article](#) [Google Scholar](#)

48. 48.

Adams, P. D. et al. PHENIX: a comprehensive Python-based system for macromolecular structure solution. *Acta Crystallogr. D* **66**, 213–221 (2010).

[CAS](#) [PubMed](#) [PubMed Central](#) [Article](#) [Google Scholar](#)

49. 49.

Shen, H. et al. Structure of a eukaryotic voltage-gated sodium channel at near-atomic resolution. *Science* **355**, eaal4326 (2017).

[PubMed](#) [Article](#) [CAS](#) [Google Scholar](#)

50. 50.

Yan, Z. et al. Structure of the Na_v1.4-β1 complex from electric eel. *Cell* **170**, 470–482.e11 (2017).

[CAS](#) [PubMed](#) [Article](#) [Google Scholar](#)

51. 51.

Shen, H., Liu, D., Wu, K., Lei, J. & Yan, N. Structures of human Na_v1.7 channel in complex with auxiliary subunits and animal toxins. *Science* **363**, 1303–1308 (2019).

[ADS](#) [CAS](#) [PubMed](#) [Article](#) [Google Scholar](#)

52. 52.

Pan, X. et al. Structure of the human voltage-gated sodium channel Na_v1.4 in complex with β1. *Science* **362**, eaau2486 (2018).

[PubMed](#) [Article](#) [CAS](#) [Google Scholar](#)

53. 53.

Jiang, D. et al. Structure of the cardiac sodium channel. *Cell* **180**, 122–134.e10 (2020).

[CAS](#) [PubMed](#) [Article](#) [Google Scholar](#)

54. 54.

Li, Z. et al. Structural basis for pore blockade of the human cardiac sodium channel Na_v1.5 by the antiarrhythmic drug quinidine. *Angew. Chem. Int. Edn Engl.* **60**, 11474–11480 (2021).

[CAS](#) [Article](#) [Google Scholar](#)

55. 55.

Pan, X. et al. Comparative structural analysis of human Na_v1.1 and Na_v1.5 reveals mutational hotspots for sodium channelopathies. *Proc. Natl Acad. Sci. USA*, **118**, e2100066118 (2021).

[CAS](#) [PubMed](#) [Article](#) [Google Scholar](#)

56. 56.

Li, Z. et al. Structure of human Na_v1.5 reveals the fast inactivation-related segments as a mutational hotspot for the long QT syndrome. *Proc. Natl Acad. Sci. USA* **118**, e2100069118 (2021).

[CAS](#) [PubMed](#) [Article](#) [Google Scholar](#)

57. 57.

DeLano, W. L. The PyMOL Molecular Graphics System, <http://www.pymol.org> (2002).

[Download references](#)

Acknowledgements

We thank X. Pan for sharing the expression plasmids for the Ca_v2.2 complex subunits as a gift; X. Fan for critical discussion on cryo-EM data processing; and the cryo-EM facility at Princeton Imaging and Analysis Center. The work was supported by a grant from the NIH (5R01GM130762).

Author information

Author notes

1. These authors contributed equally: Shuai Gao, Xia Yao

Affiliations

1. Department of Molecular Biology, Princeton University, Princeton, NJ, USA

Shuai Gao, Xia Yao & Nieng Yan

Authors

1. Shuai Gao

[View author publications](#)

You can also search for this author in [PubMed](#) [Google Scholar](#)

2. Xia Yao

[View author publications](#)

You can also search for this author in [PubMed](#) [Google Scholar](#)

3. Nieng Yan

[View author publications](#)

You can also search for this author in [PubMed](#) [Google Scholar](#)

Contributions

N.Y. conceived the project. S.G. and X.Y. together conducted all wet experiments, including molecular cloning, protein purification, cryo-sample preparation and data acquisition. S.G. performed cryo-EM data processing, model building and refinement. All authors contributed to data analysis. N.Y. wrote the manuscript.

Corresponding author

Correspondence to [Nieng Yan](#).

Ethics declarations

Competing interests

The authors declare no competing interests.

Additional information

Peer review information *Nature* thanks Annette Dolphin and the other, anonymous, reviewer(s) for their contribution to the peer review of this work.

Publisher's note Springer Nature remains neutral with regard to jurisdictional claims in published maps and institutional affiliations.

Extended data figures and tables

[Extended Data Fig. 1 Cryo-EM analysis of the human Ca_v2.2 complex alone and in the presence of ziconotide.](#)

a, Representative electron micrograph and 30 classes of 2D class averages for Ca_v2.2–ziconotide. The green circles indicate particles in distinct orientations. The box size for the 2D averages is 312 Å. Scale bar, 50 nm. Left, a half view of one micrograph out of 3,384 in total for Ca_v2.2–ziconotide. **b**, Workflow for electron microscopy data processing (Methods). **c**, The gold-standard Fourier shell correlation (FSC) curves for the 3D reconstructions. The graph was prepared in GraphPad Prism. **d**, FSC curves of the refined model versus the summed map that it was refined against (black); of the model versus the first half map (red); and of the model versus the second half map (green). Z-complex, Ca_v2.2–ziconotide.

Extended Data Fig. 2 Cryo-EM structure of the human Ca_v2.2 complex bound with ziconotide.

a, Heat map for local resolutions of the complex. The resolution map was calculated in Relion 3.0 and prepared in Chimera. Top inset, bound ziconotide (labelled as Zi) is well-resolved. Bottom inset, resolution of the β3 subunit, after a focused refinement, allows for reliable model building using the crystal structure of rat β3 (PDB code 1VYU) as a template. **b**, Overall structure of the complex at an averaged resolution of 3.0 Å. Left, the complex comprises the α1 core subunit (silver), the extracellular α2δ-1 subunit (light pink for α2 and green for δ) and the cytosolic β3 subunit (wheat). The peptide pore blocker ziconotide is coloured brown. The resolved lipid, cholesterol and CHS molecules are shown as black sticks. The bound PIP₂ is shown as black ball-and-sticks. Sugar moieties are shown as thin sticks. Right, surface presentation of the structure. The four repeats are coloured grey, cyan, yellow, and pale green. The III–IV linker and the CTD are coloured orange and pale purple, respectively.

Extended Data Fig. 3 Electron microscopy densities for representative segments of Ca_v2.2–ziconotide.

a, Electron microscopy maps for representative segments in α1 and β3. The densities for the β3 segments are from focused refinement, and the others are from the overall map. All the densities shown are contoured at 4σ. **b**,

The electron microscopy map for ziconotide. **c**, Electron microscopy densities for the bound Ca^{2+} ion and surrounding residues in the selectivity filter. The maps were prepared in PyMol.

Extended Data Fig. 4 Lipids resolved in the structures.

a, A PIP_2 molecule binds to VSD_{II} in both structures. All the densities shown are contoured at 3σ . **b**, The densities for the resolved cholesterol (Cho) and CHS molecules in $\text{Ca}_v2.2$ -ziconotide. **c**, Lipids resolved in the structure of $\text{Ca}_v2.2$ -ziconotide. The $\alpha 1$ subunit are shown in two opposite side views. The numbering for cholesterol and CHS is consistent with that in **b**. Two phospholipids are also resolved and assigned as phosphatidylethanolamine (PE).

Extended Data Fig. 5 Structural comparison of the $\text{Ca}_v1.1$ and $\text{Ca}_v2.2$ channel complexes.

a, Superimposition of the overall structures of human $\text{Ca}_v2.2$ (apo) and rabbit $\text{Ca}_v1.1$ (PDB code 5GJW). For visual clarity, the γ subunit in the endogenous $\text{Ca}_v1.1$ complex is not shown. The conformational shift of VSD_{II} from $\text{Ca}_v1.1$ (wheat) to $\text{Ca}_v2.2$ (blue) is indicated by the blue arrow. **b**, Identical structures of the $\alpha 2\delta-1$ subunit in the two channel complexes. A detailed structural description of the $\alpha 2\delta-1$ subunit can be found in a previous publication¹⁸. **c**, Structural differences of the ECLs between $\text{Ca}_v1.1$ and $\text{Ca}_v2.2$. An extracellular view of the superimposed $\alpha 1$ subunits in the two channels is shown.

Extended Data Fig. 6 Conformational shifts of $\text{Ca}_v2.2$ upon ziconotide binding.

a, ECL_I does not participate in ziconotide coordination. An extracellular view perpendicular to that in Fig. [1c](#) is shown. **b**, Slightly different mode of action of KIIIA for $\text{Na}_v1.2$ ²⁶. Lys7 in KIIIA directly blocks the outer mouth of the selectivity filter vestibule of $\text{Na}_v1.2$ (PDB code 6J8E), in a manner

similar to a cork. Ziconotide lacks an equivalent basic residue. **c**, Relative shift of $\alpha 2\delta$ -1 between apo (blue) and ziconotide-bound $\text{Ca}_v 2.2$ (domain-coloured) when the two structures are superimposed relative to the $\alpha 1$ subunit. The rest of the complex remains identical except for ECL_{III}. **d**, Concerted motion of $\alpha 2\delta$ -1 and ECL_{III} of $\alpha 1$. The $\alpha 2\delta$ -1 subunit in the two structures can be superimposed with a root mean square deviation of 0.28 Å over 847 C α atoms, indicating nearly identical conformations. When the two structures are superimposed relative to $\alpha 2\delta$ -1, the entire $\alpha 1$ undergoes a relative shift—except for ECL_{III}, which stays as a rigid body with $\alpha 2\delta$ -1.

Extended Data Fig. 7 Conformational changes of VSD_{II} and VSD_{III} between $\text{Ca}_v 1.1$ and $\text{Ca}_v 2.2$.

a, Structural comparison of $\text{Ca}_v 2.2$ VSD_{II} with other VSDs that exhibit down conformations. To make the nomenclature consistent, we define the gating charge residue on the first helical turn of the S4 segment as R1. The PDB accession codes are 6NT4 for VSD_{IV} in the chimeric $\text{Na}_v \text{PaS}-1.7$, 7K18 for toxin-bound VSD_{IV} in rat $\text{Na}_v 1.5$, 4G80 for the antibody-locked VSD of a voltage-sensitive phosphatase, and 6UQF for the VSD of HCN1 in hyperpolarized conformation. **b**, Structural comparison of $\text{Ca}_v 1.1$ and $\text{Ca}_v 2.2$ shows a slight rotation of VSD_{III} around the pore domain. The superimposed structures of the diagonal repeats I and III of $\text{Ca}_v 1.1$ (wheat) and $\text{Ca}_v 2.2$ (domain-coloured) are shown. **c**, VSD_{III} remains nearly rigid in these two structures. When the structures of VSD_{III} in the two channels are individually superimposed, the S4 segment and the gating charge residues align well. **d**, Marked shift of S4_{II} between $\text{Ca}_v 1.1$ and $\text{Ca}_v 2.2$ when the two structures are compared relative to VSD_{II}. S4_{II} undergoes a combination of spiral sliding and secondary structural transition. S1, S2 and S3 remain nearly unchanged in these two VSD_{II} structures, which suggests a concerted rotation of the other three segments pivoting around S4.

Extended Data Fig. 8 A closed pore domain with one small fenestration.

a, The pore domain is in a closed conformation. Four perpendicular side views of the pore domain are shown. S4–5_{II} is pushed downward as a result of the sliding of S4_{II}. **b**, Side walls that involve S6_{II} are sealed without fenestration. Side views of the pore domain surface are shown. There is only one fenestration on the interface of repeats III and IV.

[Extended Data Fig. 9 A PIP₂ molecule may help to stabilize the down conformation of Ca_v2.2 VSD_{II}.](#)

a, The binding pose for PIP₂ is incompatible with an up VSD_{II}. Left, coordination of the head group of PIP₂ by Ca_v2.2. Side local view of VSD_{II} is shown. Right, in an up state of VSD_{II} (as in Ca_v1.1), R4 and K5 can no longer interact with the PIP₂ head group, and S4–5_{II} directly clashes with PIP₂. Structures of Ca_v1.1 and Ca_v2.2 are superimposed relative to the α1 subunit and Ca_v2.2 is omitted to highlight the relative position of PIP₂ to Ca_v1.1. **b**, The hydrophobic tails of PIP₂ interact extensively with multiple segments in repeats II and III. Hydrophobic residues on segments S3 to S6 in repeat II and S5 and S6 in repeat III contact the two tails of PIP₂. **c**, The PIP₂ molecule in the K_v channel KCNQ1 is bound at a similar, but lower, position. The PDB code for the KCNQ1 structure is 6V01. **d**, Rearrangement of the interface of VSD_{II} and pore domain between Ca_v2.2 and Ca_v1.1. Ca_v1.1 is coloured with the same scheme as for Ca_v2.2. Alternative sets of hydrophobic residues between the gating charge residues on S4_{II} are used for interacting with S5_{III} in Ca_v1.1 and Ca_v2.2 as a result of the rotation of S4_{II}. The sequence numbers for corresponding VSD_{II} residues in these two channels differ by 50, and those for S5_{III} residues differ by 354. As labelled in the parentheses, Val1298 and Phe1292 on the S5_{III} segment of Ca_v2.2 are at loci corresponding to Cys944 and Leu938 in Ca_v1.1, respectively.

Extended Data Table 1 Statistics for data collection and structural refinement

[Full size table](#)

Supplementary information

Supplementary Figure 1

Sequence alignment of the $\alpha 1$ subunit of human Ca_v channels and rabbit $\text{Ca}_v 1.1$.

Reporting Summary

Video 1 Overall structure of the $\text{Ca}_v 2.2$ channel complex

The complex is coloured the same as in Fig. 1a.

Video 2 Conformational changes of the $\alpha 1$ subunits between $\text{Ca}_v 2.2$ and $\text{Ca}_v 1.1$

The morph was generated in PyMol using structures of human $\text{Ca}_v 2.2$ and rabbit $\text{Ca}_v 1.1$ (PDB code: 5GJW) as the first and end frames. For visual clarity, the cytosolic segments, which are poorly resolved in $\text{Ca}_v 1.1$, are omitted.

Rights and permissions

Reprints and Permissions

About this article



Check for
updates

Cite this article

Gao, S., Yao, X. & Yan, N. Structure of human $\text{Ca}_{\text{v}}2.2$ channel blocked by the painkiller ziconotide. *Nature* **596**, 143–147 (2021).
<https://doi.org/10.1038/s41586-021-03699-6>

[Download citation](#)

- Received: 16 March 2021
- Accepted: 07 June 2021
- Published: 07 July 2021
- Issue Date: 05 August 2021
- DOI: <https://doi.org/10.1038/s41586-021-03699-6>

Comments

By submitting a comment you agree to abide by our [Terms](#) and [Community Guidelines](#). If you find something abusive or that does not comply with our terms or guidelines please flag it as inappropriate.

[Access through your institution](#)

[Change institution](#)

[Buy or subscribe](#)

Advertisement

This article was downloaded by **calibre** from <https://www.nature.com/articles/s41586-021-03699-6>